Architectures of planetary systems via imaging of exoplanets and disks with SPHERE at the Very Large Telescope

Célia Desgrange

THÈSE

Pour obtenir le grade de

DOCTEUR DE L'UNIVERSITÉ GRENOBLE ALPES

École doctorale : PHYS - Physique
Spécialité : Astrophysique et Milieux Dilués
Unité de recherche : Institut de Planetologie et d'Astrophysique de Grenoble

Architectures des systèmes planétaires via l'imagerie d'exoplanètes et de disques avec SPHERE au Very Large Telescope

Architectures of planetary systems via imaging of exoplanets and disks with SPHERE at the Very Large Telescope

Présentée par :

Célia DESGRANGE

Direction de thèse :

Gaël CHAUVIN DIRECTEUR DE RECHERCHE, CNRS DELEGATION COTE D'AZUR	Directeur de thèse
JULIEN MILLI ASTRONOME ADJOINT, UNIVERSITE GRENOBLE ALPES	Co-encadrant de thèse
Thomas HENNING Institut Max-Planck d'Astronomie	Co-encadrant de thèse

Rapporteurs :

CHRISTINE CHEN
ASTRONOME ADJOINTE, SPACE TELESCOPE SCIENCE INSTITUTE
PIERRE KERVELLA
ASTRONOME, OBSERVATOIRE DE PARIS

Thèse soutenue publiquement le **23 septembre 2024**, devant le jury composé de :

JEAN-LOUIS MONIN, PROFESSEUR DES UNIVERSITES, UNIVERSITE GRENOBLE ALPES	Président
CHRISTINE CHEN, ASTRONOME ADJOINTE, SPACE TELESCOPE SCIENCE INSTITUTE	Rapporteure
PIERRE KERVELLA, ASTRONOME, OBSERVATOIRE DE PARIS	Rapporteur
SASHA HINKLEY, ASSOCIATE PROFESSOR, UNIVERSITY OF EXETER	Examinateur
FRANÇOIS MENARD, DIRECTEUR DE RECHERCHE, CNRS DELEGATION ALPES	Examinateur

Invités :

ROBERT DE ROSA
ASTRONOME ADJOINT, EUROPEAN SOUTHERN OBSERVATORY

Aux nuits étoilées

au Champ du Feu

et ailleurs

À la SAFGA

et aux wawas

aux rencontres

à l'autre

À l'horizon infini des possibles

Abstract

The direct imaging technique is the only viable method to complete our view of the planetary system architectures and to set constraints on giant planet formation scenarios at large (>5 au) separations. Direct imaging can currently detect the near- and mid-infrared emission of young self-luminous giant planets and resolve the material left over from planet formation processes, i.e., the debris disks. Those disks consist of small particles resulting from collisional cascades among planetesimals.

During my Ph.D., I focused my research on the architectures of planetary systems from an observational perspective. I used mainly the ground-based instrument SPHERE, which has now been in operation at the VLT for more than 10 years, demonstrating a high level of performance and stability. SPHERE has produced outstanding results in a variety of scientific areas, but primarily in the field of direct imaging of exoplanetary systems, including the discovery of new exoplanets and planet-forming or debris disks.

In particular, I worked on a detailed study of two specific, young systems, and also on a survey of a larger, older sample to get a statistical view of planetary system architectures. These results give constraints on theoretical models of planet formation and evolution, from grain-size to planet-size scales.

The two individual studies focused on debris disk systems, HD 120326 and HD 95086. The first one has an enigmatic, complex debris disk, with both intermediate (<100 au) and large (<1 000 au) structures, and no detected planet yet. The second one can be considered as a massive solar system analog, with a 4–5 Jupiter-mass planet lying in the cavity between two belts. In both systems, yet unseen planets are expected to sculpt the disk structures, and are prime targets for the ELT, which could detect them. In HD 120326, I focused on constraining the global morphology of the disk, by coupling SPHERE, *HST* and ALMA data, and on the dust properties, such as their scattering phase function, reflectance and degree of linear polarisation. In HD 95086, I led an in-depth SPHERE direct-imaging and spectroscopic characterization of the gas giant planet b. This planet is under-luminous and has a red color, and I showed with my collaborators that the presence of dust around it could be either located in the upper layers of the atmosphere, or in a circumplanetary disk around it.

Finally, I worked on a SPHERE survey of very nearby (< 20 pc) super-Earth and mini-Neptune hosts. The goal was to constrain the presence of giant planets in those systems, to better understand the formation of close-in low-mass planets. This project helped to understand the current detection limits of extreme adaptive optics systems in terms of planetary mass and separation for mature systems (> 500 Myr). It also helped to investigate the benefits of coupling direct imaging with radial velocity and astrometric measurements with Gaia.

As for perspectives, an important upgrade of the SPHERE instrument, named SPHERE+, is currently under development. It corresponds to the upgrade of the extreme adaptive optics (AO) system, by adding a second AO stage. This will be a technology demonstration for the second-generation spectro-imager on the ELT, named PCS, that aims to image exo-Earths. I contributed regarding the definition of future scientific cases of SPHERE+, by working on the future performances of a new, putative medium-resolution spectrograph, which would take advantage of the improved performances of the upgraded adaptive optics system.

Résumé

La technique d'imagerie directe est la seule méthode de détection viable pour sonder les parties externes des systèmes planétaires et ainsi, contraindre les scénarios de formation des planètes géantes situées loin de leur étoile (> 5 ua). À l'heure actuelle, l'imagerie directe permet de détecter l'émission dans l'infrarouge proche et moyen de jeunes planètes géantes, et de résoudre les restes des processus de formation planétaire, c'est-à-dire, les disques de débris. De ces disques, la poussière peut être détectée. Elle résulte de cascades collisionnelles entre les planétésimaux.

Ma thèse a porté sur les architectures des systèmes planétaires d'un point de vue observationnel. J'ai principalement utilisé l'instrument SPHERE, qui est situé au VLT depuis plus de 10 ans et qui a fait preuve d'un haut niveau de performance et de stabilité. SPHERE a produit des résultats remarquables dans une variété de domaines scientifiques, et principalement dans le domaine de l'imagerie directe des systèmes exoplanétaires, y compris la découverte de nouvelles exoplanètes et de disques protoplanétaires ou de débris.

En particulier, j'ai mené des études détaillées sur deux systèmes, et une étude sur un échantillon plus large, afin d'obtenir une vision statistique des architectures des systèmes planétaires. Ces résultats apportent des contraintes aux modèles théoriques de formation et d'évolution planétaires, de l'échelle du grain de poussière à celle d'une planète.

Les deux études individuelles ont porté sur des disques de débris, HD 120326 et HD 95086. Le premier possède un disque de débris complexe et énigmatique, avec des structures de taille intermédiaire (<150 ua) et grande (<1 000 ua), et dans lequel aucune exoplanète n'a encore été détectée. Le second système peut être considéré comme un analogue du Système Solaire, en plus massif, avec une exoplanète de 4 à 5 fois la masse de Jupiter. Cette exoplanète est située dans la cavité entre les deux ceintures de poussières. Dans les deux systèmes, des exoplanètes encore non-détectées sont attendues, ce sont donc des cibles de choix pour l'ELT, qui pourrait les détecter. Concernant HD 120326, j'ai contraint la morphologie globale du disque, en couplant des données SPHERE, *HST* et ALMA, et les propriétés des poussières, telles que leur fonction de phase de diffusion, leur réflectance et leur degré de polarisation linéaire. Pour HD 95086, j'ai caractérisé l'orbite et l'atmosphère de l'exoplanète géante gazeuse HD 95086 b avec des données SPHERE. Cette planète est peu lumineuse et a une couleur rouge, due à la présence de poussières autour de la planète. J'ai montré, avec mes collaborateurs, que ces poussières pourraient être situées dans un disque circumplanétaire.

Enfin, j'ai travaillé sur un relevé SPHERE d'étoiles ayant des super-Terres et des mini-Neptunes situées proches de leur étoile. J'ai contraint la présence de planètes géantes dans ces systèmes, afin de mieux comprendre la formation de planètes de faible masse à proximité. Ce projet a permis de comprendre les limites de détection actuelles de SPHERE pour des systèmes âgés (>500 Ma). Il a également permis d'étudier les avantages de coupler l'imagerie directe avec les mesures de vitesse radiale et d'astrométrie.

Concernant les perspectives, une amélioration importante de l'instrument SPHERE, appelée SPHERE+, est en cours. La mise à niveau SPHERE+ correspond à l'amélioration de son système d'optique adaptative extrême, en y ajoutant un second étage. Il s'agira d'une démonstration technologique pour le spectro-imageur de deuxième génération de l'ELT, appelé PCS, qui a pour but de photographier des exo-Terres. Durant ma thèse, j'ai contribué à la définition des futurs cas scientifiques de SPHERE+, en étudiant les performances d'un nouveau, potentiel spectrographe à moyenne résolution, qui tirerait parti des meilleures performances atteintes par l'amélioration du système d'optique adaptative.

Acknowledgements

Gaël, Julien, Thomas, merci pour votre confiance.

Merci de m'avoir permis d'effectuer cette thèse entre Grenoble et Heidelberg. Merci pour votre supervision, les diverses relectures d'articles, demandes de temps, manuscrit et dossiers de candidatures en post-doctorat, et les lettres de recommandation. Merci pour les discussions, conseils, opportunités et la liberté que vous m'avez donnée.

Gaël. Je me rappelle très bien de la première fois où nous nous sommes rencontrés, à Los Dominicos au Chili pour aller à l'observatoire Calán. C'était durant mon stage de première année de master, en 2019. Tu m'as fait découvrir SPHERE, et plus généralement le domaine de l'imagerie directe des exoplanètes. Je me rappelle nos discussions, notamment sur les points à savoir pour faire une thèse plus tard. Je me rappelle que déjà, à ce moment-là, je souhaitais être en thèse sous ta direction. Pour tout te dire, j'en rêvais, car je pressentais que cette expérience m'épanouirait. Cela l'a été. Merci Gaël. Merci mille fois.

J'en profite pour remercier ici Guillaume Laibe et Maxime Lombart, car c'est vous qui m'avez parlé la première fois de SPHERE et de Gaël. Finalement, tout a commencé grâce à une discussion post-déjeuner durant mon stage de dernière année de licence au CRAL !

Julien. Merci de m'avoir partagé ta passion pour les poussières et pas n'importe lesquelles ! Merci de ton encadrement, de ton aide, de tes idées et de ton soutien. Merci aussi pour ton engagement pour la diffusion scientifique et les actions pour limiter l'empreinte carbone. Cela me pousse aussi à réfléchir sur comment je souhaite mener et partager ma recherche. Merci pour ces moments débordants d'enthousiasme. Je me souviendrai pendant longtemps de notre exposé lors de Pint of Science. J'ai adoré pouvoir animer et partager cela avec toi et avec un public au top.

Thomas. Thank you for the opportunities you gave me. Thank you for encouraging me to think out of the box. Thank you for having funded the other half part of my Ph.D.. Carrying out half of my Ph.D. at the Max-Planck Institute for Astronomy definitively helped me to grow scientifically.

J'en profite aussi pour remercier Faustine Cantalloube, qui m'a encadrée lors d'un stage précédent mon doctorat. Tu m'as permis de connaître le MPIA, de m'y faire connaître, même si l'ambiance y était un peu particulière due aux périodes de confinements. Tu m'as beaucoup appris sur le traitement de données en imagerie à haut-contraste. Cette thèse a pu avoir lieu également grâce à toi.

On the MPIA side, first thank you to Elisabeth Matthews. Thank you for always having a door open for me. Thank you for the discussions. Thank you for having helped me with the *James Webb Space Telescope* proposals. Thank you for these crazy periods before proposal deadlines. Without you, the experience at MPIA would not have had the same taste.

Thank you also to Remo Burn, Matthias Samland, Giuila Perotti, Macla Ramirez, Roy van Boekel, Bertram Bitsch, Nicolas Kurtovic and Martin Schlecker.

Côté IPAG, un merci particulier à Mickaël Bonnefoy, Jean-Philippe Berger, Carine Babusiaux, Philippe Delorme, Nadège Meunier, Xavier Bonfils et Xavier Delfosse. Merci à toute l'équipe Exoplanètes. Merci aux membres des équipes Charm et Odyssey.

Merci à tout l'IPAG, c'est un institut où je me suis sentie particulièrement bien durant ma thèse.

Merci aux équipes administratives de l'IPAG et du MPIA.

Merci à Isabelle Boisse et Mamadou N'Diaye, d'avoir été membres de mon comité de suivi individuel de thèse et de m'avoir soutenue.

Merci aux membres du GAD.

Merci aux membres des consortia SPHERE, SPHERE+, SHARK-NIR et le Sco-Cen groupe. I would like to thank in particular Valentina D'Orazi, Dino Mesa, Jacopo Farinato, Justin Hom et également Virginie Faramaz, Johan Olofsson, Valentin Christiaens, Olivier Absil et Mamadou N'Diaye à nouveau.

Thank you to the members of my Ph.D. jury, who accepted to evaluate me.

Merci aux amis et amies en thèse. Ceux de mon année en particulier, Nicolas, Dorian, Antoine, Maxime, Tituan, Lucie, Marc, Jonah, Paulina. Merci aussi aux anciens doctorants qui nous ont accueilli à bras ouverts, Julien, Thibault, Thomas et aux nouveaux petits jeunes.
Et à celui devenu permanent depuis... merci Benjamin C., nous sommes jamais bien longtemps au même endroit en même temps... et je ne suis pas sûre que cela s'améliorera !

Thank you to Soumya, with whom I lived my first adventures at the Königstuhl, back to the day we were not yet Ph.D. students.

Merci évidemment à Marion et Valentin. Merci pour toutes ces aventures. Sur un continent ou un autre. Pour les bus de nuits, pour Huasco, pour le mistral gagnant, pour la Californie, pour croquer la vie. Merci de m'avoir montré comment être celle que je voulais être. Je vous dois beaucoup.

Merci aux amis de l'ultimate-frisbee. Ceux d'ENSpin (ou devrais-je dire d'Emergency Hammer ?), Julien, Léa, Robin et les autres. Ceux des Phoenix.

Merci à Justine, Audrey et Claire, mes amies de (très) longue date. Regardons-nous où nous en sommes aujourd'hui.

Merci à la SAFGA, la Société Astronomique de France Groupe Alsace. En particulier, merci à Frédéric D., Benoît, Boris, Julien, Dominique, Jean-Noël, Zyed, Christine mais aussi à tous les autres. J'ai sans doute grandi depuis la terminale, effectué un petit bout de chemin, mais soyez-en sûr, je ne vous oublie pas. Je me rappelle de la bonne humeur qui m'envahissait quand j'arrivais à l'observatoire de Strasbourg pour les soirées SAFGA. Et qui m'envahit toujours quand je reviens. Une pensée pour Gilbert Klein et Robert Marche.

Merci à Marine. Je crois bien que c'est toi la première qui m'a pointé le ciel étoilé, allongées sur et sous un plaid dans le verger à Aveney. Arcturus, Cassiopée. Des soirées dont la pensée aujourd'hui encore me rappelle à la plénitude.

Merci à tous ceux que j'ai pu oublier.

J'arrive au bout.

Merci à l'ESO qui me permet de passer d'un rêve à un autre.

Merci à ma famille. Celle proche comme éloignée. Un grand merci à mes parents, mon frère et à Jules. Et un autre grand merci à ma maman.

Contents

List of Figures

List of Tables

List of Abbreviations

A&A	Astronomy & Astrophysics
ADI	Angular Differential Imaging
ADU	Analog-to-Digit Unit
ALMA	Atacama Large Millimeter/submillimeter Array
AMI	Aperture Masking Interferometry
ANDROMEDA	ANgular Differential OptiMal Exoplanet Detection Algorithm
AO	Adaptive Optics
APLC	Apodized Pupil Lyot Coronagraph
AT	Auxiliary Telescope
BB	BlackBody
BD	Brown Dwarf
cADI	classic Angular Differential Imaging
CCF	Cross Correlation Function
CHARIS	Coronagraphic High Angular Resolution Imaging Spectrograph
CHEOPS	CHaracterising ExOPlanet Satellite
CGI	CoronaGraph Instrument
CJ	Cold Jupiter
CPD	CircumPlanetary Disk
CPI	Common Path and Infrastructure
CoI	Co-Investigator
DBI	Dual-Band Imaging
HC-DC	High Contrast Data Center
DD	Debris Disk
DI	Direct Imaging
DIT	Detector Integration Time
DM	Deformable Mirror
DPI	Dual-Polarization Imaging
DR	Data Release
EDR	Early Data Release
ELT	Extremely Large Telescope
ERIS	Enhanced Resolution Imaging Spectrograph
ESO	European South Observatory
ETC	Exposure Time Calculator
FLAO	First Light Adaptive Optics
FQPM	Four Quadrant Phase Mask
FWHM	Full Width at Half Maximum
GMT	Giant Magellan Telescope
GTO	Guaranteed Time Observations
GO	General Observer
GPI	Gemini Planet Imager
GreeDS	Greedy Disc Subtractio
HARMONI	High Angular Resolution Monolithic Optical and Near-infrared Integral

	field spectrograph
HiCIAO	High-Contrast Coronagraphic Imager for Adaptive Optics
HJ	Hot Jupiter
HST	*Hubble Space Telescope*
HWO	Habitable Worlds Observatory
ID	IDentification number
IRDAP	IRDIS Data reduction for Accurate Polarimetry
IFS	Integral Field Spectrograph
IPAG	Institut de Planétologie et d'Astronomie de Grenoble
I-PCA	Iterative Principal Component Analysis
IRDIS	Infra-Red Dual-band Imager and Spectrograph
IWA	Inner Working Angle
JWST	*James Webb Space Telescope*
KMTNET	Korea Microlensing Telescope Network
LBT	Large Binocular Telescope
LMIRCam	LBT Mid-InfraRed interferometric Camera
LSS	Long-Slit Spectroscopy
LWE	Low-Wind Effects
MAYONNAISE	Morphological Analysis Yielding separated Objects iN Near infrAred usIng Sources Estimation
METIS	Mid-infrared ELT Imager and Spectrograph
MICADO	Multi-AO Imaging Camera for Deep Observations
MIRI	Mid-InfraRed Instrument
MMR	Mean Motion Resonance
MN	Mini-Neptune
MPIA	Max-Planck Institute für Astronomy
NaCo	Naos-Conica
nADI	non-Angular Differential Imaging
NCPA	Non-Common Path Abberations
NICI	Near Infrared Coronagraphic Imager
NICMOS	Near Infrared Camera and Multi-Object Spectrometer
NIRCam	Near-Infrared Camera
NIRC2	Near-InfraRed Camera
NIRI	Near-InfraRed Imager
NIRSPEC	Near-InfraRed Spectrograph
NRM	Non-Redundant Masking
OGLE	Optical Gravitational Lensing Experiment
PA	Position Angle
PACO	PAtch COvariances
PCA	Principal Component Analysis
PCS	Planetary Camera and Spectrograph
PDI	Polarization Differential Imaging
PhD	Philosophiae Doctorate
PI	Principal Investigator
PMa	Proper Motion anomaly
PPD	ProtoPlanetary Disk
PSF	Point-Spread Function
RDI	Reference Differential Imaging
REXPACO	Reconstruction of EXtended features by PAtch COvariances
RST	*Roman Space Telescope*
RTC	Real-Time Computer

RV	Radial Velocity
SAM	Sparse Aperture Masking
SAXO	Sphere Adaptive-optics for eXoplanet Observation
SCExAO	Subaru Coronagraphic Extreme Adaptive Optics
SDI	Spectral Differential Imaging
SE	Super-Earth
SED	Spectral Energy Density
SHARK-NIR	System for High contrast And coronagraphy from R to K at Near-InfraRed bands
SHARK-VIS	System for High contrast And coronagraphy from R to K at VISisble bands
SHINE	SPHERE infrared survey for exoplanets
SINFONI	Spectrograph for INtegral Field Observations in the Near Infrared
SMA	Semi-Major Axis
S/N	Signal-to-Noise ratio
SpeCal	Speckle Calibration [tool]
SOUL	Single conjugated adaptive Optics Upgrade for LBT
SPF	Scattering Phase Function
SPHERE	Spectro-Polarimetric High contrast Exoplanet REsearch
STIS	Space Telescope Imaging Spectrograph
TAC	Telescope Allocation Committee
TESS	Transiting Exoplanet Survey Satellite
TLOCI	Template Locally Optimized Combination of Images
UT	Unit Telescope
VLT	Very Large Telescope
VLTI	Very Large Telescope Interferometer
VIP-HCI	Vortex Image Processing package for High-Contrast direct Imaging
WJ	Warm Jupiter
WDH	Wind-Driven Halo
WFS	Wavefront Sensor
ZELDA	Zernike sensor for Extremely Low-level Differential Aberration
ZIMPOL	Zurich IMaging Polarimeter

Chapter 1

Introduction

Contents

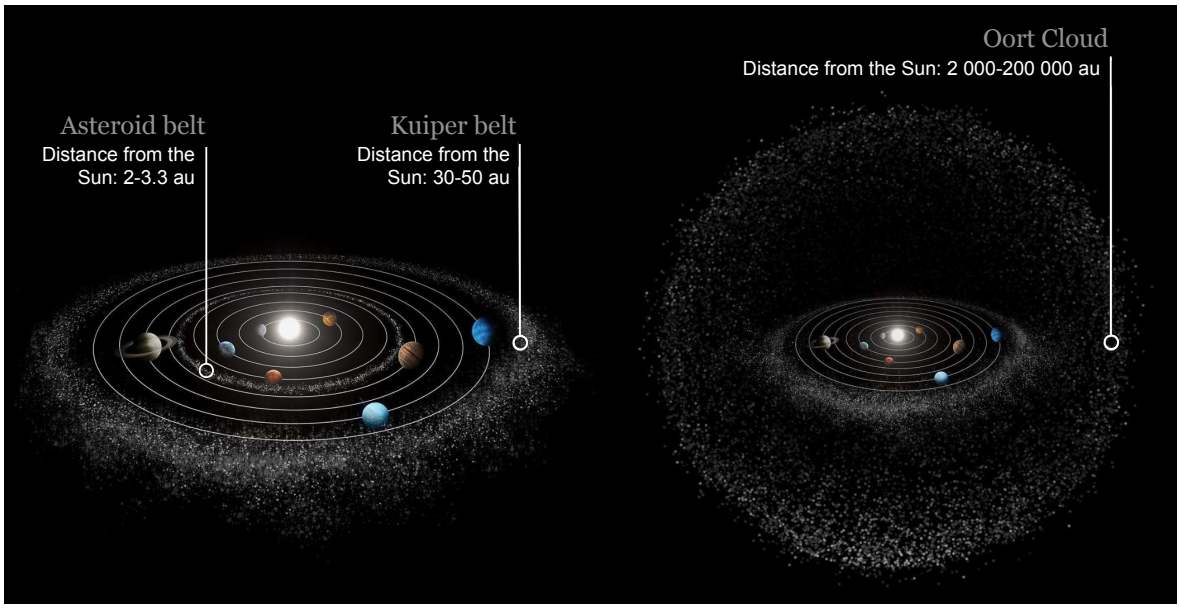

Figure 1.1: Sketch of the Solar System illustrating the architecture of the Solar System. There are eight planets, two asteroid belts and one asteroid cloud more diffused. Adapted figure from the European Space Agency (ESA).

People started to look at stars centuries ago. At that time, stars, or planets such as Venus, served as guides to find the right way to go. Nowadays, astronomers look at stars and other objects in the sky to go back into the past and try to understand the origin of the universe. Astronomers wish to understand the formation and evolution of celestial bodies, including galaxies, stars and planets, to name a few.

In my doctoral thesis, I focus my research on planetary system architectures. In particular, I show how planetary system architectures can help to constrain planet formation and evolution. In this first chapter, I introduce my research field, the exoplanets, that is to say planets orbiting stars other than the Sun. In Section 1.1, I give an overview on the Solar System, the first discoveries of exoplanets and more generally of the known exoplanets so far. In Section 1.2, I report on the main different techniques that enable the detection of exoplanets. In Section 1.3, I describe the current understanding on how planets form and evolve. Last but not least, in Section 1.4, I highlight the contribution of my research work during my doctoral thesis.

1.1 Planets and exoplanets

1.1.1 Solar System

Without a doubt, the most famous planets are the eight planets orbiting the Sun. Four of them are rocky planets, Mercury, Venus, the Earth, Mars, and the four further out are the gaseous planets Jupiter, Saturn, Uranus and Neptune. The two last ones are also called icy giant planets, because they are made of a large fraction of ice.

On top of planets, the Sun hosts many small bodies: satellite(s) orbiting around planets, such as the duo the Moon and the Earth, dwarf planets, such as Pluto and Eris, or minor bodies, consisting in comets, asteroids, pebbles or dust grains. These small objects are mainly gathered in the Asteroid Belt located between Mars and Jupiter, the Kuiper Belt located beyond Neptune, and in the Oort cloud, located further out, see Fig. 1.1. The outer border of the Oort cloud can be considered as the outer limit of the Solar System, because it represents

the end of the gravitational influence of the Sun. This frontier is located at about one light year, that is to say, roughly 10 000 billions of kilometers. In other units, at about 60 000 times the distance between the Sun and the Earth, which is defined as the astronomical unit (au).

The formation of the Sun dates back to 4.568 billions years ago (Bouvier & Wadhwa, 2010). The four giant planets formed early, in the first million years of the lifetime of the Sun. On the contrary, the timescales for the formation of rocky planets span a large range, Mars being essentially formed within 5–10 Myr (Dauphas & Pourmand, 2011), while the Earth (and the Moon) likely formed within a timescale of 50–150 Myr (Kleine et al., 2009).

The most accepted model accounting at best for the formation and evolution of the Solar System is the Nice model (Gomes et al., 2005; Tsiganis et al., 2005; Morbidelli et al., 2005), and its updated versions. The Nice model accounts for: the current orbits of the giant planets, including their orbital radii, eccentricities and inclinations (Tsiganis et al., 2005), the trojan satellites of Jupiter (Morbidelli et al., 2005), the irregular satellites of the giant planets (Nesvorný et al., 2007; Bottke et al., 2010), and the orbital structure of the Kuiper Belt including the scattered disk (Gomes et al., 2005). The Nice model assumes that the giant planets would have formed in a compact configuration between 5 and 18 au in the dusty and gaseous protoplanetary disk around the Sun. Due to a major dynamical instability, the giant planets migrated towards their current positions. In particular, Uranus and Neptune may have swapped their order, resulting in semi-major axes of 19 and 30 au, respectively (Tsiganis et al., 2005).

This dynamical instability was suggested originally to be the crossing of the Jupiter and Saturn mean motion resonance (MMR) 2:1, i.e., Jupiter does two revolutions around the Sun while Saturn does one. The MMR crossing could have happened between about 200 and 900 Myr after their formation. This is consistent with the spike of the Moon's bombardment at around 700 Myr (Hartmann et al., 2000), and that has been called the Late Heavy Bombardment (LHB, Gomes et al., 2005). However, new results reporting biases in sampling and analysis of the lunar rocks indicate that the LHB may not have existed, or not being that late or heavy (Chapman et al., 2007; Boehnke & Harrison, 2016).

Therefore, the significant dynamical instability required to explain some aspects of the architecture of the Solar System, including the orbits of the giant planets, could be different and have happened earlier. For instance, the instability could have been triggered by planet-disk interactions (Quarles & Kaib, 2019; de Sousa et al., 2020), giant planet interactions (de Sousa et al., 2020), or the inside-out photo-evaporation of the gaseous disk around the Sun (Liu et al., 2022).

Despite the fact that scientists now have some general ideas about the formation and evolution of the Solar System, some questions remain open. One of these questions relate to the small size of Mars, that could be explained by the Grand Tack model (Walsh et al., 2011), a low-mass Asteroid Belt (Hansen, 2009; Izidoro et al., 2015; Walsh & Levison, 2016; Drążkowska et al., 2016; Raymond & Izidoro, 2017) or the early instability model (Clement et al., 2018, 2021). Another question is the origin of water on Earth.

Thanks to ever more sensitive telescopes and instruments, astronomers have been able to observe other planetary systems. Some at very early stages of planet formation ($\sim$1 Myr) compared to the age of the Sun (4.6 Gyr). Looking at other planetary systems constrain how diverse they may be, and constrain theoretical models of planet formation and evolution from a general perspective. This helps to determine how the Solar System formed and evolved, but also whether the Solar System is a frequent output of planet formation and evolution processes.

1.1.2 First discoveries of extra-solar planets

Planets orbiting stars other than the Sun have been theorized centuries before the first extra-solar planet was discovered. In particular, the existence of exoplanets was associated to the question of life outside the Earth, that could have emerged and develop on other planets, not part of our Solar System.

Wolszczan & Frail (1992) discovered the first two exoplanets, of about a few Earth-masses. They orbit a pulsar, PSR1257+12. Afterwards, Mayor & Queloz (1995) discovered the first exoplanet orbiting a main-sequence star, named 51 Pegasi. This exoplanet is a gas giant planet. Both discoveries challenged the perception of astronomers of what could be extra-solar planetary systems. On the one hand, a pulsar is a massive star which ran out of fuel and exploded in a supernova to result in a neutron star, emitting a beam of electromagnetic radiation and rotating fast. On the other hand, the Jupiter-mass (M_{Jup}) giant planet 51 Pegasi b, orbits within four days around its host Sun-like star. For comparison, Jupiter orbits around the Sun in about eleven years, thus on a much longer timescale. Mercury, the closest planet to the Sun, orbits within 88 days. Therefore, first discoveries of exoplanets challenged theories on how planets may form and evolve.

Different techniques exist to detect planets, and I describe them in Section 1.2. The first exoplanets, and to date most of them, were discovered indirectly. The first direct detection of an exoplanet was made twenty years ago, around a brown dwarf[1] of about 24 M_{Jup}. Around it, Chauvin et al. (2004) directly imaged a massive giant exoplanet of 3–15 M_{Jup}, located at 55 au, hence about twice the distance from Neptune to the Sun. The first directly imaged multi-planetary system is HR 8799, hosting four massive giant planets (Marois et al., 2008, 2010), see Fig. 1.2 (*right*). The giant planets are located between two dusty belts, showing strong similarity with the architecture of the Solar System, but around a more massive star (1.5 solar mass, i.e., 1.5 $M_\odot$).

Until 2018, most of the exoplanets discovered where mainly old, several gigayears, and a few younger, down to about 15 Myr. The discoveries of the very young ($\sim$5 Myr), giant proto-planets PDS 70 b (Keppler et al., 2018; Müller et al., 2018) and PDS 70 c (Haffert et al., 2019) were breakthrough discoveries. For the first time, astronomers caught planets still at birth, in the gaseous and dusty disk surrounding their host star, called a protoplanetary disk.

1.1.3 Zoo of exoplanets

Nowadays, more than five thousands exoplanets have been discovered (see Fig. 1.3). Most of the exoplanets known so far orbit close to their host star. This is a bias of the current most efficient techniques to detect planets, based on transits and radial velocities (RV). These methods are mostly sensitive to planets orbiting within a fraction or a few astronomical units.

Both of these methods report an abundance of low-mass planets, called super-Earths or mini-Neptunes, and orbiting in less than a hundred days around their host star. A total of 20 to 50% single Sun-like stars may host such super-Earths and mini-Neptunes (Mayor et al., 2011), while it increases to almost all (90–100%) low-mass stars (Swift et al., 2013; Dressing & Charbonneau, 2015). The frontier between super-Earth and mini-Neptune is believed to be the photo-evaporation valley, also called the Fulton gap around 1.5–1.9 Earth-radius ($R_\oplus$, Fulton et al., 2017). The density value of the planet is a better estimate to distinguish between a gas-poor or a gas-rich planet. However, only the radius or the (minimal) mass of a given planet is often inferred. Roughly, super-Earths and mini-Neptunes have a mass between 1 and 20 $M_\oplus$ and a radius between 1 and 4 $R_\oplus$.

Among exoplanets orbiting very close to their host stars, there are the ultra-short-period (USP) planets with orbital periods of less than one day. They experience very high levels

[1] This brown dwarf is known as 2MASSW J1207334-393254.

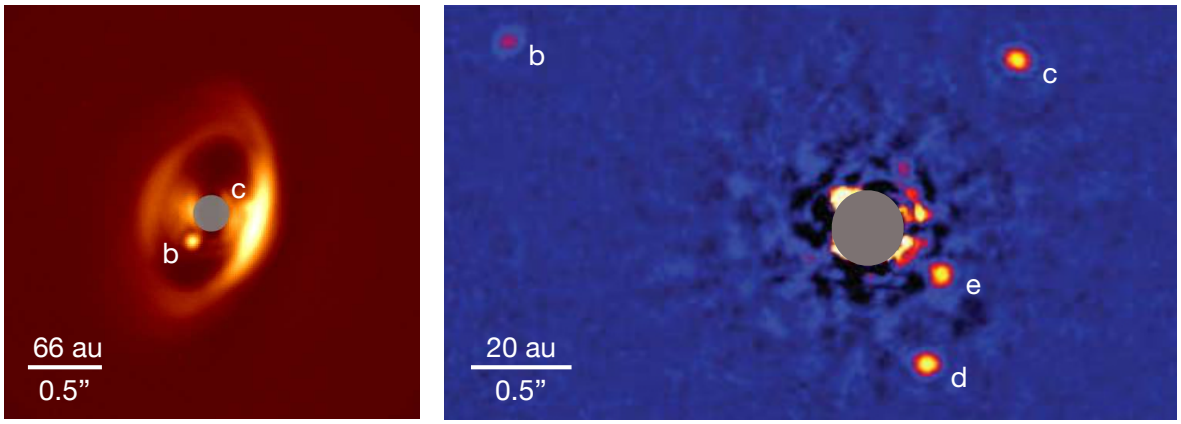

Figure 1.2: *Left*: Image of the protoplanetary disk PDS 70, hosting two giant protoplanets (Keppler et al., 2018; Müller et al., 2018; Haffert et al., 2019), PDS 70 b in the cavity and c embedded in the belt. Adapted figure from Pairet et al. (2021), based on the near-infrared (K band, 2.1 μm) VLT/SPHERE data acquired on February, 2018. *Right*: Image of the planetary system HR 8799 hosting four giant planets. Adapted figure from Marois et al. (2010), based on the near-infrared (L′ band, 3.8 μm) Keck II acquired on November 1, 2009. In both images, the grey circular mask indicates the region below the inner working angle of the coronagraph.

of irradiation and typically lie within regions where dust sublimates, opening questions on how they form (Winn et al., 2018). They are tidally locked, that is to say always showing the same face to their host star during their revolution. As a result, they have stable day and night sides, resulting in large variations in temperature across the planetary surface.

In addition, massive gas giant planets orbits have been found on short orbits too. They are often called hot or warm Jupiters, when they have orbital periods within 10 or 400 days, respectively. Giant gas planets are rarer than smaller planets, with less than 1% (respectively 10%) of FGK stars hosting a hot (warm) Jupiter (Marcy et al., 2005a; Gould et al., 2006; Mayor et al., 2011; Dai et al., 2021; Miyazaki & Masuda, 2023).

On the other hand, only a few exoplanets have been discovered orbiting at very large distances of their stars, above 10 au, due to observational biases. Those exoplanets detected using direct imaging are so far of at least a few Jupiter masses, and nicknamed super-Jupiters. There are not frequent around Sun-like stars either (2.9–8.5%, Vigan et al., 2021). Lower mass planets down to Saturn-mass, and orbiting at tens of au, are now within reach thanks to the better sensitivity of the *James Webb* space telescope (*JWST*). The *JWST* will certainly soon discover such exoplanets without any current counterparts.

Most of the exoplanets known so far orbit a star, and in some cases even two stars (Doyle et al., 2011; Welsh et al., 2012; Rodet et al., 2017). However, some exoplanets were found free-floating (e.g., the review from Miret-Roig, 2023). These free-floating planets may be quite common even though there are difficult to detect (Mróz et al., 2017, 2019; Miret-Roig et al., 2022). Exoplanets are detected around very massive stars (e.g., $\sim$3 $M_\odot$; Sato et al., 2012) down to low-mass stars, and even around the “missed stars” named brown dwarfs (Chauvin et al., 2004), because they can only fuse deuterium, not hydrogen[2].

On April 2024, the 5659 confirmed exoplanets are part of 4166 extra-solar planetary systems, including 896 systems known to host several planets[3]. Among all these planets, planets

[2]The limit between a massive gas giant planet and a brown dwarf is not cristal clear, and is astronomer-dependent. It can be based on its ability to fuse only deuterium, which implies a limit of 13 M_{Jup}-mass for a solar-metallicity object, or on its formation mechanism. The definition of the International Astronomical Union does not take into account the formation mechanism in its definition (Lecavelier des Etangs & Lissauer, 2022).

[3]from the European catalog `https://exoplanet.eu/catalog/`. In this chapter, all the numbers or percentages relative to exoplanet demographics are from April 2024.

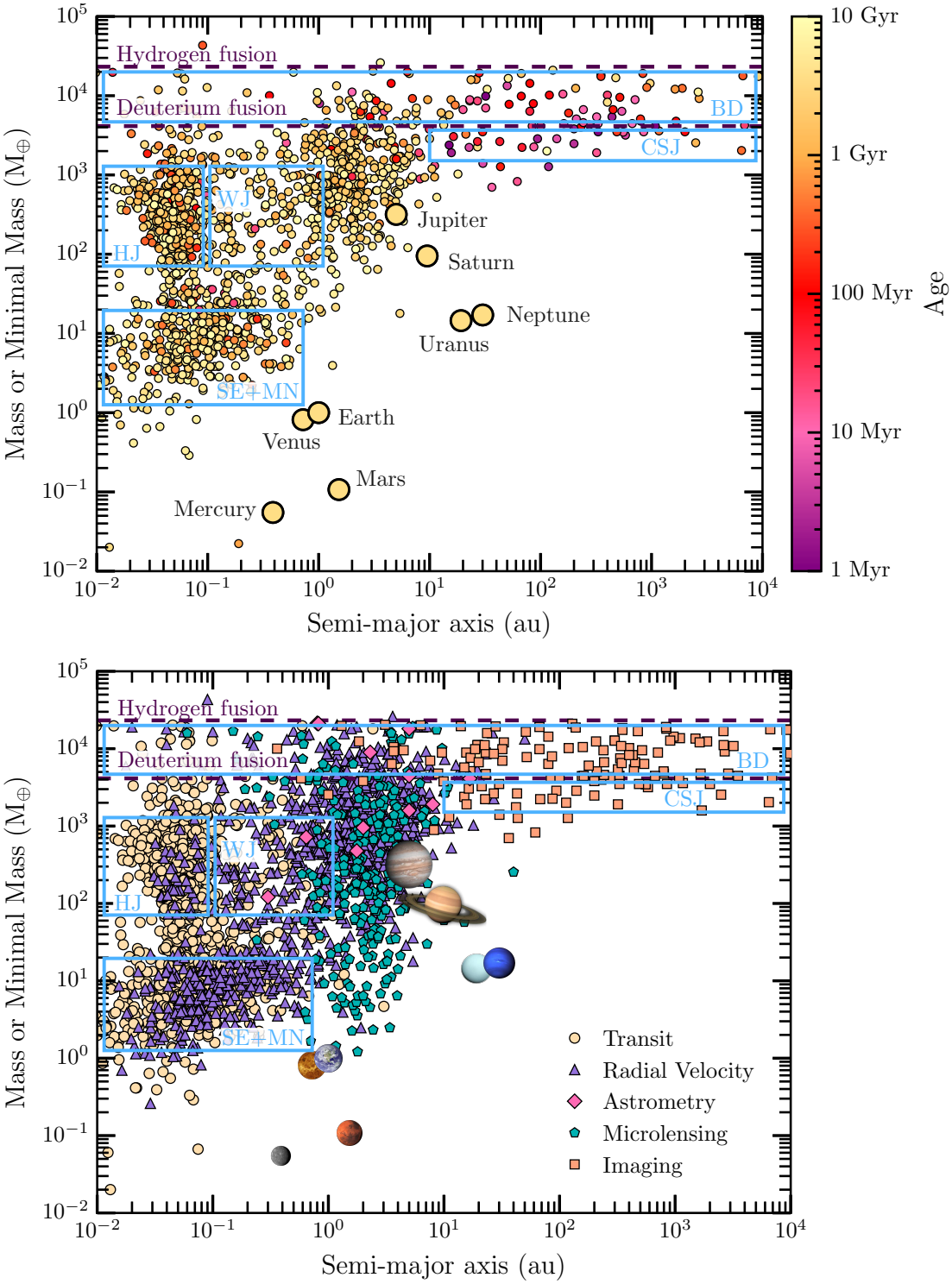

Figure 1.3: Semi-major axis of confirmed exoplanets with respect to their (minimal) mass from https://exoplanet.eu/catalog/ (April, 8 2024). Blue rectangles indicate roughly some exoplanetary groups, such as super-Earths (SE), mini-Neptunes (MN), Hot Jupiters (HJ), Warm Jupiters (WJ) and Cold super-Jupiters (CSJ). Above the deuterium fusion limit start the brown-dwarf (BD) regime, and above the hydrogen fusion limit are stars. *Top:* The color indicates the age of the host star. Most of the discovered exoplanets are part of old systems. In bigger circles, planets of the Solar System are shown for comparison. *Bottom:* The color and marker indicates the technique use to detect the planet. In my work, I focus on directly image Cold super-Jupiters. In one of my study, I search for them in systems hosting low-mass planets such as super-Earths and mini-Neptunes.

lying in the so-called habitable zone raise a particular interest in the community as life as we know might develop there. The habitable zone is defined as the region where water may be liquid on the surface of a planet that has a dense enough atmosphere (Kasting et al., 1993). The exact location depends on the stellar host properties (Underwood et al., 2003).

1.2 Detection methods

Different techniques exist to detect planets. On the one hand, direct methods such as direct imaging or interferometry take or reconstruct an image of a star and its vicinity, respectively. On the other hand, indirect methods such as transits, radial velocities or absolute astrometry reveal the presence of a planet orbiting around a star by observing regular changes in the stellar luminosity, or an anomaly in the stellar proper motion. Exoplanets can also be detected indirectly as they pass in front of a third background object, based on the gravitational microlensing technique.

I briefly present below each of these detection methods, illustrated in Fig. 1.4. I start with the direct detection techniques, then indirect, and eventually how they can be used in synergies.

1.2.1 Direct detection methods

Direct imaging

Direct imaging may be the most intuitive method to detect planets. However, imaging planets around stars face two main issues. First, a planet is much fainter than a star, which is as a dazzling light. Second, planets are located relatively close to their host star. Thus, direct imaging requires high-contrast imaging and high angular resolution to detect planets. By this way, direct imaging is sensitive to bright planets that orbit relatively far to their host star.

Current direct-imaging observations are sensitive to the thermal emission of exoplanets, and not the stellar light that is reflected upon them ("reflected light"). Consequently, it is easier to detect young exoplanets, because they are hotter and brighter than older exoplanets. For instance, evolutionary models (Linder et al., 2019) coupled to the atmospheric models `petitCODE` (Mollière et al., 2015, 2017) or `HELIOS` (Malik et al., 2017) predict that a planet of 2 M_{Jup} has an effective temperature spanning between 1 300 and 1 700 K (depending on the metallicity, presence of clouds) at 20 Myr. At 2 Gyr, the effective temperature decreases at 170–250 K.

Observational facilities image planets mainly in near- or mid-infrared wavelengths. Indeed, exoplanets emit mainly in the near- or mid-infrared, while hot enough ($\geq$ 1400 K) stars have their peak of luminosity in the optical. Therefore, it is easier to detect planets in the infrared, than in the optical. In other words, the contrast ratio defined by the flux of the planet divided by the flux of a star is more favorable in the near- or mid-infrared than in the optical.

Currently, the VLT/SPHERE and Gemini/GPI instruments are two emblematic extreme adaptive optics systems in the field, and which probed the demographics of massive giant planets beyond a few astronomical units via the SHINE (Vigan et al., 2021) and GPIES (Nielsen et al., 2019) survey, respectively. From a characterization perspective, via multi-wavelength imaging of exoplanets, one can study the emission spectroscopy of young exoplanets, to constrain its atmospheric properties such as its pressure-temperature profile, molecular composition and the cloud properties, if any (Madhusudhan, 2019). Investigating it at the early stages of planet formation and evolution can first constrain their planetary accretion from their surrounding circumplanetary disk (CPD, Miki, 1982), which confer them part of their mass, and second, also their cooling tracks (e.g., Baraffe et al., 2003; Linder et al.,

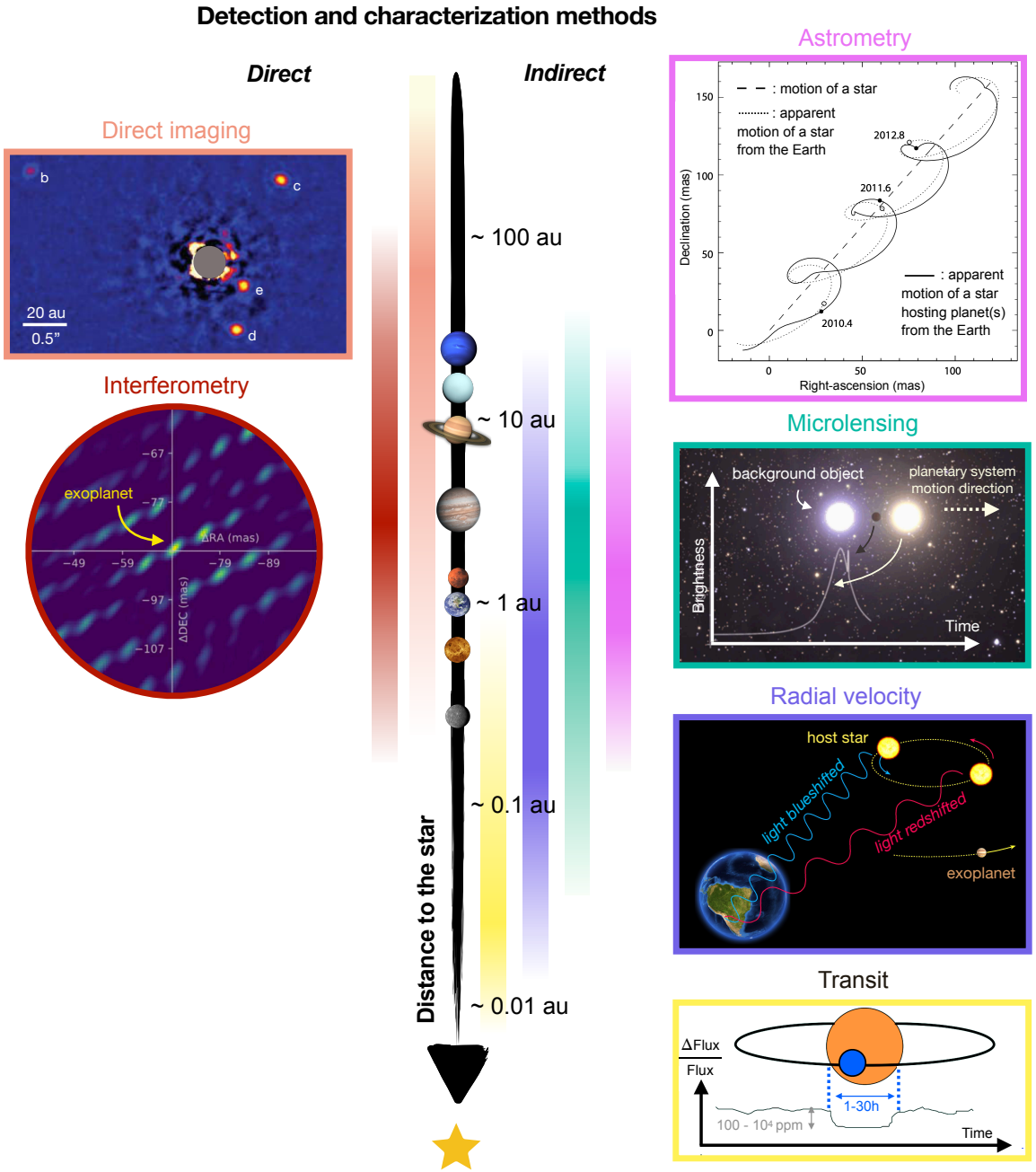

Figure 1.4: Overview of the different detection and characterization methods. This Figure is adapted from Marois et al. (2010) for the directly imaged system HR 8799, from Hinkley et al. (2023) for the interferometric detection of the exoplanet HD 206893 c, from Perryman (2012) showing how planet(s) impact the absolute astrometry of its host star, from ESO/L. Calçada for illustrating a microlensing event, from ESO explaining the principle of radial velocity using the Doppler effect, and from Rouan & Lagrange (2023) showing the lightcurve of a star which is undergoing a planetary transit.

2019). In addition, by measuring the astrometry of an exoplanet at different times, one can derive its orbital parameters (e.g., semi-major axis, eccentricity, inclination, position angle).

During my Ph.D., I mainly used the direct imaging technique to detect and characterize exoplanets, but also circumstellar disks, down to a separation of 0.1 arcsecond (″). One arcsecond corresponds to the angular diameter of the distance between the Earth and the Sun (i.e., 1 au) seen at 1 parsec (pc), 1 pc being equal to 3.26 light years. In units maybe more human friendly, 1″ corresponds the angular diameter of a one-euro coin seen at 5 km. In Chapter 2, I describe the methodology I used to directly image circumstellar signals in more details.

Interferometry

Interferometry can detect planets at separations smaller than direct imaging, and with a higher angular resolution[4].

Classical interferometry combines the signal of several telescopes. For instance, the Very Large Telescope Interferometer (VLTI) combined to the GRAVITY instrument can detect planets down to separations of 0.040″ (e.g., Fig. 12 from Pourré et al., 2024) and with a relative astrometry accuracy of 50 μas (Lacour et al., 2020; Pourré et al., 2024) which is more than one order of magnitude better than direct imaging. This is a game-changer to derive precise orbital parameters of exoplanets (e.g., Wang et al., 2021). Using GRAVITY, one can also study spectroscopy emission of young exoplanets with interferometry, to constrain exoplanetary atmospheres and/or their surrounding environment (Nasedkin et al., 2024; Wang et al., 2021).

Alternatively, sparse aperture masking (SAM), also known as aperture masking interferometry (AMI) or non-redundant masking (NRM), uses only one telescope dish with a several-hole mask. This technique loose a significant fraction of the incoming light, but is more robust to the starlight wavefront aberrations which impacts the final sensitivity of the observations (Lacour et al., 2011). Indeed, it is easier to have a flattened starlight wavefront within the size of a hole (e.g., 1.2 meter for the NaCo SAM mode), than across the whole primary diameter of the telescope (e.g., 8 meter for the VLT). In addition, the angular resolution using SAM is twice better than for classical imaging. Although still a niche method, the SAM (or AMI) technique probes a new parameter space with sensitivity to massive planets down to 50 mas (e.g., some results from the ground from Gauchet et al., 2016) and is currently the only way to do interferometry from space (Ray et al., 2023).

1.2.2 Indirect detection methods

Transit

An exoplanet can be detected when it transits in front of its host star with respect to the observer. During the transit that lasts typically between one hour and thirty hours, the light of the star decreases by 1% or less, because the transiting planet masks some part of the photosphere (see Fig. 1.4, *bottom-right*).

Although two thirds of the confirmed exoplanets have first been detected via the transit method, this method was not foreseen as efficient to discover planets, mitigated to the number of systems observed. First, the probability to have the perfect alignment telescope-exoplanet-star is most of the time low, following

$$\text{probability} \;=\; \frac{R_\star + R_\mathrm{p}}{a}\,, \tag{1.1}$$

[4]The angular resolution is λ/D for direct-imaging, and λ/B for interferometry, where λ is the wavelength, D the diameter of the telescope, and B the longest baseline between two telescopes.

where $R_\star$ and R_p are the radius of the star and the planet, respectively, and a the semi-major axis. Second, the radius of the planet must be large enough relative to the radius of its host star to result in a significant variation of the stellar flux measurement, equal to the ratio of the areas,

$$\text{variation} = \left(\frac{R_\mathrm{p}}{R_\star}\right)^2 . \tag{1.2}$$

To give a few numbers, for an external observer, the transit of Jupiter, which has a radius almost ten times smaller than the Sun's, will decrease of about 1% the received solar flux. The probability of detection of this transit is very low (0.1%), because Jupiter is far away from the Sun (5 au; 11 years). However, if Jupiter was considerably closer to the Sun, e.g., orbiting within three days, the probability of transit would be relatively high (10%).

To confirm an object first detected via transit, additional transit measurements are often required to confirm the periodicity of the object, and find its orbital period value. Furthermore, the nature of the object can be identified via the use of radial velocities, that gives then the mass of the object, e.g., a planetary, brown-dwarf or stellar mass companion. The space telescopes *Kepler* and *TESS* discovered thousands of confirmed planets, and a thousand others are still to be confirmed or rejected as false positive signal[5]. The ground-based instrument TRAPPIST also played a major role, by discovering the TRAPPIST-1 system which is an iconic system hosting seven rocky planets with similar radius and mass to the Earth, in a compact configuration around a very low-mass star (0.08 $\mathrm{M}_\odot$) located at 12 pc away (Gillon et al., 2016, 2017; Luger et al., 2017).

By observing the full orbit of a transit exoplanet, one can detect both the transit and the secondary eclipse of the exoplanet (when the exoplanet goes behind its host star)[6], and constrain its phase curve via photometry or spectroscopy. From this, one can derive precious constraints on the atmospheres of the exoplanets, and also the formation of clouds (e.g., Deming et al., 2019).

As a matter of fact, another detection technique emerged with the advent of the transit method, and is named transit-timing variation. Transit-timing variation (TTV) consists in small variations in the timing of the transits of a known planet that can then point out to the presence of an additional planet in the same system.

Radial velocity

Measuring the radial velocity (RV) of stars may indicate the presence of planets orbiting around them. Indeed, a star hosting at least one planet will orbit around the barycenter of the system, which is different from the center of the star. When the star moves toward the observer, the Doppler effect causes a blue shift of the stellar spectrum. Reciprocally, when then star moves further out, its spectrum is red shifted (see Fig. 1.4, *bottom-right*). This periodic signal is detectable for systems that are not face-on, that is to say, for which the orbital plane of the star is not orthogonal to the line of sight observer-star. The blue and red shifts in the stellar spectrum is stronger for massive exoplanets, that are seen edge-on and that orbit close to their host star.

The radial velocity technique enables the derivation of the orbital parameters of the planet, such has its period (and thus semi-major axis) and its eccentricity, as well as its minimal mass defined by its mass multiplied by the sine of its inclination. To date, more than one thousand of exoplanets have been discovered using this method.

[5] Exoplanet and candidate statistics from *Kepler* and *TESS* space telescopes are available here: https://exoplanetarchive.ipac.caltech.edu/docs/counts_detail.html

[6] For exoplanets with circular orbits, if they transit in front of the star, they also have secondary eclipse. On the other hand, eccentric exoplanets may only transit or have a secondary eclipse but not necessarily both (see the pedagogical publication from Deming et al., 2019).

Some of the high-resolution spectrometers used to detect exoplanet via RV measurements, in alphabetic order: CARMENES, ELODIE (used to discover 51 Peg b), ESPRESSO (Pepe et al., 2021), HARPS (Pepe et al., 2002), HARPS-N (Cosentino et al., 2012), HIRES (Vogt et al., 1994), NIRPS (Wildi et al., 2017), SPIRou (Donati et al., 2020), UCLES (Diego et al., 1990), UVES (Dekker et al., 2000).

Astrometry

Measuring the absolute astrometry of the star can help to discover a massive planet around it. By comparing the long-term proper motion of the star by using its position measured by *Hipparcos* (reference epoch in 1991) and *Gaia* (reference epoch in 2015) to the short term *Gaia* proper motion (baseline of about two or three years, for *Gaia* Data Release (DR) 2 and 3, respectively), the presence of a sub-stellar or stellar companion can be revealed (Brandt, 2018; Kervella et al., 2019). This effect is known as astrometric acceleration or Proper Motion anomaly (PMa).

If the star does not host a companion, its proper motion vector would be colinear between each other at the different epochs. Instead, if there is a companion, the proper motion of the star would include its motion around the center of gravity of the system. This would result in the short-term *Hipparcos* (Van Leeuwen, 2007) and *Gaia* (Gaia Collaboration et al., 2018, 2021) proper motion vectors not colinear with the long-term *Hipparcos*-*Gaia* proper motion (e.g., Fig. 1 from Kervella et al., 2019, and Fig. 1.4 *top-right*).

So far, the discovery of an exoplanet cannot be claimed by using only the astrometry method. Combined to the *Hipparcos* data, the *Gaia* DR2 and DR3 give hints for the presence of a binary companion or a massive planet, whose mass is degenerated with their distance to the star. Stars with an astrometric acceleration are prime targets for follow-up observations using radial velocity, intereferometry or direct imaging. Therefore, by avoiding blind surveys, this saves telescope time and increases the yield of exoplanets detected. In the past few years, some massive giant planets and brown dwarfs were successfully discovered by this way (Hinkley et al., 2023; Mesa et al., 2023; De Rosa et al., 2023; Franson et al., 2023; Tobin et al., 2024).

The future *Gaia* DR4 will give the first *Gaia* exoplanet list, based on five years and a half of the *Gaia* mission. The DR4 should be released at best at the end of 2025[7]. The last *Gaia* DR5 will indicate the presence of giant exoplanets with orbital periods up to about ten years, corresponding to the duration of the *Gaia* mission. The DR5 should be released at best at the end of 2030.

Microlensing

Exoplanets can also be detected by using the gravitational microlensing effect based on General Relativity (Mao & Paczynski, 1991; Gould & Loeb, 1992). A "lens" consisting in, e.g., a star hosting a planet, and passing in front of a distant background bright object, such as a star, would increase the apparent brightness of the background star. This magnification event will give specific lightcurve features (Paczynski, 1986, see Fig. 1.4): a strong bump when the two stars are perfectly aligned, and closely followed (or preceded) by a smaller and shorter bump corresponding to the perfect alignement of the planet and background star[8]. The planetary system that magnifies the light of the background object can also be a multi-planetary system, or on the contrary a free-floating planet, resulting in different multiple or single features in the lightcurve of the background object.

[7] https://www.cosmos.esa.int/web/gaia/release

[8] See the video: https://supernova.eso.org/exhibition/videos/eso50microlensingexo/ from ESO/L. Calçada

About 280 planets have been detected via the gravitational microlensing method, including a few multi-planetary systems (e.g., Gaudi et al., 2008). Unlike to the other techniques previously described, the gravitational microlensing does not rely on detection of photons from either the host of star or the planet. As such, gravitational microlensing could detect more easily planets located far from the neighborhood of our Solar System, at several kiloparsecs. The gravitational microlensing technique allows to constrain the mass and semi-major axis of the exoplanets. To date, it is the technique which discovered most of the low-mass planets such as Super-Earths between 1 and 5 au (e.g., Gaudi, 2012; Mroz & Poleski, 2023, and see Fig. 1.4).

However, microlensing events are rare, mitigated by the number of observed fields, because these events require sufficiently precise alignment between the foreground planetary system and a background bright object (e.g., Gaudi, 2012). In all likelihood, a given planetary system should be detected via the gravitational microlensing technique only once.

Two ongoing microlensing campaigns with wide-field of view are named OGLE (Optical Gravitational Lensing Experiment, Udalski et al., 2015) and KMTNET (Korea Microlensing Telescope Network, Kim et al., 2016). The forthcoming *Nancy Grace Roman Space Telescope* (launch planned in 2027) should detect analogues of the Solar System planets (except Mercury) around other stars via the microlensing technique (see Fig. 9, Penny et al., 2019).

Overall, of the more than 5 000 exoplanets (or brown dwarfs) reported on the European catalog of exoplanets, around 69% have been detected by transit, 20% by radial velocity, 5% by microlensing and 4% by direct imaging.

1.2.3 Coupling detection methods

Since no detection technique probes the full parameter space of exoplanets, combining different techniques allow to have a global view of planetary systems, both at small and large distances, from edge-on to face-on configurations. For a given exoplanet, detecting it by several methods allow to better constrain its physical, orbital and chemical parameters.

As written previously, combining detections with the radial velocity and the transit techniques constrain the mass of the detected planet. Indeed, the radial velocity method provides the minimal mass of a planet corresponding to mass $\times$ sin(inclination), while the transit technique immediately constrains the inclination to 90 deg, because the planet must be edge-on. In addition, combining both techniques gives the density of the planet, because the transit technique gives the radius of a planet normalized by the radius of its host star, that can be determined via other methods such as interferometric observations of the star (e.g., Von Braun et al., 2011). Then, the density of the planet provides constraints on its bulk composition, e.g., rocky (density of 5.5 g/cm^3 for the Earth for example) or gaseous (1–2 g/cm^3) rich.

Moreover, using in synergy the orbital constraints from direct imaging or interferometric data with radial velocity measurements or absolute astrometry from *Gaia* and *Hipparcos*, enables the determination of the dynamical mass of the planet. This dynamical mass can then be compared to the mass inferred from the evolutionary and atmospheric models using as input the thermal flux of the planet, that is provided by the direct-imaging or interferometric detection. Comparing both masses give important constraints on the mass-luminosity relationship, and in particular on the evolutionary and atmospheric models.

In addition, a long-term trend in the radial velocity series may indicate the presence of a companion located at a wide separation and with an orbital period longer than the period during which the system was monitored (e.g., the linear slopes in Fig. 3 from Teng et al., 2023). As for stars showing an astrometric acceleration based on *Gaia* and *Hipparcos*, a long-term trend in radial velocity may hint for the presence of an additional planet in the system. This guides surveys searching for planets, and so avoid blind surveys with limited success

due to the small occurence of wide-distant giant planets. Such observational strategy saves telescope time, and was successfully and independently done on AF Lep b by three different teams (Mesa et al., 2023; De Rosa et al., 2023; Franson et al., 2023).

1.3 Planet formation and evolution

Below, I first describe the current vision of the community on how planets may form around stars, and evolve. Afterwards, I shed light on observational constraints that allow to constrain planet formation, with a specific emphasis on planetary system architectures.

1.3.1 The different steps leading to planet formation

The different stages of a planetary system formation is represented on Fig. 1.5. In the following paragraphs, I briefly describe how stars form, before focussing on the dust growth within a disk, that may form planetesimals and planets.

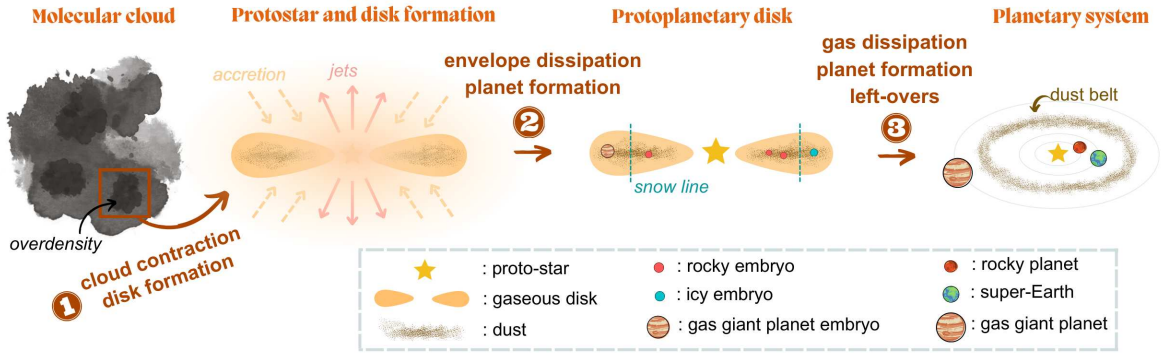

Figure 1.5: Sketch of the formation of a star, and of a possible planetary system outcome.

From molecular cloud to star and disk formation

Proto-stars are formed following gravitational collapses of molecular clouds, composed of gas and dust, e.g., the review from Kennicutt & Evans (2012) and the detailed introduction of the doctoral thesis Le Gouellec (2021). The pressure, density and temperature of the pre-stellar cores increase, until reaching the point that triggers the thermo-nuclear reactions.

The proto-star starts to shine. Except, that the photons are promptly absorbed by the surrounding material, thus the proto-star first remains invisible. Part of the gas and the dust accretes onto the proto-star, while another part is ejected via bipolar outflows, see Fig. 1.5. Due to the conservation of the angular momentum, and a balance between the gravitation, the gas pressure and the centrifugal force, the envelope around the proto-star flattens into a protoplanetary disk in which planets may later form. In addition, magnetic fields play an important, complex role to regulate star formation, from cloud to disk scales (e.g., Crutcher, 2012; Hull & Zhang, 2019).

From dust grains to planetesimals

Generally, the dust-to-gas ratio is believed to be about 1% in protoplanetary disks. The gas is subject to gravitational and centrifugal forces and to the gas pressure, that of gradient decreases at first order across the disk due to decreasing of temperature and density. This pressure gradient is the cause of the sub-Keplerian velocity of the gas. Large enough dust

particles are mostly sensitive only to gravitational and centrifugal forces, and so orbit at Keplerian velocities. The dust hence feels a headwind which results in gas drag that decelerates the dust particles and cause them to spiral inward, causing a radial drift (Weidenschilling, 1977). In addition, interactions between the dust and the gas result in the vertical settling of the dust. On the other hand, small dust particles are coupled to the gas, and so they orbit at sub-Keplerian velocities.

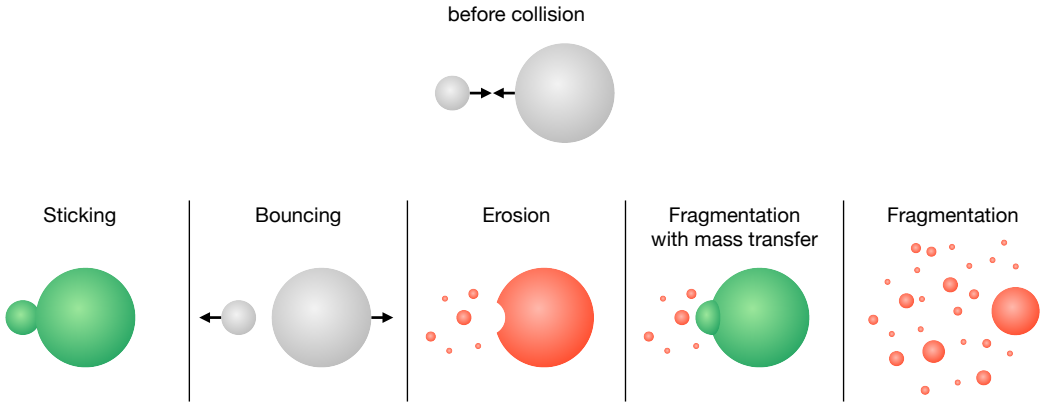

Figure 1.6: Simplified classification of collisional outcomes between dust particles. Mass gain is represented in green, mass loss in red. Figure from Birnstiel (2023).

Initially, in protoplanetary disks, dust particles are thought to have sizes of less than 1 μm (Ormel et al., 2009; Bate, 2022). Dust grains then grow bigger and bigger to form dust grain aggregates via constructive collisions, such as sticking or mass-transfer collisions. However, these constructive collisions compete with destructive collisions resulting in fragmentation and erosion of such dust aggregates (see Fig. 1.6; Güttler et al., 2010). The growth of dust aggregates faces three main barriers, named the bouncing, fragmentation and drift barriers. In short, the bouncing barrier prevents the particles to grow, the fragmentation barrier makes them smaller by destructive collisions, and eventually the drift barrier remove the bodies by making them spiral down onto the star.

In more details, the first bouncing barrier concerns grain size between about 100 μm and 1 cm, depending on the dust particle properties, such as their composition, shape, porosity, mass and velocity (e.g., Zsom et al., 2011; Drążkowska et al., 2023). At this stage, the dust grain aggregates remain in a status quo state due to mainly bouncing collisions (Zsom et al., 2010). If eventually bigger solid bodies are formed, they fragment or erode due to their higher velocities (Brauer et al., 2008). In addition, the more massive the grain particle, the faster it drifts onto the star, for instance in about one hundred years at 1 au (Weidenschilling, 1977; Nakagawa et al., 1986). This drift barrier is also known as the meter-size barrier.

In principle, those barriers prevent the formation of planetesimals and then planets. Yet, planets exist. Different dust growth scenarios have been widely investigated. For instance, the bouncing barrier could be overcome by collisions of charged or organic grains (Homma et al., 2019; Steinpilz et al., 2019). Alternatively, by taking into account the velocity dispersion of dust particles, Windmark et al. (2012b) and Garaud et al. (2013) report that the growth barriers could be circumvented for some lucky particles, that experience low-velocity constructive collisions several times in a row. Then, those particles may grow by sweeping up the other smaller dust grains trapped at the bouncing and fragmentation barriers, to finally result in planetesimal size objects (Windmark et al., 2012a). However, the drift barrier may then prevent the growth to arbitrarily large sizes (Estrada et al., 2016; Booth et al., 2018).

Another scenario that could overcome the bouncing and fragmentation barriers is described by Okuzumi et al. (2012) and Kataoka, Tanaka, Okuzumi, & Wada (2013). They favor

the growth of porous aggregates, that are stickier and have larger cross-sections. These result in higher constructive collision rates, and eventually planetesimal-sized objects. Nonetheless, such outcome is limited or prevented based on erosion (Krijt et al., 2015; Schräpler et al., 2018), rotational disruption (Tatsuuma & Kataoka, 2021), or radial drift, even though it is less influential for fractal aggregates than for compact particles (Estrada & Cuzzi, 2022).

All in all, the most popular scenario to form planetesimals may be the collapse of gravitationally bound pebble clumps. This relies on accumulation of dust in overdensities, with high dust-to-gas ratio, that may be increased via photo-evaporation (Carrera et al., 2017), dust settling, or cold-finger effects (Cuzzi & Zahnle, 2004). This can then trigger the streaming instability (Youdin & Goodman, 2005) resulting in an even higher enhancement of dust, becoming a run-away effect (e.g., the review from Simon et al., 2022). Different types of mechanisms can concentrate the solids, such as pressure bumps (e.g., Rice et al., 2006; Bai & Stone, 2010; Johansen et al., 2012), vortices (Barge & Sommeria, 1995; Meheut et al., 2012; Lyra & Lin, 2013; Raettig et al., 2015), traffic-jam at silicate and snow lines (Birnstiel et al., 2010; Schoonenberg et al., 2018; Morbidelli et al., 2021), radial drift (e.g., Youdin & Shu, 2002), or dead-zone boundaries (Kretke & Lin, 2007). The gravitational collapse of the dusty clumps can lead to the formation of planetesimals, typically of a few 100 km-size (e.g., Simon et al., 2016).

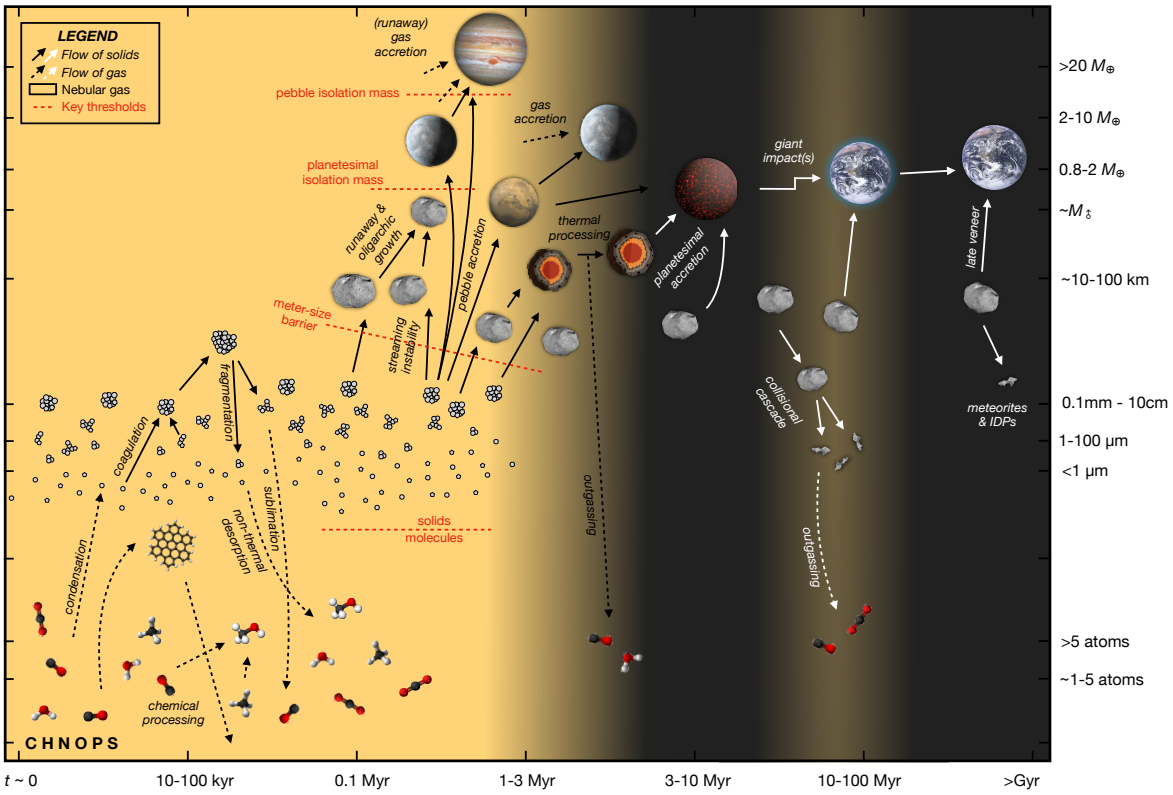

Figure 1.7: Sketch of planetary formation steps and processes. Rough sizes of bodies are indicated on the *right*, and evolution time is shown at the *bottom*. Adapted figure from the PPVII review Krijt et al. (2023).

To summarize, Figure 1.7 illustrates the growth from dust grains to planetesimals described here, and from planetesimals to planets, that I describe in the next section.

From planetesimals to planets

In the core-accretion paradigm (Pollack et al., 1996), two models compete with each other to describe how planets form: the pebble accretion (e.g., Johansen & Lacerda, 2010; Ormel & Klahr, 2010; Lambrechts & Johansen, 2012) and the planetesimal accretion (e.g., Pollack et al., 1996; Alibert et al., 2005; Emsenhuber et al., 2021) onto a planetary core (see, e.g., Drążkowska et al., 2023, for a review). Current pebble and planetesimal accretion models often initialize their simulations with Moon-mass (0.01 $M_\oplus$) planetary cores that will then accrete materials. Such cores could form via streaming instabilities followed by planetesimal constructive collisions (Liu et al., 2019).

When the planetary embryo accretes pebbles or planetesimals fast enough, it can also accrete the gas still remaining in the disk, and thus become a gas or an icy giant planet, such as Jupiter or Neptune, respectively. Otherwise, the planet can become a rocky planet, such as the Earth, or an icy Earth-mass planet, for which there is no counterpart in the Solar System, to name a few examples. While growing, a forming planet launches density spiral waves, (e.g., reviews from Kley & Nelson, 2012; Paardekooper et al., 2023). Due to gravitational interactions between the planet and the gaseous disk, the growing planet usually migrate inwards following type I migration (Goldreich & Tremaine, 1980; Tanaka et al., 2002), or type II migration if the planet is massive enough to carve a gap in the disk (Lin & Papaloizou, 1986).

Planets up to a few Jupiter mass planets are mainly produced within the core-accretion scenario, whereas larger planets ($\geq$ 4–5 M_{Jup}) and brown dwarfs ($\geq$ 13 M_{Jup}) could form via other pathways, such as gravitational disk instability (Boss, 1997) or gravo-turbulent fragmentation (Padoan & Nordlund, 2004). Gravitational disk instability consists in disk fragmentation in the early stages of stellar and disk formation. Beyond about 50 au from the host star, gravitationally unstable cold gaseous clumps can collapse to high densities (Boss, 1997; Gammie, 2001; Armitage, 2017), where planet formation can then take place. On the other hand, gravo-turbulent fragmentation of molecular clouds may result in gravitationally unstable protostellar cores of brown dwarf mass, that will then collapse and form massive giant planets, or brown dwarfs (Padoan & Nordlund, 2004).

Outcome: Planets and debris disks

Planet formation occurs during the lifetime of the protoplanetary disk (3–6 Myr, Haisch et al., 2001) for gas giant planets, while smaller, rocky planets can take longer as for the Earth in our Solar System (50-150 Myr, Kleine et al., 2009). The dispersal phase of the protoplanetary disk has been called "transition disk" or "hybrid disk". After this stage, most of the gas is gone. It has either been accreted onto the star or onto the (giant) planets or been blown away.

One open question in the field is how debris disks are related to protoplanetary disks. Do large, bright protoplanetary disks results in bright debris disks, while compact protoplanetary disks result in no debris disk? Najita et al. (2022) investigated this issue. According to them, since about 25% of young (1 Myr) single Sun-like stars host large, bright protoplanetary disks, and the same fraction of old (1 Gyr) single Sun-like stars host bright debris disks, this would be an option. However, they underline that a combination of different evolution paths with disks behaving as "early flare", "steady glow" or "late bloomer" may also describe the protoplanetary-debris disk connection, see their Fig. 12.

Around the star remain planet(s) and remnants bodies that are leftovers from planet formation, such as dwarf planets, planetesimals, pebbles and dust. They can be considered as "debris". A debris disk can represent all the debris in a system, or individual debris populations (e.g., the pedagogical review from Pearce, 2024). Planetesimals can be comets or asteroids and be located in circumstellar belts or on planetary orbits at specific locations on

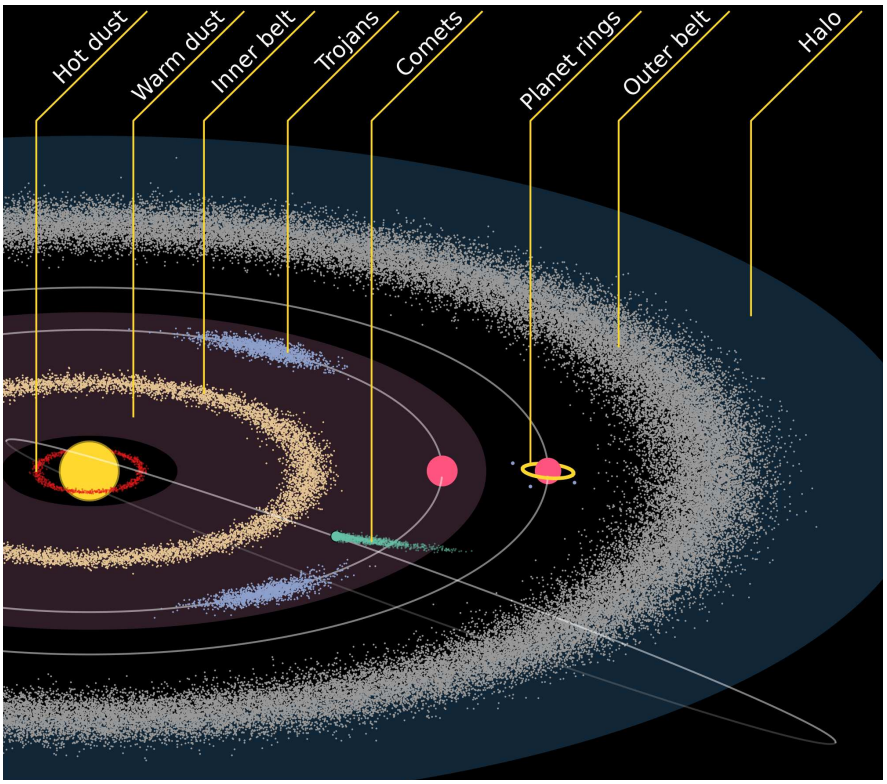

Figure 1.8: Sketch of some possible natures and locations of debris around a star. Figure from the pedagogical review on debris disks from Pearce (2024).

the same orbit of a planet (leading or trailing, so-called Trojan asteroids). Smaller bodies, such as pebbles and dust, can be located in those places, in circumplanetary disks and at lower density between belts or in the extended halo, in particular for the smaller grains, see Fig. 1.8.

After planets have formed, systems do not remain static and major events can take place, such as planet-planet collisions or scattering (Rasio & Ford, 1996), high-eccentricity migration via for instance Kozai-Lidov interactions (Kozai, 1962; Naoz et al., 2012), late in-fall of planetesimals onto planets (Gomes et al., 2005), or external perturbation such as stellar flyby (Laughlin & Adams, 1998; Hurley & Shara, 2002; Zakamska & Tremaine, 2004). This modifies the planetary system architecture, by ejecting planet(s) or changing their orbital properties. This may induce a significant variation of the temperature on the planet, which may result in a late atmospheric escape (Bourrier et al., 2018) or change the physical state of some of its content (e.g., turning oceans into steam). Late in-fall of planetesimals may update the composition of the planet, as their possible input of water on the Earth (Pepin, 1991).

As well as planets, debris disks evolve too. Collisions between planetesimals generate smaller bodies, that will undergo series of collisions and result in smaller and smaller particles (e.g., the review from Wyatt, 2008). This collisional cascade generates new populations of dust. When the dust particles are small enough, the dust grains become sensitive to additional forces than gravitation. The Poynting-Robertson drag make dust grains spiral toward the star (e.g., Klačka et al., 2014),. On the other hand, stellar winds and stellar radiation pressure are outward force opposing the stellar gravity. They push away dust grains (**?**Burns et al., 2014), in particular those below the so-called blow-out size (about 1-10 μm for G to A-stars, see the review from Pearce, 2024), and modified their orbital properties that become eccentric.

Side note: Binaries or higher-order multiple system

Previously, I have described planet formation and evolution around single stars. However, multiple-star systems are common, with 50% of Sun-like stars part of binaries or higher-order multiple systems (Heintz, 1969; Abt & Levy, 1976; Duquennoy & Mayor, 1991; Raghavan et al., 2010). More than 200 multiple systems host at least one planet (Fontanive & Bardalez Gagliuffi, 2021)[9]. In binary planetary systems, circumstellar (orbiting around one star, e.g., Patience et al., 2002; Marcy et al., 2005b) and circumbinary (around the binary pair, e.g., Doyle et al., 2011; Welsh et al., 2012; Rodet et al., 2017) planets have been detected. Higher-order stable systems are hierarchical. For instance, triple systems consist in a star in orbit with a binary pair. Planets can be part of such systems, such as for α Cen, that hosts the closest star and exoplanet from the Sun, Proxima Centauri (α Cen C) and Proxima Centauri b, respectively.

Therefore, a complete picture of how planets form and evolve cannot neglect multiple systems. The key factor is the separation between the stars, that sets if the multiplicity nature of the system tend to inhibit the planet formation to some extent (separation $\leq$ 50–100 au, Bonavita & Desidera, 2007, 2020; Kraus et al., 2012, 2016; Wang et al., 2014), influence the planet evolution (separation of about 100–1 000 au, Fabrycky & Tremaine, 2007; Naoz et al., 2012; Dong et al., 2013; Ngo et al., 2016) or have no significant consequences (separation $\geq$ 1 000 au, Bonavita & Desidera, 2007, 2020; Fontanive & Bardalez Gagliuffi, 2021).

1.3.2 Observational constraints

I present below observational results that have helped to constrain theoretical models of planet formation and evolution. First, I highlight the imaging of numerous circumstellar disks. Then, I focus on the orbital and physical properties of exoplanets, before continuing with the study of their atmosphere. Eventually, I describe how stellar parameters impact planet formation.

Circumstellar disks, and their structures

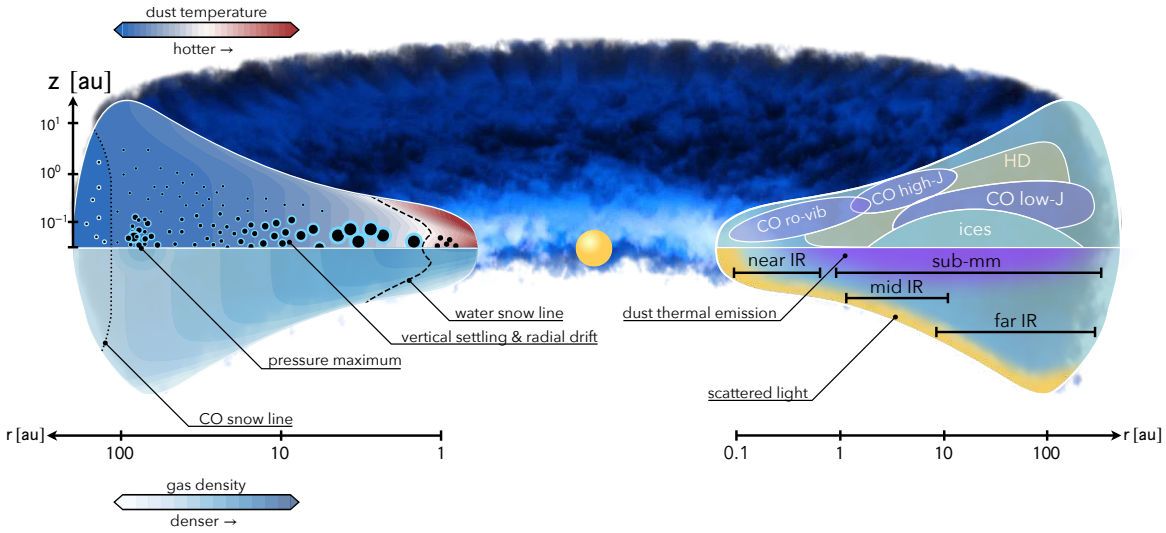

Figure 1.9: Illustration of protoplanetary disks structures and properties. *Left:* Dust temperature and gas density structure. *Right:* Simplified representation of molecular emissions, thermal emission of the dust, scattered light of the dust. Figure from the PPVII review Miotello et al. (2023).

[9] see also the following catalogue: https://exoplanet.eu/planets_binary/

To date, more than 300 circumstellar disks have been imaged in the optical, at infrared or millimeter wavelengths[10]. They cover a wide range of ages, from optically thick to optically thin disks. To give an overview: optically thick disks are younger than about 6 Myr (Haisch et al., 2001) and consist in gaseous and dusty disks in which planets may form, such as the disks in the Taurus-Auriga star-forming region (1–2 Myr, e.g., Garufi et al., 2024), or the iconic disk PDS 70 (about 5 Myr) hosting two confirmed imaged protoplanets (Keppler et al., 2018; Müller et al., 2018; Haffert et al., 2019). Then, most of the gas was either accreted onto the star or giant planets, or dissipated, resulting in little gas content in the remaining disk. Due to a decreasing of the dust density, debris disks are optically thin, as for instance the young (20–30 Myr) debris disks β Pictoris (Smith et al., 2009) and HR 8799 (Su et al., 2009) systems, and old (5–10 Gyr) debris disks GJ 581 (Lestrade et al., 2012) and HD 20794 (Kennedy et al., 2015). These four debris disks are also known to host exoplanets.

Originally, the presence of a circumstellar disk around a star was inferred by measuring the infrared excess of the system. This consists in first measuring the flux of the system at different wavelengths, that is to say the spectral energy distribution (SED). Second, in checking whether it deviates from a single black body component, that is roughly the expected SED for a single star. In practice, regarding debris disks, the presence of dust belts around a star will add blackbody components. The temperature (T) corresponding to a dust belt is related to the distance of the dust belt (r) to the star, and to the stellar luminosity ($L_\star$). Colder belts are located further out. Here, it is important to point out that the radius of a dust belt inferred by the SED modeling via the following classical equation

$$r_{\rm BB} \;=\; 1\ {\rm au} \left(\frac{T_{\rm BB}}{278\ {\rm K}}\right)^{-2} \left(\frac{L_\star}{{\rm L}_\odot}\right)^{1/2} \tag{1.3}$$

is often an underestimation of the observed radius of a dust belt, because dust belts are not perfect blackbody (BB), in particular the small grains. Multiplying the blackbody radius by a correction factor $\Gamma_{\rm BB}$ depending on the stellar luminosity and empirically calibrated (Pawellek et al., 2014; Pawellek & Krivov, 2015) offers a better estimate of the disk radii, even though still degenerate.

Contrary to these estimations, interferometry and direct imaging of circumstellar disks provide their true radius. Regarding optical and near-infrared observations, these methods are sensitive to the scattering of the stellar light on the (hot) dust particles regarding. In mid-infrared to millimeter observations, they are sensitive to the thermal emission of the (warm to cold) dust. In addition, interferometric or direct imaging observations at a given wavelength will be sensitive to grain sizes similar to this wavelength. Regarding observations sensitive to thermal emission of dust grains, they would also be sensitive to dust that has a temperature close to the temperature of a blackbody that peaks at this wavelength, and so probe a given radial region from the star (Wyatt, 2008). This can be seen as additional constraints on the dust grain properties, but also as observational biases.

The locations of dust belts indicate where materials are available. In particular, millimeter-sized grains are less sensitive to the radiation pressure and therefore trace the location of the parent belt of planetesimals, while smaller dust can be spatially more extended. Most of the disk mass is represented by the largest bodies, even though less numerous. The size distribution of particles is set by the collision cascade, and when it reaches a steady state can be expressed as

$$n(s)\, ds \propto s^{-3.5}\, ds\,, \tag{1.4}$$

[10] see the catalogues of imaged circumstellar disks: https://www.circumstellardisks.org and https://www.astro.uni-jena.de/index.php/theory/catalog-of-resolved-debris-disks.html.

where $n(s)\,ds$ represents the number of bodies with radii between s and $s + ds$ (Dohnanyi, 1969). This steep profiles means that, in scattered light the total surface area is dominated by the smallest grains, and so the brightness of the disk.

In addition, determining grain properties, such as size, porosity and composition, give clues on how planets form by constraining dust growth. For example, by assuming dust properties are sufficiently preserved while they agglomerate to form planetesimals and then when they are released through collisions (which is a strong assumption, see Blum et al., 2022), one could study the dust properties to assess whether the scenario of porous aggregates (which have higher constructive collision rates, see Section 1.3.1), is in practice realistic for dust growth.

The properties of dust particles can be inferred via data analysis. For instance, the scattering phase function of a dust belt can be compared to laboratory experiments for different types of grains to find out the composition, size, shape of dust grains (e.g., see Fig. 5 from Engler et al., 2018). The same kind of analysis can be conducted on the polarized scattering phase function (e.g., see Fig. 15 from Milli et al., 2024). This constrains the theoretical models on the dust growth.

Moreover, knowing the global architecture of circumstellar disks help to constrain where planet formation is successful by studying disk-planet interactions. In protoplanetary disks, disk structures such as gaps or cavities (Keppler et al., 2018) can be due to planets still forming, with gaps in dust and gas a possible hint for gas giant formation. Other structures such as spirals or velocity kinks (Pinte et al., 2018) could be triggered by planets, and be used to infer its position and mass. Figure 1.10 shows different types of structures detected in protoplanetary disks for BAFGKM stellar types, so high to low-mass stars.

The same goes for debris disks. Systems with single or double-belt architectures are prime targets to search for planetary companion(s) in gaps or large cavities that they may clear out, as for the benchmarks systems HR 8799, HD 95086, β Pictoris. The simultaneous presence of planets and dust belts provide sharp constraints on where those planets form and their migration history. In addition, planets shape the morphology of dust belts. Giant planets can smooth the outer edge by exciting the eccentricities of the small bodies in the belt. In the case in which the small bodies were stirred by dwarf planets, they would have low eccentricities, that would result in a sharp outer edge (Marino, 2021). Giant planet can also generate small gaps or pile-up of solids in the belt at their mean-motion resonances (Marino et al., 2018, 2019, 2020). This was also observed around the Sun in the main Asteroid Belt and in the Kuiper Belt owing to the influence of Jupiter (Delgrande & Soanes, 1943) or Neptune, respectively. Besides this, resolving spatially debris disks can also shed light on non-axisymmetric shapes in debris disks such as forks, needles or wings that could be caused by giant impacts and for which the shape depends strongly of the viewing geometry (Lee & Chiang, 2016; Jones et al., 2023). Figure 1.11 illustrates some morphologies of debris disks.

Therefore, studying circumstellar disks, from grain-size to their overall architecture, help to better understand planet formation processes at different scales and their leftovers. This can also constrain the disk-planet interactions.

Yet, we note that observations of circumstellar disks are not exception to the rule, and also suffer from multiple biases.

In general, most studies have been focused on large, bright circumstellar disks, given the resolution and imaging constraints of observational facilities. For example, current spatially resolved debris disks have a fractional luminosity between 10^{-2} and 10^{-5}, much brighter than those of the Asteroid Belt and Kuiper Belt (10^{-7}), see Fig. 1.12. The large, bright protoplanetary ($\leq$ a few Myr) and debris disks (50 Myr–10 Gyr) have both a detection rate of about

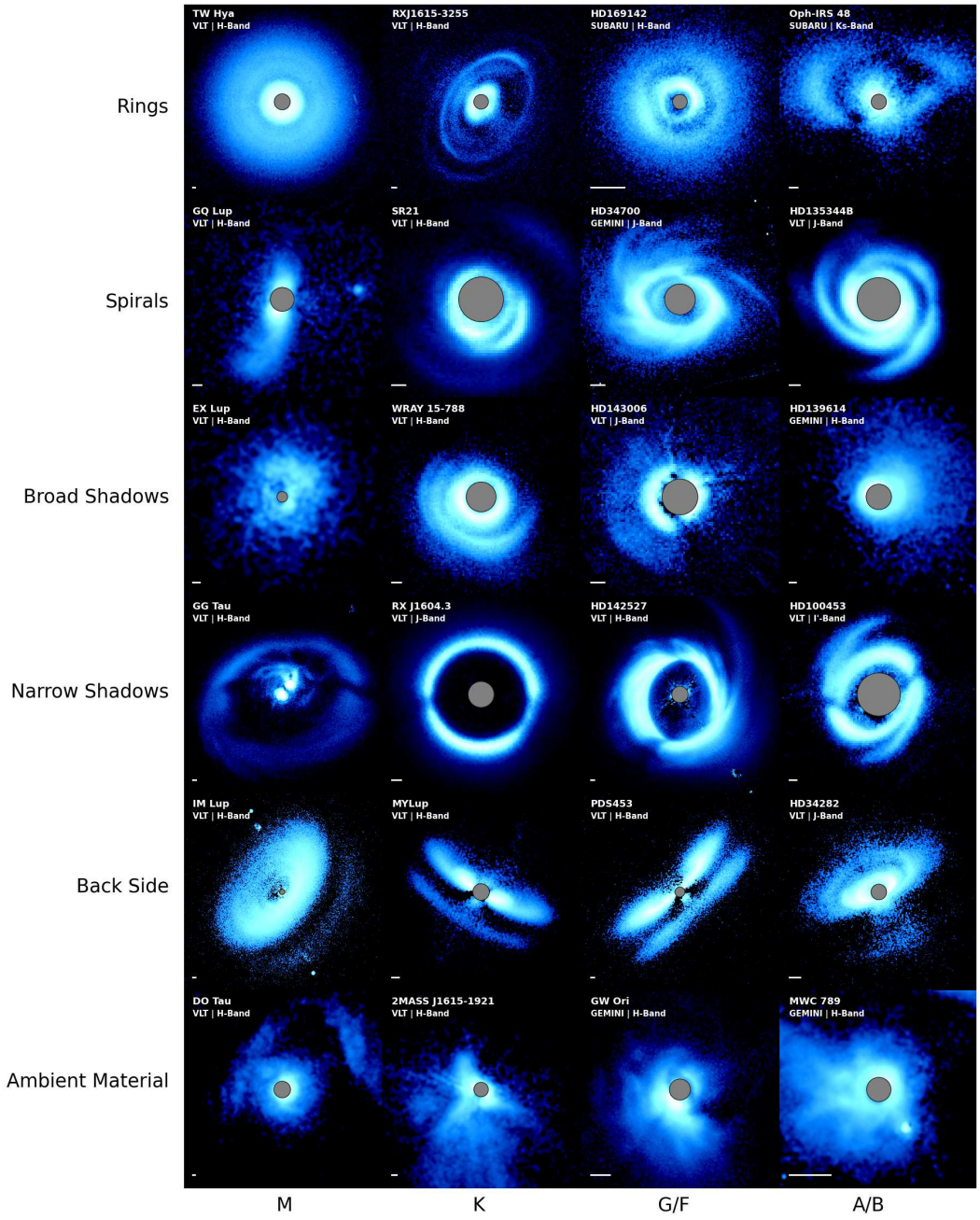

Figure 1.10: Overview of different resolved structures (*vertical axis*) in protoplanetary disks for different stellar types (*horizontal axis*). The white scalebar in the lower left corner of each image corresponds to 50 au. The grey central circles are regions masked by a coronagraph. Figure from the PPVII review Benisty et al. (2023).

References: From upper left to lower right: Rings: TW Hya (Boekel et al., 2017), RXJ1615-3255 (Avenhaus et al., 2018), HD 169142 (Momose et al., 2015), Oph IRS 48 (Follette et al., 2015). Spirals: GQ Lup (Van Holstein et al., 2021), EM* SR 21 (Muro-Arena et al., 2020), HD 34700 (Monnier et al., 2017), HD 135344B (Stolker et al., 2017). Broad shadows: EX Lup (Rigliaco et al., 2020), WRAY 15-788 (Bohn et al., 2019), HD 143006 (Benisty et al., 2018), HD 139614 (Laws et al., 2020). Narrow shadows: GG Tau (Keppler et al., 2020), RXJ 1604.3 (Pinilla et al., 2018), HD 142527 (Hunziker et al., 2021), HD 100453 (Benisty et al., 2017). Visible backside: IM Lup (Avenhaus et al., 2018), MY Lup (Avenhaus et al., 2018), PDS 453 (Benisty et al., 2023), HD 34282 (De Boer et al., 2021). Interactions with ambient material: DO Tau (Huang et al., subm.), 2MASS J1615-1921 (Garufi et al., 2020), GW Ori (Kraus et al., 2020), MWC 758 (Laws et al., 2020).

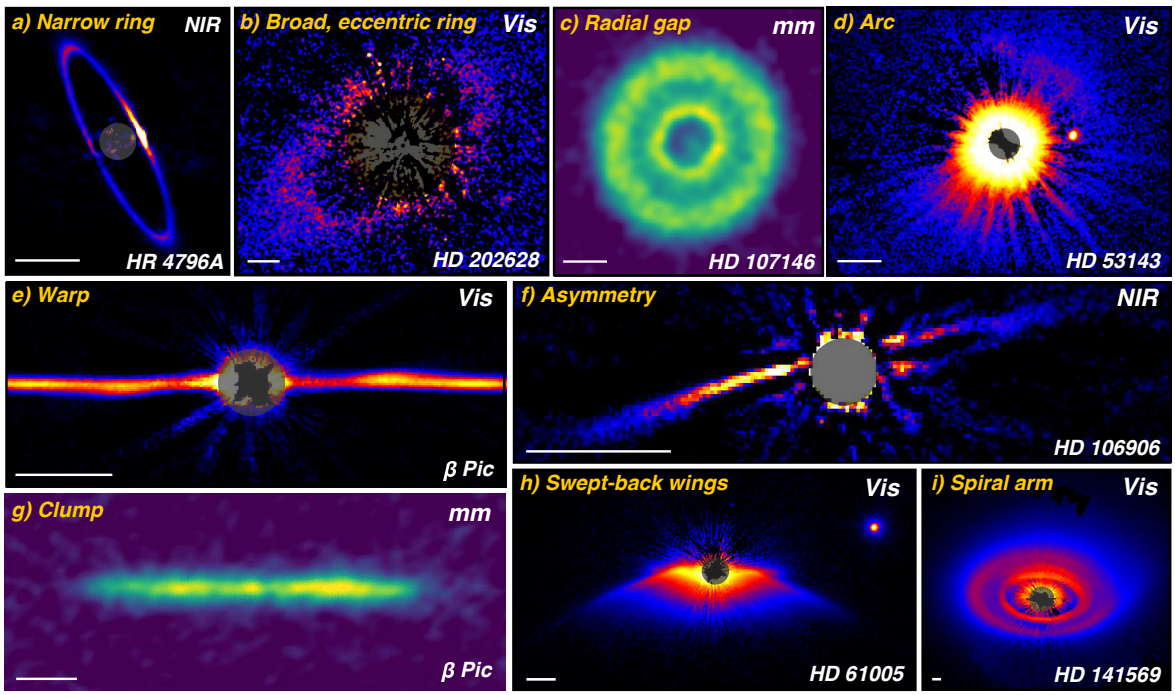

Figure 1.11: Various morphologies of debris disks based on visible (Vis), near-infrared (NIR) and millimeter (mm) observations, probing scattered starlight (Vis, NIR) on the dust grains or their thermal emission (mm). Figure from Hughes et al. (2018).
References: a) Milli et al. (2017b), b) Schneider et al. (2016), c) Marino et al. (2018), d) and h) Schneider et al. (2014), e) Apai et al. (2015), f) Kalas et al. (2015), g) Dent et al. (2014), and i) Konishi et al. (2016).

20–25% (e.g., Najita et al., 2022, and references therein)[11]. Yet, this does not mean that the 75–80% remaining stars are disk-free, because compact protoplanetary disks have been found too, but observed at a small spatial resolution compared to their size (Long et al., 2019). Thus, our view of the complete population of circumstellar disks is biased. In addition, other factors come into play and make the interpretation of circumstellar disk observations complex, because these observations provide only partial information.

For instance, regarding protoplanetary disks, different layers of the disks are probed such as the surface or mid-plane (see Fig. 1.9, *right-part*) depending on the wavelength of observation. Concerning debris disks, observations at a given wavelength will be sensitive to a given type of grain in terms of size (see Fig.), but also in temperature, that result to a grain at at given distance to the star (see Fig. 1 from Wyatt, 2008). However, the distance of the region probed around the star depend on the temperature of the star (and so its spectral type), because at a given distance to the star, the temperature is hotter around a hotter star. For instance, observations at 24 μm can detect in thermal emission a disk of a fractional luminosity equal to 10^{-3} at a distance up to 6 au around a M-star, and up to 300 au around a A-star, (see Fig. 1 from Wyatt, 2008). All in all, the detectability of a debris disk depends strongly of its brightness, its radius, the spectral type of its host star (in thermal emission), and the wavelength of observation.

[11] Younger (20–25 Myr) debris debris from the Beta Pictoris moving group have a higher detection rate (∼75 %, Pawellek et al., 2021).

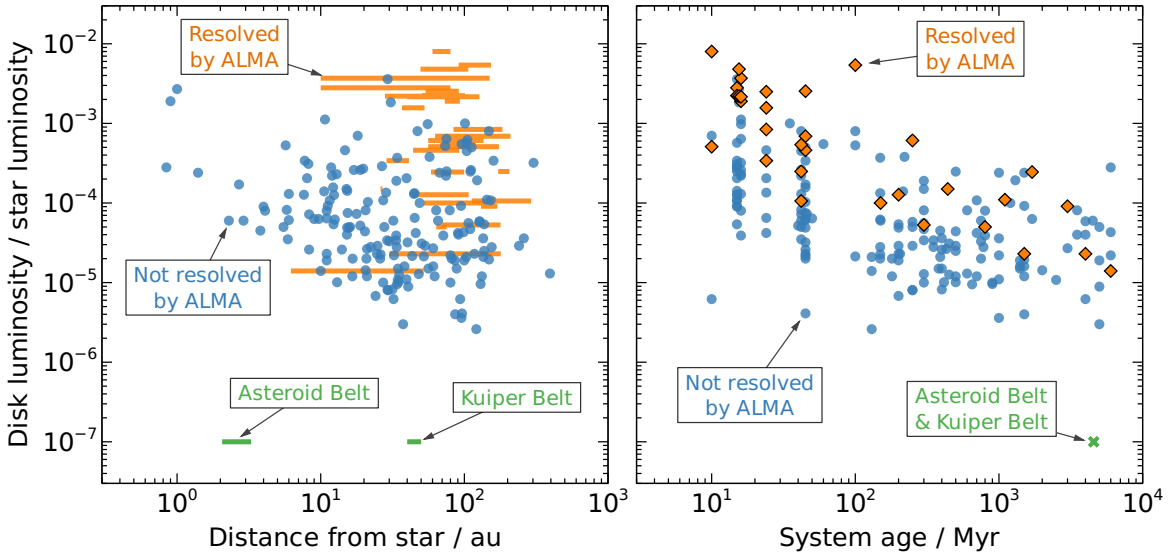

Figure 1.12: Bright and large debris disks are imaged and resolved. The luminosity of debris disks seems to decrease with time. The luminosity of the warm dust (Asteroid Belt) and the cold dust (Kuiper Belt) dust around the Sun is significantly fainter than that of the detected extrasolar disks. Figure from the review Pearce (2024).

Orbital and physical properties of exoplanets

The discovery of very close-in, massive hot Jupiters strongly challenged theories of planet formation and evolution, that had to be refined to explain the existence of such planets. Moreover, the abundance of super-Earths and mini-Neptunes on short orbits, questioned astronomers, because our Solar System does not have such types of planets (see Section 1.1.3).

In multi-planetary systems, *Kepler* discovered a significant population of compact planetary systems, that is to say, planets with close-in, tightly-packed orbits. Furthermore, planets may tend to have similar sizes and regular planet spacing in a given system, following the peas-in-a-pod pattern (Weiss et al., 2018). This statement was argued by Zhu (2020); Murchikova & Tremaine (2020) as a possible consequence of observational biases, that was then rejected (Weiss & Petigura, 2020; Weiss et al., 2022).

Unlike the iconic seven-planet system TRAPPIST-1 (Gillon et al., 2017; Luger et al., 2017), most of the planets detected with *Kepler* are not in mean-motion resonances (Lissauer et al., 2011; Fabrycky et al., 2014). During the stage of protoplanetary disk, protoplanets may migrate inwards due to disk-planet interactions. The inner proto-planet stops at the disk inner edge, and the others at specific locations in resonances, resulting in a planetary resonant chain. When the gas dissipates, the resonant chain may eventually become unstable and break, see Fig. 1.14 (*left*). Planets may then spread by mutual Hill radii instead of orbital period ratio (Izidoro et al., 2017; Pichierri et al., 2019).

While low eccentricities and mutual inclinations of the orbits indicate compact systems configurations (e.g., Weiss et al., 2022), planets with moderate or high eccentricities hint for dynamical instabilities such as planet-planet scattering (Chatterjee et al., 2008; Jurić & Tremaine, 2008; Raymond et al., 2009) and the presence of giant planets (Raymond et al., 2009; Bitsch et al., 2020; Bitsch & Izidoro, 2023), see Fig. 1.14 (*right*).

In addition, measuring the inclination of the spin axis of a planet compared to its orbital plane, i.e., its obliquity, may help to constrain the dynamical history of the planetary system (Harris & Ward, 1982; Tremaine, 1991; Dones & Tremaine, 1993). However, this assumes

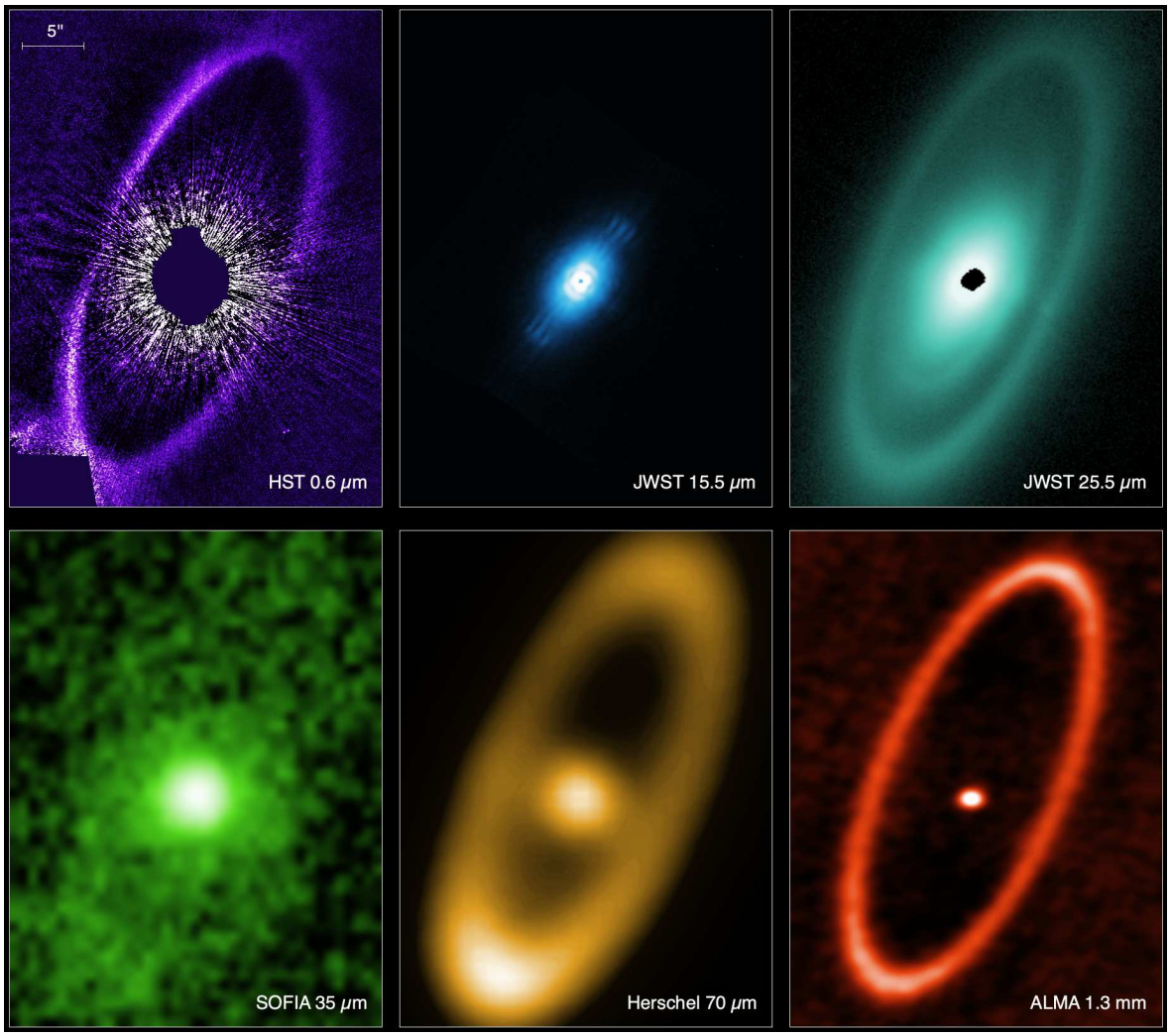

Figure 1.13: Panchromatic observations of the Fomalhaut debris disk. The *HST* observation in the optical probes the scattered starlight on small dust particles, while the mid-infrared to millimeter observations from *JWST*, *SOFIA*, *Herschel* and ALMA probe the thermal emission of larger grains. The inner belt is detected at 15.5 μm, 25.5 μm and somehow at 35 μm (see Adams et al., 2018), the intermediate belt only at 25.5 μm, and the outer belt at 0.6 μm, 35 μm (with data smoothing, Adams et al., 2018), 70 μm and 1.3 mm. Images at 0.6 μm and 15.5 μm suffer in particular of significant artifacts, whereas the image at 35 μm is very noisy. Figure from Gaspar et al. (2023).

that obliquities are primordial[12], which are not expected for instance for the four terrestrial planets in the Solar System (Laskar & Robutel, 1993). As a matter of fact, the presence of the Moon essentially stabilizes the obliquity of the Earth, and so its insulation variations on its surface, that results in a relatively stable climate (Laskar et al., 1993).

Atmospheres of exoplanets

Studying the atmospheres of (exo)planets may highlight how planets form and evolve (e.g., Gautier & Owen, 1983; Owen & Encrenaz, 2003). Comparing the metallicity of a planet to the metallicity of its host star can pinpoint to a formation based on core-accretion if they are different, or on the contrary based on gravitational instability if they are similar. In addition,

[12]Here, primordial means when the Solar System was formed, at least for the four giant planets (Laskar & Robutel, 1993).

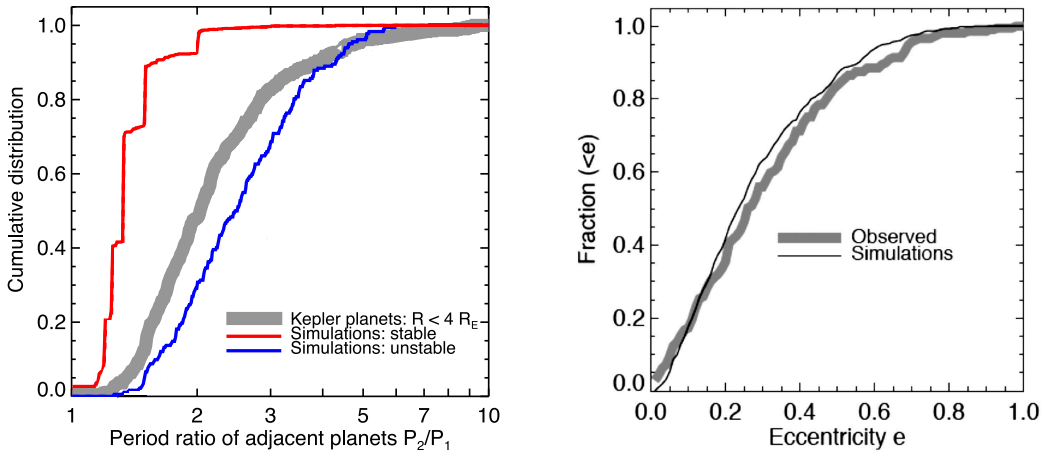

Figure 1.14: Both figures show some of the orbital properties of exoplanets retrieved by the *Kepler* mission. *Left:* Period ratio of adjacent planets from the observations (*Kepler*, gray) or from theoretical predictions in two cases, either for stable simulations (corresponding to adjacent planets that remain in resonant chain, red) or for the unstable simulations (the contrary, blue). Adapted figure from Izidoro et al. (2017). *Right:* Simulations with planet-planet scattering events can reproduce the observed (*Kepler*) cumulative eccentricity distribution of planets. Adapted figure from Raymond et al. (2009).

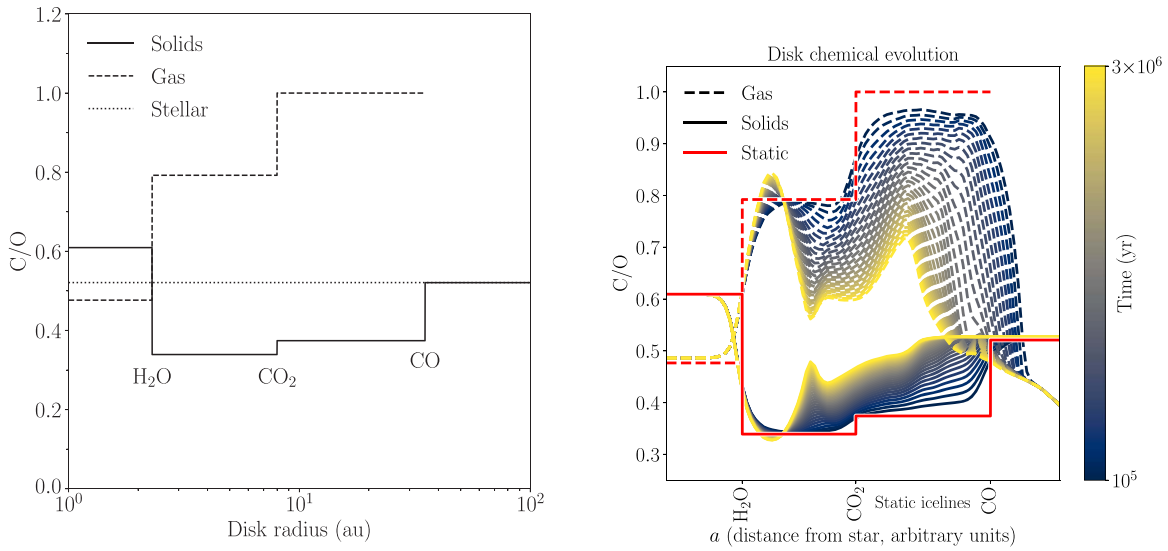

Figure 1.15: Carbon-to-oxygen ratio evolution thought the gaseous disk. Comparison between a disk composition static (Öberg et al., 2011) on the *left*, or evolving with time (Mollière et al., 2022) on the *right*. Both figures are from Mollière et al. (2022), with the first one adaptation from Öberg et al. (2011).

the location of the formation of a planet could be determined by comparing the carbon-to-oxygen ratio (C/O) with the ones expected at different regions in a protoplanetary disk, that is the stage in which most of the gas can be accreted (see Fig. 1.15, Öberg et al., 2011), or other ratios.

Based on estimations of carbon and oxygen abundances and C/O ratio from the atmosphere of a planet, Mollière et al. (2022) investigated how planet formation models could be inverted, to provide constraints on the formation pathway of a planet, such as where it accreted most of its gas and solids. They underline that the classical Fig. 1.15 (*left*) describing the C/O ratio for a static disk must be refined, to be more realistic, for instance by taking into

account the evolution of the disk composition (see Fig. 1.15, *right*) pebble drift and evaporation. However, many processes modify the chemical composition of the disk, such as disk structures (e.g., disk self-shadowing that induces lower temperatures closer to the star, Ohno & Ueda, 2021), surface reactions on grains (such as processing of the volatile gaseous CO in less volatile CO2, e.g., Eistrup et al., 2016), stellar evolution (Miley et al., 2020) or cosmic-ray ionization (Eistrup et al., 2016; Schwarz et al., 2019). Therefore, obtaining full comprehensive inverse models accounting for all processes impacting disk composition, with the corresponding numerical resources to compute them in a relatively reasonable amount of time is likely optimistic. Last, inferring the composition of the internal structure of a planet based on its atmosphere is nevertheless challenging, because connecting both is complex (e.g., the case of Jupiter, Helled et al., 2022).

Regarding planet evolution, observing atmospheric escapes in old (a few gigayear) exoplanets, could be the sign of their recent inward migration, to explain why atmospheric escape is still undergoing. Therefore, late atmospheric escape could indicate late dynamical interactions, such as high-eccentricity migration (Kozai, 1962; Naoz et al., 2012) or scattering-scattering (Rasio & Ford, 1996) events, and so the presence of additional companions in the system.

One other key goal of the community of exoplanetary atmospheric characterization, is searching for bio-signatures, that would hint for the presence of life. Answering the question "Are we alone in the universe?" will obviously raise huge interest that will go beyond the astronomer community. Nevertheless, finding extra-terrestrial life is not that straightforward, and raises philosophical questions such as, what life is, and what would be a proof of life.

Impact of stellar parameters

Several stellar parameters have a major influence on the types of planets that can form. In particular, giant planets are more likely to form around relatively massive stars, that have super-solar metallicity. Such stars have more massive disks, so more solids available for planet formation (Kennedy & Kenyon, 2008; Liu et al., 2019; Schlecker et al., 2022).

The trend regarding stellar metallicity was highlighted by theoretical (Ida & Lin, 2004) and observational (Valenti & Fischer, 2005) work. Recent population synthesis models confirm this, by reporting that the presence of sub-giant (30–100 $M_\oplus$) and giant planets ($>$ 100 $M_\oplus$) is favoured for stars with super-solar ($[Fe/H] > 0.1$) stellar metallicity (Burn et al., 2021).

Concerning stellar mass, the giant planet occurrence rate increases approximately linearly with it for stars up to 2.0 $M_\odot$, based on radial velocity and transit surveys (Johnson et al., 2010; Ghezzi et al., 2018). Still, a few Saturn-mass giant planets have been found and confirmed around very low-mass stars (e.g., 0.12 M_{Jup}, 0.15 M_{Jup} Morales et al., 2019; Lopez-Santiago et al., 2020; Quirrenbach et al., 2022). Such planets around low-mass stars cannot be formed via current population synthesis models (Burn et al., 2021), but these models do indicate that the number of giant planets increased with the stellar masses considered (0.3, 0.5, 0.7 and 1.0 $M_\odot$). Planet formation around the massive ($\geq$ 2 $M_\odot$) stars is challenging within the core-accretion paradigm, due to the shorter lifetime of gaseous disks. However, it could happen via gravitational instability that forms planets faster (e.g., in about 10^4 years for the wide distant planet b Cen (AB)b, instead of 10^6 years via a core-accretion formation, Janson et al., 2021).

1.4 Contribution of my doctoral thesis

In the previous sections, I have shown how planetary system architectures can be diverse, and to what extent they can shed light on how planets form and evolve. In this context, my research focuses on the detailed study of two specific systems and also on a survey of a larger sample to get a statistical view of planetary systems architectures to better understand planet formation and evolution from grain-size to planet-size scales.

In Chapter 3, I present my panchromatic study on the enigmatic, complex young debris disk HD 120326 with both small (30–150 au) and large ($\leq$ 1 000 au) structures. A large range of data is available on this system, including optical (*HST*/STIS), near-infrared (VLT/SPHERE) in polarized and total intensity, and millimeter observations in the dust continuum (ALMA), which I combined to offer a comprehensive view on this system (**?**). In particular, by using the VLT/SPHERE data, I modeled the debris disk to constrain the dust properties of the inner belt.

Debris disks are left-overs from planet formation. Unlike the previous system, where no planet has been discovered yet, but are likely to be there to explain the disk structures, I introduce in Chapter 4 an emblematic system known to host at least one planet and two dust belts. On this young double-belt system, HD 95086, I led an in-depth direct-imaging and spectroscopic characterization of the young gas giant planet, HD 95086 b, lying close to the inner edge of the outer belt (Desgrange et al., 2022a). Additional planets are expected to explain the width of the cavity. This system is to some extent a young, massive analogue to our Solar System, due to its double-belt architecture with giant planet(s) in the large cavity. As massive young companions detected so far, the exoplanet HD 95086 b is under-luminous and red, indicating the presence of dust around it.

Then, in Chapter 5, I focus on systems hosting low-mass planets orbiting close to their host star and already discovered via radial velocity measurements. Such systems are numerous from the *Kepler* mission or the radial velocity data. The motivation of this project was to determine how such low-mass planets, e.g., super-Earths or mini-Neptunes, could have been formed. Did they form close to their host star, despite a possible lack of solids? Or did they form further out, and then migrated inwards due to dynamical interactions with giant planets? To investigate these questions, I led the publication of a pilot survey in direct imaging using VLT/SPHERE and targetting old stars hosting low-mass planets to search for massive companions on wide orbits (Desgrange et al., 2023). The goal was to examine the correlation between the presence of low-mass planets orbiting close to their host star and outer massive companions. A positive, negative or an absence of correlation between both types of planets could indicate how the low-mass planets have formed.

In parallel of these three research projects using mostly the VLT/SPHERE instrument, I contributed to investigate how the SPHERE performances to detect and characterize exoplanets could be boosted with a medium-spectral resolution integral-field spectrograph. This work was carried out in the context of the SPHERE upgrade, named SPHERE+, and the SPHERE+ consortium. There are strong connections between SPHERE(+), and the ELT instruments, both on astrophysical and instrumental perspectives. I describe them later in the manuscript.

Let's now dive in the concepts and methods to directly image exoplanets and disks, which is the subject of the Chapter 2.

Chapter 2

Direct imaging of exoplanets and disks: concept and methods

In this chapter, I describe the methodology I used to image circumstellar signals, such as exoplanets and disks. First, in Section 2.1, I give a brief overview of high contrast facilities, both ground- or space-based. Then, in Section 2.2, I explain the necessary steps to reach the sensitivity to image exoplanets and disks. This requires high-angular resolution (Section 2.2.1), high-contrast imaging (Section 2.2.2) and specific data processing techniques using dedicated strategies of observation (Section 2.2.3). Finally, in Section 2.3, I shed light on the high-contrast imaging SPHERE instrument at the VLT, which I have mostly used during my Ph.D. for my research.

Contents

2.1 High-contrast ground- and space-based facilities

In this Section, I give some context about existing high-contrast imagers able to directly image exoplanets and circumstellar disks.

High-contrast imagers in space do not suffer from the effects of the Earth's atmosphere, which deforms the wavefront of the light and degrades the angular resolution (see Section 2.2.1). In addition, they do not suffer from the absorption of the Earth's atmosphere. Thus, they can observe celestial objects in spectral ranges unaccessible from the ground, that is to say, in γ rays, X rays, ultraviolet and in the mid- or far-infrared. In addition, the origin of spectral features in spectra acquired in space cannot be confused between true astrophysical signal (either the exoplanet itself or its host star), and terrestrial absorption from the Earth's atmosphere. Furthermore, space observations are more stable than ground-based observations. For instance, uncertainties on observables, such as the flux of an object, are smaller due to the absence of the constantly evolving atmosphere of the Earth.

However, space telescopes are long-term, expensive projects. For instance, initial designs for the *James Webb Space Telescope* (*JWST,* Gardner et al., 2006) started in 1996, whereas *JWST* was launched on December 25, 2021, for a total cost of 10 billion of United States Dollars (USD). In addition, most of the time, no repairs are possible once the space telescope is launched. The exception is the five repair (or instrumentation update) missions carried out on the *Hubble Space Telescope* (*HST*). These missions were possible due to the relative proximity of *HST*, which is located on a 590-km altitude orbit, and because maintenance missions on the *HST* using space shuttles were planned from the beginning. However, such expensive repair missions would not be conceivable before a long time for telescopes located at the Lagrange 2 point (L2, 1.5 million of kilometers) such as the *JWST*. Therefore, on-board instrumentation must be highly reliable. Consequently, when finally operated, space instrumentation can be outdated compared to what is in parallel developed, tested, and used on the ground-based facilities. Last, it is difficult and expensive to send in space a telescope with a large primary mirror. To date, *JWST* has the largest (6.2 m) primary mirror ever sent to space. It required a fine-tuned design and strategy: *JWST* was launched with the primary mirror folded, before the mirror was deployed once *JWST* had reached its final L2 location.

In my field of research, direct-imaging of exoplanets and circumstellar objects, the space facilities of particularly interest are *IRAS* (*InfraRed Astronomical Satellite*, Neugebauer et al., 1984), *Spitzer* (Werner et al., 2004), *Herschel* (Pilbratt et al., 2010), *WISE* (Wright et al., 2010), *HST*, *JWST*, and the forthcoming *Nancy Grace Roman Space Telescope* (Spergel et al., 2013) that will be launched in 2027.

In brief, *IRAS* mapped the sky and identified stars with infrared excess interpreted as cool dust surrounding stars. In particular, famous discoveries of *IRAS* are the Fabulous Four debris disks: Vega (Aumann et al., 1984), Fomalhaut, Beta Pictoris and Epsilon Eridani (e.g., Gillett, 1986; Backman & Paresce, 1993). After learning *IRAS* results, Smith & Terrile (1984) observed and resolved the Beta Pictoris debris disk, making this system the first spatially resolved debris disk ever. Later, *Spitzer*, *Herschel* and *WISE* missions helped to identify stars hosting debris disks, to remove spurious ones, and to derive minimum occurrence rates for debris disks.

Regarding (still) working space facilities, *HST*, launched in 1990, has imaged a large number of debris disks, revealing in particular halos of small particles that are pushed away due to stellar pressure and winds. Regarding *JWST*, science results have just recently started to be released. To name a few, *JWST* already imaged and resolved for the first time several disk structures, such as the inner disk in the iconic Fomalhaut system, revealing a new intermediate belt (Gaspar et al., 2023), the inner belt of the benchmark HR 8799 system (Boccaletti et al., 2024), or the so-called cat's tail in the emblematic Beta Pictoris system (Rebollido et al.,

2024). In the near future, the *Nancy Grace Roman Space Telescope* will achieve unprecedented detection limits with its coronagraphic instrument (CGI), by being sensitive in the optical to exoplanets one billion times fainter than their host star. The CGI instrument is a technology demonstrator for the Habitable Worlds Observatory (HWO), that should be launched in 2040s+. The Habitable Worlds Observatory will be fine-tuned to search for and image exo-Earths located in the habitable zones of their stars, thus where liquid water could exist.

Ground-based facilities are complementary to space-based facilities in many ways. First, facilities on the ground offer more flexibility to test new instrumentation, technologies and new strategies of observation that may even require fine-tuning during the observation (e.g., Potier et al., 2020, 2022). Second, it is less expensive to build a ground-based telescope than a space-based one. In addition, space telescopes have a limited lifetime, depending on their fuel. Finally, even if there were not financial constraints, some astronomical facilities would simply not be feasible in space given the current state of know-how. However, they could be built on the ground, as for example, the extremely large telescopes.

Table 2.1: List of current ground-based high-contrast imagers on 8–10-m class telescopes. For each high-contrast instrument, I indicate its first light, spectral range (λ) and the name of the adaptive optics (AO) system if it is a separate instrument. Some instruments do not have a particular reference paper. (*) The GPI instrument currently undergones its upgrade GPI2.0, and will be then installed on Gemini North.
Notes: Acronyms of the different instruments are: NICI: Near Infrared Coronagraphic Imager; NIRSPEC: Near-InfraRed Spectrograph; NIRC2: Near-InfraRed Camera; ALTAIR (Christou et al., 2010); NIRI: Near-InfraRed Imager; GPI: Gemini Planet Imager; SCExAO: Subaru Coronagraphic Extreme Adaptive Optics (Jovanovic et al., 2015); HiCIAO: High-Contrast Coronagraphic Imager for Adaptive Optics; CHARIS: Coronagraphic High Angular Resolution Imaging Spectrograph; FLAO: First light adaptive optics (Esposito et al., 2012); SOUL: Single conjugated adaptive Optics Upgrade for LBT (Pinna et al., 2016); LMIRCam: LBT Mid-InfraRed interferometric Camera; SHARK-NIR/VIS: System for High contrast And coronagraphy from R to K at NIR/VIS bands; SPHERE: Spectro-Polarimetric High-contrast Exoplanet REsearch.

Telescope	AO	Instrument	First light	λ (μm)	Reference paper
Northern hemisphere					
Keck		NIRSPEC	02/2000	1.0–5.5	McLean et al. (1998)
		NIRC2	07/2001	1.0–4.8	
		OSIRIS	02/2005	1.0–2.4	Larkin et al. (2006)
Gemini N.	ALTAIR	NIRI	2003	1.1–2.5	Hodapp et al. (2003)
Subaru	AO188/SCExAO	HiCIAO	12/2008	0.8–2.5	Hodapp et al. (2008)
	SCExAO	CHARIS	07/2016	1.2–2.4	Groff et al. (2016)
LBT	FLAO/SOUL	LMIRCam	05/2011	1.0–5.0	Skrutskie et al. (2010)
	SOUL	SHARK-NIR	01/2023	1.0–1.7	Farinato et al. (2015)
	SOUL	SHARK-VIS	10/2023	0.4–0.9	Pedichini et al. (2017)
Southern hemisphere					
Gemini S.		NICI	02/2007	1.1–5.0	
		GPI(*)	11/2013	1.1–2.3	Macintosh et al. (2015)
VLT		SPHERE	05/2014	0.5–2.3	Beuzit et al. (2019)
		ERIS	04/2022	1.1–5.0	Davies et al. (2023)

Current high-constrast imagers on large (8–10-meter class) telescopes are listed in Table 2.1. A review of post-2000 high-contrast instruments is available in Chauvin (2018),

and in particular addresses their constraints on planet formation and evolution models, exoplanet demographics and planetary architectures.

During my Ph.D., I have mostly used the VLT/SPHERE high-constrast instrument (see Chapters 3, 4, and 5, which include the articles Desgrange et al., 2022a, 2023; **?**). I also got deeply interested in the ground-based LBT/SHARK-NIR and LBT/LMIRCam and space-based *HST*/STIS, *JWST*/NIRCam, and *JWST*/MIRI facilities. In particular, I submitted proposals with all these facilities to obtain telescope time and initiate future research projects on which I intend to work on during my post-doctoral position. I was granted telescope time as co-PI on *JWST* (PI: Elisabeth Matthews; ID: GO 5229), and as PI on ESO (ID: 109.23F2, 113.26E1, 114.276D) and LBT (ID: MPIA-2024A-006, MPIA-2024A-007, MPIA-2024B-001) facilities, see Appendix B.

2.2 Reaching the sensitivity to image exoplanets and disks

Here, I describe the three main steps to reach the sensitivity to image circumstellar signals such as exoplanets and disks. These steps are illustrated in Fig. 2.1 for a ground-based instrument. In Section 2.2.1, I present the first step, which is reaching a high-angular resolution limited by diffraction (and not by the turbulence of the atmosphere) using an adaptive optics system. The next step is to remove most of the stellar light by using a coronagraph, see Section 2.2.2. Eventually, I end up in Section 2.2.3 with the last step, data processing, which is crucial to remove even more stellar light and detect exoplanets and disk.

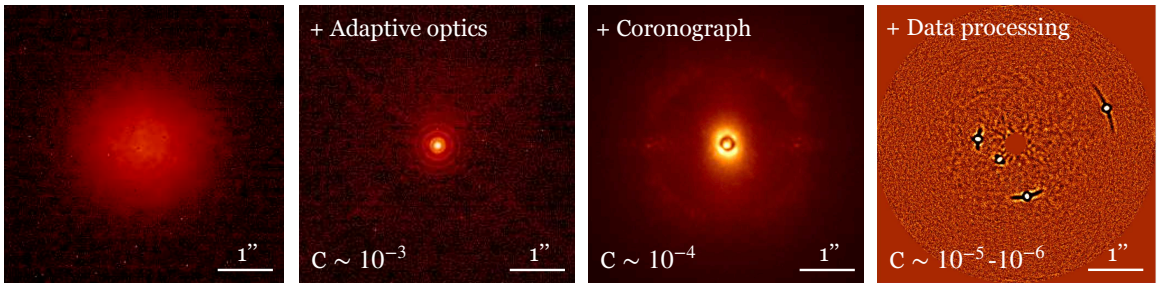

Figure 2.1: Principle of high-constrast imaging and high-angular resolution instrument. From *left* to *right*: typical image of a star from a ground-based instrument without an adaptive optics system; addition of an adaptive optics system to work at high angular resolution; addition of a coronagraph to remove the stellar halo of the star; and finally post-processed HR 8799 data. Credits: the SPHERE commissioning team and Faustine Cantalloube.

2.2.1 High-angular resolution using adaptive optics

Since exoplanets and circumstellar disks are located very close to their host star, high angular resolution is required to distinguish them from their star, as briefly written in Section 1.2.1.

In the diffraction regime, the angular resolution is determined by λ/D, where λ is the wavelength and D the diameter of the telescope. For instance, the diameter of the primary mirror of a unit telescope is 8.2 m at Paranal, where the VLT is located. Thus, the angular resolution is 0.015“ at 600 nm (visible). However, the diffraction regime is not achievable nominally from the ground, because the turbulence in the atmosphere perturbs the incoming stellar wavefront. Consequently, ground-based observations are limited by the turbulence and are not diffraction-limited: we say they are seeng limited. They have a resolution of λ/r_0, scaling as $\lambda^{6/5}$, where r_0 is the Fried parameter, which scales with $\lambda^{6/5}$, and that can be interpreted as the coherence length of the atmosphere. For instance, the coherence length

is typically 15 cm at 600 nm at Paranal in Chile, where is located the VLT, resulting in an angular resolution of 2.2", hence 55 times poorer. To summarize, the larger the primary mirror of a telescope, the more it receives photons from the celestial object. Nonetheless, in the seeing-limited regime, beyond a given diameter of the primary mirror that corresponds to r_0, a larger primary mirror does not increase anymore the angular resolution.

This is why high-contrast imagers are equipped with an adaptive optics (AO) system, that aims to restore the angular resolution allowed in the diffraction regime. In practice, an AO system is composed of a wavefront sensor (WFS), a control system being a real-time computer (RTC) and a deformable mirror (DM), see Fig. 2.2. First, the aberrations of the incoming wavefront are measured by the wavefront sensor. A widely used wavefront sensor is the Shark-Hartmann, that is an array of lenslets. The ideal sampling of the array of lenslets is set by the value of the Fried parameter r_0, and correspond to $\left(\frac{D}{r_0}\right)^2$ lenslets. Each lenslet makes an image of a star, whose centroid will be shifted due to the distorted wavefront. The displacements of each stellar centroid are derived by a real-time computer. They are corrected in a closed loop with a deformable mirror. Instead of being a flat surface, the deformable mirror can locally change of shape thanks to an array of actuators that push and pull the deformable mirror.

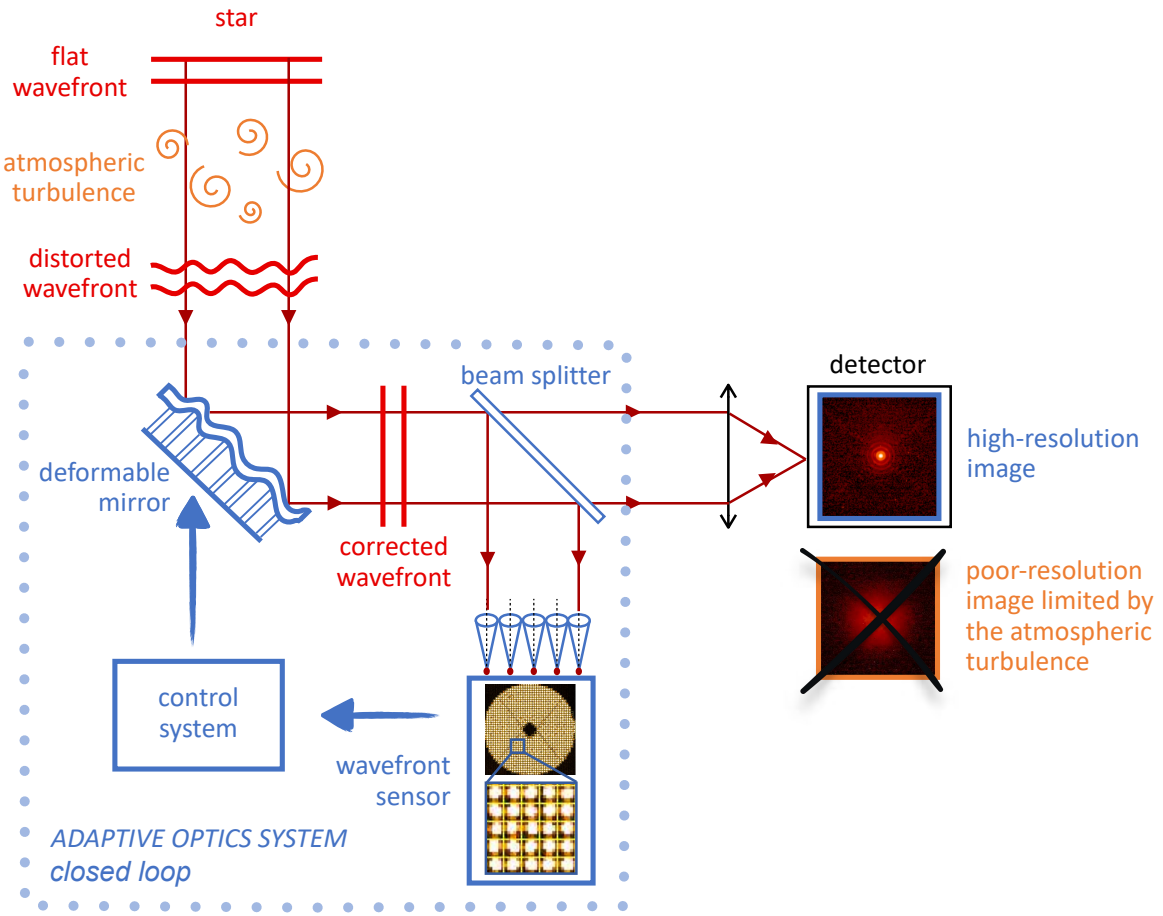

Figure 2.2: Sketch illustrating the principle of an adaptive optics system. In this set-up, there is no coronagraph. However, a coronagraph system such as the APLC (see Fig. 2.4) could be added between the beamsplitter and the lense that focuses the beam on the detector. Credits: Small square-images come from the SPHERE commissioning.

Another crucial ingredient of an effective AO system is the coherence time of the atmosphere, noted τ_0, and that is linked to r_0 via the relationship

$$\tau_0 \;=\; 0.314 \;\times\; \frac{r_0}{v_{\text{wind}}}\,, \tag{2.1}$$

where v_{wind} is the mean wind speed weighted by the turbulence profile along the line of sight (Roddier, 1981). The AO system must correct the aberrated wavefront faster than acts the turbulence of the atmosphere, to result in a correction still valid. Typically, at Paranal, the coherence time of the atmosphere is 2 ms (Fig. 2.3), requiring the sampling frequency of the AO system to be faster than 1 kHz to avoid the servolag error.

An effective correction of an aberrated wavefront of absolute star results in a quasi-flat stellar wavefront. In terms of images, instead of being a fuzzy large spot, the image of a star by the optical system (telescope+instrument) has a rather stable Airy diffraction pattern, see Fig. 2.1 (second image). This point-source image through an optical image is commonly called the point spread function (PSF). The size of the PSF is referred as the full-width at half maximum (FWHM) and is equal to the angular resolution, i.e., λ/D in the diffraction regime. A key parameter to assess the AO correction is the strehl ratio, noted Sr. This is the ratio of the peak on-axis intensity of the PSF of an aberrated wavefront, to that of a reference unaberrated wavefront.

Logically, the strehl ratio depends on the quality of the AO correction, which is related to the instrument and the observational conditions, such as the seeing and the coherence time of the atmosphere, and the brightness of the target star, see Fig. 2.3. The strehl ratio is higher for smaller seeing, higher coherence time, and brighter stars. For instance, if the star is fainter, the WFS needs more time to acquire enough photons to estimate well the centroid of the star, and so apply an appropriate AO correction. For long ($\geq$ 6 ms) coherence time and very bright (V $<$ 5 mag) stars, the strehl of SPHERE can be higher than 90% (Fig. 2.3).

Historically, the first AO-equipped instrument tested on sky was COME-ON, at the 1.52 m at the Observatoire de Haute-Provence in 1989 (Rousset et al., 1990) and afterwards on the 3.6 m at La Silla in Chile. The AO prototype COME-ON (1989-1992) had 19 actuators with a correction frequency of 100 Hz, while its upgraded versions COME-ON+ (1992-1993, Rousset et al., 1994) and ADONIS (1993-2001, Hubin et al., 1994) had 52 actuators with a correction frequency of 200 Hz. Going to larger telescopes, from the ESO 3.6-meter telescope to the VLT (8.2-meter), the first- and second-generation instruments NaCo (2001-2019, Rousset et al., 2003; Lenzen et al., 2003) and SPHERE (2014-, Beuzit et al., 2019) have respectively 185 and 1 377 actuators and correction frequency of 444 Hz and 1.3 kHz, increasing significantly high-contrast imaging performance. Yet, Fig. 2.3 shows that SPHERE is still sub-optimal for the mean of the observational conditions at Paranal ($\tau_0 \sim 2$ ms). Therefore, the AO system of SPHERE (named SAXO) has to go faster to work optimally in typical observational conditions. Hence, its forthcoming upgrade, SAXO+, which will reach a correction frequency of 3 kHz (Boccaletti et al., 2020). SAXO+ will add a second AO stage in SPHERE, consisting in a pyramid wavefront sensor and a more sensitive detector. In addition, SAXO+ will be sensitive at the beginning of the near-infrared spectral range, to be more optimal on fainter, redder stars. The SAXO+ upgrade (on-sky in 2026-2027) is considered as a technology demonstrator of the PCS second-generation instrument on the ELT.

Besides, not only instruments can be equipped of adaptive optics, but also telescopes. The M4 mirror of the ELT, is a deformable mirror with 5 352 actuators. In any case, large telescopes must be equipped with active optics technology to tackle distortion forces such as the wind, sag, thermal expansion, telescope axis deformation, this latter depending on the pointing direction. The frequency of the active optics correction is much slower, of the order

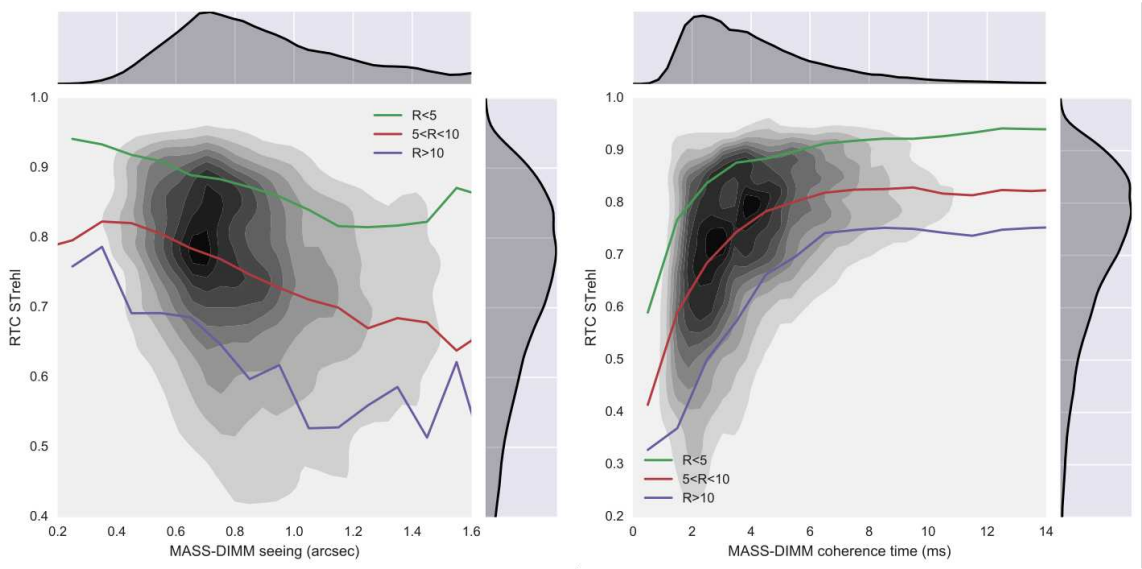

Figure 2.3: Performance of the strehl estimated by SPARTA (real-time computer of the adaptive optics system of SPHERE) as a function of the seeing (*left*) or coherence time of the atmosphere (τ_O, *right*) measured by the MASS-DIMM at Paranal in Chile, where is located the VLT. Each curve corresponds to a given magnitude range of the stars (R<5 mag: very bright,$5<$R<10 mag: medium, R>10 mag: faint). For a given brightness of star, the strehl ratio increases when the seeing decreases, or when τ_0 increases. The strehl ratio is higher for bright stars than faint ones. The typical strehl, seeing and τ_0 are between about 0.7 and 0.8, 0.6" and 0.8", and 2 and 5 ms, respectively. Figure from Mouillet et al. (2018).

of the hertz. Active optics correction ensures that large, non-self-rigid mirrors keep an optimal shape through the observation, and is a pre-requisite for the success of the observations.

To summarize, adaptive optics restore the angular resolution of large ground-based instruments to what would be achievable from space, beyond the atmosphere of the Earth. Figure 2.1 shows that using adaptive optics enables the detection of objects a thousand times fainter than the star. In other words, objects that have a contrast of 10^{-3}. Yet, young, massive giant planets are fainter, typically with contrast of 10^{-5}–10^{-6}. Additional ingredients are necessary to achieve their direct detection.

2.2.2 High-contrast imaging using a coronagraph

High-contrast imagers are equipped with coronagraphic masks, that remove about ten percent of the remaining light, resulting in an achievable contrast of about 10^{-4}.

Historically, the first coronagraph was invented and used by the French astronomer Bernard Lyot in 1931. This coronagraph, also known as the "Lyot coronagraph" is relatively intuitive. It was used to observe the solar corona by masking the solar photosphere, as does the Moon during a total eclipse. Since then, different types of coronagraphs have been developed, with different goals.

Coronagraphs can be based on pupil apodization and/or focal plane masks, or interferometers. Pupil apodization may be from amplitude, phase, or phase-induced amplitude, whereas focal plane masks apply to amplitude and/or phase (e.g., Table 2 from Ruane et al., 2018). Several aspects may be considered to evaluate the performance of a coronagraph:

its spatial coverage, which is defined by its inner and working angles (IWA and OWA, respectively)[1], the spectral bandwith over which it will work, and its resilience to low-order aberrations of the wavefront (Mawet et al., 2012).

For instance, the four-quadrant phase mask (FQPM) was designed to improve the broadband performance and robustness to tip-tilt errors, and it has a small IWA of λ/D. Nonetheless, it was only marginally used on the VLT/SPHERE (but is successful on *JWST*, e.g., Boccaletti et al., 2024), because it is very sensitive to non-common path aberrations (NCPAs), that are not corrected on SPHERE. The NCPAs consist in aberrations that are not seen by the AO system, and thus, which cannot correct them.

On the other hand, the apodized pupil Lyot coronagraph (APLC, Aime et al., 2002; Soummer et al., 2003), the coronagraph most used on SPHERE, has a higher IWA (3–4 λ/D), but overall performs better. The APLC is composed of an apodizer, a focal plane mask and a Lyot stop, see Fig. 2.4. After passing by the adaptive optics system, the corrected collimated beam goes through an apodizer, which removes the diffraction rings and smoothes the sharp edges of the telescope pupil. Then, it goes through a lens that focuses the beam on the focal plane mask. The on-axis stellar light, is blocked or diffracted beyond the nominal pupil, that is further blocked by a Lyot stop located in a pupil plane, see Fig. 2.4. The Lyot stop has a wider central obstruction, wider spiders and a smaller outer diameter. Eventually, a high-contrast image is formed and captured on the detector (see the third image in Fig. 2.1).

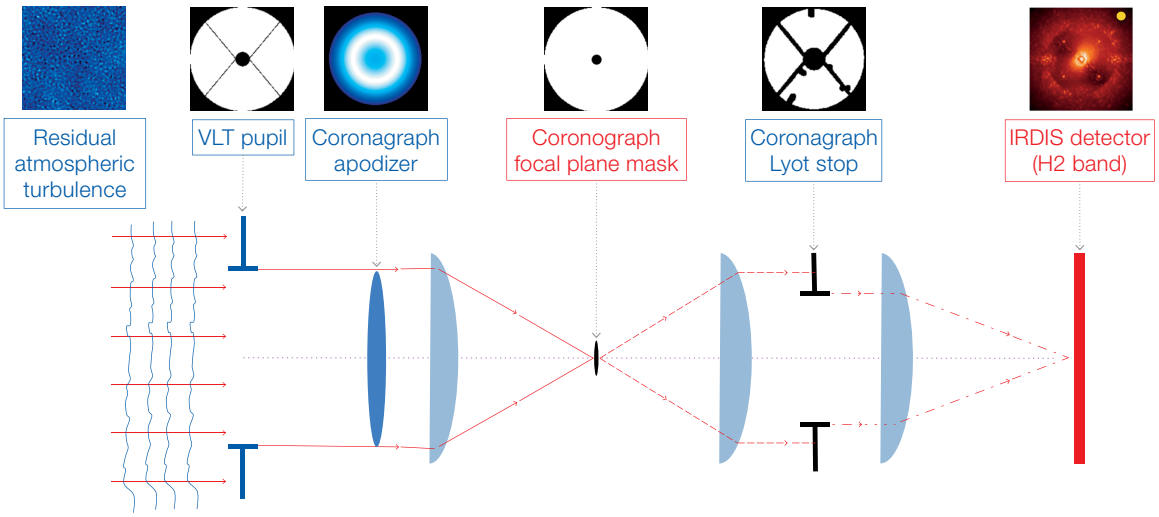

Figure 2.4: Sketch showing the set-up of the apodized Lyot coronagraph (APLC) on the VLT/SPHERE instrument. In the pupil planes (in blue) are shown the residual atmospheric turbulence (in phase and amplitude), the VLT pupil, the coronagraph apodizer and Lyot stop. In the focal planes (in red) are located the coronagraph focal plane mask and the SPHERE/IRDIS detector, on which is shown a final coronagraphic image. Figure from Cantalloube et al. (2019).

Here, it is important to underline that the coronagraph system is efficient to remove most of the stellar light, because of the high-angular resolution achieved by the AO system. Indeed, in the diffraction regime, 80% of the collected stellar energy is inside a small and sharp circular region of the PSF (radius of λ/D), while the remaining 20% is spread over the detector (Galicher & Mazoyer, 2023).

[1]The IWA is generally more crucial than the OWA to image exoplanets, even though some coronagraphic masks can reach deeper sensitivity at close separations (e.g., the asymmetric shape pupil coronagraphs on LBT/SHARK-NIR) than others (e.g., the symmetric Gaussian Lyot coronagraph on the same instrument), but they may have a smaller OWA (e.g., 300 mas instead of being limited by the edge of the field of view, which is $18 \times 18''$ for SHARK-NIR). This must be taken into account when defining the observing strategy of a target.

2.2.3 Strategies of observation and data processing

In spite of achieving better detection sensitivity thanks to the AO and coronagraph systems, circumstellar signal are still too faint or affected by too many stellar artifacts ("speckles") to enable their detection and/or characterization.

To remove even more stellar residuals, data processing plays a critical role. Data processing of high-contrast images is divided in two steps, called pre-processing and post-processing. In general, most of the data of a sequence of observation consists in several coronagraphic images of the science object of interest, which are acquired at different times, and potentially simultaneously at different wavelengths with a dual-band imager or an integral field spectrometer. On this dataset, pre-processing does relatively standard operations such as background subtraction, flat-field correction, bad-pixel correction, a re-centering of the frames, correction of the cross-talk (if relevant Greco & Brandt, 2016). It results in a four dimension dataset, with spatial, spectral and temporal dimensions (x, y, λ, t).

Afterwards, the post-processing step aims to separate the signal of the circumstellar materials (e.g., exoplanet, disk) from the stellar residuals, and results in a data cube (x, y, λ). Although different post-processing methods exist to remove the stellar light residuals, all are based on the same concept that takes advantage of the *diversity* between the properties of the star and the circumstellar signals. Applying a given post-processing technique often requires a dedicated strategy of observation.

Below, I describe the main techniques on which post-processing algorithms are based, such as Angular Differential Imaging (ADI, Marois et al., 2006), Spectral Differential Imaging (SDI, Racine et al., 1999; Sparks & Ford, 2002), Polarization Differential Imaging (PDI) and Reference Differential Imaging (RDI). In particular, regarding the ADI technique, I give more details on the different types of ADI-based algorithms, as they are many of them. I do not describe the Coherent Differential Imaging (Baudoz et al., 2012), although an intensive field of research (e.g., Potier et al., 2022).

During my Ph.D., I have been interested in the four first techniques. I used the techniques ADI and SDI in Desgrange et al. (2022a, 2023), ADI and PDI in Desgrange et al. (2025, subm.). I adopted a strategy of observation using a reference star to do RDI for future research projects that were granted telescope time, on my PI ESO/SPHERE accepted program 113.26E and LBT/SHARK-NIR and LMIRCam program MPIA-2024-006, for which some of the data have already been acquired, and on my co-PI JWST/MIRI accepted program GO 5229 (observations scheduled between January and March 2025).

Angular Differential Imaging

The ADI technique takes advantage of the angular diversity of a long enough sequence of observation when acquired in the pupil-tracking mode. In more details, an observation can be acquired either in a pupil-stabilized mode or in a field-stabilized mode. In the pupil-stabilized mode, the field of view rotates around the star with the parallactic angles through the full sequence of observation. As for the stellar light residuals, they are (quasi-)static during the observation, because most of the wavefront errors are fixed with respect to the pupil configuration. On the contrary, in the field-stabilized mode, a given location on the detector will receive the light coming from a same location in the field of view through the full sequence of observation, but for different pupil configurations. For instance, for a given field-stabilized observation, the photons thermally emitted by an exoplanet will always fall on the same pixels of the detector.

Consequently, one simple way to implement an ADI-based algorithm is to subtract the median frame of the observation sequence to each frame ("classical ADI"), see Fig. 2.5 (*top-left*). The median frame can be considered as the model of the stellar halo. Other standard

algorithms exist, such as TLOCI or PCA. Both algorithms are based on a mathematical approach involving singular value decomposition (SVD) of the covariance matrix. Regarding TLOCI (Template Locally Optimized Combination of Images, Lafreniere et al., 2007; Marois et al., 2013), the modeling of the speckle pattern is optimized in a larger region than the region of interest, to minimize the residuals. Between both regions, there is a small gap of 0.5 FWHM to avoid putative self-subtraction effects, see Fig. 2.5 (*top-right*). As for PCA, (Principal Component Analysis, Amara & Quanz, 2012; Soummer et al., 2012), the SVD is truncated, with only the most significant modes (also called components) kept. An example of such components are shown in Fig. 2.5 (*bottom*). One may often interpret the first principal components. For instance, for a full frame PCA, the first component represents the overal brightness variation of the post-coronagraphic PSFs, whereas the second and third components correspond to horizontal and vertical variations caused by small errors in the centering of the star behind the coronagraph (Bonse et al., 2024). In addition, different versions of PCA exist. The PCA algorithm can be computed either on the full frame or more locally in annuli. PCA can be iterative, to limit self-subtraction effects, by estimating and removing the astrophysical signal from the speckle-field estimation. This finally results in a better recovery of extended features (e.g., results from the algorithm GreeDS standing for Greedy Disc Subtraction from Pairet et al. (2021) or the iterative PCA "I-PCA" algorithm from Juillard et al. (2024)).

Furthermore, cutting-edge algorithms based in particular on inverse-problem methods were developed. Some are tuned to retrieve point-like sources by tracking them in the image cube, such as ANDROMEDA (ANgular Differential OptiMal Exoplanet Detection Algorithm, Cantalloube et al., 2015) and PACO (PAtch COvariances, Flasseur et al., 2018, 2020). Others were designed to retrieve extended features, such as MAYONNAISE (Morphological Analysis Yielding separated Objects iN Near infrAred usIng Sources Estimation, Pairet et al., 2021), REXPACO (Reconstruction of EXtended features by PAtch COvariances, Flasseur et al., 2021) or MUSTARD (Juillard et al., 2023).

To conclude, a large variety of ADI-based post-processing algorithms exist, with a comparison of some of them carried out in the Exoplanet Imaging Data Challenge[2] with results of the phase I (detection) in Cantalloube et al. (2020), while the phase II (characterization) is ongoing. Standard post-processing using the ADI technique tends to be particularly relevant to retrieve point-source signals, such as exoplanets. Indeed, extended features such as disks suffer more deeply of self-subtraction effects (Milli et al., 2012). Hence, fine-tuned algorithms must be used in order to retrieve their true morphology (e.g., MAYONNAISE, REXPACO, MUSTARD, GreeDS, I-PCA), or different techniques, such as PDI or RDI, that I describe below.

During my Ph.D., I mainly processed high-contrast data with standard algorithms (PCA, TLOCI, or cADI; see Chapters 3, 4 and 5) and an inverse-problem algorithm ANDROMEDA[3] (see Chapters 4 and 5). For some specific studies, I collaborated with researchers to compare my results with data reduced with other processing algorithms such as I-PCA or MUSTARD (collaboration with Sandrine Juillard and Valentin Christiaens), PACO (collaboration with Antoine Chomez and Olivier Flasseur), REXPACO (collaboration with Maud Langlois and Olivier Flasseur).

[2] https://exoplanet-imaging-challenge.github.io/

[3] Initially, I collaborated with Faustine Cantalloube to post-process data with ANDROMEDA (e.g., most of the data on HD 95086, see Chapter 4). Later, I obtained access to the ANDROMEDA pipeline and I post-processed data with ANDROMEDA on my own, e.g., for the whole survey presented in Chapter 5.

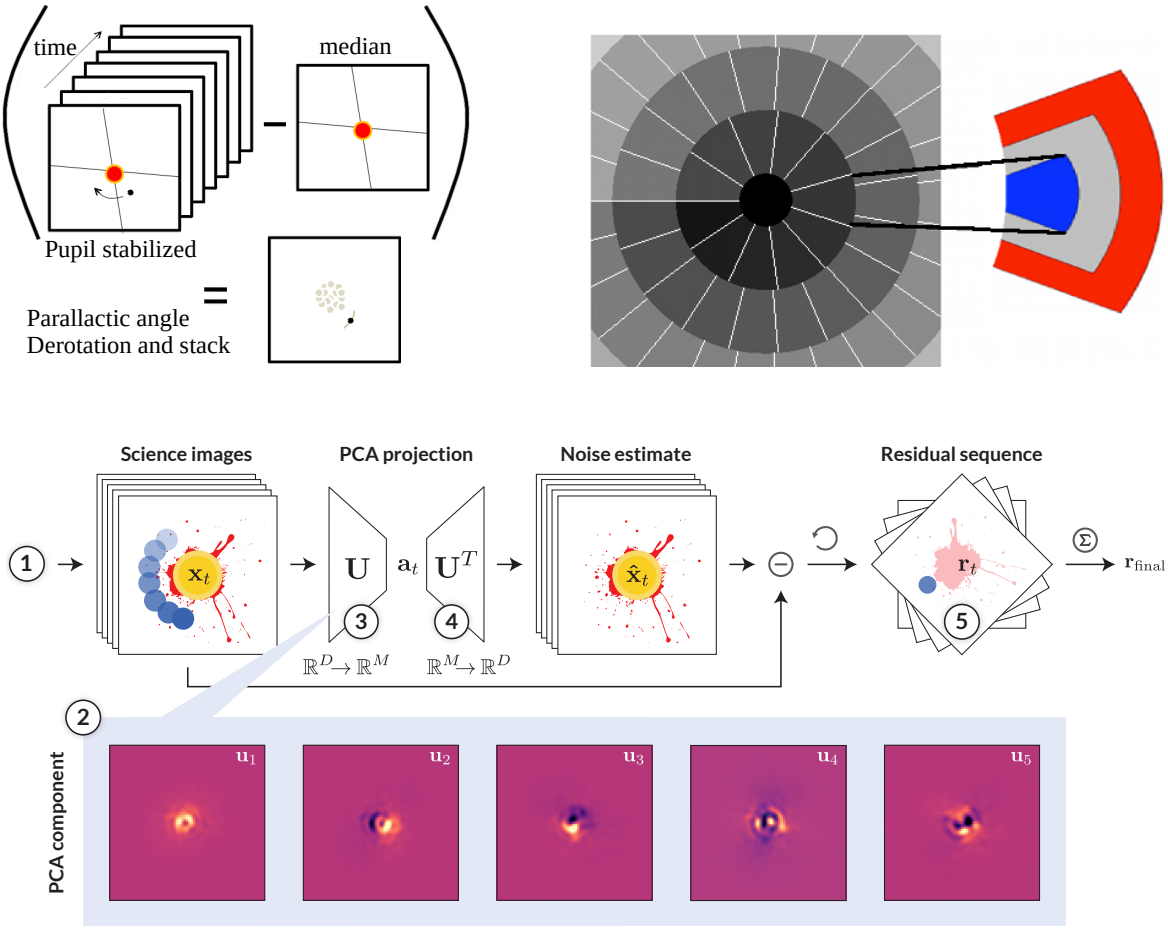

Figure 2.5: Illustration of the principle of cADI (*top-left*), TLOCI (*top-right*) and PCA (*bottom*) post-processing. These three algorithms assume that during the sequence of observations the stellar halo is (quasi)-static while the circumstellar signals rotate (in blue in cADI and PCA sketches). The remaining stellar speckles noise are represent in gray (red splash, respectively) for the cADI (PCA) sketch. Credits: Gaël Chauvin for the *top-left* image, Galicher et al. (2018) for the *top-right* image and Bonse et al. (2024) for the *bottom* image.

Spectral Differential Imaging

Post-processing based on the SDI technique concerns observations acquired simultaneously at least at two different wavelengths. Stellar residuals and circumstellar signals behave differently with respect to the wavelength. At first order, the stellar residuals spread radially in the image when the wavelength increases, while circumstellar signals remain at the same location. In addition, both the sizes of the stellar residuals and circumstellar signals increase with the wavelength, because the angular resolution increases with the wavelength in λ/D in the diffraction-limited regime, and so the typical size of the PSF (see Section 2.2.1).

The SDI technique is particularly useful to reveal point-like features, such as exoplanets. It can be used in synergy with the ADI technique, when panchromatic observations are simultaneously acquired in a pupil-stabilized sequence of observation. The combination of ADI+SDI is widely used, for instance at the VLT with the SPHERE instrument or at the Gemini observatory with the GPI instrument. The aforementioned post-processing such as PCA, TLOCI, ANDROMEDA and PACO can also take advantage of the spectral dimension to better reveal point-like features.

How exploiting the spectral information to better detect and characterize exoplanets is a

ongoing, active area. A possibility is to do molecular mapping, as first successfully done on HR 8799 b and c using Keck/OSIRIS data by (Konopacky et al., 2013; Barman et al., 2015) and Beta Pictoris b using VLT/SINFONI data by (Hoeijmakers et al., 2018). This technique concerns integral field spectrographs/units with high enough spectral resolution, that provide datacubes for which each spatial pixel ("spaxel") is a spectrum. By cross-correlating each spaxel with template spectra, that are either synthetic planetary spectra or molecule spectra, one can retrieve an exoplanet, and constrain some of its physical and/or chemical properties (if no degeneracy).

Performance of the molecular mapping technique was investigated for both ground- and space-based instrumentation, e.g., with ELT/HARMONI (Houllé et al., 2021; Bidot et al., 2024) or JWST/MIRI (Patapis et al., 2022; Mâlin et al., 2023). Some key questions are the performance of the molecular mapping technique depending on the properties of the companion (e.g., an embedded proto-planet, T- or L-type companions), and on the instrumental design (its spectral resolution, its spectral range). Landman et al. (2023) showed that the molecular mapping technique may already be powerful at a spectral resolution of ≥ 300, while before if it was commonly thought that a resolution $\geq 1\,000$ was required. They also show that the H band can be a good trade-off to detect both T- and L-type companions, because from their study T-type companions are most easily detected in the J and H bands through methane and water features, whereas L-type companions are best observed in the H and K bands through water and carbon monoxyde features.

Reference Differential Imaging

The RDI technique requires a reference cube, consisting typically from a dozen to hundreds images of one (or multiple, sometimes noted as "MRDI") reference star(s). The basic idea is to obtain similar stellar residuals in the coronagraphic image of a reference star and the coronagraphic image of a science star (i.e., the star of interest), to subtract the former from the latter (e.g., classical RDI, Galicher et al., 2018). This results in a speckle-free science image in which circumstellar signals are revealed. In practice, the reference star should not be a binary star and should share similar properties with the science star (e.g., its magnitude and spectral type), been acquired in the same telescope+instrument configuration and with similar observational conditions (seeing, turbulence, strehl, wind). This is required to obtain a similar correction of the AO system on both the science and reference stars, and so similar stellar residuals.

Different strategies of observation exist to observe a star of interest and apply RDI afterwards. For instance, a reference star can be observed before or after the observation of the science star (e.g., one hour for each sequence), or both sequences of observations can be intertwined in a star-hopping sequence (e.g., 10 minutes on the science star, 5 minutes on the reference star, this repeated several times), in order to mitigate the impact of the evolution of the observational conditions. A star-hopping sequence is particularly optimized, but requires a specific set-up to be efficient in the back and forth between the science star and the reference star, and not be too time-consuming. Regarding high-contrast spectro-imagers, the star-hopping mode is currently implemented only on the VLT/SPHERE instrument. Alternatively, reference stars can also be taken from a library of archival data, which saves telescope time. This technique may be effective when the library of archival data is large enough, in other words for instruments that have been on sky and acquire data in a similar set-up (e.g., same filter, same neutral density, same coronagraph) for a long period, and that are at least relatively stable, as for *HST*/NICMOS (Choquet et al., 2014), but also VLT/SPHERE (Xie et al., 2022; Romero et al., 2021; Stasevic et al., 2023).

In general, RDI retrieves better extended signals than ADI and SDI, as it does not suffer of self-subtraction. However, RDI is subject to oversubtraction effects, consisting in an overestimate of the fraction of stellar halo to remove. In a star-hopping sequence, the RDI-based post-processing can improve the contrast at very close separations compared to ASDI-based post-processing, e.g., be sensitive to objects of two magnitudes fainter at 0.1" (see Fig. 5 from Wahhaj et al., 2021).

Polarization Differential Imaging

Last but not least, the PDI technique is based on the fact that the stellar light is mostly unpolarized, while the light scattered on circumstellar disks is linearly polarized. In practice, simultaneous observations with orthogonal polarizers are acquired to image orthogonal polarization states on the detector and then apply PDI post-processing to remove the stellar light. To date, linear polarizers are used in high-contrast instruments, such as VLT/SPHERE and Gemini/GPI, and soon in space with *Roman Space Telescope*/CGI. In the last decade, PDI have proved to be efficient to image circumstellar disks, such as protoplanetary (e.g., Fig. 1.10, Garufi et al., 2017) or debris disks (e.g., Olofsson et al., 2022b).

To sum up, all techniques have pros and cons, with ADI and SDI suited to reveal point-like sources such as exoplanets (or background stars), while PDI is particularly efficient to retrieve circumstellar disks. The RDI technique is effective to image both disk and exoplanets, however, it can come with additional time cost if the reference images correspond to an additional reference star to observe, and not from a library of reference star images. The development of new algorithms to process high-contrast imaging observations is a very active research field. In particular, recently, scientists have been working to improve (or develop) the ADI- and RDI- based post-processing algorithms, notably to image more effectively circumstellar signals in total intensity light. This enables the characterization of the disks both in total intensity and polarimetry light, resulting in more constraints on the properties of their dust particles.

2.3 The SPHERE high-contrast instrument at the Very Large Telescope

During my Ph.D., I mostly used the high-contrast instrument SPHERE. It is an European instrument, that is operated by ESO at the VLT, and which had its first-light in 2014. SPHERE is a second-generation instrument at the VLT, which was built upon the experience acquired with the first-generation NaCo instrument, that operated between 2001 and 2019. I first give a general overview of the SPHERE instrument in Section 2.3.1, before discussing its limitations in Section 2.3.2.

2.3.1 Overview

SPHERE can image exoplanets and circumstellar disks in the optical and in the near-infrared, from 0.51 μm to 2.35 μm with broad and narrow filters. SPHERE is divided in four sub-instruments, corresponding to a Common Path and Infrastructure (CPI) that includes the adaptive optics system (SAXO), and the three sub-instruments named Infra-Red Differential Imaging Spectrometer (IRDIS, Dohlen et al., 2008), Integral Field Spectrometer (IFS, Claudi et al., 2008) and the Zurich IMaging Polarimeter (ZIMPOL, Schmid et al., 2018), see Fig. 2.6. During my Ph.D., I used the sub-instruments IRDIS and IFS, not ZIMPOL.

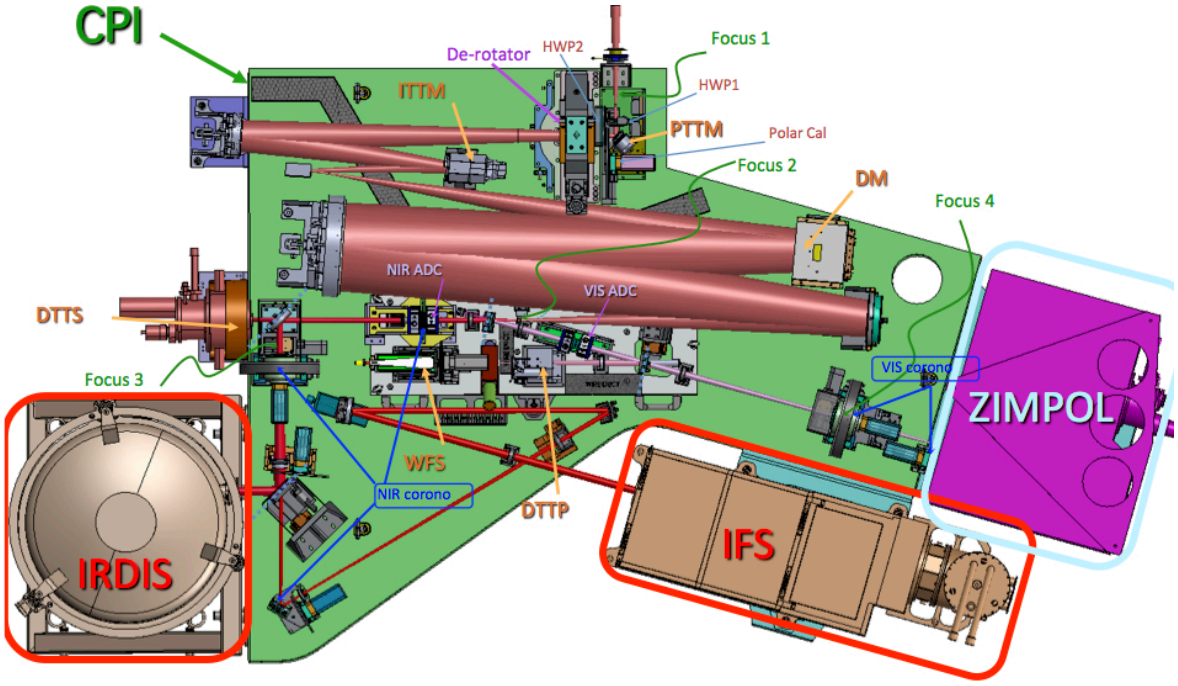

Figure 2.6: The SPHERE instrument and its three sub-instruments: IFS, IRDIS and ZIMPOL. The light enters the instrument at the top. Credits: ESO/SPHERE Manual.

The IRDIS sub-instrument is a dual-band imager in the near-infrared covering the spectral range from 0.95 μm to 2.35 μm, i.e., the YJHKs bands. IRDIS has many different modes, offering classical imaging (CI), dual-band imaging (DBI), dual linear polarization imaging (DPI, De Boer et al., 2020), and long slit spectroscopy (LSS). IRDIS has a field of view of $11"\times11"$, which is larger than that of the IFS and ZIMPOL. It has also a larger pixel size (12.25 mas x 12.25 mas).

As for the IFS, it is a low-resolution spectrograph operating either from 0.95 μm to 1.35 μm (YJ bands, resolution of about 50) or 0.95 μm to 1.65 μm (YJH bands, resolution of about 30). This is a lenslet-based spectrograph (following the BIGRE concept, Antichi et al., 2009). Each portion of the field of view is captured by a lenslet that disperses the spectrum over a rectangular area of 5.1 pixels$\times41$ pixels on the detector. This image on the detector is then resampled to obtain 4D data cube, with two spatial dimensions, one spectral corresponding to the 39 spectral channels and one temporal. The field of view is $1.7"\times1.7"$ and the final pixel size is 7.46 mas $\times$ 7.46 mas.

On the other hand, ZIMPOL is a high contrast imaging polarimeter observing in the optical (510–900 nm). ZIMPOL can do classic imaging and polarimetric differential imaging (PDI) in slow or fast modulation mode. Its field of view is $3.5"\times3.5"$, with a pixel size of 7 mas x 7 mas.

Both pupil- and field-stabilized modes are often offered for instrumental set-up with IRDIS, IFS and ZIMPOL, enabling post-processing based on the ADI technique. Multi-wavelength data cubes can be post-processed using SDI, whereas polarimetric data (from IRDIS or ZIMPOL) via PDI.

Pre- and post-processing pipelines have been developed for the SPHERE instrument, named SpeCal (Galicher et al., 2018) and IRDAP (Van Holstein et al., 2020). The SpeCal pipeline is associated to the High Contrast Data Center (HC-DC[4]), that offers a service to reduce high-contrast imaging observations, such as SPHERE data. As for the IRDAP pipeline,

[4]available at https://hc-dc.cnrs.fr/. It was previously named the SPHERE Data Center.

it was developed by Van Holstein et al. (2020) to reduce SPHERE/IRDIS polarimetric observations, by also accounting of polarization effects introduced by the telescope and instrument, and is currently beeing ingested in the HC-DC.

For my research projects, I systematically used the service of the HC-DC to obtain pre-processed total intensity SPHERE data, and often to obtain post-processed via PCA ADI or ASDI, TLOCI ADI or ASDI, cADI or nADI algorithms. I have also post-processed data on my own with the PCA algorithm using the VIP-HCI library (Gomez Gonzalez et al., 2017; Christiaens et al., 2023), see Chapter 3 and the ANDROMEDA pipeline, see Chapters 4 and 5. As for polarimetric data, I pre- and post-processed the data with the IRDAP pipeline, see Chapter 3.

2.3.2 Limitations and going beyond

After a decade of operations, the SPHERE imaged dozens of protoplanetary and debris disks, yet only a few exoplanets.

Demographic studies showed that only a few percent of stars host massive giant planets or brown dwarfs of semi-major axes greater than 10 au (Vigan et al., 2021; Nielsen et al., 2019). However, most of the massive giant planets are located between 1 and 10 au (Fulton et al., 2021), which correspond to separations of 10 mas and 100 mas for at star located at 100 pc, as roughly those in the star-forming region Sco-Cen (100–150 pc), one of the closest, large reservoir of young (5–40 Myr) stars. As the SPHERE mostly used coronagraph, the APLC, has a inner working angle of about 100 mas, the expected bulk of giant planets in Sco-Cen are located at too small separations to be reachable by SPHERE. Exoplanet demography is one of the factors that makes the probability of exoplanet detection higher for nearby stars, the other being that nearby exoplanets are brigther than distant ones, in thermal emission of reflected light. Therefore, ideal targets for SPHERE would be young stars located closer than 100 pc, such as the ones in young moving groups as Beta Pictoris (in which belong, e.g., the planetary systems Beta Pictoris and AF Leporis, discovered by direct imaging) and AB Doradus (e.g., HR 8799), but unfortunately, their number of stars is quite limited.

Consequently, increasing the detection limits at small separations (in the first few hundreds milliarcseconds) is a crucial step, as well as the number of stars that can be observed with SPHERE, i.e., for which the AO-loop can be closed. These are the two main objectives of the proposed upgrade of SPHERE, named SPHERE+: (i) to image Jupiter-mass exoplanets located down to 5 au (now $\sim$ 10 au, see Fig. 2.7, *left*), and (ii) discover new proto-planets (analogs to PDS 70) in star-forming regions, so around faint, red stars (see Fig. 2.7, *right*). In both cases, characterize them would bring strong constraints on planet formation and evolution models.

Originally, the SPHERE+ upgrade was decomposed in two main instrumental developments: SAXO+, i.e., the upgrade of the adaptive optics system named SAXO, and a medium-resolution integral field spectrograph, called MedRes. SAXO+ would be acting as an AO instrumental demonstrator for the ELT instruments, in particular PCS, as using as new, second AO stage a pyramid wavefront sensor, which is the same type of wavefront sensor that will use the ELT instruments. This new, faster and more sensitive AO stage will reduce the servolag error, mentioned in Section 2.2.1, that consists in not fast enough corrections of the atmospheric turbulence. The higher correction frequency (3 kHz instead of 1.3 kHz) will allow SPHERE to work optimally in median observational conditions. To take advantage of this improved AO correction, the medium-resolution IFS MedRes would be designed to better detect and characterize the atmosphere of exoplanets located at close separations than the current low-resolution IFS of SPHERE. With a resolution of a few hundreds to one thousand, MedRes would use more extensive spectral information with the molecular mapping technique (see Section 2.2.3). In addition, in the SPHERE+ white paper (Boccaletti et al.,

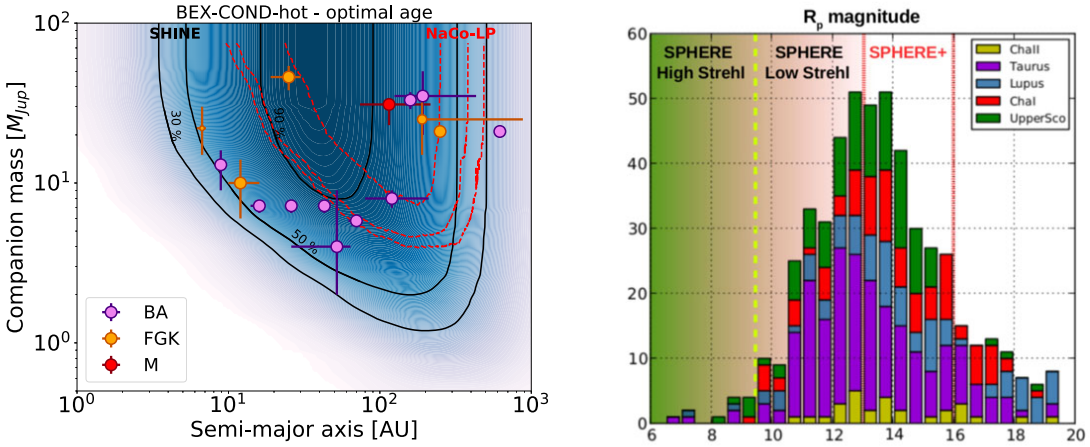

Figure 2.7: The SPHERE performances and limitations. *Left:* Completeness of the first sample of 150 stars of the SPHERE-GTO SHINE survey (black solid contours), compared to the performance of the older NaCo instrument in the Lp band (red dashed contours) for completeness at 30, 50 and 90%. At 10 au, SHINE was sensitive to companions down to at least 10 M_{Jup} for 50% of the stars. The contrast-to-mass conversion is based on the BEX-COND-hot models (Marleau et al., 2019). *Right:* The SPHERE instrument can detect stars down to a magnitude of 13 mag in the R band, missing most of the stars of the nearby, young associations while its upgrade SPHERE+ will give access to the bulk of it ($R < 16$ mag). Both figures are from the SPHERE+ white paper Boccaletti et al. (2020).

2020), new coronagraphs are also considered, such as a modified APLC (N'Diaye et al., 2015; N'Diaye et al., 2016a) and a phase apodized pupil Lyot coronagraph (Por, 2020). These coronagraphs would increase the contrast of a factor 10 between 100 and 200 mas, and for the latter one, has a smaller IWA of $1.4\,\lambda/D$. Unfortunately, the only upgrade which is in a good position to be validated by ESO is SAXO+, not MedRes, or the new coronagraphs.

Initially, half of my Ph.D. work was supposed to help on the development of the new IFS MedRes. During my first year of Ph.D., I did start to run molecular mapping simulations for different instrumental set-ups and astrophysical scenes, to determine what would be the optimized design for MedRes, in terms of spectral coverage and resolution, for exoplanet detection and characterization. As the MedRes project became more and more uncertain, my Ph.D. subject shifted and I have then fully dedicated my work towards astrophysical exploitation studies on exoplanets and debris disks.

Other effects limit the performance of the VLT/SPHERE observations and are nicely reported and illustrated in Cantalloube et al. (2019). There are the errors related to the AO such as the fitting error (due to a limited number of actuators of the deformable mirror), the aliasing error (limited spatial sampling of the wavefront sensor) and the NCPAs. The NCPAs are the main source of speckles in the AO-corrected zone in good observing conditions, and different techniques were investigated to correct them. First, a Zernike wavefront sensor (N'Diaye et al., 2013) called Zelda was developed and successfully tested on internal source (N'Diaye et al., 2016b) and on-sky (Vigan et al., 2019). Alternatively, Potier et al. (2020, 2022) demonstrated on internal source and on-sky that the NCPAs could be corrected with the dark hole technique. This technique uses a pair-wise probing estimator and a controller based on electric field conjugation, which was originally developed for space-based instrumentation. However, such calibrations and corrections of the NCPAs are still at a research and development stage. They have to be more robust to be implemented in the day-to-day operational phase of SPHERE.

On top of that, there are the jitter error, the low-wind effect, and the wind-driven halo that degrade the ultimate SPHERE performances. The wind-driven halo (WDH, Cantalloube

et al., 2020) looks like a bright butterfly pattern and is present on about 30% of the SPHERE observations. This pattern, often asymmetric and that rotates as a function of the parallactic angles, degrades the detection limits at small separations (≤ 0.5"). The WDH is caused by the displacements of the upper level atmospheric turbulence due to high wind speed of the jet stream (Madurowicz et al., 2018), and which is not corrected fast enough by the AO system. As for the jitter error, it is caused by vibrations or tip-tilt errors that miscenter the star behind the coronagraphic mask and that are not corrected by the differential tip-tilt sensor (DTTS, Baudoz et al., 2010). The low-wind effect (LWE, Pourré et al., 2022). is due to the cooler temperature of the M2-mirror spiders that then cool down the air layer next to it of about 2–3 deg compared to the ambiant air. During nights with almost no wind (≤ 5 m s^{-1}), the air does not mix properly, resulting in a higher refractive index for the cold air layer, that affects unhomogeneously the stellar wavefront, and generates speckles.

Addressing these effects is essential to limit the number and brightness of speckles, and eventually reach deeper sensitivities. The LWE is now circumvented thanks to the tape that was added on the spider holding the M2, to thermalize the M2 spider and the ambient air. As for the WDH, a new data processing strategy could be developed to model it and subtract it from the coronagraphic data (Cantalloube et al., 2020).

2.3.3 Synergies with other facilities

Understanding limits of current extreme-adaptive optics systems such are SPHERE are essential to go beyond them, for these same instruments, but not only. The extreme adaptive-optics, high-contrast, and second-generation instrument PCS at the ELT aims to reach deep contrast of 10^{-8} at 20 mas (and 10^{-9} at 100 mas), and image exo-Earths (Kasper et al., 2021). To achieve this, understanding and correcting for the NCPAs errors on PCS would be primordial. The SPHERE+ upgrade, SAXO+, is on the ESO roadmap of the development of PCS, and also share some similarities with other ELT instruments (a pyramid wavefront sensor).

Apart from instrumental perspectives and typical effects that will degrade the ultimate imaging performances, SPHERE would also be complementary in terms of strategies of observation. Indeed, SPHERE is a survey machine that can discover exoplanets and disks, to narrow down the sample of promising stars to observe with the ELT. Due to the expected very high pressure factor to have time on the ELT, large time-consuming surveys with the ELT would be hardly conceivable.

As for synergies with space facilities, SPHERE can image exoplanets at smaller separations (down to 100 mas) compared to *JWST*/NIRCam or *JWST*/MIRI coronagraphic modes (down to 300–400 mas, e.g., the detections of AF Lep b and HR 8799 e, Franson et al., 2024; Boccaletti et al., 2024). However, SPHERE is less stable than space instruments, so for instance exoplanet detections below the IWA (defined as where the coronagraphic throughput is of 50%) are not feasible for SPHERE, contrary for *JWST*, which has for the two previous cases coronagraphic throughputs of 7% and 52%, respectively. Then, the study of the variablity of the atmospheres of exoplanets are more challenging from the ground, due to the uncertainties of the source of the variability, between the exoplanet (or host star) and the variability of the Earth's atmosphere transmission. The same goes for interpreting the reflectance of circumstellar disks (that is to say, its brigthness at different wavelengths), for which measurements may not be simultaneous and hence, depend on factors (e.g., Earth's atmosphere transmission) hard to evaluate a posteriori, which challenges the data analysis. Moreover, the in-depth studies of the polarimetric mode on SPHERE/IRDIS (De Boer et al., 2020; Van Holstein et al., 2020) will give clues on possible polarization effects on the *Nancy Grace Roman Space Telescope* and targets to observe (e.g., HR 4796, Anche et al., 2023). Moreover, to image ever fainter, closer exoplanets, the correction of the NCPAs also plays a major role for space instruments.

As for other exoplanet detection techniques, as mentioned in Section 1.2.3, SPHERE is complementary, because it probes the outer part of exoplanetary systems, inaccessible by transit, radial, and, to some extent, astrometric studies. Furthermore, SPHERE provides complementary or unique constraints on the atmospheric and physical properties of a given exoplanet.

To conclude, in this Chapter, I have introduced the main instrument I have used for my research during my Ph.D., the high-angular resolution, high-contrast imager SPHERE at the VLT in Chile. I have described its main limitations and its current status in the context of the SPHERE+ upgrade. More generally, I have explained in what consist such instruments, that are able to image exoplanets and circumstellar disks. I have also given some context, about the SPHERE predecessors built and developed for ESO facilities (COME-ON, COME-ON+/ADONIS, NaCo), and more broadly, other current ground- and space-based high-contrast facilities that are particularly relevant for my research. For some of these facilities, including LBT/SHARK-NIR, LBT/LMIRCam, *HST*/STIS, *JWST*/NIRCam, and *JWST*/MIRI, I submitted proposals to obtain telescope time to initiate new research projects, and I was granted some of them.

Chapter 3

The young, multi-structured debris disk HD 120326

Contents

3.1 Context

3.1.1 Motivation

To date, more than one hundred debris disks have been spatially resolved, either in the optical, infra-red or millimeter. Debris disks are common and are more frequently detected around young ($\leq$ 25 Myr) than around older (50 Myr–10 Gyr) solar-like stars. Indeed, Pawellek et al. (2021) determined a detection rate of 75 % debris disks for the F stars of the Beta Pictoris Moving Group, whereas several studies reported a detection rate of around 25 % for other older stars (e.g., Najita et al., 2022, and references therein). However, these detection rates could be significantly different to the occurence rates, due to detection bias. For instance, current facilities are not able to detect dust belts with a similar fractional luminosity ($\sim 10^{-7}$) than that of the Asteroid Belt or the Kuiper Belt (Backman et al., 1995) around other stars (Fig. 1.12).

Studying debris disks set constraints on the architectures of planetary systems, dust and gas properties, and putative planet-disk interactions. They can be precious reservoirs of comets, and so deliver volatiles, such as water or organics, on planets when falling on them. The morphology of a debris disk can also help to trace back the formation or evolution of a system, in particular to specific features that could be related to giant impacts (Jones et al., 2023), or reveal interactions with their close neighborhood, either with stellar encounters (Bertini et al., 2023), or interactions with the interstellar medium (Maness et al., 2009).

Among nearby young and large association, Sco-Cen distinguish itself by hosting many debris disks spatially resolved and massive giant planets. Exploring such association therefore enables the study of the diversity of planetary system architectures at a young age. During my Ph.D., I work on a complex debris disk, HD 120326, having several disk structures.

3.1.2 Previous studies on HD 120326

The first image of the debris disk of HD 120326 was presented at the International Astronomical Union (IAU) by Padgett & Stapelfeldt (2016), among other debris disks imaged by *HST*/STIS in a follow-up survey of debris disks imaged previously with *WISE*, see Fig. 3.1 (*left*). The *HST*/STIS imaged the scattered-light of small dust grains in the optical, extended up to a projected separation of 900 au.

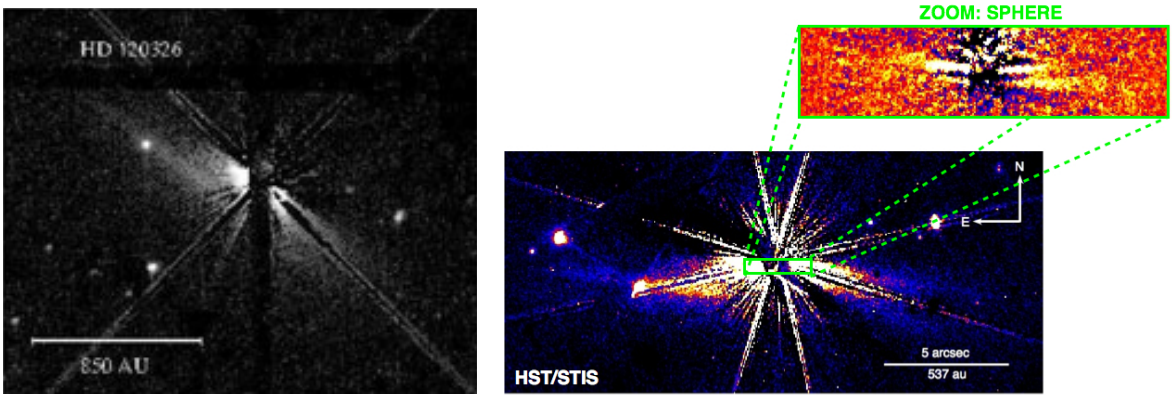

Figure 3.1: *Left: HST*/STIS image published in Padgett & Stapelfeldt (2016). *Right*: VLT/SPHERE and *HST*/STIS published in Bonnefoy et al. (2017)

Afterwards, Bonnefoy et al. (2017) published near-infrared scattered-light SPHERE observation in total intensity (Fig. 3.1, (*right*), followed by Olofsson et al. (2022b), who studied the SPHERE counterpart polarimetric data. Both studies characterized independently

the morphological parameters of the inner disk, located at a reference semi-major axis of 35 ± 4 au or 62 ± 3 au, with an estimated inclination of $76.7 \pm 0.6\,^{\circ}$ or $80 \pm 1\,^{\circ}$ and an inner and outer slopes for the belt of $\alpha_{\rm in} = 12$ and $\alpha_{\rm out} = -2$, or $\alpha_{\rm in} = 10$ and $\alpha_{\rm out} = -5$, for Olofsson et al. (2022b) and Bonnefoy et al. (2017), respectively. In addition, Bonnefoy et al. (2017) also pointed out the existence of a second, faint outer structure imaged in total intensity, but which is not detected in polarimetry (Olofsson et al., 2022b).

Previously, based notably on the *Spitzer* data, two studies modeled the SED with either a two- or one-component blackbody (Chen et al., 2014; Jang-Condell et al., 2015, respectively). Chen et al. (2014) determined a bright ($L_{\rm IR}/L_{\star} = 1.1 \times 10^{-3}$), cold ($127 \pm 5$ K) belt located at 14 au and a faint ($L_{\rm IR}/L_{\star} = 1.4 \times 10^{-4}$), colder ($63 \pm 5$ K) population at 117 au. As for Jang-Condell et al. (2015), they only recovered the inner one, at a distance of 9 ± 1 au ($L_{\rm IR}/L_{\star} = 1.5 \times 10^{-3}$, 124 ± 5 K), and by assuming a single population of dust grains, provided additional constraints on the dust properties. They estimated a grain size of 15.5 μm, with a pure olivine composition, rather than a mixture between olivine and pyroxene. In any of the SED modeling, the derived location of the dust belt is significantly lower than the one determined from the scattered-light images in the near-infrared. This is common, because small dust grains are poor emitters. The factor of difference is calibrated by Pawellek & Krivov (2015), and depends on the stellar type.

3.2 My work

As part of my Ph.D., I have peered into the young debris disk HD 120326. To characterize the morphology and dust properties on this system, I focused on the VLT/SPHERE data in total and polarized intensity. In total, there were three SPHERE observations in total intensity at 1.6 μm, either in narrow dual-bands (H2 and H3), or in the broad band H, and one in polarimetry at 1.6 μm. Using the IRDAP pipeline (De Boer et al., 2020; Van Holstein et al., 2020), I processed the polarimetric data (Section 2.1.1[1])

I spent a significant time while processing the three total-intensity epochs of observations of SPHERE/IRDIS and SPHERE/IFS, because I tested several ways to process them. By using the PCA algorithm implemented in the open-access library `VIP_HCI` (Gomez Gonzalez et al., 2017; Christiaens et al., 2023), I played over the number of components (from 1 to 20) to better reveal the faint disk structures, and I also processed individually the spectral channels, summing then the processed images (or not), or summing the spectral channels before processing the data, and see what processing set-up gave the best results (Section 2.1.2). Concerning the IRDIS data, there are two spectral channels (either H2 and H3 or two channels correponding to the BBH band), while for IFS, there are thirty nine of them. When I combined the IFS spectral channels, I applied different spectral binning, to finally converge on five IFS images made of each six spectral channels. I removed the first and last channels, and a few others that were more impacted by artifacts, see Fig. 7 (*lower-panel*) or Fig. A.3. This choice was motivated by how well the disk signal was recovered, and its S/N.

Afterwards, based on the SPHERE/IRDIS data, I constrained the morphology and photometry of the inner belt, by running first simulations using an exploration algorithm based on a `Nelder-Mead` minimization (Nelder & Mead, 1965), and then using the method `MCMC` (Markov Chain Monte Carlo) with the package `emcee` (Foreman-Mackey et al., 2013). I had six free parameters, the reference semi-major axis of the disk (r_0), its inclination (i), its position angle (PA), its slope of the outer edge of the belt ($\alpha_{\rm out}$), its flux (inferred based on

[1] All the references to Sections, Figures, Tables and Equations in this Section are from submitted paper Desgrange et al. (2025, subm.), which is added in the next Section 3.2.1.

a flux scaling factor), and the scattering anisotropy parameter (g, also called the Henyey-Greenstein parameter Henyey & Greenstein, 1941) describing its scattering phase function[2]. The simulations aimed to minimize the normalized residuals, defined as the disk model subtracted from the observations, normalized by the noise map (see Eq. (5)). I generated the disk model with the `GraTeR` code available in `VIP-HCI`.

The `Nelder-Mead`-based simulations allowed me to converge fast (about a few minutes on my laptop) to a satisfying disk model matching well the observations, whereas with `MCMC`-based simulations (about a day on the IPAG computing facilities) I could better sample the parameter space (r_0, i , PA, α_{out}, flux scaling factor, g), study the correlation between the parameters and estimate the uncertainties. I ran `Nelder-Mead` simulations in different configurations: the model had to match the observations that were either set to one epoch or a combination of some of them. This combination could be the three total-intensity observations (one in BBH, two in H23), the two epochs acquired in the broad band H (one in total intensity and one in polarimetry) or the four epochs altogether (two in BBH, two in H23). I considered for the observations either the first, second, or both channels combined, applying a PCA processing using 5 or 10 components, while carrying out the `Nelder-Mead` simulations. I ended up with a large table reporting the best-fitting parameters for different configurations of the simulations. This gave me an insight of how much the disk parameters could vary depending on the processing and observation used, and gave me confidence in my results.

As for the final best-fitting parameters of the inner belt, I decided to derive them via `MCMC` simulations, modeling jointly the polarized- and total-intensity observations of SPHERE / IRDIS in the broad band H. The simulations had to minimize the residuals of both observations (Section 3.1).

The data processing and the simulations part represented definitely a significant time of my work on this project. After these two main steps, it has been relatively straightforward to obtain additional results regarding the dust properties. Based on the best-fitting parameters (see Table 2), I obtained the scattering phase function in total and polarized intensity (Fig. 6), and extracted the maximum polarization fraction (Section 3.2).

By fixing the parameters of the inner belt to the ones derived on the IRDIS total and polarized intensity data, except the scaling factor representing the flux of the disk, I ran seven new `MCMC` simulations to determine the photometry of the inner belt at seven other wavelengths, corresponding to the disk seen in the five IFS images (from 1.0 to 1.3 μm in the YJ bands) and in the two IRDIS images (the narrow bands H2 and H3). From these results, I derived the reflectance spectrum of the inner belt from 1.0 to 1.8 μm (Fig. 7). The reflectance of the inner belt corresponds to the surface brigthness of the inner belt divided by the flux of the host star.

In addition, regarding the SPHERE data, I investigated the nature of the second disk structure seen in the SPHERE total intensity observations (Section 3.5). By assuming it is a second belt, I determined the expected flux it would have in polarimetry based on the double-belt model from Bonnefoy et al. (2017). Alternatively, I also considered the halo hypothesis, consisting in small, eccentric particles that could originate from the collisions of larger bodies within the inner belt (apocenter pile-up theory, Olofsson et al., 2023). I modeled the inner belt and the halo using the `betadisk` code[3] (Olofsson et al., 2022a).

[2]The scattering angle is defined as the angle between the incident photon's path and the scattered photon's path. For a given dust belt, the scattering angle varies with the azimuth, e.g., Fig. 12 from Perrin et al. (2015). Depending on the inclination (i) of the disk, only a given range of scattering angles are accessible for the observer. The minimum accessible scattering angle is defined as $90° - i$, of the disk (and it corresponds to the region of the belt closest to the observer), and the maximum as $90° + i$ (the region of the belt furthest away to the observer)

[3]Accessible here: https://github.com/joolof/betadisk

At the origin, my work on HD 120326 was supposed to focus only on the SPHERE data. Nonetheless, thanks to my collaborators, I was able to add ALMA and *HST*/STIS data on this system in Desgrange et al. (2025, subm.).

Regarding the ALMA data, I contacted James Miley (@USACH, Chile), who is the PI of the ALMA large program which includes data on HD 120326. He kindly gave me access to the processed ALMA data at 1.3 mm of HD 120326, yet unpublished, and in which there is a disk detection (Fig. 2). I also contacted Grant Kennedy (@Warwick University, UK), who derived the morphology of the disk seen with ALMA, and modeled the SED including the new ALMA measurement. Clearly, my collaboration with James Miley and Grant Kennedy was very fruitful, and the Sections 2.2 and 4 owe much to them.

As for the *HST*/STIS observations, they were already published in Padgett & Stapelfeldt (2016) and in Bonnefoy et al. (2017). Although some extended circumstellar signal is visible in their images (Fig. 3.1), the STIS observations are deeply impacted by the wedges. Discussions with Julien, Gaël, Mickaël Bonnefoy and Elodie Choquet made me very enthusiatic to have also a look at the STIS data. I downloaded pre-processed images from the MAST archive[4], post-processed them via a home-made routine (Section 2.3), converted them in Jy/arcsec^2 (Fig. 3) and computed the S/N map (Fig. 4).

3.2.1 Submitted in A&A: Desgrange et al. 2025 subm.

I added the submitted paper in the following pages. I submitted the paper in Astronomy & Astrophysics in October, received the positive report from the referee beginning of December[5] and will submit the paper again in January. Below the paper with most of the comments implemented.

[4] Available here: https://archive.stsci.edu/

[5] Note: in the first version of my Ph.D. manuscript submitted in July 2024, the version of the paper was the one before its submission, and before receiving the comments from most of the co-authors. I updated the paper to its version of mid-December in this second (and last) version of my Ph.D. manuscript. Please, consider as the official version of the paper the one which would be published in A&A in 2025.

Astronomy & Astrophysics manuscript no. output
December 21, 2024

Dust populations from 30 to 1 000 au in HD 120326's debris disk:

A panchromatic view with VLT/SPHERE, ALMA, and *HST*/STIS ⋆

C. Desgrange[1,2,3], J. Milli[2], G. Chauvin[3], M. Bonnefoy[2], Th. Henning[3], J. Miley[4,5,6], G. Kennedy[7,8], S. Juillard[9], J. Olofsson[10], J.-C. Augereau[2], V. Faramaz[11], V. Christiaens[9,12], A. A. Sefilian[11,13], J. Mazoyer[14], T. D. Pearce[7], H. Beust[2], F. Ménard[2], M. Booth[15]

[1] European Southern Observatory, Alonso de Córdova 3107, Vitacura, Santiago, Chile
[2] Univ. Grenoble Alpes, CNRS, IPAG, F-38000 Grenoble, France; e-mail: celia.desgrange@univ-grenoble-alpes.fr
[3] Max Planck Institute for Astronomy, Königstuhl 17, D-69117 Heidelberg, Germany
[4] Departamento de Física, Universidad de Santiago de Chile, Av. Victor Jara 3659, Santiago, Chile
[5] Millennium Nucleus on Young Exoplanets and their Moons (YEMS)
[6] Center for Interdisciplinary Research in Astrophysics Space Exploration (CIRAS), Universidad de Santiago de Chile, Chile
[7] Department of Physics, University of Warwick, Gibbet Hill Road, Coventry, CV4 7AL, UK
[8] Centre for Exoplanets and Habitability, University of Warwick, Gibbet Hill Road, Coventry CV4 7AL, UK
[9] Space sciences, Technologies and Astrophysics Research (STAR) Institute, Université de Liège, 19 Allée du Six Août, 4000 Liège, Belgium
[10] European Southern Observatory, Karl-Schwarzschild-Strasse 2, 85748 Garching bei München, Germany
[11] Department of Astronomy/Steward Observatory, The University of Arizona, 933 North Cherry Avenue, Tucson, AZ 85721, USA
[12] KU Leuven, Institute for Astronomy, Celestijnenlaan 200D, Leuven, Belgium
[13] Astrophysikalisches Institut und Universitätssternwarte, Friedrich-Schiller-Universität Jena, Schillergäßchen 2–3, D-07745 Jena, Germany
[14] LESIA, Observatoire de Paris, Université PSL, CNRS, Sorbonne Université, Université de Paris, 5 place Jules Janssen, 92195 Meudon, France
[15] UK Astronomy Technology Centre, Royal Observatory Edinburgh, Blackford Hill, Edinburgh EH9 3HJ, UK

ABSTRACT

Context. To date, more than one hundred debris disks have been spatially resolved. Among them, the young system HD 120326 stands out, by displaying different disk substructures at both intermediate (30–150 au) and large (150–1 000 au) scales.
Aims. We present new VLT/SPHERE (1.0–1.8 μm) and ALMA (1.3 mm) data of the debris disk around HD 120326. By combining them with archival *HST*/STIS (0.2–1.0 μm) and archival SPHERE data, we examine the morphology of the debris disk, and its dust properties.
Methods. Our best-fitting model of the inner belt in near-infrared data is based on a joint-modeling of the SPHERE polarized and total intensity observations. Separately, we model the ALMA data and the spectral energy distribution. We combine the results of both these analyses with the STIS data in order to establish the global architecture of HD 120326.
Results. For the inner belt, identified as a planetesimal belt, we derive a semi-major axis of 43 au, a fractional luminosity of 1.8×10^{-3}, and a maximum degree of polarization of 51 %±6 % at 1.6 μm. We find that the spectral slope of its reflectance spectrum is red between 1.0 and 1.3 μm, and then gray between 1.3 and 1.8 μm. Additionally, SPHERE data show that there could be a halo of small particles or a second belt at these distances (≤150 au). Using ALMA, we derived in the continuum (1.3 mm) an integrated flux of 561 ± 20 μJy . We do not detect any ^{12}CO emission. At larger separations (>150 au), we highlight in STIS data a spiral-like feature spanning hundreds of au.
Conclusions. Further data are needed to confirm and better constrain the dust properties and global morphology of HD 120326.

Key words. Instrumentation: adaptive optics, high angular resolution – Methods: observational – Debris disk

1. Introduction

The direct imaging technique constrains planetary system architectures by probing regions at large (> 5 au) separations from the star. It can detect the near- and mid-infrared emission of young self-luminous giant planets and resolve circumstellar disks, such as debris disks. Debris disks are leftover material from planet formation processes. They consist in volume mainly of small, dust particles resulting from the collisional cascade of larger (i.e., ∼ kilometer-sized) planetesimals (e.g., reviews from Wyatt 2008; Krivov 2010; Hughes et al. 2018; Pearce 2024).

To date, space telescopes and ground-based facilities equipped with extreme adaptive optics instruments have spatially resolved the starlight scattered off dust grains in debris disks down to separations of 0.1″and up to about 10″—

⋆ Based on observations collected at the European Southern Observatory at Paranal with SPHERE under ESO programmes 095.C-0607(A), 095.C-0487(A), 097.C-0060(A), 097.C-0949(A), 097.C-0865(F), 0101.C-0128(D), 0101.C-0016(A), and also observations collected with ALMA (project ID: 2022.1.00968.S) and with *HST*/STIS (program: 12998).

e.g., with *HST* (Schneider et al. 1999, 2014; Augereau et al. 1999a; Choquet et al. 2014, 2018; Ren et al. 2017, 2023b), *JWST*/NIRCam (Rebollido et al. 2024; Lawson et al. 2024), VLT/SPHERE (Wahhaj et al. 2016; Boccaletti et al. 2018; Xie et al. 2022; Olofsson et al. 2022b), or Gemini/GPI (Esposito et al. 2020; Crotts et al. 2024). Such images require specific strategies of observation (e.g., adaptive optics and coronagraphy) and processing, to block the stellar light and reveal the faint disk signal. Scattered-light images enable a better understanding of very small ($\lesssim$ a few μm) dust particles by determining the degree of forward scattering and linear polarization of the dust grains, and their color. This provides constraints on the properties of the dust grains, such as their size, shape and composition.

On the other hand, images of debris disks from mid-infrared to millimeter provide a complementary view, because they are sensitive mainly to the cold thermal emission of larger (sub-mm/mm) dust particles — e.g., with *JWST*/MIRI (Gaspar et al. 2023; Rebollido et al. 2024), *Spitzer* (Su et al. 2009), *Herschel* (Löhne et al. 2012; Wyatt et al. 2012; Kennedy et al. 2013, 2015, 2018), and ALMA (MacGregor et al. 2013, 2017; Su et al. 2017; Marino et al. 2017, 2019; Faramaz et al. 2019, 2021). For (sub-)mm observations, the location of the large grains seen is thought to track more reliably the parent belt of large, colliding planetesimals, as small grains are subject to stellar radiation effects that make them drift from the parent belt where they are produced, hence smearing any asymmetry gravitationally induced by massive perturbers (Thébault & Augereau 2007). The properties of debris disks, including their morphology and the properties (size, shape, composition) of the constituent dust grains can therefore be studied more comprehensively by combining multi-wavelength observations.

In total, more than one hundred debris disks have been spatially resolved[1] so far. Among them, there exists a wide diversity of morphologies: narrow or broad rings, circular, eccentric or misaligned rings, arcs, warps, clumps, swept-back wings, needles, forks or spiral arms (Hughes et al. 2018). A natural question is what causes this diversity (Wyatt et al. 1999; Lee & Chiang 2016), whether this is related mostly to the influence of planetary companions, or to other physical mechanisms such as disk self-gravity (which may or may not require the presence of planets, e.g., Ward & Hahn 1998; Hahn 2003; Jalali & Tremaine 2012; Sefilian et al. 2021, 2023), giant impacts (Jones et al. 2023), collisional dust avalanches (Grigorieva et al. 2007), stellar flybys (e.g., Kenyon & Bromley 2002; Reche et al. 2009; Lagrange et al. 2016), interstellar medium wind (Maness et al. 2009), or processes occurring during planet formation in protoplanetary disks (e.g., Najita et al. 2022).

In this context, the system HD 120326 (HIP 67497), located at 113.3 ± 0.4 pc (Gaia Collaboration et al. 2021) belongs to the Upper Centaurus Lupus sub-group in the Sco-Cen association, and hosts a debris disk around the F0V-type young (16 Myr, Mamajek et al. 2002) star of mass of 1.6 $M_\odot$ (Chen et al. 2014). Using VLT/SPHERE near-infrared imaging in scattered light, Bonnefoy et al. (2017) reported the existence at intermediate scales ($\lesssim$ 150 au) of a dust belt and a putative second dust structure, which could be another belt or a halo of dust grains. In addition, optical data seems to show scattered-light of an extended halo, up to a projected separation of 700 au (Padgett & Stapelfeldt 2016; Bonnefoy et al. 2017, using *HST*/STIS).

[1] see the catalogs: https://www.astro.uni-jena.de/index.php/theory/catalog-of-resolved-debris-disks.html and https://circumstellardisks.org/

Previously, the spectral energy distribution (SED) of HD 120326 has been modeled with either a single- (Jang-Condell et al. 2015), or a double-belt (Chen et al. 2014) architecture, by using in particular measurements of the Infrared Spectrograph (IRS) data of *Spitzer*. From their SED modeling, Chen et al. (2014) found a bright ($L_{IR}/L_\star = 1.1\times10^{-3}$), relatively cold (127 ± 5 K) belt at 13.9 au, and a dimmer ($L_{IR}/L_\star = 1.4\times10^{-4}$), colder (63 ± 5 K) belt at 116.5 au, by assuming two blackbody models. Alternatively, Jang-Condell et al. (2015) modeled the data with a single belt made of a single grain population of a given size, temperature and composition (a mixture of olivine and pyroxene). Their best fit was that of a belt with fractional luminosity of $L_{IR}/L_\star = 1.5\times10^{-3}$ located at 8.8 ± 1.0 au, dust particles of temperature of 124 ± 5 K, size of 15.5 μm, and with a composition converging to pure olivine (instead of a mixture of olivine and pyroxene).

However, both locations of the dust belt are underestimated. This is common for representative radii of dust belts inferred via SED modeling (e.g., Pawellek & Krivov 2015), because small dust particles are inefficient emitters, resulting in higher temperatures than expected based on their separation from their host star. By using SPHERE total intensity observations, Bonnefoy et al. (2017) imaged for the first time the dust belt, and derived via forward-modelling a larger reference radius r_0 of 59 ± 3 au. They also reported the possible existence of a second, outer disk component, that could be another belt ($r_0 \sim 130 \pm 8$ au) or a halo. However, Bonnefoy et al. (2017) were cautious about this second component, as it is faint, and could also be related to self-subtraction effects (Milli et al. 2012) caused by their data processing based on the angular differential imaging (ADI, Marois et al. 2006) technique. This purported second structure was not detected in polarized intensity light using the same instrument, SPHERE, at the same wavelength (1.6 μm, Olofsson et al. 2022b). This further complicates the interpretation of the dust distribution around HD 120326.

In this paper, we carry out a comprehensive, multi-wavelength study of the morphological and dust properties of the HD 120326 debris disk. We use a combination of optical, near infrared and millimeter data, including new observations using VLT/SPHERE and ALMA and archival data (*HST*/STIS and SPHERE). In Section 2, we present the data used and our reduction: SPHERE observations (Section 2.1; with SPHERE/IRDIS and SPHERE/ZIMPOL polarized intensity data in Section 2.1.1 and SPHERE/IRDIS and SPHERE/IFS total intensity data in Section 2.1.2), ALMA observations (Section 2.2), and STIS observations (Section 2.3). In Section 3, we present our joint modeling (Section 3.1) and analysis of the SPHERE total and polarized intensity observations. We derive new constraints on the properties of the inner dust belt, including at 1.6 μm its scattering phase function (Section 3.2) and maximum fraction of polarization (Section 3.3), and between 1.0 μm and 1.8 μm its reflectance spectrum (Section 3.4). We also investigate the nature of the second, faint component at larger distances (Section 3.5) first mentioned by Bonnefoy et al. (2017), which we firmly detect in our new SPHERE total intensity observations. In Section 4, we report our study of the ALMA data, including the morphological analysis of the disk (Section 4.1), the modeling of the SED (Section 4.2) and its dust mass (Section 4.3). In Section 5, we discuss the dust properties contextualized with other debris disks, and the global morphology of the debris disk around HD 120326, based on the STIS, SPHERE and ALMA images. We finally conclude in Section 6.

2. Observations and processing of the SPHERE, ALMA and STIS data

We here present the data used and our processing: VLT/SPHERE (Section 2.1), ALMA (Section 2.2) and *HST*/STIS (Section 2.3).

2.1. SPHERE near-infrared observations

The system HD 120326 (HIP 67497) was observed both in polarimetry and total intensity with the Spectro-Polarimetric High-contrast Exoplanet REsearch instrument (SPHERE, Beuzit et al. 2019) using its imager IRDIS (Dohlen et al. 2008) and its integral field spectrograph (Claudi et al. 2008, IFS) at the Very Large Telescope (VLT). The field of view of IRDIS is 11"×11" and the plate scale of its detector is 12.25 mas (Maire et al. 2016), while for the IFS, these are 1.73"×1.73" and 7.46 mas, respectively. The astrometric calibration of both IRDIS and IFS is based on past regular observations of the star crowded field 47 Tuc, and includes measurements on the true north, distortion, and plate scale (Maire et al. 2021).

We summarize the log of the observations in Table 1. The seeing and atmospheric coherence time (τ_0) are estimated by the DIMM (Differential Image Motion Monitor, Sarazin & Roddier 1990) and MASS (Multi-Aperture Scintillation Sensor, Kornilov et al. 2007) turbulence monitor at the Paranal Observatory. The Strehl ratio is computed by the real-time computer SPARTA (Standard Platform for Adaptive optics Real Time Applications, Fedrigo et al. 2006) of SAXO (SPHERE eXtreme Adaptive Optics system, Petit et al. 2014). In Section 2.1.1, we present the polarized intensity observations and our data processing, whereas in Section 2.1.2 we report the total intensity observations and our data processing, before comparing them in Section 2.1.3.

2.1.1. Polarimetric observations

As dust grains scatter light, they will polarize it, and this process will depend on their intrinsic properties. Thus, observing circumstellar disks with polarimetry enables the study of dust grain properties. Despite the stellar light being very bright, this technique is ideally suited to reveal the much dimmer signal from the disk. Indeed, since stellar light is mostly unpolarized, polarimetric observations facilitate the subtraction of the stellar light via polarization differential imaging (PDI).

Two polarimetric datasets are available on HD 120326: near-infrared data using SPHERE/IRDIS and optical data using SPHERE/ZIMPOL. Below, we first describe the IRDIS data, in which the disk signal is clear detected, and then, the ZIMPOL data, in which no disk signal is detected.

By using the near-infrared instrument SPHERE/IRDIS in its dual-beam polarimetric imaging (DPI, De Boer et al. 2020) mode, the host star of HD 120326 was observed on the night of the June 1, 2018 (PI: Boccaletti) under well-suited observation conditions, with a seeing of 0.45" and a coherence time of the atmosphere of 4.2 ms. The observation was carried out in the field-stabilized mode in the broad band filter H (λ = 1.625 μm, $\Delta\lambda$ = 0.29 μm).

The IRDIS-DPI mode allows us to image simultaneously the linearly polarized light in two orthogonal directions, by using polarizers with orthogonal transmission axes. A polarimetric observation with SPHERE/IRDIS is made of polarimetric cycles consisting of images acquired at four half-wave plate (HWP) angles to measure the Stokes parameters Q^+, Q^-, U^+, and U^-. These HWP angles are 0°, 45°, 22.5°, 67.5°, respectively, with the Q^+ vector aligned with a preferred orientation, usually the meridian on-sky (see Fig. 1 from De Boer et al. 2020). This allows us to retrieve the two linear polarization contributions, Q and U expressed as

$$Q = \frac{1}{2}(Q^+ - Q^-), \quad (1)$$

$$U = \frac{1}{2}(U^+ - U^-). \quad (2)$$

Expressing Q and U as such enables the removal of the instrumental polarization effects caused by the reflections in the instrument downstream of the HWP. From them, one can reconstruct the linearly polarized intensity via the equation $pI = \sqrt{Q^2 + U^2}$, and also the degree of linear polarization following $DoLP = pI/I$, where I is the total intensity (De Boer et al. 2020). Tackling the instrumental polarization generated by the reflections upstream of the HWP require additional corrections, which are described in Canovas et al. (2011). To process the polarimetric observations, we used the public pipeline IRDAP[2] (van Holstein et al. 2020), which corrects for instrumental polarization both upstream and downstream the HWP.

Finally in practice, we work with the azimuthal Stokes parameters Q_ϕ and U_ϕ (Schmid et al. 2006), expressed as

$$Q_\phi = -Q\cos(2\phi) - U\sin(2\phi), \quad (3)$$

$$U_\phi = +Q\sin(2\phi) - U\cos(2\phi) \quad (4)$$

where ϕ is the angle between the North and the point of interest (from the North over East direction). A positive Q_ϕ signal corresponds to polarization oriented in azimuthal direction (with respect to the position of the star), while a negative Q_ϕ corresponds to radial polarization. The U_ϕ signal corresponds to polarization angles oriented at ±45° with respect to the radial (or azimuthal) direction.

In Figure 1, we show the final Stokes vector components pI, Q_ϕ and U_ϕ resulting from the polarimetric observation acquired with 10 HWP cycles, expressed in μJy/arcsec^2. Stellar light has been subtracted in this image, which was evaluated to 0.06 ± 0.07 % at 1σ by the IRDAP pipeline. All the signal of the disk is seen positively in Q_ϕ, i.e., this corresponds to azimuthal polarization of the light scattered by the debris disk, but is not seen in U_ϕ, and so we used this polarization to estimate the noise in the polarimetric data. To convert from detector units into flux unit, we normalized the coronagraphic images with the total flux of the star computed in a circular region of radius 25 pixels summed over the two channels, and corrected from respective frame time exposure and transmission of the neutral density of the coronagraphic and non-coronagraphic observations. We multiplied this then by a stellar flux density of 0.977 ± 0.044 Jy (from Johnson H filter, Bourgés et al. 2014) and divided by the plate scale area.

To derive the signal-to-noise (S/N) map of the disk seen in polarimetry, we divide the Q_ϕ component containing the signal of the disk by the azimuthal mean of the U_ϕ representing the noise, see Fig. 1. The disk is easily detected in the IRDIS polarimetric data, with a S/N of an average value of 4.6/pixel^2 for the East-part, and 3.5/pixel^2 for the West-part of the disk.

In addition, we also processed the ZIMPOL polarimetric observations acquired on the night of August 1, 2015. The ZIMPOL data were reduced by the High-Contrast Data Centre[3] (HC-DC, Delorme et al. 2017) which implements the pipeline developed at ETH Zürich and described in Hunziker et al. (2021).

[2] https://github.com/robvanholstein/IRDAP
[3] https://hc-dc.cnrs.fr/

Table 1. Log of all the VLT/SPHERE observations on the system HD 120326.

Epoch	Instr. Filt.	N_{exp}	DIT (s)	$\Delta\pi$ (deg)	seeing (")	τ_0 (ms)	airmass	strehl (RTC)	PI	ESO program
2015-04-09	IRDIS H23	13	16	1.7	–	–	3.3	–	Bonnefoy	095.C-0607(A)
2015-04-09	IFS YJ	3	16	0.3			3.3	–	Bonnefoy	095.C-0607(A)
2015-08-01	Zimpol IPRIM	48[a]	28 × 5	–	0.65 ± 0.10	3.2 ± 0.5	1.1	–	Booth	095.C-0487(A)
2016-04-05	IRDIS H23 (†)	128	32	37	1.06 ± 0.13	3.4 ± 0.6	1.12	0.63	Bonnefoy	097.C-0060(A)
2016-04-05	IFS YJ	64	64					0.63	Bonnefoy	097.C-0060(A)
2016-06-03	IRDIS H23 (†)	80	32	22	0.72 ± 0.14	3.1 ± 0.5	1.11	–	Hinkley	097.C-0949(A)
2016-06-03	IFS YJ	40	64					–	Hinkley	097.C-0949(A)
2016-06-13	IRDIS J23	80	64	44.7	1.18 ± 0.17	2.1 ± 0.4	1.11	0.54	GTO	097.C-0865(F)
2018-06-01	IRDIS Pol. BBH (‡)	80	64	–	0.51 ± 0.06	4.4 ± 0.8	1.11	0.69	Boccaletti	0101.C-0128(D)
2019-06-26	IRDIS BBH	56	32	36	1.76 ± 0.26	2.1 ± 0.3	1.13	0.53	Bonnefoy	0101.C-0016(A)
2019-06-26	IFS YJ	28	64					0.53	Bonnefoy	0101.C-0016(A)
2019-07-09	IRDIS BBH (‡)	224	32	58	0.63 ± 0.07	3.1 ± 0.4	1.13	0.60	Bonnefoy	0101.C-0016(A)
2019-07-09	IFS YJ (‡)	112	64					0.60	Bonnefoy	0101.C-0016(A)

Notes. The results from this work are mainly based on the high-quality observations acquired on 2018-06-01 (polarized intensity) and on 2019-07-09 (total intensity), highlighted via (‡). We also successfully detect the disk in the SPHERE/IRDIS total intensity observations of 2016-04-05 and 2016-06-03 (†; see Fig. 2). The other datasets are of poorer quality with for some no (2015-08-01) or almost no (2016-06-13, 2019-06-26) recovery of disk signal. The observation acquired in 2015-04-09 is not exploitable because the focal plane mask was missing during the observation sequence. ([a]) The 48 exposures correspond to twelve HWP cycles, resulting in a total time on source of N_{exp} × DIT. GTO stands for Guaranteed Time Observations (PI: Beuzit).

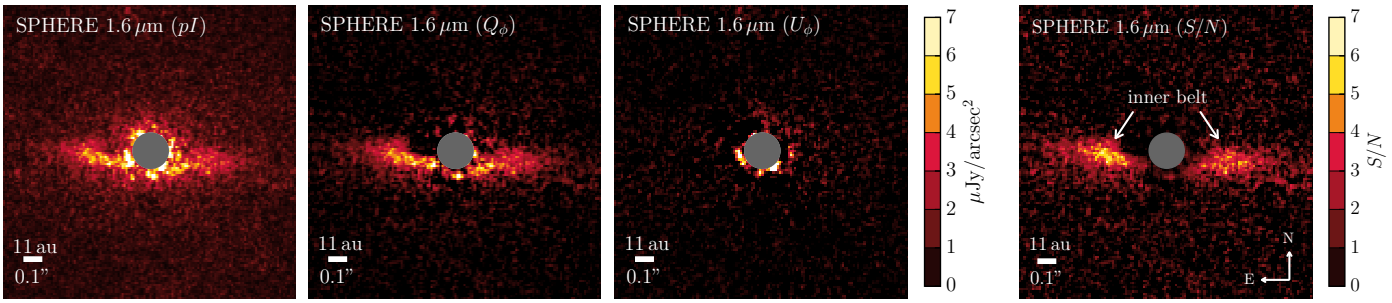

Fig. 1. Polarimetric images of the system HD 120326 using VLT/SPHERE at 1.6 μm (broad band H; scattered light; epoch 2018-06-01). We processed the data by using the pipeline IRDAP. From left to right, we show the Stokes vector components pI (intensity), Q_ϕ (azimuthal or radial polarization), and U_ϕ (polarization oriented at ±45° with respect to the azimuth) calibrated in μJy/arcsec^2, and the signal-to-noise (S/N) map, which is derived based on the Q_ϕ and U_ϕ images. For these images, as all the ones in this paper: North is up and East is left, while the gray circular mask corresponds to the region within the inner working angle of the coronagraph.

In particular, we measured and corrected the relative beam shift of the two orthogonal polarization states, subtracted the frame transfer smearing, and corrected for the residual telescope polarization and the intrinsic polarization of the star. The Stokes Q and U images were then transformed into the Q_ϕ and U_ϕ images following Eq. 4. Unfortunately no circumstellar structure is visible in the reduced Q_ϕ image and we therefore do not discuss further these data.

2.1.2. Total intensity observations

In total intensity, the star HD 120326 was observed in several modes with VLT/SPHERE: IRDIFS H23+YJ (2015-04-09, 2016-04-05, 2016-06-03), IRDIS J23 (2016-06-13), and IRDIFS BBH+YJ (2019-06-26, 2019-07-09), see Table 1. The IRDIFS mode enables simultaneous observations of the dual-band imager IRDIS in the filter doublet H2H3 (λ_{H2} = 1.593 ± 0.055 μm, λ_{H3} = 1.667 ± 0.056 μm) and of the low-resolution integral field spectrograph IFS in the band YJ (0.95–1.35 μm). The filter doublet J2J3 corresponds to λ_{J2} = 1.190 ± 0.042 μm, λ_{J3} = 1.273 ± 0.046 μm. The broad band H (BBH) filter is the same filter as that used in polarimetric mode (Section 2.1.1). All observations were carried out in the pupil-tracking mode to enable the processing of the data with the ADI technique and achieve higher contrast at sub-arcsecond separations. In pupil-tracking observations, circumstellar signal (e.g., disks or exoplanets) rotates through the sequence of observation, while the stellar halo remains quasi-static as a function of the parallactic angles. The ADI technique therefore enables the removal of most of the stellar halo and the retrieval of faint circumstellar signal. For one epoch of observation, a data set consists of the non-coronagraphic image of the star (to derive the stellar flux and have the point-spread function -PSF- of the instrument), the coronagraphic cube acquired at two (IRDIS) or thirty-nine (IFS) channels (x, y, t, λ), and the list of the parallactic angles corresponding to each temporal frame.

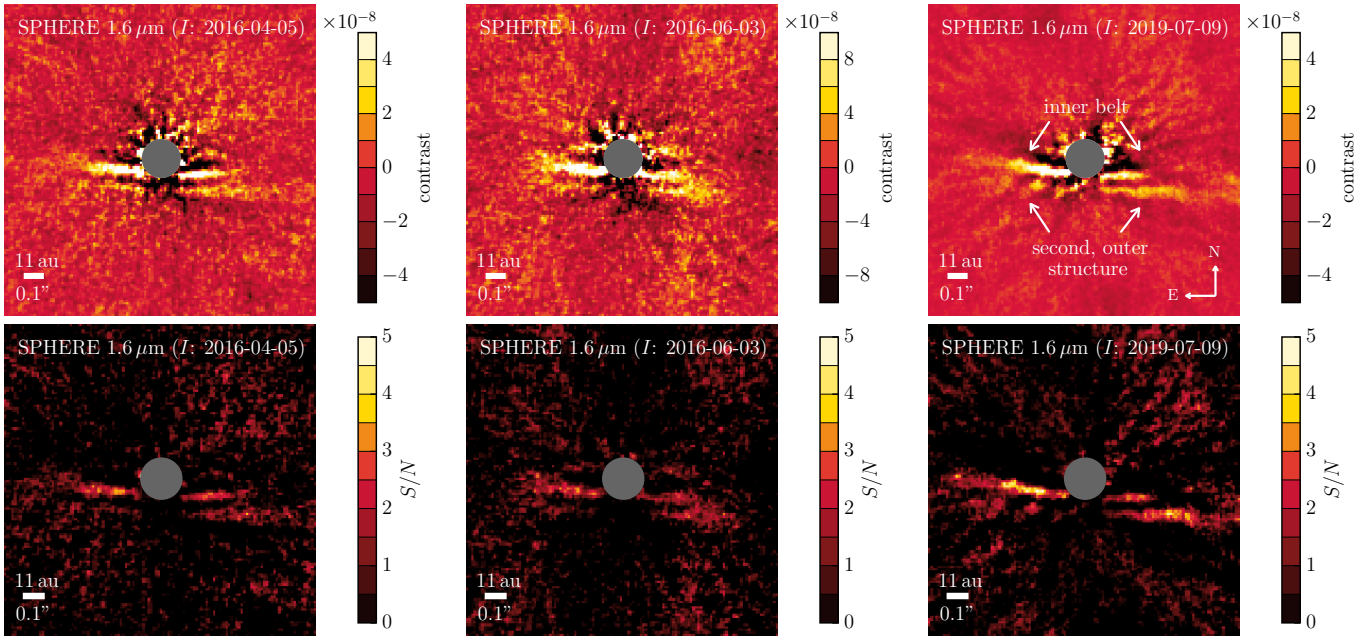

Fig. 2. Total intensity ("I") images at about 1.6 μm reduced using the processing PCA ADI on the system HD 120326, calibrated in contrast unit (*top*) or in S/N (*bottom*). Two structures can be seen, the inner belt and second, outer structure (see the labels in the *top-right* image). All images have the same orientation, with North up and East on the left.

Among the total intensity data, we mainly focus on the unpublished high-quality epoch of observation 2019-07-09, which has a total time exposure of 119 min, with an average seeing of 0.54", and a variation of parallactic angles of 58°, as displayed in Table 1. In Figure 2, we also present results on the epochs of 2016-04-05 (published in Bonnefoy et al. 2017) and 2016-06-03 (unpublished), but in which the circumstellar signal is fainter. Regarding the other datasets (see Table 1), we do not consider the observation of 2015-04-09 as the focal plane mask was missing during the observation sequence. We processed the observation 2019-06-26, but we do not present results in this paper as the data are of significantly lower quality than the one of 2019-07-09 acquired in the same band, and in which the disk is hardly detectable. We processed the epoch 2016-06-03 acquired in the J23 band, but almost no disk signal is recovered.

The data are pre-processed by the High-Contrast Data Center (Delorme et al. 2017), using the SPHERE Data Reduction and Handling pipeline (Pavlov et al. 2008). This pre-processing corrects from both IRDIS and IFS data the bad pixels, dark current, flat non-uniformity, sky background. In addition for the calibration of the IFS, the pre-processing corrects for the wavelength and cross-talk between the spectral channels. Coronagraphic images are centered via four satellite spots used to determine the accurate position of the star hidden behind the coronagraphic mask.

We homogeneously post-processed the observations in total intensity with the Principal Component Analysis (PCA, Amara & Quanz 2012; Soummer et al. 2012) algorithm as implemented in the open library `VIP`[4] (Gomez Gonzalez et al. 2017; Christiaens et al. 2023). For the SPHERE/IRDIS data, we tested several methods to process the data: first, we considered either one of the two channels (combined before or after the PCA processing), and we applied one to twenty components to model the stellar halo before its subtraction with the PCA algorithm. The ultimate goal was to have the cleanest image to retrieve the circumstellar signal. Although the circumstellar signal is drowned in the stellar light, the number of PCA components used to model the stellar halo has to be limited, because the model will capture circumstellar signal too and remove it. This effect is named self-subtraction, and is well known (Milli et al. 2012). By evaluating the S/N of the disk and examining the residuals, we concluded that applying PCA with 10 components on each of the two channels before averaging them into a final image is a relatively satisfying compromise, though some other options give comparable results.

We show the reduced SPHERE/IRDIS observations for the epochs 2016-04-05, 2016-06-03 and 2019-07-09 in Fig. 2, calibrated in contrast or in S/N. To convert to contrast, we normalized the coronagraphic observation by the stellar flux estimated in a circular aperture of 25-pixel radius, as for the polarimetric observations. To obtain the S/N map, we built the noise map by processing with PCA the coronagraphic cube for the opposite parallactic angles, to keep a similar temporal dependence of the stellar residuals and average any circumstellar signals, as done in Pairet et al. (2019). We can see that the disk has a higher S/N in the last observation (2019-07-09, H band), reaching on average about 3.9/pixel^2 for the East-part of the disk and 2.5/pixel^2 for the West-part.

From Figure 2, we can see two disk structures from the scattered total intensity light observations. These two structures will be refereed in this work as (i) "the inner belt", which was already reported by Bonnefoy et al. (2017) based on their epoch 2016-04-05, and (ii) "the second, outer structure" (see Fig. 2), which is also reported by Bonnefoy et al. (2017), but which appeared particularly faint in their observation.

For the second, outer component, we confirmed the its West-part based on the new epoch 2019-07-09, with a higher S/N of median average 3.4±0.6 per pixel, compared to a S/N of 1.5±1.0 per pixel in the previous epoch 2016-04-05.

In addition, we processed the epochs 2019-07-09 and 2016-04-05 with an iterative version of PCA (Pairet et al. 2021; Juillard et al. 2023), using ADI only (I-PCA ADI), reference differ-

[4] https://github.com/vortex-exoplanet/VIP/

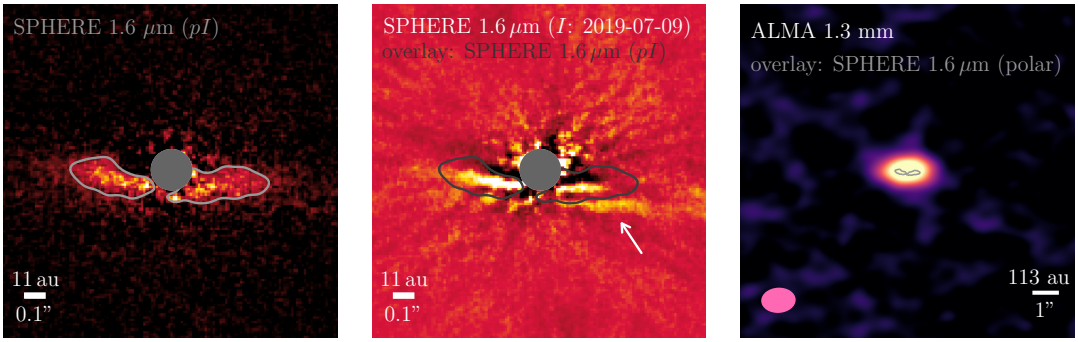

Fig. 3. Comparison of the disk structures in HD 120326 detected in scattered-light (SPHERE, 1.6 μm) and in thermal emission (ALMA, 1.3 mm). On the *left*, we show the polarized intensity SPHERE image with in overlay the contours of the inner belt determined for a signal level of 2 mJ/arcsec^2 on this image convolved with a gaussian to obtain smooth contours. The contours are added on the total intensity SPHERE image (*middle*) and on the zoom-out ALMA reconstructed image (*right*). In the *middle* image, we added a white arrow to point out the South-West part of the second structure seen in total intensity, which does not overlap with the signal seen in polarized intensity.

ential imaging (RDI, Lafrenière et al. 2009) only (I-PCA RDI) or combined (I-PCA ARDI, Juillard et al. 2024). Reference differential imaging has proved to be efficient to remove the stellar halo and retrieve extended circumstellar signal of dozen of ground-based observations (Xie et al. 2022; Ren et al. 2023a). Using an iterative approach for PCA helps to limit the effects of self-subtraction, over-subtraction and deformations of the disk. To apply I-PCA ARDI, we used a library of reference frames obtained from observations of other stars with SPHERE/IRDIS in the same filter. On HD 120326, contrary to I-PCA RDI, the processing I-PCA ADI and I-PCA ARDI retrieve the second, outer structure on the epochs 2016-04-05 and 2019-07-09, see Fig. A.1. In particular, the East and West parts of the second, outer structure are more visible than in the simple PCA ADI reductions shown in Fig. 2.

Concerning IFS observations covering Y and J bands, we processed them using PCA ADI and ten modes. Since the disk is faint, we consider only the best epoch, 2019-07-09, and we binned the spectral channels per six, to increase the signal-to-noise ratio. Over the 39 spectral channels of the IFS, we kept 30 channels, removing the first and last ones, and a few that were more impacted by artifacts. In these images (Fig. A.2, from top-left to bottom-middle), the first belt is visible, but not the second, outer disk structure. We recovered the West part of the second structure only by taking the average of the 30 spectral channels and applying a spatial binning (Fig. A.2, bottom-right).

In the rest of this work, we will mainly use for the SPHERE total intensity observation, the epoch 2019-07-09 because its signal-to-noise ratio is higher than the other exploitable observations (2016-04-05, 2016-06-03), and it is acquired in the exact same filter than the SPHERE polarized intensity data (see Table 1). We will use the PCA ADI processing to have a fast-computing processing algorithm (compared to I-PCA ADI/ARDI) when modeling the data to derive the best-fitting disk parameters (see Sections 3.1 and 3.4).

2.1.3. Comparison of polarized versus total intensity data

The striking result from the previous Sections 2.1.1 and 2.1.2 is the differences between the disk structures imaged in polarized and total intensity. Only one disk belt is seen in polarized intensity, while two components are detected in total intensity. In Fig. 3, we compare the location of both structures, and we show that the first structure in total intensity matches the location of the ring imaged in polarized intensity. The second structure is located further away.

2.2. ALMA millimeter observations

ALMA observations of HD 120326 were acquired as part of project 2022.1.00968.S (PI J. Miley). In total five separate executions were made on October 19th and 21st, and December 17th, 18th, and 27th, 2022. The observations use a spectral set-up using Band 6 receivers that include two relatively coarse resolution spectral windows with 128 channels of width 15.6 MHz placed at central frequencies of 218.0 GHz (1.375 mm) and 233.0 GHz (1.287 mm). Two further spectral windows were placed to cover any potential bright molecular lines. The first was positioned with central frequency 230.5 GHz (1.301 mm) containing 3 840 channels of width 244 kHz (1.4 μm). The final spectral window was positioned at central frequency 220.0 GHz (1.363 mm) with 1 920 channels of width 976 kHz (6.0 μm). We reduced the raw data by using the pipeline script provided by ALMA observatory using CASA version 6.4 (McMullin et al. 2007).

Although emission from molecular lines is not detected, we flag channels corresponding to ±15 km/s of the rest frequency of the bright molecular line transitions covered by channels within the spectral windows, specifically ^{12}CO at 230.538 GHz, ^{13}CO at 220.4 GHz and ^{18}CO at 219.6 GHz. This ensures that any potential contamination of the continuum image by line flux is avoided. The observed data was then averaged in frequency to produce consistent channel widths of 15.625 MHz before imaging and the five executions were then concatenated into a single data set for imaging. Images were reconstructed using `tclean` task in CASA using the Hogbom deconvolver (Högbom 1974) and natural weighting. This produced a continuum image with a synthesized beam of size of $1.321'' \times 0.950''$ ($PA = -86.729°$), and achieved a noise level of 17 μJy/beam. The clear detection of circumstellar material, which is unresolved, is shown in Figure 3 (right panel). There is no evidence of any offset from the expected stellar position.

Our measurement of the flux of the debris disk is achieved by fitting a Gaussian in the uv-plane, giving an integrated flux value of 561 ± 20 μJy in the continuum at 1.3 mm. In addition, we derived an upper limit of the ^{12}CO value of 4.8 Jy · km/s. This corresponds to three times the rms noise level measured over an area equal to the size of the synthesized beam.

2.3. HST/STIS optical observations

The archival *HST*/STIS observation of HD 120326 were already published in Padgett & Stapelfeldt (2016) and Bonnefoy et al. (2017). These coronagraphic observations were acquired on 2013-06-20 with the star centered behind the WedgeA1.0 at two different rolling angles of separation 30° and in the broad band filter centered at 0.59 μm ($d\lambda$ = 0.44 μm). Both papers published reduced images with an extended halo around HD 120326, and strong stellar artifacts at close separations.

We post-processed again the dataset with a home-made routine to remove most of the stellar light. We used as inputs the two calibrated images acquired at ORIENT1 (28°) and ORIENT2 (58°), performed a roll-subtraction (IM1-IM2) and de-rotated the image, resulting in North up and East on the left. The corresponding results are shown in Fig. 4. As can be seen, we recover the disk, which is impacted by self-subtraction (see black negatives feature at the bottom right of the wedge in Fig. 4). We derived the flux map (Fig. 4) by converting the ADU in Jy/arcsec^2, following the procedure described on the STScI website[5]. At large separations ($> 2.5''$), the disk has a flux density of a few μJy/arcsec^2.

To better distinguish the disk features from the stellar residuals, we also computed the S/N map. We defined the signal map as the reduced STIS image. Regarding the noise map, we computed radially the noise as the standard deviation in annuli. We did not consider the full image, but only the top-right quadrant, in which we masked the (small) regions defined by the location of the WedgeB1.0, one of the stellar spikes, a few background sources or suspicious, bright pixels. We applied a spatial binning of a factor four (two in height and two in width) to increase the S/N. We show the S/N map in Fig. 5. A large asymmetric disk structure extends up to a projected separation of about 700 au. Its S/N per pixel is between 5 and 8. This spiral-like feature is discussed in Section 5.2. Some signal is still visible relatively close to the star, at the East edge of the WedgeA1.0 which has a width of 1". For scale comparison, in Fig. 5, we added the image of the inner structures detected with SPHERE in total intensity (*top*) and in polarized intensity (*middle*), and with ALMA (*bottom*). In Section 5.2, we examine the global architecture of the debris disk around HD 120326.

In the next two Sections, we present our constraints on the properties of the inner disk structures of HD 120326, which are detected in the near-infrared with VLT/SPHERE (Section 3) and in the millimeter with ALMA (Section 4).

3. Morphology, photometry and polarization of the disk structures from SPHERE near-infrared data

In Sections 3.1–3.4, we constrain the morphology, polarization, and reflectance spectrum of the inner dust belt of HD 120326. To this aim, we modeled the VLT/SPHERE near-infrared polarimetric and total intensity data. Then, in Section 3.5, we examine the leftover circumstellar signal in the residuals (indicated by the white arrow in Fig. 6, *bottom-right*) and investigate its origin.

3.1. Disk modeling with one belt

To derive the disk morphology, we modeled jointly and independently the SPHERE/IRDIS total and polarized intensity observations (2019-07-09 and 2018-06-01, respectively). We first describe our methodology and results for our joint modeling, and will then briefly also mention the results obtained for the independent modeling following a similar methodology.

In our simulations, we constrained the six following parameters related to the belt: its reference radius r_0, its position angle PA, its inclination i, its scattering anisotropy parameter g, its outer slope $\alpha_{\rm out}$ and a scaling factor related to its flux. To limit the number of free parameters, we fixed the eccentricity, ascending node and argument of periastron of the ring to zero, and a steep inner slope to $\alpha_{\rm in} = 10$. We used a gaussian vertical profile ($\gamma = 2$), a linearly flared ring ($\beta = 1$) and set the scale height ξ_0 to 1.5 au at the reference radius r_0 (aspect ratio of ~3.75%), see Eqs. B.1- B.3 and Augereau et al. (1999b) for a thorough description of the model for the dust density distribution. To model the scattering phase function (SPF) of the disk in total intensity, we used the Henyey-Greenstein (HG) function (Henyey & Greenstein 1941, see Eq. (B.5)) parametrized by the scattering anisotropy parameter g. The same goes for the polarized intensity, which is modeled by this HG function multiplied by the Rayleigh scattering function, see Eq. (B.6).

Our simulations aimed to minimize the reduced $\chi^2_{r,I+pI}$ defined as

$$\chi^2_{r,I+pI} = \chi^2_{r,I} + \chi^2_{r,pI} \quad (5)$$

$$= \frac{\chi^2_I}{N_{\rm resol,I} - N_{\rm param} - 1} + \frac{\chi^2_{pI}}{N_{\rm resol,pI} - N_{\rm param} - 1} \quad (6)$$

where $N_{\rm resol,I}$ and $N_{\rm resol,pI}$ are the number of pixels considered within the regions used to model the inner belt in the total and polarized intensity images (see Fig. B.1), and $N_{\rm param}$ is the number of free parameters. The χ^2_I and χ^2_{pI} are expressed as follows

$$\chi^2_I = \sum_{\rm pixel} \left[\frac{\texttt{PCA(}\,{\rm obs}_I - M_I\,(r_0,\, PA,\, i,\, \alpha_{\rm out},\, {\rm scaling}_I)\,\texttt{)}}{\sigma_I} \right]^2 \quad (7)$$

$$\chi^2_{pI} = \sum_{\rm pixel} \left[\frac{Q_\phi - M_{pI}\,(r_0,\, PA,\, i,\, \alpha_{\rm out},\, {\rm scaling}_{pI})}{\sigma_{pI}} \right]^2 \quad (8)$$

where ${\rm obs}_I$ is the pre-processed total intensity science coronagraphic cube before applying PCA ADI, Q_ϕ is the IRDAP-processed polarized intensity image, M_I and M_{Q_ϕ} are the convolved disk models in total (I) and polarized (pI) intensity, and σ_I and σ_{pI} are the noise maps of the observation in total and polarized intensity, respectively. Both the total and polarized intensity (I and pI, respectively) terms have similar values, they therefore give an equal contribution in this merit function.

To explore the parameter space, we first ran simulations using a `Nelder-Mead` minimization (Nelder & Mead 1965), to converge quickly to a minimum, before running a Markov Chain Monte Carlo (`MCMC`) algorithm with `emcee` (Foreman-Mackey et al. 2013) to explore the space parameter more extensively. The walkers were initialized by drawing random values in the interval set by the best parameters found with `Nelder-Mead` plus or minus 10%. The random draw was linearly uniform for the reference radius, the position angle, the scattering anisotropy parameter, the outer slope, the cosine of the inclination and the logarithm in base ten of the scaling flux factor. In total, we used 100 walkers, with 3 000 iterations for each parameter. For each iteration, we generated a disk model with the radiative transfer code `GraTeR` (Augereau et al. 1999b), available in the open-access library `VIP` (Gomez Gonzalez et al. 2017; Christiaens et al. 2023).

In the case of the total intensity data, we convolved directly the disk model M_I with the SPHERE/IRDIS non-coronagraphic

[5] https://www.stsci.edu/documents/dhb/web/c03_stsdas.fm3.html

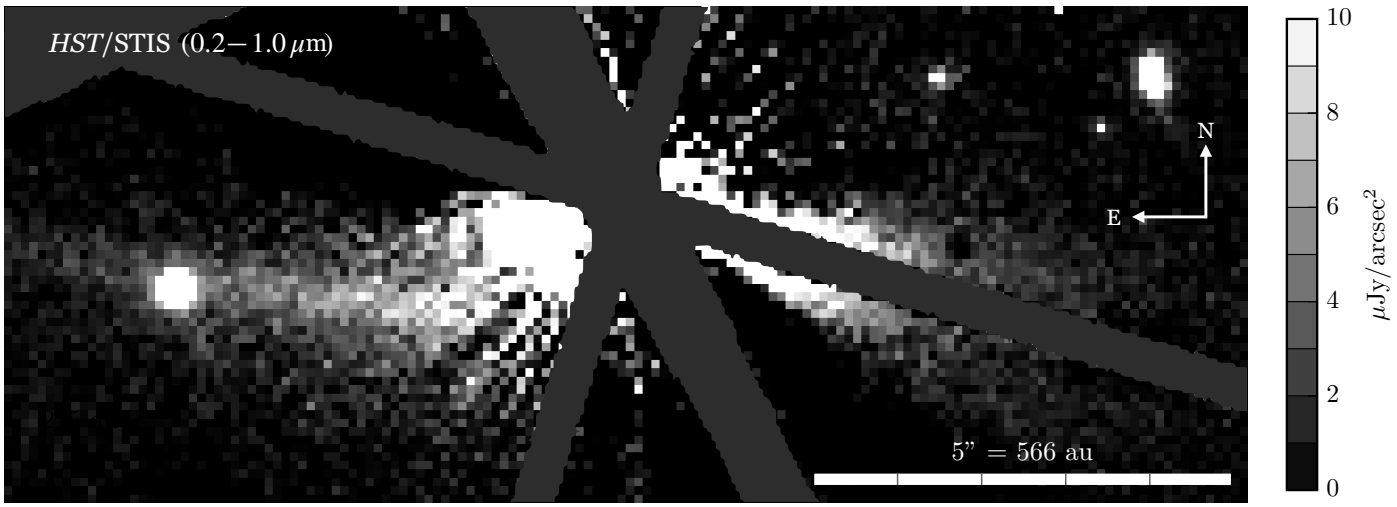

Fig. 4. Optical coronagraphic *HST*/STIS observations of HD 120326 centered behind the WedgeA1.0". We applied a spatial binning 2×2 pixels^2 → 1 × 1 pixel^2. The flux unit is μJy/arcsec^2. The areas hidden by the wedges (WedgeA and WedgeB) and the diffraction spikes (the cross-pattern) are masked in gray.

observation of the star, corresponding to the PSF of the instrument. Then, we rotated the convolved synthetic disk model for each parallactic angle of the sequence of observation, and subtracted it from the science coronagraphic cube. We processed this new cube by applying PCA using ten modes. We divided the cube by the noise map σ_I (computed in Section 2.1.2), producing a normalized residual map. If the disk model matches the observations, no circumstellar signal should remain in this normalized residuals map, that should only represent noise.

On the other hand, in the case of polarimetric observations, we matched the disk model with the Q_ϕ image obtained by processing with the IRDAP pipeline (see Section 2.1.1). To convolve robustly the disk model, we constructed the synthetic Stokes Q and U images from the disk model generated with `VIP`. We convolved those Q and U images with the PSF of the star and re-constructed the Q_ϕ image. Applying robustly the convolution on the reconstructed Stokes Q and U images is important for disks located at small separations, to account for positive and negative polarization signals that cancel each other when observed with a limited angular resolution (e.g., Engler et al. 2018; Heikamp & Keller 2019). We obtained the residual map by subtracting the synthetic image M_{pI} from the processed image Q_ϕ, and normalized it by the noise map σ_{pI} (computed in Section 2.1.1).

By considering only pixels within the region of interest (where the disk signal may be located), we summed the square value of these pixels for the total and polarized intensity, to obtain χ^2_I and χ^2_{pI}, respectively, and then $\chi^2_{r,I+pI}$ following Eq. (6). By minimizing $\chi^2_{r,I+pI}$, the `MCMC` exploration maximizes the likelihood directly related to it.

We list the best parameters derived for the dust belt in Table 2. The reference radius r_0 of $39.9^{+0.4}_{-0.8}$ au corresponds to a semi-major axis at maximum dust volume density in the mid plane of about ∼ 42.5 au with a full-width at half maximum of 24.3 au, with a shallow outer edge, thus decreasing slowly in density for higher radii. Our reference radius is consistent at 1σ with the reference radius (35.1 ± 3.4 au) derived by Olofsson et al. (2022b), and smaller than the one (61.9 ± 3.2 au) derived by Bonnefoy et al. (2017)[6], respectively for inner and outer slopes of $\alpha_{in} = 12$ and $\alpha_{out} = -2$ (Olofsson et al. 2022b) and $\alpha_{in} = 10$ and $\alpha_{out} = -5$ (Bonnefoy et al. 2017). From our disk modeling, the total surface brightness of the disk is $(1.2 \pm 0.2) \times 10^{-4}$ in polarized intensity and $(2.0 \pm 0.2) \times 10^{-3}$ in total intensity, corresponding to 0.12 ± 0.2 μJy and 2.0 ± 0.2 μJy, respectively, using a stellar flux of 0.975 mJy at 1.6 μm (Ofek 2008).

Figure 6 shows the synthetic disk models and residuals for the observations in polarized and total intensity at 1.6 μm. The posteriors are reported in Fig. B.2, for which we removed the first 2 000 iterations for each walker, considered as the burn-in phase. We can see that the reference radius is correlated with the inclination of the disk and the outer slopes. Regarding our best-fitting value of the inclination ($78.0^{+0.3}_{-0.5}$ °), it is between the values derived by Bonnefoy et al. (2017) and Olofsson et al.

Table 2. Morphology of the inner dust belt based on our `MCMC` exploration jointly fitting the SPHERE total and polarized intensity data.

Parameter	Range	Best fit $\chi^2_{r,min}$	Median ± 1σ
r_0 (au)	[10, 130]	39.9	39.7 ± 0.6
PA (°)	[−120, −60]	−94.1	−94.1 ± 0.1
i (°)	[0, 90]	78.0	77.9 ± 0.4
g	[0.05, 0.999]	0.78	0.77 ± 0.01
scaling (I)	[100, 10^8]	6.8×10^3	$(6.8 \pm 0.3) \times 10^3$
scaling (pI)	[100, 10^8]	9.6×10^4	$(9.3 \pm 0.6) \times 10^4$
α_{out}	[−20, −1.1]	−2.17	−2.18 ± 0.9
$SB_{disk,I}/F_{\star,I}$		2.0×10^{-3}	$(2.0 \pm 0.2) \times 10^{-3}$
$SB_{disk,pI}/F_{\star,pI}$		1.2×10^{-4}	$(1.2 \pm 0.2) \times 10^{-4}$

Notes. The two last lines correspond to the total surface brightness of the disk in total and polarized intensity, respectively, expressed in terms of contrast, i.e., divided by the total stellar flux. The ranges correspond to the authorized values. The disk models and residuals are shown in Fig. 6, and the corner plot of the posteriors in Fig. B.2. One may wish to compare these results with those from the `MCMC` exploration independently fitting either the total or polarized intensity, see Tables B.1 and B.2, respectively.

[6] To be consistent, we updated their original value 58.6 ± 3 au to 61.9 ± 3.2 au to take into account the different values used for the distance of HD 120326, which is 113.4 pc in this work (and in Olofsson et al. 2022b), and 107.4 pc in Bonnefoy et al. (2017).

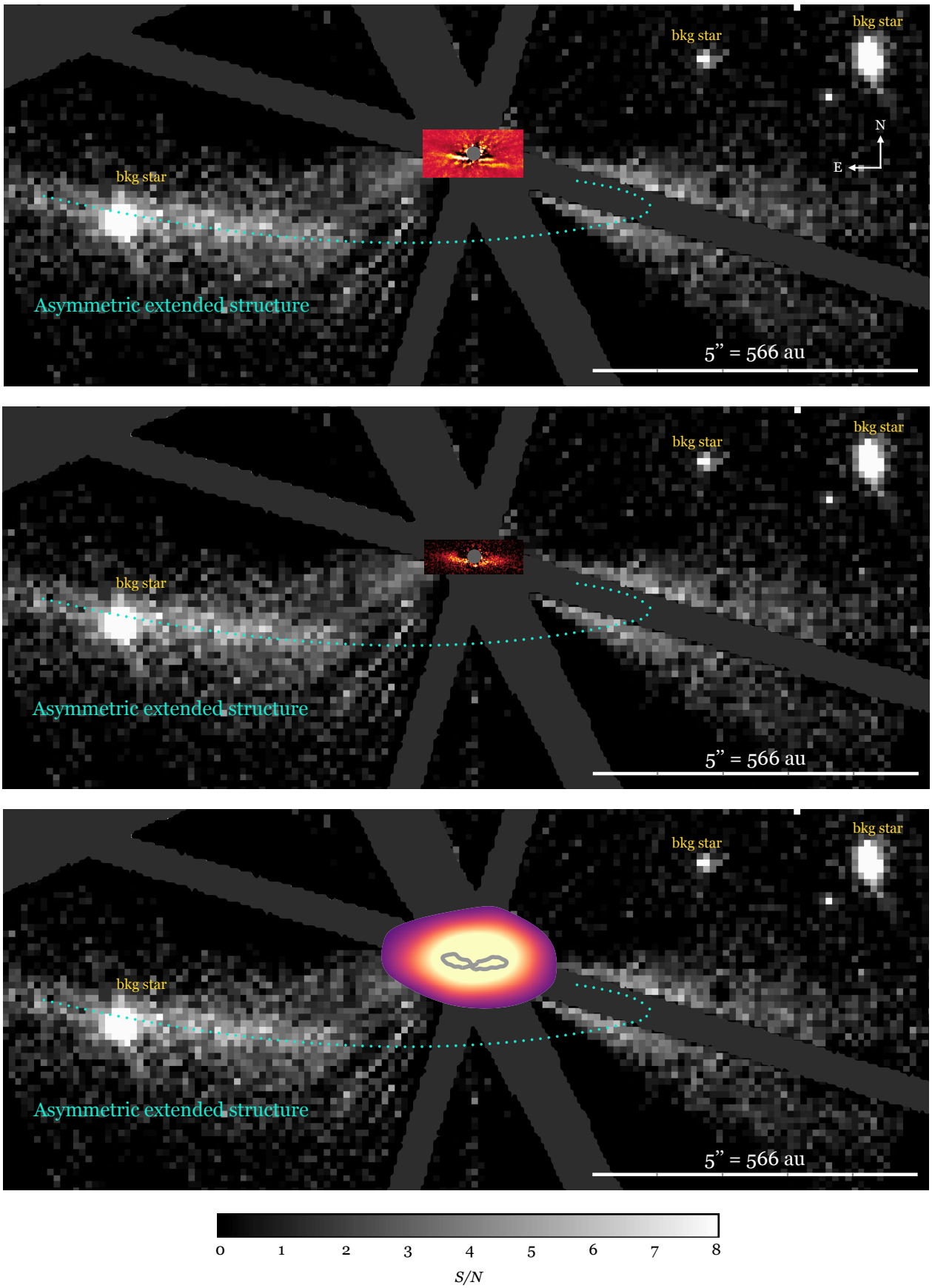

Fig. 5. Overview of the young debris disk around HD 120326. The black-to-white images are the S/N map of the optical *HST*/STIS coronagraphic data, with a spatial binning 2×2 pixels^2 $\rightarrow$ 1×1 pixel^2. For reference, in the center of the images we display the inner structures detected with SPHERE in total intensity (*top*), in polarimetry (*middle*) and with ALMA (*bottom*). The areas hidden by the coronagraphs and the *HST* diffraction spikes are masked in dark gray.

(2022b), 80° ± 1° and 76.7° ± 0.6°, derived either only based on the total or polarized intensity, respectively.

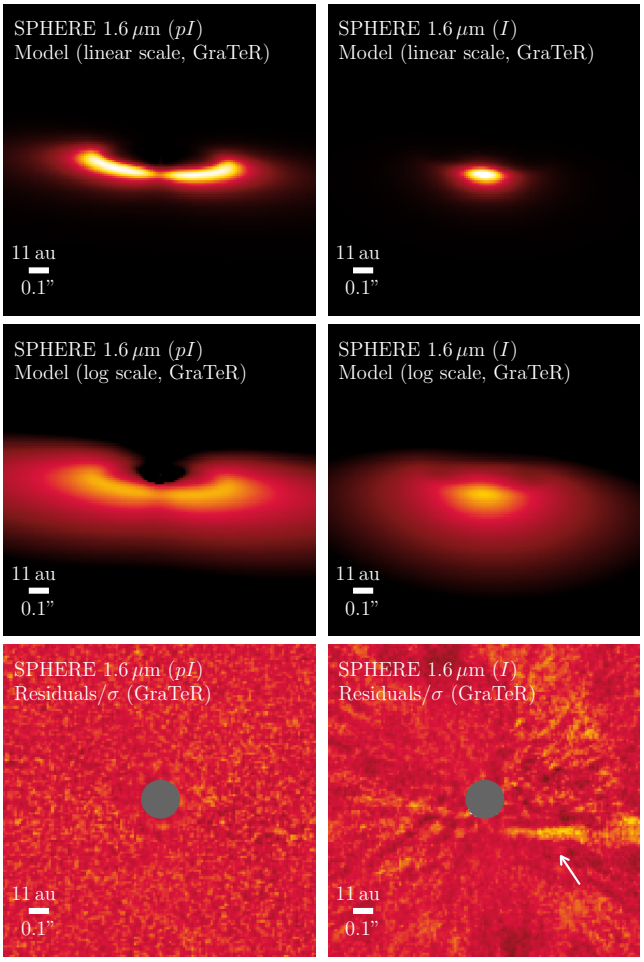

Fig. 6. Results of our MCMC simulations, using the Pythonized version of the GraTeR tool to generate the belt model. We show the best models in linear or logarithmic scales (*top* and *middle*), and the associated residuals normalized by the noise ("σ", *bottom*). Scattered light images for the polarized intensity images are on the *left* and those for total intensity images on the *right*. Some signal is still visible in the total intensity residuals, and is indicated by the white arrow. Unlike the disk model in total intensity, the disk model in polarized intensity accounts for Rayleigh scattering, hence visual brightness differences between these disk models depending on the scattering angle. The best-fitting parameters are given in Table 2. As a reminder, since the disk inclination found is 78°, the scattering angle is 12° at the closest location of the belt, 90° in the anses, and 168° at its furthest location (see also Fig. 5 from Perrin et al. 2015, to have an insight of the scattering angles around a dust belt).

For completeness, we also ran additional simulations to model independently the debris disk seen either in the SPHERE/IRDIS total intensity or polarized intensity. We display the best-fitting parameters obtained in each case in Tables B.1 and B.2, respectively. The results based on total intensity give higher values for the inclination, the reference radius and the anisotropic parameter compared to the results based on polarized intensity only: $i_I = 79.4° \pm 0.3°$ and $i_{pI} = 77.1^{+0.6°}_{-0.5}$, $r_{0,I} = 43.2^{+1.0}_{-0.9}$ au and $r_{0,pI} = 38.5^{+1.1}_{-0.7}$ au, $g_I = 0.81 \pm 0.01$ and $g_{pI} = 0.74^{+0.03}_{-0.02}$. They are consistent with each other at 3σ. Provided uncertainties from our simulations in this paper are statistical uncertainties derived from the MCMC fitting process (see Fig. B.2) and are likely underestimated, as it is common in morphological simulations of disks with MCMC exploration (see Mazoyer et al. 2020). We can see that the best parameters derived by jointly fitting the total and polarized intensity are roughly an average of the best parameters derived by independently fitting these observations (Tables 2, B.1 and B.2).

To summarize, our best model fitting jointly the observations acquired in total and polarized intensity seem to reproduce well the observed disk signals, excepting the signal in the residuals indicated by the white arrow (Fig. 6, *bottom-right*). This signal corresponds to the second, outer structure already mentioned in Section 2.1.2 (see also Fig. 2), and we will investigate its nature in Section 3.5. Since most of the signal is reproduced by modeling with one dust belt jointly the polarized and total intensity observations, the difference between both images can be mostly assigned to processing effects (Section 2.1) and the scattering phase function (Section 3.2).

3.2. Scattering phase function and degree of polarization

In Fig. 7, we compare the scattering phase function of the joint and independent modeling of the polarized and total intensity observations derived from the disk modeling described above. Using the ad-hoc formalism of Henyey-Greenstein (see Eqs. (B.5) and (B.6)), the scattering phase function is parameterized by one scattering anisotropy parameter g, which is the same for the polarized and total intensity data in the case of the joint modeling.

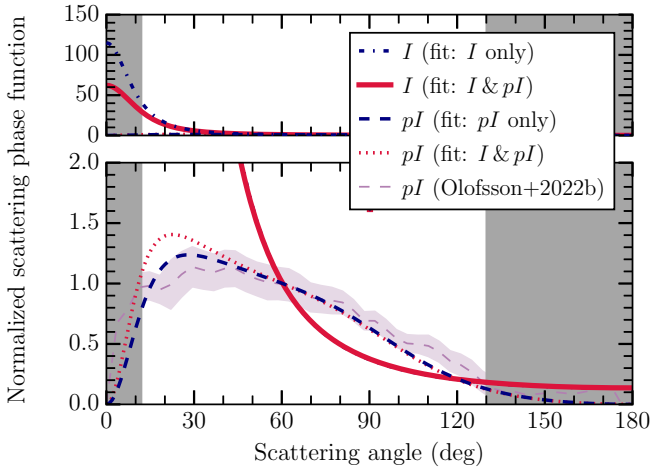

Fig. 7. Scattering phase function for our best model of the polarized and total intensity observation, fit independently or jointly. For comparison, we added the model retrieved by Olofsson et al. (2022b) for the polarized intensity data. We hide the part below 12° and above 130°, because we do not detect the disk for such scattering angles, neither in polarized or total intensity light (see text).

Both polarized SPF mostly agree with each other, with some differences at low scattering angles (10–30°) that correspond to a region of the disk close to or below the inner working angle of the coronagraph. In Fig. 7, we also compare our polarized SPF with the one derived by Olofsson et al. (2022b). They are consistent with each other at 2σ, and mostly at 1σ, with differences for scattering angles between 105° and 125°, corresponding to backward scattering from the disk. We hide in the Fig. 7 (and Fig. 8) the parts of the SPFs for which we do not have access to the scattering angles, that is to say, below 12° (i.e., 90° − inclination) and above 178° (i.e., 90° + inclination) due to geometrical effects, and also above 130°, because no disk signal is detected in either polarized or total intensity data.

As for total intensity, the scattering anisotropy parameter g increases when modeling independently the total intensity data, compared to modeling it jointly with polarimetric observations (see Tables 2 and B.1). This results in a disk which seems even more strongly forward scattering, i.e., a SPF steeper at low scattering angles (Fig. 7). Nonetheless, the height of the peak must be taken with caution, first because it cannot be constrained below 12° (geometrical effects). Second, the inner belt of HD 120326 at low scattering angles (10–30°) corresponds to a projected separation below or at the edge of the inner working angle of the coronagraph. Moreover, at small separations, the self-subtraction effects caused by ADI removes most of the light (Milli et al. 2012). Estimating the SPF of the inner belt of HD 120326 is therefore particularly challenging at low scattering angles.

Figure 8 shows the comparison of the SPF of HD 120326 in total intensity at 1.6 μm with that of other extrasolar debris disks and dust populations in the Solar System. The dust populations in the Solar System include the zodiacal dust (Leinert et al. 1976), the ring D68 of Saturn (Hedman & Stark 2015), the comet 67/Churyumov-Gerasimenko (using the dataset MTP020 acquired on 2015-08-28, Bertini et al. 2017), and microasteroids of diameter 10 μm, 30 μm, and 100 μm (Min et al. 2010). The SPFs of these microasteroids, corresponding to dust grains covered by small regolith particles, were derived theoretically using Fraunhofer diffraction model and Hapke reflectance theory (Hapke 1981) by Min et al. (2010). All SPFs are normalized at 60° for easier comparison.

Based on Fig. 8, one can see that the SPF of HD 120326 is somehow similar to the SPFs of HD 35841 (Esposito et al. 2018), HD 61005 (Olofsson et al. 2016) and HD 114082 (Engler et al. 2023), with a significant forward scattering peak and a continuous decline as the scattering angle increases. Nonetheless, we note that the derived SPF of HD 120326 is limited by the one-component HG function we used in our modeling, which prevents us from obtaining both forward and backward scattering contributions for the inner belt of HD 120326, as observed e.g. for HR 4796 (Milli et al. 2017) and HD 11721 (Engler et al. 2020). Even though we do not observe any backward scattering for HD 120326 in the images, there may be some to a lower level, for which our observations are not sensitive to. Regarding the dust populations in the Solar System, the SPF of HD 120326 is very similar to that of the zodiacal dust, as already reported for other debris disks in Hughes et al. (2018).

3.3. Maximum degree of linear polarization

We here derived the maximum polarization fraction of the inner belt, defined as the maximum of the linear degree of polarization over the scattering angles. We divided the scattering phase function of the polarized intensity data by that of the total intensity data for our best synthetic models, using the scaling flux found in our modeling to express them in the same unit. This led us to obtain the linear degree of polarization for our best disk model.

The maximum polarization fraction occurs at a scattering angle of 90°, because of the Rayleigh scattering assumed in our formalism to model the polarized SPF (Eq. B.6), and the fixed scattering anisotropy parameter g for both total and polarized intensity models. This sets the bell shape of the linear degree of polarization of the inner belt.

We found that the inner belt of HD 120326 has a maximum polarization fraction of 51 ± 6 %. The 1σ uncertainty accounts for the error of the flux in total and polarized intensity (Table 2). This maximum polarization fraction is similar to HR 4796 A (50 % ± 3 % at 1.9–2.19 μm, Perrin et al. 2015), and higher than other debris disks (10–20 % in the near-infrared, e.g., Beta Pictoris, HD 15115, HD 32297, HD 114082, see Tamura et al. 2006; Asensio-Torres et al. 2016; Bhowmik et al. 2019; Engler et al. 2023). A high maximum polarization fraction can for instance be associated to a low albedo of dust particles (Umov 1905), or also to small monomers in dust grain aggregates (Tobon Valencia et al. 2022).

3.4. Reflectance of the inner belt

We derived the reflectance of the inner ring based on the spectroscopic SPHERE/IFS (YJ bands) and photometric SPHERE/IRDIS (broad band H) data acquired simultaneous during the best epoch of observation (2019-07-09) in total intensity, and the additional photometric points acquired in 2016-04-05 in the narrow bands H2 and H3. The reflectance represents the surface brightness of the disk ($SB_{\rm disk}$) divided by the total stellar flux ($F_\star$).

In practice, we ran new `MCMC` simulations for the five IFS images (Fig. A.2) to estimate the surface brightness of the inner belt. In the `MCMC` simulations, one free parameter (the flux scaling factor) was used, and the five others (r_0, PA, i, g, $\alpha_{\rm out}$) were fixed to the best fitting values (Table 2) found previously (Section 3.1) based on our modeling of the joint total and polarized intensity observations in the broad band H. We determined the surface brightness of the inner belt as the total flux of the best synthetic belt model. Then, we divided the surface brightness of the belt by the stellar flux estimated within a large circular region of diameter 12 FWHM, representing between 20 and 27 pixels depending on the wavelength and plate scale of the instrument (IFS or IRDIS).

We show the reflectance spectrum of the inner ring between 1.0 and 1.8 μm in Fig. 9. Based on the SPHERE data, we conclude that the inner belt seems to have a red color at 1σ between 1.0 and 1.3 μm, and a gray color between 1.3 and 1.8 μm. Although there are large uncertainties on the 1.6 μm measurement, there might be a tentative evidence of a break in the reflectance spectrum between 1.3 and 1.5 μm. Such a break could be caused by an absorption band around 1.5 μm, possibly due to H_2O in water ice (Ciarniello et al. 2021) or in minerals (e.g., phyllosilicates, Hu et al. 2012; Lane et al. 2024). The red spectral slope from 1.3 to 1.5 μm would be due to additional compound(s) mixed with H_2O ice or H_2O-bearing minerals, possibly opaque minerals or organic matter (e.g., mixture of water ice and kerite in Ciarniello et al. 2021)

Regarding the uncertainties on $SB_{\rm disk}/F_\star$, we derived them by including the errors on the estimations of the surface brightness of the disk and the stellar flux. Concerning the surface brightness, we estimated the error via the posteriors of the `MCMC` simulations. The lower and upper errors are defined to cover an interval of 68% of the posteriors, centered on their median value (e.g., Fig. B.2). As for the stellar flux, we considered a conservative 5% variation during the sequence of observation, based on empirical experience.

3.5. Nature of the second component of the disk (seen in the SPHERE total intensity data)

By examining the residual image in Fig. 6 (*bottom-right*), one can see that there is still some signal in the South-West region of the disk, indicated by the white arrow. Such signal is located beyond the inner belt seen in polarimetry (Fig. 1), and is unlikely

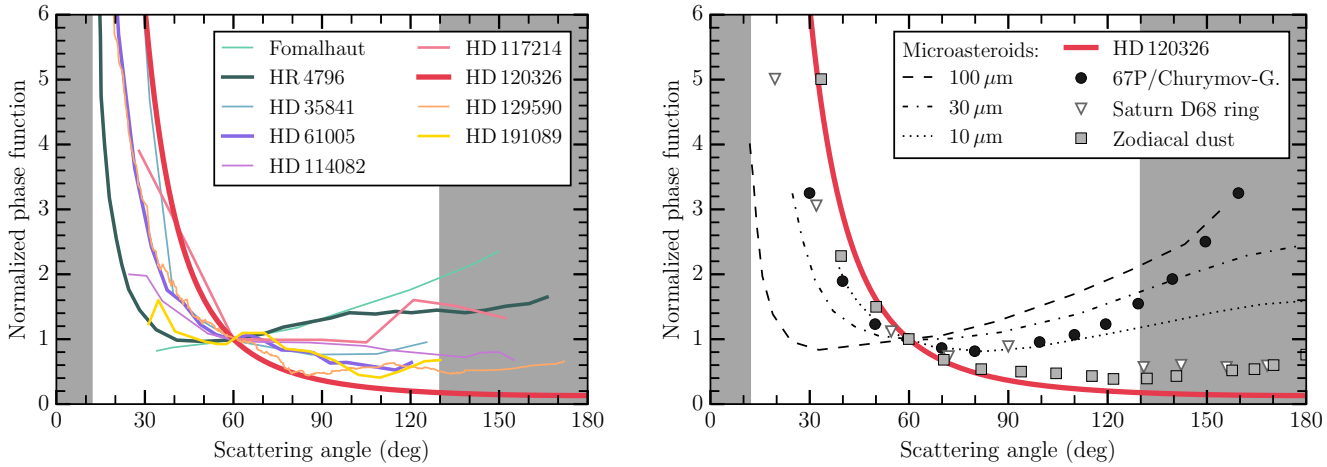

Fig. 8. Scattering phase function of the inner belt of HD 120326 seen in total intensity compared to other extrasolar debris disks (*left*) and different dust populations in the Solar System (*right*).

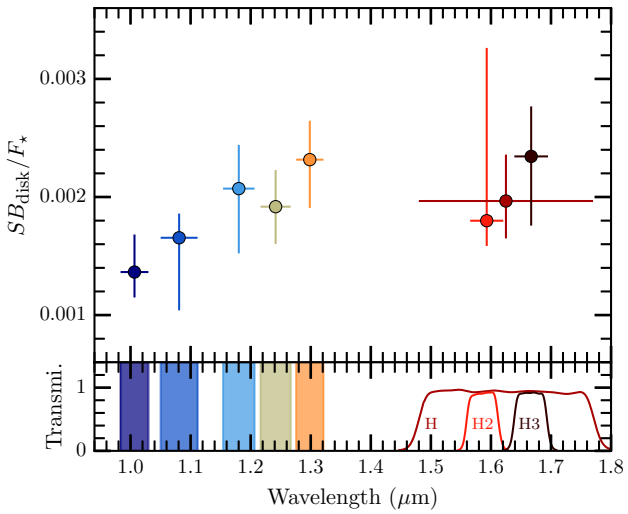

Fig. 9. Reflectance spectrum of the inner belt of HD 120326. For each point, we derive the surface brightness of the disk (SB_{disk}) and the stellar flux ($F_\star$) over a spectral range shown by the horizontal line around each point, and also by the colored areas (IFS) or the filter transmission (IRDIS) at the bottom.

to be caused by an effect of the ADI post-processing on the inner belt. Indeed, the residual image is obtained by processing a inner-belt-free cube, since we subtracted the disk model to the cube of observation, before processing it with PCA ADI (Section 3.1). In addition, this second structure is imaged at different epochs and with different algorithms (Figs. 2 and A.1).

Therefore, we firmly confirmed this second disk structure, whose exact nature remains to be determined. Previously, Bonnefoy et al. (2017) considered whether it could be a halo of dust grains, or, a second belt. We revisit both options below, by using in particular the fact that the second structure is not detected in the polarimetric data (Olofsson et al. 2022b, and this work).

3.5.1. Hypothesis: second belt

By assuming that the second structure is an additional belt, Bonnefoy et al. (2017) found out that its reference radius would be 137 ± 9 au[7] and its flux ratio relative to the inner one would be 0.08 ± 0.03 at the scattering angle for which the flux is maximum in total intensity. By using their disk models, we checked that this value of flux ratio is the same at scattering angles of ∼30°, i.e., the maximum of the polarization intensity peak based on Fig. 7, and ∼ 70°, which still has a high level of polarization intensity and at which we do not detect the second structure in Fig. 1.

Thus, by assuming that the dust particles of the second belt have the same polarimetric properties as those of the inner disk, we expect the flux of the second belt to be 8 ± 3% of the flux of the inner belt, i.e., 12.5 times smaller. However, such flux is too faint to be recovered in our polarimetric data, because we only detect the inner belt with a S/N of 3–7 per pixel (see Fig. 1), so a flux 12.5 times smaller results in a S/N below one per pixel. Therefore, the second structure seen in total intensity could be a second ring, that remains undetected in our SPHERE polarimetric (2018-06-01) observations due to a lack of sensitivity.

3.5.2. Hypothesis: Apocenter pile-up of small particles originating from the inner belt

Alternatively, the second structure could be a halo of small particles related to the inner belt. Indeed, these small particles could originate from the collisions of larger bodies within the inner belt ("birth ring", Strubbe & Chiang 2006, see also Lecavelier Des Etangs et al. (1996); Augereau et al. (2001)) similarly to the debris disk around HD 129590 (Olofsson et al. 2023). This halo would correspond to the eccentric orbits of small particles, whose size sets their eccentricity. Instead of a smooth continuous halo, it could have a visual gap between the birth belt and the second disk structure. This could be explained by the apocenter pile-up model (Olofsson et al. 2023), that uses the fact that the small, eccentric particles spend most of the time at their apocenter. By considering many small particles in a narrow range of sizes, their eccentricities would be similar, and so too their apocenter distances (but with arguments of pericenter uniformly distributed between [0, 2π]). This results in a visual arc structure located at their apocenter distance for scattering angles giving a bright enough SPF. This arc structure could be enhanced by

[7] To be consistent, we updated their original value 130 ± 8 au to 137 ± 9 au using the most recent distance estimation of 113.4 pc (and not 107.4 pc as in Bonnefoy et al. (2017)).

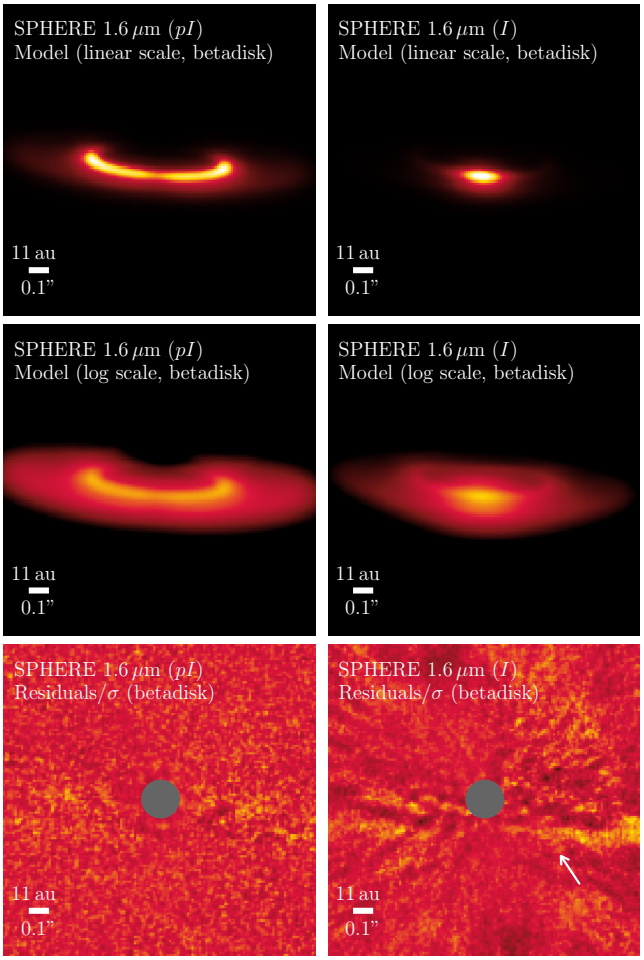

Fig. 10. Scattered light images of one dust belt generated using the code `betadisk`, with the associated residual map normalized by the noise ("σ"), in polarized and total intensity (*left* and *right*, respectively). The second structure seen with SPHERE (indicated by the white arrow) is somehow more removed, compared to the `GraTeR` modeling (Fig. 6, *bottom-right*).

scattering efficiencies that depend on the size (and composition, porosity) of dust particles (Olofsson et al. 2023) and the wavelength of observation. We stress that the apocenter pile-up model introduces a visual pile-up (not a dynamical one), and that it is different to the apocenter glow, which requires an asymmetric disk (Pan et al. 2016, see also Wyatt et al. (1999)).

To investigate this, we used the open-access `betadisk` tool[8] (Olofsson et al. 2022a). This code can compute scattered light images for different grain sizes, parametrized by the parameter β. This parameter is the ratio between the stellar radiation pressure and gravitational forces. It is inversely proportional to the particle size s in the case of stars bright enough, $\beta < 0.5$ and $s \gtrsim 0.5$ μm (e.g., Burns et al. (1979), Figs. 1 and 2 from Artymowicz (1988), and Fig. 7 from Löhne et al. (2012)).

By assuming the disk parameters determined in Section 3.1 (disk inclination, position angle, reference radius, and the scattering anisotropy parameter), we modeled the inner belt with `betadisk`. This synthetic disk is a linear combination of 14 scattered light images computed for different grain sizes, corresponding to β from 0.01 to 0.4. We found out that a combination of large particles, mainly in the parent bodies corresponding to the inner belt, and eccentric, small particles could better model the disk structures than the previous model generated with the radiative transfer `GraTeR` code, for which we used its fast-computing version. This version does not assume any size distribution, but an overall scattering efficiency for the dust without any underlying assumption on the grains. We can indeed see that the residual map corresponding to the `betadisk` model (Fig. 10) is to some extent cleaner than the one corresponding to the `GraTeR` model (Fig. 6). The apocenter pile-up model may therefore explain some signal of the second structure.

Yet, this second structure is asymmetric, with a higher flux and larger extension in the West than in the East. In addition, this asymmetry is reversed for the inner belt, which is brighter and more extended in the East than in the West, see Fig. 2 and the Fig. 2 from Bonnefoy et al. (2017). This still remains to be explained.

[8] Accessible here https://github.com/joolof/betadisk

4. Morphology and photometry of the dust belt seen with ALMA millimeter observations

In Section 4.1, we constrain the morphology of the disk detected with ALMA (Fig. 3). Then, in Section 4.2, we model the SED by taking into account the new ALMA measurement. Last, in Section 4.3, we derive the dust mass of HD 120326.

4.1. Morphology of the disk

The ALMA observation does not resolve the disk (or only very marginally, see Fig. 3), so we used parametric modeling of the visibilities to obtain constraints on the disk parameters. We used an optically thin 3D model that takes line of sight effects into account, which was previously used to model debris disks (e.g., Kennedy 2020). To obtain constraints on parameters, we modeled the data using `galario` (Tazzari et al. 2018) to Fourier transform the model images and compare them to the observed visibilities, and `emcee` to perform Markov-Chain Monte-Carlo sampling and extract posterior distributions for parameters. We assumed a Gaussian torus model, for which the model parameters are x/y offsets from the observation phase center, the disk inclination and position angle, the disk flux, the ring radius and width. The scale height (H/r) was restricted to be small (< 0.05). We did not include the stellar flux as it is ~100 times fainter than the disk at 1 mm. We ran the `MCMC` until all parameters converged, and then continued sampling to build up the posterior distributions.

Posterior distributions from the modeling are shown in Fig. C.1. The inclination ($70 \pm 5°$) and position angle ($-91.7 \pm 4.5°$) are consistent at 2σ with the scattered light results. While the resolution clearly limits the conclusions that can be drawn, the disk detected with ALMA peaks at radii of 35 ± 25 au at 1σ based on our modeling. At 1σ, the outer edge of the disk in the millimeter is 75 au at most, thus closer to the star than the second structure seen with SPHERE, which peaks at radii larger than 100 au (Section 3.5).

In particular, the mm-wave emission peaks at a location consistent with that of the inner belt seen in the near-infrared, for which scattered light models give disk radii between 30 and 65 au at 1σ, depending on the modeling and the SPHERE data used (see Section 3.1). By assuming millimeter dust traces the presence of planetesimals, we would expect that the inner belt resolved with SPHERE is a planetesimal belt. To be more confident would require higher resolution ALMA observations.

4.2. Modelling of the spectral energy distribution

To construct a spectral energy distribution, we collected photometry from various sources, e.g. *UBV*, *Stromgren*, *Hipparcos*, *Gaia*, *2MASS*, *WISE*, *Spitzer*, and *Herschel*. We also used the new ALMA photometric point derived in this work, and a *Spitzer* IRS spectrum. These data were fit with stellar and blackbody disk models as described previously by Yelverton et al. (2019). The best fitting model is shown in Fig. 11. The disk model used is a single component modified blackbody, as we found that this was sufficient to explain the data. We determined that the star has an effective temperature of 6 940 ± 100 K, and a luminosity of 4.5±0.1 $L_\odot$. We derived for the disk a temperature of 110±1 K and a fractional luminosity of 1.8×10^{-3}. The ALMA photometry is somewhat lower than expected for a pure blackbody, but this is expected for debris disks where much of the emission comes from bodies that are significantly smaller than 1 mm.

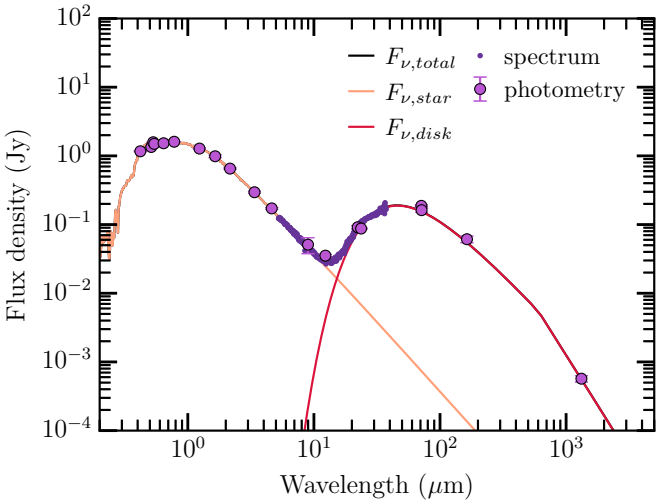

Fig. 11. Spectral energy distribution of HD 120326 based on archival data (see main text) and the new ALMA measurement at 1.3 mm.

Assuming blackbody absorption and emission, the dust temperature implies a dust population at 13 au from the star, which is clearly closer than it is observed. However, the small dust sizes also mean that their temperatures are higher than a blackbody at the same stellocentric distance, meaning that the 13 au distance is a lower limit. Empirically, Pawellek & Krivov (2015) found that the difference in disk radii at 4.5 $L_\odot$ is about a factor of four, which would make the SED estimate consistent with the semi-major axis derived for the SPHERE or ALMA data.

4.3. Dust mass

Based on the results from our SED modeling, we derived the dust mass, which consists of the mass of dust particles of size below a few millimeters. This is a significant underestimation of the total mass budget of the debris disk, as most of the mass is represented by the largest bodies (e.g., planetary embryos or kilometer-size planetesimals). The dust mass is regularly derived in the literature, expressed as

$$M_{\rm dust} = \frac{F_\nu d^2}{\kappa B_\nu(T_{\rm dust})}, \quad (9)$$

where F_ν is the flux density of the dust belt in W.m^{-2}.Hz^{-1}, d is the distance of the star hosting the dust belt, κ_ν is the dust opacity assumed to be 1.7 cm^{2}g^{-1} (850 μm/$\lambda_{\rm obs}$) from Beckwith et al. (1990) (also assumed in Krivov & Wyatt (2020)), $B_\nu(T_{\rm dust})$ is the Planck function, and $T_{\rm dust}$ is the temperature of the dust grains chosen to be consistent with the observed SED (110 K, see Section 4.2).

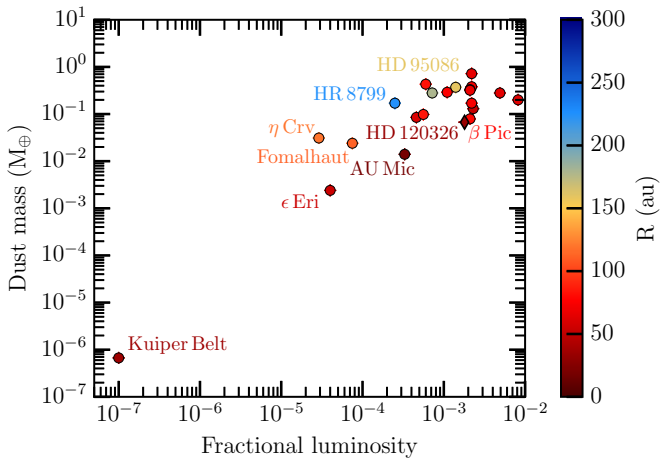

Fig. 12. Dust mass and fractional luminosity of the debris disk around HD 120326 (diamond marker) compared to those of the sample used in Krivov & Wyatt (2020) (circle markers). The dust mass and fractional luminosity of HD 120326 is in particular very similar to β Pic. The color represents the location of the dust belt relative to its host star.

We obtained a dust mass for HD 120326 of 0.067 M$_\oplus$. In Figure 12, we compare this dust mass to the sample from Krivov & Wyatt (2020), which is restricted to the best-quality ALMA data from Matrà et al. (2018), observed either in band 6 ($\lambda \sim$ 1.3 mm) or 7 ($\lambda \sim$ 850 μm). From Figure 12, HD 120326 has a fractional luminosity and dust mass very similar to β Pictoris (2.1×10^{-3} and 0.079 M$_\oplus$; A6V-type star), and for the two next closest matches, to HD 61005 (2.3×10^{-3} and 0.13 M$_\oplus$; G8Vk star) and HD 146181 (2.2×10^{-3} and 0.17 M$_\oplus$; F6V star), based on the values derived in Krivov & Wyatt (2020) (dust mass) and Matrà et al. (2018) (fractional luminosity).

5. Discussion

We discuss below our results on the inner belt (Section 5.1) and on the global morphology of the debris disk around HD 120326 (Section 5.2).

5.1. Inner belt

In Sections 3.1-3.4, we constrained different properties of the inner belt based on the VLT/SPHERE data, which we then identified as a planetesimal belt based on the ALMA data (Section 4.1). To summarize the results from SPHERE, the inner belt has a semi-major axis of 42.5 au, with a FWHM of 24.3 au (fractional width of 0.57). Its dust grains are strongly forward scattering in total intensity. Assuming a Rayleigh scattering for the SPF in polarized intensity data does match well the polarized intensity data. Their relatively high maximum degree of polarization (51% ± 6%) can be related to various physical properties (e.g., low albedo or small monomers if particles are structured in dust aggregates; Section 3.3). The red (1.0–1.3 μm) and then gray (1.5–1.8 μm) slopes of the dust particles can be interpreted as either related to the size or the composition of the dust grains. In the former case, dust particles would rather have a size (s)

equal or larger than the one defined by the size parameter size ($2\pi s/\lambda \sim 1$) at the turnover wavelength 1.3 μm (see Fig. 9). On the other hand, in the latter case, the slope and tentative break in the reflectance spectrum could be caused by absorption related to the presence of H_2O (see Section 3.4). Increasing the wavelength coverage and/or the spectral resolution could help to leverage the degeneracies between different dust grain properties.

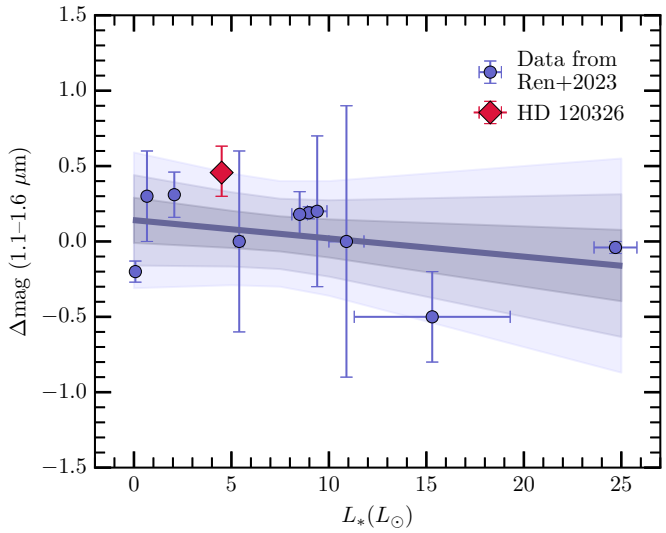

Fig. 13. Dust color at scattering angles between 80 and 100° for the debris disk around HD 120326 compared to other debris disks (Ren et al. 2023b). The trend and shaded areas corresponding to the uncertainties of the trend at 1σ, 2σ, and 3σ are from Ren et al. (2023b) based on their analysis (see their Section 3.2).

We compare the color 1.1−1.6 μm of the inner belt of HD 120326 with other debris disks (Ren et al. 2023b) in Fig. 13. The inner belt of HD 120326 has a color redder than 0.36 mag compared to what is predicted from Ren et al. (2023b) for a star of 4.5 $L_\odot$, lying at 3σ of their confidence region. Nonetheless, as highlighted by Ren et al. (2023b), the trend is based on a relatively small sample (ten disks), and some systematics could occur, as their data are from a different instrument, *HST*/NICMOS (but with a similar spectral coverage, with the filters F110W and F160W).

We point out that it would be particularly interesting to image the inner belt of HD 120326 with *HST*/STIS, which has a wavelength range centered at 0.59 μm ($d\lambda$ = 0.44 μm), using a mask with a smaller inner working angle (e.g., the Cbar5). Indeed, Ren et al. (2023b) derived the color 0.59 − 1.1 μm for twenty debris disks, and reported that debris disks with stellar luminosity of 4.5 $L_\odot$ have a bluer color of 0.7 mag at these spectral ranges. If HD 120326 would also have a blue color 0.59 − 1.1 μm and assuming the color is mainly related to the size of dust grains rather than their composition, this could hint at two different dust populations (e.g., Fig. 2 from Thébault & Kral 2019). Very small grains would be responsible for a blue color between 0.59 and 1.1 μm, and larger ones would be responsible for a red color between 1.1 and 1.6 μm.

5.2. Overall picture of the debris disk around HD 120326

The complex, global morphology of the debris disk around HD 120326 is illustrated in Fig. 5. Two key questions are, first, what is the nature of the extended asymmetric structure seen with *HST*/STIS at 100s of au and the second one seen with SPHERE in total intensity at smaller distances, and second, to what extent the inner structures detected with SPHERE and ALMA connect with the outer one seen with STIS.

Regarding the first question, the extended, asymmetric structure could be an eccentric or misaligned ring, or a spiral. The onset of an eccentric or misaligned disk is preceded by the appearance of spirals (Wyatt 2005b, assuming massless disks), and requires timescales an order of magnitude greater than the appearance of spirals, typically several 10–100 Myr at the reaches ($\gtrsim$ 100 au) of planetary systems (e.g., Pearce & Wyatt 2014). Thus, dynamical timescales are shorter to create a spiral than an eccentric or misaligned disk. Therefore, considering the young age (16 Myr) of the HD 120326 system, the asymmetric structure could be more likely to be a spiral than an eccentric or misaligned disk.

While spirals are regularly observed in gas rich protoplanetary disks, their detection is much rarer in debris disks. The reason for this is still unclear. The argument usually advanced is that they are only transient (Wyatt 2005b; Farhat et al. 2023), however, theoretical studies of planet debris disk interactions indicate that these features can be more persistent depending on the importance of disk self-gravity (Hahn 2003; Ward & Hahn 1998; Jalali & Tremaine 2012; Sefilian 2022). Notably, HD 120326 is one of the very rare debris disks with an imaged spiral-like feature. The other ones are the debris disks around TWA 7 (Olofsson et al. 2018), and possibly HD 106906 (Rodet et al. 2017; Farhat et al. 2023), and the gas-rich debris disk around HD 141569 (Konishi et al. 2016, but this one could be considered as a transition disk as with an age of 5 Myr). Among all of them, HD 120326 is the only one with a spiral-like feature spanning over hundreds of au, up to 1 000 au if co-planar with the inner belt. By assuming it is indeed a spiral, different mechanisms of dynamical interactions could be outlined to shape it. Stellar flybys can generate spirals (e.g., HD 141569, Reche et al. 2009), but this scenario remains very unlikely for HD 120326 based on the extensive search for such a dynamical perturber by Bertini et al. (2023).

As a result, the likely remaining possible mechanisms are, first, secular dynamical interactions with a planet (Wyatt 2005b; Farhat et al. 2023) possibly combined to disk self-gravity (Hahn 2003; Ward & Hahn 1998; Sefilian 2022; Sefilian et al. 2021, 2023), or considering disk self-gravity alone (Jalali & Tremaine 2012). It could also be collisional dust avalanches following the breakup of a large planetesimal-like object (Artymowicz 1997; Grigorieva et al. 2007), giant impacts (Jones et al. 2023), interstellar medium wind (as for HD 61005, Maness et al. 2009), or it could be potentially inherited from the protoplanetary disk phase (e.g., Najita et al. 2022).

Alternatively, we point out that the location of a bright point-like source overlays with the South-East end of the spiral-like feature (see Figs. 4 and 5). This bright source was determined to be a background star (see Appendix D and in particular Fig. D.1). We investigated whether the asymmetry of this extended disk structure could be caused by a fortuitous alignment of the background star with dust grains from the halo of dust grains around HD 120326. In such case, the strongly forward-scattering dust grains could scatter some of the light from the background star. This could result in more scattered-light on the South-East grains than on the South-West ones, because there is no bright background star there. This would mean that the spiral-like feature seen might actually be a fraction of an outer belt. However, from our modeling in Appendix D, this seems very unlikely that the asymmetry could be explained by the fortuitous alignment with the background star. In short, the scattering an-

gles of dust grains located in the South-East (at a close projected distance of the background star) and the South-West (at a far projected distance of the background star) are too close to each other to explain the asymmetry.

To determine what is the true morphology of the extended debris disk around HD 120326, and ultimately identify the mechanism causing it, new *HST*/STIS data are required. Indeed, large areas where disk signal is expected are masked by the WedgeA1.0 or the cross-pattern of the spiders, or are affected by self-subtraction effects from the data processing (see Section 2.3 and Fig 5). The new STIS data should be acquired with an optimized strategy of observation, using a color-matched reference star, more angular diversity (e.g., with three rolling angles instead of two), and an appropriate position of the wedges relatively to the disk, to probe a larger spatial coverage (e.g., Schneider et al. 2009).

Concerning the second, enigmatic structure seen with SPHERE in total intensity at smaller radii (e.g., Section 2.1.2), we investigated its nature in Section 3.5. Analysing this faint structure requires pushing SPHERE to its limits in terms of sensitivity, so we could not draw decisive conclusions about its true nature. We confirmed that the second structure could be a second ring, which was previously hypothesized by Bonnefoy et al. (2017), and we showed that due to its faintness, it is not expected to be detected in the SPHERE polarimetric observations (see Section 3.5.1). Alternatively, instead of a second ring, it could also be a halo of small particles that originate from the birth ring (see Section 3.5.2), identified as a planetesimal belt (see Section 4.1). This is supported by the apocenter pile-up model (Olofsson et al. 2023). Furthermore, this second structure is asymmetric, with a higher flux and larger extension in the South-West region. This could be explained by a giant impact at the opposite direction in the birth ring, generating small, eccentric dust particles pushed away by the stellar radiation pressure (Jones et al. 2023).

As for the second question, regarding whether both the outer (imaged with STIS) and inner (detected with SPHERE and ALMA) structures connect with each other, tackling it also suffers from the lack of spatial coverage of STIS, and in particular at small separations, hidden by the too large mask WedgeA1.0. In addition, some parts of the spiders coincide with the spiral-like feature, in particular in the region where it seems it could connect with the inner ring, see Fig. 5.

Concerning the SPHERE and ALMA images, in both images we do not detect a disk structure above a projected separation of 1.0–1.5″, where it could overlay with the disk signal detected with STIS data. Nonetheless, the second structure detected with SPHERE in total intensity is intriguing, and is in the direction where starts the spiral-like feature. Current observations cannot distinguish whether they are connected or not. However, new STIS data using masks with a smaller inner working angle such as the Cbar5 or WedgeA0.6, may provide crucial constraints.

6. Conclusion

In this paper, we presented a panchromatic study of the young (16 Myr) debris disk around HD 120326 surrounding a F5V-type star and located in the Sco-Cen OB association. We used optical (*HST*/STIS), near-infrared (VLT/SPHERE, both in total and polarized intensity) and millimeter (ALMA) data, some published for the first time in this work. These observations were sensitive either to the scattered starlight on dust grains (STIS, SPHERE) or their thermal emission (ALMA).

The debris disk around HD 120326 shows substructures both at intermediate and large distances, imaged with SPHERE and ALMA (30–150 au) and STIS ($\leq 1\,000$ au). From our analysis, we showed that modeling the ALMA data with one belt results in a belt morphology and location consistent with that of the inner belt imaged with SPHERE. By assuming millimeter dust particles trace the location of planetesimals, we identified the inner belt as a planetesimal belt. This belt has a semi-major axis at maximum dust volume density of ~ 42.5 au and an inclination of $\sim 78°$ from SPHERE near-infrared data. Constraints on the belt morphology using millimeter data are looser, and thus higher resolution ALMA observations are needed to be more accurate. Moreover, we derived from the ALMA data an integrated flux value of 561 ± 20 μJy in the continuum at 1.3 mm and an upper limit of ^{12}CO emission of 4.8 Jy $\cdot$ km/s. Using the new photometric ALMA measurement, we modeled the SED and determined a fractional luminosity of 1.8×10^{-3} and a dust mass of 0.067 $M_\oplus$, both values being very similar to the debris disk around β Pictoris.

Based on the SPHERE data, still regarding the inner belt, we derived its scattering phase function both in total and polarized intensity and its maximum degree of polarization ($51\,\% \pm 6\,\%$) at 1.6 μm. We derived its reflectance spectrum, which seems to show a red color between 1.0 and 1.3 μm and a gray color between 1.5 and 1.8 μm. There might also be a tentative evidence of break in the reflectance between about 1.3 and 1.5 μm. Such a break could be caused by various absorption features, for instance water in hydrated minerals (e.g., phyllosilicates) or opaque mixtures of water ice and kerite.

Furthermore, we also explored the nature of the second faint structure (≤ 150 au), seen in several SPHERE epochs in total intensity, with various processing algorithms. We confirmed it could be a second dust belt or a halo of small particles. In the context of the halo hypothesis, the asymmetry structure, which is brighter and more extended in the South-East than in the South-West part, may be explained by a giant impact that could have happened in the opposite direction in the inner ring (North-East), and that would generate small, eccentric dust particles pushed away by the stellar radiation pressure (Jones et al. 2023). We showed that the non-detection in the polarized intensity data of the second structure is not contradictory with the halo or second belt hypotheses. As for the extended asymmetric-like feature ($\leq 1\,000$ au), we investigated what its morphology could be based on a new processing of the STIS archival data, and theoretical considerations. New, optimized STIS observations are required to precisely constrain its morphology, and the physical mechanisms that could generate and shape it. If the spiral feature is confirmed, HD 120326 would be one of the very rare debris disks with an imaged spiral feature so far, and the only one with a spiral spanning over hundreds of au, up to 1 000 au. Yet, it is interesting to note that spiral features are a common outcome of planet-debris disk interactions, both in massless (e.g., Wyatt 2005a; Pearce & Wyatt 2014; Farhat et al. 2023) and massive disks (with or without planets; e.g., Ward & Hahn 1998; Hahn 2003; Jalali & Tremaine 2012; Sefilian 2022).

To date, no planet has been discovered in HD 120326. Bonnefoy et al. (2017) ruled out the presence of > 2 M_{Jup} companions beyond projected separations of 50 au (and below 750 au). Future observations with the upgrade of SPHERE (SPHERE+, Boccaletti et al. 2020), high-contrast imaging instruments on the extremely large telescopes (ELT, GMT) or on the *JWST* and *Nancy Grace Roman Space Telescope* would be sensitive to less massive exoplanets in HD 120326, and/or located closer to the host star. Such observations will provide major constraints on

the global architecture of HD 120326, including on any potential disk-planet interactions that could sculpt the observed disk structures. Ultimately, this would help to determine how unique is the architecture of the young system HD 120326.

Acknowledgements. C.D. thanks for fruitful discussions Elodie Choquet regarding handling *HST*/STIS data, Gaspard Duchêne concerning scattering phase function and disk modeling, Veronica Roccatagliata concerning any potential flybys, Natalia Engler about albedo derivation for dust grains, and Anne-Marie Lagrange, regarding the presence of putative planets in HD 120326. C.D. also thanks Karl Stapelfeldt, Elisabeth Matthews, Sophia Stasevic, Xie Chen, Bin Ren, and Oliver Absil for useful discussions. C.D. is also grateful to Anthony Boccaletti, Deborah Padgett, and Sasha Hinkley, who obtained as PI some of the datasets used in this papers. This work has made use of the High Contrast Data Centre, jointly operated by OSUG/IPAG (Grenoble), PYTHEAS/LAM/CeSAM (Marseille), OCA/Lagrange (Nice), Observatoire de Paris/LESIA (Paris), and Observatoire de Lyon/CRAL, and supported by a grant from Labex OSUG@2020 (Investissements d'avenir – ANR10 LABX56). This paper makes use of the following ALMA data: ADS/JAO.ALMA#2022.1.00968.1. ALMA is a partnership of ESO (representing its member states), NSF (USA) and NINS (Japan), together with NRC (Canada), MOST and ASIAA (Taiwan), and KASI (Republic of Korea), in cooperation with the Republic of Chile. The Joint ALMA Observatory is operated by ESO, AUI/NRAO and NAOJ. The National Radio Astronomy Observatory is a facility of the National Science Foundation operated under cooperative agreement by Associated Universities, Inc. C.D. is part of Labex OSUG (ANR10 LABX56). C.D. acknowledges support from the European Research Council under the European Union's Horizon 2020 research and innovation program under grant agreement No. 832428-Origins. G.M.K. is supported by the Royal Society as a Royal Society University Research Fellow. A.A.S. is supported by the Heising-Simons Foundation through a 51 Pegasi b Fellowship and acknowledges financial support from the Alexander von Humboldt Foundation in the early stages of this work. T.D.P. is supported by a UKRI/EPSRC Stephen Hawking Fellowship. F.M. has received funding from the European Research Council (ERC) under the European Union's Horizon Europe research and innovation program (grant agreement No. 101053020, project Dust2Planets). J.M. acknowledges support from FONDECYT de Postdoctorado 2024 #3240612 V.F. acknowledges funding from the National Aeronautics and Space Administration through the Exoplanet Research Program under Grants No. 80NSSC21K0394 (PI: S. Ertel) and No 80NSSC23K0288 (PI: V. Faramaz). M.B. is supported by the European Union's Horizon 2020 research and innovation programme under grant agreement no. 951815 (AtLAST).

References

Amara, A. & Quanz, S. P. 2012, Monthly Notices of the Royal Astronomical Society, 427, 948
Artymowicz, P. 1988, Astrophysical Journal Letters, 335, L79
Artymowicz, P. 1997, Annual Review of Earth and Planetary Sciences, 25, 175
Asensio-Torres, R., Janson, M., Hashimoto, J., et al. 2016, Astronomy & Astrophysics, 593, A73
Augereau, J. C., Lagrange, A. M., Mouillet, D., & Ménard, F. 1999a, Astronomy & Astrophysics, 350, L51, _eprint: astro-ph/9909423
Augereau, J. C., Lagrange, A. M., Mouillet, D., Papaloizou, J. C. B., & Grorod, P. A. 1999b, Astronomy & Astrophysics, 348, 557
Augereau, J. C., Nelson, R. P., Lagrange, A. M., Papaloizou, J. C. B., & Mouillet, D. 2001, Astronomy & Astrophysics, 370, 447
Beckwith, S. V. W., Sargent, A. I., Chini, R. S., & Guesten, R. 1990, Astronomical Journal, 99, 924
Bertini, I., La Forgia, F., Tubiana, C., et al. 2017, Monthly Notices of the Royal Astronomical Society, 469, S404
Bertini, L., Roccatagliata, V., & Kim, M. 2023, Astronomy & Astrophysics, 671, L2, arXiv:2302.06302 [astro-ph]
Beuzit, J.-L., Vigan, A., Mouillet, D., et al. 2019, Astronomy & Astrophysics, 631, A155
Bhowmik, T., Boccaletti, A., Thébault, P., et al. 2019, Astronomy & Astrophysics, 630, A85
Boccaletti, A., Chauvin, G., Mouillet, D., et al. 2020, SPHERE+: Imaging young Jupiters down to the snowline, arXiv:2003.05714 [astro-ph]
Boccaletti, A., Sezestre, E., Lagrange, A.-M., et al. 2018, Astronomy & Astrophysics, 614, A52
Bonnefoy, M., Milli, J., Ménard, F., et al. 2017, Astronomy & Astrophysics, 597, L7
Bourgés, L., Lafrasse, S., Mella, G., et al. 2014, Astronomical Data Analysis Software and Systems XXIII, 485, 223
Burns, J. A., Lamy, P. L., & Soter, S. 1979, Icarus, 40, 1
Canovas, H., Rodenhuis, M., Jeffers, S. V., Min, M., & Keller, C. U. 2011, Astronomy & Astrophysics, 531, A102
Chen, C. H., Mittal, T., Kuchner, M., et al. 2014, The Astrophysical Journal Supplement Series, 211, 25
Choquet, E., Pueyo, L., Hagan, J. B., et al. 2014, Proceedings of the SPIE, 914357, arXiv:1407.0617 [astro-ph]
Choquet, , Bryden, G., Perrin, M. D., et al. 2018, The Astrophysical Journal, 854, 53
Christiaens, V., Gonzalez, C. A. G., Farkas, R., et al. 2023, Journal of Open Source Software, 8, 4774
Ciarniello, M., Moroz, L. V., Poch, O., et al. 2021, Minerals, 11, 1222
Claudi, R. U., Turatto, M., Gratton, R. G., et al. 2008, Proceedings of the SPIE, 7014, edited by McLean, Ian S.; Casali, Mark M.
Crotts, K. A., Matthews, B. C., Duchêne, G., et al. 2024, The Astrophysical Journal, 961, 245
De Boer, J., Langlois, M., Van Holstein, R. G., et al. 2020, Astronomy & Astrophysics, 633, A63
Delorme, P., Meunier, N., Albert, D., et al. 2017
Dohlen, K., Langlois, M., Saisse, M., et al. 2008, Proceedings of the SPIE, 7014, edited by McLean, Ian S.; Casali, Mark M.
Dominik, C., Min, M., & Tazaki, R. 2021, published: Astrophysics Source Code Library, record ascl:2104.010
Engler, N., Lazzoni, C., Gratton, R., et al. 2020, Astronomy & Astrophysics, 635, A19
Engler, N., Milli, J., Gratton, R., et al. 2023, Astronomy & Astrophysics, 672, A1, arXiv:2211.11767 [astro-ph]
Engler, N., Schmid, H. M., Quanz, S. P., Avenhaus, H., & Bazzon, A. 2018, Astronomy & Astrophysics, 618, A151
Esposito, T. M., Duchêne, G., Kalas, P., et al. 2018, The Astronomical Journal, 156, 47
Esposito, T. M., Kalas, P., Fitzgerald, M. P., et al. 2020, The Astronomical Journal, 160, 24
Faramaz, V., Krist, J., Stapelfeldt, K. R., et al. 2019, The Astronomical Journal, 158, 162
Faramaz, V., Marino, S., Booth, M., et al. 2021, The Astronomical Journal, 161, 271
Farhat, M., Sefilian, A., & Touma, J. 2023, Monthly Notices of the Royal Astronomical Society, 521, 2067, arXiv:2210.07395 [astro-ph]
Fedrigo, E., Donaldson, R., Soenke, C., et al. 2006, Society of Photo-Optical Instrumentation Engineers (SPIE) Conference Series, 6272, 627210
Foreman-Mackey, D., Hogg, D. W., Lang, D., & Goodman, J. 2013, Publications of the Astronomical Society of the Pacific, 125, 306
Gaia Collaboration, Brown, A. G. A., Vallenari, A., et al. 2021, Astronomy & Astrophysics, 649, A1
Gaspar, A., Wolff, S. G., Rieke, G. H., et al. 2023, Nature Astronomy, arXiv:2305.03789 [astro-ph]
Gomez Gonzalez, C. A., Wertz, O., Absil, O., et al. 2017, The Astronomical Journal, 154, 7
Grigorieva, A., Artymowicz, P., & Thébault, P. 2007, Astronomy & Astrophysics, 461, 537
Hahn, J. M. 2003, The Astrophysical Journal, 595, 531
Hapke, B. 1981, Journal of Geophysical Research, 86, 4571
Hedman, M. M. & Stark, C. C. 2015, The Astrophysical Journal, 811, 67
Heikamp, S. & Keller, C. U. 2019, Astronomy & Astrophysics, 627, A156
Henyey, L. G. & Greenstein, J. L. 1941, Astrophysical Journal, 93, 70
Hu, R., Ehlmann, B. L., & Seager, S. 2012, The Astrophysical Journal, 752, 7
Hughes, A. M., Duchene, G., & Matthews, B. 2018, Annual Review of Astronomy and Astrophysics, 56, 541, arXiv:1802.04313 [astro-ph]
Hunziker, S., Schmid, H. M., Ma, J., et al. 2021, Astronomy & Astrophysics, 648, A110
Högbom, J. A. 1974, Astronomy & Astrophysics Supplement, 15, 417
Jalali, M. A. & Tremaine, S. 2012, Monthly Notices of the Royal Astronomical Society, 421, 2368
Jang-Condell, H., Chen, C. H., Mittal, T., et al. 2015, The Astrophysical Journal, 808, 167
Jones, J. W., Chiang, E., Duchêne, G., Kalas, P., & Esposito, T. M. 2023, The Astrophysical Journal, 948, 102
Juillard, S., Christiaens, V., & Absil, O. 2023, Astronomy & Astrophysics, 679, A52
Juillard, S., Stasevic, S., Christiaens, V., Absil, O., & Milli, J. 2024, Combining reference-star and angular differential imaging for high-contrast imaging of extended sources, arXiv:2406.14444 [astro-ph]
Kennedy, G. M. 2020, Royal Society Open Science, 7, 200063
Kennedy, G. M., Bryden, G., Ardila, D., et al. 2018, Monthly Notices of the Royal Astronomical Society, 476, 4584, arXiv:1803.02832 [astro-ph]
Kennedy, G. M., Matrà, L., Marmier, M., et al. 2015, Monthly Notices of the Royal Astronomical Society, 449, 3121
Kennedy, G. M., Wyatt, M. C., Kalas, P., et al. 2013, Monthly Notices of the Royal Astronomical Society: Letters, 438, L96, arXiv:1312.5315 [astro-ph]

Kenyon, S. J. & Bromley, B. C. 2002, The Astronomical Journal, 123, 1757
Konishi, M., Grady, C. A., Schneider, G., et al. 2016, The Astrophysical Journal, 818, L23
Kornilov, V., Tokovinin, A., Shatsky, N., et al. 2007, Monthly Notices of the Royal Astronomical Society, 382, 1268
Krivov, A. V. 2010, Research in Astronomy and Astrophysics, 10, 383
Krivov, A. V. & Wyatt, M. C. 2020, Monthly Notices of the Royal Astronomical Society, 500, 718
Lafrenière, D., Marois, C., Doyon, R., & Barman, T. 2009, The Astrophysical Journal, 694, L148
Lagrange, A.-M., Langlois, M., Gratton, R., et al. 2016, Astronomy & Astrophysics, 586, L8
Lane, M. D., Cloutis, E. A., R. N., C., et al. 2024, Planetary Science Journal, accepted
Lawson, K., Schlieder, J. E., Leisenring, J. M., et al. 2024, The Astrophysical Journal Letters, 967, L8
Lecavelier Des Etangs, A., Vidal-Madjar, A., & Ferlet, R. 1996, Astronomy & Astrophysics, 307, 542
Lee, E. J. & Chiang, E. 2016, The Astrophysical Journal, 827, 125
Leinert, C., Link, H., Pitz, E., & Giese, R. H. 1976, Astronomy & Astrophysics, 47, 221
Löhne, T., Augereau, J.-C., Ertel, S., et al. 2012, Astronomy & Astrophysics, 537, A110
MacGregor, M. A., Matrà, L., Kalas, P., et al. 2017, The Astrophysical Journal, 842, 8
MacGregor, M. A., Wilner, D. J., Rosenfeld, K. A., et al. 2013, The Astrophysical Journal, 762, L21
Maire, A.-L., Bonnefoy, M., Ginski, C., et al. 2016, Astronomy & Astrophysics, 587, A56
Maire, A.-L., Langlois, M., Delorme, P., et al. 2021, Journal of Astronomical Telescopes, Instruments, and Systems, 7
Mamajek, E. E., Meyer, M. R., & Liebert, J. 2002, The Astronomical Journal, 124, 1670
Maness, H. L., Kalas, P., Peek, K. M. G., et al. 2009, The Astrophysical Journal, 707, 1098
Marino, S., Wyatt, M. C., Panić, O., et al. 2017, Monthly Notices of the Royal Astronomical Society, 465, 2595
Marino, S., Yelverton, B., Booth, M., et al. 2019, Monthly Notices of the Royal Astronomical Society, 484, 1257
Marois, C., Lafreniere, D., Doyon, R., Macintosh, B., & Nadeau, D. 2006, The Astrophysical Journal, 641, 556
Matrà, L., Marino, S., Kennedy, G. M., et al. 2018, The Astrophysical Journal, 859, 72
Mazoyer, J., Arriaga, P., Hom, J., et al. 2020, Proceedings of the SPIE, 251, arXiv:2012.06790 [astro-ph]
McMullin, J. P., Waters, B., Schiebel, D., Young, W., & Golap, K. 2007, Astronomical Data Analysis Software and Systems XVI ASP Conference Series, 376, 127
Milli, J., Mouillet, D., Lagrange, A.-M., et al. 2012, Astronomy & Astrophysics, 545, A111
Milli, J., Vigan, A., Mouillet, D., et al. 2017, Astronomy & Astrophysics, 599, A108
Min, M., Kama, M., Dominik, C., & Waters, L. B. F. M. 2010, Astronomy and Astrophysics, 509, L6
Najita, J. R., Kenyon, S. J., & Bromley, B. C. 2022, The Astrophysical Journal, 925, 45
Nelder, J. A. & Mead, R. 1965, Computer Journal, 7, 308
Ofek, E. O. 2008, Publications of the Astronomical Society of the Pacific, 120, 1128
Olofsson, J., Samland, M., Avenhaus, H., et al. 2016, Astronomy & Astrophysics, 591, A108
Olofsson, J., Thébault, P., Bayo, A., et al. 2023, Astronomy & Astrophysics, 674, A84
Olofsson, J., Thébault, P., Kennedy, G. M., & Bayo, A. 2022a, Astronomy & Astrophysics, 664, A122
Olofsson, J., Thébault, P., Kral, Q., et al. 2022b, Monthly Notices of the Royal Astronomical Society, 513, 713
Olofsson, J., van Holstein, R. G., Boccaletti, A., et al. 2018, Astronomy & Astrophysics, 617, A109
Padgett, D. & Stapelfeldt, K. 2016, Proceedings of the International Astronomical Union, 10, 175
Pairet, B., Cantalloube, F., Gomez Gonzalez, C. A., Absil, O., & Jacques, L. 2019, Monthly Notices of the Royal Astronomical Society, 487, 2262
Pairet, B., Cantalloube, F., & Jacques, L. 2021, Monthly Notices of the Royal Astronomical Society, 503, 3724
Pan, M., Nesvold, E. R., & Kuchner, M. J. 2016, The Astrophysical Journal, 832, 81
Pavlov, A., Feldt, M., & Henning, T. 2008, Proceedings of the SPIE, 394, 581
Pawellek, N. & Krivov, A. V. 2015, Monthly Notices of the Royal Astronomical Society, 454, 3207
Pearce, T. D. 2024, in Encyclopedia of Astrophysics (arXiv), arXiv:2403.11804 [astro-ph]
Pearce, T. D. & Wyatt, M. C. 2014, Monthly Notices of the Royal Astronomical Society, 443, 2541
Perrin, M. D., Duchene, G., Millar-Blanchaer, M., et al. 2015, The Astrophysical Journal, 799, 182
Petit, C., Sauvage, J.-F., Fusco, T., et al. 2014, Proceedings of the SPIE, 91480O
Rebollido, I., Stark, C. C., Kammerer, J., et al. 2024, The Astronomical Journal, 167, 69
Reche, R., Beust, H., & Augereau, J.-C. 2009, Astronomy & Astrophysics, 493, 661
Ren, B., Pueyo, L., Perrin, M. D., Debes, J. H., & Choquet, E. 2017, Proceedings of the SPIE, 10400, 1040021
Ren, B. B., Benisty, M., Ginski, C., et al. 2023a, Astronomy & Astrophysics, 680, A114
Ren, B. B., Rebollido, I., Choquet, , et al. 2023b, Astronomy & Astrophysics, 672, A114
Rodet, L., Beust, H., Bonnefoy, M., et al. 2017, Astronomy & Astrophysics, 602, A12
Sarazin, M. & Roddier, F. 1990, Astronomy and Astrophysics, 227, 294
Schmid, H. M., Joos, F., & Tschan, D. 2006, Astronomy & Astrophysics, 452, 657
Schneider, G., Grady, C. A., Hines, D. C., et al. 2014, The Astronomical Journal, 148, 59
Schneider, G., Smith, B. A., Becklin, E. E., et al. 1999, The Astrophysical Journal, 513, L127
Schneider, G., Weinberger, A. J., Becklin, E. E., Debes, J. H., & Smith, B. A. 2009, The Astronomical Journal, 137, 53
Sefilian, A. A. 2022, University of Cambridge, UK
Sefilian, A. A., Rafikov, R. R., & Wyatt, M. C. 2021, The Astrophysical Journal, 910, 13
Sefilian, A. A., Rafikov, R. R., & Wyatt, M. C. 2023, The Astrophysical Journal, 954, 100
Soummer, R., Pueyo, L., & Larkin, J. 2012, The Astrophysical Journal, 755, L28
Strubbe, L. E. & Chiang, E. I. 2006, The Astrophysical Journal, 648, 652
Su, K. Y. L., MacGregor, M. A., Booth, M., et al. 2017, The Astronomical Journal, 154, 225
Su, K. Y. L., Rieke, G. H., Stapelfeldt, K. R., et al. 2009, The Astrophysical Journal, 705, 314
Tamura, M., Fukagawa, M., Kimura, H., et al. 2006, Astronomy and Astrophysics, 641, 1172, _eprint: astro-ph/0603344
Tazzari, M., Beaujean, F., & Testi, L. 2018, Monthly Notices of the Royal Astronomical Society, 476, 4527
Thébault, P. & Augereau, J.-C. 2007, Astronomy & Astrophysics, 472, 169
Thébault, P. & Kral, Q. 2019, Astronomy & Astrophysics, 626, A24
Tobon Valencia, V., Geffrin, J.-M., Ménard, F., et al. 2022, åp, 666, A68
Umov, N. 1905, Phys. Z., 6, 674
van Holstein, R. G., Girard, J. H., De Boer, J., et al. 2020, Astronomy & Astrophysics, 633, A64
Wahhaj, Z., Milli, J., Kennedy, G., et al. 2016, Astronomy & Astrophysics, 596, L4
Ward, W. R. & Hahn, J. M. 1998, The Astronomical Journal, 116, 489
Wyatt, M. C. 2005a, Astronomy & Astrophysics, 433, 1007
Wyatt, M. C. 2005b, Astronomy & Astrophysics, 440, 937
Wyatt, M. C. 2008, Annual Review of Astronomy and Astrophysics, 46, 339
Wyatt, M. C., Dermott, S. F., Telesco, C. M., et al. 1999, The Astrophysical Journal, 527, 918
Wyatt, M. C., Kennedy, G., Sibthorpe, B., et al. 2012, Monthly Notices of the Royal Astronomical Society, 424, 1206
Xie, C., Choquet, E., Vigan, A., et al. 2022, Astronomy & Astrophysics, 666, A32
Yelverton, B., Kennedy, G. M., Su, K. Y. L., & Wyatt, M. C. 2019, Monthly Notices of the Royal Astronomical Society, 488, 3588

Appendix A: Near-infrared total intensity SPHERE observations

In the main text, we showed our PCA ADI processing of the SPHERE/IRDIS data of the epochs acquired in total intensity in Fig. 2. For the best epoch in the dual band H23 (2016-04-05) and the epoch in the broad band H (2019-07-09), we also processed the data with an iterative PCA, using ADI, RDI or ADI+RDI (ARDI) techniques. We only show the I-PCA ADI and ARDI reductions in Fig. A.1, because our I-PCA RDI processing is not able to retrieve the disk.

Concerning SPHERE/IFS observations, we show our PCA ADI processing of the best epoch 2019-07-09 in Fig. A.2. There are five IFS images with sub-coverages corresponding to binning of six spectral channels in the Y or J bands. The sixth IFS image is a mean of these thirty channels, thus covering YJ. We did not consider the first and last channels of the IFS, nor a few that are more impacted by artifacts.

Appendix B: Morphological parameters of the belt based on SPHERE data

We add in this appendix materials regarding our morphological analysis of the inner dust belt carried out in Section 3.1.

First, Figure B.1 show the areas considered to model the inner dust belt. Second, we describe below the equations setting the geometry of the disk, show the posteriors of our simulations jointly modeling the total and polarized intensity observations in Fig. B.2. Third, in Tables B.1 and B.2, we display the best-fitting parameters obtained when we independently modeled either the total or polarized intensity observations, respectively.

Following Augereau et al. (1999b), the dust density distribution may be expressed in cylindrical coordinates as,

$$\rho(r,\theta,z) \;=\; \rho_0 \;\times\; R(r,\theta) \;\times\; Z(r,z)\,, \tag{B.1}$$

where $R(r,\theta)$ and $Z(r,z)$ describe the radial and vertical distribution profile, respectively, and ρ_0 is the normalized grain density. This can be expressed as

$$\rho(r,\theta,z) \;=\; \rho_0 \times \left[\frac{2}{\left(\frac{r}{\tilde{r}(\theta)}\right)^{-2\alpha_{\rm in}} + \left(\frac{r}{\tilde{r}(\theta)}\right)^{-2\alpha_{\rm out}}}\right]^{1/2} \times \exp\left[-\left(\frac{z}{\xi(r)}\right)^{\gamma}\right], \tag{B.2}$$

where γ accounts for the shape of the vertical profile, either gaussian ($\gamma = 2$), spread out ($\gamma >> 2$) or stepped ($\gamma << 2$), $\xi(r)$ is the scale height of the ring. It is parameterized with β the flaring of the disk a the semi-major axis, and e the eccentricity as

$$\xi(r) \;=\; \xi_0 \left(\frac{r}{a\,(1 \,-\, e^2)}\right)^{\beta}. \tag{B.3}$$

If the disk is circular, $\tilde{r}(\theta)$ is equal to the constant reference radius r_0, and otherwise parameterized following Milli et al. (2017) via

$$\tilde{r}(\theta) \;=\; \frac{a\,(1 \,-\, e^2)}{1 \,+\, e\cos(\theta)}\,, \tag{B.4}$$

where θ is the polar angle.

In near-infrared observations, disk structures are seen via the scattering of the stellar light on the dust particles of the disk. The scattering phase function of a debris disk in total intensity light may be modeled for the sake of convenience with the Henyey-Greenstein (HG) function (Henyey & Greenstein 1941) as follows

$$\mathrm{HG}(g,\phi) \;=\; \frac{1}{4\pi} \times \frac{1 \,-\, g^2}{(1 \,-\, 2\,g\cos(\phi) \,+\, g^2)^{3/2}}\,, \tag{B.5}$$

which is parameterized by the HG scattering anisotropy parameter g. If there is only backward scattering, g is equal to -1, if only forward scattering, g is equal to 1, and if the scattering is isotropic, g is equal to 0. For debris disks, g is typically greater than 0 because small dust grains are known to be forward scattering.

For polarimetric observations, we multiply the SPF by the Rayleigh scattering function as follows

$$\mathrm{HG}(g,\phi) \;\rightarrow\; \mathrm{HG}(g,\phi) \;\times\; \frac{1 \,-\, (\cos(\phi))^2}{1 \,+\, (\cos(\phi))^2}\,. \tag{B.6}$$

Table B.1. Morphology of the belt based on the MCMC exploration fitting the SPHERE near-infrared observation in total intensity (2019-07-09) only.

Parameter	Range	Best fit $\chi^2_{\rm r,min}$	Median $\pm$ 1σ
r_0 (au)	[10, 130]	42.8	$43.2^{+1.0}_{-0.9}$
PA (°)	[−120, −60]	−94.5	$-94.5^{+0.1}_{-0.2}$
i (°)	[0, 90]	79.4	79.4 ± 0.3
g	[0.05, 0.999]	0.81	0.81 ± 0.01
scaling (I)	[100, 10^8]	6.2×10^3	$(6.0^{+0.4}_{-0.3}) \times 10^3$
$\alpha_{\rm out}$	[−20, −1.1]	−2.27	$-2.34^{+0.10}_{-0.13}$

Table B.2. Morphology of the belt based on the MCMC exploration fitting the SPHERE near-infrared observation in polarized intensity (2018-06-01) only.

Parameter	Range	Best fit $\chi^2_{\rm r,min}$	Median $\pm$ 1σ
r_0 (au)	[10, 130]	38.3	$38.5^{+1.1}_{-0.7}$
PA (°)	[−120, −60]	−93.5	$-93.6^{+0.2}_{-0.3}$
i (°)	[0, 90]	77.0	$77.1^{+0.6}_{-0.5}$
g	[0.05, 0.999]	0.73	$0.74^{+0.03}_{-0.02}$
scaling (pI)	[100, 10^8]	7.8×10^4	$(7.9^{+0.4}_{-0.6}) \times 10^4$
$\alpha_{\rm out}$	[−20, −1.1]	−2.01	−2.00 ± 0.12

Appendix C: Morphological parameters of the belt based on ALMA data

Figure C.1 shows some of the posteriors of the simulations constraining the morphology of the debris disk based on the ALMA data (Section 4.1).

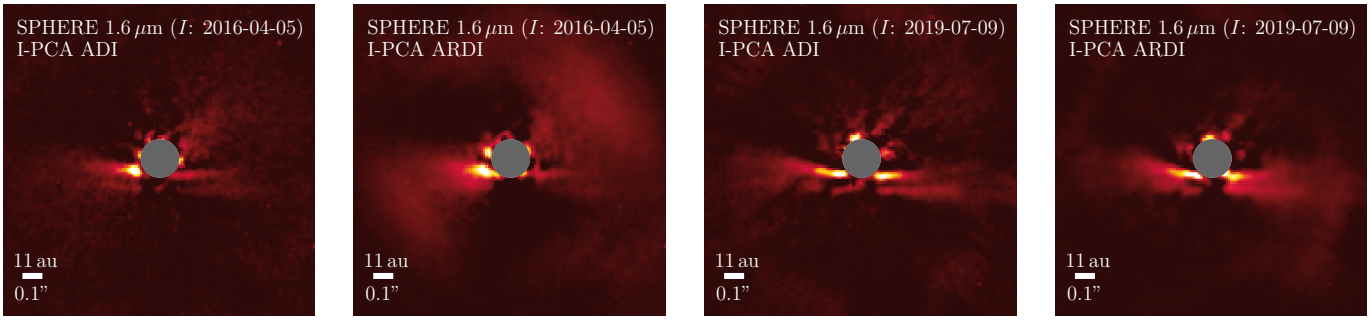

Fig. A.1. Total intensity images in the broad band H and reduced using an iterative PCA ADI or ADI+RDI algorithm.

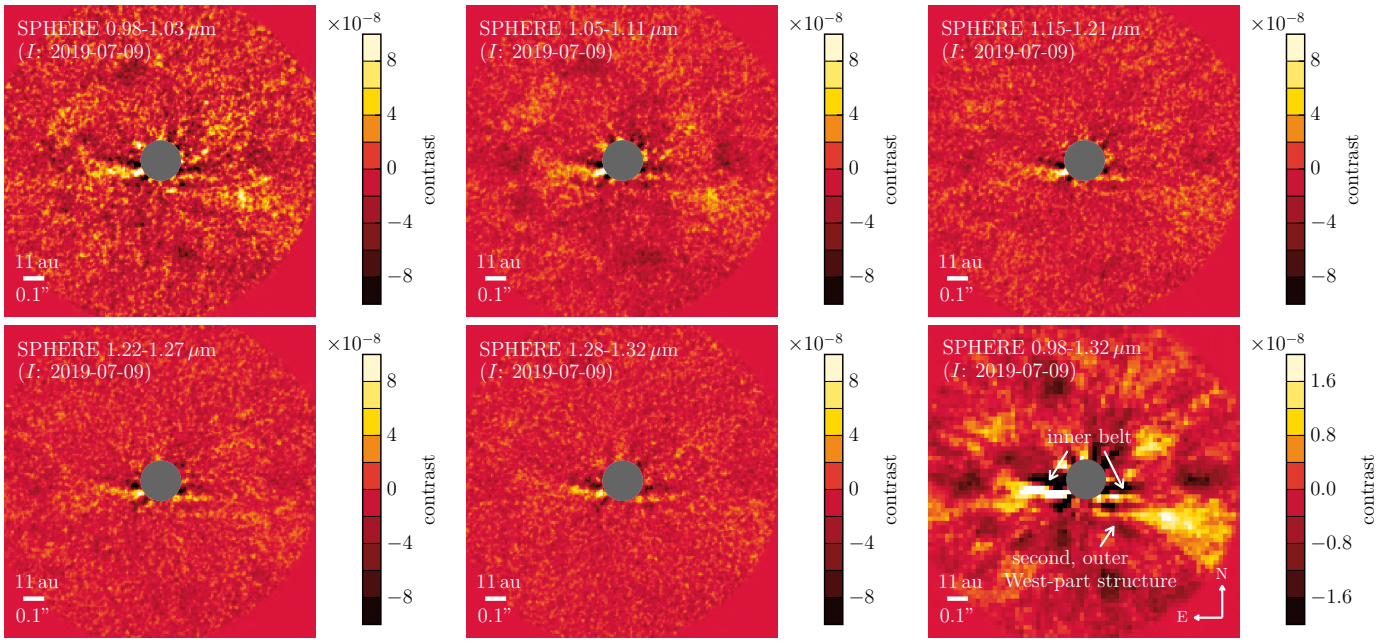

Fig. A.2. From *top-left* to *bottom-middle* images: total intensity ("*I*") images in different sub-coverages of the bands Y and J, reduced using PCA ADI. The *bottom-right* image corresponds to the average of the PCA ADI processed images over the full YJ bands, and that we spatially binned (3×3 pixels^2 $\rightarrow$ 1×1 pixel^2) to reveal the West-part of the second, outer structure. North is up, East is left for all the images.

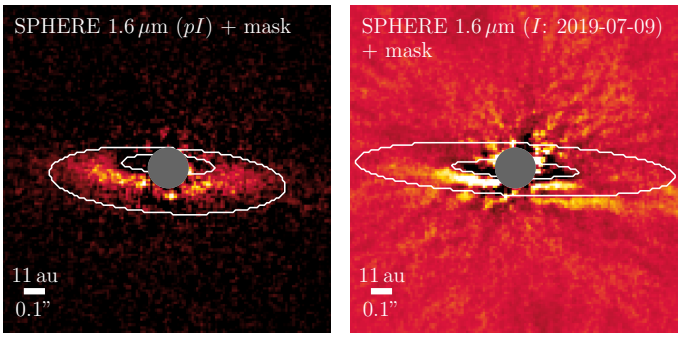

Fig. B.1. Region of the SPHERE polarized (*left*) and total (*right*) intensity images considered to model the inner belt in Section 3.1.

Appendix D: The background contaminant

We show here that the bright point-like source on the extended spiral-like feature (see Fig. 4) is a background star and investigate whether it could explain the asymmetry of the extended feature seen with *HST*/STIS. This bright point-like source was detected in the five epochs *HST*/STIS and SPHERE/IRDIS from 2013 to 2019. By comparing the relative motion of this bright point source for different epochs, we show in Fig. D.1 that this bright source follows the track of a background object. This track is determined by using the parallactic and proper motions of the primary star. HD 120326 has a proper motion of (−29.0 mas/yr in right-ascension, and −21.0 mas/yr in declination (Gaia Collaboration et al. 2021).

We investigate below whether the alignment of the background star with the South-East part of the dust seen with *HST*/STIS could explain why the disk is brighter in the South-East part than in the South-West part, which would results in a visual (and not dynamical) asymmetry. We stress that such investigation is limited because the South-West part of the disk lacks of spatial coverage in the *HST*/STIS image.

We consider two regions of interest where there are dust grains, one located at a close projected separation of the background star and another one located further away (see Fig. D.2). By deriving the mean average flux within each of this circular aperture (of radius five pixels, i.e., 210 mas), we obtained a flux of 4.8 ± 0.5 mJy and 3.0 ± 0.3 mJy, respectively. These locations correspond to scattering angles of 0.0085° and 0.062°, respectively, using geometrical relationships given below.

The goal is to express the scattering angle (ϕ) as a function of the distance between the system HD 120326 and the observer

($d_{\mathrm{HD\,120326}}$), the distance between the background object and the observer ($d_{\mathrm{background}}$), the angular separation between the background star and the dust grain of interest (θ, which also represents the angle between the line of sight observer-background object and the scattered wave on the dust grain of interest), see Fig. D.3.

By considering the triangle whose corners are the background star, the dust grain of interest and the observer, and the fact that the sum of angles in a triangle is equal to 180°, one can express

$$\theta + \psi + (180 - \phi) = 180\,, \tag{D.1}$$

$$\psi = \phi - \theta\,, \tag{D.2}$$

where ψ is the angle between the line of sight observer-background star and the incident wave from the background star on the dust grain of interest. As ψ is very small, $\tan(\psi) \sim \psi$, hence one can express

$$\psi \sim \frac{d_{\mathrm{HD\,120326}} \times \theta}{d_{\mathrm{background}} - d_{\mathrm{HD\,120326}}}\,, \tag{D.3}$$

and so by injecting Eq. D.2 in Eq. D.3, one gets

$$\phi \sim \theta + \frac{\theta}{d_{\mathrm{background}} - d_{\mathrm{HD\,120326}}}\,, \tag{D.4}$$

This results in the following expression for the scattering angle ϕ,

$$\phi \sim \frac{\theta}{1 - d_{\mathrm{HD\,120326}} / d_{\mathrm{background}}}\,. \tag{D.5}$$

Our numerical applications use θ = 26 pixels = 1.3" = 0.0085° (the STIS plate scale is 0.05078 pixels/arcsec^2) and θ = 186 pixels = 222" = 0.062° for the dust grains at close and far projected separations, respectively, $d_{\mathrm{HD\,120326}}$ = 113.3 pc and $d_{\mathrm{background}}$ = 118.3 pc, so assuming a background star at 5pc further away than the system HD 120326. The distance of the background star is very likely underestimated, but this is done on purpose to maximize the difference of the scattering angles and so to maximize the difference of the scattering phase function values, to be able to explain the difference observed.

By assuming Mie's theory, astrosilicate grains distributed from 0.1 to 100 μm with a power law in −3.5, we computed the scattering phase function using the open-access tool `optool`[9] (Dominik et al. 2021) at the central wavelength of the STIS filter, 0.59 μm. The tool `optool` provides scattering phase functions sampled between 0.5° and 179.5° with step of 1°. In particular, we used its input file for `RADMC-3d`, for which `optool` extrapolates and reinterpolates the previous grid between 0° and 180°, with step of 1°[10].

For scattering angles of 0° and 1°, the SPF values are $1.13 \cdot 10^5$ and $6.79 \cdot 10^4$, which correspond to a ratio of 1.67. By considering the scattering angles of interest, 0.0085° and 0.062°, the ratio is therefore $1.67 \times (0.062 - 0.0085) = 0.089$. Consequently, we expect that the dust grains having a scattering angle of 0.062° scatter 8.9% less than those with a scattering angle of 0.0085°. This results in a flux of $4.8 - 4.8 \times 0.089 = 3.9$ mJy at 0.062°. This is higher than the flux (3.0 ± 0.3 mJy) measured in the STIS image at such location.

We also tested different distributions of dust grains (0.1–1 μm, 0.1–50 μm, 1–10 μm, 1–50 μm, 1–100 μm). At 0° and 1°, their SPF results in ratio values smaller or similar to that of 1.67, obtained for the grain distribution 0.1–100 μm. Hence the ratio 1.67 is a conservative value, which maximizes the slope of the SPF between 0° and 1°, and thus the variation of flux observed at the scattering angles of interest, 0.0085° and 0.062°.

In addition, we stress that if the background star is located further away than 118.3 pc, the expected asymmetry in flux that it would cause would be much less. For example, for a background star located at 123.3 pc (i.e., 10 pc further away than HD 120326) the scattering angles are 0.0045° and 0.032°, resulting in a flux ratio of 4.6% instead of 8.9%; if the background star is located at 163.3 pc (i.e., 50 pc further away than HD 120326), scattering angles are 0.0012° and 0.0085° and the flux ratio is 1.2%. Considering the Figure D.1, we do not expect the background star to be located particularly close ($\lesssim$ 5 pc) to the star HD 120326, because the background star follows well the background track without showing additional proper motion.

[9] avalaible here https://github.com/cdominik/optool/

[10] see the Appendix B.3 of the User Guide of `optool`, located on the github repository

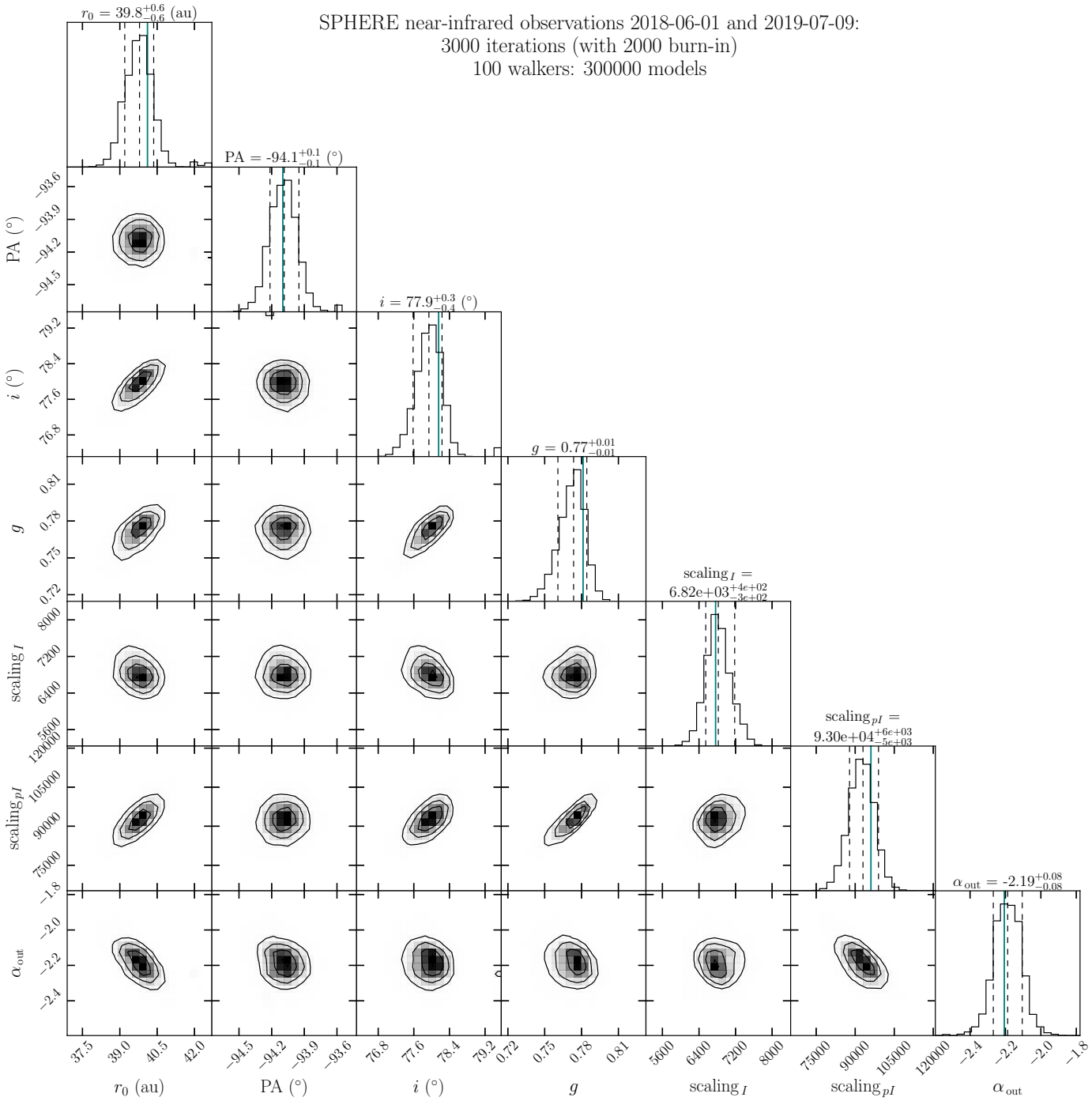

Fig. B.2. Posteriors of the MCMC exploration of the parameter space for the disk seen in near-infrared (1.6 μm) SPHERE observations in polarized and total intensity. The vertical dashed lines represents the values of the median and at $\pm1\sigma$, which are defined as the 15.9% and 84.1% percentiles to encompass 68.2% of the solutions for a given parameter. The blue vertical line represent the best-fitting parameters, which are the values minimizing the χ^2_r.

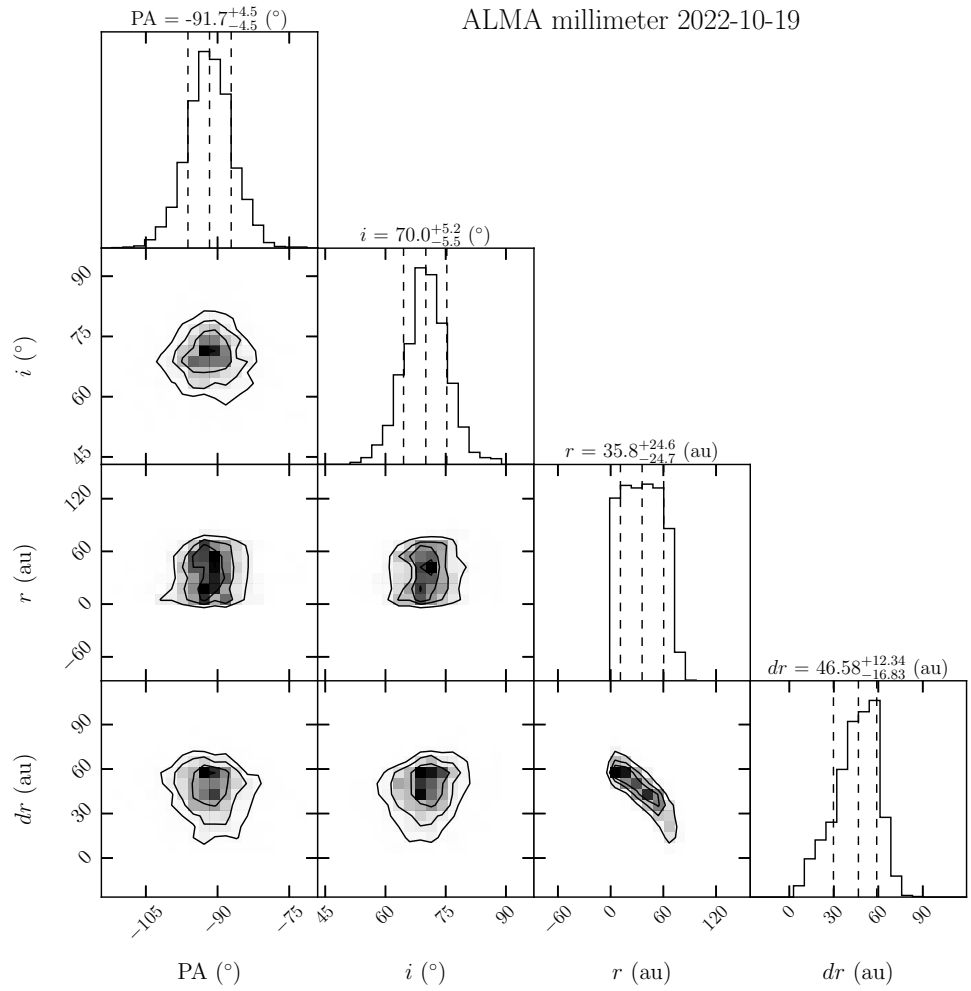

Fig. C.1. Posteriors of the `MCMC` exploration of the parameter space for the disk seen in continuum millimeter (1.3 mm) interferometric ALMA observations. The parameters are: position angle (PA), inclination (i), radius (r), and width (dr).

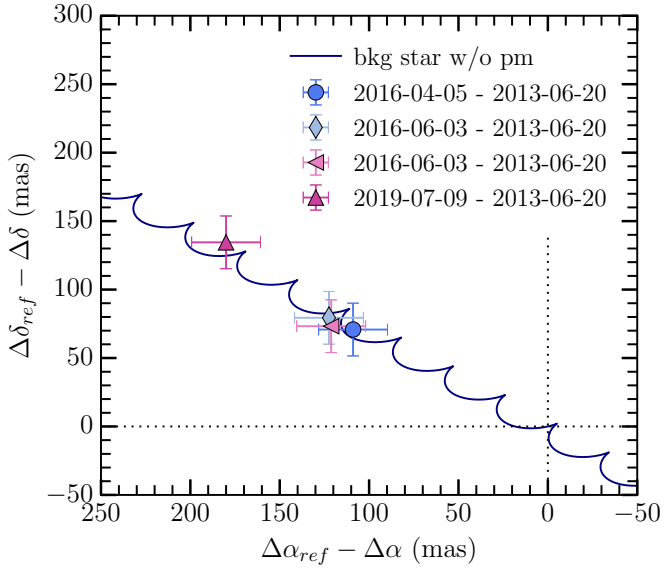

Fig. D.1. Difference of the relative astrometry of the bright point-source lying on the spiral-like feature (see Fig. 4) between the *HST*/STIS epoch (2013-06-20, used as reference) and the SPHERE/IRDIS epochs (2016 to 2019, see Table 1). The blue solid curve shows the expected track of a background object, based on the parallactic and proper motions of the primary star HD 120326. The point source is clearly identified as a background object.

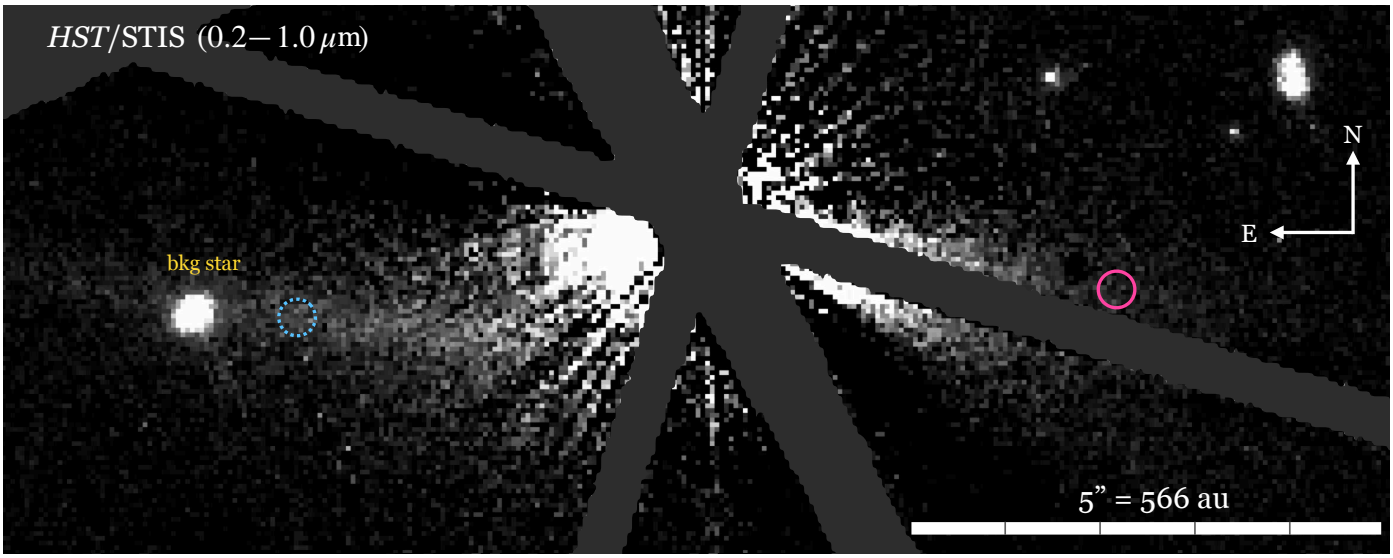

Fig. D.2. Location of the two regions of interest of dust grains in the extended dust emission seen in the *HST*/STIS reduced image. The dotted blue circle corresponds to the region located at a projected distance close to the background star, while the solid pink circle corresponds to the region located a projected distance far to the background star. Unlike to Fig. 4, no spatial binning was applied on this image.

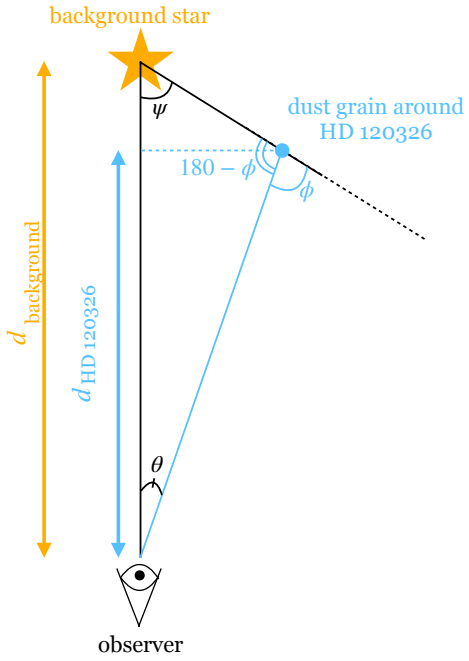

Fig. D.3. The sketch represents the parameters (angles and distances) used to express the scattering angle ϕ of the background stellar light scattered by a dust grain in the system HD 120326.

3.2.2 Main results

In Desgrange et al. (2025, subm.), I investigated the dust properties and morphology of the disk structures of HD 120326.

I confirmed that HD 120326 has two intermediate scale (30–150 au) disk structures. I found the inner dust belt a semi-major axis at maximum dust density in the mid-plane of $\sim$42.5 au and an inclination of $\sim$78° au by jointly-modeling the polarized and total intensity observations. As for the second, faint structure located further away, I showed that its non-detection in polarized intensity is not contradictory with its detection in total intensity, either if it is a second belt or halo of small, eccentric dust grains originating from collisions within the inner belt. The second structure is asymmetric, it is brighter and more extended in the South-West than in the South-East part. This may be explained by a giant impact of planetesimals that could have happened in the North-East part of the inner ring, i.e., the direction opposite to where the dust particle density is highest (see the giant impact simulations from Jones et al., 2023).

As for the large-scale (up to 1 000 au) asymmetric structure, I processed and calibrated the *HST*/STIS flux map in μJy/arcsec^2 (Fig. 3), and derived its S/N map (Fig. 4), which revealed an extended spiral-like feature. The nature and origin of this structure is of utmost interest. Is it indeed a spiral? Spirals are predicted to be common in debris disks, either if they are seen as transient (Wyatt, 2005) or persistent (Ward & Hahn, 1998; Sefilian, 2022) features based on numerical simulations of debris disks involving giant planets on wide orbits. Yet, they are rarely observed so far in debris disks, and HD 120326 is the only detected one with a spiral-like feature spanning over hundreds of astronomical units (Section 5.2).

Alternatively, perhaps the seen asymmetry of the extended feature might be just an alignment coincidence. In the South-East part of the disk, there is a background star overlaying with the spiral-like feature. Due to strong forward scattering of small dust grains, the background star might significantly increase the brightness of small particles closed to be aligned with the background star. This could explained why in the opposite South-West part, there is no similarly bright disk signal.

Regarding the dust properties of the inner belt, I constrained their polarization and color properties. I determined a maximum polarization fraction of $51\,\% \pm 6\,\%$. In addition, I derived a red color between 1.0 and 1.3 μm and a grey color between 1.3 and 1.8 μm (Fig. 7). The maximum polarization fraction is similar to HR 4796 A ($50\,\% \pm 3\,\%$ at 1.9-–2.19 μm Perrin et al., 2015), but is higher than other disks (10–20 % in the near-infrared, for Beta Pictoris, HD15115, HD 32297, HD114082, Tamura et al., 2006; Asensio-Torres et al., 2016; Bhowmik et al., 2019; Engler et al., 2023). Interpreting the color of dust particles is a degenerated problem, in particular with low-resolution spectra, between dust size, composition and shape. Between 1.3 and 1.5 μm, there might be a tentative evidence of a break in the reflectance spectrum. This could be caused by an absorption feature, such as opaque mixtures of water ice and kerite (Ciarniello et al., 2021) or water in hydrated minerals (e.g., Hu et al., 2012; Lane et al., 2024).

Last, Figure 3.2 shows that the inner belt of HD 120326 seems large compared to other spatially resolved disks in scattered light that have a dust belt between 20 and 60 au.

3.3 Perspectives

Obtaining new observations on this disk would be key to constrain more precisely the morphology of the disk. In particular, optimized *HST*/STIS observations acquired with a color-matched reference star, three rolling angles, and the star centered behind the WedgeA1.0

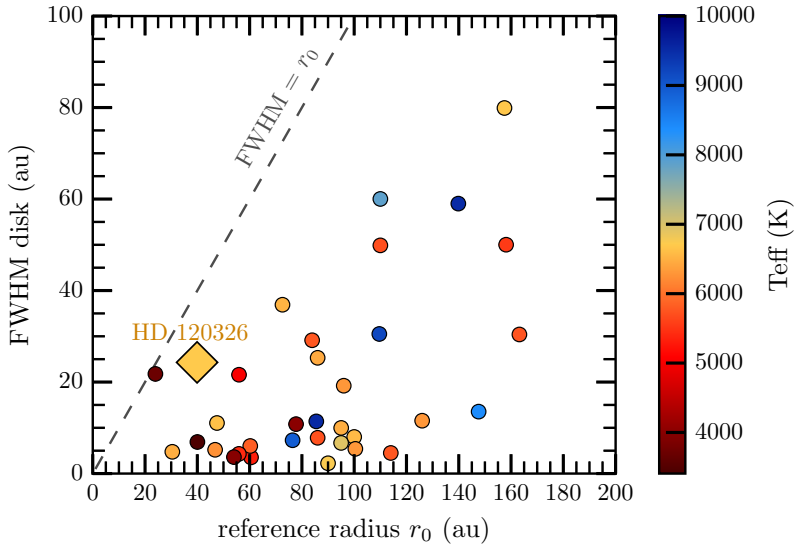

Figure 3.2: Reference radius (r_0) and full width at half maximum (FWHM) of the inner belt of HD 120326 (diamond) compared to other debris disks spatially resolved in scattered light (colored circles). The color indicates the effective temperature of the host star. Data from the R2D2 catalogue from Julien Milli, and which are listed and referenced in the Table E.1 from Adam et al. (2021). Two important caveats of this comparison are the lack of error bars on the values of the FWHM and r_0, and the heterogeneous disk modeling based on different studies.

(IWA $\sim 1''$) will provide important constraints on the spiral-like feature, by avoiding self-subtraction effects, having a larger spatial coverage and being more sensitive. Using a similar strategy but with the star centered behind the Cbar5, which has an IWA of $0.2''$, will help to discriminate whether the South-West part of the second small structure (seen with SPHERE in total intensity) connects with the spiral-like feature (seen with *HST*/STIS).

Moreover, constraining the photometry of the inner belt and second disk structure in the STIS broad band filter at 0.59 μm ($d\lambda = 0.44$ μm) would help to determine the size of dust particles by studying the color 0.59–1.1 μm and/or 0.59–1.6 μm. It could be compared to dozens of other known debris disks (e.g., Ren et al., 2023).

In this perspective, in March 2024, I submitted a *HST* proposal during Cycle 32 to obtain such new optimized *HST*/STIS data, which was unfortunately not granted. Previously, in *JWST* Cycle 3, I submitted a joint *JWST*+*HST* proposal, to characterize both the disk morphology and dust properties with *HST* and search for giant (≤ 2 M_{Jup}[6]) planets that could shape the disk structures, in particular the extended spiral-like one, with *JWST*. This proposal was not accepted. Better constraining the mass and semi-major axis of the predicted companion(s) based on a better characterization of the morphology and the nature of the spiral-like would certainly be more convincing for the Telescope Allocation Committee (TAC). Acquiring therefore first new *HST* data based on an optimized observation strategy is primordial to my mind.

In addition, new, higher-resolution ALMA data would able to better constrain the location of the dust belt while tracing the thermal emission of millimeter-size grains. This could then be compared to the results from the scattered light of smaller grains seen in the near-infrared.

One common argument to explain the disk structures in debris disks are the presence of

[6]Previously, Bonnefoy et al. (2017) excluded the presence of ≥ 2 M_{Jup} companions between projected separations of 50 and 750 au based on the `COND` evolutionary models to convert the contrast to mass detection limits.

planets that could sculpt or stir the dust belts. Regarding HD 120326, no exoplanet was yet discovered, but a significant part of the parameter space remains to be explored.

By inferring the presence of exoplanets owing to planet-disk interactions, Pearce et al. (2022) predicted that many inferred exoplanets could lie between 10 and 100 au, see Fig. 3.3. To shape a given dust belt, the mass and semi-major axis of an inferred exoplanet can differ depending on the interaction (e.g., stirring or sculpting by one planet, or multiple planets involved). Before the *JWST*, most of these planetary candidates fell below the detection limits achievable with observational facilities. Since the *JWST*, several programs have been accepted to detect these inferred exoplanets in debris disks, down to Neptune-mass planets (e.g., Fig. 9 from Kammerer et al., 2024). Even non-detections will bring valuable information, as it will rule out hypotheses regarding the properties of the putative planet (or chain of planets), which could shape the dust belt, and so constrain planet-disk interactions.

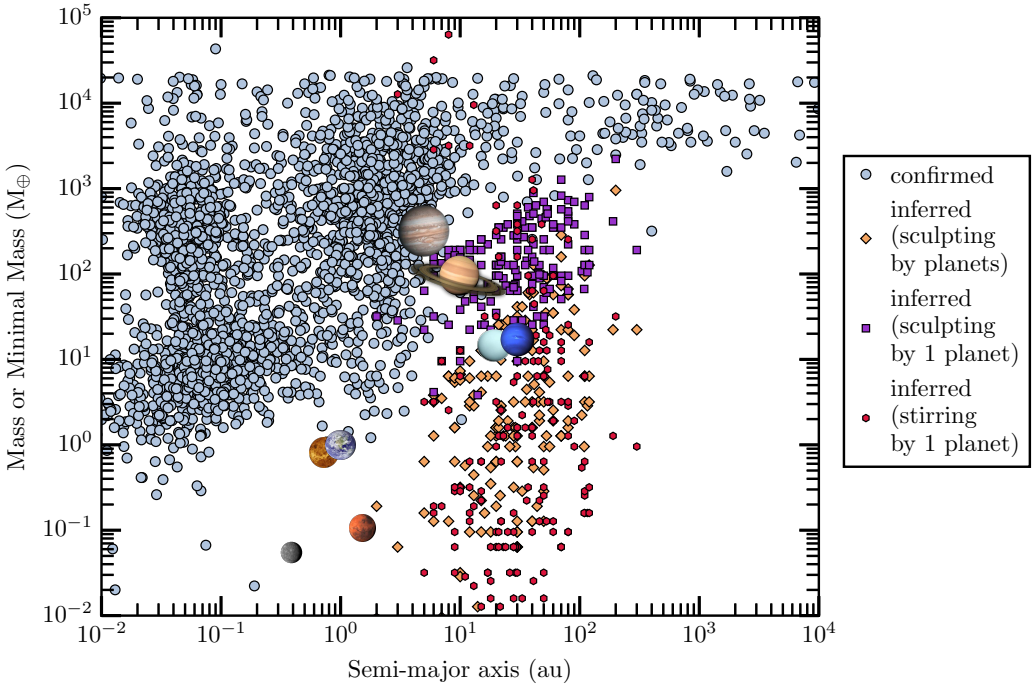

Figure 3.3: Exoplanets inferred via planet-disk interactions from the catalogue of Pearce et al. (2022). The color indicates the mechanism assumed for the planet-disk interaction: either via stirring by one planet, sculpting by one planet or sculpting by multiple planets.

In the next chapter, I focus on a young, massive giant planet, HD 95086 b, which could carve the inner edge of the outer belt in the system HD 95086.

Chapter 4

The young Solar System analog HD 95086

Contents

4.1 Context

4.1.1 Motivation

Young Solar System analogs offer the way to go back in time to try to understand how such systems form and evolve at early stages (1–500 Myr). This provides a unique perspective to complete and re-fine our understanding of the formation of our Solar System, the Earth, and the origins of life.

To date, for diverse young systems, having circumstellar disks and / or planets, astronomers have been able to constrain:

1. The orbital properties of the young giants planets, in particular whether they are in mean-motion resonances, which could provide a stable dynamical configuration (Wang et al., 2021; Nowak et al., 2020; Beust et al., 2024), or their eccentricity (De Rosa et al., 2020b), which could trace back dynamical interactions such as scattering events (e.g., Raymond et al., 2009) or Kozai-Lidov interactions (e.g., Beust et al., 2012; De Rosa et al., 2020a).

2. The presence of circumplanetary disks, in which exo-Moons could form (Benisty et al., 2021).

3. The atmospheres of young exoplanets and the presence of clouds (e.g., Crossfield et al., 2014; Petrus et al., 2021; Huang et al., 2023; Palma-Bifani et al., 2024; Nasedkin et al., 2024, for mostly recent characterizations).

4. The hot or warm dust located at a fraction or a few astronomical units, respectively. Such dust as a fraction of a few 1% of the stellar flux in the near infrared based on interferometric data (Absil et al., 2013, 2021; Ertel et al., 2014, 2016). Its frequent detection raises questions, because this dust should dissipate fast, and so replenishment mechanisms are required (e.g., see Section 3.5 from Pearce, 2024).

5. The cold reservoirs of asteroids, by studying the dust generated by collisions (Chen et al., 2020; Milli et al., 2015, 2017a, 2019, 2024; Engler et al., 2023; Wu et al., 2024). Investigating dust properties help to constrain how porous dust particles could be, and help to understand better dust growth, by assuming that their structure is somehow preserved since the protoplanetary disk phase. Furthermore, constraining dust properties help to determine whether they could contain hydrated minerals, which may also represent a source of water for rocky planets, when asteroids fall onto them (e.g., the Late Heavy Bombardment).

6. The reservoirs of comets[1] by studying the gas released by collisions or when falling onto their host star (Matrà et al., 2017, 2019; Rebollido et al., 2020; Beust et al., 2024). Second-generation gas can also contribute to modify the atmospheric composition of rocky planets which may partially accrete this gas (Kral et al., 2020). Comets are particularly interesting as they could deliver volatiles such as water on inner, rocky planets, when falling onto them.

Such studies on young Solar System analogs are of prime interest. Unfortunately, only a handful of planetary systems showing to some extent similar properties to our Solar System have been discovered. The most iconic one is HR 8799 (Marois et al., 2008, 2010), with four massive giant planets lying in between two dust belts. Another double-belt planetary system

[1] I make here the distinction between a comet and an asteroid, even though I am aware that the difference may not be that clear anymore. I intend by comets, bodies rich in volatiles, contrary to asteroids.

is HD 95086, hosting so far one known giant exoplanet (Rameau et al., 2013), and which also lies in the cavity. Both HR 8799 and HD 95086 orbit A-stars, and so are considered are massive analogs of the Solar System.

4.1.2 Previous studies on HD 95086

Regarding the global system properties, Booth et al. (2021) reported that this young system, is more likely to be located in the Carina association than in Lower Centaurus Crux in the Sco-Cen association as previously thought (De Zeeuw et al., 1999; Madsen et al., 2002). This corresponds to small differences in distance and age, with an updated distance of 86.2 ± 0.3 pc (Bailer-Jones et al., 2018) and an age of $13.3^{+1.1}_{-0.6}$ Myr (Booth et al., 2021), while before it was 83.8 ± 2.9 pc (Chauvin et al., 2018) and 17 ± 2 Myr (Pecaut et al., 2012).

Since the discovery of the 4–5 M_{Jup} gas giant planet with the imager VLT/NaCo (Rameau et al., 2013), several observational or theoretical studies have been focused on HD 95086. They aimed to: characterize the orbital properties (Rameau et al., 2016; Chauvin et al., 2018) and the atmosphere (Galicher et al., 2014; De Rosa et al., 2016; Chauvin et al., 2018) of the giant exoplanet b, study the debris disk (Su et al., 2015, 2017; Zapata et al., 2018; Booth et al., 2019; Chen et al., 2012; Jang-Condell et al., 2015), investigate whether additional exoplanets are expected to explain the width of the cavity based on dynamical arguments (Su et al., 2015), and search for them observationally (Rameau et al., 2016; Chauvin et al., 2018).

Spectral properties of the giant planet b show that this companion is between the late L to L/T transition and is a red, underluminous object compared to other field dwarfs (Galicher et al., 2014; De Rosa et al., 2016; Chauvin et al., 2018). It orbits at a semi-major axis of 52^{+13}_{-24} au, with an eccentricity peaking at zero (but, constrained to < 0.5 at 1σ) and an inclination of $140.7^{+14.8}_{-13.3}$ °. Therefore, the exoplanet b lies between the inner and outer belts, which are located at 7–10 au and 106–320 au, respectively, and could carve the inner edge of the outer belt (Su et al., 2015, 2017). No CO gas was detected with ALMA (J=3-2, J=2-1, and/or J=1-0 Su et al., 2017; Zapata et al., 2018; Booth et al., 2019), or only tentatively (J=2-1 Booth et al., 2019), which exclude the presence of primordial gas in HD 95086 (Zapata et al., 2018; Booth et al., 2019).

In the cavity, the presence of one or two additional giant planets is expected (Su et al., 2015), and given direct imaging detection limits, could be possible between 10 and 30 au (Chauvin et al., 2018; Rameau et al., 2016). Such additional exoplanets would have to be dynamically stable with the outer exoplanet b, and possibly contribute in the replenishment of the inner belt.

4.2 My work

My work on HD 95086 aimed to carry-out an in-depth spectrocopy and orbital characterization of the exoplanet b, and to search for the presence of the expected additional exoplanets. To accomplish these goals, I used 10 observations of VLT/SPHERE, acquired between 2015 and 2019 as part of the Guaranteed Time Observations (GTO) of the consortium SPHERE. They were simultaneously acquired with the dual-band imager SPHERE/IRDIS (in the K1 and K2 bands) and the integral field spectrograph SPHERE/IFS (covering the YJH bands). The last five epochs (January 2018, February 2018, March 2018, April 2019 and May 2019) were unpublished data.

I started to work on HD 95086 before my Ph.D., in the context of my first-year Master project between March and July 2019 at the Universidad de Chile with Gaël Chauvin and Patricio Rojo. I continued to work on it afterwards, submitting and publishing the paper in

Astronomy & Astrophysics during my first year of Ph.D., as a paper of the SPHERE consortium.

In practice for this work, I collaborated with the HC-DC to obtain the pre-processing and post-processing of the data via the SpeCal tool, with Faustine Cantalloube (@MPIA[2]) for the post-processing with the ANDROMEDA pipeline. I analyzed the SPHERE/IRDIS and SPHERE/IFS data, evaluating their quality based on the detection limits and observational conditions. I extracted the astrometric and spectral information of the exoplanet b, and collaborated with Hervé Beust (@IPAG), Laëtitia Rodet (@Cornwell University, USA) and Valentin Christiaens (@Monash University, in Australia) to constrain the orbital parameters and the properties of the atmosphere based on my results. I compared the results from the atmospherics models with predicted physical properties from evolutionary models, to study their consistency. To search for the presence of additional companions, I collaborated with Hervé Le Coroller (Laboratoire d'Astronomie de Marseille, France) to combine several epochs of observations and search the presence of any additional companions with his K-Stacker tool. Last, I computed the detection limits in terms of mass and semi-major axis, based on direct imaging and radial velocity data, using the private MESS2 tool that Anne-Marie Lagrange (@IPAG) and Pascal Rubini shared to me.

The full article is available in the next section. I summarize the main results in Section 4.2.2 and discuss the perspectives in Section 4.3.

4.2.1 Publication in A&A: Desgrange, Chauvin, Christiaens et al. 2022

[2]The affiliations stated in this chapter correspond to the ones at the time of the collaboration.

A&A 664, A139 (2022)
https://doi.org/10.1051/0004-6361/202243097

Astronomy & Astrophysics

In-depth direct imaging and spectroscopic characterization of the young Solar System analog HD 95086

C. Desgrange[1,2,3], G. Chauvin[1,3], V. Christiaens[4], F. Cantalloube[5], L.-X. Lefranc[6], H. Le Coroller[5], P. Rubini[7], G. P. P. L. Otten[5,8], H. Beust[1], M. Bonavita[9], P. Delorme[1], M. Devinat[7], R. Gratton[10], A.-M. Lagrange[1,11], M. Langlois[12], D. Mesa[10], J. Milli[1], J. Szulágyi[13], M. Nowak[14], L. Rodet[15], P. Rojo[3], S. Petrus[1], M. Janson[16], T. Henning[2], Q. Kral[11], R. G. van Holstein[17], F. Ménard[1], J.-L. Beuzit[6], B. Biller[2,18,19], A. Boccaletti[11], M. Bonnefoy[1], S. Brown[2], A. Costille[5], A. Delboulbe[1], S. Desidera[10], V. D'Orazi[10], M. Feldt[3], T. Fusco[20], R. Galicher[11], J. Hagelberg[21], C. Lazzoni[22], R. Ligi[23], A.-L. Maire[1], S. Messina[24], M. Meyer[25], A. Potier[26], J. Ramos[2], D. Rouan[11], T. Schmidt[11], A. Vigan[5], and A. Zurlo[5,27,28]

(Affiliations can be found after the references)

Received 12 January 2022 / Accepted 25 April 2022

ABSTRACT

Context. HD 95086 is a young nearby Solar System analog hosting a giant exoplanet orbiting at 57 au from the star between an inner and outer debris belt. The existence of additional planets has been suggested as the mechanism that maintains the broad cavity between the two belts.

Aims. We present a dedicated monitoring of HD 95086 with the VLT/SPHERE instrument to refine the orbital and atmospheric properties of HD 95086 b, and to search for additional planets in this system.

Methods. SPHERE observations, spread over ten epochs from 2015 to 2019 and including five new datasets, were used. Combined with archival observations, from VLT/NaCo (2012–2013) and Gemini/GPI (2013–2016), the extended set of astrometric measurements allowed us to refine the orbital properties of HD 95086 b. We also investigated the spectral properties and the presence of a circumplanetary disk around HD 95086 b by using the `special` fitting tool exploring the diversity of several atmospheric models. In addition, we improved our detection limits in order to search for a putative planet c via the `K-Stacker` algorithm.

Results. We extracted for the first time the JH low-resolution spectrum of HD 95086 b by stacking the six best epochs, and confirm its very red spectral energy distribution. Combined with additional datasets from GPI and NaCo, our analysis indicates that this very red color can be explained by the presence of a circumplanetary disk around planet b, with a range of high-temperature solutions (1400–1600 K) and significant extinction ($A_V \gtrsim 10$ mag), or by a super-solar metallicity atmosphere with lower temperatures (800–1300 K), and small to medium amount of extinction ($A_V \lesssim 10$ mag). We do not find any robust candidates for planet c, but give updated constraints on its potential mass and location.

Key words. instrumentation: adaptive optics – instrumentation: high angular resolution – methods: observational – stars: individual: HD95086 – planetary systems

1. Introduction

Direct imaging has proven to be successful at imaging and characterizing the properties of young planetary system architectures, and young (≤100 Myr) gaseous giant planets orbiting at large distances from their host stars ($a \gtrsim 10$ au). Large-scale surveys of several hundreds of young nearby stars (<150 pc), such as SHINE (Chauvin et al. 2017; Desidera et al. 2021; Langlois et al. 2021; Vigan et al. 2021) and GPIES (Nielsen et al. 2019), have now extended our vision of the giant planet demographics down to 10 au. The goal is to access the bulk of the giant planet population close to the snowline and to bridge the gap with complementary indirect detection methods such as radial velocity, transit, micro-lensing, and soon astrometry (with the Gaia Data Release 4) that are sensitive to planets closer to their stars (≲10 au). Over the last two decades discoveries of emblematic planetary systems such as HR 8799 (Marois et al. 2008, 2010), β Pictoris (Lagrange et al. 2010), HD 95086 (Rameau et al. 2013a), 51 Eri (Macintosh et al. 2015), and PDS 70 (Keppler et al. 2018; Müller et al. 2018) have offered rich opportunities to explore the diversity of young Solar System analogs, containing giant planets and circumstellar disks shaped with cavities and belts. HR 8799 hosts four exoplanets (Marois et al. 2008, 2010), whereas 51 Eridani hosts one exoplanet (Macintosh et al. 2015). A second planet has been recently detected by the radial velocity technique in the β Pictoris system (Lagrange et al. 2019) and confirmed with interferometric observations (Nowak et al. 2020), while a second forming planet has been detected with MUSE in the PDS 70 system (Haffert et al. 2019). The mass of these protoplanets is highly uncertain, with estimates ranging from 1 to 17 $M_{\rm Jup}$ (Müller et al. 2018; Christiaens et al. 2019; Mesa et al. 2019; Isella et al. 2019; Stolker et al. 2020b; Wang et al. 2021). These young, planetary systems are benchmark laboratories for exploring the formation and evolution of young giant planets with the current large telescopes and instruments. They are prime targets for upcoming telescopes, such as the *James Webb* Space Telescope (JWST, first light 2022) and the Extremely Large Telescope (ELT, first light 2027). From that perspective, the hunt for additional planets in the young system HD 95086 is very interesting.

Table 1. Physical properties of the HD 95086 system from Chauvin et al. (2018); Su et al. (2017, 2015); Rameau et al. (2013a); De Rosa et al. (2016); Bailer-Jones et al. (2018); Booth et al. (2021); Swatik et al. (2021).

The HD 95086 exoplanetary system	
Star	
Spectral type	A
Teff (K)	7883^{+43}_{-65}
log(g) (dex)	$4.58^{+0.02}_{-0.06}$
Distance (pc)	86.2 ± 0.3
Age (Myr)	$13.3^{+1.1}_{-0.6}$
Mass ($M_\odot$)	1.6 ± 0.1
Luminosity ($L_\odot$)	5.7 ± 1.7
Metallicity ([Fe/H])	$0.14^{+0.05}_{-0.04}$
Debris disk – Innermost belt (?)	
Location (au)	2
Temperature (K)	300
– Warm belt	
Location (au)	7–10
Temperature (K)	187 ± 26
– Cold belt	
Location (au)	106–320
Temperature (K)	57 ± 2
Inclination (°)	30 ± 3
Position Angle (°)	97 ± 3
– Stellar halo (?)	
Location (au)	300–800
HD 95086 b	
Spectral type	$L6 \pm 1$
Teff (K)	800–1300 K
log(g) (dex)	$\lesssim 4.5$
Semimajor axis (au)	52^{+13}_{-24}
Eccentricity	$0.2^{+0.3}_{-0.2}$
Inclination (°)	141^{+15}_{-13}
Period (years)	289^{+12}_{-177}
Mass ($M_{\rm Jup}$)	4–5

Notes. $T_{\rm eff}$ corresponds to the effective temperature when assuming the blackbody hypothesis; log(g) corresponds to the logarithm of the surface or photosphere gravity. To avoid confusion, it should be noted that the inclination i could as well be $180° - i$ owing to projection on the sky.

Since 2013, and since the discovery of a 4–5 $M_{\rm Jup}$ exoplanet HD 95086 b in thermal imaging using the NaCo instrument (Rousset et al. 2003; Lenzen et al. 2003) at the Very Large Telescope (VLT), the HD 95086 planetary system has become a reference to investigate the processes of planetary formation and evolution, and to characterize young planetary architectures. The star is an A-type star with an approximate effective temperature of 7750 K and a mass of 1.6 $M_\odot$. Until very recently, the star was identified as a young star located at the border of the Lower Centaurus Crux (LCC) association and thus with an age of 17 ± 2 Myr (Pecaut et al. 2012). However, based on the *Gaia* Data Release 2, Booth et al. (2021) showed that the star could instead belong to the Carina association, which

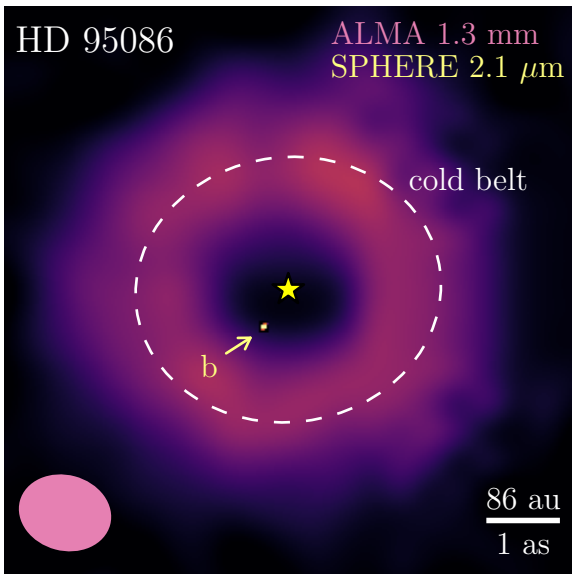

Fig. 1. Composite ALMA-continuum (at 1.3 mm) and SPHERE/IRDIS (at 2.1 μm) observations of HD 95086 (see Su et al. 2017; Chauvin et al. 2018). The exoplanet b is detected at the $K1$ band (red dot). The white dashed ring at 180 au represents the peak location of the outer cold belt located from 106 ± 6 au to 320 ± 20 au. The inner warm belt is not resolved with ALMA. The pink ellipse represents the ALMA synthetic beam.

according to their age estimation would make it a few million years younger, $13.3^{+1.1}_{-0.6}$ Myr. By using a self-consistent Bayesian analysis, Swatik et al. (2021) derived a new estimation of the stellar parameters consistent with the literature but more accurate, and in particular a stellar metallicity of $0.14^{+0.05}_{-0.04}$. The physical parameters of the star are summarized in Table 1.

HD 95086 hosts a double-belt debris disk architecture, very similar to that of our Solar System, with an outer belt resolved by the Atacama Large Millimeter Array (ALMA) in the continuum at 1.3 mm (Su et al. 2017; see Fig. 1). The inner warm belt is located at 8 ± 2 au (187 ± 26 K), and the large outer, colder belt between 106 ± 6 au and 320 ± 20 au (57 ± 2 K). Their existence was originally identified from the analysis of *Herschel* observations, in combination with the characterization of the spectral energy distribution (SED) of HD 95086 (Moór et al. 2013). Based on SED modeling from Herschel, Spitzer, WISE, and APEX observations, the existence of a third belt at 2 au (300 K), has been also proposed by Su et al. (2015), together with a disk halo component that could extend up to 800 au (Su et al. 2017), but this innermost belt has not been confirmed to date. Recently, Zapata et al. (2018) added new constraints on the structure of the outer belt at submillimeter and millimeter wavelengths with ALMA observations at 0.9 and 1.3 mm, and derived a dust-to-gas ratio ≥50. Moreover, Zapata et al. (2018) and Booth et al. (2019) did not detect CO (J = 2–1) and (J = 3–2) emissions, excluding the possibility of HD 95086 being an evolved gaseous primordial disk. By using spectro-spatial filter on ALMA observations, Booth et al. (2019) found tentative evidence of CO (J = 2–1) emission with an integrated line flux of 9.5 ± 3.6 mJy km s^{-1}. It corresponds to a CO mass of (1.4–13) × 10^{-6} $M_\oplus$, which they determined to be consistent with second-generation production of gas through collisional cascade (Kral et al. 2017). According to Su et al. (2015), the collisions in the HD 95086 disk might also explain their detection of a 69 μm crystalline olivine feature from the outer disk with the *Spitzer* telescope as the crystallization of olivine requires a high

temperature, as is the case for instance in the core of planetary bodies after their disruption. Finally, the outer belt has also been marginally detected in polarized scattered light in the near-infrared (J band) by SPHERE differential polarimetric imaging (DPI) observations (Chauvin et al. 2018) colocated with the thermal emission seen by ALMA. The physical parameters of the debris disk architecture are given in Table 1.

At infrared wavelengths, following the discovery of HD 95086 b with VLT/NaCo (Rameau et al. 2013a) in the L' band (3.8 µm), the planet was re-imaged using Gemini/GPI in the H band (1.5–1.8 µm) and in the $K1$ band (1.9–2.2 µm) (Rameau et al. 2016; De Rosa et al. 2016), and using VLT/SPHERE with IRDIS in H2H3 filters (λ_{H2} = 1.593 µm, λ_{H3} = 1.667 µm) and in $K1K2$ filters (λ_{K1} = 2.103 µm, λ_{K2} = 2.255 µm), and with the integral field spectrograph (IFS) in the YJ (0.95–1.35 µm), and YJH (0.97–1.66 µm) settings (Chauvin et al. 2018). The combination of different photometric measurements in the infrared enabled De Rosa et al. (2016) and Chauvin et al. (2018) to confirm the late L spectral type of HD 95086 b, which is consistent with a dusty atmosphere of about 800–1300 K.

The first orbital fitting of HD 95086 b was performed by Rameau et al. (2016) from previous NaCo astrometric data (epochs 2012 to 2013 from Rameau et al. 2013a) and GPI astrometric monitoring between 2013 and 2016 (published partially in Galicher et al. 2014). They found a semimajor axis of 62^{+21}_{-8} au, an eccentricity less than 0.21, and an inclination of $153^{+10\circ}_{-14}$ at the 68% confidence interval by using Monte Carlo methods. Chauvin et al. (2018) updated the orbital solution using a larger orbital coverage, this time combining NaCo and SPHERE astrometric measurements. This recent MCMC analysis gave consistent results and showed that the planet is orbiting with a period of about 289^{+12}_{-177} years, a semimajor axis of 52^{+13}_{-24} au, a relatively low eccentricity ($0.2^{+0.3}_{-0.2}$), and with an inclination of $141^{+15\circ}_{-13}$ at the 68% confidence interval, compatible with a coplanar orbit with the debris disk plane. The physical parameters of the exoplanet are summarized in Table 1. In addition, Chauvin et al. (2018) used the High Accuracy Radial velocity Planet Searcher (HARPS) high-resolution optical spectrograph to search for additional exoplanets with the radial velocity (RV) technique, and could exclude the presence of a very massive ($>10\ M_{\rm Jup}$), coplanar inner giant planets at less than 1 au.

Given the large cavity seen in ALMA images inside the cold outer belt (see Fig. 1), the system HD 95086 very likely hosts at least one or perhaps two additional planets closer to the star than HD 95086 b, which would explain the architecture of the two debris belts. Su et al. (2015), Rameau et al. (2016), and Chauvin et al. (2018) investigated this possibility by considering various locations, eccentricities, and masses for the inner planets, the physical properties of b, and the characteristics of the inner and outer belts together with the detection performance of current planet imagers. A configuration with one or two additional inner planets between 10 and 30 au, dynamically stable with b carving the outer belt, and participating in the replenishment of the inner belt is possible and worth investigating.

In this paper we extend the study of Chauvin et al. (2018) to revisit the orbital and atmospheric properties of HD 95086 b, and the presence of additional inner giant planets, considering a total of ten epochs acquired with the VLT/SPHERE instrument (Beuzit et al. 2019) between February 2015 and May 2019. These datasets include five new unpublished epochs covering January 2018 to May 2019. In Sect. 2 we present the data acquired, together with the archival data used for this analysis. In Sect. 3 we describe the image processing methods used, along with our data selection and the decision to combine the different datasets considering the individual epoch contrast performance and adaptive optics (AO) correction quality. In Sect. 4 we present the updated astrometry for the exoplanet HD 95086 b based on VLT/NaCo and VLT/SPHERE data, covering a total of seven years of monitoring between 2012 and 2019, and determine the best orbital solution. In Sect. 5 we present for the first time the SPHERE-JH (1.2–1.6 µm) spectroscopic observations of HD 95086 b. Using the MCMC `special` code (Christiaens et al. 2021) applied to the combined spectrum, we re-analyze the physical parameters of the planet and investigate the presence of a circumplanetary disk around it. In Sect. 6 we finally look for the hypothetical exoplanets c and d in the system by updating the HARPS and SPHERE combined observations, and also by applying the K-Stacker algorithm (Le Coroller et al. 2015) to the SPHERE multi-epoch datasets.

2. Observations

2.1. VLT/SPHERE data

The HD 95086 system was monitored during the SHINE survey at 13 different epochs between February 2015 and May 2019 (see Table 2) using the VLT/SPHERE high-contrast instrument (Beuzit et al. 2019). The observations were obtained with the modes IRDIFS (3 epochs) and IRDIFS-EXT (11 epochs) that combine simultaneously the IRDIS (Dohlen et al. 2008) and IFS instruments (Claudi et al. 2008). The IRDIFS-EXT mode combines IRDIS in dual-band imaging (DBI; Vigan et al. 2010) mode with the $K1K2$ filter doublet λ_{K1} = 2.103 ± 0.102 µm, λ_{K2} = 2.255 ± 0.109 µm, and IFS in the YJH (0.97–1.66 µm) setting. The IRDIFS mode combines IRDIS in DBI with H2H3 filters (λ_{H2} = 1.593 ± 0.055 µm, λ_{H3} = 1.667 ± 0.056 µm), and IFS in the YJ (0.95–1.35 µm) setting. Each observing sequence was performed with the pupil-tracking mode. This combination enables the use of angular (Marois et al. 2006) and/or spectral differential imaging techniques (Racine et al. 1999; Sparks et al. 2002) to reach higher contrast at subarcsecond separations. The details of the observations are reported in Table 2.

In this work we focused our analysis on data acquired with the IRDIFS-EXT mode as HD 95086 b, and any expected inner planet in the system, are L-type planets, expected to be particularly red and therefore easier to detect at longer wavelengths. A total of ten epochs are considered as the data acquired on May 3, 2017, are not exploitable owing to very poor observational conditions. The observing conditions are summarized in Table 2 and Fig. A.1. The Strehl ratio (SR) and the wind parameters are measured by the SPHERE eXtreme AO (SAXO, Petit et al. 2014) real-time computer named Standard Platform for Adaptive optics Real Time Applications (SPARTA, Fedrigo et al. 2006), while the seeing (ϵ) and the atmospheric coherence time parameters (τ_0) were obtained by the Differential Image Motion Monitor (DIMM) and the Multi-Aperture Scintillation Sensor (MASS, Kornilov et al. 2007) turbulence monitor at the Paranal Observatory.

2.2. Archival data: VLT/NaCo and Gemini-South/GPI

To revisit the orbital and spectral properties of HD 95086 b, we analyzed archival data from the VLT/NaCo imager obtained in 2012 and 2013 (Rameau et al. 2013a,b), together with Gemini-S/GPI observations obtained between 2013 and 2016 (Rameau et al. 2016; De Rosa et al. 2016). A summary of these observations and the astrometric and spectro-photometric results used for this work are reported in Table 3.

Table 2. Summary of all SPHERE observations of HD 95086 in the *K*1*K*2 (IRDIS) and *YJH* bands (IFS), as well as the mean observational conditions when available.

Epoch	Instr.	Filter	Coronagraph	Satellite spots	NDIT × DIT number × s	N_{exp}	$\Delta\pi$ (°)	ϵ (″)	τ_0 (ms)	Sr (%)	Airmass
2015-02-03	IFS	YJH	N_ALC_YJH_S	No	1 × 64	26	22.4	–	–	–	1.41
2015-02-03	IRDIS	DB *K*12	N_ALC_YJH_S	No	1 × 16	26	22.4	–	–	–	1.41
2015-05-05	IFS	YJH	N_ALC_YJH_S	No	4 × 64	13	18.2	0.79	2.1	75	1.40
2015-05-05	IRDIS	DB *K*12	N_ALC_YJH_S	No	4 × 64	13	18.2	0.45	2.1	75	1.40
2015-05-12	IFS	YJH	N_ALC_YJH_S	No	4 × 64	No	22.5	1.07	3.0	–	1.41
2015-05-12	IRDIS	DB *H*23	N_ALC_YJH_S	No	4 × 64	No	22.5	1.07	3.0	–	1.41
2016-01-18	IFS	YJH	N_ALC_YJH_S	No	5 × 64	19	28.1	0.33	1.8	81	1.41
2016-01-18	IRDIS	DB *K*12	N_ALC_YJH_S	No	5 × 64	19	28.1	0.33	1.8	81	1.41
2016-05-31	IFS	YJH	N_ALC_Ks	Yes	10 × 64	7	25.2	0.64	3.4	61	1.43
2016-05-31	IRDIS	DB *K*12	N_ALC_Ks	Yes	10 × 64	7	25.2	0.64	3.4	61	1.43
2017-05-03	IFS	YJH	N_ALC_Ks	No	7 × 12	No	2.1	2.15	1.6	47	1.40
2017-05-03	IRDIS	DB *K*12	N_ALC_Ks	No	7 × 12	No	2.1	2.15	1.6	47	1.40
2017-05-10	IFS	YJH	N_ALC_Ks	Yes	10 × 64	7	36.6	0.89	3.3	73	1.40
2017-05-10	IRDIS	DB *K*12	N_ALC_Ks	Yes	10 × 64	7	36.6	0.89	3.3	73	1.40
2018-01-06	IFS	YJH	N_ALC_Ks	Yes	10 × 96	7	41.0	0.30	10.1	83	1.40
2018-01-06	IRDIS	DB *K*12	N_ALC_Ks	Yes	10 × 96	7	41.0	0.30	10.1	83	1.40
2018-02-24	IFS	YJH	N_ALC_Ks	No	4 × 96	16	33.4	0.38	9.0	–	1.41
2018-02-24	IRDIS	DB *K*12	N_ALC_Ks	No	4 × 96	16	33.4	0.38	9.0	–	1.41
2018-03-28	IFS	YJH	N_ALC_YJH_S	No	4 × 96	16	33.3	0.51	9.3	82	1.41
2018-03-28	IRDIS	DB *K*12	N_ALC_YJH_S	No	4 × 96	16	33.3	0.51	9.3	82	1.41
2019-04-13	IFS	YJH	N_ALC_YJH_S	Yes	9 × 96	16	33.8	0.76	3.0	70	1.42
2019-04-13	IRDIS	DB *K*12	N_ALC_YJH_S	Yes	9 × 96	16	33.8	0.76	3.0	70	1.42
2019-05-18	IFS	YJH	N_ALC_YJH_S	No	4 × 96	16.	33.8	0.63	3.2	72	1.42
2019-05-18	IRDIS	DB *K*12	N_ALC_YJH_S	No	4 × 96	16	33.8	0.63	3.2	72	1.42

Notes. NDIT represents the number of frames in the data cube, DIT the exposure time for one frame, Nexp the number of cubes, $\Delta\pi$ the variation of the parallactic angle, ϵ the seeing (at λ = 550 nm), τ_0 the atmospheric coherence time, and SR the Strehl ratio after the AO correction.

3. Data reduction and analysis

3.1. Pre-processing

All SPHERE observations of HD 95086 were reduced by the SPHERE Data Center (Delorme et al. 2017a), using the SPHERE Data Reduction and Handling pipeline (Pavlov et al. 2008), following the same approach as described by Chauvin et al. (2018). To summarize, the pre-processing corrects the non-coronagraphic point spread function (PSF) and the coronagraphic image cube for bad pixels, dark current, flat non-uniformity; the sky background for both IRDIS and IFS; and the wavelength and cross-talk between spectral channel calibration for IFS. A normalization is applied to calibrate the coronagraphic images in intensity relative to the star (i.e., in terms of contrast). The coronagraphic images are centered by using the four satellite spots to accurately determine the position of the star behind the coronagraphic mask, as also described in Chauvin et al. (2018). To calibrate the astrometry of both IRDIS and IFS on the sky, a star-crowded field (47 Tuc) is regularly observed as part of the long-term analysis of the SPHERE guaranteed time observation (GTO) astrometric calibration described in Maire et al. (2016, 2021a) to measure the detector plate scale, true north, and distortion. The plate scale and true north solutions at each epoch are reported in Table 3.

3.2. Image processing

To detect and characterize potential planetary signals in the images, we used two dedicated pipelines, namely ANDROMEDA (Cantalloube et al. 2015) and SpeCal (Galicher et al. 2018). Both are based on the angular differential imaging (ADI) technique, which removes the starlight residuals in the coronagraphic images. ANDROMEDA is a forward-modeling approach based on a maximum likelihood estimator (Mugnier et al. 2009). It first performs a simple pair-wise subtraction. Then, it searches for the specific signature that would appear in the presence of an unresolved point-source in the residual image, and estimates its probability, jointly for all pairs of subtracted images. The SpeCal pipeline combines a set of different algorithms like classical ADI (cADI, Marois et al. 2006), locally optimized combination of images (LOCI/TLOCI, Lafrenière et al. 2007), and principal component analysis (PCA, Amara & Quanz 2012; Soummer et al. 2012). To exploit the spectral diversity given by the IFS and the IRDIS-DBI modes, in addition to the temporal dimension as done in ADI, SpeCal has been developed to apply LOCI/TLOCI and PCA in angular and spectral differential imaging (ASDI; Mesa et al. 2015). For the analysis of the SHINE survey, the reference algorithms benchmarked with various blind tests are the TLOCI-ADI and the PCA-ASDI algorithms (Langlois et al. 2021). For IRDIS,

Table 3. Relative astrometry and photometry of the star and planet b for NaCo, GPI, and SPHERE at 68% confidence level.

UT Date	Ins.-Filter	Algo.[(a)]	$\Delta\alpha$ (mas)	$\Delta\delta$ (mas)	Sep. (mas)	PA (°)	Contrast (mag)	True North (deg)	Plate scale (mas)	Ref.
12-01-2012	NaCo-L'	sADI	294 ± 8	−550 ± 8	624 ± 8	151.9 ± 0.8	9.8 ± 0.4	−0.57 ± 0.10	27.11 ± 0.06	1
12-01-2012	NaCo-L'	sADI	–	–	–	–	9.5 ± 0.2	–	–	3
14-03-2013	NaCo-L'	sADI	305 ± 13	−546 ± 13	626 ± 13	150.8 ± 1.3	9.7 ± 0.6	−0.58 ± 0.10	27.10 ± 0.03	1
27-06-2013	NaCo-L'	sADI	291 ± 8	−525 ± 8	600 ± 11	151.0 ± 1.2	9.2 ± 0.8	−0.65 ± 0.10	27.10 ± 0.04	1
10-12-2013	GPI-K_1	LOCI	301 ± 5	−541 ± 5	619 ± 5	150.9 ± 0.5	12.1 ± 0.5	−0.10 ± 0.13	14.17 ± 0.01	2, 3, 7
11-12-2013	GPI-H	LOCI	306 ± 11	−537 ± 11	618 ± 11	150.3 ± 1.1	13.1 ± 0.9	−0.10 ± 0.13	14.17 ± 0.01	2, 3, 7
13-05-2014	GPI-K_1	LOCI	307 ± 8	−536 ± 8	618 ± 8	150.2 ± 0.7	–	−0.10 ± 0.13	14.17 ± 0.01	3, 7
06-04-2015	GPI-K_1	LOCI	322 ± 7	−532 ± 7	622 ± 7	148.8 ± 0.6	–	−0.10 ± 0.13	14.17 ± 0.01	3, 7
08-04-2015	GPI-K_1	LOCI	320 ± 4	−533 ± 4	622 ± 4	149.0 ± 0.4	12.2 ± 0.2	−0.10 ± 0.13	14.17 ± 0.01	3, 4, 7
29-02-2016	GPI-H	LOCI	330 ± 5	−525 ± 5	621 ± 5	147.8 ± 0.5	13.7 ± 0.2	−0.10 ± 0.13	14.17 ± 0.01	3, 4, 7
06-03-2016	GPI-H	LOCI	336 ± 3	−521 ± 3	620 ± 5	147.2 ± 0.5	–	−0.10 ± 0.13	12.17 ± 0.01	3, 7
03-02-2015	IRDIS-K_1	TLOCI	322 ± 4	−532 ± 4	621 ± 4	148.7 ± 0.3	12.2 ± 0.1	−1.72 ± 0.06	12.25 ± 0.03	5
03-02-2015	IRDIS-K_1	ANDR	–	–	620 ± 4	148.9 ± 0.4	12.6 ± 0.5	−1.72 ± 0.06	12.25 ± 0.03	6
05-05-2015	IRDIS-K_1	TLOCI	324 ± 4	−530 ± 6	621 ± 5	148.5 ± 0.4	12.4 ± 0.2	−1.71 ± 0.06	12.25 ± 0.06	5
05-05-2015	IRDIS-K_1	ANDR	–	–	619 ± 7	148.6 ± 0.5	12.0 ± 0.5	−1.71 ± 0.06	12.25 ± 0.06	6
18-01-2016	IRDIS-K_1	TLOCI	326 ± 4	−532 ± 4	625 ± 4	148.4 ± 0.3	12.3 ± 0.2	−1.74 ± 0.07	12.27 ± 0.03	5, 7
18-01-2016	IRDIS-K_1	ANDR	–	–	623 ± 4	148.7 ± 0.4	11.6 ± 0.9	−1.74 ± 0.07	12.27 ± 0.03	6
31-05-2016	IRDIS-K_1	TLOCI	333 ± 2	−519 ± 2	618 ± 2	147.3 ± 0.2	12.2 ± 0.2	−1.81 ± 0.05	12.26 ± 0.01	5
31-05-2016	IRDIS-K_1	ANDR	–	–	621 ± 3	147.4 ± 0.3	12.2 ± 0.3	−1.81 ± 0.05	12.26 ± 0.01	6
10-05-2017	IRDIS-K_1	TLOCI	341 ± 2	−517 ± 3	620 ± 3	146.6 ± 0.2	12.3 ± 0.2	−1.78 ± 0.06	12.25 ± 0.02	5
10-05-2017	IRDIS-K_1	ANDR	–	–	624 ± 3	146.7 ± 0.3	12.2 ± 0.2	−1.78 ± 0.06	12.25 ± 0.02	6
06-01-2018	IRDIS-K_1	TLOCI	351 ± 2	−514 ± 2	622 ± 2	145.6 ± 0.2	12.3 ± 0.1	−1.83 ± 0.05	12.26 ± 0.01	5
06-01-2018	IRDIS-K_1	ANDR	–	–	625 ± 4	145.6 ± 0.3	12.2 ± 0.1	−1.83 ± 0.05	12.26 ± 0.01	6
24-02-2018	IRDIS-K_1	TLOCI	353 ± 3	−517 ± 3	627 ± 3	145.6 ± 0.3	12.2 ± 0.1	−1.75 ± 0.06	12.25 ± 0.01	5, 7
24-02-2018	IRDIS-K_1	ANDR	–	–	625 ± 4	145.7 ± 0.4	12.1 ± 0.1	−1.75 ± 0.06	12.25 ± 0.01	6, 7
28-03-2018	IRDIS-K_1	TLOCI	357 ± 4	−521 ± 4	632 ± 4	145.5 ± 0.3	12.3 ± 0.1	−1.73 ± 0.07	12.26 ± 0.02	5, 7
28-03-2018	IRDIS-K_1	ANDR	–	–	631 ± 4	145.6 ± 0.4	12.3 ± 0.1	−1.73 ± 0.07	12.26 ± 0.02	6, 7
13-04-2019	IRDIS-K_1	TLOCI	368 ± 3	−508 ± 3	623 ± 3	144.1 ± 0.2	12.3 ± 0.2	−1.78 ± 0.07	12.25 ± 0.02	5
13-04-2019	IRDIS-K_1	ANDR	–	–	627 ± 3	144.1 ± 0.3	12.2 ± 0.2	−1.78 ± 0.07	12.25 ± 0.02	6
18-05-2019	IRDIS-K_1	TLOCI	368 ± 4	−509 ± 4	630 ± 4	144.1 ± 0.3	12.2 ± 0.1	−1.78 ± 0.07	12.26 ± 0.01	5, 7
18-05-2019	IRDIS-K_1	ANDR	–	–	628 ± 4	144.3 ± 0.4	12.1 ± 0.1	−1.77 ± 0.07	12.26 ± 0.01	6

Notes. [(a)]Algo. refers to the algorithms used for the reduction: smart ADI (sADI; Rameau et al. 2013b), TLOCI (Lafrenière et al. 2007), and ANDROMEDA (ANDR; Mugnier et al. 2009).

References. (1) Astrometric and photometric results from Rameau et al. (2013a); (2, 3) Astrometric results processed by Rameau et al. (2016) and photometric results from Galicher et al. (2014); (4) Photometric results reported by De Rosa et al. (2016); (5,6) This work: astrometric and photometric results done automatically with pipeline (5) SpeCal-TLOCI or (6) ANDROMEDA. The 2018 and 2019 data have not been reported and exploited yet. The 2015, 2016, and 2017 data are reported by Chauvin et al. (2018), but they reduced the data with the IPAG-ADI pipeline; (7) These epochs are not used for the orbital fit of the HD 95086 b exoplanet (see Sect. 3.3).

the contrast performance showed that ANDROMEDA-ADI performs better than TLOCI-ADI (see Figs. 2 and 3), and in addition provides a more robust estimate of the statistical threshold for the candidate detection. The signal-to-noise ratio maps (S/N maps) obtained with TLOCI-ADI for IRDIS and PCA-ASDI for IFS using SpeCal are shown in Fig. B.1. The S/N maps obtained for ANDROMEDA in ADI for IRDIS and IFS (consisting of a combination of the IFS channels after processing individual each channel) are shown in Fig. 2.

3.3. Multi-epoch selection and combination

Given the very red spectrum of HD 95086 b, the planet is clearly detected for each individual epoch (with $S/N > 10$) in the $K1$ and $K2$ bands with SPHERE, and in the K band with GPI. This band ($K1$, where the background noise is lower than in $K2$) is therefore used to extract the planet's relative astrometry at each epoch, and derive its updated orbital properties (see below). The detection becomes more challenging at the H band ($S/N \sim 3$–7) for both SPHERE and GPI, but remains possible for good-quality observation (January 2018, February 2018, March 2018, April 2019 and May 2019). At the J band the planet is currently detected only by stacking reduced SPHERE-IFS images taken at various epochs to optimize the speckle cancelation, as done by Chauvin et al. (2018). Following a similar multi-epoch strategy, we first selected the best observing epochs obtained by SPHERE between 2015 and 2019, then re-aligned each final IFS datacubes correcting for the planet's orbital motion, and stacking them to extract the JH spectrum of the planet.

To investigate the contrast performance at each epoch, we considered as the first criterion the contrast curves determined with TLOCI-ADI and ANDROMEDA-ADI for IRDIS, and PCA-ASDI and ANDROMEDA-ADI for IFS (Fig. 3). The observing conditions (atmospheric turbulence conditions and

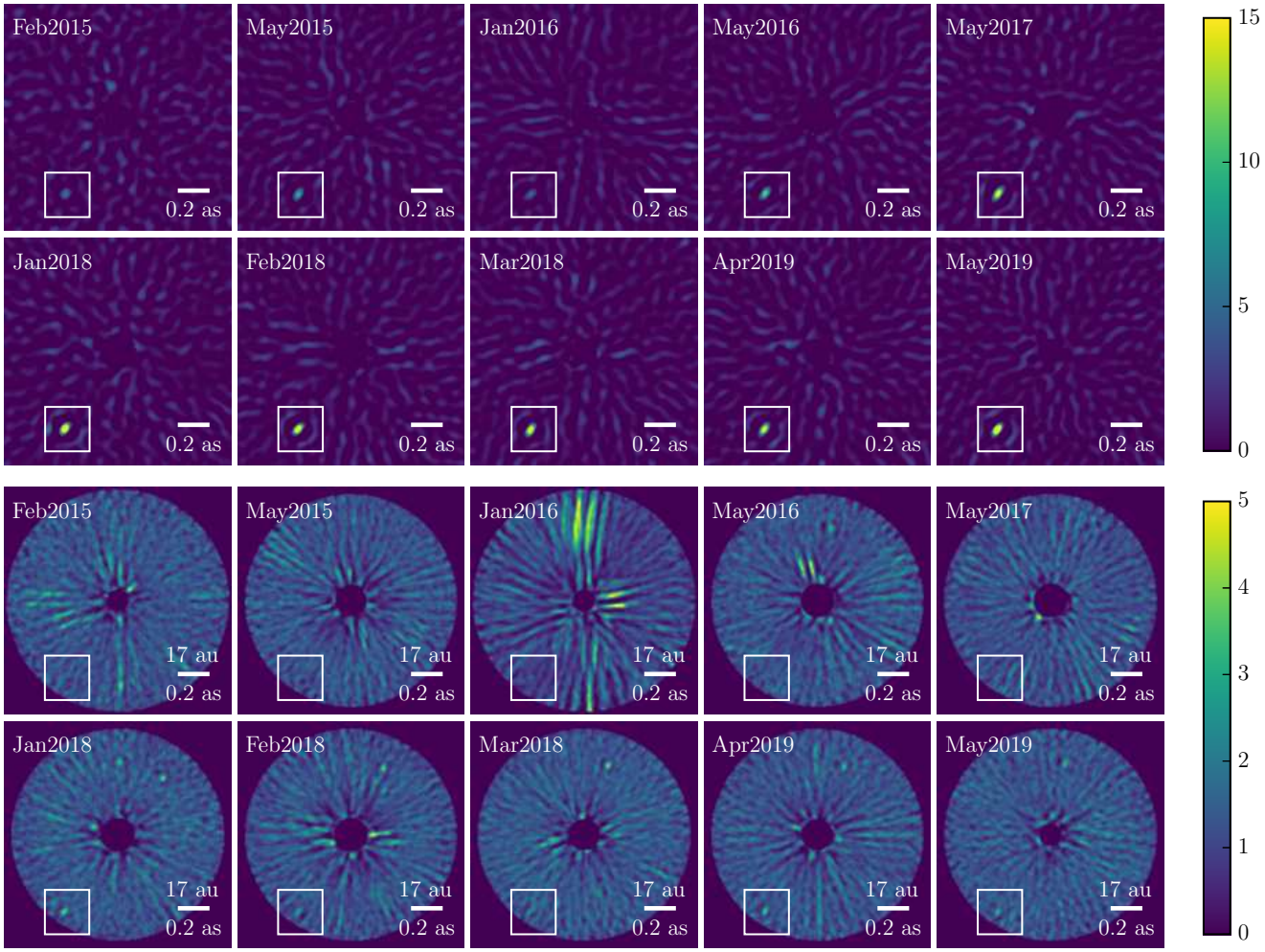

Fig. 2. Signal-to-noise ratio maps for all the SPHERE epochs. At the *top*, SPHERE-IRDIS in the $K1$ band and at the *bottom*, SPHERE-IFS in the *YJH* bands, both reduced by the pipeline ANDROMEDA. The color bar corresponds to the signal-to-noise ratio, 0–15 for IRDIS and 0–5 for the IFS. Planet b is located in the white square. The region below the inner working angle of the coronagraph is masked. In the top right corner of the IFS data, the one (or two) point-like feature(s) correspond to the remanent of the star on the IFS detector.

AO telemetry, summarized in Table 2 and in Fig. A.1) were used as a consistency check. From a total of ten epochs, a subsample clearly emerges of six very good epochs. The best epoch is January 2018, followed by February 2018, March 2018, April 2019, May 2019, and May 2017. The worst epochs are January 2016 and February 2015. Despite the very good Strehl ratio (81%) and seeing (0.33 as) for the January 2016 epoch, the atmospheric coherence time is very fast (1.8 ms), producing a wind-driven halo, which degrades the contrast performance by about one order of magnitude at the planet location (Cantalloube et al. 2020).

The 5σ detection limits are 1×10^{-6} and 2×10^{-6} at $0.6''$ respectively with the IFS and IRDIS for the best epoch (January 2018). IFS performs better in contrast at close separations as PCA-ASDI exploits the spectral diversity of 39 spectral channels to remove the speckles, while TLOCI-ADI does not for the IRDIS dual-band $K12$. We note that the IFS and IRDIS contrast curves are coherent with each other: the best contrast curves with IFS are the same as with IRDIS (see Fig. 3). In summary, the best epochs for extracting the spectrum of the exoplanet HD 95086 b are the last six: May 2017, January 2018, February 2018, March 2018, April 2019, and May 2019. To extract the astrometry, we preferred the epochs acquired with the satellite spots for the whole sequence of observation (and not only at the beginning and/or the end of the observation) to ensure a correct astrometric calibration for the whole sequence of observation (May 2016, May 2017, January 2018, and April 2019), as well as the two epochs in 2015 (February 2015 and May 2015), as in 2015 no observation with satellite spots for the whole sequence was acquired. We note that the position of the star on the detector can marginally evolve during the sequence of observation due to optomechanical and thermal variations that slightly move the optics. The Differential Tip Tilt Sensor (DTTS, Baudoz et al. 2010) aims to ensure its centering, but a centroid variation can be expected. We adopted the conservative error on the centroid position of 0.2 pixel corresponding to 2.5 mas for the epochs acquired without the continuous satellite spots mode, as done in Chauvin et al. (2018). This value is taken into account in the astrometric calibration error budget, as well as the errors on the true north, plate scale, and pupil offset, following Maire et al. (2021b). In addition, it should be noted that the epoch of March 2018 suffers from a higher centroid variation, which is a rare problem, but even so occurred in a few observations over the whole seven years of exploitation of the SPHERE instrument. This higher centroid variation is about 5 mas both in declination and right ascension based on

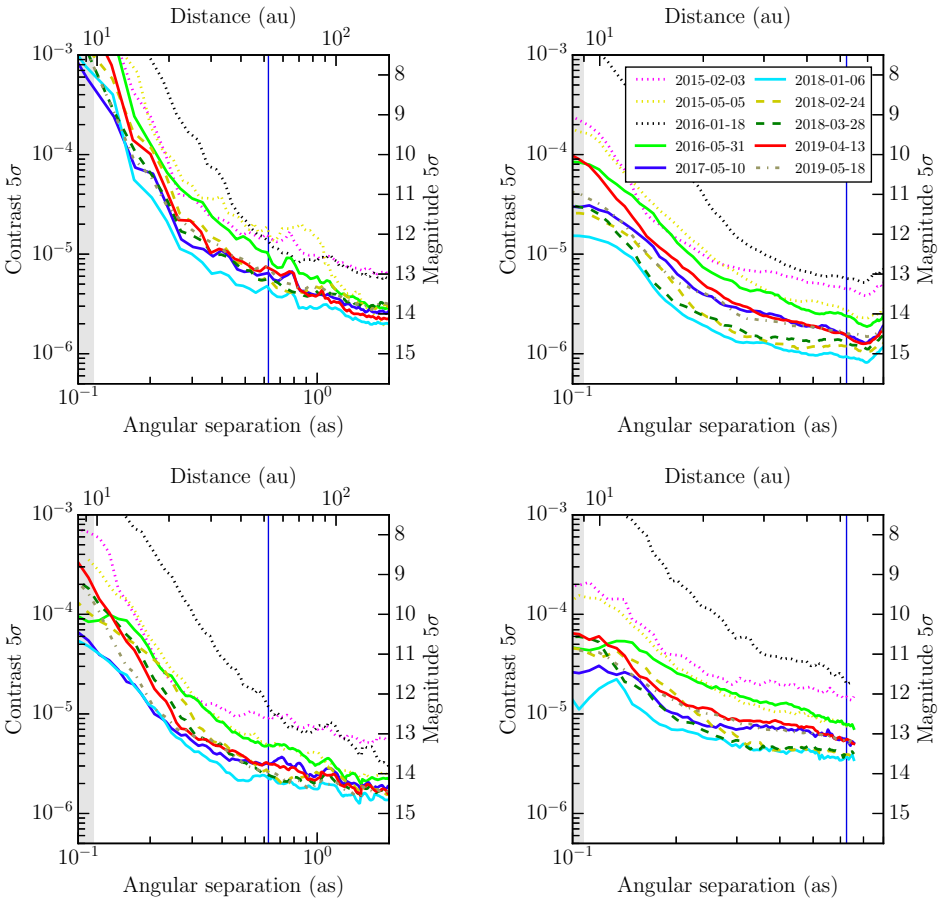

Fig. 3. Detection limits at 5σ for IRDIS in the $K1$ band on the *left* and IFS in the *YJH* bands on the *right*. Data are reduced at the *top* by the pipeline SpeCal-TLOCI (for IRDIS) or SpeCal-PCAPad (for IFS) and at the *bottom* by the pipeline ANDROMEDA. The gray area corresponds to the area hidden by the larger coronagraph used for all the epochs (i.e., N_ALC_Ks) which has an inner working angle of 0.107″ and 0.116″ for IFS and IRDIS, respectively. The blue vertical line corresponds to the position of the planet HD 95086 b at the best epoch January 2018 (cyan, 0.625″).

the expected position of HD 95086 b in March 2018 considering the epochs better calibrated in astrometry, as of January 2018 and April 2019.

The relative astrometry and photometry of the exoplanet HD 95086 b to its host star are gathered in Table 3 for all the epochs obtained with SPHERE-IRDIS in the $K1$ band, using ANDROMEDA and SpeCal-TLOCI image processing, along with the measurements from archival NaCo and GPI observations. The ANDROMEDA and SpeCal-TLOCI astrometric and photometric measurements from 2015 to 2019 are consistent with each other (see Table 3).

3.4. The 1.2–3.8 μm spectrum of HD 95086 b

For the first time, we have extracted the spectrum of the planet HD 95086 b in the J and H bands. This was achieved on the SpeCal-PCA ADI reduced images by measuring the contrast of the planet in an aperture of 1 FWHM of the six-epoch averaged image in which we corrected for the exoplanet's orbital motion by using its precise astrometry through time before stacking. The exoplanet is still not detectable in the Y band, hardly in the J band, and with a signal-to-noise ratio of about 5 per spectral channel in the H band. By using the BT-NEXTGEN synthetic spectrum of the star HD 95086 A, we converted the contrast values to flux values. We completed the SPHERE-IFS *YJH* (0.96–1.64 μm, resolution 30) and SPHERE-IRDIS K12 photometric points (2.10 and 2.26 μm) with archival data from GPI, which provides the spectrum of the exoplanet HD 95086 b in the $K1$ band at low resolution (1.95–2.20 μm, resolution 66), and from NaCo, which provides a photometric measurement in the L' band (3.80 μm, bandwidth 0.62 μm). The complete spectrum of HD 95086 b is shown in Fig. 4; a zoomed-in image of the J and H bands is shown in Fig. 5. The increasing slope in the spectroscopic $K1$ and photometric $K12$ and L' points acknowledges the redness of exoplanet b (De Rosa et al. 2016) and seems to be verified in our H-band spectrum as well, even though the uncertainties are significant. We empirically estimated the spectral correlation matrix as in Greco & Brandt (2016) and De Rosa et al. (2016) for the measurements obtained with the IFS of SPHERE and GPI (see Appendix C), and used it to compute the covariance matrix used for spectral fitting of HD 95086 b (see Sect. 5).

4. Orbital analysis

We ran the Markov chain Monte Carlo (MCMC) orbital fit (Ford 2005, 2006), as done in Chauvin et al. (2012). We used previous NaCo astrometric data (epochs 2012 to 2013 from Rameau et al. 2013a) and SPHERE measurements (epochs February 2015, May 2015, May 2016, and May 2017 from Chauvin et al. 2018) including two new astrometric points from the SPHERE-IRDIS images obtained in the $K1$ band (January 2018 and April 2019) with the updated distance value of 86.2 pc from Bailer-Jones et al. (2018). In this run the stellar mass was fixed to its mean value 1.6 $M_\odot$ and to the stellar distance (86.2 pc). It would have been technically possible to leave the stellar mass free and to let the code redetermine it, but this turned out to be inaccurate. The reason is

[1] The transmission curves are available at https://www.eso.org/sci/facilities/paranal/instruments/sphere/inst/filters.html

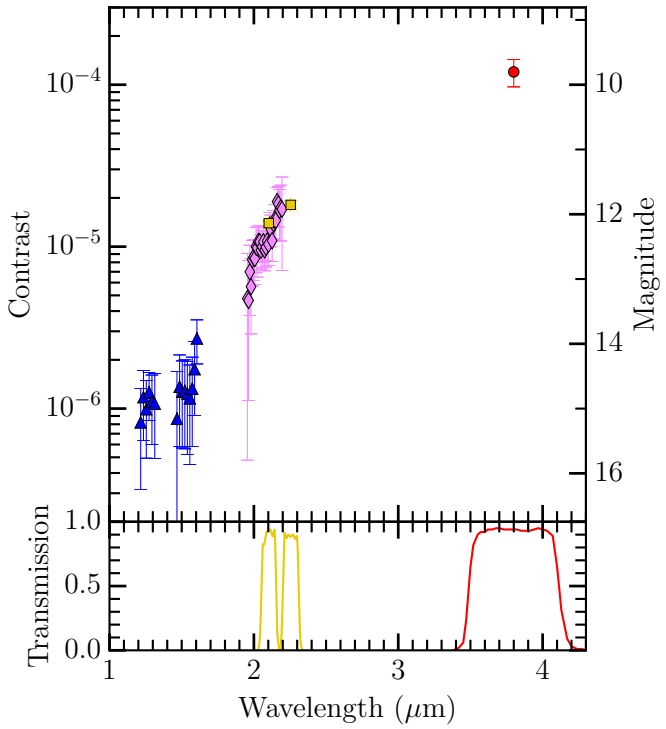

Fig. 4. Spectroscopic and photometric values of the exoplanet HD 95086 b expressed in contrast relative to the host star from 1.2 μm to 3.8 μm with SPHERE-IFS (blue triangles), SPHERE-IRDIS (yellow squares), GPI (pink diamonds), and NaCo (red circle) in the bands *JH*, *K*, *K*12, and *L*′ at the *top*. At the *bottom*, the transmission curves of the filters *K*1, *K*2, and *L*′ are shown[1]. Results are extracted from an averaged stacking of the six best epochs for the SPHERE data, and for one single epoch for the GPI and NaCo data.

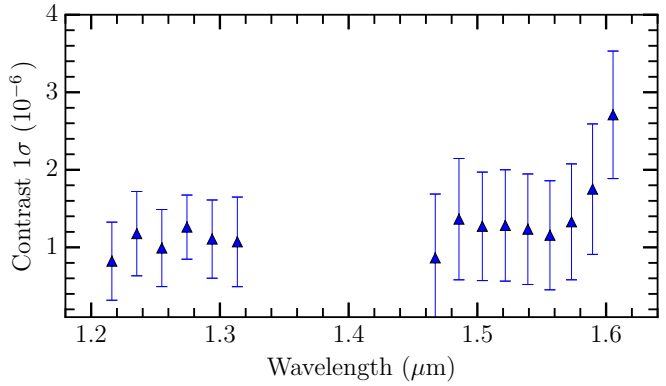

Fig. 5. Spectrum of the exoplanet HD 95086 b expressed in contrast relative to the host star from SPHERE-IFS data in the *J* band (1.21–1.32 μm) and in the *H* band (1.46–1.62 μm) at a 68% confidence level. The contrast is given in units of 10^{-6}. The data are reduced by the pipeline SpeCal-PCA ADI where a six-epoch averaged stack was made before extracting the spectrum to boost the S/N.

that only a tiny part of the orbital period is covered by the observations, leading to a degeneracy between the central mass and the inclination.

The priors assumed for this run were logarithmic between 1 and 4000 yr; linear for the eccentricity e between 0 and 1; $\propto \sin i$ for the inclination i between 0 and 180°; and linear between −180° and 180° for the longitude of ascending node Ω, the argument of periastron ω, and for the mean anomaly at the time of the first observation epoch (related to the time of periastron passage T_p). We note that the MCMC run is represented by taking the orbital period P as variable instead of the semimajor axis a. Both approaches are equivalent as P and a are linked via Kepler's third law.

In addition, when dealing with pure relative astrometric data as we do here, it is well known that there is a ±180° degeneracy between solutions in the longitude of ascending node Ω and the argument of periastron ω. Each solution with (Ω, ω) yields exactly the same projected orbit as the same solution, but with $(\Omega + 180°, \omega + 180°)$. To overcome this difficulty, as explained in Chauvin et al. (2012), the code actually fits $\Omega + \omega$ and $\omega - \Omega$ rather than Ω and ω directly. The former angles are indeed unambiguously determined contrary to ω and Ω. Then, each root solution with fitted values for $\Omega + \omega$ and $\omega - \Omega$ is declined as two final separate solutions, one with (Ω, ω) and the other with $(\Omega + 180°, \omega + 180°)$.

The updated orbital parameters and confident regions from the MCMC orbital fit with the two new astrometric measurements in 2018 and 2019 are shown in Table 4. A sample of the orbit solutions is displayed in Fig. 6, as is the orbit given in Table 4, which corresponds to the maximum a priori probability (MAP). By using both the prior and the reduced chi-squared (χ^2_r) information, the MAP maximizes the probability given in Eq. (1) used in the MCMC:

$$\text{probability} = \frac{\sin(i)}{P} \times \exp\left(-\chi^2_r/2\right). \quad (1)$$

As the MAP gives the peak of probability in the 6D orbital parameter space, the MAP may not correspond to the peak of each 1D distribution (see black vertical lines in diagonal panels in Fig. 7), due to the correlation between the orbital fitted elements. Nevertheless, the 2D distributions in Fig. 7 indicate that the MAP solution (black star) corresponds better to the 2D peaks, which is closer to the 6D reality.

Table 4. Comparison of the MCMC and K-Stacker solutions within the 68% confidence interval for the orbital parameters of HD 95086 b.

Orbital parameter	MCMC solutions (2012–2019)	K-Stacker solutions (2016–2019)
a (au)	72^{+1}_{-21}	51 ± 2
e	≤0.18	0.12 ± 0.03
i (°)	144^{+18}_{-4}	180 ± 15
Ω (°)	72^{+53}_{-27} (+180)	-137 ± 62 (+180)
ω (°)	-89^{+110}_{-2} (+180)	-43 ± 62 (+180)
T_p (yr AD)	2004^{+105}_{-45}	2100 ± 28
star mass ($M_\odot$)	–	1.56

Notes. The astrometric data used regarding MCMC solutions (*middle column*) are NaCo (Rameau et al. 2013b) and SPHERE (Chauvin et al. 2018, and this work) spanning from 2012 to 2019. As for K-Stacker solutions (*right column*), only the SPHERE data acquired with satellite spots (2016–2019) were considered. The orbital parameters are: the semimajor axis (a), the eccentricity (e), the inclination (i), the longitude of ascending node (Ω), the argument of periastron (ω), the time of periastron passage (T_p). If (Ω, ω) is a solution, due to their degeneracy, $(\Omega + 180°, \omega + 180°)$ will be a solution as well (see text for additional details).

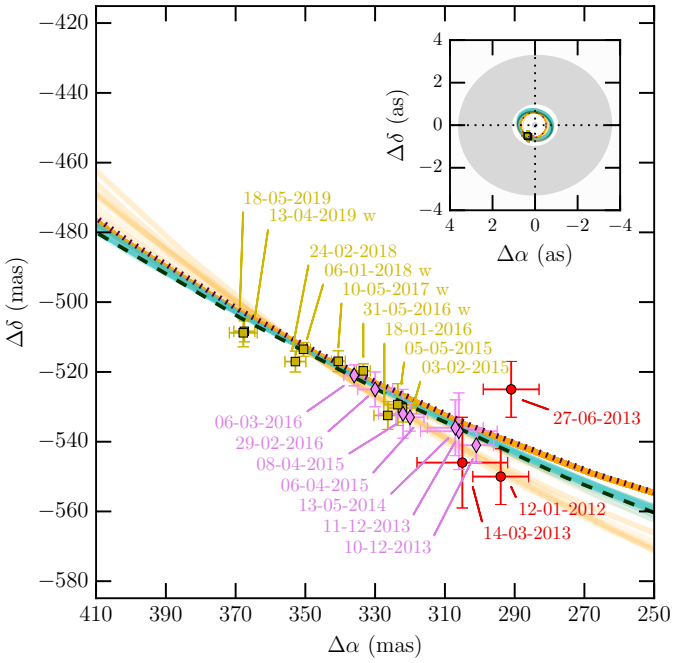

Fig. 6. Astrometric positions of the planet HD 95086 b between 2012 and 2020 with three different instruments: SPHERE (yellow squares), GPI (pink diamonds), and NaCo (red circles) with 1σ error bars. The astrometric positions from SPHERE were computed with the SpeCal-TLOCI pipeline. The letter "w" in the legend indicates the observations imaged with satellite spots that enable finding the exact position of the star during the whole sequence and later recenter the frames if necessary. The green and orange solid lines correspond to a sample of the orbital solutions found by the MCMC orbital fit and the K-Stacker tools, respectively. The black dashed and dotted lines respectively represent the MCMC and K-Stacker orbits for which the corresponding orbital parameters are given in Table 4. For the MCMC tool, the orbit corresponds to the MAP (see text), whereas for K-Stacker it is the orbit closest to the mean of the orbital solutions. Both of these orbits are by construction true orbital solutions. Notes: The Feb2015 point from SPHERE is hidden by the two 2015 points from GPI; the two 2019 points are very close to each other. The insert (in the top right corner) shows the location of the planet relative to the cold outer belt and warm inner belt from Su et al. (2017).

The results are consistent with the previous analysis led by Chauvin et al. (2018). This is expected, first because the fit corresponds to a linear part of the orbit, and second because it only covers a small percent of its whole orbit. In Fig. 7 we can see that a subsample of very eccentric solutions are found ($e \geq 0.4$), but they are correlated with lower inclinations ($i \leq 140°$) than the inclination of the outer belt (147–153°). Hence, these orbital solutions could still be consistent with the double-belt architecture of the system, even though they represent a small subsample of the MCMC orbital fit solutions.

All in all, these solutions confirm that the exoplanet HD 95086 b, located at a semimajor axis 51–73 au and with a low eccentricity ($e \leq 0.18$), is likely sculpting the inner edge of the outer ring, and cannot alone sustain the large cavity observed between 10 and 106 au (Su et al. 2015; Rameau et al. 2016).

By using only the four epochs imaged with SPHERE-IRDIS in the $K1$ band and acquired with the satellite spots enabling a better astrometric calibration (see Table 2), we also obtained the orbital parameters of HD 95086 b as a by-product of the K-Stacker algorithm (Le Coroller et al. 2015), which is used below in the search for one or two additional inner planets in the system (see Sect. 5). K-Stacker is an optimization algorithm that takes advantage of the Keplerian motion of exoplanets on several epochs to then recenter the images according to their Keplerian motion. Thus, it differs from other classical orbital fitting methods, such as MCMC, as it takes as input images from several epochs instead of derived astrometric positions, and consequently can detect objects otherwise unreachable in each observation considered individually. Hence, the coherence of the orbits found by K-Stacker (within 2σ) illustrates its ability to constrain objects with small orbital motion between epochs (50 mas, i.e., $\sim$ 1 FWHM in the $K1$ band) and very faint objects as well; about the same orbit has been found in the H band, where HD 95086 b is hardly detectable (i.e., $S/N \leq 5$ for each epoch taken individually, see Fig. 2). Within the error bars from orbital parameters similar results to the MCMC solutions are found, although the MCMC fit uses the NaCo and SPHERE data, which covers a longer timescale 2012–2019 (instead of 2016–2019 for K-Stacker). In addition, K-Stacker allows us to constrain the star mass between 1.56 and 1.59 $M_\odot$ (as described in Le Coroller et al. 2020, Sect. 3.4).

5. Spectral characterization

The first studies of the infrared colors of HD 95086 b rapidly showed that the spectral properties of the planet fall at the late L to L/T transition and that the planet is underluminous compared to the field dwarfs of similar spectral types (Galicher et al. 2014; De Rosa et al. 2016; Chauvin et al. 2018). The red colors and underluminosity, as shown in Fig. 8, are characteristic of young L/T objects, and are often associated with the inhibited settling of dust in the upper parts of low surface gravity atmospheres. Based on photometric H (1.5–1.8 μm) and spectroscopic $K1$ (1.9–2.2 μm) observations of HD 95086 b with GPI, De Rosa et al. (2016) confirmed the L-type dusty atmosphere, as evidenced by a featureless low-resolution spectrum and a monotonically increasing pseudo-continuum in the $K1$ band consistent with a cloudy atmosphere. Considering the 1.2–1.6 μm spectrum extracted in this work, we propose below to reinvestigate the spectral properties of HD 95086 b. We will consider the best atmosphere models fitting current observations from 1.2 to 3.8 μm, as well as the possibility of having a circumplanetary disk around the planet b, as seen for instance in the younger Solar System analog PDS 70, also a member of Sco-Cen for the planet c (Keppler et al. 2018; Isella et al. 2019).

5.1. Comparison to models

To constrain the physical properties of the exoplanet HD 95086 b with atmospheric and circumplanetary disk models, we used the `special` package (Christiaens et al. 2021), first known as `specfit`, a module of the open-source python package `VIP`[2] (Gomez Gonzalez et al. 2017) and now available as a distinct package[3]. The `special` package is compatible with any atmospheric grid if a snippet function which reads the input grid files is provided. It can also fit for blackbody components (either alone or as additional component(s) to the atmosphere), the optical extinction A_V, the optical-to-selective extinction ratio R_V, or the intensity of emission lines that are provided in a dictionary. `special` utilizes the MCMC sampler `emcee` (Foreman-Mackey et al. 2013) to retrieve in a Bayesian framework the most likely physical parameters of any stellar or substellar object based on its spectral energy distribution. Models are linearly interpolated

[2] Available at https://github.com/vortex-exoplanet/VIP
[3] Available at https://github.com/VChristiaens/special

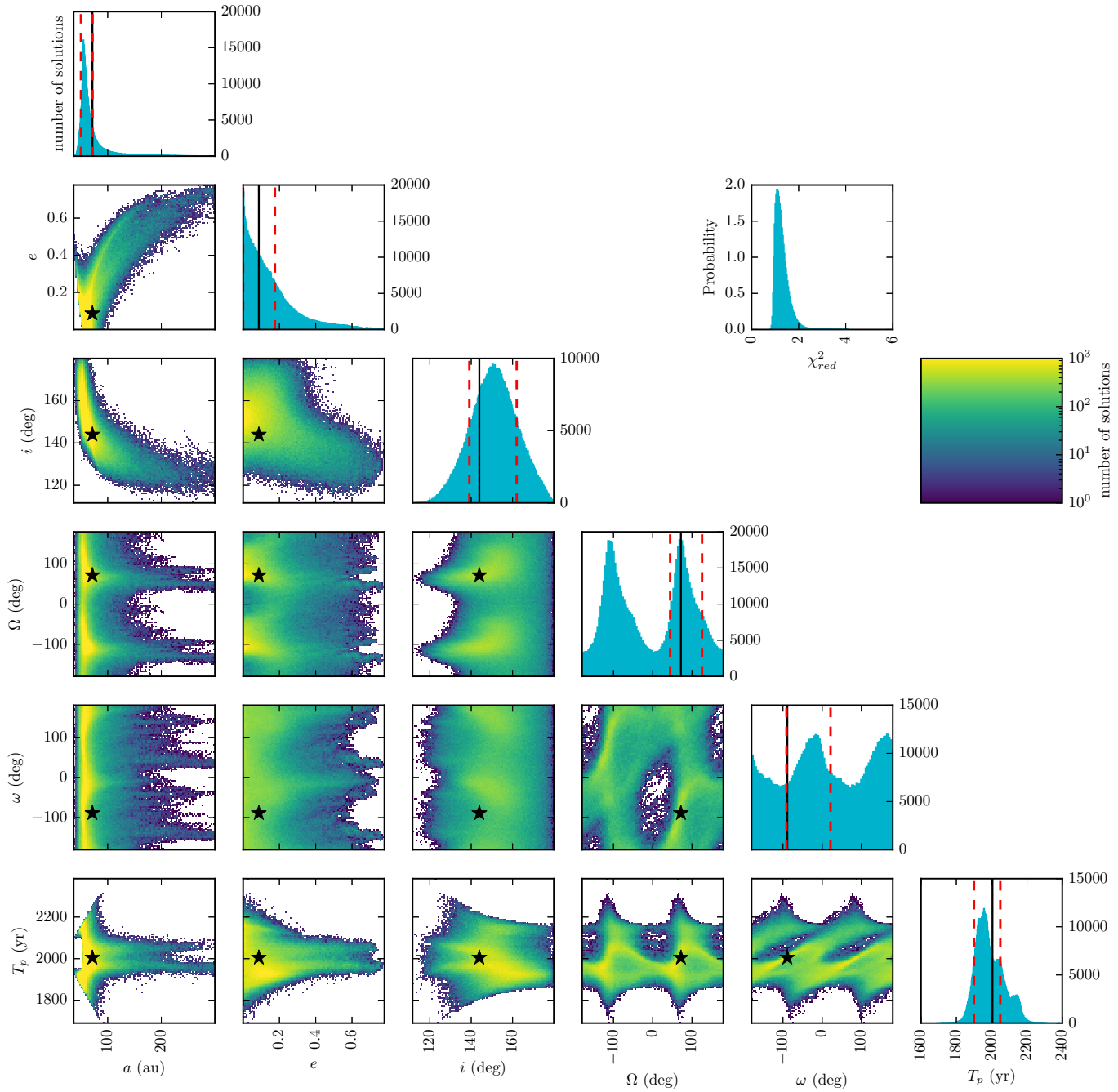

Fig. 7. Results of the MCMC orbital fitting of HD 95086 based on the NaCo archive data (epochs 2012–2013) and our SPHERE-IRDIS astrometric results obtained in the $K1$ band with the SpeCal-TLOCI pipeline (epochs 2015–2019). The orbital parameters are: the orbital period (P (yr)), the eccentricity (e), the inclination (i (°)), the longitude of ascending node (Ω (°)), the argument of periastron (ω (°)), the time of periastron passage (T_p (yr AD)). The best orbital fit solution is given by the MAP as black stars in the non-diagonal panels, and as the solid black vertical lines in the diagonal panels. The 1σ confidence region defined as the shortest interval comprising 68% of the probability around the MAP solution is shown with the vertical dashed red lines in the diagonal panels. As Ω and ω are degenerated; confidence regions of 34% are given for both. If (Ω, ω) is a solution, then (Ω + 180°, ω + 180°) is a solution as well. The color bar (on the *right*) indicates the number of solutions corresponding to a given color for each subplot.

between grid points. The log-likelihood expression provided to the sampler is

$$\log \mathcal{L}(D|M) = -\frac{1}{2}[\mathbf{W}(\mathbf{F}_{\rm obs} - \mathbf{F}_{\rm mod})^T]\mathbf{C}^{-1}[\mathbf{W}^T(\mathbf{F}_{\rm obs} - \mathbf{F}_{\rm mod})], \quad (2)$$

where $F_{\rm obs}$ and $F_{\rm mod}$ are the observed and model fluxes; $\mathbf{C}$ is the spectral covariance matrix (see Appendix C); and $\mathbf{W}$ is a vector of normalized weights that are proportional to the relative width $\delta\lambda/\lambda$ of each spectral channel or photometric filter. The last prevents the fit from putting too much emphasis on the IFS points (higher density of measurements) at the expense of the photometric points, which cover a wider spectral range (e.g., Ballering et al. 2013; Olofsson et al. 2016). Nevertheless, to test their effect on the fits to the HD 95086 b spectrum, we show in Appendix D a comparison of the best-fit models obtained with and without these additional weighting coefficients.

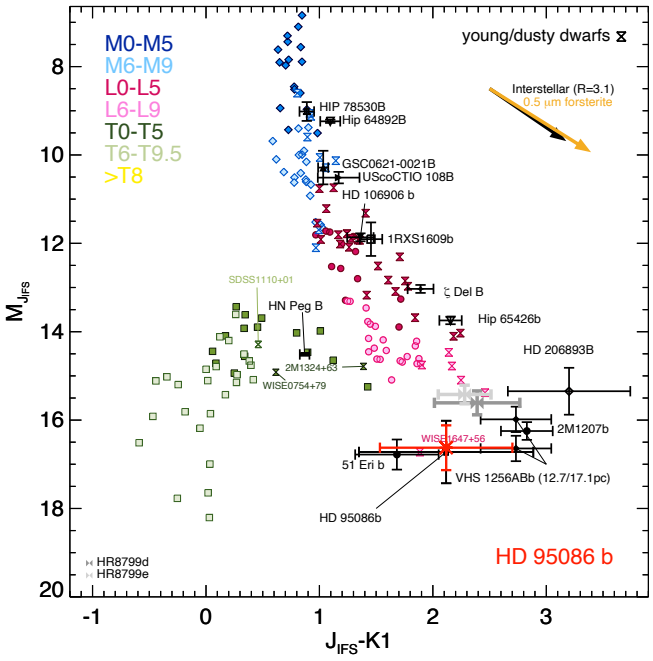

Fig. 8. Color-magnitude diagram considering the SPHERE-IRDIS *K1* photometry, and the J_{IFS} photometry from 1.2 to 1.32 µm as extracted from the SPHERE-IFS datacubes.

For each fit the MCMC was run with 100 walkers until the number of steps met a criterion based on autocorrelation time for convergence. The adopted criterion is that the number of steps is 50 times larger than the autocorrelation time for all free parameters (see, e.g., documentation of `emcee`; Foreman-Mackey et al. 2013). This resulted in 5000–20 000 steps for atmospheric models and 100 000–250 000 steps for the atmospheric+circumplanetary disk models. We then used a "burn-in" factor of 0.5.

5.1.1. Atmospheric models

We provided the following public grids of atmospheric models as input to `special`: BT-SETTL (Allard et al. 2012; Allard 2014), DRIFT-PHOENIX (Woitke & Helling 2003, 2004; Helling & Woitke 2006; Helling et al. 2008), and the grids of A and AE forsterite cloud models with 60 µm modal grain size distribution from Madhusudhan et al. (2011, hereafter M11).

These grids have different prescriptions for clouds, opacity, and dust. The BT-SETTL and DRIFT-PHOENIX models both rely on the PHOENIX atmosphere model (Hauschildt 1992), while the M11 models use a modified version of the TLUSTY atmosphere model (Hubeny 1988; Hubeny & Lanz 1995). The BT-SETTL models consider dust formation using cloud microphysics (condensation and sedimentation mixing timescales) to compute dust grain sizes in a self-consistent way. The DRIFT-PHOENIX models rely on the non-equilibrium cloud model DRIFT and account for the formation of dust grains through a kinetic approach (grain formation, growth, settling, advection, and evaporation). Seven different solids are considered for dust and cloud formation: $MgSiO_3$[s], Mg_2SiO_4[s], MgO[s], SiO_2[s], SiO[s], Al_2O_3[s], and TiO_2[s]. In the M11 grids, different distributions of the grain sizes and vertical extent are considered. The A and AE cloud models correspond to clouds extending to the top of the atmosphere and half the pressure scale height, respectively. In this work we only consider the M11 grids calculated using forsterite (Mg_2SiO_4[s]) clouds owing to the completeness of the grids. Given the very red slope of the spectrum of HD 95086 b and the better fits obtained with the cloud-A grid (see below), we did not consider the grids with thinner and/or lower cloud distributions presented in M11.

Table 5. Parameter ranges probed with the different grids of atmospheric models.

Model	$T_{\rm eff}$ (K)	$\log(g)$	$\log(Z/Z_\odot)$
D-P [a]	1000...2000 [100] [b]	3.0...5.5 [0.5]	−0.3...0.3 [0.3]
BT-SETTL	1200...4000 [100]	2.5...5.0 [0.5]	(0) [c]
M11 c-A	600...1700 [100]	(4.0) [c]	0.0...1.0 [0.5]
M11 c-AE	700...1700 [100]	3.5...5.0 [100]	(0) [c]

Notes. [a]D-P stands for DRIFT-PHOENIX. [b]Step of the grid provided in square brackets. [c]Grid only available with the value provided in parentheses.

All grids consider effective temperature ($T_{\rm eff}$) and surface gravity ($\log(g)$) as free parameters, except for the M11 forsterite cloud-A models ($\log(g)$ fixed to 4.0). The DRIFT-PHOENIX and M11 forsterite cloud-A grids also include metallicity ($\log(Z/Z_\odot)$) as a free parameter. The photometric radius $R_{\rm phot}$ was allowed to take values between 0.1 $R_{\rm Jup}$ and 5 $R_{\rm Jup}$, the lower bound allowing for the possibility of a fraction of the emission not reaching the observer (e.g., in the presence of a large amount of dust around the planet). Table 5 summarizes the sampling of the free parameters for each grid. For each model grid, we carried out two types of fits; the optical extinction A_V was either fixed to 0 (the value estimated for the star; Chen et al. 2012) or left as a free parameter to account for the possible presence of dust around the planet. We considered the Cardelli et al. (1989) extinction law and allowed the value of A_V to span from 0 to 20 mag.

The best-fit models retrieved by `special` for each grid of atmospheric models are presented in the top four panels of Fig. 9. The solid and dashed green lines correspond to the maximum-likelihood samples among all posterior samples, when A_V is included as a free parameter and set to 0 mag, respectively. In order to visualize the uncertainties on the retrieved physical parameters, we also plotted 200 random samples from the posterior distribution inferred by the MCMC in the free A_V case (cyan curves in Fig. 9). Table 6 reports the most likely parameters for each type of model based on their marginalized distribution (some of which are shown in Figs. D.1–D.4).

For each type of model we computed the Akaike information criterion (AIC; Akaike 1974) to evaluate which models reproduced the observed spectrum better. The definition of the AIC takes into account the number of free parameters in order to avoid overfitting. Low values of AIC correspond to a good fit with a relatively small number of free parameters. For each type of model we report $\Delta{\rm AIC} = {\rm AIC}_{\rm model} - {\rm AIC}_{BB}$ in Table 6, where ${\rm AIC}_{BB}$ is the AIC obtained for a fit to a single blackbody component (no atmospheric model).

We show in Figs. D.1–D.4. the corner plots retrieved by `special` for some of the models with minimum AIC values, to show the degeneracy between some parameters. When $\log(g)$ is a free parameter, an additional panel is shown for the mass posterior distribution estimated from the $\log(g)$ and $R_{\rm phot}$ posterior distributions (i.e., not a free parameter of the fit).

Inspection of Figs. 9 and D.2 and Table 6 reveal two types of models with high support. Depending on the assumed atmospheric grid, either the planet is found to have a relatively low

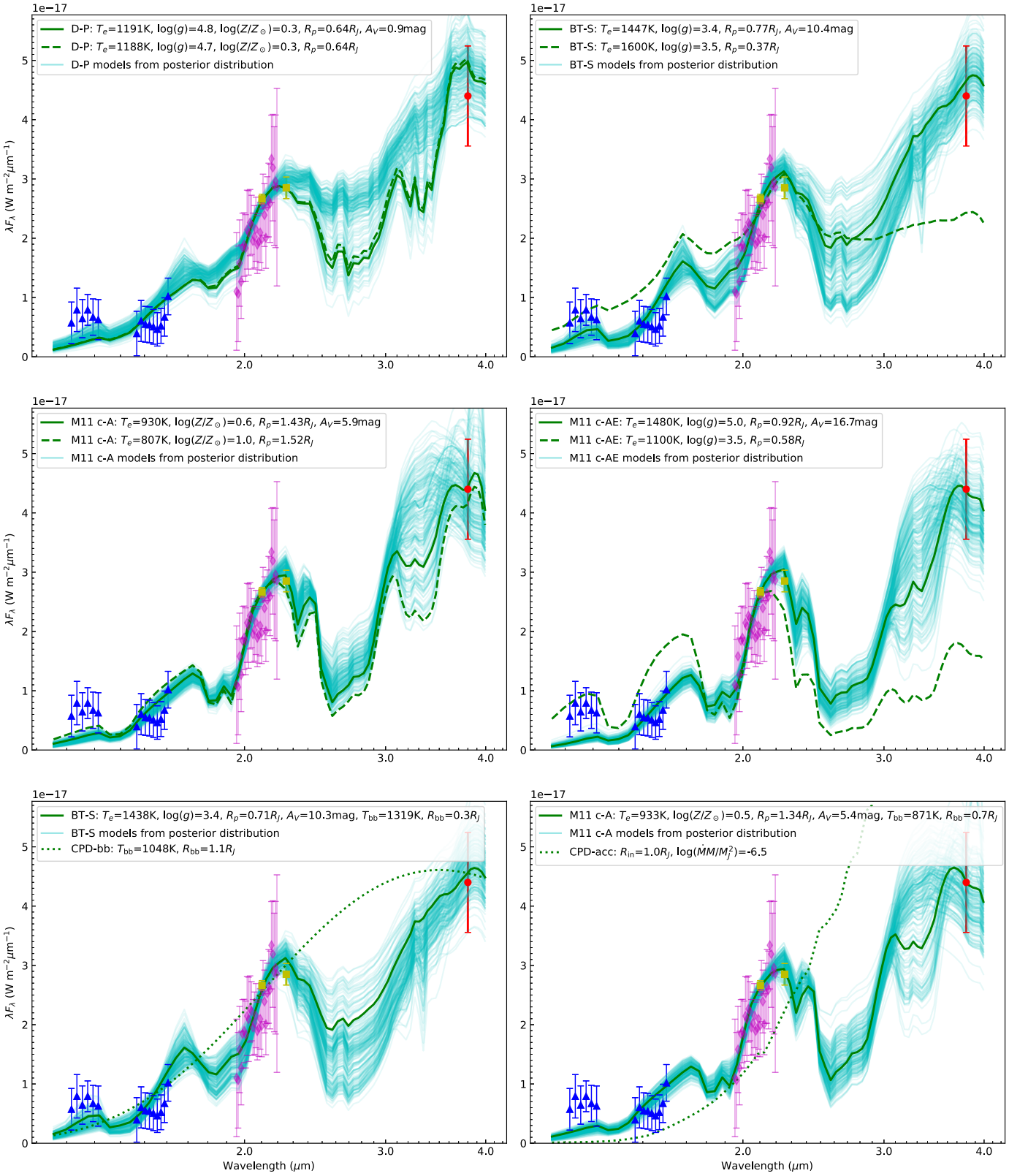

Fig. 9. Measured spectrum of HD 95086 b (see Fig. 4 for legend information) compared to the best-fit models retrieved by `specIal` for each atmospheric model grid considered in this work (*top four panels*: DRIFT-PHOENIX, BT-SETTL, M11 cloud-A, M11 cloud-AE), and for different circumplanetary disk models (*bottom two panels*). All solid lines correspond to extinction A_V considered as a free parameter, while the dashed lines correspond to a fixed extinction of A_V = 0 mag. The circumplanetary disk models consist of either mixed atmosphere (BT-SETTL or M11 c-A) + extra blackbody models (solid lines) or CPD-only models (dotted lines). The latter correspond to either a debris CPD model (*bottom left panel*) or a viscous CPD model (*bottom right panel*; Zhu et al. 2015), where the parameter log($\dot{M}M/M_J^2$) corresponds to the mass accretion rate. All types of models have a similar level of support, except for the BT-SETTL and M11 c-AE models without extinction, and the viscous CPD model (Table 6).

Table 6. Physical parameters of HD 95086 b retrieved by `special` for different atmospheric and CPD models.

Model	$T_{\rm eff}$ (K)	$\log(g)$	$R_{\rm p}$ ($R_{\rm Jup}$)	$\log(Z/Z_\odot)$	$A_{\rm V}$ (mag)	$T_{\rm bb}$ (K)	$R_{\rm bb}$ ($R_{\rm Jup}$)	M_b ($M_{\rm Jup}$)	ΔAIC [a]
Blackbody	–	–	–	–	(0)	1032^{+45}_{-45}	1.1 ± 0.2	–	0
D-P ($A_{\rm V} = 0$) [b]	1247^{+56}_{-89}	$4.71^{+0.46}_{-0.51}$	$0.61^{+0.09}_{-0.06}$	$0.3^{+0.0}_{-0.6}$	(0)	–	–	$2.9^{+7.8}_{-2.8}$	0.4
BT-SETTL ($A_{\rm V} = 0$)	1600^{+3}_{-20}	$3.50^{+0.0}_{-0.1}$	0.38 ± 0.01	(0)	(0)	–	–	$0.2^{+0.0}_{-0.0}$	52.5
M11-cA ($A_{\rm V} = 0$) [b]	808^{+43}_{-35}	(4.0)	$1.59^{+0.07}_{-0.32}$	$1.0^{+0.0}_{-0.1}$	(0)	–	–	$7.8^{+3.0}_{-1.7}$	1.9
M11-cAE ($A_{\rm V} = 0$) [b]	1101^{+7}_{-29}	3.5 ± 0.0	0.59 ± 0.02	(0)	(0)	–	–	$0.5^{+0.0}_{-0.0}$	98.9
D-P [b]	1549^{+150}_{-353}	$5.0^{+0.5}_{-0.6}$	$0.66^{+0.05}_{-0.08}$	$0.3^{+0.0}_{-0.4}$	$1.2^{+13.1}_{-1.2}$	–	–	$0.6^{+17.7}_{-0.4}$	2.4
BT-SETTL	1456^{+99}_{-91}	$3.4^{+1.6}_{-0.9}$	$0.79^{+0.11}_{-0.12}$	(0)	$11.5^{+1.7}_{-2.1}$	–	–	$0.3^{+1.7}_{-0.2}$	–0.8
M11-cA	977^{+241}_{-113}	(4.0)	$1.32^{+0.16}_{-0.31}$	$0.5^{+0.4}_{-0.3}$	$8.7^{+4.5}_{-3.5}$	–	–	$6.9^{+1.5}_{-3.5}$	–0.6
M11-cAE [b]	1383^{+223}_{-110}	$3.5^{+1.4}_{-0.0}$	0.91 ± 0.12	(0)	$16.0^{+1.7}_{-1.8}$	–	–	$1.5^{+9.5}_{-0.9}$	2.2
D-P + BB	1600^{+143}_{-271}	$5.0^{+0.5}_{-0.6}$	$0.66^{+0.05}_{-0.07}$	$0.0^{+0.3}_{-0.2}$	$1.9^{+13.1}_{-1.9}$	110^{+327}_{-9}	$0.3^{+2.4}_{-0.3}$	$0.6^{+17.5}_{-0.4}$	6.3
BT-SETTL + BB	1451^{+101}_{-86}	$3.3^{+1.7}_{-0.8}$	$0.80^{+0.09}_{-0.14}$	(0)	$10.8^{+2.4}_{-1.3}$	108^{+324}_{-8}	$0.2^{+2.6}_{-0.2}$	$0.3^{+1.8}_{-0.2}$	2.9
M11-cA + BB	979^{+276}_{-111}	(4.0)	$1.28^{+0.19}_{-0.32}$	$0.5^{+0.4}_{-0.3}$	$8.9^{+5.1}_{-3.1}$	187^{+229}_{-87}	$0.4^{+2.4}_{-0.4}$	$6.6^{+1.4}_{-3.5}$	3.2
M11-cAE + BB	1421^{+187}_{-128}	$3.6^{+1.3}_{-0.1}$	$0.87^{+0.16}_{-0.10}$	(0)	$16.1^{+1.8}_{-1.7}$	156^{+357}_{-56}	$0.4^{+2.3}_{-0.4}$	$1.5^{+9.3}_{-1.0}$	5.5

Notes. [a] ΔAIC = AIC – $\rm AIC_{bb}$. Bold font is used to highlight models with ΔAIC–$\Delta\rm AIC_{min} < 10$ (i.e., models with the most support). [b] The MCMC converged at the edge of the allowed range for at least one parameter; uncertainties are likely underestimated for all parameters of this model.

effective temperature (800–1200 K), small to medium amount of extinction ($A_{\rm V} \lesssim 10$ mag), and super-solar metallicity (DRIFT-PHOENIX and M11 forsterite cloud-A models; e.g., Figs. D.2 and D.3) or it has a higher effective temperature (1200–1600 K) and a high level of extinction by surrounding dust ($A_{\rm V} \gtrsim 10$ mag) for a solar metallicity (BT-SETTL and M11 forsterite cloud-AE models; e.g., Fig. D.1). In particular, we find that only the DRIFT-PHOENIX and M11 forsterite cloud-A models can reproduce the red slope of the spectrum when the extinction is set to $A_{\rm V} = 0$ mag (dashed lines in Fig. 9), while the BT-SETTL and M11 cloud-AE models are unable to account for the observed spectrum without extinction (ΔAIC > 10; Burnham & Anderson 2002). These two solutions can also be seen in the DRIFT-PHOENIX posterior samples (top left panel of Fig. 9) and corner plot (Fig. D.2) obtained when $A_{\rm V}$ is set as a free parameter: two clusters of solutions can be seen corresponding to low $T_{\rm eff}$, high $\log(g)$, high $\log(Z/Z_\odot)$, and low $A_{\rm V}$ on the one hand, and high $T_{\rm eff}$, unconstrained $\log(Z/Z_\odot)$, and high $A_{\rm V}$ on the other hand.

Our results suggest that a large amount of dust is present, either in the upper part of the atmosphere (super-solar metallicity; see details in Sect. 5.2) and/or around the planet (to account for the extinction). Whether circumplanetary dust could emit an additional thermal component detectable in our spectrum is further investigated in the next section.

5.1.2. Circumplanetary disk models

HD 95086 b is located between two debris disk belts. As it is one of the reddest substellar object known (De Rosa et al. 2016), and a large amount of dust appears to be necessary to account for the observed spectrum (see previous section), we also investigated the possible presence of a circumplanetary disk (CPD) signature in our spectrum. We considered two types of CPDs: a circumplanetary primary viscous disk, in which the exoplanet b still accretes material, and a circumplanetary debris disk consisting of heated grains and modeled by a blackbody component.

We used the SED predictions from the grid of accreting CPD models presented in Zhu (2015), which are characterized by two free parameters: the inner truncation radius of the CPD and the mass accretion rate, spanning 1 to 4 $R_{\rm Jup}$ and 10^{-4} to 10^{-7} $M_{\rm Jup}^2$ yr^{-1}, respectively. For debris CPDs we considered either a single blackbody component (without atmospheric model), as performed recently for PDS 70 b (Wang et al. 2020; Stolker et al. 2020a), or an additional blackbody component besides the emission from the atmosphere. We allowed the values of the blackbody temperature $T_{\rm bb}$ to range between 100 K and 2000 K and a blackbody radius between 0.1 and 10 $R_{\rm Jup}$, with the condition that $T_{\rm bb}$ is lower than or equal to $T_{\rm eq}$, where $T_{\rm eq}$ is the equilibrium temperature corresponding to a distance of $R_{\rm bb}$ (i.e., the extreme case of a spherical shell of optically thick hot dust). If the condition is not met for a particular sample, its log-likelihood is set to minus infinity.

For viscous CPD models the MCMC converged at the edge of the parameter space in terms of inner truncation radius ($1.0\ R_{\rm Jup}$) for a mass accretion rate of $\sim 10^{-6.5}$ ${M_{\rm Jup}}^2$ yr^{-1}. However, the slope of the viscous CPD models is too red to reproduce the observed spectrum on its own (dotted line in bottom right panel of Fig. 9), leading to a poor fit (ΔAIC ~ 636). This does not prevent the possibility of a combination of atmospheric and viscous CPD emission. Future measurements in the Hα filter are required to constrain the accretion rate and definitely rule out this hypothesis.

The single-blackbody model leads to a satisfactory fit for a temperature of 1032 ± 45 K and a photometric radius of $1.1 \pm 0.2\ R_{\rm Jup}$ (bottom left panel of Fig. 9 and Fig. D.1). It is one of the models that minimizes the ΔAIC. For atmospheric+debris CPD models, we find that the addition of a blackbody component can also reproduce the observed spectrum without significantly

increasing the ΔAIC value. The minor improvement for the maximum-likelihood atmospheric+debris CPD models is such that ΔAIC is still lower than 10, hence implying a similar level of support as models with fewer free parameters (see bold values of ΔAIC in Table 6), including super-solar metallicity atmosphere models. The corner plots associated with atmosphere+debris CPD models (e.g., Fig. D.4 for M11 c-A+debris CPD) show that a number of solutions correspond to negligible contribution from the additional blackbody. However, some high-likelihood solutions involve values of T_{bb} ~ 800–1300 K and R_{bb} ~ 0.3–0.7 R_{Jup} that are comparable to T_{eff} and R_{phot}, respectively. This is the case in particular for the maximum-likelihood BT-SETTL+CPD and M11c-A+CPD models, shown as a green curve in the bottom two panels of Fig. 9. Considering the blackbody temperature to be the equilibrium temperature of the dust, $T_{bb} \approx 1319$ K (resp. 871 K) for $T_{eff} \approx 1438$ K (resp. 933 K) would imply that the heated dust is located near the top of the atmosphere in either case.

5.1.3. Evolutionary models

Atmosphere modeling of exoplanets and brown dwarfs consists in describing the physical and chemical processes at play in substellar atmospheres using radiative-convective equilibrium models, which can include non-equilibrium chemistry processes, the effect of stellar irradiation, cloud formation, dust settling, and/or mixing to simulate spectra. Even so, their results must be compared to predictions of evolutionary models, which give the evolution of the internal structure of exoplanets and brown dwarfs in time, to exclude non-physical solutions. To do so, based on the apparent photometry, age, and distance of HD 95086 b, we used the Bern EXoplanet cooling tracks (BEX, Marleau et al. 2019) with the AMES-COND atmospheres (Baraffe et al. 2003), corresponding to hot or warm start initial conditions, to derive the predicted bulk properties of the planet (luminosity, mass, effective temperature, surface gravity, and radius). Following a similar approach to Delorme et al. (2017b), we compared the regime of solutions between the two atmosphere and evolutionary models for the predicted surface gravity and radius, as shown in Fig. 10. At the age of HD 95086, BEX models predict for effective temperatures between 800 and 1600 K, typical values of 1.2–1.5 R_{Jup} and $\log(g)$ between 3.6 and 4.2, with a predicted mass of 3–12 M_{Jup} for HD 95086 b.

From the best-fit solutions of the atmosphere models shown in Fig. 10 and reported in Table 6, the only model consistent with the BEX predictions is M11 with forsterite cloud-A models. The spectrum of HD 95086 b is well reproduced by a super-solar metallicity 800–1200 K atmosphere, with only a small to medium amount of additional extinction required. The atmospheric fits lead to values of radii ($1.32^{+0.16}_{-0.31}$ R_{Jup}) comparable to the physical radius predicted by the BEX models. For all other grids of models, the favored values of photometric radius (0.6–1.0 R_{Jup}) appear smaller than expected, which may either suggest that the M11 forsterite cloud-A models are the most appropriate for the case of HD 95086 b or that a fraction of the atmospheric flux is obscured by circumplanetary dust, as we discuss below.

5.2. Origin of the red spectral slope of b

5.2.1. Super-solar metallicity atmosphere

The good fit to high-metallicity atmospheric models suggests that HD 95086 b could be somewhat similar to the unusually red L dwarfs (e.g., Gizis et al. 2012; Marocco et al. 2014, and references therein). Looper et al. (2008) and Stephens et al. (2009) suggested that a high metallicity was indeed responsible for the unusually red slope of the field L dwarfs in their samples (for which a low gravity appeared unlikely). A high metallicity facilitates the production of dust grains in the atmosphere, hence clouds. To reproduce the spectrum of unusually red L dwarfs, Marocco et al. (2014) tested different extinction laws corresponding to different dust compositions, namely corundum (Al_2O_3), enstatite ($MgSiO_3$), iron, and ISM-like ($R_V = 3.1$). They found that dereddening with any of these extinction laws (including ISM) makes the spectra consistent with that of standard field L dwarfs. Their findings also corroborate our two categories of best-fit models. It appears observationally difficult from the near-infrared spectrum alone to constrain where the dust is located, either in the upper atmosphere (super-solar metallicity enhancing cloud formation) or around the planet (high circumplanetary extinction).

5.2.2. Circumplanetary disk

The first evidence for the presence of a viscous circumplanetary disk was presented in Christiaens et al. (2019) and Isella et al. (2019) for the case of protoplanet PDS 70 b. This is consistent with the estimated young age of the system (~5 Myr) and the presence of a large amount of gas in the protoplanetary disk. Since the HD 95086 system is older (~13.3 Myr), and a low amount of CO has been observed (Booth et al. 2019), the viscous disk is not favored. Our best-fit viscous CPD model also appears too red on its own to account for the observed near-infrared spectrum. Nonetheless, considering that Chinchilla et al. (2021) and Eriksson et al. (2020) find evidence for ongoing accretion onto a planetary-mass object with a main estimated age of 25 Myr and 30–40 Myr, respectively, future measurements in the Hα filter are required to constrain the accretion rate of HD 95086 b, and definitively rule out the possibility of a combined atmosphere+viscous CPD model. We note that the comparison with the studied system by Eriksson et al. (2020) could be nuanced as they studied a binary system of two M stars that could keep the gas-rich disk longer (e.g., known as the Peter Pan disks, Silverberg et al. 2020), and whose age is poorly constrained and debated. It could be younger, with a recent averaged age estimated at about 20 Myr (and an age range of 3–65 Myr, Ujjwal et al. 2020). Finally, if H-alpha measurements are necessary to measure the accretion rate, they could also be a sign of chromospheric activity as it is a common feature in late M and early L objects (Chinchilla et al. 2021).

An alternative explanation for the red slope of HD 95086 b is the presence of circumplanetary dust causing high extinction. In this scenario we can expect the dust located the closest to the planet to be heated to high enough temperatures to show a signature corresponding to an IR excess comparable to the atmospheric emission alone. We find in Sect. 5 that the addition of a second blackbody component to model a circumplanetary debris disk around HD 95086 b can also reproduce the observed spectrum with a similar level of support to models with fewer free parameters (i.e., without an extra blackbody component). In particular, the solution from the model of atmosphere M11 with cloud-A and an extra blackbody component and optical extinction A_V is consistent with predictions from evolutionary models. This model favors a super-solar metallicity ($0.5^{+0.4}_{-0.3}$) with a medium level of extinction ($A_V = 8.9^{+5.1}_{-3.1}$ mag). Hence, both a circumplanetary disk and a super-solar metallicity could account for the red spectral slope of b, and both could be present together; if there is a debris CPD, some of this debris might have been

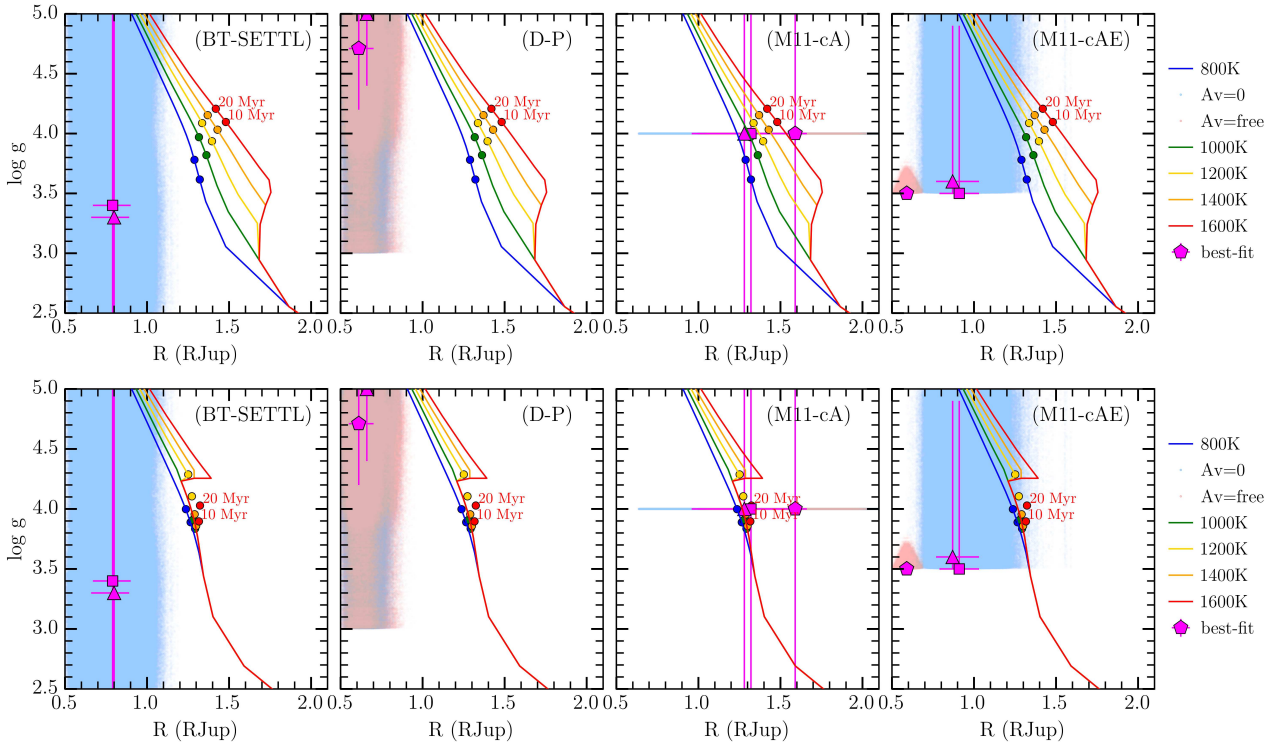

Fig. 10. Comparison of the solutions for the different models of atmosphere (*left:* BT-SETTL, *middle left:* DRIFT-PHOENIX, *middle right:* M11 cloud-A, and *right:* M11 cloud-AE) and models of evolution (*top panel*: BEX-Hot and *bottom panel:* BEX-Warm). As for the atmospheric models, the best-fit solutions are shown in pink, with a pentagon if the optical extinction $A_V = 0$, a square if the extinction is a free parameter, and a triangle if there is an additional blackbody fitted; the samples of solutions are in red if the extinction $A_V = 0$ and in blue if the extinction is a free parameter. For the evolutionary models, the solid curves represent the surface gravity as a function of the planetary radius given different effective temperature (blue for the coolest to red for the hottest). The colored circles represent the expected log g and R at a given age (10 or 20 Myr): hence lower and upper values expected for HD 95086 aged 13.3 Myr.

accreted onto the planet's atmosphere, which naturally increases the metallicity.

A small subset of the debris disk CPD solutions from models of atmosphere is expected to have a non-negligible signature at near-IR wavelengths (solutions with large T_{bb} and R_{bb} similar to R_{phot}, as shown in the bottom panels of Fig. 9). In these cases, considering the blackbody temperature to correspond to the equilibrium temperature at the separation of the dust implies that the heated dust would be located near the top of the atmosphere (within ~1 R_{Jup} distance above the atmosphere). However, since a significant fraction of posterior samples corresponds to no significant excess at near-IR wavelengths, it is also possible that only cold circumplanetary dust is present. We note that Pérez et al. (2019) used ALMA 1.3 mm observations from Su et al. (2017) to search for the presence of a circumplanetary disk around HD 95086 b, and derived an upper limit of 30 µJy at the planet location. All the models retrieved by `special` are consistent with this non-detection, being over three orders of magnitude fainter than their upper limit.

To test whether longer infrared wavelength observations may allow us to distinguish between high-metallicity cold circumplanetary dust and hot+cold circumplanetary dust, we show in Fig. 11 the predictions at longer wavelengths for the highest-likelihood models of each type. The predicted spectra for six of the most likely models are reported up to 11 µm: two models with high metallicity only and no extinction (in cyan), two models with mid to high extinction (i.e., cold circumplanetary dust), and two models with both extinction and an extra blackbody component (i.e., both hot and cold circumplanetary dust). We see that multiple accurate measurements at longer wavelengths, possibly including a spectrum, would be required to distinguish between the different scenarios since the predicted fluxes are still relatively similar for the different scenarios.

On the other hand, observations at short wavelengths in the visible and the near-infrared may also reveal the presence of a CPD. If there is a similar disk around HD 95086 b, it should be polarized, and also detectable at short wavelengths based on Mie's theory, for example by ZIMPOL and SPHERE-IRDIS in dual-polarization imaging mode (van Holstein et al. 2021). In particular, we note the excess of flux at the shorter wavelengths (below 1.4 µm), with respect to the best-fit models (within 1–2σ) in Fig. 11, which would be consistent with a debris disk. However, this CPD should be modeled with a more tuned model than the additional blackbody component used in this work to account for the observed spectrum.

Future ground-based observations with ERIS at the VLT, METIS at the ELT, and JWST in space, should soon enable us to unambiguously confirm the origin of the very red spectrum of HD 95086 b. This is indeed highlighted by synthetic observations of CPD from Szulágyi et al. (2019, for the ERIS instrument) and Chen & Szulágyi (2021, for the JWST and ELT telescopes).

6. Searching for planet c

The architecture of the young planetary system HD 95086 offers an interesting comparison case with two emblematic systems HR 8799 (Götberg et al. 2016; Su et al. 2015) and PDS 70 (Keppler et al. 2018), and more generally with the interpretation that these multiple-belt debris disks are young analogs to our

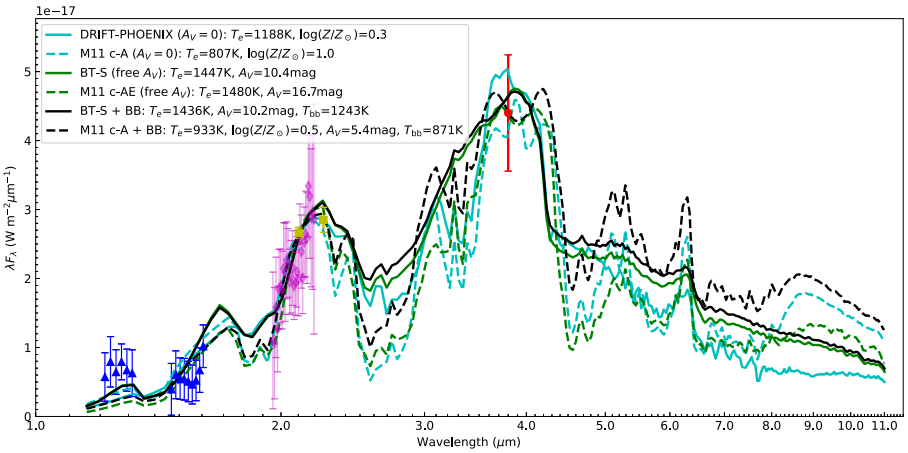

Fig. 11. Spectrum of HD 95086 b compared to the most likely models retrieved by `special` with the highest-likelihood atmospheric and CPD models, extended up to 11 µm. Cyan curves show models with high metallicity but no extinction: DRIFT-PHOENIX (solid line) and M11 cloud-A (dashed line). Green curves show models with mid to high extinction: BT-SETTL (solid line) and M11 cloud-AE (dashed line). Black curves show models with both extinction and an extra blackbody component: BT-SETTL (solid line) and M11 cloud-A (dashed line). There is no atmospheric model+viscous CPD reported here as their best model does not represent a good enough fit to the data with respect to the other models.

Solar System. The imaged giant planets would be responsible for the dynamical clearing of the debris disks and the formation of observed multiple-belt architecture, as suggested by Kennedy & Wyatt (2014) and Shannon et al. (2016). For HD 95086 the observed planet–belt architecture composed of a warm and relatively narrow inner belt at ∼8 au, a broad cavity from typically 10–100 au inside which the massive (4–5 $M_{\rm Jup}$, $a \sim 53 \pm 16$ au and $e \leq 0.17$, see Table 4) planet HD 95086 b orbits, and finally, a cold outer belt lying between 106 and 320 au, suggests that probably more than one giant planet is orbiting in this system (Su et al. 2017; Rameau et al. 2016; Chauvin et al. 2018).

Applying Eqs. (4) and (5) of Shannon et al. (2016) to the case of HD 95086 (1.6 $M_\odot$, 14.3 ± 2 Myr, cavity from 10 to 100 au), Chauvin et al. (2018) derived a minimum mass of the planets in the cavity of 0.35 $M_{\rm Jup}$ and a typical number of required planets of 2.4 (i.e., 2–3 giant planets depending on their respective separation). Comparing these results to the outcome of HARPS and SPHERE combined detection limits (up to 2017) in the context of a planet–disk coplanar configuration, they found that there might still be room for two additional stable planets c and d in the cavity in addition to b with typical masses between 0.35 $M_{\rm Jup}$ (dynamical clearing constraint) and 6 $M_{\rm Jup}$ for a semimajor axis between 10 and 30 au or 0.35 $M_{\rm Jup}$ and 5 $M_{\rm Jup}$ beyond 30 au.

Considering the most recent SPHERE multi-epoch observations (up to May 2019) and including the deepest high-contrast images obtained so far with SPHERE (in early 2018), we revisit here the search for planet c (and d) beyond the inner warm narrow belt at ∼8 au, that is beyond ∼100 mas for the HD 95086 system. We first push the current exploration of the close environment to search for c using the K-Stacker algorithm. With no clear detection, we then set new upper limits on the potential masses of inner giant planets in the system.

6.1. K-Stacker exploration

The existence of HD 95086 c has been investigated by Le Coroller et al. (2020) using the K-Stacker algorithm (Nowak et al. 2018). The code was applied to a combination of six IFS observations (median over Y-H wavelengths) obtained at different epochs (from February 2015 to May 2017). Following a similar strategy, the complete set of observations reported in Table 2 is now considered for both IFS and IRDIS. They represent a total of ten epochs between February 2015 and May 2019. Based on the detection limits achieved with SpeCal-PCAPad and SpeCal-TLOCI in the H and $K1$ bands with IFS and IRDIS, respectively (see Fig. 3), we selected the eight best ones, rejecting February 2015 and January 2016. For IFS, the choice of

Table 7. Orbital parameter ranges for the research of exoplanet c.

Orbital parameter	Interval in K range	Interval in H range	Distribution type
a (au)	[10.5, 14]	[9.5, 14]	Uniform
e	[0, 0.6]	[0, 0.6]	Uniform
$inc.$ (rad)	$[0, \pi]$	$[0, \pi]$	Uniform
Ω (rad)	$[-\pi, \pi]$	$[-\pi, \pi]$	Uniform
ω (rad)	$[-\pi, \pi]$	$[-\pi, \pi]$	Uniform
t_0 (yr)	[0, 42]	[0, 42]	Uniform
Stellar mass ($M_\odot$)	1.54	1.54	Fixed value
Star distance (pc)	86.2	86.2	Fixed value

Notes. The origin of times is set at May 5, 2015.

H band (median over the channels between 1.47 and 1.59 µm) over Y and J bands was motivated by deeper sensitivities down to masses of 2 $M_{\rm Jup}$ given the very red colors (mid-L to L/T types) expected for the detectable planets according to the SPHERE detection limits. As fixed parameters for K-Stacker, the recent *Gaia*-DR2 distance and the primary stellar mass derived in this work (see Sect. 4) were used, together with an exploration range of orbital parameters for HD 95086 c compatible with stable dynamical orbits considering the system architecture and the presence of HD 95086 b (see Table 7).

For both K-Stacker runs, IRDIS at the $K1$ band and IFS at the H band, we do not detect any clear point-source signal with a signal-to-noise ratio higher than 5, which could indicate the probable presence of a closer-in planet. Further characterization to improve the detection limits in the 100–300 mas regime using either reference differential imaging with star-hopping (Wahhaj et al. 2021) or molecular mapping techniques (Petrus et al. 2021) will be needed.

6.2. Detection probabilities

Without any clear detection of additional planets orbiting HD 95086 on individual epochs or using K-Stacker and all the best epochs available, we now explore the completeness of previous HARPS and new SPHERE observations using the pyMESS2 code (A.-M. Lagrange, priv. comm.), a Pythonized version of the MESS2 code (Lannier et al. 2017), together with the Exoplanet Detection Map Calculator (Exo-DMC Bonavita 2020)[4]. Both codes are the latest versions of the Multi-purpose Exoplanet

[4] https://github.com/mbonav/Exo_DMC

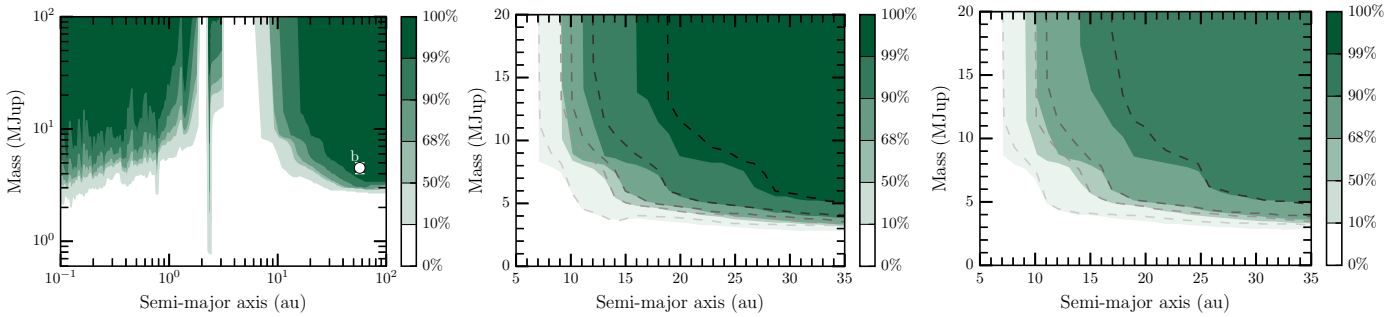

Fig. 12. Probability of companion detection as a function of the distance to the star from pyMESS2. On the *left*, overview of the detection limit results based on radial velocity (≤ 5 au) and direct imaging (all SPHERE+NaCo observations, ≥5 au) data for the whole HD 95086 system. In the *middle* and *right*, direct imaging results are zoomed between 5 and 35 au. In the *left* and *middle*, coplanarity is assumed between the researched exoplanets and the outer belt (i.e., with $i = -30 \pm 3°$ and $\Omega = 97 \pm 3°$), but not on the *right*. The results without the last five epochs imaged with SPHERE (in 2018 and 2019) are shown in gray to black contours for a given probability of 10%, 50%, 68%, 90%, and if coplanarity is assumed 99%. The color bars show the levels of probability detection.

Simulation System (MESS; Bonavita et al. 2012), a Monte Carlo tool for the statistical analysis of direct imaging survey results. In a similar fashion to its predecessors, both codes combine the information on the target stars with the instrument detection limits to estimate the probability of detection of a given synthetic planet population, ultimately generating detection probability maps.

For each star in the sample, they generate a grid of masses and physical separations of synthetic companions, then estimate the probability of detection given the provided detection limits at each epoch. The default setup uses a flat distribution in log space for both the mass and semimajor axis, but in a similar fashion to their predecessors, they allow for a high level of flexibility in terms of possible assumptions on the synthetic planet population to be used for the determination of the detection probability. For each point in the mass–semimajor axis grid, pyMESS2 and DMC generate a fixed number of sets of orbital parameters. By default all the orbital parameters are uniformly distributed except for the eccentricity, which is generated using a Gaussian eccentricity distribution with $\mu = 0$ and $\sigma = 0.3$ (constraint: $e \geq 0$), following the approach by Hogg et al. (2010) (see Bonavita et al. 2013, for details). This allows us to properly take into account the effects of projection when estimating the detection probability using the contrast limits in Fig. 3. They calculate the projected separations corresponding to each orbital set for all the values of the semimajor axis in the grid (see Bonavita et al. 2012, for a detailed description of the method used for the projection). This allows us to estimate the probability that each synthetic companion is truly in the instrument field of view and therefore that it will be detected if the value of the mass is higher than the limit. In this specific case, we chose to restrict the inclination and the longitude of the node of each orbital set to make sure that all companions in the population would lie in the same orbital plane as the disk (i.e., with $i = -30 \pm 3°$ and $\Omega = 97 \pm 3°$) for one run, and consider no a priori information on the system's orientation for a second run. We also assumed a uniform distribution for the eccentricity, with a maximum value of 0.6.

While MESS was limited in its use to direct imaging, both DMC and pyMESS2 can also be used to draw similar constraints using other kinds of datasets, including radial velocity (RV) data. Given the provided RV time series, both codes use the local power analysis (LPA) approach described by Meunier et al. (2012) to estimate, for each mass and separation in the grid, for what fraction of the generated orbital sets the signal generated by the companion would be compatible with the data. DMC at this stage is limited to an independent determination of the detection probability for each technique that is later combined. The two sets of maps are merged by considering, for each point in the grid, the best value of the probability. With pyMESS2 (and MESS2), the detection probability directly combines the detectability of each generated planet by checking if each planet can be detectable at least in one DI epoch or in the RV epochs. The probability is then derived by counting, for each [mass,a], how many of the generated planets are detected with either technique. In the end, combining the two methods allows a more accurate determination of the detection probability.

Figure 12 (left) illustrates the advantages of combining HARPS radial velocity observations with direct imaging, as shown by Chauvin et al. (2018), but here updating their results with the latest SPHERE measurements. The detection probability gain with the new SPHERE epochs is shown in the middle (coplanar case) and right (no orbital constraints) panels for the specific region of interest between 5 and 35 au, where the presence of inner giant planets is suspected. The contrast gain of about 1.0 mag at typically 100–200 mas with both IFS and IRDIS presented in Fig. 3, with the multi-epoch combination, enables us to nail down the detection probability map by a fraction of Jupiter mass and au. A further relevant gain would likely imply using alternative observing strategies, such as star-hopping (Wahhaj et al. 2021) or molecular mapping (Hoeijmakers et al. 2018; Petrus et al. 2021), before the arrival of the extremely large telescopes (Chauvin 2018).

7. Conclusion

In this work we presented and analyzed five new observations from SPHERE (2018–2019) on the young Solar System analog HD 95086, as well as a re-analysis of the five previous SPHERE observations (2015–2017), and the results from archival data from the GPI and NaCo instruments. We reported an in-depth characterization of the system HD 95086:

1. Regarding the exoplanet HD 95086 b, we extracted for the first time its spectrum in the J and *H* bands by combining six epochs imaged with SPHERE-IFS to maximize the signal-to-noise ratio of the planet as it is hardly detectable in these bands.
2. We constrained the physical properties of HD 95086 b providing spectroscopic and photometric measurements in *J*, *H*, *K*1, *K*2, and *L*′ bands from the SPHERE-IFS, GPI, SPHERE-IRDIS, and NaCo instruments. We obtained two

types of solutions: for a surface gravity log(g) between 3.3–5.0, either the exoplanet seems to have a high effective temperature between 1400–1600 K and a significant extinction ($\gtrsim$10), or lower temperatures between 800–1200 K with a small to medium level of extinction ($\lesssim$10) and a super-solar metallicity. Both of these solutions reveal the presence of significant dust, which can explain the redness of the exoplanet b. The dust could be present either in the upper layers of the atmosphere, explaining the super-solar metallicity atmosphere found for some atmospheric model best solutions, or around the exoplanet HD 95086 b with the presence of a circumplanetary disk, explaining the high extinction found for the other atmospheric models.

3. Additional modeling combining at the same time models of atmospheres and circumplanetary disks confirm the possibility of the presence of a debris circumplanetary disk around the exoplanet HD 95086 b since the solution is as likely as the other solutions found without it based on the Akaike information criterion. Considering the age of the system, the nature of this possible circumplanetary disk suggested by our modeling is more likely to be a debris disk than a viscous disk. Nevertheless, future measurements sufficiently precise in the Hα filter are required to constrain the accretion rate of HD 95086 b and rule out definitively the possibility of a viscous circumplanetary disk combined with specific atmospheric models. Other future measurements, particularly in M and N bands, are necessary to discriminate between our remaining best-fit atmospheric models.
4. We updated the orbital parameters for the exoplanet b, adding two additional monitoring years from SPHERE. Our best orbital solutions are consistent with previous published orbital parameters.
5. As for additional exoplanets in the system, we pushed the detection performance by combining the best epochs using the K-Stacker algorithm, which combines the best observations through different Keplerian motions to correct for the orbit of any additional exoplanet. We also applied several post-processing algorithms, but we did not find any robust candidates. Nonetheless, we put new constraints on the masses and locations of putative additional exoplanets in the system, and we ruled out any other 5 $M_{\rm Jup}$ inner planet in the system located at a distance greater than 17 au at a 50% confidence level (or 9 $M_{\rm Jup}$ inner planet at a distance greater than 10 au at a 50% confidence level).

Future observations with the JWST (GTO target), at the VLT/I with GRAVITY, ERIS, SPHERE and its potential upgrade, and with the first light instruments of the ELT, should enable us to understand the global architecture and origin of HD 95086, and its commonality with our own Solar System.

Acknowledgements. We would like to thank Kate Su for sharing the ALMA continuum image used in Fig. 1 together with the SPHERE-IRDIS high-contrast image at $K1$-band. We acknowledge financial support from the Programme National de Planétologie (PNP) and the Programme National de Physique Stellaire (PNPS) of CNRS-INSU. The project is supported by CNRS, by the Agence Nationale de la Recherche (ANR-14-CE33-0018). This work is partly based on data products produced at the SPHERE Data Center hosted at OSUG/IPAG, Grenoble. SPHERE is an instrument designed and built by a consortium consisting of IPAG (Grenoble, France), MPIA (Heidelberg, Germany), LAM (Marseille, France), LESIA (Paris, France), Laboratoire Lagrange (Nice, France), INAF – Osservatorio di Padova (Italy), Observatoire de Genève (Switzerland), ETH Zurich (Switzerland), NOVA (Netherlands), ONERA (France) and ASTRON (Netherlands) in collaboration with ESO. SPHERE was funded by ESO, with additional contributions from CNRS (France), MPIA (Germany), INAF (Italy), FINES (Switzerland) and NOVA (Netherlands). SPHERE also received funding from the European Commission Sixth and Seventh Framework Programmes as part of the Optical Infrared Coordination Network for Astronomy (OPTICON) under grant number RII3-Ct-2004-001566 for FP6 (2004–2008), grant number 226604 for FP7 (2009–2012) and grant number 312430 for FP7 (2013–2016). This project has received funding from the European Research Council (ERC) under the European Union's Horizon 2020 research and innovation programme (COBREX; grant agreement n° 885593). V.C. acknowledges funding from the Australian Research Council via DP180104235. A.V. and G.P.P.L.O. acknowledge funding from the European Research Council (ERC) under the European Union's Horizon 2020 research and innovation programme (grant agreement No. 757561). Finally, we would like to thank the anonymous referee and the editor for their helpful comments.

References

Akaike, H. 1974, IEEE Trans. Automat. Control, 19, 716
Allard, F. 2014, IAU Symp., 299, 271
Allard, F., Homeier, D., & Freytag, B. 2012, Philos. Trans. R. Soc. London Ser. A, 370, 2765
Amara, A., & Quanz, S. P. 2012, MNRAS, 427, 948
Bailer-Jones, C. A. L., Rybizki, J., Fouesneau, M., Mantelet, G., & Andrae, R. 2018, AJ, 156, 58
Ballering, N. P., Rieke, G. H., Su, K. Y. L., & Montiel, E. 2013, ApJ, 775, 55
Baraffe, I., Chabrier, G., Barman, T. S., Allard, F., & Hauschildt, P. H. 2003, A&A, 402, 701
Baudoz, P., Dorn, R. J., Lizon, J.-L. et al. 2010, SPIE Conf. Ser., 7735, 77355B
Beuzit, J. L., Vigan, A., Mouillet, D., et al. 2019, A&A, 631, A155
Bonavita, M. 2020, Astrophysics Source Code Library [record ascl:2010.008]
Bonavita, M., Chauvin, G., Desidera, S., et al. 2012, A&A, 537, A67
Bonavita, M., de Mooij, E. J. W., & Jayawardhana, R. 2013, PASP, 125, 849
Booth, M., Matrà, L., Su, K. Y. L., et al. 2019, MNRAS, 482, 3443
Booth, M., del Burgo, C., & Hambaryan, V. V. 2021, MNRAS, 500, 5552
Burnham, K. P., & Anderson, D. R., 2002, Information and Likelihood Theory: a Basis for Model Selection and Inference (New York, NY: Springer), 49
Cantalloube, F., Mouillet, D., Mugnier, L. M., et al. 2015, A&A, 582, A89
Cantalloube, F., Farley, O., Milli, J., et al. 2020, A&A, 638, A98
Cardelli, J. A., Clayton, G. C., & Mathis, J. S. 1989, ApJ, 345, 245
Chauvin, G. 2018, ArXiv e-prints [arXiv:1810.02031]
Chauvin, G., Lagrange, A. M., Beust, H., et al. 2012, A&A, 542, A41
Chauvin, G., Desidera, S., Lagrange, A. M., et al. 2017, in SF2A-2017: Proceedings of the Annual meeting of the French Society of Astronomy and Astrophysics, eds. C. Reylé, P. Di Matteo, F. Herpin, E. Lagadec, A. Lançon, Z. Meliani and F. Royer, 331
Chauvin, G., Gratton, R., Bonnefoy, M., et al. 2018, A&A, 617, A76
Chen, X., & Szulágyi, J. 2021, MNRAS, accepted [arXiv:2112.12821]
Chen, C. H., Pecaut, M., Mamajek, E. E., Su, K. Y. L., & Bitner, M. 2012, ApJ, 756, 133
Chen, C. H., Mittal, T., Kuchner, M., et al. 2014, ApJS, 211, 25
Chinchilla, P., Béjar, V. J. S., Lodieu, N., Zapatero Osorio, M. R., & Gauza, B. 2021, A&A, 645, A17
Christiaens, V., Cantalloube, F., Casassus, S., et al. 2019, ApJ, 877, L33
Christiaens, V., Ubeira-Gabellini, M. G., Cánovas, H., et al. 2021, MNRAS, 502, 6117
Claudi, R. U., Turatto, M., Gratton, R. G., et al. 2008, SPIE Conf. Ser., 7014
Delorme, P., Meunier, N., Albert, D., et al. 2017a, in SF2A-2017: Proceedings of the Annual meeting of the French Society of Astronomy and Astrophysics, eds. C. Reylé, P. Di Matteo, F. Herpin, E. Lagadec, A. Lançon, Z. Meliani and F. Royer, 347
Delorme, P., Schmidt, T., Bonnefoy, M., et al. 2017b, A&A, 608, A79
De Rosa, R. J., Rameau, J., Patience, J., et al. 2016, ApJ, 824, 121
Desidera, S., Chauvin, G., Bonavita, M., et al. 2021, A&A, 651, A70
Dohlen, K., Langlois, M., Saisse, M., et al. 2008, Proc. SPIE, 7014, 70143L
Eriksson, S. C., Asensio Torres, R., Janson, M., et al. 2020, A&A, 638, L6
Fedrigo, E., Donaldson, R., Soenke, C., et al. 2006, SPIE Conf. Ser., 6272, 627210
Ford, E. B. 2005, AJ, 129, 1706
Ford, E. B. 2006, ApJ, 642, 505
Foreman-Mackey, D., Hogg, D. W., Lang, D., & Goodman, J. 2013, PASP, 125, 306
Galicher, R., Rameau, J., Bonnefoy, M., et al. 2014, A&A, 565, L4
Galicher, R., Boccaletti, A., Mesa, D., et al. 2018, A&A, 615, A92
Gizis, J. E., Faherty, J. K., Liu, M. C., et al. 2012, AJ, 144, 94
Gomez Gonzalez, C. A., Wertz, O., Absil, O., et al. 2017, AJ, 154, 7
Götberg, Y., Davies, M. B., Mustill, A. J., Johansen, A., & Church, R. P. 2016, A&A, 592, A147
Greco, J. P., & Brandt, T. D. 2016, ApJ, 833, 134
Haffert, S. Y., Bohn, A. J., de Boer, J., et al. 2019, Nat. Astron., 329, 749

Hauschildt, P. H. 1992, J. Quant. Spec. Rad. Transf., 47, 433
Helling, C., & Woitke, P. 2006, A&A, 455, 325
Helling, C., Dehn, M., Woitke, P., & Hauschildt, P. H. 2008, ApJ, 675, L105
Hoeijmakers, H. J., Schwarz, H., Snellen, I. A. G., et al. 2018, A&A, 617, A144
Hogg, D. W., Myers, A. D., & Bovy, J. 2010, ApJ, 725, 2166
Hubeny, I. 1988, Comput. Phys. Commun., 52, 103
Hubeny, I., & Lanz, T. 1995, ApJ, 439, 875
Isella, A., Benisty, M., Teague, R., et al. 2019, ApJ, 879, L25
Kammerer, J., Lacour, S., Stolker, T., et al. 2021, A&A, 652, A57
Kennedy, G. M., & Wyatt, M. C. 2014, MNRAS, 444, 3164
Keppler, M., Benisty, M., Müller, A., et al. 2018, A&A, 617, A44
Kornilov, V., Tokovinin, A., Shatsky, N., et al. 2007, MNRAS, 382, 1268
Kral, Q., Matrà, L., Wyatt, M. C., & Kennedy, G. M. 2017, MNRAS, 469, 521
Lafrenière, D., Marois, C., Doyon, R., Nadeau, D., & Artigau, É. 2007, ApJ, 660, 770
Lagrange, A. M., Bonnefoy, M., Chauvin, G., et al. 2010, Science, 329, 57
Lagrange, A. M., Meunier, N., Rubini, P., et al. 2019, Nat. Astron., 3, 1135
Langlois, M., Gratton, R., Lagrange, A. M., et al. 2021, A&A, 651, A71
Lannier, J., Lagrange, A. M., Bonavita, M., et al. 2017, A&A, 603, A54
Le Coroller, H., Nowak, M., Arnold, L., et al. 2015, in Proceedings of colloquium 'Twenty years of giant exoplanets' held at Observatoire de Haute Provence, 59
Le Coroller, H., Nowak, M., Delorme, P., et al. 2020, A&A, 639, A113
Lenzen, R., Hartung, M., Brandner, W., et al. 2003, SPIE Conf. Ser., 4841, 944
Looper, D. L., Kirkpatrick, J. D., Cutri, R. M., et al. 2008, ApJ, 686, 528
Macintosh, B., Graham, J. R., Barman, T., et al. 2015, Science, 350, 64
Madhusudhan, N., Burrows, A., & Currie, T. 2011, ApJ, 737, 34
Maire, A.-L., Langlois, M., Dohlen, K., et al. 2016, SPIE Conf. Ser., 9908, 990834
Maire, A. L., Chauvin, G., Vigan, A., et al. 2021a, The Messenger, 183, 7
Maire, A.-L., Langlois, M., Delorme, P., et al. 2021b, J. Astron. Telesc. Instrum. Syst., 7, 035004
Marleau, G.-D., Coleman, G. A. L., Leleu, A., & Mordasini, C. 2019, A&A, 624, A20
Marocco, F., Day-Jones, A. C., Lucas, P. W., et al. 2014, MNRAS, 439, 372
Marois, C., Lafrenière, D., Doyon, R., Macintosh, B., & Nadeau, D. 2006, ApJ, 641, 556
Marois, C., Macintosh, B., Barman, T., et al. 2008, Science, 322, 1348
Marois, C., Zuckerman, B., Konopacky, Q. M., Macintosh, B., & Barman, T. 2010, Nature, 468, 1080
Mesa, D., Gratton, R., Zurlo, A., et al. 2015, A&A, 576, A121
Mesa, D., Keppler, M., Cantalloube, F., et al. 2019, A&A, 632, A25
Meunier, N., Lagrange, A. M., & De Bondt, K. 2012, A&A, 545, A87
Milli, J., Hibon, P., Christiaens, V., et al. 2017, A&A, 597, L2
Moór, A., Ábrahám, P., Kóspál, Á., et al. 2013, ApJ, 775, L51
Mugnier, L. M., Cornia, A., Sauvage, J.-F., et al. 2009, J. Opt. Soc. Am. A, 26, 1326
Müller, A., Keppler, M., Henning, T., et al. 2018, A&A, 617, L2
Nielsen, E. L., De Rosa, R. J., Macintosh, B., et al. 2019, AJ, 158, 13
Nowak, M., Le Coroller, H., Arnold, L., et al. 2018, A&A, 615, A144
Nowak, M., Lacour, S., Lagrange, A. M., et al. 2020, A&A, 642, L2
Olofsson, J., Samland, M., Avenhaus, H., et al. 2016, A&A, 591, A108
Pavlov, A., Möller-Nilsson, O., Feldt, M., et al. 2008, SPIE Conf. Ser., 7019, 701939
Pecaut, M. J., Mamajek, E. E., & Bubar, E. J. 2012, ApJ, 746, 154
Pérez, S., Marino, S., Casassus, S., et al. 2019, MNRAS, 488, 1005
Petit, C., Sauvage, J.-F., Fusco, T., et al. 2014, Proc. SPIE, 9148, 91480O
Petrus, S., Bonnefoy, M., Chauvin, G., et al. 2021, A&A, 648, A59
Racine, R., Walker, G. A. H., Nadeau, D., Doyon, R., & Marois, C. 1999, PASP, 111, 587
Rameau, J., Chauvin, G., Lagrange, A. M., et al. 2013a, ApJ, 772, L15
Rameau, J., Chauvin, G., Lagrange, A. M., et al. 2013b, A&A, 553, A60
Rameau, J., Nielsen, E. L., De Rosa, R. J., et al. 2016, ApJ, 822, L29
Rousset, G., Lacombe, F., Puget, P., et al. 2003, SPIE Conf. Ser., 4839, 140
Shannon, A., Bonsor, A., Kral, Q., & Matthews, E. 2016, MNRAS, 462, L116
Silverberg, S. M., Wisniewski, J. P., Kuchner, M. J., et al. 2020, ApJ, 890, 106
Soummer, R., Pueyo, L., & Larkin, J. 2012, ApJ, 755, L28
Sparks, W. B., Ford, H. C., Krist, J., Clampin, M., & Golimowski, D. 2002, AAS Meeting Abs., 201, 21.03
Stephens, D. C., Leggett, S. K., Cushing, M. C., et al. 2009, ApJ, 702, 154
Stolker, T., Marleau, G. D., Cugno, G., et al. 2020a, A&A, 644, A13
Stolker, T., Quanz, S. P., Todorov, K. O., et al. 2020b, A&A, 635, A182
Su, K. Y. L., Morrison, S., Malhotra, R., et al. 2015, ApJ, 799, 146
Su, K. Y. L., MacGregor, M. A., Booth, M., et al. 2017, AJ, 154, 225
Swastik, C., Banyal, R. K., Narang, M. et al. 2021, AJ, 161, 114
Szulágyi, J., Dullemond, C. P., Pohl, A., & Quanz, S. P. 2019, MNRAS, 487, 1248
Ujjwal, K., Kartha, S. S., Mathew, B., Manoj, P., & Narang, M. 2020, AJ, 159, 166
van Holstein, R. G., Stolker, T., Jensen-Clem, R., et al. 2021, A&A, 647, A21
Vigan, A., Moutou, C., Langlois, M., et al. 2010, MNRAS, 407, 71
Vigan, A., Fontanive, C., Meyer, M., et al. 2021, A&A, 651, A72
Wahhaj, Z., Milli, J., Romero, C., et al. 2021, A&A, 648, A26
Wang, J. J., Ginzburg, S., Ren, B., et al. 2020, AJ, 159, 263
Wang, J. J., Vigan, A., Lacour, S., et al. 2021, AJ, 161, 148
Woitke, P., & Helling, C. 2003, A&A, 399, 297
Woitke, P., & Helling, C. 2004, A&A, 414, 335
Zapata, L. A., Ho, P. T. P., & Rodríguez, L. F. 2018, MNRAS, 476, 5382
Zhu, Z. 2015, ApJ, 799, 16
Zhu, Z., Dong, R., Stone, J. M., & Rafikov, R. R. 2015, ApJ, 813, 88

[1] Univ. Grenoble Alpes, CNRS, IPAG, 38000 Grenoble, France
e-mail: celia.desgrange@univ-grenoble-alpes.fr
[2] Max Planck Institute for Astronomy, Königstuhl 17, 69117 Heidelberg, Germany
[3] Unidad Mixta Internacional Franco-Chilena de Astronomía, CNRS/INSU UMI 3386 and Departamento de Astronomía, Universidad de Chile, Casilla 36-D, Santiago, Chile
[4] Space sciences, Technologies and Astrophysics Research (STAR) Institute, Université de Liège, 19 Allée du Six Août, 4000 Liège, Belgium
[5] Aix Marseille Univ, CNRS, CNES, LAM, Marseille, France
[6] Univ. Paris-Saclay, ENS de Paris-Saclay, Paris-Saclay, France
[7] Pixyl, 5 Avenue du Grand Sablon, 38700 La Tronche, France
[8] Academia Sinica Institute of Astronomy and Astrophysics, 11F Astronomy-Mathematics Building, NTU/AS campus, No. 1, Section 4, Roosevelt Rd., Taipei 10617, Taiwan
[9] School of Physical Sciences, The Open University, Walton Hall, Milton Keynes MK7 6AA, UK
[10] INAF – Osservatorio Astronomico di Padova, Vicolo dell' Osservatorio 5, 35122 Padova, Italy
[11] LESIA, Observatoire de Paris, Université PSL, CNRS, Sorbonne Université, Université de Paris, 5 place Jules Janssen, 92195 Meudon, France
[12] CRAL, UMR 5574, CNRS, Université de Lyon, École Normale Supérieure de Lyon, 46 Allée d'Italie, 69364 Lyon Cedex 07, France
[13] Institute for Particle Physics and Astrophysics, ETH Zürich, Wolfgang-Pauli-Strasse 27, 8093, Zürich, Switzerland
[14] Institute of Astronomy, University of Cambridge, Madingley Road, Cambridge CB3 0HA, UK
[15] Cornell Center for Astrophysics and Planetary Science, Department of Astronomy, Cornell University, Ithaca, NY 14853, USA
[16] Institutionen för astronomi, Stockholms Universitet, Stockholm, Sweden
[17] European Southern Observatory, Alonso de Cordova 3107, Casilla 19001, Vitacura, Santiago, Chile
[18] SUPA, Institute for Astronomy, University of Edinburgh, Blackford Hill, Edinburgh EH9 3HJ, UK
[19] Centre for Exoplanet Science, University of Edinburgh, Edinburgh, UK
[20] DOTA, ONERA, Université Paris Saclay, 91123 Palaiseau, France
[21] Geneva Observatory, University of Geneva, 51 ch. Pegasi, 1290 Versoix, Switzerland
[22] Dipartimento di Fisica a Astronomia "G. Galilei", Università di Padova, Via Marzolo, 8, 35121 Padova, Italy
[23] Université Côte d'Azur, Observatoire de la Côte d'Azur, CNRS, Laboratoire Lagrange, Bd de l'Observatoire, CS 34229, 06304 Nice cedex 4, France
[24] INAF – Osservatorio Astrofisico di Catania, via Santa Sofia, 78 Catania, Italy
[25] European Southern Observatory (ESO), Karl-Schwarzschild-Str. 2, 85748 Garching, Germany
[26] Jet Propulsion Laboratory, California Institute of Technology, 4800 Oak Grove Drive, Pasadena, CA 91109, USA
[27] Núcleo de Astronomía, Facultad de Ingeniería y Ciencias, Universidad Diego Portales, Av. Ejercito 441, Santiago, Chile
[28] Escuela de Ingeniería Industrial, Facultad de Ingeniería y Ciencias, Universidad Diego Portales, Av. Ejercito 441, Santiago, Chile

Appendix A: Observational conditions

Figure A.1 shows the observation conditions for all the available SPHERE epochs used.

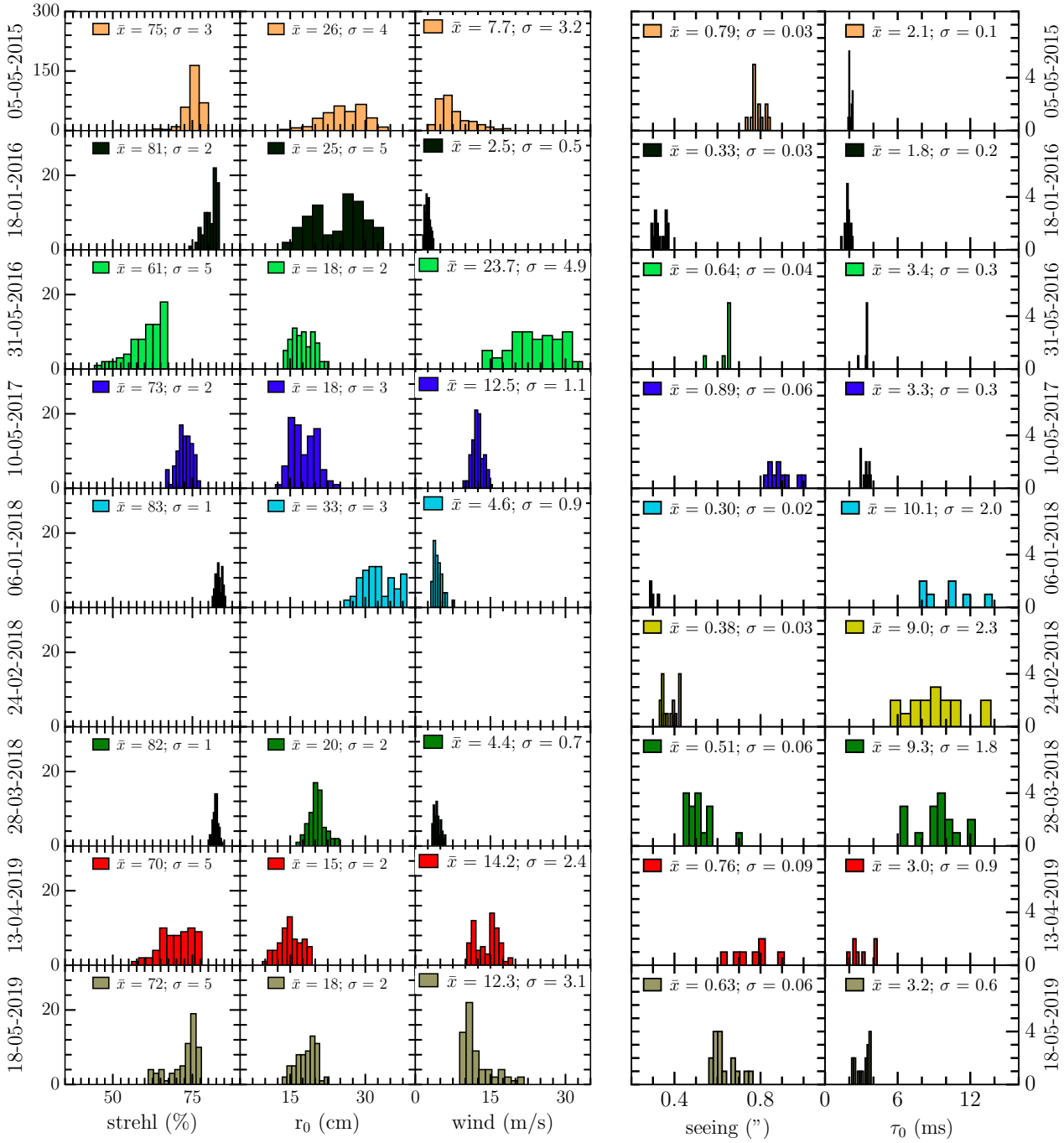

Fig. A.1. Distribution of the observational conditions (when available) for all the epochs: Strehl ratio, atmospheric coherence length r_0, wind, seeing, and atmospheric coherence time τ_0. The Strehl ratio, atmospheric coherence length, and wind were all measured by SPARTA, the computer of the adaptive system of SPHERE, while both the seeing and atmospheric coherence time were measured by the DIMM telescope at Paranal. A wind ≤ 3 m $\cdot$ s^{-1} indicates the presence of low wind effect (Milli et al. 2017), while a coherence time ≤ 3 ms indicates the presence of wind-driven halo (Cantalloube et al. 2020).

Appendix B: Reduced images with SpeCal

Figure B.1 shows the images reduced with the pipelines SpeCal-TLOCI and SpeCal-PCAPad for the IRDIS and IFS data, respectively.

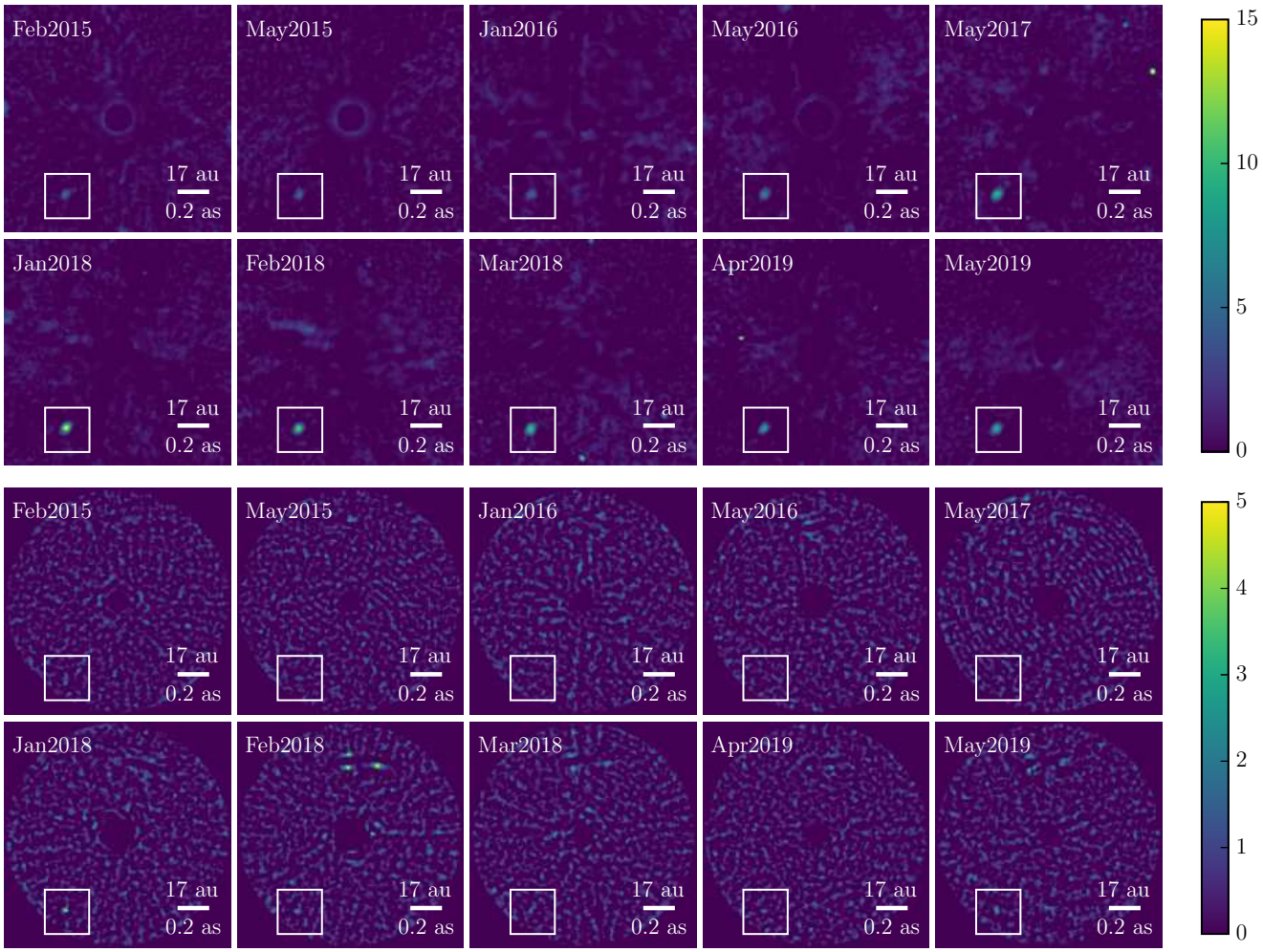

Fig. B.1. Signal-to-noise ratio maps for all the SPHERE epochs (*top*: IRDIS in the K1 band reduced by the pipeline SpeCal-TLOCI, and *bottom*: IFS in the YJH bands) reduced by the pipeline SpeCal-PCAPad (PCA ADI+SDI). The color bar corresponds to the signal-to-noise ratio. The region below the inner working angle of the coronagraph is masked.

Appendix C: Spectral correlation matrix

Figure C.1 shows the spectral correlation matrix (ϕ) empirically estimated from our IFS datasets, as in Greco & Brandt (2016) and De Rosa et al. (2016). The spectral covariance matrix C used for spectral fits is obtained as $C_{ij} = \phi_{ij}\sigma_i\sigma_j$, where σ_i and σ_j correspond to the reported uncertainties in flux measurements for points i and j.

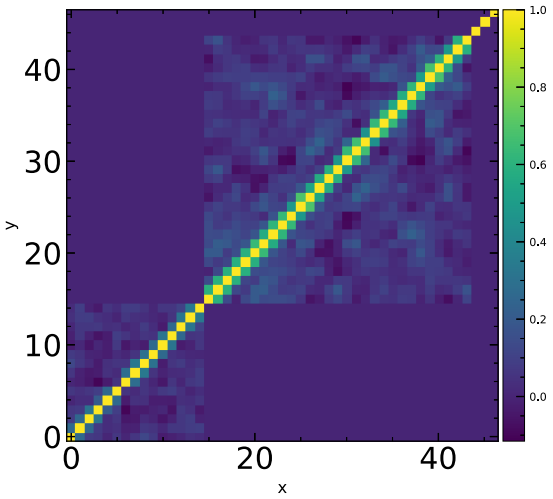

Fig. C.1. Spectral correlation matrix computed from our SPHERE/IFS (first 15 points) and GPI/IFS (points 15–43) data. For IRDIS and NACO, $C_{ij} = \delta_{ij}$, where δ_{ij} is the Kroenecker symbol.

Appendix D: Corner plots of the posteriors of the atmospheric models

In this appendix we show the posteriors of the atmospheric models retrieved by `specIal` for some of the best models at reproducing the observed spectrum: the single-blackbody model and the BT-SETTL model with free extinction (both in Fig. D.1); the DRIFT-PHOENIX model with free extinction (Fig. D.2); and the M11 cloud-A model with free extinction, without and with an extra blackbody component (Figs. D.3 and D.4, respectively). In each case the mass is not a free parameter of the fit, but is calculated from the $\log(g)$ and R_p posterior distributions.

We note that in Eq. (2), which represents the log-likelihood expression provided to the sampler, in addition to the spectral covariance matrix, additional weighting coefficients are used. These coefficients can account for the fact that absolute flux calibration is performed instrument per instrument (i.e., it is not specific to each spectroscopic point), whose individual uncertainties and covariances are not properly accounted for in the fit. In the hypothetical case where the uncertainty on absolute flux calibration is the same for the spectrograph and the photometers involved in acquiring the combined spectrum, but dominates over individual statistical uncertainties, the absence of additional weights would typically pin the absolute flux calibration to that of the spectrograph, given the significantly larger number of data points.

This absolute flux calibration uncertainty can be difficult to assess. It was noted when comparing Spitzer/IRS versus Spitzer/MIPS measurements, a case for which the use of additional weights was suggested (e.g., Ballering et al. 2013; Chen et al. 2014). However, it is known to still be an issue when comparing measurements obtained by the latest generation of high-contrast imagers. The amplitude of the systematic bias between the overlapping SPHERE and GPI spectra of HD 206893 B is on the same order as the total estimated (statistical+systematic) uncertainties (Kammerer et al. 2021). This kind of bias has also been noted when comparing the spectrum of PDS 70 b obtained by SINFONI and SPHERE (Christiaens et al. 2019).

Assigning weights such that their sum is 1 for all measurements obtained by a given instrument (i.e., 1 per photometric measurement and 1/N_spec for each spectrograph measurement, where N_spec is the number of channels) would correspond to assigning the same level of confidence for the absolute flux calibration of each instrument. However, this would too severely undermine the significance of the spectroscopic data in the fit. It would indeed make all measurements of a given spectrograph as significant as a single photometric measurement, while spectrographs provide more than just an absolute flux measurement; they also provide information about the shape of the spectrum.

Therefore, as a compromise we opted for weights that are proportional to the spectral bandwidth, as in Ballering et al. (2013) and Olofsson et al. (2016). Some estimated model parameters are dependent on the absolute flux calibration (e.g., photometric radius), on the features, and/or shape of the spectrum (e.g., surface gravity), or on both together (effective temperature and extinction). Therefore, a certain choice of weights may in principle change the estimated best-fit parameters.

To test in practice the effect of the additional weighting coefficients on the fits to the HD 95086 b spectrum, we show in Figs. D.4 and D.5 the best-fit solutions obtained with and without the additional weighting coefficients, respectively. The best-fit parameters show only minor differences, which may have been expected given the good match between most near-IR spectroscopic and photometric points of HD 95086 b (Fig. 4). The largest relative differences correspond to the estimated radius and mass of the planet, although all parameters still remain within the 1σ error bars of the estimates obtained with and without weights.

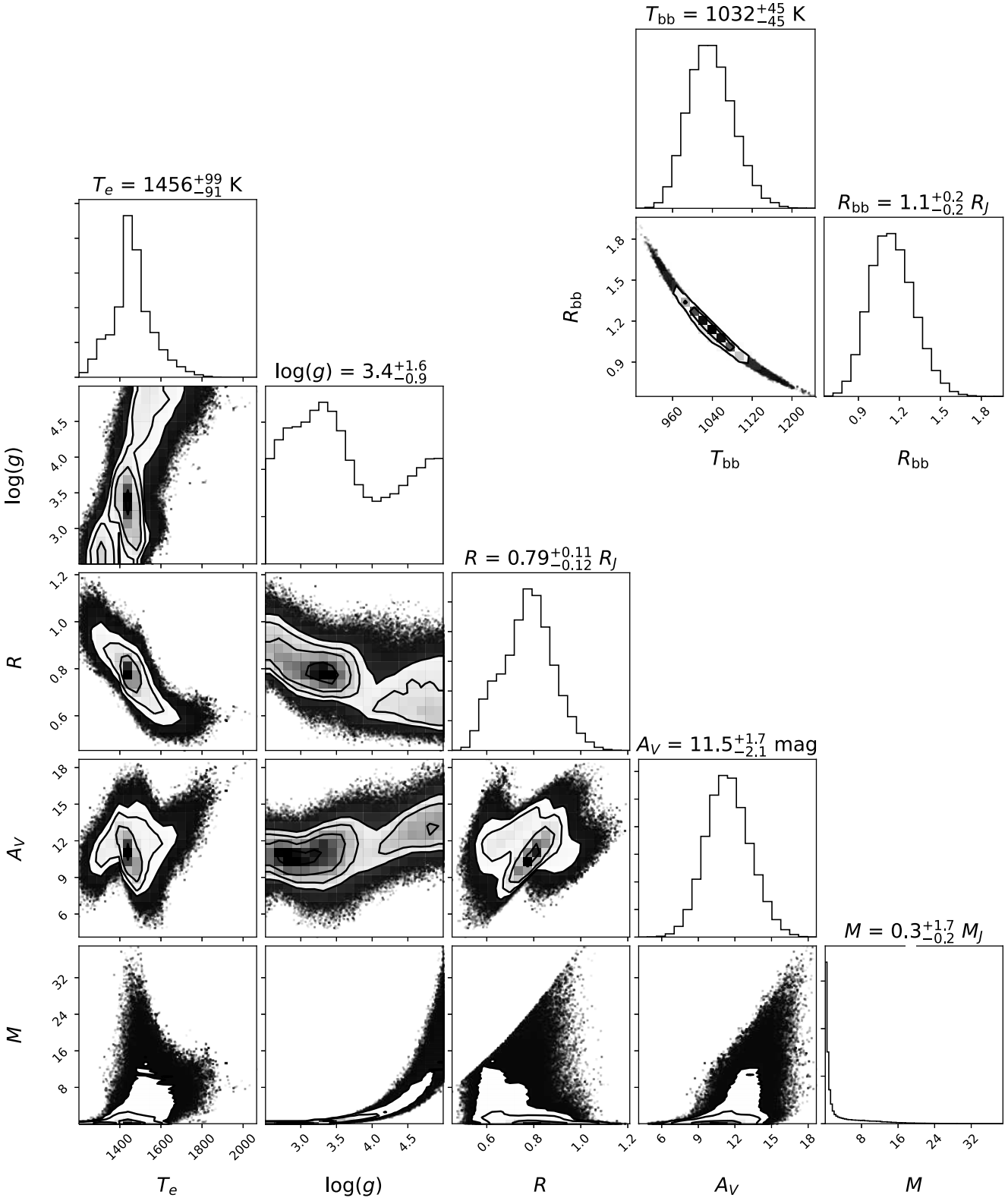

Fig. D.1. Corner plots retrieved by `special` for the single-blackbody model at the *top right*, BT-SETTL with free extinction A_V model at the *bottom left*.

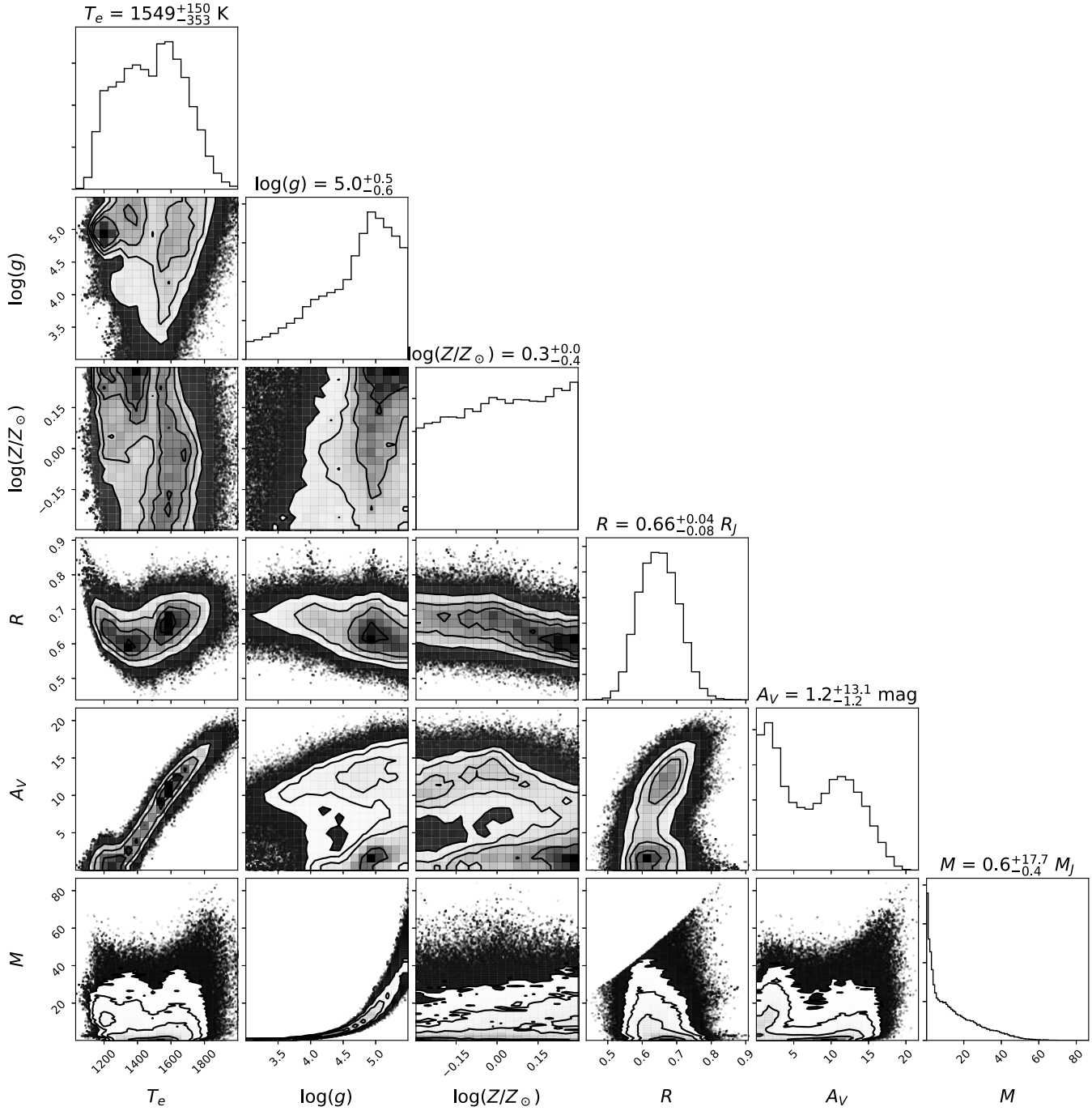

Fig. D.2. Corner plot retrieved by `special` for the DRIFT-PHOENIX model with free extinction A_V.

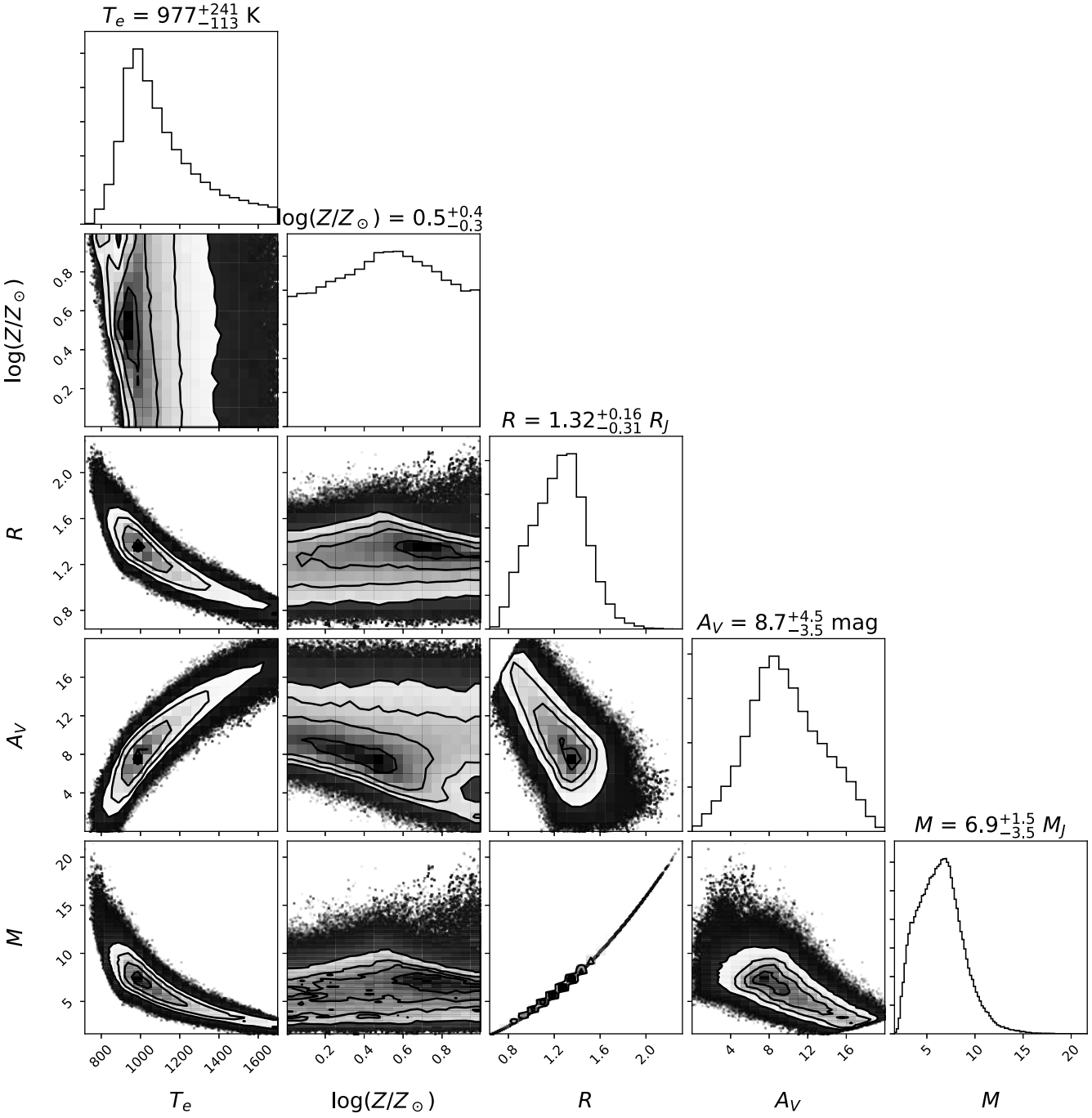

Fig. D.3. Corner plot retrieved by `specIal` for the M11 cloud-A model with free extinction A_V.

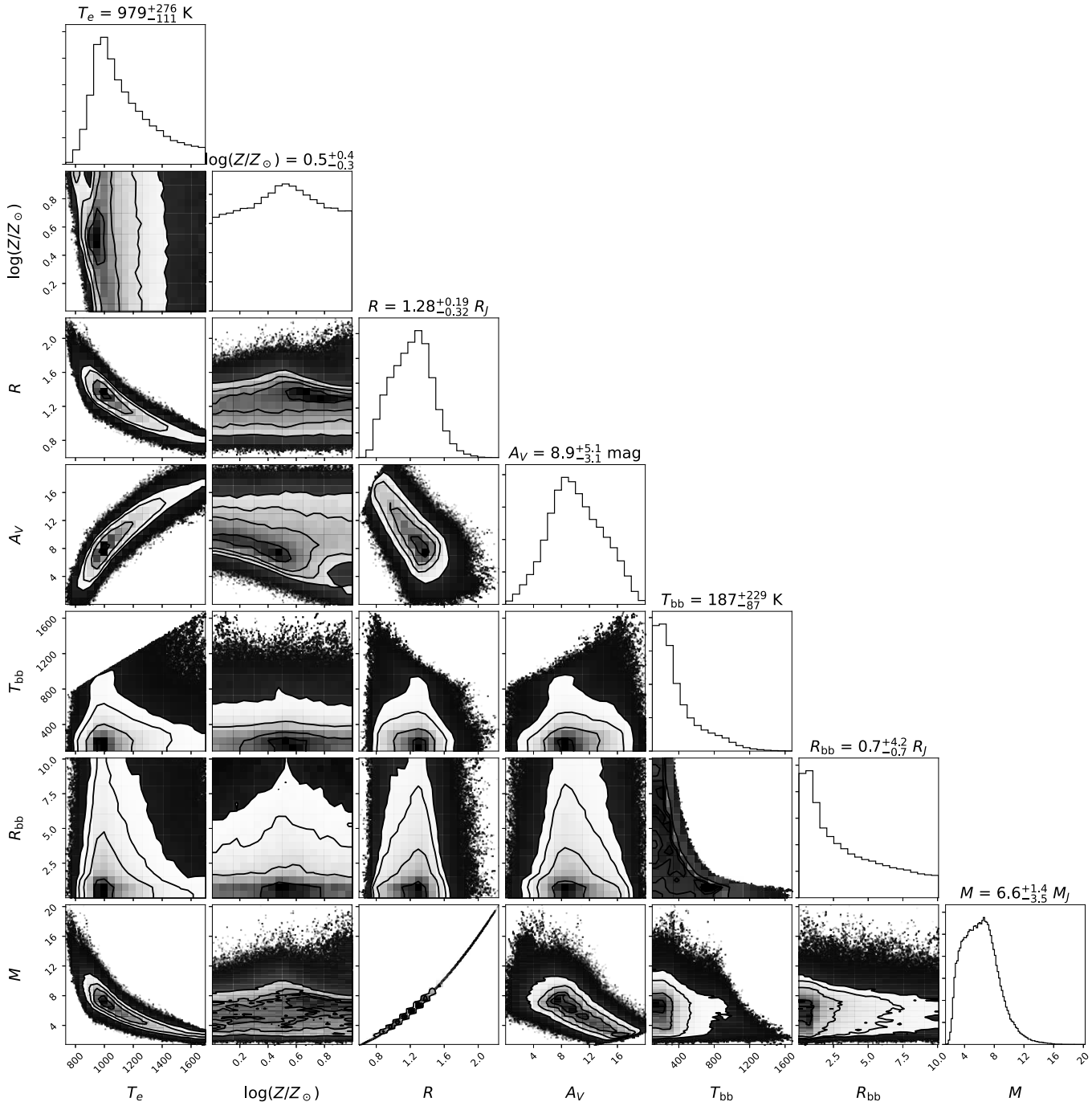

Fig. D.4. Corner plot retrieved by `specal` for the M11 cloud-A model with free extinction A_V and with an extra blackbody component.

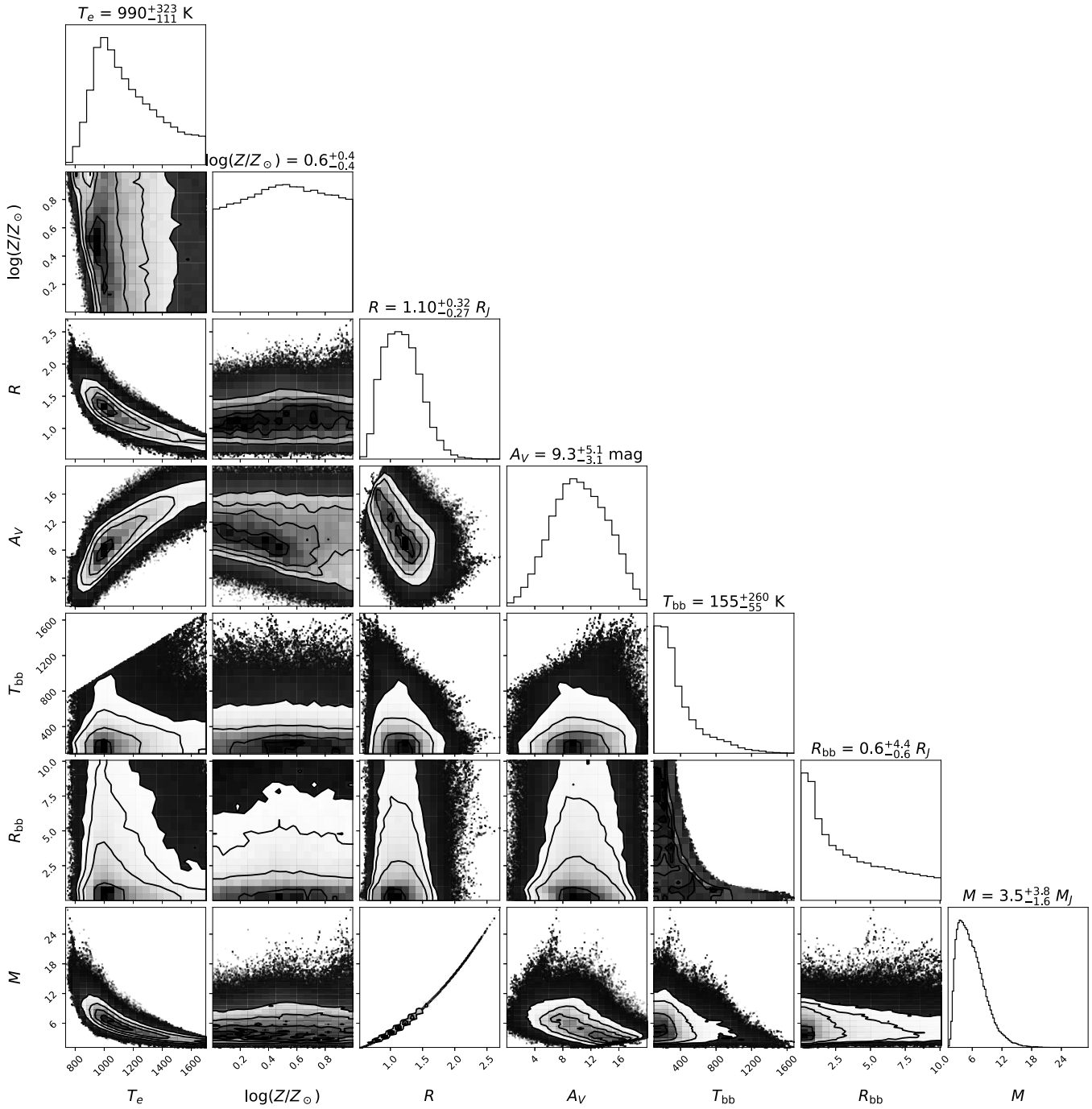

Fig. D.5. Corner plot retrieved by `special` for the M11 cloud-A model with free extinction A_V and with an extra blackbody component without additional weighting coefficients.

4.2.2 Main results

In Desgrange et al. (2022a), my collaborators and I showed that the under-luminosity and redness of the young giant exoplanet HD 95086 b (see Fig. 8 from Desgrange et al., 2022a) could be either caused by the presence of a second-generation circumplanetary disk around the planet, or dust in the upper layers of the atmosphere. Both solutions are indistinguishable (Table 6, Fig. 11 from the paper[3]) from our modeling of the spectoscopic and photometric data.

These data correspond to my extraction of the spectoscopic and photometric measurements of SPHERE, including the first-time extracted JH spectrum of b (Fig. 5), and coupled to GPI and NaCo archive data (Fig. 4). This was challenging to extract the JH spectrum of the planet b, because it is very faint. I had to couple the best epochs of observation to do so, by correcting from the orbital motion. I also tried in the Y band to extract the low-resolution spectrum, but did not consider this region of the SPHERE/IFS spectum eventually, because the combined-epoch data are not sensitive enough in this band.

The data modeling consists in fitting atmospheric models with different configurations: all were fit either with an extinction A_V set to zero or free, some of the atmospheric models providing also a constraint on the metallicity, with or without a blackbody component to mimic a second-generation CPD. My collaborators and I identified two possible scenarios to explain the atmosphere of HD 95086 b: either an atmosphere with a high effective temperature (> 1400 K) and a high-extinction ($A_V > 10$), or a colder effective temperature (800–1 300 K) with an extra-solar metallicity, see Table 6. We point out that future observations with the *JWST* and the ELT should unambiguously discriminate between both scenarios.

One classical issue while modeling atmospheres of exoplanets, is obtaining inconsistent physical parameters (e.g., the surface of gravity and the radius of exoplanet) with what is predicted based on evolutionary models. I showed that among the different atmospheric grids fitting well our data, the only ones that are consistent with evolutionary models are the grids from Madhusudhan et al. (2011), with fosterite cloud-A models (Fig. 10). These models favor the atmosphere with the lower effective temperature solution (800–1 200 K at 1σ).

As for orbital properties, we spanned the orbital coverage from 2012–2017 to 2012–2019, and in particular by adding more accurate astrometric measurements. We confirmed that HD 95086 b, has a low-eccenticity with a higher confidence (at 1σ, ≤ 0.18 instead of ≤ 0.5 from Chauvin et al., 2018), and a semi-major axis of 51–73 au (Table 4 and Fig. 6). Hence, the planet b is likely carving the inner edge of the outer belt, but could not maintain the wide cavity by itself.

Last but not least, I provided constraints on the presence of additional companions in the system. In coplanar configuration, I ruled out at a 90% confidence level exoplanets above 9 M_{Jup} at semi-major axis between 13 and 20 au, and above 5 M_{Jup} beyond 20 au.

4.3 Perspectives

In the course of this work, we had a promising 5σ detection of a point-like source at a projected separation of 168 ± 6 mas (~ 14 au), by collaborating with Olivier Flasseur (@CRAL). We only detected this candidate in the best epoch of observation (January 2018) with the cutting-edge post-processing PACO (see Fig. 4.1) and at a lower S/N with ANDROMEDA (see Fig. 2 from Desgrange et al., 2022a). Still, this detection motivated the writing of a ESO DDT (PI: Gaël Chauvin, cycle P106), to confirm this exoplanet candidate c in HD 95086. To

[3] All the references to Figures and Tables in this Section is from the paper Desgrange et al. (2022a), which is added in the previous Section 4.2.1.

maximize our chances of success to confirm it, we asked for exquisite conditions of observation (i.e., turbulence category of 10%, with a seeing inferior to $0.5''$ and a coherence time of the AO system superior to 5.2 ms) and the star-hopping strategy of observation, at that time only recently offered on SPHERE. Coupling the RDI to ADI and SDI techniques would boost the SPHERE performances at 100–300 mas.

The DDT was accepted, and the observations were acquired in 2021-03-10 and 2022-02-26. We had two epochs, because the requirements regarding the conditions of observation were not met the first time. A fast processing of the data did not recover the promising detection of the exoplanet candidate c. Currently, between April and September 2024, with Gaël Chauvin and Valentina D'Orazi (@Rome University), I am co-supervising a Master student, Macarena Vega, who works on a more fine-tuned processing and analysis of these star-hopping observations.

Figure 4.1 shows the architecture of the multi-belt planetary system HD 95086, as we understand it when we published Desgrange et al. (2022a), and what I see as future directions to constrain more the system. Regarding the additional planets, one hot question will be which facility will discover the exoplanet c: the current VLT/SPHERE observations, or its upgrade VLT/SPHERE+, the upgrade VLTI/GRAVITY+, instruments on the ELT (HARMONI, METIS, MICADO), or space-based facilities, such as *JWST*/NIRISS/AMI or the *RST*/CGI. Bets are opened. Moreover, additional planets could be discovered in the system, as for instance rocky planets between the star and the inner belt, confirming HD 95086 as a massive Solar System analog, or potentially icy exoplanets located beyond the outer belt (e.g., with the *JWST*).

As for the known HD 95086 b, other orbital and spectroscopic studies are ongoing or planned. For instance, I collaborated with Gilles Otten (@Taïwan), who have been working on GRAVITY data on this exoplanet. He extracted and analysed the medium-resolution GRAVITY spectrum in the K band, and derived with high accuracy the astrometry of the planet. In July 2022, during the In Spirit of Lyot conference, in Leiden in the Neverthelands, I presented a poster showing my orbital and spectroscopic results based on SPHERE, along to the work in progress of Gilles, see Fig. 4.2. The GRAVITY astrometry falls on the best orbital solutions obtained in Desgrange et al. (2022a), and new orbital analysis include the GRAVITY data, offer consistent orbital parameters, in particular with smaller uncertainties on the eccentricity (≤ 0.13 instead of < 0.18). Since then, new GRAVITY observations occured on HD 95086 b, that would certainly result in a publication at some point.

Regarding the double-belt architecture, up to 2023, only the outer belt has been detected and published, based on ALMA data. Very recently, work from Mathilde Mâlin (@STScI) shows that the inner belt, previously inferred from the SED modeling, is now also imaged with *JWST*/MIRI (Mâlin et al., 2024), similarly to the inner belt of HR 8799 (Boccaletti et al., 2024). Another very exciting result is that the new modeling of the atmosphere of HD 95086 b with the *JWST*/MIRI photometric points, seems to confirm that the exoplanet b has a low effective temperature with a super-solar metallicity.

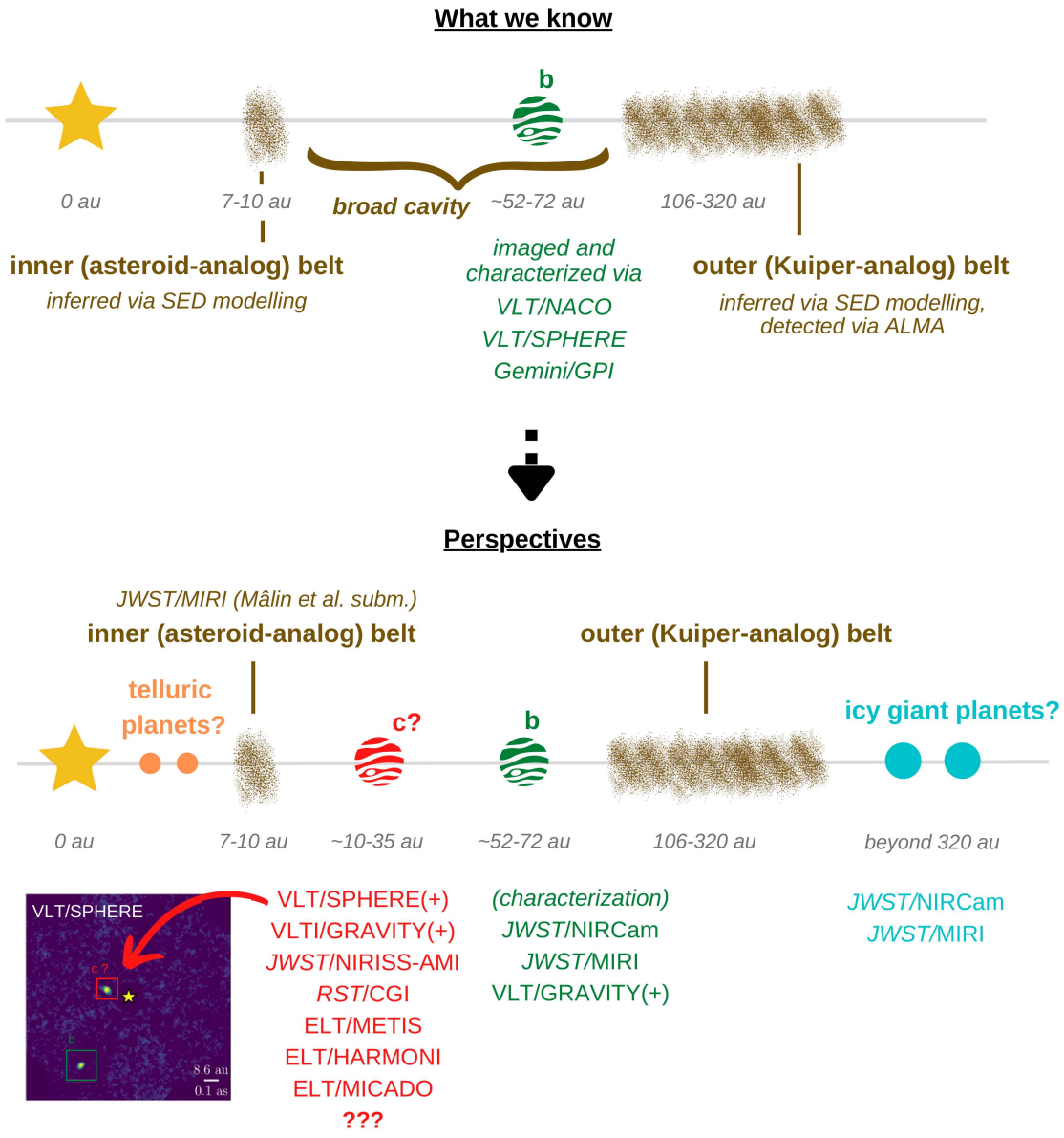

Figure 4.1: Architecture of the planetary multi-belt system HD 95086 as we know it (*top*), and example of what it could be, with in highlight telescopes and instruments which could make major discoveries (*bottom*). The inserted image shows the planetary candidate c, located at a projected separation of $168pm6$ mas ($\sim$ 14 au) to its host star, and that we detected by post-processing the best epoch of observation with PACO.

In-depth direct imaging and spectroscopic characterization of the young Solar System analog HD 95086

Célia Desgrange, Gilles Otten, Gaël Chauvin, Valentin Christiaens, Faustine Cantalloube,
SPHERE Consortium, ExoGRAVITY and GRAVITY Collaborations.
contact: celia.desgrange@univ-grenoble-alpes.fr

The system HD 95086

In this poster, we present our results on HD 95086 obtained with SPHERE and published in A&A (Desgrange+2022). We confront them with ongoing work on GRAVITY (Otten+, in prep).

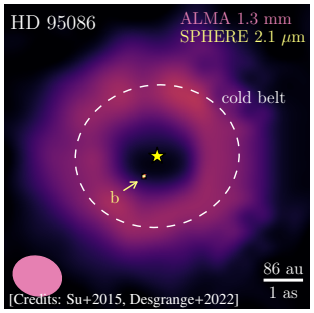

The HD 95086 exoplanetary system

Star	
Spectral type	A
Teff (K)	7750 ± 250
log(g) (dex)	4.0 ± 0.5
Distance (pc)	86.2 ± 0.3
Age (Myr)	$13.3^{+1.1}_{-0.6}$
Mass ($M_\odot$)	1.6 ± 0.1
Luminosity ($L_\odot$)	5.7 ± 1.7
Metallicity [Fe/H]	0.25 ± 0.5

Debris disk

– Warm belt

Location (au)	7 – 10
Temperature (K)	187 ± 26

– Cold belt

Location (au)	106 – 320
Temperature (K)	57 ± 2
Inclination (°)	30 ± 3
Position Angle (°)	97 ± 3

– Stellar halo (?)

Location (au)	300 – 800

HD 95086 b

Spectral type	L6 ± 1
Teff (K)	800 – 1300 K
log(g) (dex)	$\lesssim 4.5$
Mass (M_{Jup})	4 – 5

(from Rameau+2013a; Su+2015,2017; De Rosa+2016; Chauvin+2018; Bailer-Jones+2018; Booth+2021; Swastik+2021)

Observations & data processing

We used **10 observations from SPHERE-IRDIS (K12 band) and SPHERE-IFS (YJH)**. Data processing was performed by the SPHERE Data Center (Delorme+2017) and post-processing with ANDROMEDA (Cantalloube+2015) and SpeCal (Galicher+2018) pipelines. As the exoplanet b is hardly detectable in YJH ($S/N = 4.3$), we corrected the epochs from the orbital movement of the planet and stacked them to **extract for the first time the spectrum of b in JH**.

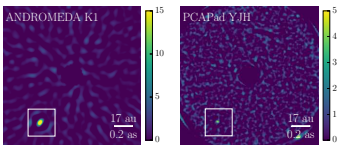

Atmospheric properties

From Galicher+2014, De Rosa+2016, and Chauvin+2018, **the exoplanet HD 95086 b**:

- falls at the **late-L to L/T transition**
- is **under-luminous** compared to the field dwarfs of similar spectral types
- is **red**

We investigated the origin of the red spectral slope in the spectrum of the HD 95086 b. by using atmospheric grids and circumplanetary disk models. We considered two types of CPDs: a "primordial" CPD, in which the exoplanet b still accretes material (models from Zhu+2015), and "debris" consisting of heated grains and modeled by a blackbody component. **We found the redness of the exoplanet HD 95086 b could be explained by a super-solar metallicity atmosphere or a circumplanetary disk.**

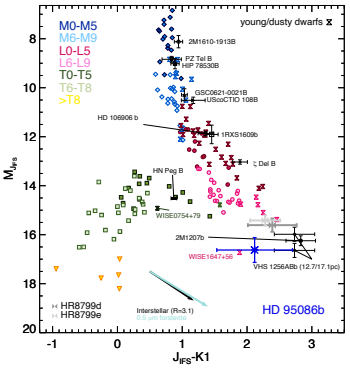

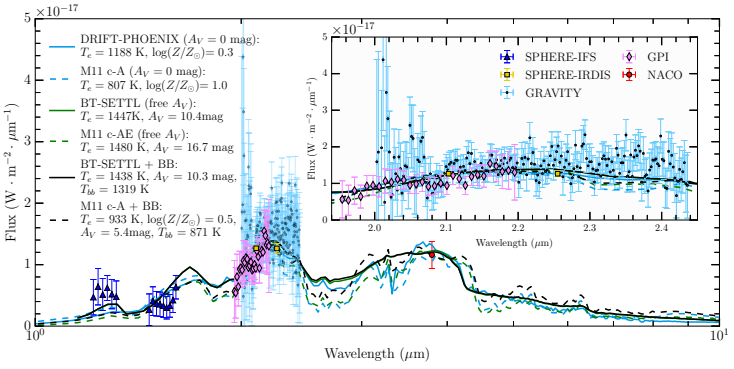

Astrometry and orbital fitting

Orbital fitting from measurements of SPHERE and NACO alone or couple to GRAVITY give **consistent orbital parameters**.

Orbital Parameter	MCMC solutions SPH.+NA. (2012–2019)	OFTI solutions GRA.+SPH.+NA. (2012–2022)
a (au)	72^{+1}_{-21}	57^{+14}_{-5}
e	≤ 0.18	≤ 0.13
i (°)	144^{+18}_{-4}	156^{+9}_{-10}
Ω (°)	72^{+53}_{-27}	87^{+52}_{-42}
ω (°)	-89^{+110}_{-2}	-66^{+49}_{-81}
T_p (yr AD)	2004^{+105}_{-45}	1972^{+78}_{-64}

Note: if (ω, Ω) is solution, ($\omega + 180$, $\Omega + 180$) is solution as well.

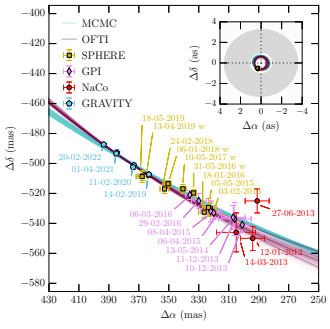

Exploration & sensitivities

The system HD 95086 very likely hosts at least one additional planet closer to the star than HD 95086 b to explain the architecture of the two debris belts (Su+2015). We searched it unsuccessfully but we put new constraints on the masses and locations of its/their putative presence. **We ruled out any other 5 M_{Jup} (9 M_{Jup}) inner planet in the system located at a distance greater than 17 au** (10 au, respectively) **at a 50% confidence level.**

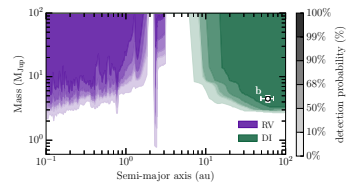

Figure 4.2: Poster on HD 95086, coupling SPHERE (Desgrange et al., 2022a) and GRAVITY (Otten et al. in prep.). I presented this poster during the conference In the Spirit of Lyot, in Leiden, Neverthelands, in 2022.

Chapter 5

Architectures of planetary systems hosting close-in low-mass planets

Contents

5.1 Context

5.1.1 Motivation

A striking result of the *Kepler* mission was the abundance of low-mass planets found orbiting their host star in less than 100 days. These low-mass planets, that can be called super-Earths, mini-Neptunes or Neptunes by referring to their mass and/or radius, could orbit around about 50% of single Sun-like stars based on radial velocity detection methods (Mayor et al., 2011). This may hold true for M stars too, though based on small sample statistics (Bonfils et al., 2013). On the contrary, the transit detection method indicates a higher occurence of close-in super-Earths and mini-Neptunes for M stars than for solar-like stars when compared at similar orbital periods (Mulders et al., 2015). However, for similar insolation values, the occurence of close-in super-Earths and mini-Neptunes orbiting M stars or solar-like stars are nearly equal within uncertainties (Hsu et al., 2019, 2020).

The short orbital periods of many super-Earths and mini-Neptunes in extrasolar systems is a surprise when compared to the location of the Earth and Neptune in our Solar System. The formation of such close-in super-Earths and mini-Neptunes is still an open question, and thus a very active topic of research (e.g., Haghighipour, 2013; Zhu & Wu, 2018; Schlecker et al., 2021). On the one hand, close-in super-Earth and Neptune-mass planets could form at about the radial location where there have been detected, that is to say within 100 day-orbital periods. Alternatively, they could have formed in the outer part of the system, and then migrated inwards. This migration could be assisted or prevented by the presence of an distant giant planet.

These different scenarios can be investigated by studying the correlation between the presence of close-in low-mass planets, and outer giant planets. I give some examples below, and illustrate them in Fig. 5.1.

Positive correlation

A positive correlation would imply that conditions that make the growth of a giant planet possible are also favorable for the growth of low-mass planets in the inner disk (Chiang & Laughlin, 2013; Schlecker et al., 2021), or that an outer giant planet could favor the presence of an inner low-mass planet.

For instance, while forming, the low-mass planet could be located in the outer part of the system, but closer to its host star than the giant planet. Its formation would be favored via the inward sweeping of secular resonances (Nagasawa et al., 2005; Best et al., 2024). The sweeping of the secular resonances is related to the relative apsidal precession rates between the outer giant planet, and the embryos and planetesimals (Ward et al., 1976; Ward, 1981; Heppenheimer, 1980). When these rates coincide, the eccentricity of embryos and planetesimals is greatly excited, increasing their encounter frequency. The gas drag from the disk damp the eccentricities of embryos and planetesimals, causing their orbital decay. As the gas depletes, the location of the secular resonances propagates toward the star. Eventually, this process may result in the presence of super-Earth-mass planets orbiting close to their host star (see Fig. 5.1, *first row*).

In another scenario, the low-mass planet could be formed further away than the giant planet, before being scattered to the inner part of the system. There, it could undergo orbital circularization from the star via tidal interactions (Terquem & Papaloizou, 2007; Kennedy & Kenyon, 2008) or from the disk via gas damping (Izidoro et al., 2015), see Fig. 5.1 (*second row*).

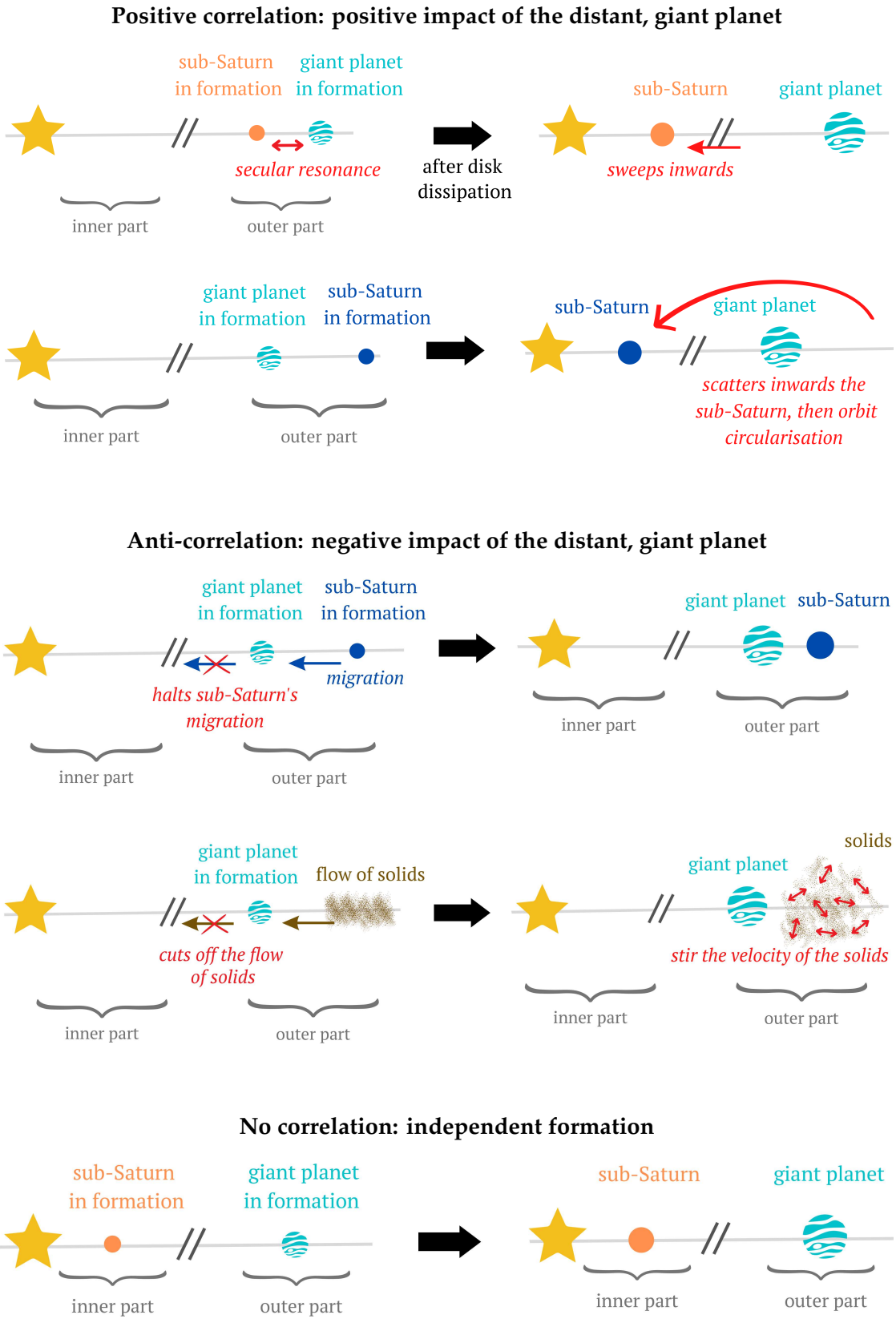

Figure 5.1: Examples of different mechanisms of planet formation and evolution that could trace a positive correlation (*top*), anti-correlation (*middle*) or no correlation (*bottom*) between the presence of a close-in low-mass planet ($< 95\ M_\oplus$) and a distant, massive giant planet.

Anti-correlation

If both planets are formed in the outer part of the system, with the low-mass planet farther away, its putative migration towards the host star could be halted by the presence of a giant planet. This giant planet would be seen as a barrier (Izidoro et al., 2015), see Fig. 5.1 (*third row*).

Another possibility would be that the close-in low-mass planet may never form, because an outer forming giant planet would cut off the flow of solids toward the inner part of the system, acting again as a barrier (Morbidelli et al., 2016; Izidoro et al., 2021), and stir the velocity distribution of solids (Mustill & Wyatt, 2009), see Fig. 5.1 (*fourth row*).

No correlation

Both the presence of a close-in low-mass planet and a distant giant planet could be independent if initial conditions for the formation of both types of planets are uncorrelated (Schlaufman, 2014). The low-mass planet could form in the inner part of the system, while the giant planet would form in the outer part (Raymond et al., 2008; Lee et al., 2014), see Fig. 5.1 (*last row*). This would require very high initial protoplanetary disk masses or an enhancement in the density of solids in its inner regions, with the latter supported by the inward drift of pebble sized objects (Chiang & Laughlin, 2013; Lee et al., 2014; Schlichting, 2014; Hansen & Murray, 2013).

Alternatively, a mixture of previous planet formation mechanisms (with positive or negative impact of a giant planet) could result statistically to an absence of correlation between the presence of both types of planets.

Therefore, studying whether the presence of a short-period low-mass planet is correlated with the presence of an outer giant planet could help to understand how close-in low-mass planets form. This is of particular interest, because such planets are very numerous based on current transit and radial velocity studies.

5.1.2 Previous studies on the correlation of inner super-Earths and outer Jupiters

Several studies investigated the simultaneous presence of at least one super-Earth located close to their host stars, and an outer distant giant planet, which are sometimes referred to as cold Jupiters (CJ). They aimed to find whether the presence of both types of planets were correlated. Table 5.1 summarizes the findings of these studies, which are mostly based on radial velocity and/or transit observations, and one on planet population models.

I would like to stress that the definition of what is called a super-Earth or a distant giant planet depends on the study, increasing the complexity to compare fairly their results. Actually, a planet which is called a super-Earth may in some cases refer to a small giant planet, such as Neptune, because the upper limit on the *minimal* mass may be as high as 30 $M_{\oplus}$, i.e., 1.7 $M_{Neptune}$, depending on the study.

On the one hand, Zhu & Wu (2018), Bryan et al. (2019), and Rosenthal et al. (2022) derived a positive correlation between the presence of both planets around solar-type stars, with a probability ranging from 21 to 32% for super-Earth hosts to also have a giant planet (noted P(CJ | SE)), higher than the probability of having an outer gas giant planet irrespective of the low-mass planet presence, which ranges from 6 to 10% (noted P(CJ)). Such results indicate that the presence of a gas giant planet enhances the presence of at least one inner super-Earth, either by a direct positive impact, or because the conditions resulting in the presence of an inner super-Earth are also favorable for the presence of a distant giant planet.

On the other hand, Bonomo et al. (2023) reported at first sight contradictory results with those just mentioned. They found that there is no excess of giant planets in systems having

Table 5.1: Previous observational studies on the conditional and absolute probabilities of the presence of inner super-Earths (SE) and outer giant (CJ) planets.

Study and Method	Sample	Parameter space	P(CJ | SE) (%)	P(CJ) (%)	P(SE | CJ) (%)	P(SE) (%)
Zhu & Wu (2018) RV and Transit	31 FGK	SE: 1–20 $M_\oplus$, < 400 days CJ: 0.3–15 M_{Jup}, 1–7 au	32 ± 8	10 [a]	90 ± 20 [(*)]	30 ± 3 [b]
Barbato et al. (2018) RV	20 FGK	SE: 10–30 $M_\oplus$, < 150 days CJ: 0.2–10 M_{Jup}, 1–6 au			< 10	
Bryan et al. (2019) RV and Transit	65 FGKM	SE: 1–10 $M_\oplus$, 1–4 $R_\oplus$ CJ: 0.3–13 M_{Jup}, 3–7 au	34 ± 7 [(†)] 21 ± 4 [(‡)]	6^{+3}_{-2} [c]	164^{+83}_{-57} [(*,†)] 102^{+51}_{-34} [(*,‡)]	30 ± 3 [b]
Rosenthal et al. (2022) RV	719 FGKM	SE: 2–30 $M_\oplus$, 0.02–1 au CJ: 0.3–13 M_{Jup}, 3–7 au	13^{+10}_{-7}	7^{+2}_{-2}	32^{+24}_{-16}	28^{+6}_{-5}
Rosenthal et al. (2022) RV	719 FGKM	SE: 2–30 $M_\oplus$, 0.02–1 au CJ: 30 $M_\oplus$–19 M_{Jup}, 0.23–10 au	41^{+15}_{-13}	18^{+3}_{-2}	42^{+17}_{-13}	28^{+6}_{-5}
Bonomo et al. (2023) RV	37 FGK	SE: 1–20 $M_\oplus$, 1–4 $R_\oplus$, < 100 d CJ: 0.3–13 M_{Jup}, 1–10 au	9^{+8}_{-3} 12^{+8}_{-4} [(†)]	20^{+7}_{-3} [(d)]		
Zhu (2023) RV	17 FGK	SE: 1–10 $M_\oplus$, 1–4 $R_\oplus$, < 100 d CJ: 0.3–13 M_{Jup}, 1–10 au	39^{+12}_{-11}	≤ 20		
Schlecker et al. (2021) Bern models	1 000 G	SE: 2–20 $M_\oplus$, < 400 days CJ: 0.3–31 M_{Jup}, > 400 days	16 ± 3	29 ± 2	34 ± 6	14 ± 1

Notes: The observational studies are based on RV and/or Transit data to search for the outer giant planets. Rosenthal et al. (2022) is the only observational study, which directly derived both the conditional (P(CJ | SE), P(SE | CJ)) and absolute (P(CJ), P(SE)) probabilities, without using the Bayes theorem (*) or absolute probabilities derived in other studies (a,b,c,d). The size of the sample indicates the number of stars with close-in low-mass planets for the studies of Zhu et al. (2018), Bryan et al. (2019), Bonomo et al. (2023) and Zhu (2023) based on their definition, and wide-orbit giant planets for Barbato et al. (2018). As for Rosenthal et al. (2022), the sample of 719 stars is the sample for their whole RV blind survey (in which they found 43 low-mass planets). Regarding Schlecker et al. (2021), this corresponds to the number of systems they simulated.
(*) These conditional properties are inferred by using the Bayes theorem. This can lead to probabilities higher than 100%.
Conditional probabilities without the symbols (†) or (‡) do not include RV trends. (†) or (‡): Bryan et al. (2019) computed conditional probabilities either by including (†) all giant planets that they inferred from the RV trends (but that could lie outside 3–7 au), or (‡) only a fraction of them. Bonomo et al. (2023) derived in one case (†) a conditional probability with one RV trend that is compatible with its parameter of space, but that could also lie beyond.

Additional references: (a) Cumming et al. (2008), (b) Zhu et al. (2018), (c) Wittenmyer et al. (2016), (d) Wittenmyer et al. (2020).

super-Earths, as they determined that P(CJ | SE) is equal to 9^{+8}_{-3} %, which they compared to P(CJ) equal to 20^{+7}_{-3} % based on the occurrences from Wittenmyer et al. (2020). Nonetheless, later results from Zhu (2023) indicated that those from Bonomo et al. (2023) are biased by their sample design. He showed that Bonomo et al. (2023) considered many stars with subsolar metallicity ($22/37 = 59\,\%$), which are anti-correlated with the presence of giant planets (Fischer et al., 2003; Santos et al., 2004). By considering only the stars with solar or supersolar metallicity of their sample ($[Fe/H] > 0$, 17 stars), Zhu (2023) found that there is indeed a positive correlation, P(CJ | SE) = 39^{+12}_{-11} %, while P(CJ) $\leq 20\,\%$.

Nevertheless, I think these results should be taken with some caution, and by having in

mind several factors. First, Zhu (2023) also removed three multiple systems corresponding to solar-rich stars with four close-in low-mass planets and no giant planets from the sample of Bonomo et al. (2023). Zhu (2023) justified it to remove some biases from the HARPS-N campaigns that targetted too often multiple systems, but this also goes to the point he wanted to prove, that inner low-mass planets and outer giant ones are correlated. This results in a very small sample of 17 stars. In addition, in a previous study, Zhu & Wu (2018) found a positive correlation ($P(CJ \mid SE) = 32 \pm 8\,\%$ versus $P(CJ) \sim 10\,\%$) with a sample including both metal-poor ($12/31 = 39\,\%$) and metal-rich ($19/31 = 61\,\%$) stars. When Zhu & Wu (2018) restricted the sample only towards the more metal-rich stars ($[Fe/H] > 0.1$), and increased the upper limit in minimal mass of a super-Earth from 20 $M_\oplus$ to 47 $M_\oplus$, which resulted in a sample of 29 stars, Zhu & Wu (2018) found a (very) high conditional probability $P(CJ \mid SE)$ of about $60\,\%$, while $P(CJ)$ was estimated to about $20\,\%$. This seems significantly higher than the conditional probability $P(CJ \mid SE)$ that Zhu (2023) derived for the sample of Bonomo et al. (2023), though no uncertainties were given. Perhaps this might be explained by small sample statistics and small changes in the probed parameter of space (in planet mass and stellar metallicity).

Last but not least, it is interesting to report that results based on planet population models do not report a correlation between the presence of close-in low-mass planets, and outer giant ones at 1σ (Schlecker et al., 2021). By considering only metal-rich stars ($[Fe/H] > 0.2$), they even found an anti-correlation, with $P(CJ \mid SE) = 24 \pm 7\,\%$ and $P(CJ) = 42 \pm 5\,\%$, contradictory with results from Zhu & Wu (2018) and Zhu (2023). As a matter of fact, Schlecker et al. (2021) rather emphasized a correlation regarding the composition of an inner super-Earth planet with respect to the presence of an outer giant planet. They found that short-period super-Earths are drier when there is an outer giant planet, and icier when there is not.

Conversely, these studies also investigated the presence of a close-in super-Earth depending on the presence of a distant giant planet. At the beginning, this conditional probability, noted $P(SE \mid CJ)$, was inferred by using the Bayesian theorem. Zhu & Wu (2018) and Bryan et al. (2019) reported that almost all systems hosting cold Jupiters should also host super-Earths.

This was later denied by results from Rosenthal et al. (2022), who directly derived for the first time the presence of super-Earth when there are cold Jupiters, finding $P(SE \mid CJ) = 32^{+24}_{-16}\,\%$ or $P(SE \mid CJ) = 42^{+17}_{-13}\,\%$, depending on their definition of a cold Jupiter. To some extent, this is also contradictory with the results from Barbato et al. (2018), who found $P(SE \mid CJ) \leq 10\,\%$, even though they later pointed out in Barbato et al. (2020) this could have been too underestimated.

All in all, I hope this section has shown that it is not straigthforward to derive the correlation between the presence of short-period, low-mass planets and distant, giant planets. When we considered both observational and numerical studies, there is not yet a clear consensus in the literature. One strong factor limiting the observational studies are the small-size sample of systems hosting close-in, low-mass planets and/or distant giant planets. This also makes it difficult to compare consistently their results by using the same parameter space (in terms of mass, periods, metallicity of the host star, stellar mass...). Strong limitations also concern the determination of wide-orbit companions based on radial velocity measurements. The semi-major axis derived for long-period companions based on radial-velocity method only could be significantly different (even of 2σ) to the ones estimated with additional constraints such as absolute astrometry (see Fig. 8 from Philipot et al., 2023). Beyond 5–8 au, deriving demographics based on RV measurements only is not secured according to Lagrange et al. (2023).

The use of the names of super-Earths and cold Jupiters can be somewhat misleading, because the planets designated by these names can be very different from what one might

think at first glance. Related to this, and to conclude with a last example, Zhu & Wu (2018) highlighted that Solar System analogs should be very rare: about 1% when considering single Sun-like stars. This is because there is a cold Jupiter but no short-period super-Earth in our Solar System. However, based on their definition of a super-Earth (a mass between 1 and 20 $M_\oplus$ and an orbital period of less than 400 days), the Earth could be considered as a super-Earth, and so our Solar System would host one.

To my mind, one of the main caveats when speaking about super-Earths, is their definition. The upper limit of a super-Earth could be set by a threshold in density, separating rocky-rich to gas-rich planets, or the Fulton radius (roughly 1.7 $R_\oplus$), that corresponds to the photo-evaporation valley which divides super-Earths and mini-Neptunes. However, the lower limit of a super-Earth, either in mass or radius, is far less clear. A super-Earth should be larger (or more massive) than the Earth, but such definition might be too simple, and not satisfying enough when thinking to its physical motivation.

5.2 My work

5.2.1 Overview of the project and the sample of stars

During my Ph.D., I brought another perspective regarding this question about the correlation of the presence of both short-period, low-mass planets ($\leq 95\,M_\oplus$, ≤ 1 au), and the presence of outer, massive companions (≥ 1 au, $\geq 10\,M_{Jup}$). I searched for the outer, massive companions by using VLT/SPHERE direct imaging observations, instead of the RV or transit methods, in a sample of close-in low-mass planets already discovered via RV campaigns (see Fig. 1 from the paper added in Section 5.2.5[1]). Contrary to transit or RV methods, direct imaging can detect planets up to the field of view of the instrument (e.g., ≤ 5", corresponding to ≤ 50 au at 10 pc). This is much further away than RV or transit methods ($\leq$ 10 au and $\leq$ 1 au, respectively).

I work on a sample of 27 stars, with spectral type spanning from GK stars (12/27) to M stars (15/27), with a stellar mass from 0.94 to 0.31 $M_\odot$ (see Fig. 2). All stars are suspected to host low-mass planets at the time of the sample definition. In total, this sample hosts 44 confirmed and 72 unconfirmed low-mass exoplanets, which could be identified as super-Earths or sub-Saturns based on their mass (see Table 1 and Table 2, Fig. 1). A few of the stars also have a debris disk, or could be considered as wide binaries (except GJ 229), either with another star or with a massive (20–75 M_{Jup}) brown dwarf (see Table 1 and Fig. 3).

This project, based on 47 simultaneous observations of VLT/SPHERE/IRDIS and VLT/SPHERE/IFS, was a long-run project, which started in 2016 and finished in 2023 with the publication of my paper, Desgrange et al. (2023). The idea at the origin of this project grew out of interactions between observers in Chile familiar with SPHERE (Luca Matrà and Julien Milli) and theorists in the United Kingdom, who wished to test planet formation and migration models (Mark Wyatt et Grant Kennedy).

In 2016, the sample was designed and the first ESO VLT/SPHERE proposal submitted. The first observations were acquired in April 2017, while the last ones in July 2022. On my side, I started to work on this project in March 2021, during my internship with Julien and Gaël before starting officially my Ph.D. with them and Thomas in October 2021. I jumped in the project at a stage where most of the data were already acquired, but I did write the last proposal on GJ 832, for which I found a very promising imaged exoplanet candidate (see Fig. 9). The proposal was granted (Program ID 109.23F2, PI: Desgrange), and the observations were acquired in June and July 2022.

[1] All the references to Figures and Tables in the Sections 5.2.1-5.2.4 and 5.2.6 concern Figures and Tables from the paper Desgrange et al. (2023), which is added in Section 5.2.5.

To familiarize myself with each planetary system of the sample, I carried out a significant investigation of what has been done in the literature for each system. I summarized it in the Appendix A of the paper. While some systems have only a handful of peer-reviewed publications, others (e.g., GJ 581, GJ 832, HD 40307, and HD 69830) had more than 30 peer-reviewed publications[2]. Although it was to some extent repetitive, carefully checking the literature for each system was a mandatory step to my mind. In particular, to assess what was the status of the exoplanets reported so far (confirmed or unconfirmed), but also to save in a table the information regarding the properties of each planet (e.g., mass, orbital properties, discovery paper, the most relevant characterization paper for which I took from the values of the physical properties). This research also triggered discussions with other researchers at IPAG, experts in the radial velocity method and/or stellar activity (Xavier Bonfils, Xavier Delfosse and Lucile Mignon, Nadège Meunier). Based on this work, I realized that some of the systems which were reported to host short-period, low-mass planets in 2016, may actually not, owing to more recent results. For instance, GJ 832 c, GJ 682 b and c were refuted by Gorrini et al. (2022) and Feng et al. (2020) and attributed to stellar activity.

5.2.2 Identification of the companion candidates

One of the main time-consuming task was to process all the data and identify of the point-sources that could be bound companion candidates. I processed myself the IRDIS and IFS observations (in total, 2×47 datasets) with the pipeline ANDROMEDA (Fig. E.3 and E.5) , and the HC-DC processed them with the SpeCal pipeline, including cADI (Fig. E.1), TLOCI (Fig. E.2), PCA ASDI (Fig. E.4), and nADI algorithms. Figure 5 shows the performance in contrast of the different processing for all the IRDIS and IFS observations of the survey.

Then, the companion candidates were identified by two methods, based on either ANDROMEDA or SpeCal. Regarding ANDROMEDA, I identified all the companion candidates, while for SpeCal only for some observations, as Julien and his previous Master intern, Anna Luashvili, already did this for most of the observations. Regarding SpeCal, all the candidates must be identified by hand. In total, this amounts to 366 candidates in the IRDIS observations, and a handful in the IFS data.

As for ANDROMEDA, even though the pipeline identifies by itself point-sources with high enough S/N, this also considers as potential companion candidates other bright features that are close to the inner working angle of the coronagraph, secondary lobes of the main candidate, or caused by processing effects. ANDROMEDA has various flags to pinpoint the relevant candidates, but in spite of this, it does still consider some that should not be companion candidates. Thereby, I visually checked all the ANDROMEDA candidates to keep only relevant ones. This results in a final number of 232 relevant companion candidates in the IRDIS data and a handful in the IFS data.

In Appendix F, I compared the results of the identification of companion candidates between ANDROMEDA and SpeCal, as a function of the separation. ANDROMEDA detects more candidates below 2″ than SpeCal cADI, which is expected (e.g., Cantalloube et al., 2015). I noticed that there was a bias between the photometry derived by ANDROMEDA compared to SpeCal candidates for bright candidates (contrast $> 10^{-5}$ with respect to their host star) imaged in the H2 and H3 bands. The photometry derived by ANDROMEDA is fainter up to 1.3 mag than the SpeCal one (e.g., Fig. F.1). I investigated this, which could be related to some extent to the high-pass filtering applied in ANDROMEDA but not in SpeCal, nonetheless, further analysis is needed to identify the source of this discrepancy.

[2] I looked for them in ADS by a making a selection of peer-reviewed papers having the name of the system in the abstract, such as: `abs:"HD 40307"` or `(abs:"GJ 581" OR abs:"Gl 581")`, and some time in the full text, in particular when there were only a few papers.

This had an impact on my method to list all the candidates of the survey and their properties. I decided to use the ANDROMEDA outputs for faint companion candidates (contrast $\leq 10^{-5}$), located at relatively small separations ($\leq 2''$), and SpeCal-cADI information otherwise (Section 4.1).

5.2.3 Classification of the companion candidates

I then classified the status of each candidate, as either a bound companion, a background star, an instrumental artifact, or ambiguous (Fig. 6). I used two criteria, based on the photometric properties of the candidates using a color magnitude diagram (CMD), or its relative motion between two epochs (see Section 5.1, Figs. 7, A.1–A.7).

By using the CMD in the H2 and H3 bands (or in K1 and K2), I compared the photometric properties of the companion candidates to the empirical sequence of known brown dwarfs[3] or to the theoretical predictions based on the isochrones from the evolutionary models `COND` (Baraffe et al., 2003). The CMD criterion can be used for candidates detected in two bands. However, this is an indicative and not absolute criterion. For instance, a bright background star (11–14 mag in the H2 or K1 bands) could mimic a L-type dwarf, or a faint one (11–14 mag in K1) could be confused with a TY dwarf (Fig. 7).

The relative motion criterion is the most conclusive criterion. However, it requires to have detected the companion candidate in two epochs, which was not always the case in our observations. This implied to obtain a second epoch of observation, and so submit a new proposal, resulting at the end in a relatively long process. By using the proper and parallactic motion of the host star, I determined whether the companion candidates followed the expected track of a background star, or whether they were located at about the same separation than before, which would have suggested there were bound to the host star (Figs. A.1–A.7). As all the stars from our sample are very nearby (≤ 20 pc), they have a high proper motion, from a few hundred to one thousand milliarcseconds per year in right ascension or in declination.

5.2.4 Analysis of the results

As eventually I did not detect new robust companions, I was only able to set constraints on the architectures of the planetary systems. I first used the `MESS2` tool (Section 5.3), as for HD 95086 (see Chapter 4), by combining the direct imaging observations and radial velocities measurements. For the direct-imaging data, I converted all the detection limit maps expressed in contrast to mass, by using the evolutionary models `COND`. As for RV, I downloaded all the HARPS data from the ESO archive, and processed them, to result for each system in a time series (Sections 3.2 and 4.2). For each system, I used altogether the SPHERE detection limit maps and HARPS time series as inputs in `MESS2`. I obtain detection probability maps, that illustrate what planet (in terms of semi-major axis and mass) the SPHERE or HARPS observations are able to detect, and with what probability.

This work was then updated, as my collaborators and I decided to include the constraints from the *Gaia* and *Hipparcos* data, derived by the `GaiaPMEX` tool (Kiefer et al. subm.). Flavien Kiefer (@LESIA) derived for each star the *Gaia* and *Hipparcos* constraints based on the Proper Motion anomaly and excess noise. His work hinted for the presence of companions around GJ 229 and GJ 832, both consistent with the presence of the known companions GJ 229 B and GJ 832 b. Unfortunately, he did not find hints of new companions around other stars in our sample.

The development of `GaiaPMEX` led to the development of a new version of the `MESS` tool, called `MESS3`, that takes into account the direct imaging, radial velocity and astrometry data.

[3] available here https://cass.ucsd.edu/~ajb/browndwarfs/spexprism/index.html

This tool, still private, was used by Anne-Marie Lagrange (@LESIA) and Pascal Rubini to derive detection probability maps, based on the SPHERE, HARPS, *Gaia* and *Hipparcos* data. There are shown in Fig. 10 for each system. I also showed the constraints from SPHERE observations only for each system in Fig. H.2. In addition, I compared the detection probability performance of each detection method in Fig. H.1, for M and GK stars respectively.

Furthermore, I compared my results with observational and theoretical studies (Section 6.1). In particular, I compared the detection probabilities from our direct imaging observations with planetary population models from Burn et al. (2021). Given the SPHERE sensitivity, I showed that the non-detection of a distant massive giant planet in our SPHERE observations are consistent with theoretical predictions. Last, I led a discussion on which systems from our sample would be the more likely to host gas giant planets based on the constraints of the debris disk and the impact of the stellar duplicity or multiplicity (when relevant), the stellar metallicity and mass, and the influence of the planet multiplicity and eccentricity (Section 6.2).

5.2.5 Publication in A&A: Desgrange, Milli, Chauvin et al. 2023

The publication resulting from this work is a significant paper of 46 pages. However, the main text corresponds only to 19 pages. In the Appendices, there are:

- the Appendix A (8 pages), which reports the literature on each system and showing figures with the relative motion of companion candidates;
- the Appendices B (4 pages) and C (2 pages), in which Sergio Messina (@INAF Catania) derived homogeneously the age of each star and Valentina D'Orazi (@INAF Roma and Padova) the metallicity of each GK star;
- the Appendices D (2 pages) and E (5 pages), in which there are the log of the 2×47 direct imaging observations and the mosaics of the reduced data;
- the Appendix F (1 page), in which I compared the companion candidates retrieved by the two pipelines ANDROMEDA and SpeCal;
- the Appendix G (1 page), parameters used with the tool `GaiaPMEX`;
- and the Appendix H, which contains some additional Figures illustrating the performance of different detection methods, and that completes the Fig. 11 shown in the main text.

A&A, 680, A64 (2023)
https://doi.org/10.1051/0004-6361/202346863

Astronomy & Astrophysics

Planetary system architectures with low-mass inner planets

Direct imaging exploration of mature systems beyond 1 au⋆

C. Desgrange[1,2], J. Milli[1], G. Chauvin[3], Th. Henning[2], A. Luashvili[4], M. Read[5], M. Wyatt[6], G. Kennedy[7,8], R. Burn[2], M. Schlecker[9], F. Kiefer[10], V. D'Orazi[11,12], S. Messina[13], P. Rubini[14], A.-M. Lagrange[10], C. Babusiaux[1], L. Matrà[15], B. Bitsch[2], M. Bonavita[12,16], P. Delorme[1], E. Matthews[2], P. Palma-Bifani[3], and A. Vigan[17]

[1] Univ. Grenoble Alpes, CNRS, IPAG, 38000 Grenoble, France
e-mail: celia.desgrange@univ-grenoble-alpes.fr
[2] Max Planck Institute for Astronomy, Königstuhl 17, 69117 Heidelberg, Germany
[3] Laboratoire Lagrange, UMR7293, Université Côte d'Azur, CNRS, Observatoire de la Côte d'Azur, Boulevard de l'Observatoire, 06304 Nice, France
[4] Laboratoire Univers et Théories, Observatoire de Paris, Université PSL, CNRS, Université Paris Cité, 92190 Meudon, France
[5] Space Research and Planetology Division, Physikalisches Inst., Universität Bern, Switzerland
[6] Institute of Astronomy, University of Cambridge, Madingley Road, Cambridge CB3 0HA, UK
[7] Department of Physics, University of Warwick, Gibbet Hill Road, Coventry, CV4 7AL, UK
[8] Centre for Exoplanets and Habitability, University of Warwick, Gibbet Hill Road, Coventry CV4 7AL, UK
[9] Department of Astronomy/Steward Observatory, The University of Arizona, 933 North Cherry Avenue, Tucson, AZ 85721, USA
[10] LESIA, Observatoire de Paris, Université PSL, CNRS, Sorbonne Université, Université de Paris, 5 place Jules Janssen, 92195 Meudon, France
[11] Department of Physics, University of Rome Tor Vergata, Via della Ricerca Scientifica 1, 00133 Rome, Italy
[12] INAF - Osservatorio Astronomico di Padova, Vicolo dell' Osservatorio 5, 35122 Padova, Italy
[13] INAF - Osservatorio Astrofisico di Catania, via Santa Sofia, 78 Catania, Italy
[14] Pixyl, 5 avenue du Grand Sablon, 38700 La Tronche, France
[15] School of Physics, Trinity College Dublin, The University of Dublin, College Green, Dublin 2, Ireland
[16] School of Physical Sciences, The Open University, Walton Hall, Milton Keynes, MK7 6AA, UK
[17] Aix-Marseille Univ, CNRS, CNES, LAM, Marseille, France

Received 10 May 2023 / Accepted 3 October 2023

ABSTRACT

Context. The discovery of planets orbiting at less than 1 au from their host star and less massive than Saturn in various exoplanetary systems revolutionized our theories of planetary formation. The fundamental question is whether these close-in low-mass planets could have formed in the inner disk interior to 1 au, or whether they formed further out in the planet-forming disk and migrated inward. Exploring the role of additional giant planet(s) in these systems may help us to pinpoint their global formation and evolution.
Aims. We searched for additional substellar companions by using direct imaging in systems known to host close-in small planets. The use of direct imaging complemented by radial velocity and astrometric detection limits enabled us to explore the giant planet and brown dwarf demographics around these hosts to investigate the potential connection between both populations.
Methods. We carried out a direct imaging survey with SPHERE at VLT to look for outer giant planets and brown dwarf companions in 27 systems hosting close-in low-mass planets discovered by radial velocity. Our sample is composed of very nearby (<20 pc) planetary systems, orbiting G-, K-, and M-type mature (0.5–10 Gyr) stellar hosts. We performed homogeneous direct imaging data reduction and analysis to search for and characterize point sources, and derived robust statistical detection limits. The final direct imaging detection performances were globally considered together with radial velocity and astrometric sensitivity.
Results. Of 337 point-source detections, we do not find any new bound companions. We recovered the emblematic very cool T-type brown dwarf GJ 229 B. Our typical sensitivities in direct imaging range from 5 to 30 $M_{\rm Jup}$ beyond 2 au. The non-detection of massive companions is consistent with predictions based on models of planet formation by core accretion. Our pilot study opens the way to a multi-technique approach for the exploration of very nearby exoplanetary systems with future ground-based and space observatories.

Key words. planetary systems – instrumentation: adaptive optics – instrumentation: high angular resolution – methods: observational

1. Introduction

A striking result of the *Kepler* mission is the detection of numerous small planets, mini-Neptunes and super-Earths, separated by the so-called photo-evaporation valley ($R \sim 1.8\ R_\oplus$, referred to as the Fulton gap), and orbiting very close to their host star with a period less than 100 days (Fulton et al. 2017). One fundamental question of particular interest is related to the correlation between the presence of inner super-Earths and outer giant planets from observational and theoretical perspectives.

A positive correlation would imply that outer giant planet(s) could enhance the occurrence of inner low-mass planets, or that conditions that make the growth of giants possible are also

⋆ Based on observations collected at the European Southern Observatory under ESO programmes 099.C-0255(A) 102.C-0489(A), 103.C-0484 (A and B), and 109.23F2.

favorable for the growth of planets to the inner disk (Chiang & Laughlin 2013; Schlecker et al. 2021). Close-in planets could still have formed in the outer parts of the system, inside or outside the giant planet orbit(s). Secular resonances or Kozai interactions with outer giants can promote excitation and growth of inner, low-mass planets to the observable regime (Nagasawa et al. 2005; Muñoz et al. 2016; Best et al. 2023). If formed farther out, the lower-mass planets could have been scattered to the inner part of the system, and then undergone orbital circularization (Terquem & Papaloizou 2007; Kennedy & Kenyon 2008a).

Conversely, giant planets can be detrimental to the existence of close-in small planets, since they could halt their migration from the outer to inner regions (Izidoro et al. 2015; Schlecker et al. 2021). They could cut off the flow of solids toward the inner regions (Morbidelli et al. 2016), and/or stir the velocity distribution of the solids (Mustill & Wyatt 2009). These negative impacts take place only if the giant planet forms before or at the same time as the small planet. Finally, formation in the inner disk of low-mass close-in planets would be independent of the presence of a distant giant planet if initial conditions between those regions are uncorrelated (Schlaufman 2014).

Zhu & Wu (2018) and Bryan et al. (2019) looked for giant planets via the radial velocity (RV) method in samples of 31 and 65 systems, respectively, known to host at least one super-Earth by radial velocity and/or transit techniques. Both of these studies found a positive correlation between the presence of inner super-Earths (SE) and outer massive giant planets called cold Jupiters (CJ). They derived conditional probabilities of hosting at least one outer giant planet in systems known to harbor super-Earth(s), which is mathematically represented by the probability P(CJ|SE) and compared it to the absolute probability of a system to host at least one giant planet, noted as P(CJ). These studies have consistent results because Zhu & Wu (2018) found a conditional probability P(CJ|SE) of 29 ± 18% around Sun-like stars which is greater than the absolute probability of finding at least one giant planet, that is, P(CJ) = 10% (Cumming et al. 2008), whereas Bryan et al. (2019) found P(CJ|SE) = 34 ± 7%. They compared it to P(CJ) = 7 ± 3% from Wittenmyer et al. (2016) to be consistent with their definition of cold Jupiter and the spectral type of the sample of host stars considered, FGKM. In addition, they both derived, indirectly, the probability of having super-Earth planets in systems known to host outer giant planets and found that systems possessing outer giant planets are very likely to be accompanied by inner super-Earth(s) as well (P(SE|CJ) = 90 ± 20% from Zhu & Wu 2018). On the other hand, Barbato et al. (2018) looked for inner super-Earth planets in a sample of 20 systems known to host distant giant planets and did not find any. They concluded that the probability of detecting a super-Earth planet in a system known to host a distant giant planet is small (P(SE|CJ) < 9.84%). However, this is statistically not at odds with previous observational studies due to observational biases, the limited size of the sample (Zhu & Wu 2018; Barbato et al. 2020), the eccentricity distribution of the giant planets in those surveys (Bitsch et al. 2020; Bitsch & Izidoro 2023), and the definition of planet categories (i.e., lower and upper bound in planet mass and semi-major axis to define, e.g., a "super-Earth").

As Zhu & Wu (2018) and Bryan et al. (2019), Rosenthal et al. (2022) recently concluded based on their large California Legacy Survey (719 systems) that systems with inner low-mass planets are more likely to host outer giant ones. In addition, Rosenthal et al. (2022) derived the conditional probability P(SE|CJ) both directly via measurement, and indirectly from Bayesian inference. They found a mismatch of 20–30% between the maximum of the conditional probability density measured via direct or indirect measurements. The difference depends on the definition of an outer giant planet, in particular the range of semi-major axis and masses (3–7 au and 95–4130 $M_\oplus$, i.e., 0.3–13 $M_{\rm Jup}$, or 0.23–10 au and 30–6000 $M_\oplus$, i.e., 0.09–18.9 $M_{\rm Jup}$).

On the other hand, Bonomo et al. (2023) argued for the absence of an excess of cold Jupiters in small-planet systems based on their RV survey on planet-transiting systems. However, Bitsch & Izidoro (2023) highlighted that the survey from Bonomo et al. (2023) might have been biased in the first place, as the eccentricities of their transiting low-mass planets are mainly low, hinting to the presence of only a few giant planets (see Sect. 6.2.4). In other ways, Zhu (2023) indicated that the metallicity dimension could resolve the discrepancy between Bonomo et al. (2023) and previous works, stating that the positive correlation of close-in super-Earths and distant cold Jupiters is verified around metal-rich hosts.

Despite those investigations to name a few, the origin of the architectures of exoplanetary systems is still an open question. The link between close-in small mass planets and distant giant planets, hence the conclusions on their formation and evolution, depend on the definition of the planet categories (e.g., Rosenthal et al. 2022; Schlecker et al. 2021), and on observational biases (e.g., Barbato et al. 2018; Zhu & Wu 2018; Bryan et al. 2019). To date, observational studies on this correlation mainly used RV and transit detection methods, which are limited somehow to the inner regions of exoplanetary systems.

In this paper, we look for outer giant planets or brown dwarfs with direct imaging in 27 nearby exoplanetary systems known to harbour close-in ($\lesssim$1 au) low-mass ($\lesssim$95 $M_\oplus$) planet(s) by the RV detection method. We complement our direct imaging observations (VLT/SPHERE) with archival data from RVs (HARPS) and proper motion coupled to the excess noise (*Gaia* and HIPPARCOS) to illustrate the global parameter space explored in these exoplanetary systems. In Sect. 2, we introduce our direct imaging survey, and the properties of the targeted systems. In Sect. 3, we present the high-contrast imaging observations and archival data, while in Sect. 4, we describe the data reduction. In Sect. 5, we report our observational results, including the directly imaged point-source detections, and the status of these planetary or substellar companion candidates based on two criteria: the color magnitude diagram (CMD), and the proper motion diagram (PMD). We indicate the detection limits for each system by combining the direct imaging, radial velocity and astrometry detection methods. In Sect. 6, we discuss our results. We compare our direct-imaging results with previous studies, including theoretical predictions in Sect. 6.1. In Sect. 6.2, we consider constraints from intrinsic parameters of the planetary systems in the presence of additional planets. In Sect. 7, we conclude on how this survey and in-depth study is particularly relevant to demonstrate to what extent current observational facilities used in synergy can challenge the current global vision of planetary formation.

2. Sample and target properties

We describe here how we selected the systems of our sample, and their known architectures and properties.

2.1. Sample selection

Our direct imaging survey aims to explore the link between close-in low-mass planets and outer giant planets, as it could

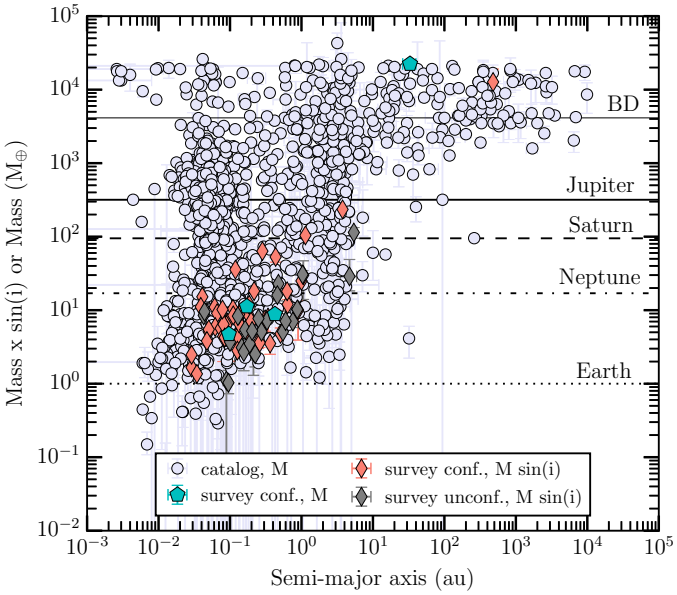

Fig. 1. Masses and semi-major axes of the planets in our sample. Minimal masses of both confirmed ("conf.") and unconfirmed ("unconf.") planets are shown in orange and gray diamonds, respectively, and absolute masses of the confirmed companions GJ 229 B and in HD 136352 are represented in blue pentagons, in the context of all the exoplanets known so far from the catalog (http://exoplanet.eu/catalog/).

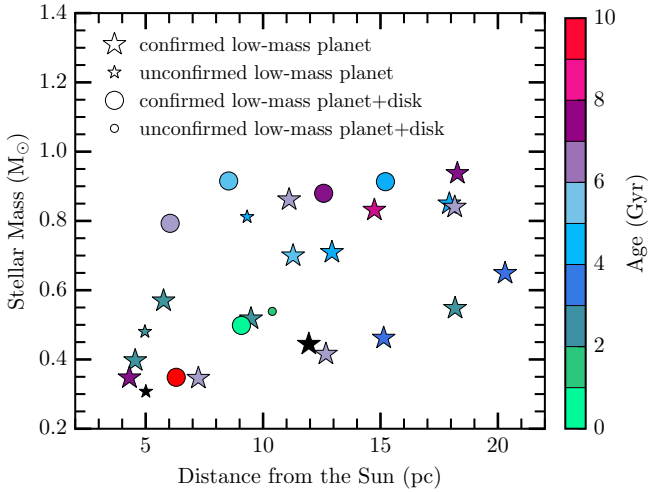

Fig. 2. Target properties of our sample: star (circle) markers correspond to systems without (with) a debris disk discovered. The four small markers corresponds to the four systems for which only suggested or debatted low-mass planets exist based on the literature (see Appendix A).

inform us on how the close-in low-mass planets formed. Therefore, we built a sample of 27 exoplanetary systems suspected to harbour at least one close-in ($\lesssim$1 au) low-mass ($\lesssim$95 $M_\oplus$, i.e., sub-Saturn mass, see Fig. 1) planet revealed by various RV spectrographs (see Table 1), and observable from the southern hemisphere at the Very Large Telescope (VLT). To maximize the sensitivity of high-contrast imaging observations, we restricted the sample to stars within 20 pc. The sample includes stars covering a relatively broad range of stellar masses, from 0.3 $M_\odot$ to 1 $M_\odot$ corresponding to spectral types from M, K and G types (see Fig. 2).

The challenge of this survey is to directly image planets around relatively mature and quiet stars where high-precision RV monitoring detected low-mass planets. Indeed old systems (>100 Myr) are rarely observed in direct imaging to search for planets. With time, giant exoplanets cool down and their emitted light decreases, making their detection more difficult given current XAO planet imager performance. In addition, we note that RV-based low-mass planets come with a bias, because the presence of a signal from a giant planet may often lead to a stop of the observations on this system (see the discussion in Sect. 6.1).

We derived homogeneously the masses for each star in the sample by following the method from Gaia Collaboration (2023), see their Appendix E. This uses the magnitude in the G band from the *Gaia* Data Release 3, as well as the age and the metallicity of the stars homogeneously re-analyzed in the following sections. This is the first time that the mass of GJ 649 is estimated. As for the other stars of the sample, the masses derived are consistent with the previous ones published at 1σ or 2σ when considering only the *Gaia* uncertainty, as the uncertainty value from the literature is not always available.

The detailed target properties (distance, spectral type, stellar host mass and radius, duplicity or multiplicity, number of planets and presence of a debris disk) are reported in Table 1. We derived homogeneously the age for each star of our sample and the metallicity for each GK star. Both methods are described in Appendices B and C, respectively, and associated results in Tables B.1 and C.1, and in Figs. B.1 and C.1. We note that three out of the twelve GK stars from our sample have super-solar metallicity (HD 102365, HD 154088 and HD 3651), two consistent with solar-like metallicity (HD 69830, 61 Vir) and for the fifteen M-stars, no reliable metallicity constraints (see Appendix C). This could impact our results concerning the GK-stars, because the presence of giant planets if formed via core-accretion (Pollack et al. 1996) is correlated with super-solar metallicity (see e.g., Fischer & Valenti 2003, and our discussion in Sect. 6.2.2). Stellar metallicity was not a criterion back to the time of the sample design, already restricted to 27 systems owing to required visibility from the VLT, presence of suggested close-in low-mass planets and the very nearby location of the systems (within 20 pc) to maximize high-contrast imaging sensitivity. Below, we describe the architectures of the systems from our sample.

2.2. Prior knowledge of the planetary system architectures

We point out that the systems in our sample show a diversity of architectures, see Fig. 3. Some systems are known to host a debris disk (61 Vir, GJ 433, GJ 581, GJ 649, HD 20794, HD 38858 and HD 69830), others to be part of binary (GJ 229, HD 3651, HD 99492, and HD 102365) or even multiple-star (GJ 667 C) system. Table 1 gives details on the architecture of each system in our sample, whereas Table 2 summarizes the number of systems with a specific architecture. We provide a review on the state of the art of each system in the Appendix A.

Regarding the planets known in our sample, we note that some are debated in the literature, and thus we label them as unconfirmed. In the 27 systems of the survey, four systems have only unconfirmed low-mass planets, while the 23 other systems are known to host such confirmed planets (see Fig. 4). We define in this work low (minimal) mass planets as being less massive than 95 $M_\oplus$ (i.e., sub-Saturn-mass planets). Some of the known planets in our sample correspond to the so called super-Earth (rocky) or sub-Neptune planets (with a gaseous envelope). We consider (e.g., in Tables 1 and 2) as super-Earth a planet with a

Table 1. Target properties, including both stellar and system properties.

System	Distance (pc)	Spectral type	Stellar mass ($M_\odot$)	Stellar radius ($R_\odot$)	Super-Earth conf.	Super-Earth unconf.	Sub-Saturn conf.	Sub-Saturn unconf.	Ref.	Debris disk	Binary system
GJ 163	15.14	M3.5	0.46 ± 0.05	–	2	2	3	2	1, *a*	–	–
GJ 176	9.49	M2.5	0.52 ± 0.05	–	1	0	1	1	2, *b*	–	–
GJ 180	11.95	M2	0.44 ± 0.05	–	2	1	2	1	3, *ac*	–	–
BD-061339	20.31	M0V	0.65 ± 0.05	–	0	1	1	2	4, *ad*, 5, *ad*	–	–
GJ 229	5.76	M2	0.57 ± 0.05	–	2	0	2	0	3, *ac*	–	Yes
GJ 422	12.68	M3.5	0.42 ± 0.05	–	1	0	1	0	6, *ac*	–	–
GJ 433	9.08	M1.5	0.50 ± 0.05	–	2	0	2	1	7, *a*	Yes	–
GJ 581	6.30	M3	0.35 ± 0.05	0.30 ± 0.01	3	3	3	3	8, *a*	Yes	–
Wolf 1061	4.31	M3V-M4.5V	0.35 ± 0.05	0.33 ± 0.01	2	1	2	1	9, *a*	–	–
GJ 649	10.39	M1.5	0.54 ± 0.05	0.54 ± 0.02	0	1	0	1	10, *e*	Yes	–
GJ 667C	7.24	M1.5	0.35 ± 0.05	0.30 ± 0.02	2	5	2	5	11, *ade*	–	Yes
GJ 674	4.55	M2.5V	0.40 ± 0.05	–	1	0	1	0	12, *a*	–	–
GJ 682	5.01	M3.5	0.31 ± 0.05	–	0	2	0	2	3, *ac*	–	–
GJ 832	4.97	M1.5	0.48 ± 0.05	0.50 ± 0.02	0	1	0	1	13, *adf*	–	–
GJ 3998	18.18	M1.5	0.55 ± 0.05	–	2	0	2	0	14, *g*	–	–
HD 20794	6.04	G8V	0.79 ± 0.05	–	3	3	3	3	15, *a*	Yes	–
HD 3651	11.11	K0V	0.86 ± 0.06	–	0	0	1	0	16, *h*	–	Yes
HD 38858	15.21	G2V	0.91 ± 0.06	–	1	0	1	1	17, *a*	Yes	–
HD 40307	12.93	K2.5V	0.71 ± 0.05	–	4	2	4	2	18, *a*	–	–
HD 69830	12.58	G8	0.88 ± 0.06	0.91 ± 0.02	3	0	3	0	19, *a*	Yes	–
HD 85512	11.28	K6V	0.70 ± 0.05	–	1	0	1	0	15, *a*	–	–
HD 99492	18.16	K2V	0.84 ± 0.05	–	0	0	1	0	20, *e*	–	Yes
HD 102365	9.32	G3V-G5V	0.81 ± 0.05	–	0	1	0	1	21, *f*	–	Yes
61 Vir	8.53	G7V	0.92 ± 0.05	–	2	0	2	1	22, *f*	Yes	–
HD 136352	14.74	G2V	0.83 ± 0.05	–	3	0	3	0	23, *a*	–	–
HD 154088	18.27	K0IV-V	0.94 ± 0.05	–	1	0	1	0	24, *a*	–	–
HD 189567	17.93	G2V	0.85 ± 0.05	–	2	0	2	0	24, *a*	–	–

Notes. For each system, we indicate the presence of confirmed ("conf.") or debated ("unconf.") super-Earth and sub-Saturn mass planets, and if it is known to host a debris disk (see the references in Appendix A). The system is marked as binary if it is bound to a star or brown dwarf with a mass $\gtrsim$20 $M_{\rm Jup}$ (references in Appendix A). We give the references for the first planet discovered (even if the planet was debated afterwards) for each system in the column "Ref." and the RV instrument(s) enabling the discovery. We review the literature on the presence of additional planet(s) and their (un)confirmed status in Appendix A, with corresponding references therein. The stellar masses come from this work. The distances are taken from the *Gaia* Early Data Release 3, with distance uncertainties given in Appendix A.

References. Discovery papers: 1 = Bonfils et al. (2013b), 2 = Endl et al. (2008), 3 = Tuomi et al. (2014), 4 = Lo Curto et al. (2013), 5 = Arriagada et al. (2013), 6 = Feng et al. (2020), 7 = Delfosse et al. (2013), 8 = Bonfils et al. (2005), 9 = Wright et al. (2016), 10 = Johnson et al. (2010b), 11 = Anglada-Escudé et al. (2012), 12 = Bonfils et al. (2007), 13 = Wittenmyer et al. (2014), 14 = Affer et al. (2016), 15 = Pepe et al. (2011), 16 = Fischer et al. (2003), 17 = Mayor et al. (2011), 18 = Mayor et al. (2009b), 19 = Lovis et al. (2006), 20 = Marcy et al. (2005), 21 = Tinney et al. (2011), 22 = Vogt et al. (2010b), 23 = Udry et al. (2019), 24 = Unger et al. (2021). Instruments used for the discovery paper: *a* = ESO/HARPS, *b* = *Hobby-Eberly* Telescope (HET, Ramsey et al. 1998) with the High-Resolution Spectrograph (HRS, Tull 1998), *c* = Ultraviolet and Visual Echelle Spectrograph (UVES, Dekker et al. 2000), *d* = *Magellan Clay* telescope Planet Finder Spectrograph (Crane et al. 2006, 2008, 2010), *e* = *Keck* Observatory High-Resolution Echelle spectrometer (HIRES, Vogt et al. 1994), *f* = Anglo-Australian Telescope (AAT) with the University College London Echelle Spectrograph (UCLES, Diego et al. 1990), *g* = Telescopi Nazionale *Galileo* (TNG) HARPS-N (Cosentino et al. 2012), *h* = *Lick Hamilton* spectrometer (Vogt 1987).

(minimal) mass less than 20 $M_\oplus$, and stress that this definition differs in studies (e.g., Izidoro et al. 2015; Schlecker et al. 2021; Mayor et al. 2011; Bryan et al. 2019; Burn et al. 2021).

For a handful of companions in our sample, the absolute masses are known via transit or astrometry. The transiting planets are the three known planets in the system HD 136352 (transits seen with TESS and CHEOPS; Kane et al. 2020; Lovos et al. 2022; Delrez et al. 2021). In particular, the planet HD 136352 b has a radius of 1.66 ± 0.05 $R_\oplus$ (see Appendix A), i.e., close to the photo-evaporation valley observed at about 1.8 $R_\oplus$ for close-in planets. The photo-evaporation valley is believed to represent the separation between super-Earth and sub-Neptune-like planets (Fulton et al. 2017). In addition, by combining RV measurements with the astrometry from *Gaia* and HIPPARCOS, the absolute mass of the brown dwarf GJ 229 B was constrained to 71.4 ± 0.6 $M_{\rm Jup}$ (Brandt et al. 2021).

3. Observations

We first present the 47 VLT/SPHERE observations from our survey, then the archival data used (HARPS, *Gaia* and HIPPARCOS).

3.1. VLT/SPHERE

Our survey was conducted between 2017 and 2022. The observations were acquired with the VLT/SPHERE high-contrast

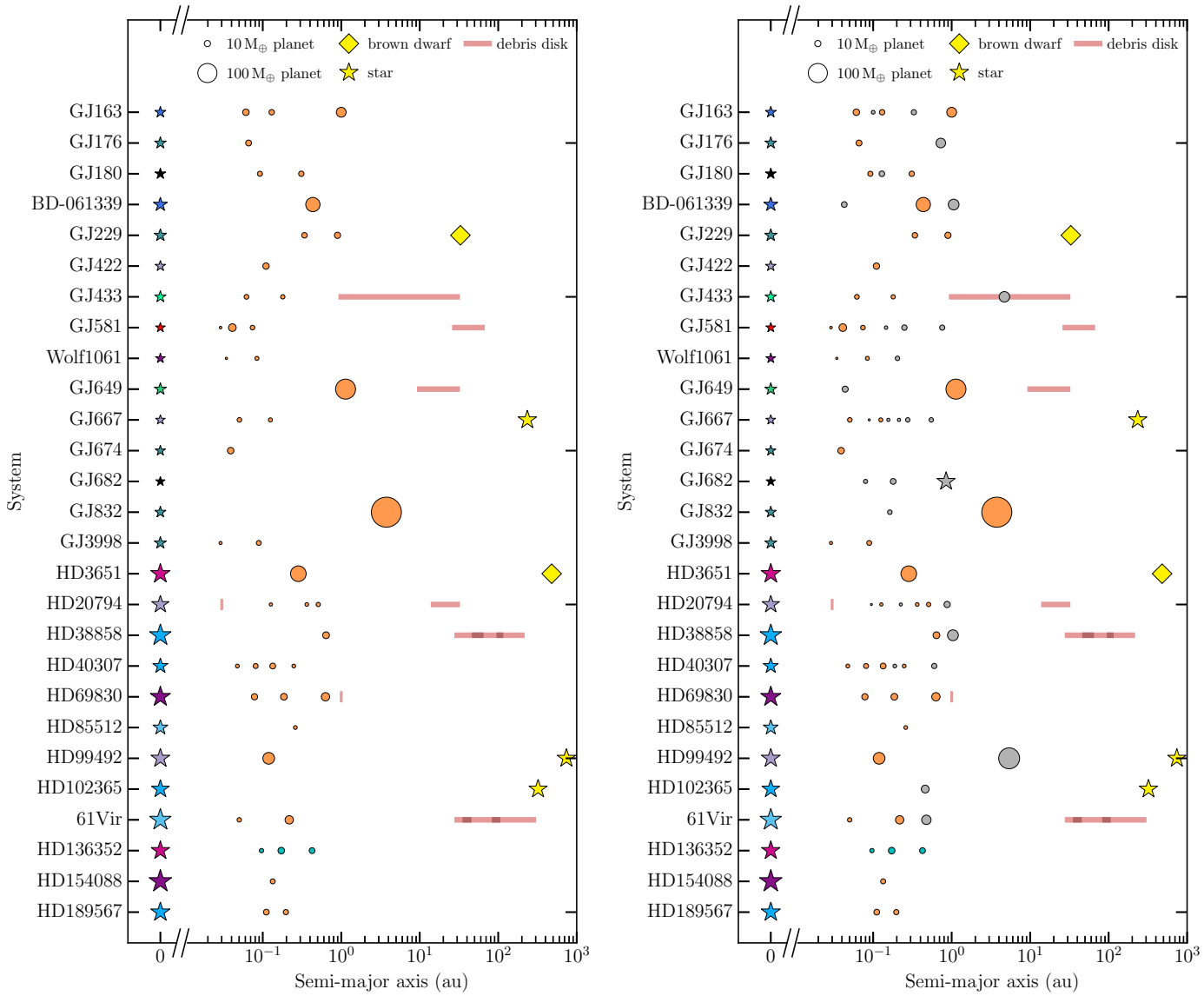

Fig. 3. Overview of the 27 systems in our sample. The planets are represented in orange if the minimal mass is used to scale the circle radius, in blue (HD 136352) if the absolute mass is used instead. On the right image, we added the unconfirmed planets in gray. We indicate the expected locations of the known debris disk(s) with red horizontal rectangles, with two possible structures for 61 Vir and HD 38858, either a single-belt or a two-belt (darker region only) architecture. For the host star, the color code is the same than in Fig. 2, and the bigger the star marker is, the higher the stellar mass. The references for each system (star, planet, debris disk and/or binary companion) are indicated in Appendix A.

Table 2. Summary of the characteristics of the systems in our sample.

Planetary systems considered	Total	Debris disk	Binary system
All the systems	27	7	5
Systems with confirmed sub-Saturn	23	6	4
Systems with confirmed super-Earth	19	6	1

instrument (Beuzit et al. 2019). All first-epoch observations were obtained with the IRDIFS mode, while additional observations to confirm the status of the point-source detections were acquired either with the IRDIFS or IRDIFS-EXT modes. Both of the modes combine simultaneously the IRDIS (Dohlen et al. 2008) and IFS instruments (Claudi et al. 2008). The IRDIFS mode uses IRDIS in dual-band imaging (DBI, Vigan et al. 2010) with the H2H3 filter doublet (λ_{H2} = 1.593 ± 0.055 µm, λ_{H3} = 1.667 ± 0.056 µm), and IFS in the YJ (0.95–1.35 µm) spectral bands, while the IRDIFS-EXT mode operates for IRDIS with the K1K2 filter (λ_{K1} = 2.103 ± 0.102 µm, λ_{K2} = 2.255 ± 0.109 µm) and for IFS with the YJH (0.97–1.66 µm) bands. We used the pupil-tracking mode for each observational sequence. This strategy of observation enables to process the data with the angular (ADI, Marois et al. 2006) and/or spectral differential imaging techniques (SDI, Racine et al. 1999; Sparks et al. 2002), with the combination of ADI and SDI noted ASDI, to achieve higher contrast at sub-arcsecond separations.

Table D.1 reports the individual setup of the 47 observations, as well as the observational conditions; those distributions are shown in Fig. D.1. The seeing (ϵ) and the atmospheric coherence time parameters (τ_0) were obtained from the Atmospheric Site Monitor on the platform of the Paranal observatory, whereas

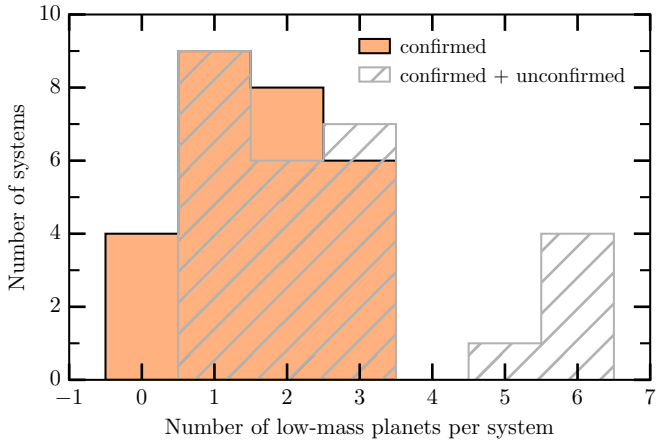

Fig. 4. Number of close-in ($\lesssim$1 au) low-mass ($\lesssim$95 $M_\oplus$) planets per system in our sample. In orange is indicated the multiplicity based on the confirmed planets, while in gray, it is based on both confirmed and unconfirmed planets. Bins are centered on their corresponding multiplicity value, i.e., four systems do not have confirmed low-mass planets (GJ 649, GJ 682, GJ 832, HD 102365), even though at least one has been suggested in the literature (see details in Appendix A).

the Strehl ratio (Sr) is measured by the SPHERE eXtreme AO (SAXO, Petit et al. 2014) real-time computer (SPARTA, Fedrigo et al. 2006).

Most of the systems were observed once, while a few up to three or even five times, due to companion candidates or because the observations were repeated as the observational conditions degraded, and hence the requirements were not matched.

3.2. Archival data (HARPS, Gaia, and HIPPARCOS)

In synergy with direct imaging observations, we use radial velocity and astrometric measurements to better constrain the presence of giant companions.

All the systems of the survey have low-mass planets discovered by radial velocity, and except HD 3651, all the systems of the survey were observed at least with HARPS. In this work, we use the RV data to set constraints on the detection limits in terms of planet mass and location in each system of the survey. We only use RV data from HARPS to avoid potential biases between instruments, though we note a possible bias between before and after the change of fiber in May 2015 (Lo Curto et al. 2013). A more complete analysis using all available RV measurements would be optimal, but this is beyond the scope of this paper focused on the direct imaging exploration of these mature systems. We note that in-depth studies exploiting various RV spectrographs have already been published in the literature on the systems from our sample, see Appendix A.

In addition, *Gaia* and HIPPARCOS data measurements exist for all the targets except GJ 667C. We use both the proper motion anomaly, (Kervella et al. 2019, 2022) and excess noise (Kiefer et al., in prep.) to look for the evidence of the presence of a binary companion, and to set constraints on the presence of planets for each system. The proper motion anomaly is computed by using long-term proper motion, i.e., the difference between HIPPARCOS and *Gaia* measurements (over a baseline of 2015.5 − 1991.25 = 24.25 yr) and near-instantaneous proper motions. Regarding the excess noise, this represents the difference between the dispersion of the estimated *Gaia* measurements at the estimated times of observations and the instrumental and intrinsic *Gaia* noise (Kiefer et al., in prep). We note that from the *Gaia* Data Release 3, none of our targets is classified as a non-single star, either via astrometry or spectroscopy.

4. Data reduction

In the following sections, we describe the data reduction regarding the high-contrast imaging observations, more briefly the one for the radial velocity measurements.

4.1. Direct imaging

The SPHERE observations were first pre-processed by the SPHERE Data Center (Delorme et al. 2017), using the SPHERE Data Reduction and Handling pipeline (Pavlov et al. 2008). The pre-processing includes correction for bad pixels, dark current, flat non-uniformity, the sky background for both IRDIS and IFS, and for the wavelength and cross-talk between spectral channels in the calibration for IFS. The centering of the coronagraphic images is carried out by means of the four satellite spots which determine the precise position of the star behind the coronagraphic mask. The astrometry of both IRDIS and IFS on sky is calibrated with past regular observations of a star crowded field (47 Tuc) as described in Maire et al. (2016, 2021). It includes measurements of the detector plate scale, true north and distortion.

Second, we independently applied on all the observations two post-processing pipelines named ANDROMEDA (Cantalloube et al. 2015) and SpeCal (Galicher et al. 2018) to remove the starlight residuals in the coronagraphic images via the ADI or ASDI techniques, and to reveal putative planetary companions. ANDROMEDA is a forward-modelling approach using the maximum likelihood estimator (Mugnier et al. 2009). It performs a simple pair-wise subtraction before tracking for the specific planetary signature that appears after the subtraction. Jointly for all pair of subtracted images, it fits the flux and position of each planetary signature. The SpeCal pipeline includes a set of different baseline algorithms such as classical ADI (cADI, Marois et al. 2006), locally optimized combination of images (LOCI/TLOCI, Lafrenière et al. 2007) and principal component analysis (PCA, Amara & Quanz 2012; Soummer et al. 2012).

The detection limits of the different post-processing techniques are shown in Fig. 5. Regarding IRDIS observations, ANDROMEDA-ASDI and ADI perform better than SpeCal-cADI and SpeCal-TLOCI-ADI at close separations, while for IFS data, SpeCal-PCA-ASDI (Mesa et al. 2015) performs better than ANDROMEDA-ASDI or ADI. For the sake of completeness, we show the IRDIS and IFS reduced images in terms of contrast relative to the host star in Figs. E.1, E.2 and E.4, for the mentioned SpeCal algorithms, and in Figs. E.3 and E.5 the signal-to-noise ratio (S/N) maps for ANDROMEDA-ADI, respectively.

Companion candidates are identified based on the following methodology: detection of close ($\lesssim 2''$) and faint ($\lesssim 10^{-5}$) point-like sources are estimated from the more sophisticated processing ANDROMEDA (both ADI and ASDI versions), whereas easier point-source detections (farther out or brighter) are considered from the baseline processing cADI. A comparison between ANDROMEDA and cADI detections is shown in Fig. F.1, with a few additional point-source detections in ANDROMEDA reduced images.

4.2. Radial velocities

The HARPS RV data were processed following the ESO pipeline to obtain time series of the RV signals and uncertainties. The

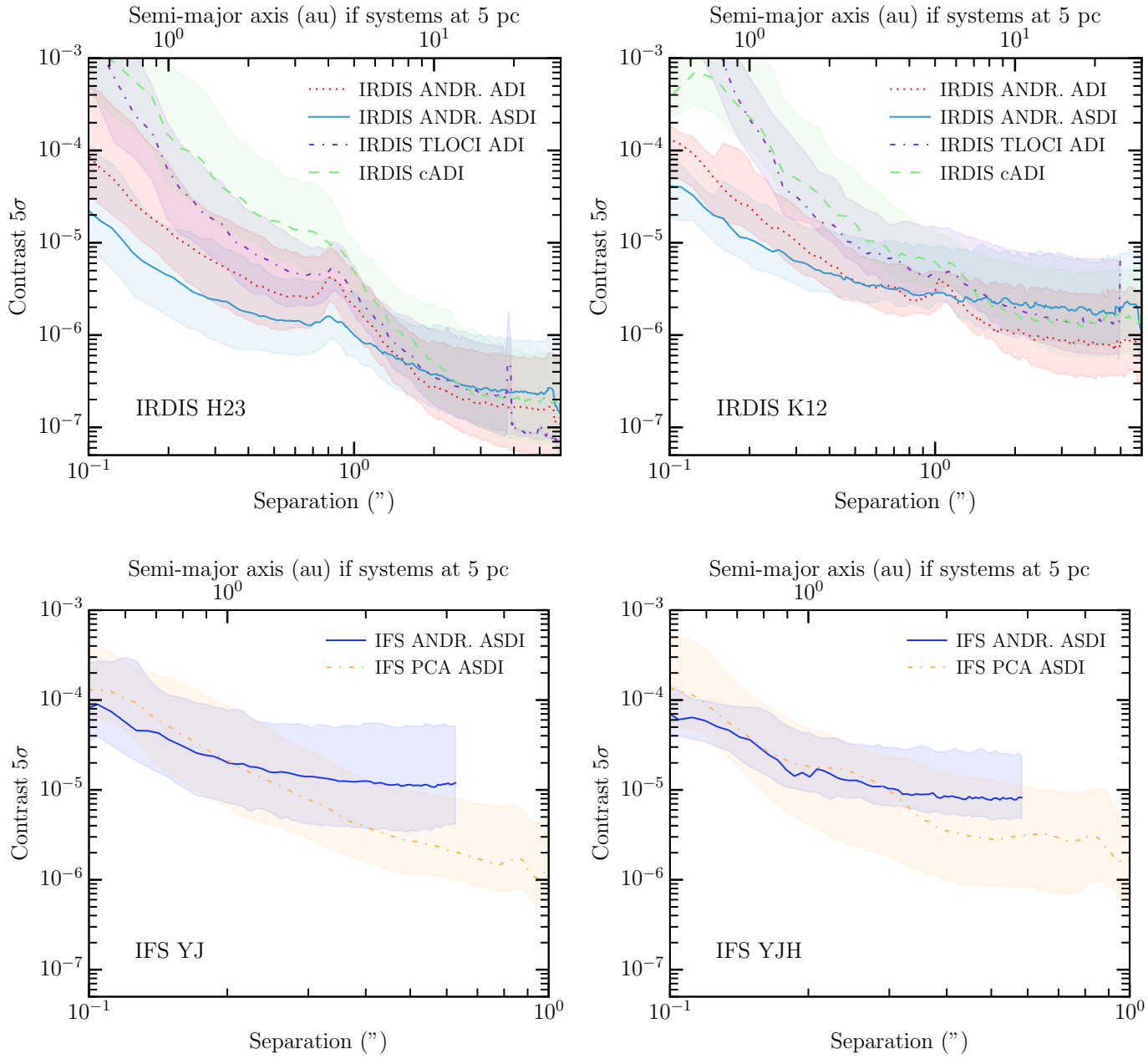

Fig. 5. Sensitivity of our observations in terms of contrast with respect to the host star for the whole survey. Top panels: detection limits from SPHERE-IRDIS in the H23 (on the left) and K12 (on the right) bands for ANDROMEDA-ADI, ANDROMEDA-ASDI, SpeCal-TLOCI ADI and SpeCal-cADI post-processing. Bottom panels: detection limits from SPHERE-IFS in YJ (on the left) and in YJH (on the right) for ANDROMEDA-ASDI and SpeCal-PCA-ASDI reductions. The detection limits are given as a function of the separation to the star, also expressed as semi-major axis for systems located at 5 pc, following semi-major axis (au) = separation (″) × distance (pc).

RV measurements were mainly used to estimate the RV detection limits described in Sect. 5.4. By using the `DACE` tool (Buchschacher et al. 2015), we removed from the time series the Keplerian signal associated with the planets already discovered and confirmed by RV based on the literature values, except for GJ 649 and GJ 3998 as only a limited number of HARPS measurements are available. This step enables to remove the impact of known confirmed planets on determination of the detection limits.

The change of fiber in HARPS in May 2015 may cause some differences in the RV signal measured between before and after the operation (Lo Curto et al. 2015). This can result in an offset between both measurements of about 20–50 m s^{-1}. We added the offset as a free parameter when relevant. If only a negligible number of measurements have been acquired after the fiber operation, we did not consider them in our RV time series.

5. Results

We describe the classification of our detections of giant planet or brown dwarf candidates in Sect. 5.1. In Sect. 5.2, we report the bound and ambiguous point-source detections, and the ones likely caused by instrumental artifacts. In Sect. 5.3, we derive constraints on the potential companions consistent with measurements from *Gaia* and HIPPARCOS for each system of our sample. Last in Sect. 5.4, we derive the probability of detection

Table 3. Overview of the SPHERE-IRDIS and SPHERE-IFS point-source detections per observation, as well as the status of these detections.

Observation information				Detections	Status of the detections							
					(CMD)		(PM)		(CMD and/or PM)			
Target	Date	Instru.	Filter	Total	Bkg.	Promising	Bkg.	Not re-det.	Bkg.	Inst. Art.	Bound	Ambi.
GJ 176	2018-10-08	IRDIS	H23	1	1	0	0	0	1	0	0	0
BD-061339	2018-11-24	IRDIS	H23	2	2	0	0	0	2	0	0	0
GJ 229	2018-11-27	IRDIS	H23	2	1	1	0	0	1	0	1	0
GJ 422	2018-01-28	IRDIS	H23	13	12	1	2	11	13	0	0	0
GJ 422	2019-11-25	IRDIS	K12	2	1	0	2	0	2	0	0	0
GJ 422	2020-01-18	IRDIS	K12	3	2	0	3	0	3	0	0	0
GJ 433	2018-02-02	IRDIS	H23	1	1	0	1	0	1	0	0	0
GJ 433	2019-06-08	IRDIS	K12	1	0	0	1	0	1	0	0	0
GJ 433	2020-01-20	IRDIS	K12	1	0	0	1	0	1	0	0	0
Wolf 1061	2017-07-28	IRDIS	H23	1	1	0	0	0	1	0	0	0
GJ 667	2017-06-27	IRDIS	H23	142	138	0	0	0	138	0	0	4
GJ 667	2017-06-27	IFS	YJ	1	0	0	0	0	0	0	0	1
GJ 674	2017-07-14	IRDIS	H23	18	18	0	5	13	18	0	0	0
GJ 674	2021-07-04	IRDIS	K12	11	4	0	4	7	6	0	0	5
GJ 674	2021-07-04	IFS	YJH	1	0	0	1	0	1	0	0	0
GJ 682	2017-06-23	IRDIS	H23	20	19	1	20	0	20	0	0	0
GJ 682	2017-07-20	IRDIS	H23	26	24	1	19	7	25	0	0	1
GJ 682	2019-07-05	IRDIS	K12	10	6	1	10	0	10	0	0	0
GJ 832	2017-05-27	IFS	YJ	1	0	0	0	1	0	1	0	0
GJ 832	2022-07-29	IRDIS	H23	1	1	0	0	1	1	0	0	0
GJ 3998	2017-05-14	IRDIS	H23	1	1	0	0	0	1	0	0	0
HD 38858	2018-11-23	IRDIS	H23	1	1	0	0	0	1	0	0	0
HD 85512	2017-04-01	IRDIS	H23	3	3	0	1	2	3	0	0	0
HD 85512	2017-12-30	IRDIS	H23	3	3	0	1	2	3	0	0	0
HD 85512	2019-11-25	IRDIS	K12	2	1	0	1	1	1	1	0	0
HD 85512	2020-01-03	IRDIS	K12	1	1	0	1	0	1	0	0	0
HD 99492	2018-02-03	IRDIS	H23	1	1	0	0	0	1	0	0	0
HD 136352	2017-07-14	IRDIS	H23	17	17	0	7	10	17	0	0	0
HD 136352	2020-03-16	IRDIS	K12	5	1	0	5	0	5	0	0	0
HD 154088	2017-06-21	IRDIS	H23	29	27	2	9	20	29	0	0	0
HD 154088	2019-07-22	IRDIS	K12	5	1	0	5	0	5	0	0	0
HD 154088	2021-07-04	IRDIS	K12	11	1	3	10	1	10	0	0	1

Notes. The observations with non-detections are not listed. More details on the classification of the companion candidates are given in Sects. 5.1 and 5.2. "Bkg." stands for a background star; "Not re-det." for not re-detected; "Inst. Art." for instrumental artifact, "Ambi." for ambiguous, "CMD" for Color Magnitude Diagram; "PM" for Proper Motion.

in terms of mass and semi-major axis for each system providing the detection sensitivities of our VLT/SPHERE high-contrast imaging observations, the *Gaia* and HIPPARCOS data, and the HARPS radial velocity measurements.

5.1. Overview of the direct imaging results

Over 47 SPHERE observations, 337 point sources have been detected by SpeCal (bright or large-separation companion candidates) and ANDROMEDA (faint and close candidates). Table 3 lists the number of companion candidates for each observation both for the IRDIS and IFS instruments, as well as their detection status (background contaminant, companion, instrumental artifact or ambiguous), also shown in Fig. 6.

We used two independent criteria to find out about the nature of the companion candidates. The first criterion consists in extracting the photometry in two bands, H2H3 (or K1K2), and comparing it with empirical and theoretical predictions on a CMD, see Fig. 7. The empirical expectation is based on a sequence of old known brown dwarfs and substellar objects for different spectral types (symbols). The theoretical predictions are from the COND evolutionary model (lines, Baraffe et al. 2003). This model describes the evolution of the internal structure of a planet with time, and gives constraints on the physical properties of the planet, such as its luminosity, mass, effective temperature, surface gravity, and radius. The promising point-source detections are defined as having similar photometric magnitudes than the empirical sequence of known substellar objects, while the other detections are likely to be background contaminants. In particular, one can define the area of background contaminants as the one corresponding to faint objects ($M_{H2} \gtrsim 15$ mag) and without color (H2-H3 $\lesssim -1$ mag). Reciprocally, the brighter point-source detections or with a significant color are considered as promising. For promising detections, we asked for additional epochs in the K12 dualband, such as for the systems GJ 422, GJ 682, and HD 154088.

The same principle applies for K12 observations, except some difficulties arise to define a background contaminant zone.

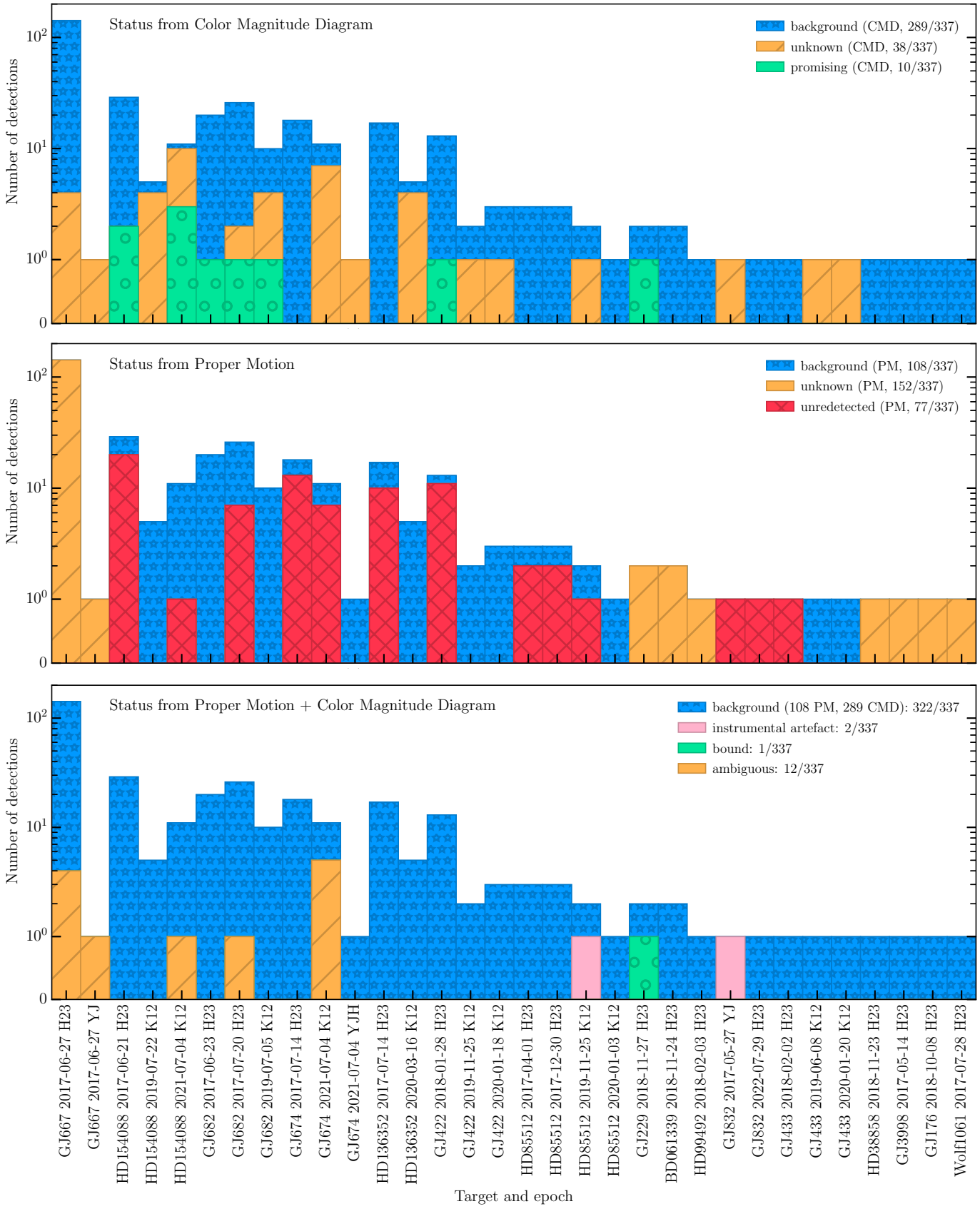

Fig. 6. Status of all the point-source detections with SPHERE-IRDIS and SPHERE-IFS ranked by system, epoch of observation and filter. Top panel: based only on the Color Magnitude Diagram criterion. Middle panel: based only on the Proper Motion Diagram criterion. Bottom panel: Final status of the point-source detections based on both criteria. There is one already known bound companion, corresponding to the brown dwarf GJ 229 B, and none new.

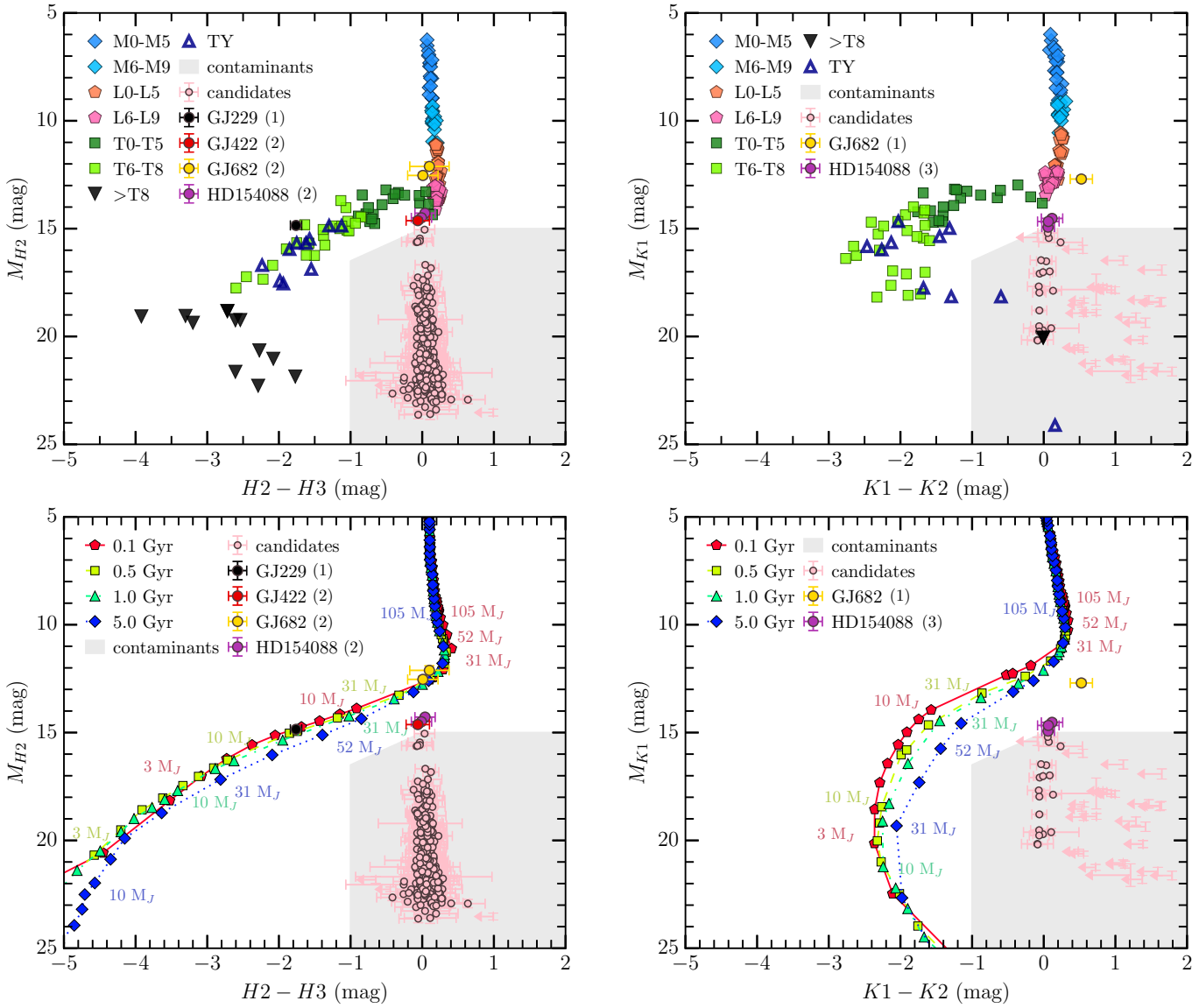

Fig. 7. Color Magnitude Diagram in the band H23 (left) and K12 (right) for all the point sources detected in the H2 and/or K1 band over the whole survey. Top panel: the sequence of known giant planets and brown dwarfs of different spectral types is shown (the photometry from MLTY brown dwarfs is taken from https://cass.ucsd.edu/~ajb/browndwarfs/spexprism/index.html). Bottom panel: isochrones from the evolutionary models COND (Baraffe et al. 2003) are plotted for different object masses.

Indeed, our direct imaging observations are sensitive to companions with an effective temperature down to 400 K (see Fig. 8) corresponding to giant planets of TY spectral type. Those objects are very faint in the K1 band, and some of them with a color K1–K2 close to zero, hence they could be confused with background stars (see Fig. 7). In addition, another issue arose, as a dozen point-source detections are only detected in the K1 band (and not in the K2 band). On the one hand, this could be interpreted positively as the K2 band corresponds to methane absorption. Thus, it may advocate for the presence of an exoplanet with methane in its atmosphere. On the other hand, if the point-source detection is faint in the K1 band, the absence of detection in the K2 band could suggest that the detection is rather an instrumental artifact than a real object. We note that both the GJ 682 and HD 154088 systems possess promising point-source detections based on the CMD in the K12 bands, coinciding with the promising detections in the H23 bands. In summary, we could flag 289 companion candidates as background contaminants, 10 as promising, and 38 remain as unknown as only detected with the IFS, or in one of the IRDIS dual band, H2 or K1 (see Fig. 6, top panel).

The second criterion is the relative motion of the point-source detections with respect to their host stars when comparing at least two epochs. If a detection is a background star, its expected location in the second epoch can be derived by knowing the proper and parallactic motion of its host star. Conversely, if a companion candidate is detected at about the same location relative to the star between two epochs, it suggests it is bound to the star, by assuming its orbital motion is small. Of the 27 systems of our sample, 11 have been observed at least twice, either as having promising companion candidates or because the observational conditions did not satisfy the requirements asked for. We have 108 point-source detections flagged as background contaminants based on this absolute criterion, summarized in Fig. 6. Proper motion diagrams are shown in Figs. A.1–A.7. For 77 companion candidates, new observations were acquired at a second epoch, but the companion candidates were not

Table 4. Relative astrometry and photometry with respect to their host star of the point-source detections in our SPHERE survey labeled as promising, ambiguous or instrumental artifacts.

Target	Epoch	Instr.-Filt.	$\Delta\alpha$ (mas)	$\Delta\delta$ (mas)	Separation (mas)	PA (°)	Contrast	*S/N*	Status	ID
GJ 229	2018-11-27	IRDIS-H2	228 ± 12	−5204 ± 3	5209 ± 12	177.5 ± 0.8	$(2.0 \pm 0.1) \times 10^{-4}$	88	bound	–
GJ 667	2017-06-27	IFS-YJ	−535 ± 3	−159 ± 3	558 ± 3	253.5 ± 0.3	$(3.1 \pm 0.4) \times 10^{-5}$	7	ambi.	1
GJ 667	2017-06-27	IRDIS-H2	−2526 ± 15	−1437 ± 10	2906 ± 15	240.4 ± 0.2	$(8.0 \pm 0.1) \times 10^{-7}$	13	ambi.	2
GJ 667	2017-06-27	IRDIS-H2	−3462 ± 8	587 ± 8	3511 ± 8	279.6 ± 0.1	$(4.3 \pm 0.8) \times 10^{-7}$	6	ambi.	3
GJ 667	2017-06-27	IRDIS-H2	3760 ± 40	3004 ± 12	4813 ± 40	51.4 ± 0.2	$(6.8 \pm 1.0) \times 10^{-7}$	8	ambi.	4
GJ 667	2017-06-27	IRDIS-H2	5885 ± 8	−424 ± 8	5901 ± 8	94.1 ± 0.1	$(1.2 \pm 0.2) \times 10^{-6}$	7	ambi.	5
GJ 674	2021-07-04	IRDIS-K1	−1550 ± 27	−2677 ± 6	3093 ± 27	210.1 ± 0.2	$(9.4 \pm 1.7) \times 10^{-7}$	6	ambi.	6
GJ 674	2021-07-04	IRDIS-K1	986 ± 10	−5092 ± 10	5187 ± 10	169.0 ± 0.6	$(2.4 \pm 0.2) \times 10^{-6}$	12	ambi.	7
GJ 674	2021-07-04	IRDIS-K1	−2382 ± 9	−2825 ± 9	3695 ± 9	220.1 ± 0.2	$(2.6 \pm 0.3) \times 10^{-6}$	12	ambi.	8
GJ 674	2021-07-04	IRDIS-K1	−3206 ± 11	−4354 ± 11	5407 ± 11	216.4 ± 0.2	$(2.6 \pm 0.3) \times 10^{-6}$	12	ambi.	9
GJ 674	2021-07-04	IRDIS-K1	226 ± 7	−2601 ± 7	2611 ± 7	175 ± 2	$(1.6 \pm 0.2) \times 10^{-6}$	9	ambi.	10
GJ 682	2017-07-20	IRDIS-H2	3571 ± 5	1667 ± 6	3941 ± 5	65.0 ± 0.1	$(3.6 \pm 0.5) \times 10^{-7}$	8	ambi.	11
GJ 832	2017-05-27	IFS-YJ	487 ± 3	194 ± 3	524 ± 3	68.3 ± 0.3	$(2.7 \pm 0.9) \times 10^{-6}$	4	inst. art.	–
HD 85512	2019-11-25	IRDIS-K1	911 ± 7	11 ± 4	912 ± 6	89.3 ± 0.2	$(4.5 \pm 2.2) \times 10^{-6}$	6	inst. art.	–
HD 154088	2021-07-04	IRDIS-K1	3525 ± 8	−4408 ± 7	5644 ± 8	141.3 ± 0.1	$(1.0 \pm 0.2) \times 10^{-6}$	6	ambi.	12

Notes. More information on the "Status" column is given in Sects. 5.1 and 5.2.

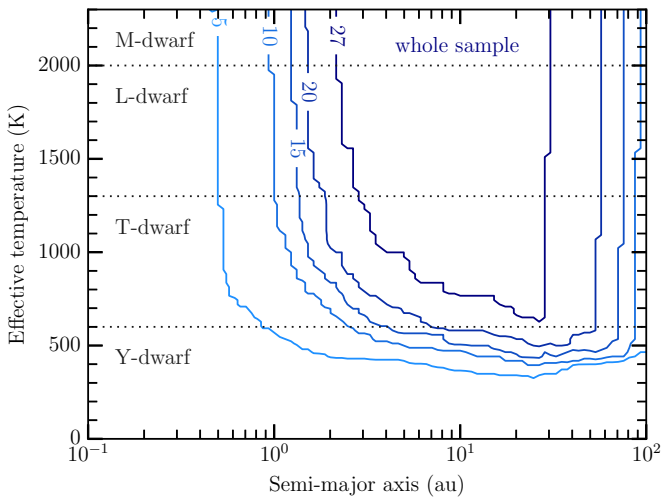

Fig. 8. Sensitivity for our direct imaging survey. The isocontours give the number of stars that have the sensitivity to detect companions at a probability of 50% for this given semi-major axis and effective temperature. The dotted lines represent the indicative effective temperatures of the transitions between Y and T-dwarfs (~600 K), T and L-dwarfs (~300 K), L and M-dwarfs (~2000 K).

re-detected at the expected location for a bound object and/or a stationary background contaminant. For some cases, the predicted location for a background contaminant was out of the field of view given the high proper motion of the star (see next section). The 152 "unknown" point-source detections correspond to companion candidates in system observed only once.

In total, we were able to flag 322/337 point-source detections as background contaminants, with 289 being from the CMD only and 108 from proper motion. We discuss the other 15 remaining companion candidates in the following section.

5.2. Substellar companion candidates

Of the 337 point-source detections with SPHERE-IRDIS and SPHERE-IFS, one is already known as the companion GJ 229 B (Nakajima et al. 1995), two are identified as instrumental artifacts (GJ 832, HD 85512), and the twelve others remain with an ambiguous nature, as we lack sufficient information to conclude definitively. Table 4 lists these 15 point-source detections, labeled as "bound", "instrumental artifact" "ambiguous", respectively, along with their relative astrometry and contrast with respect to their host star.

We list below the reasons why ambiguous companion candidates are labeled as such. We note that the ambiguous companion candidates are all detected in systems with a crowded field of view (see Table 3).

Candidate 1 (GJ 667): detected only with the IFS in the combined YJ bands in 2017-06-27, so we could not use the CMD criterion. There is no additional epoch of observation on the system GJ 667.

Candidate 2 (GJ 667): detected only in the band H2 (and not in the band H3) in 2017-06-27, hence we cannot conclude to its color H2-H3. There is no second epoch on the system GJ 667.

Candidates 3–5 (GJ 667): detected only in the band H2 in 2017-06-27 (and not in the band H3), hence we cannot use their color H2–H3 to conclude. There is no additional epoch of observation on the system GJ 667. We note these candidates are at separations $\gtrsim 3''$, and what should look like point sources are in practice elongated azimuthally for separations $\gtrsim 3''$ for the observation on GJ 667. This is caused by a too fast rotation of the field of view with respect to the frame exposure time. The greater the separation, the stronger the effect is. This could bias our flux estimation of the companion candidates 3, 4 and 5.

Candidates 6–10 (GJ 674): candidates detected only in the K1 band in 2021-07-04. If the companion candidates are

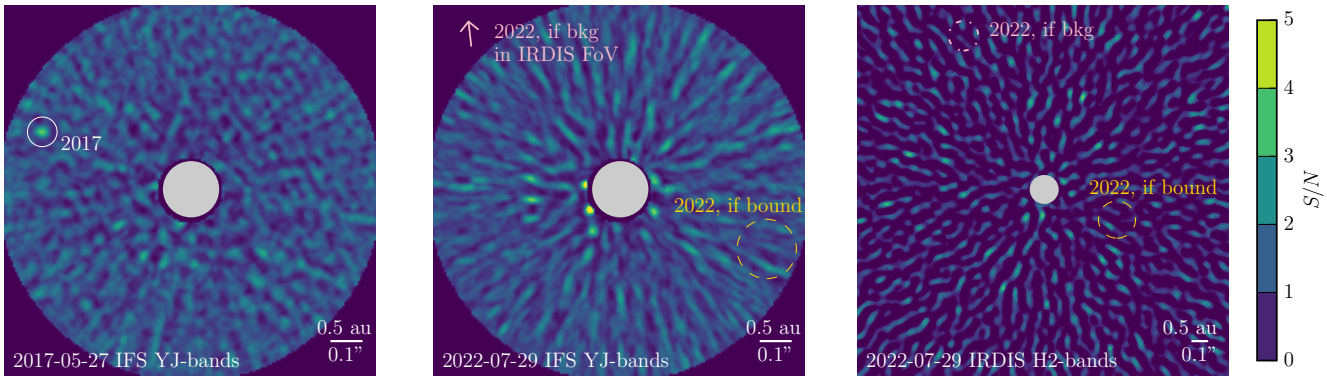

Fig. 9. Companion candidate in the system GJ 832: detected in the epoch 2017-05-27 (in the white circle) but not in 2022-07-29, neither at the expected location if bound (yellow dashed circle) or if a background contaminant ("bkg", in the pink dashed circle visible only in the IRDIS field of view) in spite of better conditions of observation and higher detection sensitivity (see text for more information).

background stars, there are not expected to be in the field of view (11″×11″ for IRDIS) of our other epoch of observation, 2017-07-14, acquired in H23, considering their location and the fact that the star GJ 674 A moves of 0.57″ yr^{-1} in right-ascension, and −0.88″ yr^{-1} in declination (Gaia Collaboration 2020).

Candidate 11 (GJ 682): faint companion candidate detected only in the H2 band in 2017-07-20. The companion candidate is in the field of view of the previous epoch of observation 2017-06-23, but the epoch was acquired under poorer observation conditions which lead to poorer detection sensitivity. The companion candidate is out of the field of view of the third epoch of observation, 2019-07-05, as the proper motion of the star GJ 682 A is high (0.71″ yr^{-1} in right-ascension, −0.94″ yr^{-1} in declination, Gaia Collaboration 2020)

Candidate 12 (HD 154088): companion candidate detected both in K1 and K2 bands in 2021-07-04 with a promising CMD, but not detected in the epoch of observation 2019-07-22 in K12 dual band (acquired with poorer condition of observations) or in the other dual band H23 in 2017-06-21. Due to the proper motion of the star HD 154088 A (0.83″ yr^{-1} in right-ascension, −0.27″ yr^{-1} in declination, Gaia Collaboration 2020), if the companion candidate is a background star, it is expected to be out of the field of view.

Regarding the point-source detection in GJ 832 that we classified as an instrumental artifact, this was detected in the IFS data (epoch 2017-05-27) at a separation of 524 mas (i.e., 2.7 au), which could have been consistent with the giant planet already known from RV measurements ($m \times \sin(i) = 0.74 \pm 0.06\ M_{\rm Jup}$). However, if the imaged companion candidate was indeed the RV planet, the system GJ 832 should have been much younger (about 100 Myr), than the age estimation of 2.4 ± 0.3 Gyr (see Table B.1). Indeed, at 100 Myr, the imaged companion candidate could correspond to a planet of 1 $M_{\rm Jup}$ based on the evolutionary models `COND`, and be consistent with a RV-planet seen with an inclination of about 50 deg. Unfortunately, we did not detect the companion candidate again in the latter observation which was acquired under better observing conditions (2022-07-29), and reached better detection sensitivity. There was no detection either at the expected location of a background object, or at its expected location if bound and coinciding with GJ 832 b (see Fig. 9). This location was expected in the epoch 2022-07-29 on the opposite side of the star to its location in the epoch 2017-05-27, as the period of GJ 832 b is about ten years from RV measurements, and the observations were taken five years apart. Therefore, this point-source detection at low S/N ($S/N \sim 4$) is likely to be an instrumental artifact. The same conclusion applies to the point-source detection in HD 85512 (epoch 2019-11-25). This companion candidate was not re-detected in the later epoch acquired with better observational conditions and in the same filter, either as a bound or background object, thereby we conclude this to be an artifact.

5.3. Results from proper motion anomaly and excess noise (*Gaia*-HIPPARCOS)

The *Gaia* and HIPPARCOS data were analyzed with the `GaiaPMEX` tool (Kiefer et al., in prep) to determine the possible mass and semi-major axis (sma, hereafter) of candidate companions within the selected systems using the proper motion anomaly (PMa, hereafter) from the Kervella et al. (2022) catalog and the `astrometric_excess_noise` (AEN, hereafter; for a definition see Lindegren et al. 2018 and Kiefer 2019) from the *Gaia* DR3 (Gaia Collaboration 2021).

In a nutshell, the `GaiaPMEX` tool models the AEN and PMa on a grid of possible mass and semi-major axis of a hypothetical companion orbiting the targeted star. It will be described in depth in Kiefer et al. (in prep.). For each (mass, sma)-node of the grid, all parameters, including e the eccentricity, ω the periastron longitude, Ω the longitude of ascending node, ϕ the phase, I the orbital inclination, $M_\star$ the stellar mass, and ϖ the parallax, are drawn randomly from prior-distributions shown in Table 5. Astrometric and spacecraft attitude noises (Lindegren et al. 2021), and other non-astrophysical jitters that participate to the generation of an AEN and a PMa, are estimated for the targeted stars given their G-mag, $G_{bp} - G_{rp}$ color, RA and DEC (Kiefer et al., in prep.). Table G.1 summarizes the parameters used for running `GaiaPMEX` for GJ 832 and GJ 229 the only two that led to a positive detection (see Sect. 5.3). Based on those parameters, the *Gaia* DR3 observations and the HIPPARCOS position at epoch J1991.25 of the targeted stars are simulated 1000 times per node, leading to theoretical distributions of AEN and PMa at all nodes. From those distributions, the likelihoods of the observed AEN and PMa are obtained and then further transformed into a posterior probability of the given companion mass and semi-major axis, through a Bayesian framework that will be thoroughly explained in Kiefer et al. (in prep.). Resulting posterior maps for the GJ 832 and GJ 229 companions are shown in Fig. 10, with the presence of a companion

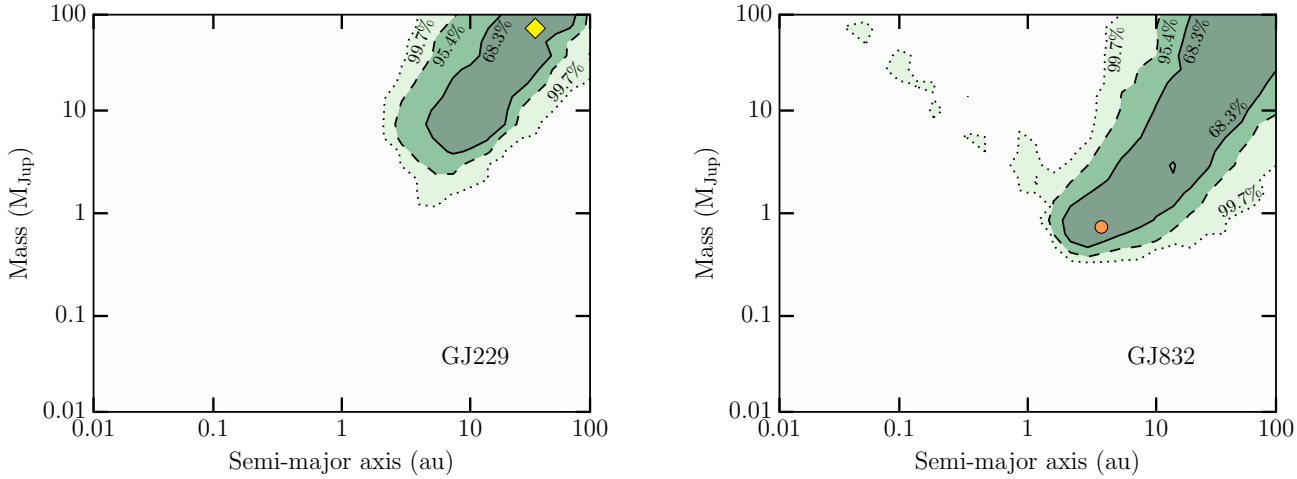

Fig. 10. Constraints derived on the presence of a substellar companion in the systems GJ 229 (left) and GJ 832 (right), by using the tool `GaiaPMEX` based on the proper motion anomaly and excess noise from *Gaia* and HIPPARCOS. The known massive companions are represented with the yellow diamond for GJ 229 B and the orange circle for GJ 832 b, consistent with the `GaiaPMEX` constraints.

Table 5. Distribution of parameters sampled at each tested bin of the mass – semi major axis ("sma") grid with the `GaiaPMEX` tool.

Parameter	Type	Bounds or law
$\log M_c$	Uniform	$\log M_c \pm \Delta \log M_c$
log sma	Uniform	log sma $\pm \Delta$ log sma
e	Uniform	[0, 0.9]
ω	Uniform	$[0, \pi]$
Ω	Uniform	$[0, 2\pi]$
ϕ	Uniform	[0, 1]
I_c	Uniform or sin i	$[0, \pi/2]$
ϖ	Normal	$\mathcal{N}(\mathrm{PLX}, \sigma^2_{\mathrm{PLX}})$
$M_\star$	Normal	$\mathcal{N}(M_\star, \sigma^2_{M_\star})$

Notes. "M_c" stands for the mass of the companion, other parameters are defined in Sect. 5.3.

at a significance of 8.8 σ and 51 σ, respectively, both consistent with objects already known: the radial velocity discovered Jovian planet GJ 832 b (Bailey et al. 2009) and the imaged brown dwarf GJ 229 B (Nakajima et al. 1995). The other systems from our survey do not show strong proper motion anomaly and/or excess noise (<2 σ).

5.4. Detection limits from direct imaging, radial velocity and proper motion anomaly and excess noise

Although we did not detect a new companion bound to its host star, we can set constraints on the presence of outer companions in the different systems.

Regarding our direct imaging observations, we used the evolutionary models `COND` (Baraffe et al. 2003), to convert our ANDROMEDA detection limit maps given in contrast relative to the host star into masses, both for SPHERE-IRDIS and SPHERE-IFS observations. This conversion depends in particular on the age of the system, as the older the system is, the fainter the companion in the near infrared, and thus the poorer is the mass sensitivity of direct imaging observations. However, mature systems are generally required for RV observations to be sensitive to low-mass planets, as the host stars must be stable enough.

We used our `MESS3` tool that can combine the available RV data with the high contrast imaging data and with the *Gaia*-HIPPARCOS data to derive the detection limits associated to each target (see Fig. 11). The `MESS3` tool is an extension of `MESS2`, described in Lannier et al. (2017) based on RV and high contrast imaging data. `MESS3`, as previous `MESS` versions, generates synthetic planets on a grid of semi-major axes and masses, with orbital parameters drawn from prior distributions, and it tests their detectability based on observations given as inputs. Direct imaging inputs are the detection limit maps expressed in terms of mass via evolutionary models. RV inputs are the RV time series that will be combined in `MESS3` with the local power analysis (LPA) approach described in Meunier et al. (2012) to assess planet detectability. Long-term trends do not count as detections, because only planets with periods lower than two times the time baseline are considered (Lannier et al. 2017). As for *Gaia* and HIPPARCOS inputs, these are detection limit maps based on the proper motion anomaly and *Gaia* astrometric excess noise.

From Figs. 11 and H.1, we have the following results: RV measurements are sensitive between 0.01 and 1 au to planets down to a few Earth-masses, between 1 and 5 au to giant planets down to about 30 Earth-masses (RV). *Gaia* and HIPPARCOS set constraints mainly between 0.1 and 30 au, down to about one Jupiter mass. Eventually, direct imaging observations provide constraints beyond 1 au down to mostly companions of 20 M_{Jup} (see Fig. 12), and in the most favorable systems, of a few Jupiter masses beyond a few astronomical units (GJ 433) or dozen of astronomical units (e.g., GJ 229, GJ 649, GJ 674, GJ 832), see Fig. H.2.

6. Discussion

We discuss our results using a generic approach in Sect. 6.1 by considering studies on other surveys and planet population models. In Sect. 6.2, we use an individual approach by looking into the intrinsic parameters of the planetary systems from our sample.

6.1. Comparison to theories and surveys

Our results do not contradict previous observational studies as we are sensitive to a different companion category, typically

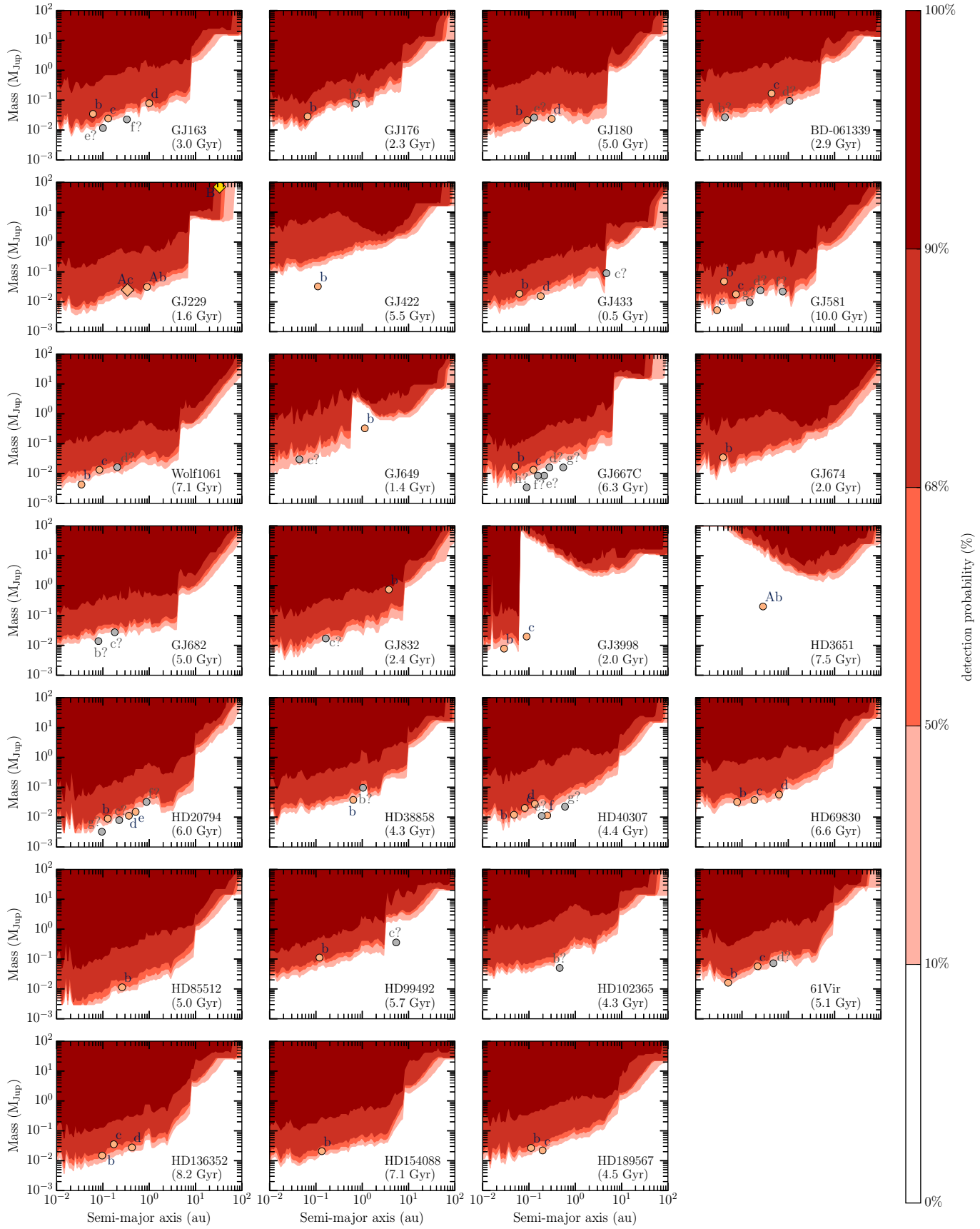

Fig. 11. Detection limits from RV (HARPS) + DI (SPHERE-IRDIS and SPHERE-IFS) + astrometric (*Gaia* and HIPPARCOS) data for the whole survey. Already known planets are overplotted in a filled orange (gray) circle if confirmed (unconfirmed). Although some planets seem beyond the reach of RV data, they were all detected with RV data (except the brown dwarf GJ 229 B) by using different RV instruments, whereas the limits plotted here only considered HARPS measurements.

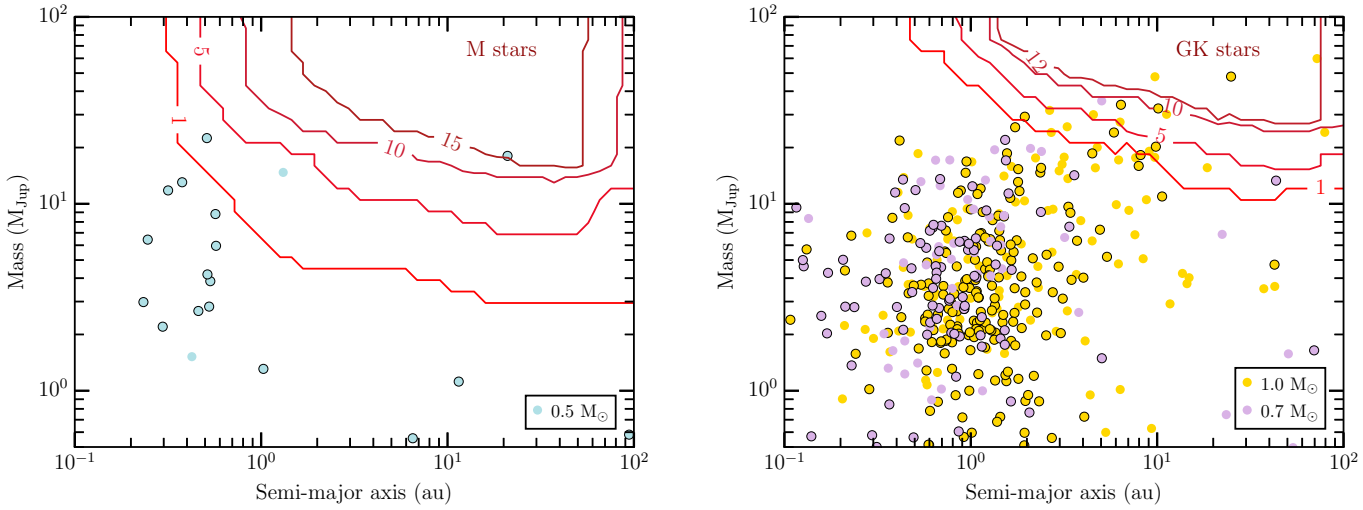

Fig. 12. Detection sensitivity of companions for our direct imaging SPHERE observations of 15 M-stars (left) and 12 GK-stars (right). The isocontours give the number of stars from our survey that have the sensitivity to detect companions at a probability of 50%. The theoretical population of companions formed via the Bern core-accretion models considering 1000 systems are indicated in circles of colors associated to stellar masses (Burn et al. 2021). These symbols have a black outline if the systems also host close-in (≤1 au) low-mass (≤95 $M_\oplus$) planets.

beyond 1 au and only massive objects (at least a few Jupiter-masses and mostly above 20 M_{Jup}, see Fig. 12). This survey is complementary, as RV measurements to date can only detect planets up to about a dozen of astronomical units, and only suggest trends for any planets further out.

Twelve of our systems are part of the survey from Bryan et al. (2019), and five from Zhu & Wu (2018), who both did not find additional distant giant planets in their analysis of RV measurements for these systems. We note that past RV studies have often been biased positively or negatively for systems hosting Jupiter-mass planets. In some RV surveys, the primary goal was to find Earth-like objects in the so-called habitable zone of their host star. Thus, if a massive giant planet was identified in the measurements, the RV-monitoring of the system would be stopped, because it would have been much more difficult to find an Earth-like planet. On the contrary, some other RV surveys would have kept the system and observed it more extensively. In the former case, the systems with small planets discovered so far with RV may be biased toward systems without giant planets easily accessible to RV measurements, and the contrary would happen in the latter case. Taking into account these biases in RV-monitored systems is challenging.

From a theoretical perspective, models of planetary population synthesis give predictions for the architectures of planetary systems based on current knowledge and in the limits of computational capacities. The New Generation Planetary Population Synthesis (NGPPS, Emsenhuber et al. 2021a), latest version of the Bern models, aim to be a comprehensive global end-to-end model of planetary system formation and evolution in the core-accretion framework. By coupling N-body interactions, internal structure calculations, and long-term thermodynamical evolution model, with the initial system parameters (e.g., stellar mass and metallicity, disk mass), the Bern models predict the architecture of planetary systems, and in particular physical and observable quantities for the planets at different ages. Based on these models, Schlecker et al. (2021) suggested a weak positive correlation between the presence of super-Earths and cold-Jupiters around Sun-like stars, but this correlation depends of the range of masses and periods defining each planet category, as also highlighted in Rosenthal et al. (2022) from their large RV survey. A more robust prediction of their study is the link between the composition of close-in super-Earths and the presence of an outer Jupiter-mass planet. If a distant giant planet is present, the inner super-Earth is denser, volatile-depleted. The formation of each category is driven by the disk mass, with both super-Earths and cold Jupiters forming preferentially in an intermediate mass disk.

Additional parameters influence the presence of a given type of planet, such as the stellar metallicity and stellar mass, or can give constraints on the presence of planets, as the multiplicity of planets investigated in Burn et al. (2021), the existence of debris disks (e.g., Marino et al. 2017; Pearce et al. 2022) or the stellar duplicity or multiplicity (e.g., Zucker & Mazeh 2002; Eggenberger et al. 2004; Fontanive et al. 2019). By using New Generation Planetary Population Synthesis (NGPPS) simulations, Burn et al. (2021) found that super-solar stellar metallicity ([Fe/H] > 0.1) favors the presence of sub giant (30–100 $M_\oplus$) and giant planets (>100 $M_\oplus$), in agreement with previous theoretical (Ida & Lin 2004) and observational (Valenti & Fischer 2005) studies. In addition, the more massive the star, the greater the fraction of systems with planets more massive than 2 $M_\oplus$. A striking result is the absence of formation of (sub) giant planet around 0.1 and 0.3 $M_\odot$-stars in the NGPPS simulations. Yet, Morales et al. (2019) discovered via RV with CARMENES observations two giant planets of minimal mass 0.46 ± 0.02 M_{Jup} and 0.20 ± 0.02 M_{Jup} around a 0.12 $M_\odot$ star in the system GJ 3512, and those exoplanets are confirmed by Lopez-Santiago et al. (2020). Another giant exoplanet of minimal mass 0.21 ± 0.02 M_{Jup} orbiting a 0.15 M_{Jup} star was recently discovered (Quirrenbach et al. 2022). This highlights the discrepancies still to be solved between theoretical predictions and observations, or the existence of alternative formation mechanisms (Schlecker et al. 2022).

By comparing the detection probabilities from our direct imaging observations obtained with `MESS3` (Fig. 12) to massive companions obtained in systems hosting close-in low-mass planets from Bern population models, we see that only a few of those companions are reachable by our observations. In more detail, we use the grids from Burn et al. (2021) synthesized for a population of 1000 planetary systems around a host star of 1.0 $M_\odot$,

0.7 $M_\odot$, 0.5 $M_\odot$, and 0.3 $M_\odot$, to match our sample. The Bern grids directly give the mass and semi-major axis of the planets of the 1000 systems at different ages. We consider the surviving planets at the age of 5 Gyr that are displayed in circles of different colors in Fig. 12, and we highlight the ones in systems hosting as well close-in ($\leq$1 au) low-mass ($\leq$95 $M_\oplus$) planets by circles with black outline. The more massive the star is, the greater the number of massive companions orbiting within a few astronomical units, as underlined in Burn et al. (2021). We can see that the best sensitivities in our survey are reached for M stars, i.e., low-mass stars (see Fig. H.2, e.g., GJ 433, GJ 674).

We computed the number of planets that these model predict should have been detected given our detection performance from the direct imaging SPHERE observations. For each system, we used the grid with the closest stellar mass, and at the corresponding age. This gives a probability of detecting at least one planet at a confidence level of 504 of 0.8% for the most favorable system (the solar-mass star HD 154088) from our sample, while the detection probability is 0% for the least favorable systems, corresponding mainly to low-mass stars, because Bern models do not form giant planets for such stars (Burn et al. 2021). Overall, this results in a probability of 3.7% to detect at least one massive distant planet in one of our systems at a confidence level of 50%. A more faithful comparison to our sample would be to look at theoretical predictions only for the planetary systems with close-in low-mass planets ($\lesssim$1 au, $\lesssim$95 $M_\oplus$). In this case, the detection performance for each system increases at best to 0.9% at a confidence level of 50%. On the whole, this results in a probability of 4.5% to detect at least one massive distant planet in one of our systems at a confidence level of 50%. The probabilities slightly increase with respect to planetary systems for which we do not assume that already close-in low-mass planet(s) exist. This is due to the weak positive correlation of inner low-mass planets and outer giant planets in the Bern models (Schlecker et al. 2021). Overall, the non-detection of a distant massive giant planet in our high-contrast imaging observations is compatible with predictions based on core-accretion models of planet formation. Nonetheless, we note that the formation of large planets and brown dwarfs could be enhanced by other formation pathways, such as gravitational disk instability (e.g., Boss 1997) or gravo-turbulent fragmentation (e.g., Padoan & Nordlund 2004), not discussed in this work.

Based on the sensitivity of our SPHERE observations to mostly brown dwarfs in the mature systems of our sample, and the biases of RV surveys disregarding systems with massive companions when looking for Earth-like planets, looking into the correlation between the presence of close-in small planets and outer massive companions is highly challenging. A detailed statistical study taking into account the observational biases, as well as the formation and evolution of planets and brown dwarfs from different pathways applied to different stellar types (Solar-like to M stars), from population or parametric models (e.g., Vigan et al. 2021) is beyond the scope of this paper, and could be addressed in a future work.

6.2. Constraints from intrinsic parameters of the planetary systems

In this section, we peer into the architecture of the planetary systems of our sample to get an insight on where we could expect additional companions. We first focus on the stellar parameters such as the stellar multiplicity, metallicity and mass, then on the presence of a debris disk, eventually on the multiplicity and eccentricity of the known planet(s).

From a larger point of view, we note that the stellar neighborhood can play a role to shape planetary systems, for instance with flyby events (Kalas 1996) consisting in an encounter between a given system and a perturber such as a star. In our sample, Bertini et al. (2023) reported that the systems HD 20794, HD 38858, and HD 69830 have experienced (or will) one to six flybys. The consequence of flyby events can be similar to the presence of a binary star and is described below.

6.2.1. Influence of the stellar duplicity or multiplicity

Since about 50% of Sun-like stars are part of binaries or higher-order multiple system, binaries cannot be neglected to have a complete picture of planet formation and evolution (e.g., Heintz 1969; Abt & Levy 1976; Duquennoy & Mayor 1991; Raghavan et al. 2010; Tokovinin 2014).

One of the key parameters is the separation of the two binary-components. Close binaries ($\lesssim$50–100 au) inhibit planet formation (e.g., Kraus et al. 2012, 2016; Wang et al. 2014; Bonavita & Desidera 2007, 2020). In the Milky Way, Kraus et al. (2016) reported that 20% of all the solar-type stars cannot host planetary systems owing to the influence of a binary companion. A relatively wide binary (about 100–1000 au) may impact the evolution of the planet via the high-eccentricity migration, as it may facilitate the planet's migration via dynamical interactions, by increasing its eccentricity until it undergoes circularization from the primary star (as could do flybys). This migration may be caused by Kozai-Lidov process (e.g., Fabrycky & Tremaine 2007; Naoz et al. 2012; Dong et al. 2014), but not only (Ngo et al. 2016). On the contrary, very wide binaries ($\gtrsim$1000 au) may not have consequences on planetary formation and evolution, as exoplanets in these systems have the same properties as the ones around single stars (Fontanive & Bardalez Gagliuffi 2021; Bonavita & Desidera 2007, 2020).

In this context, the outer wide (200–1000 au) binary dwarf or stellar companion in the systems HD 3651, HD 99492, and HD 102365 from our sample should not prevent the formation of planets, nor have a significant impact on the formation of giant exoplanets beyond $\gtrsim$0.5 au (Fontanive & Bardalez Gagliuffi 2021), but could influence their evolution. In particular, the binary dwarf HD 3651 B could explain the high eccentricity (0.63 ± 0.04, Fischer et al. 2003) of the close-in giant planet HD 3651 A b if induced via the high-eccentricity migration process mentioned previously. On the other hand, in spite of the proximity of the binary companion GJ 229 B to its host star ($33.3^{+0.4}_{-0.3}$ au), the small mass ratio (0.1, see dedicated paragraph in Appendix A) relative to GJ 229 A could explain the formation of small inner planets in the system, especially if the brown dwarf forming during the disk phase was on a circular orbit and inclined with respect to the disk (Cadman et al. 2022).

Regarding GJ 667 AB+C, the hierarchical triple stellar system in our sample, this has one central binary AB (semi-major axis of 13 au, total mass of 1.27 $M_\odot$), and a third star C of 0.35 $M_\odot$, located at a projected distance of 235 au (Delfosse et al. 2013; Söderhjelm 1999). The close binary GJ 667 AB can be treated dynamically as a single object and thus previous conclusions for binary systems hold for this system as well. Planet formation is not inhibited in triple systems, nor in GJ 667 or in others (e.g., Mugrauer et al. 2007a,b).

6.2.2. Influence of the stellar metallicity and mass

It is now well established observationally that the occurrence rate of a giant planet is strongly dependent on the stellar metallicity

(e.g., Fischer & Valenti 2003; Santos et al. 2004). The host star metallicity also increases with increasing planet mass or radius (e.g., Narang et al. 2018). These trends are often interpreted as a direct signature of the core accretion (Pollack et al. 1996) formation paradigm explained by a more massive and frequent core assembly at higher metallicities (e.g., Ida & Lin 2004; Bitsch et al. 2015; Ndugu et al. 2018; Emsenhuber et al. 2021b; Schlecker et al. 2021). This correlation however reverses for planet masses greater than 4–5 $M_{\rm Jup}$, as the averaged host star metallicity decreases with increasing planetary mass (Santos et al. 2017; Narang et al. 2018; Schlaufman 2018; Swastik et al. 2021). They suggest that this turn-over traces different formation pathways for super-Jupiter and brown dwarf companions. These companions with masses larger than 4–5 $M_{\rm Jup}$ would be formed by gravitational instability or even gravo-turbulent fragmentation. In our context, detection limits are mainly limited to these massive companions (see Fig. 12) and the metallicity of the stellar host probably has little impact on our chances of maximizing the discovery rate.

From radial velocity and transit surveys, it is also known that the giant planet occurrence rate increases approximately linearly with stellar mass from low-mass stars up to intermediate-mass stars (Johnson et al. 2010a; Ghezzi et al. 2018). The trend is also predicted by core accretion theory due to a more massive initial reservoir of solids available to their formation (Kennedy & Kenyon 2008b; Liu et al. 2019; Schlecker et al. 2022). For the low-mass stars in our sample, however, we expect a very low occurrence, almost null, of giant planets formed by core accretion (see Fig. 12). For solar-type stars, despite an increasing rate of giant planets formed by core accretion, our sensitivities degrade significantly and remain mainly sensitive to the population of super-Jupiters or brown dwarfs, here again preferably formed by gravitational instability or gravo-turbulent fragmentation and for which a universal distribution of the companion mass ratio, which is roughly flat (e.g., Reggiani & Meyer 2013), is expected.

6.2.3. Constraints from a debris disk

The presence of a debris belt is helpful to constrain the location and mass of putative planets in the system. Those planets may sculpt the belts, and/or stir them via secular interactions, in particular their edges.

In our sample, seven systems are known to harbour a debris disk: GJ 433, GJ 581, GJ 649, HD 20794, HD 38858, HD 69830, 61 Vir. The system HD 69830 is a specific case because there is no significant level of cool dust detected (e.g., Marshall et al. 2014), unlike the others. The existence of the hot belt in the mature HD 69830 system raised particular interests in the literature (see Appendix A), since it cannot be replenished, and may be explained by recent collisions between planetesimals (Wyatt et al. 2007, 2010; Heng & Tremaine 2010). A comparison of the four debris disks around GK stars (HD 69830, 61 Vir, HD 20794, and HD 38858) from our sample can be found in Kennedy et al. (2015), while the observations of the three debris disks around M stars (GJ 433, GJ 581, and GJ 649) are presented in Kennedy et al. (2018).

Pearce et al. (2022) provided constraints on the location and mass required for planets in four of our studied systems (GJ 581, GJ 649, HD 69830, and 61 Vir), by assuming the belts are sculpted or stirred by one or several planets. The outermost planet HD 69830 c (a = 0.63 au, $m \sin i$ = 18 $M_\oplus$) could have stirred and sculpted its disk, while GJ 649 b a = 1.1 au, $m \sin i$ = 0.33 $M_{\rm Jup}$) could have stirred its disk, and maybe sculpted it. Although, the outermost planets 61 Vir c (yet unconfirmed: a = 0.49 au, $m \sin i$ = 23 $M_\oplus$), and GJ 581 d (a = 0.074 au, $m \sin i$ = 5.7 $M_\oplus$) have in principle a minimal mass sufficient to sculpt their debris disk, they are located too far and inside of the belts for this sculpting to have been effective over the system ages. As a matter of fact, Marino et al. (2017) showed that a >10 $M_\oplus$ stirring planet in 61 Vir should be located between 10 and 20 au. In short, no giant planets are required to explain the single/multi-belt architecture in those four systems, even though such planets are not ruled out.

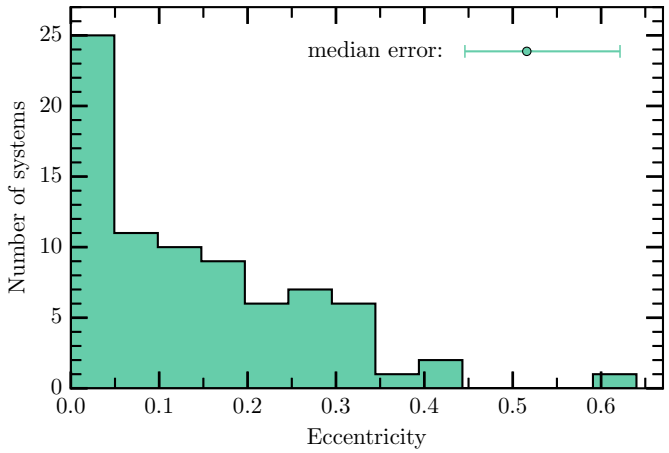

Fig. 13. Distribution of the eccentricity of the close-in (≲1 au) low-mass (≲95 $M_\oplus$) planets known in our sample. We indicate the median error in the upper right corner.

6.2.4. Influence of the planet multiplicity or eccentricity

From theoretical predictions, the multiplicity of small inner planets may be reduced by the presence of outer giant planet(s) in a given system (Schlecker et al. 2021; Bitsch & Izidoro 2023), also reported in a combined theoretical and observational analysis of the *Kepler* results from Hansen (2017), or tentatively from observations by Zhu & Wu (2018).

Figure 4 represents the distribution of the multiplicity of the known low-mass planets in our sample. All the systems have less than 3 low-mass planets confirmed, and a few up to 6 planets but with some controversy in the literature (see our review in Appendix A). In particular, the systems GJ 176, GJ 422, GJ 674, HD 154088 only host one close-in small mass planet so far, while in BD-061339 or HD 99492 a second companion is suggested but debated. Hence, this low-multiplicity may hint toward the presence of a yet to be discovered distant giant planet.

Furthermore, the eccentricity of known planets can help to constrain the presence of additional planets, as an eccentric orbit may result from scattering with another planet (e.g., Raymond et al. 2009). Thus, an eccentric close-in small planet may hint at the presence of an outer more massive companion (Bitsch et al. 2020; Bitsch & Izidoro 2023). In our sample, most planets have low to moderate eccentricities (see Fig. 13). The more eccentric confirmed low-mass planets are GJ 163 d (e = 0.41 ± 0.07, $m \sin i$ = 25 $M_\oplus$) and GJ 667 C c (e = 0.34 ± 0.10, $m \sin i$ = 4.25 $M_\oplus$). Even though both planets are part of multi-planetary systems, since GJ 163 hosts between 3 and 5 planets (of minimal masses ≤25 $M_\oplus$), while GJ 667 C between 2 and 7 (of minimal masses ≤7 $M_\oplus$), see Appendix A and Fig. 3, scattering events only between these small planets cannot explain the large observed eccentricity of GJ 163 d and GJ 667 C c. This would

require the presence of an outer giant planet (Bitsch & Izidoro 2023).

Conversely, if eccentric giant planets are not sufficiently dynamically separated from inner systems of low-mass planets, they may disrupt the latter. Both planetesimal and pebble accretion based formation models robustly predict this disruption, which becomes more likely the more eccentric, massive, and closer in the giant planet is Schlecker et al. (2021); Bitsch et al. (2020). Thus, we do not expect inner low-mass planets in the system HD 3651 ($e = 0.64 \pm 0.04$, $m \sin i = 0.20\ M_{\rm Jup}$, $a = 0.28$ au) even though the star has a slightly super-solar metallicity (0.08 ± 0.06) and is relatively massive ($0.86 \pm 0.06\ M_{\odot}$). In addition, this should also be unlikely in GJ 649 ($e = 0.30 \pm 0.08$, $m \sin i = 0.33\ M_{\rm Jup}$, $a = 1.14$ au) or BD-061339 ($e = 0.31 \pm 0.11$, $m \sin i = 0.17\ M_{\rm Jup}$, $a = 0.44$ au).

However, we note that there are observational biases in the estimation of planet eccentricities from RV measurements. Zakamska et al. (2011) reported that the eccentricity of single-planets may be overestimated, and that the conclusions of their analysis may be applied to multi-planet systems too. In addition, the RV signal of two circular planets can be confused with the RV signal of one eccentric planet (e.g., Wittenmyer et al. 2007, 2013; Anglada-Escudé et al. 2010). These biases depend on the quality of the RV measurements, their number and sampling. In any case, measuring the eccentricity at a given time period only gives partial information as the eccentricities of planets in multi-planet systems can oscillate through time owing to secular perturbations (e.g., Zakamska et al. 2011; Read & Wyatt 2016).

Regarding the systems in our sample, an in-depth study of secular perturbations can help to provide constraints on the presence of additional planets. For instance, Read & Wyatt (2016) showed that for the single planetary system HD 38858, the presence of an outer eccentric planet c is unlikely as secular perturbations would have excited the planet b which is known to have a circular orbit. If such an additional planet exists, it could point out to the presence of a third inner planet d, close to the HD 38858 b, that would stabilize it. Regarding two-planet systems, Read & Wyatt (2016) highlighted that it is complex to constrain deeply the presence of an outer eccentric planet based on secular interactions only, such as for the system 61 Vir, and that instead, the structure of an outer debris disk is more restrictive.

7. Conclusion and perspectives

We carried out a survey on 27 very nearby systems. Although all these systems are suspected to host at least one low (minimal) mass ($\lesssim 95\ M_{\oplus}$) planet orbiting on a small orbit (<1 au), they depict diverse planetary architectures: seven harbor a debris disk, five are part of a binary or triple hierarchical stellar system, and two host a brown dwarf companion beyond 10 au. In this work, we homogeneously derived target properties (age, stellar mass, stellar metallicity), processed data reduction and analyzed them. We also provide a complete review of the literature on each system in Appendix A.

Our main findings are as follows:

1. In the 47 epochs of observation in the near infrared with VLT/SPHERE-IRDIS and IFS published for the first time in this paper, we detected 337 point sources. We did not discover new bound companions even though 12 remain pending, as information is missing to conclude. We detected the already known brown dwarf GJ 229 B. We classified two companion candidates as instrumental artifacts, whereas the 328 others are classed as background stars based on analysis of their proper motion or location in a Color Magnitude Diagram.
2. By combining direct imaging (SPHERE), radial velocity (HARPS), and proper motion coupled to excess noise (*Gaia* and HIPPARCOS) observations, the existence of planets in each system is constrained down to a few Earth-masses between 0.01 and 1 au, down to about 30 $M_{\oplus}$ between 1 and 10 au, and down to about a dozen of Jupiter-masses beyond 10 au. Regarding the high-contrast imaging observations alone, we are sensitive down to 3 to 30 $M_{\rm Jup}$ beyond 0.5 or 2 au depending on the system.
3. Given these detection limits, our non-detection of new giant planets is consistent with state-of-the-art planet formation models following the core accretion paradigm (Burn et al. 2021).
4. If additional planets yet undiscovered exist in some systems of our sample, by examining the properties and architecture of each system, and previous work from the literature, we identified several particularly promising targets for follow-up. First, we could preferentially expect additional planets in GJ 163 and GJ 667C. Both systems have eccentric low-mass planets (0.41 ± 0.07 and 0.34 ± 0.10, respectively). The multiplicity of GJ 667 C should not have prevented the formation of massive planets as the two components GJ 667 AB and GJ 667 C are distant enough from each other ($\gtrsim$235 au). Second, we could expect additional planets in 61 Vir and GJ 581. By assuming the inner edge of the debris disk is sculpted by a planet, this would require a planet of $\gtrsim 19\ M_{\oplus}$ if located at 30 ± 10 au (61 Vir) or $\gtrsim 3.4\ M_{\oplus}$ if located at 14 ± 6 au (GJ 581). It would need to be more massive if the planet is closer-in (Pearce et al. 2022).

Very nearby planetary systems offer unique possibilities to couple direct imaging, radial velocity and astrometry from *Gaia* and HIPPARCOS. This is true not only across a system, but also for the coupled characterization of a single exoplanet. In the coming years, *Gaia* would hint for giant exoplanets with orbital periods up to about 10 yr, and direct imaging and interferometric instruments, such as for instance the future upgrades VLT/SPHERE+ (Boccaletti et al. 2020) and VLTI/GRAVITY+ (Eisenhauer 2019). They will be able to explore the population of massive giant planets down to the snowline expanding the current overlap between these techniques (but again mainly for the youngest systems). This is of utmost importance as different detection techniques provide diverse physical information on the exoplanet, and particularly a measurement of the dynamical mass, the luminosity and the atmospheric properties, which can help to constrain theoretical models of formation and evolution.

With this work, we have not answered our initial question set in the introduction concerning the correlation between close-in low-mass planets and giant outer planets. We however showed that, with the current state-of-the-art instrumentation, the high-contrast imaging detection limits are mainly sensitive to companions down to 20 $M_{\rm Jup}$ around mature stars. The question remains open from a direct imaging perspective, though radial velocity and transit studies seem to suggest a tentative positive correlation, that would require larger samples to be fully established. For the decades to come, the *James Webb* Space Telescope with the MIRI instrument or the forthcoming high-contrast imagers such as METIS (2030+) or PCS (2035+) on the ELT will pave the way for the imaging in thermal and/or reflected light, and the demographics characterization of more mature and smaller planets around very nearby stars.

Acknowledgements. C.D. and J.M. thank Lucile Mignon, Xavier Bonfils and Xavier Delfosse for constructive discussions on radial velocity data. C.D., J.M. and G.C. thank Faustine Cantalloube for sharing the ANDROMEDA pipeline with us to process the SPHERE data from this paper, and for useful discussions. C.D., J.M. and G.C. thank Clémence Fontanive for discussions on exoplanet demographics and multiple systems. C.D. and J.M. thank Pierre Kervella for his help on *Gaia* data. Last, C.D. is grateful to Mickaël Bonnefoy, Nadège Meunier, Nicolas Cuello, Melissa Hobson, and Aurélia Leclerc for fruitful discussions on this paper. This work has made use of the SPHERE Data Centre, jointly operated by OSUG/IPAG (Grenoble), PYTHEAS/LAM/CESAM (Marseille), OCA/Lagrange (Nice), Observatoire de Paris/LESIA (Paris), and Observatoire de Lyon. This work has made use of data from the European Space Agency (ESA) space mission *Gaia* (https://www.cosmos.esa.int/gaia), processed by the *Gaia* Data Processing and Analysis Consortium (DPAC). This work has been supported by a grant from Labex OSUG (Investissements d'avenir – ANR10 LABX56). This project has received funding from the European Research Council (ERC) under the European Union's Horizon 2020 research and innovation programme (COBREX; grant agreement n° 885593) C.D., T.H., R.B. acknowledge support from the European Research Council under the European Union's Horizon 2020 research and innovation program under grant agreement No. 832428-Origins. G.M.K. is supported by the Royal Society as a Royal Society University Research Fellow. The results reported herein benefited from collaborations and/or information exchange within the program "Alien Earths" (supported by the National Aeronautics and Space Administration under agreement No. 80NSSC21K0593) for NASA's Nexus for Exoplanet System Science (NExSS) research coordination network sponsored by NASA's Science Mission Directorate. B.B. thanks the European Research Council (ERC Starting Grant 757448-PAMDORA) for their financial support.

References

Absil, O., Marion, L., Ertel, S., et al. 2021, A&A, 651, A45
Abt, H. A., & Levy, S. G. 1976, ApJS, 30, 273
Affer, L., Micela, G., Damasso, M., et al. 2016, A&A, 593, A117
Alibert, Y., Baraffe, I., Benz, W., et al. 2006, A&A, 455, L25
Amara, A., & Quanz, S. P. 2012, MNRAS, 427, 948
Anglada-Escudé, G., López-Morales, M., & Chambers, J. E. 2010, ApJ, 709, 168
Anglada-Escudé, G., Arriagada, P., Vogt, S. S., et al. 2012, ApJ, 751, L16
Anglada-Escudé, G., Tuomi, M., Gerlach, E., et al. 2013, A&A, 556, A126
Angus, R., Aigrain, S., Foreman-Mackey, D., & McQuillan, A. 2015, MNRAS, 450, 1787
Arriagada, P., Anglada-Escudé, G., Butler, R. P., et al. 2013, ApJ, 771, 42
Asplund, M., Grevesse, N., Sauval, A. J., & Scott, P. 2009, ARA&A, 47, 481
Astudillo-Defru, N., Delfosse, X., Bonfils, X., et al. 2017a, A&A, 600, A13
Astudillo-Defru, N., Forveille, T., Bonfils, X., et al. 2017b, A&A, 602, A88
Bailey, J., Butler, R. P., Tinney, C. G., et al. 2009, ApJ, 690, 743
Baliunas, S., Sokoloff, D., & Soon, W. 1996, ApJ, 457, L99
Baluev, R. V. 2012, MNRAS, 429, 2052
Baraffe, I., Chabrier, G., Barman, T. S., Allard, F., & Hauschildt, P. H. 2003, A&A, 402, 701
Baratella, M., D'Orazi, V., Carraro, G., et al. 2020, A&A, 634, A34
Barbato, D., Sozzetti, A., Desidera, S., et al. 2018, A&A, 615, A175
Barbato, D., Pinamonti, M., Sozzetti, A., et al. 2020, A&A, 641, A68
Barnes, R., Jackson, B., Raymond, S. N., West, A. A., & Greenberg, R. 2009, ApJ, 695, 1006
Beichman, C. A., Bryden, G., Gautier, T. N., et al. 2005, ApJ, 626, 1061
Beichman, C. A., Bryden, G., Stapelfeldt, K. R., et al. 2006, ApJ, 652, 1674
Beichman, C. A., Lisse, C. M., Tanner, A. M., et al. 2011, ApJ, 743, 85
Bertini, L., Roccatagliata, V., & Kim, M. 2023, A&A, 671, L2
Best, S., Sefilian, A. A., & Petrovich, C. 2023, ApJ, submitted, [arXiv:2304.02045]
Beuzit, J. L., Vigan, A., Mouillet, D., et al. 2019, A&A, 631, A155
Bitsch, B., & Izidoro, A. 2023, A&A, 674, A178
Bitsch, B., Johansen, A., Lambrechts, M., & Morbidelli, A. 2015, A&A, 575, A28
Bitsch, B., Trifonov, T., & Izidoro, A. 2020, A&A, 643, A66
Boccaletti, A., Chauvin, G., Mouillet, D., et al. 2020, arXiv e-prints [arXiv:2003.05714]
Bonavita, M., & Desidera, S. 2007, A&A, 468, 721
Bonavita, M., & Desidera, S. 2020, Galaxies, 8, 16
Bonfanti, A., Ortolani, S., & Nascimbeni, V. 2016, A&A, 585, A5
Bonfils, X., Forveille, T., Delfosse, X., et al. 2005, A&A, 443, L15
Bonfils, X., Mayor, M., Delfosse, X., et al. 2007, A&A, 474, 293
Bonfils, X., Delfosse, X., Udry, S., et al. 2013a, A&A, 549, A109
Bonfils, X., Lo Curto, G., Correia, A. C. M., et al. 2013b, A&A, 556, A110
Bonomo, A. S., Dumusque, X., Massa, A., et al. 2023, A&A, 677, A33
Boro Saikia, S., Marvin, C. J., Jeffers, S. V., et al. 2018, A&A, 616, A108
Boss, A. P. 1997, Science, 276, 1836
Brandt, T. D., Dupuy, T. J., Bowler, B. P., et al. 2020, AJ, 160, 196
Brandt, G. M., Dupuy, T. J., Li, Y., et al. 2021, AJ, 162, 301
Brasser, R., Ida, S., & Kokubo, E. 2014, MNRAS, 440, 3685
Brewer, J. M., Fischer, D. A., Blackman, R. T., et al. 2020, AJ, 160, 67
Bryan, M. L., Knutson, H. A., Lee, E. J., et al. 2019, AJ, 157, 52
Bryden, G., Beichman, C. A., Trilling, D. E., et al. 2006, ApJ, 636, 1098
Bryden, G., Beichman, C. A., Carpenter, J. M., et al. 2009, ApJ, 705, 1226
Buchschacher, N., Ségransan, D., Udry, S., & Díaz, R. 2015, ASP Conf. Ser., 495, 7
Burgasser, A. J. 2007, ApJ, 658, 617
Burn, R., Schlecker, M., Mordasini, C., et al. 2021, A&A, 656, A72
Butler, R. P., Tinney, C. G., Marcy, G. W., et al. 2001, ApJ, 555, 410
Butler, R. P., Howard, A. W., Vogt, S. S., & Wright, J. T. 2009, ApJ, 691, 1738
Cadman, J., Hall, C., Fontanive, C., & Rice, K. 2022, MNRAS, 511, 457
Cantalloube, F., Mouillet, D., Mugnier, L. M., et al. 2015, A&A, 582, A89
Casagrande, L., & VandenBerg, D. A. 2014, MNRAS, 444, 392
Casagrande, L., & VandenBerg, D. A. 2018, MNRAS, 475, 5023
Casagrande, L., Schönrich, R., Asplund, M., et al. 2011, A&A, 530, A138
Casagrande, L., Lin, J., Rains, A. D., et al. 2021, MNRAS, 507, 2684
Chiang, E., & Laughlin, G. 2013, MNRAS, 431, 3444
Claudi, R. U., Turatto, M., Gratton, R. G., et al. 2008, SPIE Conf. Ser., 7014, 701401
Cosentino, R., Lovis, C., Pepe, F., et al. 2012, SPIE Conf. Ser., 8446, 84461V
Crane, J. D., Shectman, S. A., & Butler, R. P. 2006, SPIE Conf. Ser., 6269, 626931
Crane, J. D., Shectman, S. A., Butler, R. P., Thompson, I. B., & Burley, G. S. 2008, SPIE Conf. Ser., 7014, 701479
Crane, J. D., Shectman, S. A., Butler, R. P., et al. 2010, SPIE Conf. Ser., 7735, 773553
Cumming, A., Butler, R. P., Marcy, G. W., et al. 2008, PASP, 120, 531
Díaz, R. F., Ségransan, D., Udry, S., et al. 2016, A&A, 585, A134
Dekker, H., D'Odorico, S., Kaufer, A., Delabre, B., & Kotzlowski, H. 2000, SPIE Conf. Ser., 4008, 534
Delfosse, X., Bonfils, X., Forveille, T., et al. 2013, A&A, 553, A8
Delorme, P., Meunier, N., Albert, D., et al. 2017, in SF2A-2017: Proceedings of the Annual meeting of the French Society of Astronomy and Astrophysics, eds. C. Reylé, P. Di Matteo, & F. Herpin, et al., 347
Delrez, L., Ehrenreich, D., Alibert, Y., et al. 2021, Nat. Astron., 5, 775
Diego, F., Charalambous, A., Fish, A. C., & Walker, D. D. 1990, SPIE Conf. Ser., 1235, 562
Dietrich, J. & Ginski, C. 2018, A&A, 620, A102
Díez Alonso, E., Caballero, J. A., Montes, D., et al. 2019, A&A, 621, A126
Dohlen, K., Langlois, M., Saisse, M., et al. 2008, Proc. SPIE, 7014, 70143L
Dong, S., Katz, B., & Socrates, A. 2014, ApJ, 781, L5
D'Orazi, V., Oliva, E., Bragaglia, A., et al. 2020, A&A, 633, A38
Duncan, D. K., Vaughan, A. H., Wilson, O. C., et al. 1991, ApJS, 76, 383
Duquennoy, A., & Mayor, M. 1991, A&A, 248, 485
Eggenberger, A., Udry, S., & Mayor, M. 2004, A&A, 417, 353
Eisenhauer, F. 2019, The Very Large Telescope in 2030, 30
Emsenhuber, A., Mordasini, C., Burn, R., et al. 2021a, A&A, 656, A69
Emsenhuber, A., Mordasini, C., Burn, R., et al. 2021b, A&A, 656, A70
Endl, M., Cochran, W. D., Wittenmyer, R. A., & Boss, A. P. 2008, ApJ, 673, 1165
Engle, S. G., & Guinan, E. F. 2011, ASP Conf. Ser., 451, 285
Ertel, S., Absil, O., Defrère, D., et al. 2014, A&A, 570, A128
Ertel, S., Defrère, D., Absil, O., et al. 2016, A&A, 595, A44
Evans, D. S., Menzies, A., & Stoy, R. H. 1957, MNRAS, 117, 534
Fabrycky, D., & Tremaine, S. 2007, ApJ, 669, 1298
Faherty, J. K., Burgasser, A. J., Walter, F. M., et al. 2012, ApJ, 752, 56
Fedrigo, E., Donaldson, R., Soenke, C., et al. 2006, SPIE Conf. Ser., 6272, 627210
Feng, F., Tuomi, M., & Jones, H. R. A. 2017, A&A, 605, A103
Feng, F., Butler, R. P., Shectman, S. A., et al. 2020, ApJS, 246, 11
Feng, F., Butler, R. P., Vogt, S. S., et al. 2022, ApJS, 262, 21
Fischer, D. A., & Valenti, J. A. 2003, ASP Conf. Ser., 294, 117
Fischer, D. A., Butler, R. P., Marcy, G. W., Vogt, S. S., & Henry, G. W. 2003, ApJ, 590, 1081
Fontanive, C., & Bardalez Gagliuffi, D. 2021, Front. Astron. Space Sci., 8, 16
Fontanive, C., Rice, K., Bonavita, M., et al. 2019, MNRAS, 485, 4967
Forveille, T., Bonfils, X., Delfosse, X., et al. 2009, A&A, 493, 645
Forveille, T., Bonfils, X., Delfosse, X., et al. 2011, arXiv e-prints [arXiv:1109.2505]
Fossati, L., Kochukhov, O., Jenkins, J. S., et al. 2013, A&A, 551, A85
France, K., Froning, C. S., Linsky, J. L., et al. 2013, ApJ, 763, 149
Froning, C. S., Kowalski, A., France, K., et al. 2019, ApJ, 871, L26
Fulton, B. J., Petigura, E. A., Howard, A. W., et al. 2017, AJ, 154, 109

Gaia Collaboration 2020, VizieR Online Data Catalog: I/350
Gaia Collaboration (Brown, A. G. A., et al.) 2021, A&A, 649, A1
Gaia Collaboration (Arenou, F., et al.) 2023, A&A, 674, A34
Gaidos, E., Mann, A. W., Lépine, S., et al. 2014, MNRAS, 443, 2561
Galicher, R., Boccaletti, A., Mesa, D., et al. 2018, A&A, 615, A92
Geballe, T. R., Knapp, G. R., Leggett, S. K., et al. 2002, ApJ, 564, 466
Ghezzi, L., Montet, B. T., & Johnson, J. A. 2018, ApJ, 860, 109
Giacobbe, P., Benedetto, M., Damasso, M., et al. 2020, MNRAS, 491, 5216
Gomes da Silva, J., Santos, N. C., Bonfils, X., et al. 2011, A&A, 534, A30
Gomes da Silva, J., Santos, N. C., Boisse, I., Dumusque, X., & Lovis, C. 2014, A&A, 566, A66
Gondoin, P. 2020, A&A, 641, A110
Gorrini, P., Astudillo-Defru, N., Dreizler, S., et al. 2022, A&A, 664, A64
Gray, R. O., Corbally, C. J., Garrison, R. F., McFadden, M. T., & Robinson, P. E. 2003, AJ, 126, 2048
Gray, R. O., Corbally, C. J., Garrison, R. F., et al. 2006, AJ, 132, 161
Gustafsson, B., Edvardsson, B., Eriksson, K., et al. 2008, A&A, 486, 951
Hansen, B. M. S. 2017, MNRAS, 467, 1531
Hara, N. C., Delisle, J.-B., Unger, N., & Dumusque, X. 2022, A&A, 658, A177
Hatzes, A. P. 2016, A&A, 585, A144
Hawley, S. L., Gizis, J. E., & Reid, I. N. 1996, AJ, 112, 2799
Heintz, W. D. 1969, JRASC, 63, 275
Heng, K. 2011, MNRAS, 415, 3365
Heng, K., & Tremaine, S. 2010, MNRAS, 401, 867
Henry, T. J., Soderblom, D. R., Donahue, R. A., & Baliunas, S. L. 1996, AJ, 111, 439
Henry, T. J., Walkowicz, L. M., Barto, T. C., & Golimowski, D. A. 2002, AJ, 123, 2002
Herrero, A., Garcia, M., Puls, J., et al. 2012, A&A, 543, A85
Hojjatpanah, S., Figueira, P., Santos, N. C., et al. 2019, A&A, 629, A80
Houdebine, E. R., Mullan, D. J., Bercu, B., Paletou, F., & Gebran, M. 2017, ApJ, 837, 96
Ida, S., & Lin, D. N. C. 2004, ApJ, 616, 567
Ingersoll, A. P. 1969, J. Atmos. Sci., 26, 1191
Isaacson, H., & Fischer, D. 2010, ApJ, 725, 875
Izidoro, A., Raymond, S. N., Morbidelli, A., Hersant, F., & Pierens, A. 2015, ApJ, 800, L22
Jenkins, J. S., Jones, H. R. A., Tinney, C. G., et al. 2006, MNRAS, 372, 163
Ji, J., Kinoshita, H., Liu, L., & Li, G. 2007, ApJ, 657, 1092
Johnson, J. A., Aller, K. M., Howard, A. W., & Crepp, J. R. 2010a, PASP, 122, 905
Johnson, J. A., Howard, A. W., Marcy, G. W., et al. 2010b, PASP, 122, 149
Joy, A. H., & Abt, H. A. 1974, ApJS, 28, 1
Kalas, P. G. 1996, PhD thesis, Max-Planck-Institute for Astronomy, Germany
Kane, S. R., Thirumalachari, B., Henry, G. W., et al. 2016, ApJ, 820, L5
Kane, S. R., von Braun, K., Henry, G. W., et al. 2017, ApJ, 835, 200
Kane, S. R., Yalçınkaya, S., Osborn, H. P., et al. 2020, AJ, 160, 129
Kasting, J. F. 1988, Icarus, 74, 472
Katsova, M. M., & Livshits, M. A. 2011, Astron. Rep., 55, 1123
Keenan, P. C., & McNeil, R. C. 1989, ApJS, 71, 245
Kennedy, G. M., & Kenyon, S. J. 2008a, ApJ, 682, 1264
Kennedy, G. M., & Kenyon, S. J. 2008b, ApJ, 673, 502
Kennedy, G. M., Matrà, L., Marmier, M., et al. 2015, MNRAS, 449, 3121
Kennedy, G. M., Bryden, G., Ardila, D., et al. 2018, MNRAS, 476, 4584
Kervella, P., Arenou, F., Mignard, F., et al. 2019, Mem. Soc. Astron. It., 90, 340
Kervella, P., Arenou, F., & Thévenin, F. 2022, A&A, 657, A7
Kiefer, F. 2019, A&A, 632, L9
Kiraga, M., & Stepien, K. 2007, Acta Astron., 57, 149
Krasinsky, G. A., Pitjeva, E. V., Vasilyev, M. V., & Yagudina, E. I. 2002, Icarus, 158, 98
Kraus, A. L., Ireland, M. J., Hillenbrand, L. A., & Martinache, F. 2012, ApJ, 745, 19
Kraus, A. L., Ireland, M. J., Huber, D., Mann, A. W., & Dupuy, T. J. 2016, AJ, 152, 8
Krist, J. E., Stapelfeldt, K. R., Bryden, G., & Plavchan, P. 2012, AJ, 144, 45
Lafrenière, D., Marois, C., Doyon, R., Nadeau, D., & Artigau, É. 2007, ApJ, 660, 770
Lannier, J., Lagrange, A. M., Bonavita, M., et al. 2017, A&A, 603, A54
Lecavelier Des Etangs, A. 2007, A&A, 461, 1185
Leconte, J., Forget, F., Charnay, B., et al. 2013, A&A, 554, A69
Leggett, S. K. 1992, ApJS, 82, 351
Lestrade, J. F., Matthews, B. C., Sibthorpe, B., et al. 2012, A&A, 548, A86
Lind, K., Asplund, M., Barklem, P. S., & Belyaev, A. K. 2011, A&A, 528, A103
Lindegren, L., Hernández, J., Bombrun, A., et al. 2018, A&A, 616, A2
Lindegren, L., Klioner, S. A., Hernández, J., et al. 2021, A&A, 649, A2
Line, M. R., Teske, J., Burningham, B., Fortney, J. J., & Marley, M. S. 2015, ApJ, 807, 183
Lisse, C. M., Beichman, C. A., Bryden, G., & Wyatt, M. C. 2007, ApJ, 658, 584
Liu, M. C., Leggett, S. K., & Chiu, K. 2007, ApJ, 660, 1507
Liu, B., Lambrechts, M., Johansen, A., & Liu, F. 2019, A&A, 632, A7
Lo Curto, G., Mayor, M., Benz, W., et al. 2013, A&A, 551, A59
Lo Curto, G., Pepe, F., Avila, G., et al. 2015, The Messenger, 162, 9
Lopez-Santiago, J., Martino, L., Míguez, J., & Vázquez, M. A. 2020, AJ, 160, 273
Lovis, C., Mayor, M., Pepe, F., et al. 2006, Nature, 441, 305
Lovis, C., Dumusque, X., Santos, N. C., et al. 2011, arXiv e-prints [arXiv:1107.5325]
Lovos, F. V., Díaz, R. F., & Nieto, L. A. 2022, A&A, 665, A157
Luhman, K. L., Patten, B. M., Marengo, M., et al. 2007, ApJ, 654, 570
Luna, S. H., Melita, M. D., & Navone, H. D. 2016, Boletin de la Asociacion Argentina de Astronomia La Plata Argentina, 58, 310
Maire, A.-L., Langlois, M., Dohlen, K., et al. 2016, SPIE Conf. Ser., 9908, 990834
Maire, A. L., Chauvin, G., Vigan, A., et al. 2021, The Messenger, 183, 7
Maldonado, J., Micela, G., Baratella, M., et al. 2020, A&A, 644, A68
Mamajek, E. E., & Hillenbrand, L. A. 2008, ApJ, 687, 1264
Marcy, G. W., Butler, R. P., Vogt, S. S., et al. 2005, ApJ, 619, 570
Marino, S., Wyatt, M. C., Kennedy, G. M., et al. 2017, MNRAS, 469, 3518
Marois, C., Lafrenière, D., Doyon, R., Macintosh, B., & Nadeau, D. 2006, ApJ, 641, 556
Marsden, S. C., Petit, P., Jeffers, S. V., et al. 2014, MNRAS, 444, 3517
Marshall, J. P., Moro-Martín, A., Eiroa, C., et al. 2014, A&A, 565, A15
Mayor, M., Bonfils, X., Forveille, T., et al. 2009a, A&A, 507, 487
Mayor, M., Udry, S., Lovis, C., et al. 2009b, A&A, 493, 639
Mayor, M., Marmier, M., Lovis, C., et al. 2011, arXiv e-prints [arXiv:1109.2497]
Mesa, D., Gratton, R., Zurlo, A., et al. 2015, A&A, 576, A121
Meschiari, S., Laughlin, G., Vogt, S. S., et al. 2011, ApJ, 727, 117
Meunier, N., Lagrange, A. M., & De Bondt, K. 2012, A&A, 545, A87
Meunier, N., Lagrange, A. M., Mbemba Kabuiku, L., et al. 2017, A&A, 597, A52
Miller, B. P., Gallo, E., Wright, J. T., & Pearson, E. G. 2015, ApJ, 799, 163
Morales, J. C., Mustill, A. J., Ribas, I., et al. 2019, Science, 365, 1441
Morbidelli, A., Bitsch, B., Crida, A., et al. 2016, Icarus, 267, 368
Muñoz, D. J., Lai, D., & Liu, B. 2016, MNRAS, 460, 1086
Mugrauer, M., Seifahrt, A., Neuhäuser, R., & Mazeh, T. 2006, MNRAS, 373, L31
Mugrauer, M., Neuhäuser, R., & Mazeh, T. 2007a, A&A, 469, 755
Mugrauer, M., Seifahrt, A., & Neuhäuser, R. 2007b, MNRAS, 378, 1328
Mugnier, L. M., Cornia, A., Sauvage, J.-F., et al. 2009, J. Opt. Soc. Am. A, 26, 1326
Mustill, A. J., & Wyatt, M. C. 2009, MNRAS, 399, 1403
Nagasawa, M., Lin, D. N. C., & Thommes, E. 2005, ApJ, 635, 578
Nakajima, T., Oppenheimer, B. R., Kulkarni, S. R., et al. 1995, Nature, 378, 463
Naoz, S., Farr, W. M., & Rasio, F. A. 2012, ApJ, 754, L36
Narang, M., Manoj, P., Furlan, E., et al. 2018, AJ, 156, 221
Ndugu, N., Bitsch, B., & Jurua, E. 2018, MNRAS, 474, 886
Ngo, H., Knutson, H. A., Hinkley, S., et al. 2016, ApJ, 827, 8
Oelkers, R. J., Rodriguez, J. E., Stassun, K. G., et al. 2018, AJ, 155, 39
Padoan, P., & Nordlund, Å. 2004, ApJ, 617, 559
Papaloizou, J. C. B., & Terquem, C. 2010, MNRAS, 405, 573
Passegger, V. M., Schweitzer, A., Shulyak, D., et al. 2019, A&A, 627, A161
Pavlov, A., Möller-Nilsson, O., Feldt, M., et al. 2008, Proc. SPIE, 7019, 701939
Payne, M. J., Ford, E. B., Wyatt, M. C., & Booth, M. 2009, MNRAS, 393, 1219
Peacock, S., Barman, T., Shkolnik, E. L., et al. 2019, ApJ, 886, 77
Pearce, T. D., Launhardt, R., Ostermann, R., et al. 2022, A&A, 659, A135
Pepe, F., Lovis, C., Ségransan, D., et al. 2011, A&A, 534, A58
Petit, C., Sauvage, J.-F., Fusco, T., et al. 2014, Proc. SPIE, 9148, 91480O
Pollack, J. B., Hubickyj, O., Bodenheimer, P., et al. 1996, Icarus, 124, 62
Quirrenbach, A., Passegger, V. M., Trifonov, T., et al. 2022, A&A, 663, A48
Racine, R., Walker, G. A. H., Nadeau, D., Doyon, R., & Marois, C. 1999, PASP, 111, 587
Radick, R. R., Lockwood, G. W., Henry, G. W., Hall, J. C., & Pevtsov, A. A. 2018, ApJ, 855, 75
Raghavan, D., McAlister, H. A., Henry, T. J., et al. 2010, ApJS, 190, 1
Ramírez, I., Meléndez, J., Bean, J., et al. 2014, A&A, 572, A48
Ramsey, L. W., Adams, M. T., Barnes, T. G., et al. 1998, SPIE Conf. Ser., 3352, 34
Raymond, S. N., Armitage, P. J., & Gorelick, N. 2009, ApJ, 699, L88
Read, M. J., & Wyatt, M. C. 2016, MNRAS, 457, 465
Reggiani, M., & Meyer, M. R. 2013, A&A, 553, A124
Robertson, P., Mahadevan, S., Endl, M., & Roy, A. 2014, Science, 345, 440
Robertson, P., Endl, M., Henry, G. W., et al. 2015, ApJ, 801, 79
Rocha-Pinto, H. J., Flynn, C., Scalo, J., et al. 2004, A&A, 423, 517
Rosenthal, L. J., Knutson, H. A., Chachan, Y., et al. 2022, ApJS, 262, 1
Saar, S. H., & Osten, R. A. 1997, MNRAS, 284, 803
Santos, N. C., Israelian, G., & Mayor, M. 2004, A&A, 415, 1153

Santos, N. C., Sousa, S. G., Mortier, A., et al. 2013, A&A, 556, A150
Santos, N. C., Adibekyan, V., Figueira, P., et al. 2017, A&A, 603, A30
Schlaufman, K. C. 2014, ApJ, 790, 91
Schlaufman, K. C. 2018, ApJ, 853, 37
Schlecker, M., Mordasini, C., Emsenhuber, A., et al. 2021, A&A, 656, A71
Schlecker, M., Burn, R., Sabotta, S., et al. 2022, A&A, 664, A180
Schlecker, M., Apai, D., Lichtenberg, T., et al. 2023, arXiv e-prints [arXiv:2309.04518]
Simpson, E. R., Fetherolf, T., Kane, S. R., et al. 2022, AJ, 163, 215
Smith, R., Wyatt, M. C., & Haniff, C. A. 2009, A&A, 503, 265
Sneden, C. A. 1973, PhD thesis, The University of Texas at Austin, USA
Söderhjelm, S. 1999, A&A, 341, 121
Soummer, R., Pueyo, L., & Larkin, J. 2012, ApJ, 755, L28
Sousa, S. G., Santos, N. C., Mayor, M., et al. 2008, A&A, 487, 373
Sousa, S. G., Santos, N. C., Adibekyan, V., Delgado-Mena, E., & Israelian, G. 2015, A&A, 577, A67
Sparks, W. B., Ford, H. C., Krist, J., Clampin, M., & Golimowski, D. 2002, AAS Meeting Abstracts, 201, 21.03
Stephenson, C. B. 1986, AJ, 92, 139
Suárez Mascareño, A., Rebolo, R., González Hernández, J. I., & Esposito, M. 2015, MNRAS, 452, 2745
Suárez Mascareño, A., Rebolo, R., & González Hernández, J. I. 2016, A&A, 595, A12
Suárez Mascareño, A., Rebolo, R., González Hernández, J. I., & Esposito, M. 2017, MNRAS, 468, 4772
Swastik, C., Banyal, R. K., Narang, M., et al. 2021, AJ, 161, 114
Takeda, G., Ford, E. B., Sills, A., et al. 2007, ApJS, 168, 297
Tanner, A., Boyajian, T. S., von Braun, K., et al. 2015, ApJ, 800, 115
Terquem, C., & Papaloizou, J. C. B. 2007, ApJ, 654, 1110
Tilipman, D., Vieytes, M., Linsky, J. L., Buccino, A. P., & France, K. 2021, ApJ, 909, 61
Tinney, C. G., Butler, R. P., Jones, H. R. A., et al. 2011, ApJ, 727, 103
Tokovinin, A. 2014, AJ, 147, 86
Trifonov, T., Kürster, M., Zechmeister, M., et al. 2018, A&A, 609, A117
Tull, R. G. 1998, SPIE Conf. Ser., 3355, 387
Tuomi, M. 2011, A&A, 528, L5
Tuomi, M. 2014, MNRAS, 440, L1
Tuomi, M., & Anglada-Escudé, G. 2013, A&A, 556, A111
Tuomi, M., Anglada-Escudé, G., Gerlach, E., et al. 2013, A&A, 549, A48
Tuomi, M., Jones, H. R. A., Barnes, J. R., Anglada-Escudé, G., & Jenkins, J. S. 2014, MNRAS, 441, 1545
Turbet, M., Ehrenreich, D., Lovis, C., Bolmont, E., & Fauchez, T. 2019, A&A, 628, A12
Turbet, M., Bolmont, E., Ehrenreich, D., et al. 2020, A&A, 638, A41
Udry, S., Bonfils, X., Delfosse, X., et al. 2007, A&A, 469, L43
Udry, S., Dumusque, X., Lovis, C., et al. 2019, A&A, 622, A37
Unger, N., Díaz, R. F., Segránsan, D., Delisle, J. B., & Hara, N. 2020, Boletin de la Asociacion Argentina de Astronomia La Plata Argentina, 61B, 27
Unger, N., Ségransan, D., Queloz, D., et al. 2021, A&A, 654, A104
Valenti, J. A., & Fischer, D. A. 2005, ApJS, 159, 141
van Biesbroeck, G. 1961, AJ, 66, 528
Veyette, M. J., & Muirhead, P. S. 2018, ApJ, 863, 166
Vican, L. 2012, AJ, 143, 135
Vidotto, A. A., Gregory, S. G., Jardine, M., et al. 2014, MNRAS, 441, 2361
Vidotto, A. A., Feeney, N., & Groh, J. H. 2019, MNRAS, 488, 633
Vigan, A., Moutou, C., Langlois, M., et al. 2010, MNRAS, 407, 71
Vigan, A., Fontanive, C., Meyer, M., et al. 2021, A&A, 651, A72
Vogt, S. S. 1987, PASP, 99, 1214
Vogt, S. S., Allen, S. L., Bigelow, B. C., et al. 1994, SPIE Conf. Ser., 2198, 362
Vogt, S. S., Butler, R. P., Rivera, E. J., et al. 2010a, ApJ, 723, 954
Vogt, S. S., Wittenmyer, R. A., Butler, R. P., et al. 2010b, ApJ, 708, 1366
von Braun, K., Boyajian, T. S., Kane, S. R., et al. 2011, ApJ, 729, L26
von Braun, K., Boyajian, T. S., & van Belle, G. T. 2013, EAS Pub. Ser., 64, 429
von Braun, K., Boyajian, T. S., van Belle, G. T., et al. 2014, MNRAS, 438, 2413
Wang, J., Xie, J.-W., Barclay, T., & Fischer, D. A. 2014, ApJ, 783, 4
Ward-Duong, K., Patience, J., De Rosa, R. J., et al. 2015, MNRAS, 449, 2618
Wittenmyer, R. A., Endl, M., Cochran, W. D., & Levison, H. F. 2007, AJ, 134, 1276
Wittenmyer, R. A., Wang, S., Horner, J., et al. 2013, ApJS, 208, 2
Wittenmyer, R. A., Tuomi, M., Butler, R. P., et al. 2014, ApJ, 791, 114
Wittenmyer, R. A., Butler, R. P., Tinney, C. G., et al. 2016, ApJ, 819, 28
Wright, J. T., Marcy, G. W., Butler, R. P., & Vogt, S. S. 2004, ApJS, 152, 261
Wright, N. J., Drake, J. J., Mamajek, E. E., & Henry, G. W. 2011, ApJ, 743, 48
Wright, D. J., Wittenmyer, R. A., Tinney, C. G., Bentley, J. S., & Zhao, J. 2016, ApJ, 817, L20
Wyatt, M. C., Smith, R., Greaves, J. S., et al. 2007, ApJ, 658, 569
Wyatt, M. C., Booth, M., Payne, M. J., & Churcher, L. J. 2010, MNRAS, 402, 657
Wyatt, M. C., Kennedy, G., Sibthorpe, B., et al. 2012, MNRAS, 424, 1206
Yee, S. W., Petigura, E. A., & von Braun, K. 2017, ApJ, 836, 77
Yuan-Yuan, C., Ji-Lin, Z., & Yue-Hua, M. 2014, arXiv e-prints [arXiv:1408.4228]
Zakamska, N. L., Pan, M., & Ford, E. B. 2011, MNRAS, 410, 1895
Zechmeister, M., Kürster, M., & Endl, M. 2009, A&A, 505, 859
Zechmeister, M., Kürster, M., Endl, M., et al. 2013, A&A, 552, A78
Zhou, J.-L. 2010, EAS Pub. Ser., 42, 255
Zhu, W. 2023, arXiv e-prints [arXiv:2306.16691]
Zhu, W., & Wu, Y. 2018, AJ, 156, 92
Zucker, S., & Mazeh, T. 2002, ApJ, 568, L113

Appendix A: State of the art of each system

In this appendix, we briefly describe each system of the survey, and state-of-the-art studies on it.

GJ 163. The system GJ 163 is located at 15.135 ± 0.004 pc (Gaia Collaboration 2021). The host star is a M3.5 dwarf (Hawley et al. 1996). We estimated the mass of the star to 0.46 ± 0.05 $M_\odot$ and its age via gyrochronology to 3 ± 7 Gyr. Both are consistent with the previous estimates from Bonfils et al. (2013b) and Tuomi & Anglada-Escudé (2013). The question of GJ 163's membership of the old disk or halo populations has been discussed in the literature (e.g., Leggett 1992; Bonfils et al. 2013b; Tuomi & Anglada-Escudé 2013) based on its relatively high UVW galactic velocities, and is still debated. GJ 163 could be either a rather young star accelerated to the typical velocity of an old dynamical population, or belong to the metal-rich tail of an old population of stars.
Bonfils et al. (2013b) discovered three planets, GJ 163 b, GJ 163 c and GJ 163 d with minimum masses of 11 $M_\oplus$, 7.7 $M_\oplus$ and 25 $M_\oplus$ and semi-major axes of 0.061 au, 0.13 au, and 1.0 au, respectively. Two additional planets may be present, GJ 163 e (11 $M_\oplus$, 0.10 au) and GJ 163 f (7.2 $M_\oplus$, 1.0 au). Tuomi & Anglada-Escudé (2013) confirmed the presence of three planets b, c and d, and have tentative evidence for the planet f. Thus, in our work, we consider the planets b, c and d as confirmed and the planets e and f as unconfirmed.

GJ 176. The system GJ 176 is located at 9.485 ± 0.002 pc (Gaia Collaboration 2021). Its host star is a M2.5 dwarf (Joy & Abt 1974). We estimated the stellar mass to 0.52 ± 0.05 $M_\odot$, consistent with the previous estimate from Astudillo-Defru et al. (2017a). However, our age estimate based on gyrochronology gives a younger age of 2.3 ± 0.6 Gyr compared with $8.8^{+2.5}_{-2.8}$ Gyr from Veyette & Muirhead (2018). von Braun et al. (2014) derived a stellar radius of 0.45 ± 0.02 $R_\odot$. Peacock et al. (2019) investigated the extreme ultraviolet (EUV) emission of the star, that plays a key role in the stability and photochemistry of exoplanet atmospheres.
Endl et al. (2008) discovered one Neptune-like planet with a minimum mass of 24.1 ± 3.1 $M_\oplus$ at a period of 10.2 days. However, this planet has been called into question by Butler et al. (2009) and Forveille et al. (2009). Forveille et al. (2009) found the planet b to be rather a super-Earth-like planet (8.4 $M_\oplus$, 8.8 days) by using HARPS RV measurements. Robertson et al. (2015) and Trifonov et al. (2018) confirmed the existence of the planet b by studying the stellar activity for the former or by adding CARMENES measurements for the latter. They reported a minimal mass of $9.06^{+1.54}_{-0.70}$ $M_\oplus$ at a semi-major axis of 0.066 ± 0.001 au (period of 8.8 days).

GJ 180. The system GJ 180 is located at 11.949 ± 0.002 pc (Gaia Collaboration 2021). The host star is a M2 dwarf (Gaidos et al. 2014), and has a stellar mass estimated in our work of 0.44 ± 0.05 $M_\odot$ which is consistent with the previous estimate from Zechmeister et al. (2009).
The system hosts two or three known planets discovered by radial velocity measurements. The planets b and c were found by Tuomi et al. (2014), while Feng et al. (2020) confirmed the existence of b ($m \sin i$ = $6.75^{+1.37}_{-1.78}$ $M_\oplus$, a = 0.092 ± 0.008 au, P = 17.132 ± 0.008 days), found no evidence significant enough for c ($8.3^{+3.5}_{-5.3}$ $M_\oplus$, 0.129 ± 0.017 au, 24.33 ± 0.07 days from Tuomi et al. (2014)), and discovered an additional planet d ($7.49^{+2.66}_{-2.33}$ $M_\oplus$, 0.31 ± 0.03 au, 106.34 ± 0.03 days).

BD-06 1339 (GJ 221). The system BD-06 1339 (also known as GJ 221) is the furthest from the Sun in our sample, at 20.305 ± 0.008 pc (Gaia Collaboration 2021). We estimated an age of 2.9 ± 1.2 Gyr by using chromospheric activity, a stellar mass of 0.65 ± 0.05 $M_\odot$, and a sub-solar stellar metallicity [Fe/H] of −0.20 ± 0.10, all in agreement with Lo Curto et al. (2013) and/or Arriagada et al. (2013). The star is a K7 dwarf (Stephenson 1986).
It hosts one confirmed planet named c (minimal mass of 53 $M_\oplus$ at a semi-major axis of 0.44 au, period of 126 days), and putatively two additional planets, b (8.5 $M_\oplus$, 0.04 au, 3.9 days) and d (30 $M_\oplus$, 1.1 au, 1496 days). The planets b and c were found simultaneously by Arriagada et al. (2013); Lo Curto et al. (2013). Tuomi (2014) indicated the presence of the third planet d. However, this planet d is ignored in the later paper from Simpson et al. (2022), who recently reported that the planet b is likely to be a false alarm caused by stellar activity. The only confirmed planet in this system is the one known as BD-06 1339 c which has a mass between Neptune and Saturn.

GJ 229. The system GJ 229 is located at 5.7612 ± 0.0004 pc (Gaia Collaboration 2021). Its host star GJ 229 A is a M1 dwarf (Henry et al. 2002), with a mass estimated in this work of 0.57 ± 0.05 $M_\odot$ consistent with the previous estimate from Zechmeister et al. (2009). By using gyrochronology, we found an age of 1.6 ± 0.4 Gyr, at 2 σ consistent with Brandt et al. (2020) who suggested an age of 2.6 ± 0.5 Gyr from stellar activity measurements.
Nakajima et al. (1995) imaged GJ 229 B at a distance of 44.3 au from the star GJ 229 A. From their mass estimation of 20–50 M_{Jup} via cooling models of brown dwarfs, GJ 229 B is the first T-type brown dwarf with clear signs of methane (T6 according to Geballe et al. 2002).

By combining imaging, RV, and *Gaia* and HIPPARCOS data, different dynamical masses are found for GJ 229 B. On one hand, Brandt et al. (2020) measured a dynamical mass of 70.4 ± 4.8 M_{Jup}, updated to 71.4 ± 0.6 M_{Jup} by Brandt et al. (2021). This value is significantly higher than the previous estimate and the minimal mass found by Feng et al. (2020) of 1.62 M_{Jup}, but consistent with the inclination of $7.7^{+7.6}_{-4.4}$ ° found by orbital fitting (Brandt et al. 2021). Nonetheless, their value is inconsistent with the value determined by using cooling models (64.8 ± 0.1 M_{Jup}, Brandt et al. 2021). On the other hand, Feng et al. (2022) recently derived a dynamical mass of 60.4 ± 2.4 M_{Jup}, consistent only at 4 σ with the value derived from Brandt et al. (2021). The brown dwarf is a bit closer than originally thought, as at 33 au (e.g., Brandt et al. 2020, 2021).

The system hosts as well two additional planets, GJ 229 A b first discovered by Tuomi et al. (2014) and confirmed later by Feng et al. (2020), who found as well the planet GJ 229 A c. Respectively, their minimal masses are $10.0^{+3.4}_{-6.1}$ $M_\oplus$ and $7.9^{+2.4}_{-3.4}$ $M_\oplus$, while their semi-major axes are 0.90 ± 0.07 au and 0.34 ± 0.03 au. If their orbits are coplanar with the orbit of GJ 229 B, hence face-on (inclination of $7.7^{+7.6}_{-4.4}$ °, Brandt et al. 2021), their masses would be of 73^{+67}_{-16} $M_\oplus$ and 57^{+17}_{-13} $M_\oplus$, respectively.

GJ 422. The system GJ 422 is located at 12.676 ± 0.005 pc (Gaia Collaboration 2021). By using stellar activity, we estimated for the first time the age of the system to 5.5 ± 0.8 Gyr. The host star GJ 422 corresponds to a M3.5 dwarf (Hawley et al. 1996), with a mass estimated in this work of 0.42 ± 0.05 $M_\odot$ slightly higher but consistent with the previous estimate from Zechmeister et al. (2009).
To date, one planet b has been discovered but its location is debated: either at a 26-day period (Tuomi et al. 2014) or at a 20-day period (Feng et al. 2020). In both cases, the minimal mass is about 10 $M_\oplus$. We consider in this study the planet from Feng et al. (2020) ($10.4^{+3.3}_{-1.9}$ $M_\oplus$, 0.11 ± 0.01 au) as they used more observations (76 measurements by combining UVES and HARPS instruments) than Tuomi et al. (2014) (49, same instruments but on a shorter timeline).

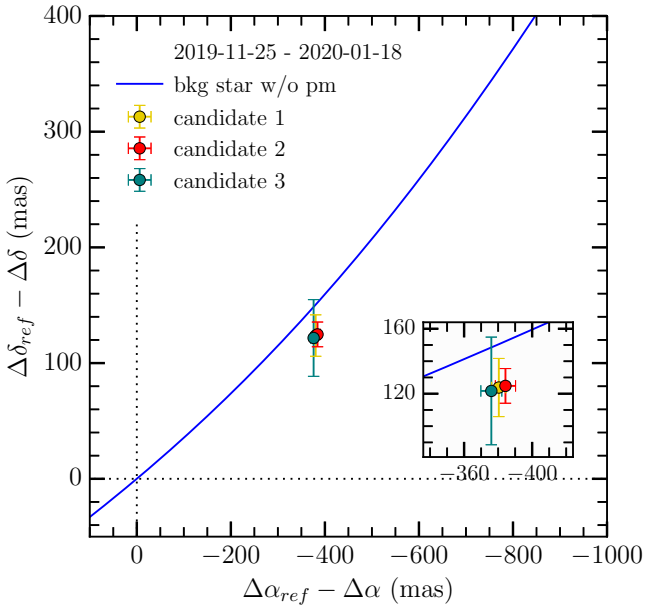

Fig. A.1. SPHERE/IRDIS relative astrometry differences of the offset positions of all the point-like sources detected around GJ 422 in both the second and third epochs (2018-01-28 and 2020-01-18).The expected variation of offset positions, if the companion candidates are stationary background objects are shown in blue solid line. The variation is estimated based on the parallactic and proper motions of the primary star. The five companion candidates are clearly identified as background contaminants. At the *bottom-right* corner, the insert shows a zoom on the location of the candidates.

GJ 433. The system GJ 433 is located at 9.077 ± 0.002 pc (Gaia Collaboration 2021). By using gyrochronology, we estimated for the first time the age of the system to 500 ± 150 Myr. The host star GJ 433 corresponds to a M1.5 dwarf (Hawley et al. 1996), with a mass estimated in this work of 0.50 ± 0.05 $M_\odot$ consistent with the previous estimate from Zechmeister et al. (2009). GJ 433 was reported to host a low-mass planet GJ 433 b with a minimal mass of 5.8 $M_\oplus$ at a semi-major axis of 0.058 au (period of 20.1 days, Delfosse et al. 2013). They detected an additional significant signal with a much longer period of 10 years. Yet, based on the variation of activity indices on a similar timescale reported by Gomes da Silva et al. (2011), they concluded that a magnetic cycle of the star was a more likely origin. Tuomi et al. (2014) recovered the same signals and considered the longer period signal to be a planet candidate, and called it GJ 433 c. If the planet GJ 443 c is real and the system close to edge-on, the planet c would be a cold super-Neptune (minimal mass of $28.8^{+19.2}_{-10.5}$ $M_\oplus$) belonging to an unexplored population of Neptune-like planets. Regarding its separation of 0.5" from its host star (corresponding to a semi-major axis of $4.7^{+1.2}_{-0.8}$ au), the putative planet c is probably the first realistic candidate for the direct imaging of cold Neptunes (Feng et al. 2020). In addition, Feng et al. (2020) may have discovered a third planet in the system, GJ 433 d, likely a super-earth with a minimal mass of $4.9^{+2.5}_{-1.8}$ $M_\oplus$ at a semi-major axis of $0.18^{+0.01}_{-0.02}$ au (36-day period). Furthermore, Kennedy et al. (2018) discovered an unresolved debris disk with a radius between 1 and 30 au by using Herschel.

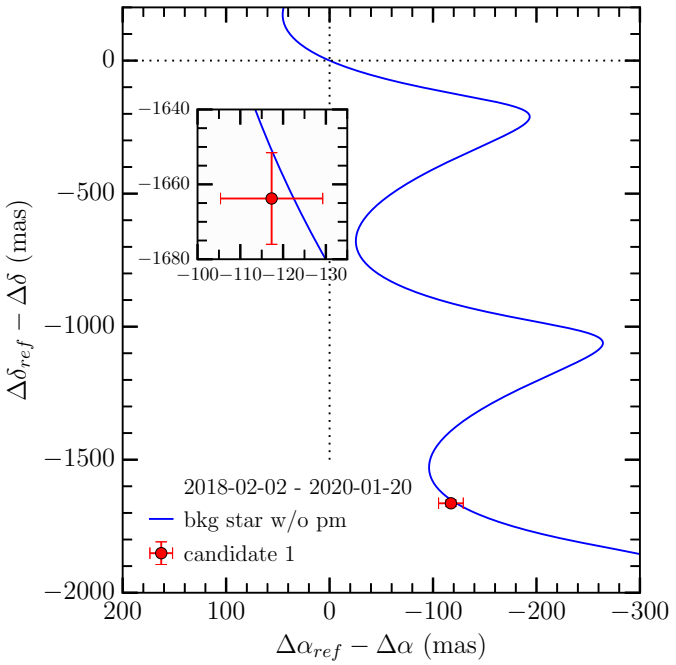

Fig. A.2. SPHERE/IRDIS relative astrometry differences of the offset positions of the point-like source detected around GJ 433 between the first epoch considered as reference 2018-02-02 and the second epoch 2020-01-20. (See caption from Fig. A.1)

GJ 581. The system GJ 581 is located at 6.301 ± 0.001 pc (Gaia Collaboration 2021). We estimated the stellar age at 10 ± 1 Gyr by using chromospheric activity which is consistent at 1 σ with Veyette & Muirhead (2018) based on chemo-kinematics ($6.9^{+2.5}_{-2.3}$ Gyr) but not with the estimation based on isochrones (4.1 ± 0.3 Gyr) from Yee et al. (2017). Our new determination of the stellar mass (0.35 ± 0.05 $M_\odot$) is consistent with Astudillo-Defru et al. (2017a). The star is a M3 star (Trifonov et al. 2018), and its radius is 0.30 ± 0.01 $R_\odot$ (von Braun et al. 2011). By looking into the atmospheric structures on the star based on observations in the visible, ultraviolet (UV), and X-ray, and especially by synthesizing integrated extreme-ultraviolet (EUV) fluxes, Tilipman et al. (2021) found the star GJ 581 to be relatively inactive compared to other M dwarfs of similar spectral types (e.g., GJ 644 B, GJ 588, GJ 887, or GJ 205), with H_2 fluorescent emission (France et al. 2013).
Over potentially six low-mass planets discovered, three are confirmed in the system. The GJ 581 b (15.7-$M_\oplus$ minimal mass, 5.4-day period) was discovered by Bonfils et al. (2005), while GJ 581 c (5.0-$M_\oplus$ minimal mass, 13-day period) and GJ 581 d (7.7-$M_\oplus$ minimal mass, 84-day period) by Udry et al.

(2007), and GJ 581 e (1.7 $M_\oplus$-minimal mass, 3.2-day period) by Mayor et al. (2009a). Vogt et al. (2010a) proposed the existence of two additional planets, GJ 581 f and GJ 581 g with orbital periods of 433 days and 37 days, respectively, but their existence is not supported by Forveille et al. (2011), nor by Tuomi (2011). In addition, later studies reconsidered the existence of the planet d (e.g., Baluev 2012; Robertson et al. 2014; Hatzes 2016). As did Trifonov et al. (2018), we only consider the planets GJ 581 b, GJ 581 c and GJ 581 e as confirmed and we use their derivation of the orbital values, i.e., minimal masses of 15.2 ± 0.3 $M_\oplus$, 5.7 ± 0.3 $M_\oplus$, and 1.7 ± 0.2 $M_\oplus$, and semi-major axes of 0.041 ± 0.001 au, 0.074 ± 0.001 au, and 0.029 ± 0.001 au, respectively. The planet GJ 581 c has been more in-depth studied in the literature: its spin-orbit resonance is likely to be 3:2, and the presence of liquid water has been investigated, including through 3D global climate models (Leconte et al. 2013).

Furthermore, Lestrade et al. (2012) discovered and resolved a debris disk extending from 25 au to more than 60 au by using Herschel. Its inclination is estimated to be between 30 and 70°.

Wolf 1061 (GJ 628). The system Wolf 1061 (GJ 628) is the closest system to the Sun from our sample, located at 4.3078 ± 0.0005 pc (Gaia Collaboration 2021). By using gyrochronology, we estimated an age of 7.1 ± 2.0 Gyr, consistent with the previous estimate from Veyette & Muirhead (2018) based on chemo-kinematics. We derive the stellar mass to a value of 0.35 ± 0.05 $M_\odot$, which is higher but in agreement with the value from Maldonado et al. (2020) of 0.25 ± 0.12 $M_\odot$. The stellar spectral type is between M3V and M4.5V spectral types (e.g., Joy & Abt 1974; Henry et al. 2002), while the stellar radius is 0.325 ± 0.012 $R_\odot$ (Kane et al. 2017).
Wright et al. (2016) discovered three planets Wolf 1061 b ($m \sin(i) = 1.4 \pm 0.3$ $M_\oplus$, $a \sim 0.04$ au, $P \sim 4.9$ days), Wolf 1061 c (4.3 ± 0.4 $M_\oplus$, 0.08 au, 18 days) and Wolf 1061 d (5.21 ± 0.68 $M_\oplus$, 0.20 au, 67 days). However, Astudillo-Defru et al. (2017b) called into issue the existence of the planet d, which could be caused by aliases. Hence, we consider in this paper only the planets b and c as confirmed.

GJ 649. The system GJ 649 is located at 10.391 ± 0.003 pc (Gaia Collaboration 2021). We derived an age of 1.40 ± 0.35 Gyr based on gyrochronology, which is in agreement with its membership to the "old disk" following kinematics (Leggett 1992) but younger than the age of $4.5^{+3.0}_{-2.0}$ Gyr determined by Veyette & Muirhead (2018) following a combined chemo-kinematic approach (consistent at $2\,\sigma$). Our stellar mass measurement of 0.54 ± 0.05 $M_\odot$ is consistent with previous estimate from Johnson et al. (2010b) and von Braun et al. (2014). Its spectral type is M1.5 (Johnson et al. 2010b), while von Braun et al. (2014) found a stellar radius equal to 0.54 ± 0.02 $R_\odot$.
The system hosts one giant planet with a minimal mass of 0.328 M_{Jup} at a semi-major axis equal to 1.135 au and eccentricity of 0.30 ± 0.08 (Johnson et al. 2010b). As the RV signal of two circular planets can mimic the signal of one eccentric planet, Wittenmyer et al. (2013) proposed the existence of an inner smaller planet, with a minimal mass of about 9.5 $M_\oplus$ at a semi-major axis of about 0.043 au based on a statistical approach. However, this planet has not been confirmed yet.
By using Herschel, Kennedy et al. (2018) discovered and marginally resolved a debris disk with a radius between 6 and 30 au, likely to be edge-on.

GJ 667 C. The system GJ 667 is a multi-stellar and planetary system located at 7.2429 ± 0.0015 pc (Gaia Collaboration 2021). The stars GJ 667 A and GJ 667 B form a binary pair with a total dynamically derived mass of 1.27 $M_\odot$ (Söderhjelm 1999) and a semi-major axis of 13.1 au (period of 42.15 years, Delfosse et al. 2013), around which a third star, GJ 667 C, orbits at a projected angular separation of about 32.4", i.e., at a minimal distance of 235 au.

In this work, we focused on GJ 667 C, which is a M1.5 star (Hawley et al. 1996). We estimated its mass to 0.346 ± 0.050 $M_\odot$, consistent with previous estimates (Anglada-Escudé et al. 2012; Delfosse et al. 2013). Our age determination (6.3 ± 4.0 Gyr) via gyronochronology is in agreement with Anglada-Escudé et al. (2012). We derived a sub-solar stellar metallicity [Fe/H] of -0.48 ± 0.10. The stellar radius is equal to 0.30 ± 0.02 $R_\odot$ (von Braun et al. 2013). In addition, France et al. (2013) noticed moderate level of UV emission from the chromospheric and transition regions of GJ 667 C.
The star GJ 667 C is known to host two confirmed planets (b and c), while five other ones (d, e, f, g and h) have been proposed. The planets b and c have been discovered by Anglada-Escudé et al. (2012) with minimal masses of 5.46 $M_\oplus$ and 4.25 $M_\oplus$, and at periods of about 7.2 days and 28.1 days (semi-major axes of about 0.05 au and 0.13 au), respectively. They were confirmed by Delfosse et al. (2013), Bonfils et al. (2013a), and Robertson et al. (2014). Anglada-Escudé et al. (2013) suggested the existence of the planet d ($5.1^{+1.8}_{-1.7}$ $M_\oplus$, at 0.28 au, 92-day period), planet e ($2.7^{+1.6}_{-1.4}$ $M_\oplus$, 0.21 au, 62 days), planet f ($2.7^{+1.4}_{-1.2}$ $M_\oplus$, 0.16 au, 39 days), planet g ($5.1^{+1.8}_{-1.5}$ $M_\oplus$, 0.55 au, 256 days), and planet h (tentative evidence of a $1.1^{+1.0}_{-0.9}$ $M_\oplus$, 0.09 au, 17 days). However, Delfosse et al. (2013) and Robertson et al. (2014) reported the RV signal associated to the planet d as to be in reality an artifact caused by stellar rotation, harmonics, or aliases. After correcting from stellar activity, Robertson et al. (2014) were not able to confirm the other planetary candidates (e, f, g and h), thereby we consider them as unconfirmed.

GJ 674. The system GJ 674 is the second closest system in our sample, as at 4.5528 ± 0.0005 pc from the Sun (Gaia Collaboration 2021). The stellar spectral type is M2.5 (Hawley et al. 1996). Our stellar mass measurement of 0.40 ± 0.05 $M_\odot$ is consistent with the previous estimate from Bonfils et al. (2007). We estimated an age of 2.0 ± 0.5 Gyr based on gyrochronology, moderately higher than its previous value spanning between 0.1 and 1.0 Gyr (Bonfils et al. 2007), who considered the UVW galactic velocities corresponding to the transition between young and old disk populations (Leggett 1992). Although the star is not supposed to be in its most active period, Froning et al. (2019) reported a large flare and several small ones in far-ultraviolet (FUV) monitoring observations with the Hubble Space Telescope, highlighting the importance of considering the FUV emission for exoplanet atmospheric heating and chemistry.

The system GJ 674 hosts at least one planet b of minimal mass 11.1 $M_\oplus$ at a semi-major axis of about 0.039 au (4.69-day period, Bonfils et al. 2007). Vidotto et al. (2019) pointed out that GJ 674 b would be a relevant planet to try to detect aurora in radio, provided that the wind of the host star is not too strong.

GJ 682. The system GJ 682 (HIP 86214) located at 5.008 ± 0.001 pc (Gaia Collaboration 2021) has a M3.5 star (Hawley et al. 1996). In our work, we estimated the stellar

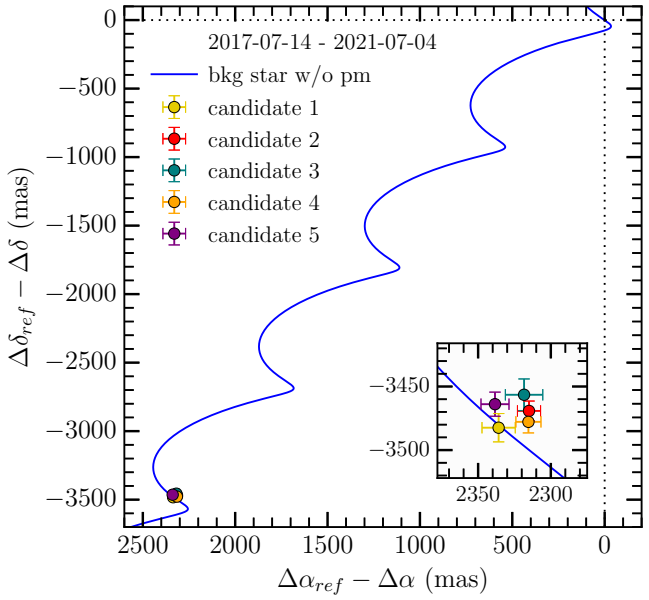

Fig. A.3. SPHERE/IRDIS relative astrometry differences of the offset positions of the point-like source detected around GJ 674 between the first epoch considered as reference 2017-07-14 and the second epoch 2021-07-04. (See caption from Fig. A.1)

mass to 0.30 ± 0.05 $M_\odot$, consistent with the previous estimate from Zechmeister et al. (2009), but higher than Ward-Duong et al. (2015), estimated at 0.23 $M_\odot$. By using either activity or gyrochronology-based methods, we were not able to estimate a robust age for this system. Thus, in this study we consider the default age of 5 ± 4 Gyr, as no estimate is given in the literature. Ward-Duong et al. (2015) proposed a 0.14 $M_\odot$ binary companion orbiting at a projected distance of 0.85 au (0.17"). Since we did not re-detect it in any of our three epochs, and the field of view of GJ 682 is crowded (10–26 detections, see Table 3, Figs. E.1 and E.3), and RV measurements did not reveal the presence of such binary companion, we consider it was a background contaminant in their 2005-05-01 epoch of observation.
Tuomi et al. (2014) discovered two low-mass planets in this system, GJ 682 b and GJ 682 c with minimal masses of $4.4^{+3.7}_{-2.4}$ $M_\oplus$ and $8.7^{+5.8}_{-4.6}$ $M_\oplus$, at semi-major axes of $0.080^{+0.014}_{-0.004}$ au and $0.176^{+0.030}_{-0.003}$ au (17.5-day and 57-day periods), respectively. However, the planets b and c have not been confirmed in a ulterior study. Feng et al. (2020) in their updated UCLES measurements and additional HARPS data did not identify them as planetary signal, but rather as caused by stellar activity. Thus, we considered the planets GJ 682 b and GJ 682 c as unconfirmed, that means the system GJ 682 might not be planetary.

GJ 832. The system GJ 832 is located at 4.9671 ± 0.0006 pc (Gaia Collaboration 2021). We estimated the stellar age at 2.4 ± 0.3 Gyr by using gyrochronology. We found a stellar mass of 0.48 ± 0.05 $M_\odot$ consistent with the previous estimate from Bonfils et al. (2013a). The stellar type is M2.5 (Hawley et al. 1996), while the stellar radius is 0.50 ± 0.02 $R_\odot$ (von Braun et al. 2011). Peacock et al. (2019) investigated the extreme ultraviolet radiation environment around, whereas afterwards Tilipman et al. (2021) focused on the stellar atmospheric structures as for GJ 581. Tilipman et al. (2021) found the star GJ 832 to be relatively inactive, but still more than GJ 581, and have as well a H_2 fluorescent emission (France et al. 2013).

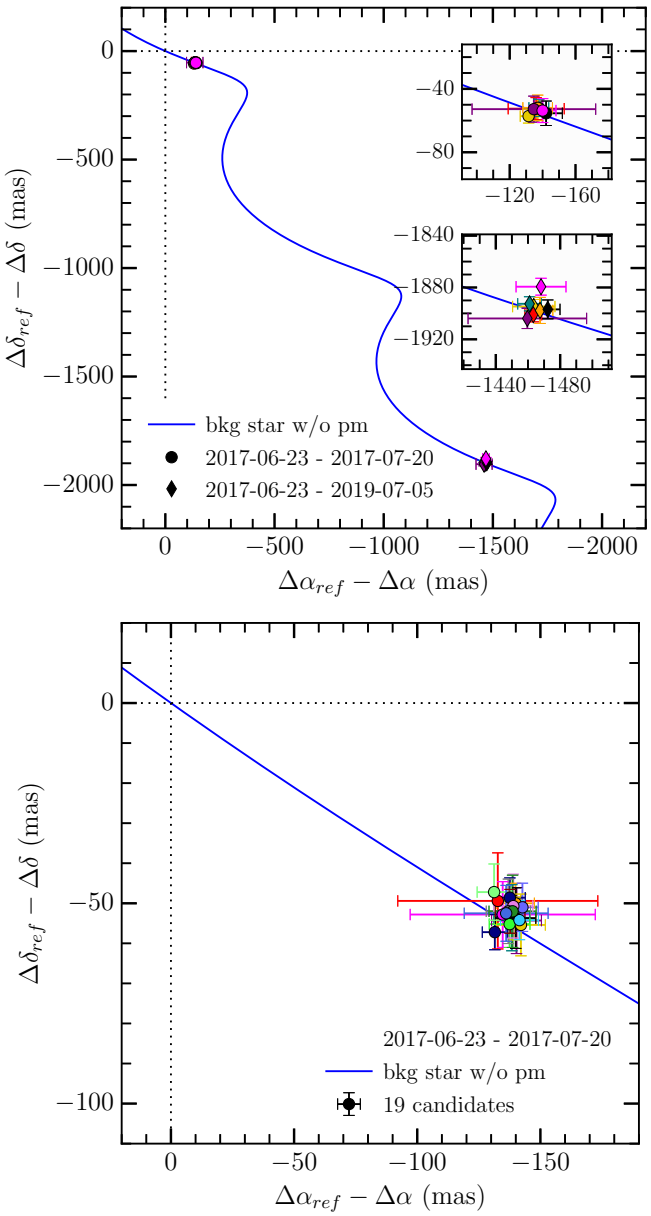

Fig. A.4. SPHERE/IRDIS relative astrometry differences of the offset positions of the point-like source detected around GJ 682 in the three epochs (at the *top*) and only in the first and third epochs (at the *bottom*). The first epoch is considered as reference, i.e., 2017-06-22; the second epoch is 2017-06-23, and the third epoch 2019-07-05. (See caption from Fig. A.1)

The system GJ 832 hosts a long-period planet named GJ 832 b. This planet b was discovered by Bailey et al. (2009) using radial velocity measurements: it has a minimal mass of 0.74 ± 0.06 M_{Jup} orbiting at a period of 3 838 ± 49 days (a semi-major axis of 3.79 ± 0.03 au) with a low eccentricity (0.02–0.06) from the most recent study Gorrini et al. (2022). Bonfils et al. (2013a) confirmed the signal, and indicated a possible second signal at a 35-day period, but which could yet be linked to stellar activity. This signal was considered by Wittenmyer et al. (2014) as the planet c, an inner super-Earth (5.4 ± 1.0 $M_\oplus$, 0.16 ± 0.01 au). Recently, this planet c have be debated by Gorrini et al. (2022) arguing for stellar activity. Hence, we only consider the planet b as confirmed, and we removed the system GJ 832 in our statistical study of systems hosting known sub-Saturn(s). Nonetheless,

we stress the fact that the system GJ 832 is one of the four systems in our full sample with a significant proper motion anomaly signature (signal-to-noise ratio equal to 14.1, Kervella et al. 2022). This is consistent with the radial velocity measurements of the planet b, assuming a circular orbit and an inclination of about 60° (Kervella et al. 2019). The planet GJ 832 b has not yet been imaged - even though we had a detection plausible in our first epoch with SPHERE, we were not able to recover it in the best observation (see Section 5.2).

GJ 3998. The system GJ 3998 located at 18.18 ± 0.01 pc (Gaia Collaboration 2021) has a M1.5 star (Gaidos et al. 2014). In our work, we estimated the stellar mass to 0.55 ± 0.05 $M_\odot$, consistent with the previous estimate from Affer et al. (2016). By using gyrochronology, we estimated for the first time an age of 2.0 ± 0.5 Gyr for this system.
Affer et al. (2016) discovered two low-mass planets in this system, GJ 3998 b and GJ 3998 c with minimal masses of 2.5 ± 0.3 $M_\oplus$ and 6.3 ± 0.8 $M_\oplus$, at semi-major axes of 0.029 ± 0.001 au and 0.089 ± 0.003 au (i.e., about 2.6-day and 13.7-day periods), respectively.

HD 3651. The system HD 3651 located at 11.108 ± 0.006 pc (Gaia Collaboration 2021) has a K0V star (Gray et al. 2003). By using gyrochronology and chromospheric activity, we estimated an age of 7.5 ± 2.2 Gyr for the system, consistent with values from the literature (e.g., Valenti & Fischer 2005; Liu et al. 2007; Vidotto et al. 2014; Bonfanti et al. 2016). We determined a stellar mass 0.86 ± 0.06 $M_\odot$, higher than the previous estimate (0.79 ± 0.06 $M_\odot$) from Fischer et al. (2003) and a stellar metallicity [Fe/H] close to the solar one (0.08 ± 0.06).

The system HD 3651 hosts one eccentric (0.63 ± 0.04) Saturn-mass planet b (0.20 M_{Jup}) at 0.28 au (period of 62-day) discovered by Fischer et al. (2003) using radial velocity measurements from the Lick and Keck observatories. In addition, Mugrauer et al. (2006) and Luhman et al. (2007) independently discovered by direct imaging a wide-orbit brown dwarf (20–60 M_{Jup}, projected separation of 43" corresponding to 480 au). Its spectral type is T7.5 ± 0.5 (Liu et al. 2007; Burgasser 2007). Line et al. (2015) retrieved ammonia in low-resolution near infrared spectrum for this brown dwarf, and found a good agreement between the values of the carbon-to-oxygen ratio of the brown dwarf and the host star. Wittenmyer et al. (2013) proposed the existence of an inner planet (minimal mass of 0.09 M_{Jup}) at a period of 31 days (0.19 au) based on the same statistical approach than for GJ 649. Yet, they retracted in Wittenmyer et al. (2007), stating that radial velocity signal from a planet with an eccentricity higher than 0.5 cannot be explained by an architecture of two circular planets from updated simulations. It is consistent with results from Brewer et al. (2020), who did no expect an inner planet to HD 3651 b from their radial-velocities measurements coupled to their N-body simulations, since it would be dynamically unstable.

HD 20794. The system HD 20794 located at 6.041 ± 0.003 pc (Gaia Collaboration 2021) has a G8V star (Pepe et al. 2011). In our work, we estimated the stellar mass to 0.79 ± 0.05 $M_\odot$, lower but consistent at 1σ with the previous estimate (0.85 ± 0.02 $M_\odot$) from Takeda et al. (2007), and a metallicity [Fe/H] of −0.36 ± 0.05. By using chromospheric activity, we estimated an age of 6.0 ± 0.3 Gyr for the system, younger than the previous age (11.6 ± 1.5 Gyr) from Bonfanti et al. (2016). As HD 20794 is particularly stable over long time baselines (Butler et al. 2001), the system has been selected as a special star reference for radial velocity measurements, which explains the high number of observations with HARPS (> 7500).

The system hosts several super-Earths. Pepe et al. (2011) reported the discovery of three planets, HD 20794 b, HD 20794 c and HD 20794 d at 0.12 au (18-day period), 0.20 au (18-day period) and 0.35 au (90-day period), and with minimal masses of 2.7 $M_\oplus$, 2.4 $M_\oplus$ and 4.7 $M_\oplus$, respectively. They are cautious regarding their planet c, due to faint amplitude signal and as it could be linked to the stellar rotation. Feng et al. (2017) is suspicious as well regarding the existence of the planet c, but points out the existence of at least one additional planet HD 20794 e at 0.51 au (147-day period), and possibly two, HD 20794 f and HD 20794 g, at 0.88 au (331-day period) and 0.09 au (12-day period), having minimal masses of 4.8 $M_\oplus$, 10.3 $M_\oplus$, and 1.0 $M_\oplus$, respectively. In this work, we consider the planets b, d, and e as confirmed detections, the others as unconfirmed.

In addition, the star hosts a cold (about 80 K) debris disk spanning between roughly 15 and 40 au (Wyatt et al. 2012; Kennedy et al. 2015). Hot dust was detected with VLTI/PIONIER with an excess of 1.64 ± 0.37% (Ertel et al. 2014) and a variability over two years (Ertel et al. 2016). This hot dust could be located between 0.01 and 0.1 au (Kennedy et al. 2015), with the sublimation radius estimate at 0.03 au (Absil et al. 2021).

HD 38858. The system HD 38858 is located at 15.210 ± 0.007 pc (Gaia Collaboration 2021) and has a G2V star (Gray et al. 2003). We derived an age of 4.3 ± 1.0 Gyr based on gyrochronology and chromospheric activity, in agreement with previous estimates from Takeda et al. (2007) and Lovis et al. (2011), but significantly older than the estimate from Casagrande et al. (2011) of 200 Myr based on isochrones. In addition, we estimated a stellar mass of 0.91 ± 0.06 $M_\odot$, consistent with Takeda et al. (2007), and a metallicity [Fe/H] of −0.21 ± 0.05.

The system hosts at least a low-mass planet named HD 38858 b discovered by Kennedy et al. (2015) at 0.64 au (198-day period) and with a minimum mass of 12 ± 2 $M_\oplus$. Previously, Mayor et al. (2011) announced the discovery of a planet with a semi-major axis of 1.04 au (407-day period) and a minimal mass of 30.6 ± 4.1 $M_\oplus$. However, by using additional data (96 instead of 52 measurements) Kennedy et al. (2015) revealed this signal to be caused by stellar activity. Read & Wyatt (2016) put constraints on the presence of additional low-mass planets in the system from a theoretical perspective. They reported that an eccentric (0.2–0.8) planet located between 1 and 10 au and with a minimal mass of 3–10 $M_\oplus$ would be unlikely, as secular interactions with the planet HD 38858 b would cause a significant eccentricity for the planet b that is not observed. Nonetheless, if such planet did exist, it would point for the existence of a third planet, in the vicinity of the planet HD 38858 b, and stabilizing it.

Furthermore, Beichman et al. (2006) discovered with *Spitzer* a cool debris disk around the star, marginally resolved (Krist et al. 2012), and better resolved at the same wavelength (70 μm) with Herschel Kennedy et al. (2015). These latter observations constrained the disk geometry and radial structure.

HD 40307. The system HD 40307 is located at 12.932 ± 0.003 pc (Gaia Collaboration 2021), and hosts a K2.5V star (Gray et al. 2006). We derived an age of 4.4 ± 2.0 Gyr based on chromospheric activity and gyrochronology which is consistent with e.g., Lovis et al. (2011) and Bonfanti et al. (2016).

We estimated the stellar mass to 0.71 ± 0.05 $M_\odot$, in agreement with Takeda et al. (2007), and determined a stellar sub-solar metallicity [Fe/H] of −0.30 ± 0.05.

By using HARPS RV measurements, four to six super-Earths and/or mini-Neptunes may have been discovered in the system. In short, the three inner ones b, c, and d are discovered by Mayor et al. (2009b) and the three outer ones e, f and g by Tuomi et al. (2013) who used a new analysis method. However, the existence of the planets HD 40307 e, and HD 40307 g is debated (Díaz et al. 2016; Unger et al. 2020). Regarding the confirmed planets HD 40307 b, HD 40307 c, HD 40307 d, and HD 40307 f, Unger et al. (2020) reported minimal masses of about 3.81 $M_\oplus$, 6.43 $M_\oplus$, 8.74 $M_\oplus$, and 3.63 $M_\oplus$, semi-major axes of about 0.05 au, 0.08 au, 0.13 au, and 0.25 au (periods of 4.3 days, 9.6 days, 20.4 days, and 51.6 days), respectively. As for the unconfirmed planets HD 40307 e and HD 40307 g, they would have a minimal mass of 3.5$M_\oplus$, and 7.1$M_\oplus$, and semi-major axis of 0.19 au and 0.60 au (period of 34.6 day, and 198 day) following Tuomi et al. (2013).

Concerning their formation history, Barnes et al. (2009) found that the planets b, c, and d likely formed at larger radii and migrated inward into their current orbits owing to disk interactions. The dynamics of this multiple system with at that time three planets discovered has been also investigated by Papaloizou & Terquem (2010), Zhou (2010), and Yuan-Yuan et al. (2014). On the other hand, Brasser et al. (2014) investigated the stability of the system based on a 6-planet configuration.

Furthermore, the system HD 40307 was imaged by VLT/NaCo (Dietrich & Ginski 2018). Nonetheless, the reported companion candidate found at a separation of 13.35" and position angle of 146° was classified as a background object.

HD 69830. The system HD 69830 is located at 12.579 ± 0.006 pc (Gaia Collaboration 2021). We derived an age of 6.6 ± 1.5 Gyr based on gyrochronology and chromospheric activity, which is younger than the age estimated from Takeda et al. (2007) of 10.4 ± 2.5 Gyr but consistent with the one from e.g., Tanner et al. (2015). Our stellar mass estimation of 0.88 ± 0.06 $M_\odot$ is consistent with the value from e.g., Tanner et al. (2015). We determined a stellar metallicity [Fe/H] consistent with the solar one (−0.03 ± 0.05). The star has a spectral type of is G8V (Gray et al. 2006) or K0V Tanner et al. (2015). From interferometric measurements with the CHARA array, Tanner et al. (2015) estimated a physical radius of 0.906 ± 0.019 $R_\odot$. In addition, the system HD 69830 underwent an encounter 0.31 ± 0.01 Myr ago at a minimal distance of $0.43^{+0.06}_{-0.02}$ pc with the star HD 57901 (Bertini et al. 2023).

Lovis et al. (2006) discovered three planets b, c and d with minimum masses of 10.2 $M_\oplus$, 11.8 $M_\oplus$ and 18.1 $M_\oplus$ and semi-major axis of about 0.08 au, 0.19 au and 0.63 au i.e., periods of 8.7, 31.6 and 197 days, respectively. Lovis et al. (2006), Alibert et al. (2006) and Lecavelier Des Etangs (2007) concluded that HD 69830 b must have a mainly rocky composition such as a super-Earth, while the two outermost planets HD 69830 c and HD 69830 d should more look like super-Neptunes. Those planets have been confirmed in later studies, e.g., Hara et al. (2022) who led an in-depth study of stellar activity. By using 254 HARPS RV measurements (acquired before the change of fiber in 2015) spanning over 11.5 years, they demonstrated that the RV periodic signals associated to the three planets have a stable amplitude, phase and period, which strengthens their planetary origin over a stellar one. Moreover, this configuration of three planets is dynamically stable even if planetary masses are shifted to Jupiter masses in case of a face-on system (Ji et al. 2007). Payne et al. (2009) reported that the three planets may have migrated through the disk.

Furthermore, the system hosts a warm belt, external to the three low-mass planets known, and first constrained by Beichman et al. (2005) via SED modelling of *Spitzer* observations. They show the star to harbour within 1 au warm dust grains from an exozodiacal disk (exozodi), which would represent a total mass of about 4.6×10^{-9} $M_\oplus$ by assuming only 0.25 µm-sized dust grains. The exozodi could be explained by a recent collision between planetesimals (Wyatt et al. 2007, 2010; Heng & Tremaine 2010). Beichman et al. (2006) pointed out that over 41 stars hosting planets, and later on Bryden et al. (2009) for an additional 105 stars hosting planets, that HD 69830 is the only one among 14 systems with a debris disk to have this IR excess exclusively at 24 µm. This means the system has a hot belt and insignificant amounts of cool dust. The absence of a large and cold reservoir of cometary bodies is also reported by Marshall et al. (2014) based on Herschel data. This makes replenishing the exozodi challenging. Hence, the discovery from Lisse et al. (2007) with *Spitzer* of icy dusty grains may indicate that a recent disruptive event happened within the year of the observation. Yet, follow-up observations at higher signal-to-noise ratio still with *Spitzer* were not able to detect water ice again or any change in the emission spectrum (Beichman et al. 2011). These latter indicate that the disruption of C-type asteroid(s) formed in dry and inner regions could explain the exozodi.

The status of a short-lived exozodi (e.g., Beichman et al. 2005) is debated by Heng (2011) which argued that the age of the system is poorly constrained and thus could be up to about 1 Gyr. Such an age might point the hypothesis of a non-transient exozodi. In this case, the exozodi would have a mass of 3–4×10^{-3} $M_\oplus$ i.e., from 7 to 10 times the one from the asteroid belt in our Solar system (Krasinsky et al. 2002).

Complementary observations in the mid infrared with VLTI/MIDI have enabled to resolve the dust emission of the exozodi at 8-13 µm, but not with VISIR at 18.7 µm, consistent with the radius of 1 au derived by SED modelling (Smith et al. 2009). In addition, Beichman et al. (2011) reported no variability of the amount of dust or its composition over 4 year period with *Spitzer* (upper limit of 3.3% at 1σ-level).

HD 85512. The system HD 85512 is located at 11.277 ± 0.003 pc (Gaia Collaboration 2021). We derived an age of 5.1 ± 1.0 Gyr based on gyrochronology and chromospheric activity, and a stellar mass of 0.70 ± 0.05 $M_\odot$, both consistent with e.g., Pepe et al. (2011). We found a sub-solar metallicity [Fe/H] of −0.28 ± 0.12. The star has a K5V spectral type, and is even more stable than HD 20794 (Pepe et al. 2011).

The system is known to harbour one planet HD 85512 b of minimal mass 3.6 ± 0.5 $M_\oplus$ at 0.26 ± 0.01 au (~ 58-day period) on a possible circular orbit (e = 0.11 ± 0.1) and rocky (Pepe et al. 2011). The spin-orbit resonance of the planet b is likely to be 3:2 (Luna et al. 2016). In addition, Leconte et al. (2013) investigated the habitability of the planet using 3D global climate models, arguing it cannot be ruled out even if the planet b is closer than the inner edge of the classically defined habitable zone, which corresponds to a predicted runaway greenhouse transition that remains to be empirically tested (Ingersoll 1969; Kasting 1988; Turbet et al. 2019, 2020; Schlecker et al. 2023).

HD 99492. The system HD 99492 is located at a distance of 18.16 ± 0.01 pc (Gaia Collaboration 2021). We derived an age of

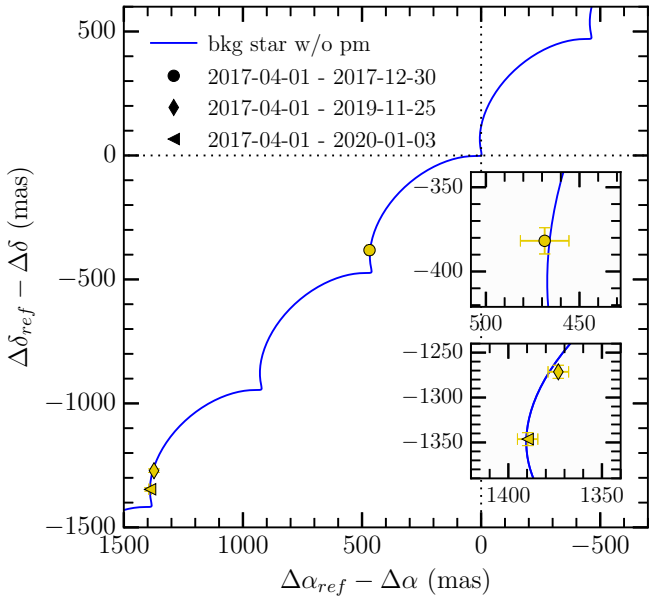

Fig. A.5. SPHERE/IRDIS relative astrometry differences of the offset positions of all the point-like sources detected around HD 85512 between the first epoch considered as reference 2017-04-01 and the three epochs after, 2017-12-30, 2019-11-25, and 2020-01-03. (See caption from Fig. A.1)

5.7 ± 1.0 Gyr from gyrochronology and chromospheric activity, which is consistent with Marcy et al. (2005) and Bonfanti et al. (2016). Its star has a mass of 0.84 ± 0.05 $M_\odot$ in agreement with Takeda et al. (2007) and a spectral type K2V (Marcy et al. 2005). We found a super-solar metallicity [Fe/H] of 0.27 ± 0.09. The star is in a binary orbit with HD 99491, both also known as 83 Leonis B and A, respectively, separated by about 40.76" corresponding to an average projected separation of ∼ 740 au.

The system hosts one planet HD 99492 b of minimal mass 35.6 $M_\oplus$ at 0.12 au (17-day period) discovered by Marcy et al. (2005). The hypothetical outer planet HD 99492 c suggested via RV trend (Marcy et al. 2005), is claimed by Meschiari et al. (2011) as a giant planet of 0.36 M_{Jup} minimal mass orbiting at 5.4 ± 0.5 au (about 5000-day period). However, Kane et al. (2016) reported the radial velocity signal associated previously to HD 99492 c to be caused by a stellar activity cycle of about 13 years.

HD 102365. The system HD 102365 (also known as HR 4523) is located at a distance of 9.320 ± 0.008 pc (Gaia Collaboration 2021). We derived an age of 4.3 ± 0.8 Gyr based on chromospheric activity and gyrochronology, younger than the age estimated from Takeda et al. (2007) of 9.5 ± 3.0 Gyr. We estimated a stellar mass of 0.81 ± 0.05 $M_\odot$, consistent with Takeda et al. (2007), and a sub-solar metallicity [Fe/H] of −0.35 ± 0.03. The star is classified as a G3V and G5V star (Keenan & McNeil 1989; Evans et al. 1957). In addition, the star is part of a binary system with a M4V companion located at projected separation of 322 au (van Biesbroeck 1961; Hawley et al. 1996).

Based on 149 UCLES radial velocities measurements spanning over 12 years, Tinney et al. (2011) reported the existence of HD 102365 b of minimal mass 16.0 ± 2.6 $M_\oplus$ orbiting at 0.46 ± 0.04 au (122.1 ± 0.3-day period) with an eccentricity of 0.34 ± 0.14. However, Zechmeister et al. (2013) did not find evidence for the signal with their 62 HARPS RV measurements spanning over 4.4 years, hence the system HD 102365 may not be planetary.

61 Vir (HD 115617). The system 61 Vir (HD 115617) is located at 8.53 ± 0.01 pc (Gaia Collaboration 2021). In this work we estimated the stellar age (5.1 ± 1.3 Gyr) based on gyrochonology and stellar activity, as well as the stellar mass (0.915 ± 0.053 $M_\odot$) and the metallicity [Fe/H] (−0.03 ± 0.04). Our results are consistent with previous estimates from Wright et al. (2011), Vican (2012), Vogt et al. (2010b), Valenti & Fischer (2005), and Sousa et al. (2008).
The star has a spectral type between G5V and G7V (e.g., Gray et al. 2006) and its stellar radius is estimated to 0.987 ± 0.005 $R_\odot$ (von Braun et al. 2014). By using radial velocity measurements, Vogt et al. (2010b) discovered three planets b, c, and d at minimal masses of 5, 18 and 23 $M_\oplus$ and semi-major axes of 0.05, 0.22 and 0.49 au, respectively. Wyatt et al. (2012) confirmed the planets b and c but not the planet d, therefore we consider in this work 61 Vir d as unconfirmed.

In addition, Bryden et al. (2006) discovered with *Spitzer* a debris disk surrounding the star with a fractional luminosity L_{dust}/L_{star} of $2.7 \cdot 10^{-5}$. By using Herschel, Wyatt et al. (2012) reported that the disk density peaks between 30 and 100 au (and even up to 150 au from ALMA observations according to Marino et al. (2017)). Wyatt et al. (2012) found that the disk is inclined by 77° with respect to the plane of the sky which gives a slight underestimation of 3% for the planet masses by assuming the disk and the orbits of these planets to be coplanar.

HD 136352. The system HD 136352 is located at 14.74 ± 0.02 pc (Gaia Collaboration 2021) and hosts a G2V star (Gray et al. 2006). We derived an age of 0.57 ± 0.17 Gyr based on chromospheric activity, which is significantly younger than the age estimated from Lovis et al. (2011) or Kane et al. (2020), respectively 4.37 ± 0.5 Gyr and 8.3 ± 3.2 Gyr. Our stellar mass estimation of 0.83 ± 0.05 $M_\odot$ is consistent with Delrez et al. (2021). We found a sub-solar metallicity [Fe/H] of −0.37 ± 0.03.

The system hosts three planets b, c, and d discovered by Mayor et al. (2011) via RV measurements. Udry et al. (2019) reported minimal masses of 4.8 ± 0.6 $M_\oplus$, 10.8 ± 1.0 $M_\oplus$, and 8.6 ± 1.2 $M_\oplus$, orbiting at about 0.09 au, 0.17 au, and 0.41 au (period of about 11.6 days, 27.6 days, and 107.6 days), respectively. In addition, the three planets transit. The two inner ones were first detected via TESS photometry (Kane et al. 2020; Lovos et al. 2022), while the outer one via CHEOPS (Delrez et al. 2021). The updated parameters derived by combining CHEOPS and TESS photometric and HARPS RV measurements do not change significantly from Udry et al. (2019) but indicate as well an absolute mass of 4.7 ± 0.4 $M_\oplus$, 11.2 ± 0.7 $M_\oplus$, and 8.8 ± 0.9 $M_\oplus$, with radii of 1.66 ± 0.05 $R_\oplus$, 2.92 ± 0.08 $R_\oplus$, and 2.56 ± 0.09 $R_\oplus$, and mean density of 1.02 ± 0.13 $\rho_\oplus$, 0.45 ± 0.05 $\rho_\oplus$, and 0.52 ± 0.08 $\rho_\oplus$, respectively (Delrez et al. 2021). More precisely, Delrez et al. (2021) indicated that the planet b is a rocky mostly dry planet unlike the planets c and d that are likely to have small hydrogen-helium envelopes, and a possible water content. They reported no major eccentricity for the three planets (up to 0.25 at 2σ).

HD 154088. The system HD 154088 is located at 18.273 ± 0.008 pc (Gaia Collaboration 2021). We derive an age of 7.1 ± 0.5 Gyr based on chromospheric activity and a stellar mass of 0.94 ± 0.05$M_\odot$, both consistent with previous estimates from e.g., Unger et al. (2021), who indicated as well the stellar spectral

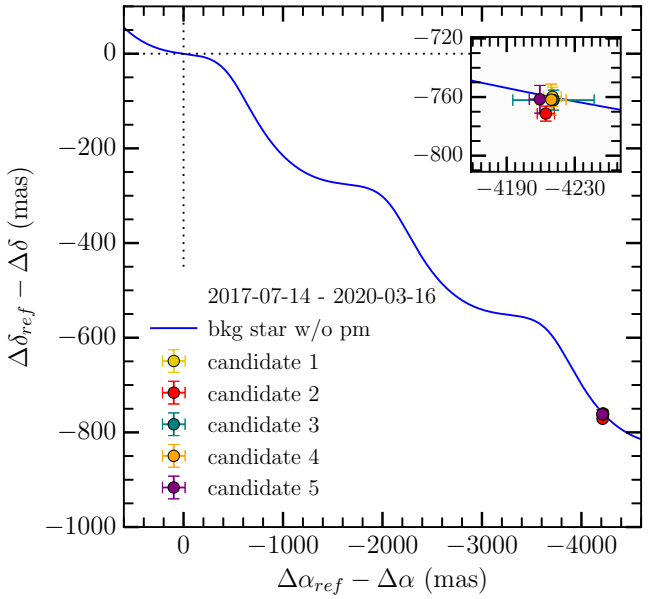

Fig. A.6. SPHERE/IRDIS relative astrometry differences of the offset positions of all the point-like sources detected around HD 136352 between the first epoch 2017-07-14 considered as reference and the second epoch 2020-03-16. (See caption from Fig. A.1)

type to be K0IV-V. We estimate a super solar metallicity [Fe/H] of 0.25 ± 0.06. Fossati et al. (2013) reported the detection of the stellar magnetic field.

The system hosts one planet HD 154088 b with a minimal mass of 6.6 $M_\oplus$ at 0.134 au (18.6-day period) discovered by Mayor et al. (2011) and confirmed by Unger et al. (2021). The latter constrain the eccentricity below 0.19 (0.34) at the 68% (95%) level.

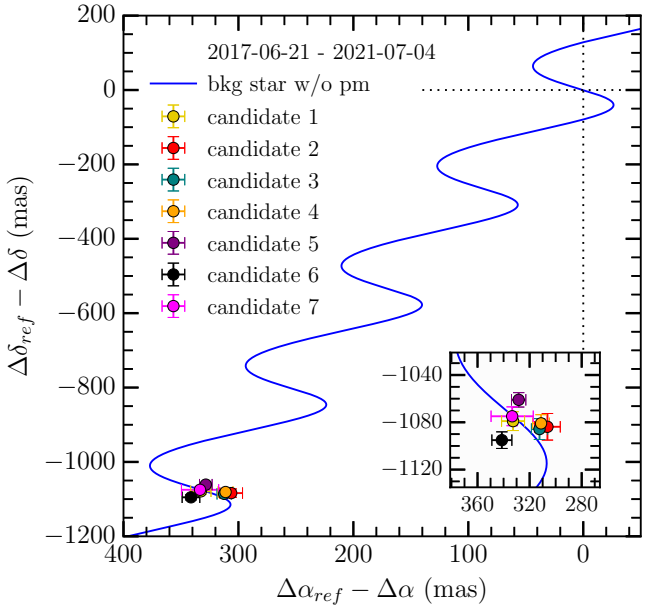

Fig. A.7. SPHERE/IRDIS relative astrometry differences of the offset positions of all the point-like sources detected around HD 154088 in the first and third epochs (2017-06-21, 2021-07-04). (See caption from Fig. A.1)

HD 189567. The system HD 189567 is located at 17.93 ± 0.01 pc (Gaia Collaboration 2021). Based on chromospheric activity, we derive an age of 4.5 ± 0.5 Gyr, younger than Takeda et al. (9.8 ± 2.1 Gyr 2007). We estimate a stellar mass of 0.85 ± 0.05 $M_\odot$ consistent with literature, and a metallicity [Fe/H] of −0.27 ± 0.05. The stellar type is a G2V (Gray et al. 2006).

The system hosts two planets, HD 189567 b and HD 189567 c discovered by Mayor et al. (2011) and Unger et al. (2021), respectively. Unger et al. (2021) derived for the planets b and c a minimal mass of 8.5 ± 0.6 $M_\oplus$ and 7.0 ± 0.9 $M_\oplus$ at a semi-major axis of about 0.11 au and 0.20 au (period of 14.2 days and 33.7 days), respectively.

Appendix B: Age estimation

The stellar age is an important parameter in high-contrast imaging observations to convert observed fluxes into masses of putative companion candidates, as well as the sensitivity in terms of mass of given observation. For our sample, ages from the literature were heterogeneously derived, and sometimes poorly constrained or disagreeing with each other. For these reasons, we have revisited in this work the ages of all the stars based on two different methods: gyrochronology and stellar activity.

B.1. Gyrochronology

Gyrochronology uses the empirical rotation period-color relation to estimate the age. This technique is calibrated by using a few age-benchmark open clusters, such as the Pleiades, the Hyades or Praesepe, can be also used to estimate the age of individual stars, possibly complementary to other independent techniques. In the present study, considering the wide color range spanned by our targets (0.64 < B−V < 1.65 mag), we had to use three different gyrochronologic relations to infer the age.

In the color range 0.5 < B−V < 1.40 mag, corresponding to the F5–K9 spectral types, we have used the relation:

$$Age(Gyr) = \sqrt[1/n]{\frac{P(d)}{a(B-V-c)^b}}, \quad \text{(B.1)}$$

using the coefficients $a = 0.407$, $b = 0.325$, $c = 0.495$, and $n = 0.566$ (Mamajek & Hillenbrand 2008) and $a = 0.40$, $b = 0.31$, $c = 0.45$, and $n = 0.55$ (Angus et al. 2015).

For the M0–M1-type stars in our sample, we used the relation of Engle & Guinan (2011):

$$Age(Gyr) = \sqrt[1/c]{\frac{P(d)-a}{b}}, \quad \text{(B.2)}$$

with $a = -4.14$, $b = 15.57$ and $c = 0.688$,

As for the M2.5–M5.5-type stars, we used the linear relation of Engle & Guinan (2011):

$$Age(Gyr) = \frac{P(d)-a}{b}, \quad \text{(B.3)}$$

with $a = 0.88$ and $b = 16.542$.

As the input rotation period for each target, we used the average value if more periods were available from the literature (see Table B.1). By exploring the existing literature on our stellar sample to gather the values of their stellar rotation periods, we found rotation periods (P) measured by using periodogram analysis of three different types of data time series: photometric ($P_{\rm ph}$), activity index ($P_{\rm ac}$), and radial velocity ($P_{\rm RV}$). In Table B.2, we list the B−V color and the photometric rotation period $P_{\rm ph}$, together with its uncertainty σ_P, when known, and the corresponding references for each target.

On a total of 27 targets, we retrieved information on the photometric rotation period $P_{\rm ph}$ for ten targets. The main reason for this low detection rate is that our targeted stars are relatively old and are expected to have very low-level photometric variability, below the current sensitivity of ground or space-based telescopes.

We retrieved information on the rotation period $P_{\rm ac}$ from the activity index time series for 13 targets, six of which with $P_{\rm ph}$ known, which are listed in Table B.2 together with their respective references. The activity index mostly measured for the selected targets is R'_{HK}. The main reason is again linked to the old age of our targeted stars, which translates into long rotation periods, combined with the scarcity of spectroscopic time series long enough to allow a meaningful measurement of rotation.

Finally, for seven targets we found rotation period measurements $P_{\rm RV}$ from RV time series (see Table B.2). In fact, the periodic modulation of visibility of surface magnetic inhomogeneities gives rise to quasi-periodic jitters in the RV measurements, which allow the stellar rotation period to be measured. Out of seven targets with $P_{\rm RV}$ known, four also have $P_{\rm ph}$ and $P_{\rm ac}$ both known, and two have only $P_{\rm ac}$ known.

To summarize, we have the rotation period required for an estimation of the age via gyrochronology for a total of 17 targets. We found that rotation periods measured by different methods (when available) are generally in good agreement with each other.

B.2. Stellar activity

The second approach to measure the age of our targets is the use of calibrated age-activity relations. In this work, we used the relation by Mamajek & Hillenbrand (2008) which is calibrated in the color range $0.5 < \mathrm{B-V} < 1.40$ mag:

$$\log Age(Gyr) = -38.053 - 17.912 \log R'_{HK} - 1.6675 \log (R'_{HK})^2 , \quad \text{(B.4)}$$

where R'_{HK} is the chromospheric activity index.

We have explored the existing literature on the selected targets to gather measurements of magnetic activity indices. As mentioned, the most widely measured index is the chromospheric activity index R'_{HK}, which is the width of the activity sensitive Ca II H&K lines normalized by the bolometric flux and corrected for a photospheric contribution. Except the single measurement for GJ 3998 and GJ 667C, all the other targets have numerous values of R'_{HK}. In Table B.2, we list for each target the R'_{HK} values and the corresponding references, and in Table B.1 the average value.

The age based on stellar activity was derived for 15 targets, whose color is within the validity of the Mamajek & Hillenbrand (2008) relation. We stress that the age of HD 136352 is likely to be underestimated by our method as our age estimation gives a rather young star of 0.57 ± 0.17 Gyr, which is discrepent by 3σ with the age from the literature ($8.2^{+3.2}_{-3.1}$ Gyr), and may not be consistent with its subsolar metallicity (see Table C.1 and Appendix C).

Both chromospheric and gyrochronologic ages were inferred for a subsample of 7 targets (without considering GJ 581). The gyrochronologic ages inferred by Mamajek & Hillenbrand (2008) and Angus et al. (2015) are generally in agreement within 20%, while chromospheric and gyrochronologic ages are also in agreement within 30%.

As final age for each system, we adopt either the gyrochronologic age, the chromospheric age, or the average value in the cases with independent realistic measurements (see Table B.1 and Fig. B.1). By using our methods, we are not able to estimate robust ages for GJ 180, GJ 682 or HD 136352. Regarding HD 136352, we use the age of 8.3 ± 3.2 Gyr from Kane et al. (2020), while considering GJ 180 and GJ 682 we use a default age of 5 ± 4 Gyr. Except GJ 433 (0.50 ± 0.15 Gyr), all of our systems have ages between 1 Gyr and 10 Gyr, with uncertainties up to a few gigayears.

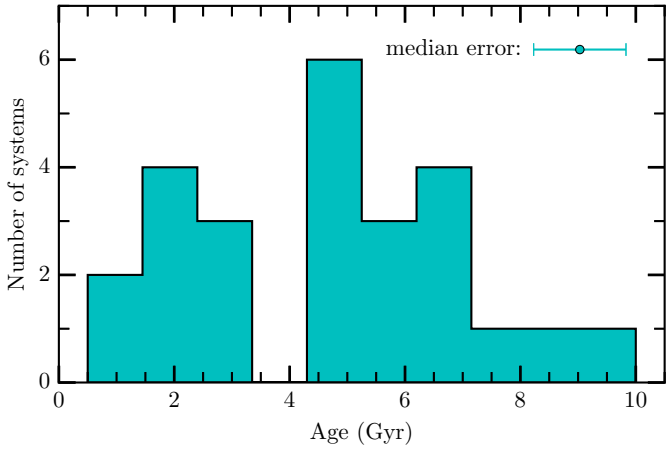

Fig. B.1. Distribution of the age of the stars in our sample re-determined homogeneously in this work (see values in Table B.1). We indicate the median error on the age in the upper right corner.

Table B.1. Average rotation period and activity and corresponding activity and gyrochronologic ages (according to M: Mamajek & Hillenbrand (2008); A: Angus et al. (2015); S: Engle & Guinan (2011).

System	B − V (mag)	$< P_{\rm rot} >$ (d)	$< R'_{HK} >$	$\rm Age_{Chromo}$ (Gyr)	$\rm Age_{Gyr0}$ (Gyr)			$<$ Age $>$
					M	A	S	this work
GJ 163	1.49	50	−5.540 ± 0.084				3.0	3.0 ± 0.7
GJ 176	1.54	39.5 ± 1.3	−4.955 ± 0.063				2.3	2.3 ± 0.6
GJ 180	1.55		−5.341 ± 0.082					
BD-061339	1.35		−4.778 ± 0.096	2.9 ± 1.2				2.9 ± 1.2
GJ 229	1.48	27.2 ± 1.6	−4.861 ± 0.131				1.6	1.6 ± 0.4
GJ 422	1.33		−5.800 ± 0.044	5.5 ± 0.8				5.5 ± 0.8
GJ 433	1.51	7.94	−5.284 ± 0.192				0.50	0.50 ± 0.15
GJ 581	1.20	130 ± 2	−5.459 ± 0.219	10 ± 1			7.8	8.9 ± 1.1
Wolf 1061	1.57	119.1 ± 1	−5.219 ± 0.209				7.1	7.1 ± 2
GJ 649	1.48	23.8 ± 0.1	−4.944 ± 0.101				1.40	1.40 ± 0.35
GJ 667C	1.57	105	−5.33				6.3	6.3 ± 2
GJ 674	1.57	34.1 ± 1.3	−5.013 ± 0.086				2.0	2.0 ± 0.5
GJ 682	1.65		−5.363 ± 0.342					
GJ 832	1.50	41 ± 4	−5.215 ± 0.085				2.4	2.4 ± 0.3
GJ 3998	1.51	32.99	−4.82				2	2 ± 0.5
HD 3651	0.83	43 ± 2	−4.979 ± 0.09	6.2 ± 1.7	7 ± 1	8.5		7.5 ± 2.2
HD 20794	0.71		−4.971 ± 0.017	6 ± 0.3				6 ± 0.3
HD 38858	0.64	24	−4.921 ± 0.043	5.1 ± 0.8	4.1 ± 0.5	4.3		4.3 ± 1
HD 40307	0.95	34.4 ± 2.4	−4.980 ± 0.144	6 ± 2	4 ± 0.4	4.8		4.4 ± 2
HD 69830	0.79	42	−4.963 ± 0.029	5.9 ± 0.5	7.3 ± 1	8.7		6.6 ± 1.5
HD 85512	1.18	42 ± 6	−4.953 ± 0.060	5.7 ± 1	4.5 ± 0.3	5.6		5 ± 1
HD 99492	1.02		−4.953 ± 0.055	5.7 ± 1.0				5.7 ± 1.0
HD 102365	0.67	24	−4.931 ± 0.026	5.3 ± 0.5	3.6 ± 0.5	4.0		4.3 ± 0.8
61 Vir	0.70	29	−4.973 ± 0.056	6 ± 1	4.7 ± 0.6	5.3		5.1 ± 1.3
HD 136352	0.65		−4.941 ± 0.044	0.57 ± 0.17				0.57 ± 0.17
HD 154088	0.83		−5.026 ± 0.027	7.1 ± 0.5				7.1 ± 0.5
HD 189567	0.64		−4.885 ± 0.028	4.5 ± 0.5				4.5 ± 0.5

Table B.2. Information from the literature on the stellar rotation period and activity as measured by means of $\rm R'_{HK}$

Name	B−V	P_{ph}	σ	ref	P_{ac}	σ	ref	P_{RV}	σ	ref	R'_{HK}	ref
GJ 163	1.49	50	—	P8	—	—	—	—	—	—	-5.480	P5
	—	—	—	—	—	—	—	—	—	—	-5.600	A7
GJ 176	1.54	38.92	—	P3	37	—	P5	39.2	0.2	P2	-4.911	P5
	—	40.7	0.4	P6	40.6	—	P7	—	—	—	-5.00	P2
	—	40.8	0.1	P4	39.3	0.1	P1	—	—	—	—	—
GJ180	1.55	—	—	—	—	—	—	—	—	—	-5.283	P5
	—	—	—	—	—	—	—	—	—	—	-5.40	A6
GJ229	1.48	27.7	0.2	P6	25	—	P5	29.4	0.1	P2	-4.90	A6
	—	27.3	0.1	P4	26.7	2.4	P2	—	—	—	-4.669	P5
	—	—	—	—	—	—	—	—	—	—	-4.965	A7
	—	—	—	—	—	—	—	—	—	—	-4.91	P2
BD-061339	1.35	—	—	—	—	—	—	—	—	—	-4.846	A7
	—	—	—	—	—	—	—	—	—	—	-4.710	A17
GJ422	1.33	—	—	—	—	—	—	—	—	—	-5.769	P5
	—	—	—	—	—	—	—	—	—	—	-5.832	A7
GJ433	1.51	7.94	—	P8	—	—	—	—	—	—	-5.148	P5
	—	—	—	—	—	—	—	—	—	—	-5.420	A7
GJ581	1.20	—	—	—	130	2	P5	—	—	—	-5.776	P5

Table B.2. continued.

Name	B−V	P_{ph}	σ	ref	P_{ac}	σ	ref	P_{RV}	σ	ref	R'_{HK}	ref
	—	—	—	—	132.5	6.3	P1	—	—	—	-5.436	A17
	—	—	—	—	—	—	—	—	—	—	-5.321	A17
	—	—	—	—	—	—	—	—	—	—	-5.304	A17
Wolf1061	1.57	119	1	P6	119	—	P5	—	—	—	-5.523	P5
	—	119.3	—	P4	—	—	—	—	—	—	-5.088	A17
	—	—	—	—	—	—	—	—	—	—	-5.075	A17
	—	—	—	—	—	—	—	—	—	—	-5.190	A17
GJ649	1.48	23.8	0.1	P6	—	—	—	—	—	—	-4.872	A8
	—	23.9	—	P8	—	—	—	—	—	—	-5.016	A7
GJ667C	1.57	—	—	—	—	—	—	105	—	P9	-5.334	A17
GJ674	1.57	33.29	—	P3	35	—	P5	36.2	0.1	P2	-5.05	A6
	—	35	1	P4	32.9	0.1	P1	—	—	—	-4.885	P5
	—	—	—	—	33.0	0.7	P2	—	—	—	-5.077	A7
	—	—	—	—	—	—	—	—	—	—	-5.04	P2
GJ682	1.65	—	—	—	—	—	—	—	—	—	-4.99	A6
	—	—	—	—	—	—	—	—	—	—	-5.438	P5
	—	—	—	—	—	—	—	—	—	—	-5.662	A7
GJ832	1.50	—	—	—	55	—	P5	39.1	0.1	P2	-5.23	A6
	—	—	—	—	45.7	9.3	P1	—	—	—	-5.10	A4
	—	—	—	—	39.2	9.4	P2	—	—	—	-5.182	P5
	—	—	—	—	—	—	—	—	—	—	-5.336	A7
	—	—	—	—	—	—	—	—	—	—	-5.23	P2
GJ3998	1.51	32.99	—	P15	—	—	—	—	—	—	-4.82	P5
HD3651	0.83	41	—	P8	43.4	—	P11	—	—	—	-4.991*	A8
	—	—	—	—	44	0.4	P10	—	—	—	-5.020	A9
	—	—	—	—	44	—	P12	—	—	—	-4.85	A10
	—	—	—	—	—	—	—	—	—	—	-5.02	A3
	—	—	—	—	—	—	—	—	—		-4.823	A13
	—	—	—	—	—	—	—	—	—	—	-5.087	A12
	—	—	—	—	—	—	—	—	—	—	-5.00	P10
	—	—	—	—	—	—	—	—	—	—	-5.04	A11
HD20794	0.71	—	—	—	—	—	—	—	—	—	-4.98	A10
	—	—	—	—	—	—	—	—	—	—	-4.981*	A1
	—	—	—	—	—	—	—	—	—	—	-4.946*	A2
	—	—	—	—	—	—	—	—	—	—	-4.98	A3
HD38858	0.64	—	—	—	24	—	P13	—	—	—	-4.95	A9
	—	—	—	—	—	—	—	—	—	—	-4.918*	A1
	—	—	—	—	—	—	—	—	—	—	-4.855*	A2
	—	—	—	—	—	—	—	—	—	—	-4.968	A12
	—	—	—	—	—	—	—	—	—	—	-4.89	A14
	—	—	—	—	—	—	—	—	—	—	-4.950	A11
HD40307	0.95	31.8	3.7	P1	36.5	2.3	P2	35.0	0.1	P2	-4.949*	A1
	—	—	—	—	—	—	—	—	—	—	-4.934*	A2
	—	—	—	—	—	—	—	—	—	—	-4.99	A3
	—	—	—	—	—	—	—	—	—	—	-4.83	A4
	—	—	—	—	—	—	—	—	—	—	-4.85	A4
	—	—	—	—	—	—	—	—	—	—	-5.259	A5
	—	—	—	—	—	—	—	—	—	—	-5.05	P2
HD69830	0.79	—	—	—	42	—	P13	—	—	—	-4.95	A9
	—	—	—	—	—	—	—	—	—	—	-4.991	A12
	—	—	—	—	—	—	—	—	—	—	-4.971	A12
	—	—	—	—	—	—	—	—	—	—	-4.94	A6
	—	—	—	—	—	—	—	—	—	—	-4.92	A3

Table B.2. continued.

Name	B−V	P_{ph}	σ	ref	P_{ac}	σ	ref	P_{RV}	σ	ref	R'_{HK}	ref
	—	—	—	—	—	—	—	—	—	—	-5.005*	A15
	—	—	—	—	—	—	—	—	—	—	-4.945	A5
	—	—	—	—	—	—	—	—	—	—	-4.98	A11
HD85512	1.18	—	—	—	45.9	0.4	P1	34.8	0.1	P2	-4.905*	A1
	—	—	—	—	45.8	5.2	P2	—	—	—	-4.90	A3
	—	—	—	—	—	—	—	—	—	—	-4.96	A4
	—	—	—	—	—	—	—	—	—	—	-4.95	P2
HD99492	1.02	—	—	—	—	—	—	—	—	-4.93	—	A3
	—	—	—	—	—	—	—	—	—	—	-4.889	A17
	—	—	—	—	—	—	—	—	—	—	-5.015	A17
	—	—	—	—	—	—	—	—	—	—	-4.978	A17
HD102365	0.67	—	—	—	24	—	P14	—	—	—	-4.957	A12
	—	—	—	—	—	—	—	—	—	—	-4.95	A16
	—	—	—	—	—	—	—	—	—	—	-4.944*	A1
	—	—	—	—	—	—	—	—	—	—	-4.916	A2
	—	—	—	—	—	—	—	—	—	—	-4.88	A6
	—	—	—	—	—	—	—	—	—	—	-4.93	A3
	—	—	—	—	—	—	—	—	—	—	-4.942	A15
61Vir	0.70	—	—	—	29	—	P12	—	—	—	-5.001*	A8
	—	—	—	—	—	—	—	—	—	—	-5.011	A12
	—	—	—	—	—	—	—	—	—	—	-5.04	A9
	—	—	—	—	—	—	—	—	—	—	-5.00	A10
	—	—	—	—	—	—	—	—	—	—	-4.87	A16
	—	—	—	—	—	—	—	—	—	—	-4.99*	A1
	—	—	—	—	—	—	—	—	—	—	-4.967*	A2
	—	—	—	—	—	—	—	—	—	—	-4.91	A6
HD136352	0.65	—	—	—	—	—	—	—	—	—	-4.91	A16
	—	—	—	—	—	—	—	—	—	—	-5.013	A12
	—	—	—	—	—	—	—	—	—	—	-4.949*	A1
	—	—	—	—	—	—	—	—	—	—	-4.932*	A2
	—	—	—	—	—	—	—	—	—	—	–4.90	A4
HD154088	0.83	—	—	—	—	—	—	—	—	—	-5.02	A9
	—	—	—	—	—	—	—	—	—	—	-5.00	A10
	—	—	—	—	—	—	—	—	—	—	-5.064*	A1
	—	—	—	—	—	—	—	—	—	—	-5.02	A6
HD189567	0.64	—	—	—	—	—	—	—	—	—	-4.86	A10
	—	—	—	—	—	—	—	—	—	—	-4.916*	A1
	—	—	—	—	—	—	—	—	—	—	-4.878*	A2

* average value

References. References given in the columns "ref" are the following: P1 = Suárez Mascareño et al. (2015), P2 = Suárez Mascareño et al. (2017), P3 = Kiraga & Stepien (2007), P4 = Suárez Mascareño et al. (2016), P5 = Astudillo-Defru et al. (2017a), P6 = Díez Alonso et al. (2019), P7 = Trifonov et al. (2018), P8 = Oelkers et al. (2018), P9 = Anglada-Escudé et al. (2013), P10 = Marsden et al. (2014), P11 = Vidotto et al. (2014), P12 = Baliunas et al. (1996), P13 = Isaacson & Fischer (2010), P14 = Saar & Osten (1997), P15 = Giacobbe et al. (2020), A1 = Gomes da Silva et al. (2014), A2 = Meunier et al. (2017), A3 = Miller et al. (2015), A4 = Jenkins et al. (2006), A5 = Gondoin (2020), A6 = Hojjatpanah et al. (2019), A7 = Houdebine et al. (2017), A8 = Duncan et al. (1991), A9 = Wright et al. (2004), A10 = Rocha-Pinto et al. (2004), A11 = Katsova & Livshits (2011), A12 = Gray et al. (2003), A13 = Herrero et al. (2012), A14 = Radick et al. (2018), A15 = Zechmeister et al. (2013), A16 = Henry et al. (1996), and A17 = Boro Saikia et al. (2018).

Appendix C: Stellar metallicity derivation

A correlation between the presence of giant planet and the metallicity of the host star is well known (Fischer & Valenti 2003). That is why we determine homogeneously the metallicity of all the GK stars in our sample, along with their atmospheric properties.

We exploited archival high-resolution, high signal-to-noise ratio (S/N) spectra for our GK stars to derive atmospheric parameters and metallicity ([Fe/H]). Given the dominance of molecular bands, M-type dwarfs require a dedicated approach and cannot be analyzed in the same way (see Maldonado et al. 2020, and references therein). Our M dwarf targets have been extensively investigated through the literature in terms of their atmospheric

parameters and chemical composition. However, due to the intrinsic issues related to their analysis, different studies have provided very different results (see e.g., the exemplary case of GJ 176 with differences of 600 K in T_{eff}, 0.6 dex in $\log(g)$ and 0.6 dex in metallicity [Fe/H]; Santos et al. 2013; Passegger et al. 2019). Thus, we do not discuss their composition because large systematic uncertainties plague the comparison with GK stars.

For stars warmer than $T_{eff} \gtrsim 5\,000$ K we obtained spectroscopic parameters by performing a differential analysis using the MOOG (Sneden 1973; 2019 version) python wrapper q^2 (Ramírez et al. 2014) and the `marcs` grid of model atmospheres (Gustafsson et al. 2008). The Fe I/Fe II line list comes from a compilation published in our recent works (sources for atomic parameters of the 90 iron transitions can be found in D'Orazi et al. 2020; Baratella et al. 2020). The equivalent widths (EWs) have been measured with `ares` (Sousa et al. 2015) and carefully checked trough the IRAF[1] task *splot*. We derived stellar parameters T_{eff}, and $\log(g)$ by imposing excitation and ionization equilibrium, respectively; microturbulence velocities (V_t) were gathered by removing spurious trends between the reduced EWs of Fe I lines and the corresponding abundances. We adopted $\log(n(\mathrm{Fe}))_\odot = 7.50$ dex as a reference solar abundance (Asplund et al. 2009). For this sample, we also determined abundances for Na I (non-LTE corrections have been applied following Lind et al. 2011), Mg I, Si I, Ca I, Ti I, Ti II, Cr I, Cr II, and Ni I, adopting the same model atmosphere and code that is described above. As for Fe, we assumed solar reference abundances from Asplund et al. (2009). Results are reported in Table C.2.

Errors on the stellar parameters, metallicity [Fe/H], and elemental abundances have been calculated in the standard way: they include internal errors due to the EW measurements and the propagation of uncertainties related to the atmospheric parameters. We refer the reader to our previous investigations, e.g., D'Orazi et al. (2020) and Baratella et al. (2020). Regarding the four cooler stars of this GK-type sub-sample (namely GJ 667C, HD 40307, HD 85512, and BD-061339), we instead fixed atmospheric parameters from photometry: T_{eff} are from *Gaia* (DR2 or eDR3 depending on availability for each target) and 2MASS JHK colors using the relationship by Casagrande et al. (2021). We exploited the `colte` python program developed and maintained by L. Casagrande[2] in order to obtain average T_{eff} with weighted errors calculated through Monte Carlo method. Surface gravities have been calculated starting from those T_{eff}, masses as given in Table 1, *Gaia* parallaxes and bolometric correction for K band photometry (Casagrande & VandenBerg 2014, 2018). We then measured EWs of neutral iron lines and found the [Fe/H] values as reported in Table C.1.

Overall, we note that in our sample only three GK host stars have a super-solar metallicity: HD 99492, HD 154088, and HD 3651, the latter one only at a $2\,\sigma$ level (see Table C.1 and Fig. C.1). We also notice that two of them (HD 99492 and HD 3651) are in a wide binary system. On the contrary, 9 GK host stars have a significant ($> 4\,\sigma$) sub-solar metallicity.

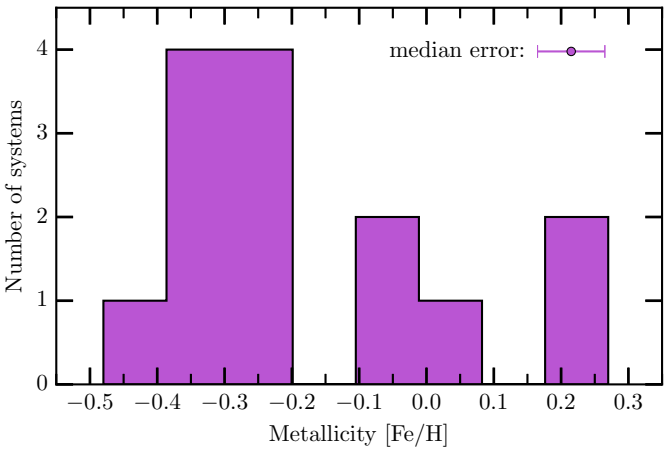

Fig. C.1. Distribution of the metallicity of the GK host stars in our sample that we estimated in this work (see values in Table C.1). We indicate the median error on the metallicity in the upper right corner.

[1] IRAF is distributed by NOAO, which is operated by AURA under a cooperative agreement with the NSF.
[2] https://github.com/casaluca/colte

Table C.1. Atmospheric parameters and metallicity [Fe/H] for the GK star sample.

Star	$T_{\rm eff}$ (K)	$\log g$ (dex)	V_t (km s^{-1})	[Fe/H] (dex)	Spectrum	S/N (per pixel)
HD 3651	5274 ± 107	4.42 ± 0.20	0.87 ± 0.25	+0.08 ± 0.06	HARPN	280
HD 20794	5501 ± 66	4.49 ± 0.15	0.88 ± 0.11	−0.36 ± 0.05	HARPS	350
HD 38858	5788 ± 75	4.56 ± 0.11	0.95 ± 0.11	−0.21 ± 0.05	HARPS	400
HD 69830	5458 ± 72	4.55 ± 0.12	0.76 ± 0.15	−0.03 ± 0.05	HARPS	380
HD 99492	5562 ± 120	4.58 ± 0.19	1.06 ± 20	+0.27 ± 0.09	HARPS	250
HD 102365	5608 ± 50	4.27 ± 0.12	0.91 ± 0.07	−0.35 ± 0.03	HARPS	350
61 Vir	5557 ± 48	4.40 ± 0.12	0.82 ± 0.10	−0.03 ± 0.04	HARPS	300
HD 136352	5655 ± 48	4.24 ± 0.12	0.88 ± 0.06	−0.37 ± 0.03	HARPS	345
HD 154088	5416 ± 70	4.46 ± 0.20	0.96 ± 0.20	+0.25 ± 0.06	HARPS	312
HD 189567	5715 ± 45	4.36 ± 0.13	0.92 ± 0.07	−0.27 ± 0.03	HARPS	330
BD-061339	4061 ± 52	4.68 ± 0.05	0.79 ± 0.12	−0.20 ± 0.10	HARPS	60
GJ 667 C	4939 ± 41	4.50 ± 0.10	0.90 ± 0.10	−0.48 ± 0.10	HARPS	290
HD 40307	4871 ± 65	4.61 ± 0.05	0.89 ± 0.10	−0.30 ± 0.05	ESPRESSO	1000
HD 85512	4389 ± 115	4.48 ± 0.10	0.75 ± 0.10	−0.28 ± 0.12	HARPS	195

Table C.2. Elemental abundances with corresponding errors for the G-type stars in our sample.

Star	[Na/Fe]$_{\rm NLTE}$	[Mg/Fe]	[Si/Fe]	[Ca/Fe]	[Ti/Fe]	[Cr/Fe]	[Ni/Fe]
HD 3651	0.11 ± 0.05	0.10 ± 0.07	0.00 ± 0.05	0.04 ± 0.06	0.04 ± 0.05	0.11 ± 0.08	0.10 ± 0.08
HD 20794	0.06 ± 0.05	0.25 ± 0.04	0.14 ± 0.05	0.18 ± 0.07	0.28 ± 0.05	0.04 ± 0.05	0.08 ± 0.04
HD 69830	0.03 ± 0.05	−0.01 ± 0.04	−0.01 ± 0.04	0.00 ± 0.05	0.05 ± 0.06	0.05 ± 0.06	0.04 ± 0.05
HD 38858	−0.01 ± 0.05	−0.03 ± 0.06	−0.03 ± 0.07	0.03 ± 0.08	0.04 ± 0.04	0.04 ± 0.08	−0.01 ± 0.08
HD 99492	0.12 ± 0.04	−0.03 ± 0.06	0.06 ± 0.06	−0.04 ± 0.07	0.05 ± 0.06	0.08 ± 0.06	0.10 ± 0.06
HD 102365	0.08 ± 0.05	0.18 ± 0.04	0.11 ± 0.05	0.12 ± 0.16	0.13 ± 0.05	0.01 ± 0.03	0.06 ± 0.07
61 Vir	0.06 ± 0.05	−0.01 ± 0.06	−0.01 ± 0.05	0.03 ± 0.05	0.06 ± 0.05	0.00 ± 0.05	0.03 ± 0.06
HD 136352	0.13 ± 0.06	0.24 ± 0.05	0.13 ± 0.06	0.14 ± 0.10	0.17 ± 0.06	0.05 ± 0.04	0.05 ± 0.06
HD 154088	0.15 ± 0.06	0.07 ± 0.06	0.12 ± 0.04	0.04 ± 0.05	0.07 ± 0.08	0.16 ± 0.07	0.10 ± 0.10
HD 189567	0.08 ± 0.09	0.05 ± 0.04	0.05 ± 0.04	0.06 ± 0.10	0.08 ± 0.10	0.01 ± 0.05	0.01 ± 0.07

Appendix D: Log of the VLT/SPHERE observations

Table D.1 lists the 94 observations with VLT/SPHERE, including the observational conditions, represented in Fig. D.1 too.

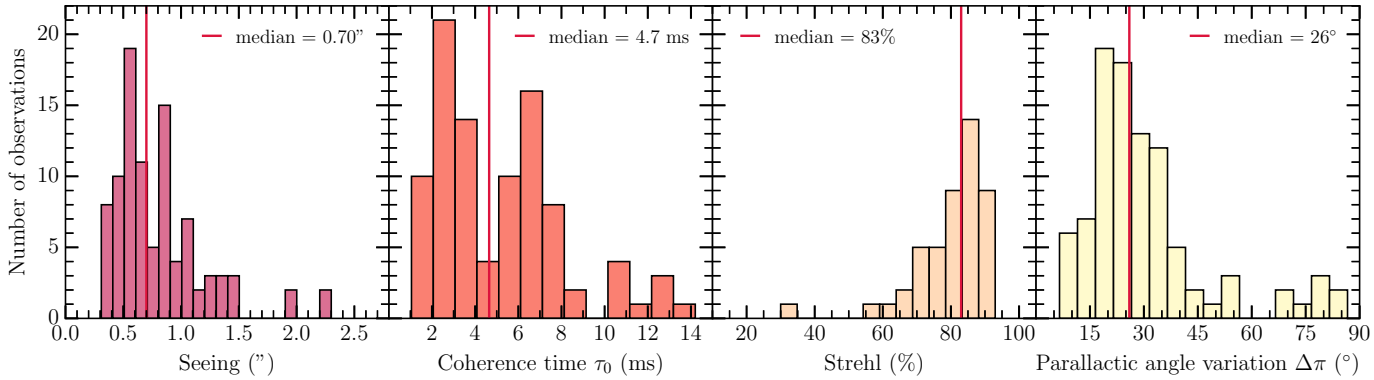

Fig. D.1. Distribution of the observing conditions: seeing, coherence time of the adaptive optic system, strehl, and parallactic angle variation.

Table D.1. Log of the 94 observations with the instrument VLT/SPHERE.

System	Date	Instru.	Filter	N_{exp}	DIT (s)	Grade	$\Delta\pi$ (°)	ϵ (")	τ_0 (ms)	Sr (%)	airmass
GJ 163	2018-10-12	IRDIS	H23	32	96	B	23.7	0.68	2.4	30	1.14
GJ 163	2018-10-12	IFS	YJ	32	96	B	23.8	0.70	2.4	–	1.14
GJ 176	2018-10-08	IRDIS	H23	64	48	A	16.9	0.90	3.7	77	1.38
GJ 176	2018-10-08	IFS	YJ	32	96	A	16.6	0.88	3.8	–	1.39
GJ 180	2018-10-09	IRDIS	H23	32	96	A	78.3	0.77	3.2	73	1.01
GJ 180	2018-10-09	IFS	YJ	32	96	A	78.4	0.84	2.5	–	1.01
BD-061339	2018-11-24	IRDIS	H23	32	96	A	31.3	0.59	12.0	84	1.06
BD-061339	2018-11-24	IFS	YJ	32	96	A	31.7	0.53	14.2	–	1.07
GJ 229	2018-11-27	IRDIS	H23	48	64	A	9.0	0.59	4.4	87	1.03
GJ 229	2018-11-27	IFS	YJ	32	96	A	9.2	0.63	4.0	–	1.03
GJ 422	2018-01-28	IRDIS	H23	30	96	A	19.4	0.38	10.2	75	1.20
GJ 422	2018-01-28	IFS	YJ	30	96	A	19.6	0.38	10.2	–	1.20
GJ 422	2019-11-25	IRDIS	K12	24	96	C	8.4	0.57	5.8	84	1.79
GJ 422	2019-11-25	IFS	YJH	24	96	C	8.4	0.65	3.9	–	1.79
GJ 422	2020-01-18	IRDIS	K12	24	96	A	15.4	0.47	10.7	87	1.20
GJ 422	2020-01-18	IFS	YJH	24	96	A	15.4	0.44	8.7	–	1.20
GJ 433	2018-02-02	IRDIS	H23	30	96	A	68.0	1.01	6.7	84	1.01
GJ 433	2018-02-02	IFS	YJ	30	96	A	68.4	1.01	6.7	–	1.01
GJ 433	2019-06-08	IRDIS	K12	15	64	C	23.9	0.86	3.7	82	1.01
GJ 433	2019-06-08	IFS	YJH	10	96	C	23.3	0.86	3.7	–	1.01
GJ 433	2020-01-20	IRDIS	K12	15	64	C	21.6	0.36	12.3	91	1.01
GJ 433	2020-01-20	IFS	YJH	10	96	C	20.6	0.36	12.3	–	1.01
GJ 581	2017-07-21	IRDIS	H23	30	96	A	35.3	0.55	6.9	81	1.05
GJ 581	2017-07-21	IFS	YJ	30	96	A	35.6	0.56	6.4	–	1.05
Wolf 1061	2017-07-28	IRDIS	H23	120	24	A	34.9	0.82	4.0	79	1.04
Wolf 1061	2017-07-28	IFS	YJ	30	96	A	34.1	0.78	4.5	–	1.04
GJ 649	2017-08-20	IRDIS	H23	60	48	B	14.1	0.84	5.6	81	1.57
GJ 649	2017-08-20	IFS	YJ	30	96	B	13.9	0.84	5.6	–	1.57
GJ 667	2017-06-27	IRDIS	H23	30	96	A	53.6	1.36	2.6	66	1.02
GJ 667	2017-06-27	IFS	YJ	30	96	A	54.2	1.36	2.6	–	1.02
GJ 674	2017-07-14	IRDIS	H23	30	96	A	27.2	0.67	3.2	73	1.08
GJ 674	2017-07-14	IFS	YJ	30	96	A	27.4	0.67	3.2	–	1.08
GJ 674	2021-07-04	IRDIS	K12	68	32	A	21.2	0.54	5.8	85	1.08
GJ 674	2021-07-04	IFS	YJH	23	96	A	21.2	0.54	5.8	–	1.08
GJ 682	2017-06-23	IRDIS	H23	60	48	C	31.5	1.95	1.4	58	1.07
GJ 682	2017-06-23	IFS	YJ	30	96	C	31.0	1.95	1.4	–	1.07
GJ 682	2017-07-20	IRDIS	H23	30	96	B	30.7	0.55	6.5	72	1.07
GJ 682	2017-07-20	IFS	YJ	30	96	B	31.0	0.55	6.5	–	1.07
GJ 682	2019-07-05	IRDIS	K12	24	96	B	25.0	0.54	6.5	88	1.06
GJ 682	2019-07-05	IFS	YJH	24	96	B	25.1	0.52	6.5	–	1.06
GJ 832	2017-05-27	IRDIS	H23	46	64	A	26.7	1.06	2.5	78	1.10

Table D.1. continued.

System	Date	Instru.	Filter	N_{exp}	DIT (s)	Grade	$\Delta\pi$ (°)	ϵ (")	τ_0 (ms)	Sr (%)	airmass
GJ 832	2017-05-27	IFS	YJ	30	96	A	25.9	0.97	2.9	–	1.10
GJ 832	2017-06-21	IRDIS	H23	184	16	C	27.7	2.30	1.1	61	1.10
GJ 832	2017-06-21	IFS	YJ	90	32	C	26.9	2.30	1.4	–	1.10
GJ 832	2017-06-27	IRDIS	H23	46	64	C	26.7	1.50	1.9	71	1.10
GJ 832	2017-06-27	IFS	YJ	30	96	C	25.9	1.50	1.9	–	1.10
GJ 832	2017-07-03	IRDIS	H23	46	64	B	25.9	1.42	1.8	75	1.10
GJ 832	2017-07-03	IFS	YJ	30	96	B	25.0	1.30	1.9	–	1.10
GJ 832	2022-07-29	IRDIS	H23	95	64	A	55.4	0.53	7.6	83	1.10
GJ 832	2022-07-29	IFS	YJ	56	96	A	47.3	0.56	7.2	–	1.10
GJ 3998	2017-05-14	IRDIS	H23	30	96	B	18.2	1.29	2.5	67	1.23
GJ 3998	2017-05-14	IFS	YJ	30	96	B	18.3	1.37	1.9	–	1.23
GJ 3998	2019-07-27	IRDIS	K12	24	96	B	14.4	0.59	4.8	85	1.23
GJ 3998	2019-07-27	IFS	YJH	24	96	B	14.4	0.68	3.6	–	1.24
HD 3651	2017-07-11	IRDIS	H23	332	10	A	18.8	1.22	2.0	78	1.45
HD 3651	2017-07-11	IFS	YJ	66	48	A	16.8	1.08	2.4	–	1.45
HD 20794	2017-09-03	IRDIS	H23	736	3	C	34.4	0.45	7.2	89	1.06
HD 20794	2017-09-03	IFS	YJ	406	6	C	37.5	0.47	6.8	–	1.06
HD 20794	2017-09-04	IRDIS	H23	552	6	B	44.9	0.88	2.2	87	1.06
HD 20794	2017-09-04	IFS	YJ	261	12	B	42.3	0.90	2.1	–	1.06
HD 38858	2018-11-23	IRDIS	H23	48	64	A	26.2	0.31	6.6	89	1.09
HD 38858	2018-11-23	IFS	YJ	32	96	A	26.1	0.32	7.7	–	1.09
HD 40307	2018-12-22	IRDIS	H23	48	64	A	18.2	0.48	8.7	89	1.27
HD 40307	2018-12-22	IFS	YJ	32	96	A	18.1	0.52	8.1	–	1.27
HD 69830	2018-12-18	IRDIS	H23	96	32	A	37.2	0.64	5.8	84	1.04
HD 69830	2018-12-18	IFS	YJ	32	96	A	36.7	0.70	5.5	–	1.04
HD 85512	2017-04-01	IRDIS	H23	60	48	C	32.8	1.04	2.4	80	1.06
HD 85512	2017-04-01	IFS	YJ	30	96	C	32.3	1.04	2.4	–	1.06
HD 85512	2017-12-30	IRDIS	H23	60	48	B	32.8	0.46	6.5	86	1.06
HD 85512	2017-12-30	IFS	YJ	30	96	B	32.2	0.46	6.5	–	1.06
HD 85512	2019-11-25	IRDIS	K12	136	16	C	7.0	0.39	7.9	91	1.55
HD 85512	2019-11-25	IFS	YJH	34	64	C	6.5	0.38	7.7	–	1.56
HD 85512	2020-01-03	IRDIS	K12	102	32	B	78.4	0.74	12.6	93	1.13
HD 85512	2020-01-03	IFS	YJH	34	64	B	24.6	0.82	10.3	–	1.06
HD 99492	2018-02-03	IRDIS	H23	30	96	A	22.7	0.94	5.8	85	1.13
HD 99492	2018-02-03	IFS	YJ	30	96	A	22.9	0.92	6.3	–	1.13
HD 99492	2020-03-16	IRDIS	K12	24	96	B	17.5	0.80	4.8	87	1.13
HD 99492	2020-03-16	IFS	YJH	24	96	B	17.6	1.06	3.4	–	1.14
HD 102365	2018-04-07	IRDIS	H23	136	24	A	40.1	0.44	7.7	91	1.05
HD 102365	2018-04-07	IFS	YJ	135	24	A	40.9	0.46	7.1	–	1.05
61 Vir	2017-06-28	IRDIS	H23	208	16	A	76.1	0.83	2.6	87	1.01
61 Vir	2017-06-28	IFS	YJ	203	16	A	15.8	0.78	2.9	–	1.01
HD 136352	2017-07-14	IRDIS	H23	70	48	A	31.2	0.82	2.9	80	1.10
HD 136352	2017-07-14	IFS	YJ	68	48	A	30.8	0.88	2.8	–	1.10
HD 136352	2020-03-16	IRDIS	K12	84	24	A	19.3	0.65	6.1	91	1.09
HD 136352	2020-03-16	IFS	YJH	64	32	A	19.7	0.64	6.1	–	1.10
HD 154088	2017-06-21	IRDIS	H23	90	32	A	21.6	1.20	2.6	73	1.03
HD 154088	2017-06-21	IFS	YJ	90	32	A	22.1	1.20	2.4	–	1.03
HD 154088	2019-07-22	IRDIS	K12	56	32	C	86.6	0.50	3.4	80	1.00
HD 154088	2019-07-22	IFS	YJH	28	64	C	84.1	0.51	3.5	–	1.00
HD 154088	2021-07-04	IRDIS	K12	28	32	A	34.6	0.55	6.6	91	1.00
HD 154088	2021-07-04	IFS	YJH	14	64	A	34.6	0.55	6.6	–	1.00
HD 189567	2017-05-29	IRDIS	H23	368	8	A	18.2	0.90	2.5	83	1.37
HD 189567	2017-05-29	IFS	YJ	60	12	A	18.1	0.93	2.5	–	1.37

Appendix E: Reduced observations

Figures E.1–E.3 show the reduced images via SpeCal-cADI, SpeCal-TLOCI, ANDROMEDA ADI algorithms for all the IRDIS observations. In addition, Figs. E.4 and E.5 show the reduced images via SpeCal-PCA ASDI and ANDROMEDA ASDI algorithms for all the IFS observations.

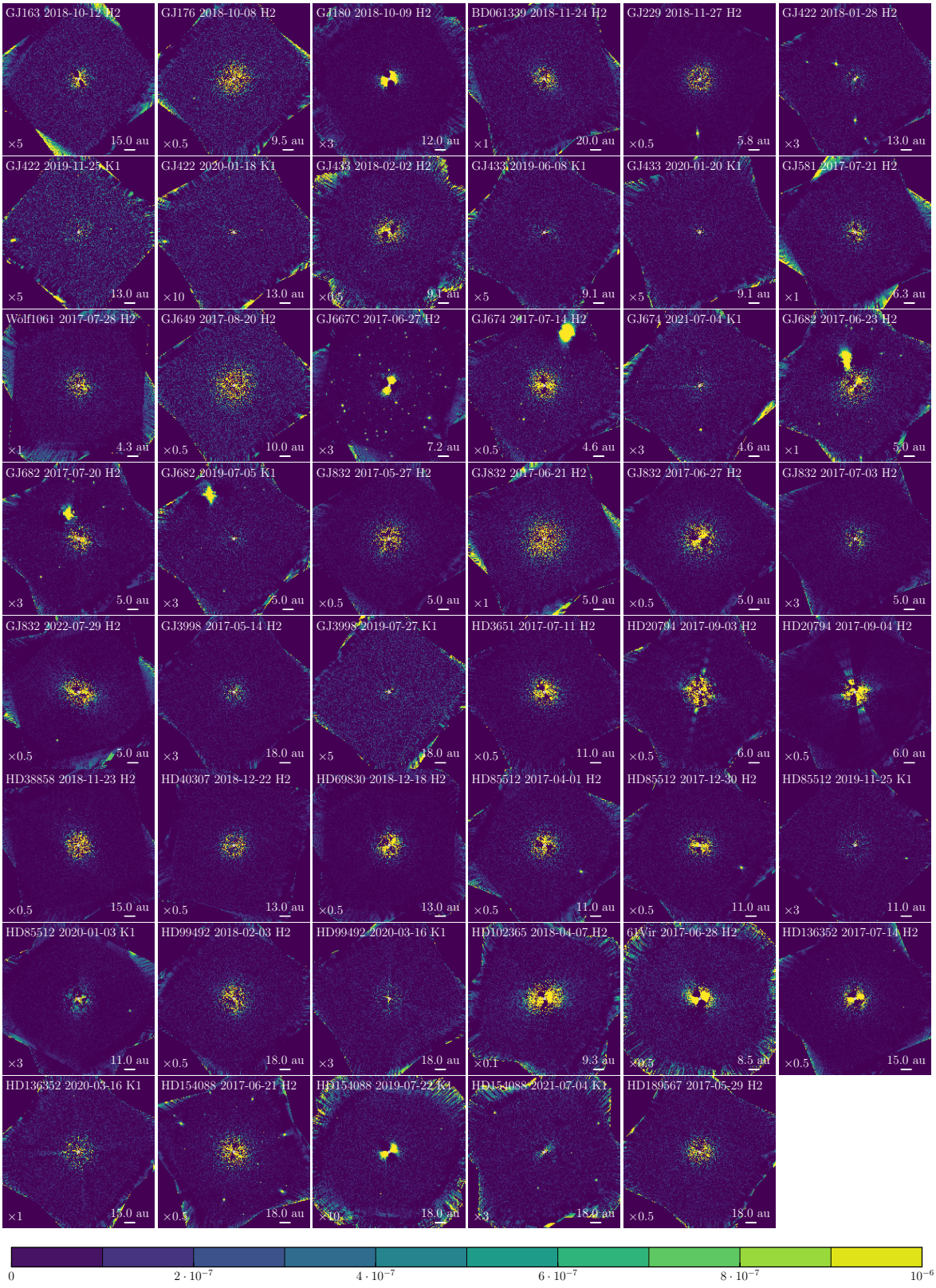

Fig. E.1. Reduced images from SPHERE-IRDIS for the whole survey for SpeCal-cADI reductions. The factor in the bottom left hand corner of each figure indicates the number by which to multiply the color bar to have the corresponding contrast values.

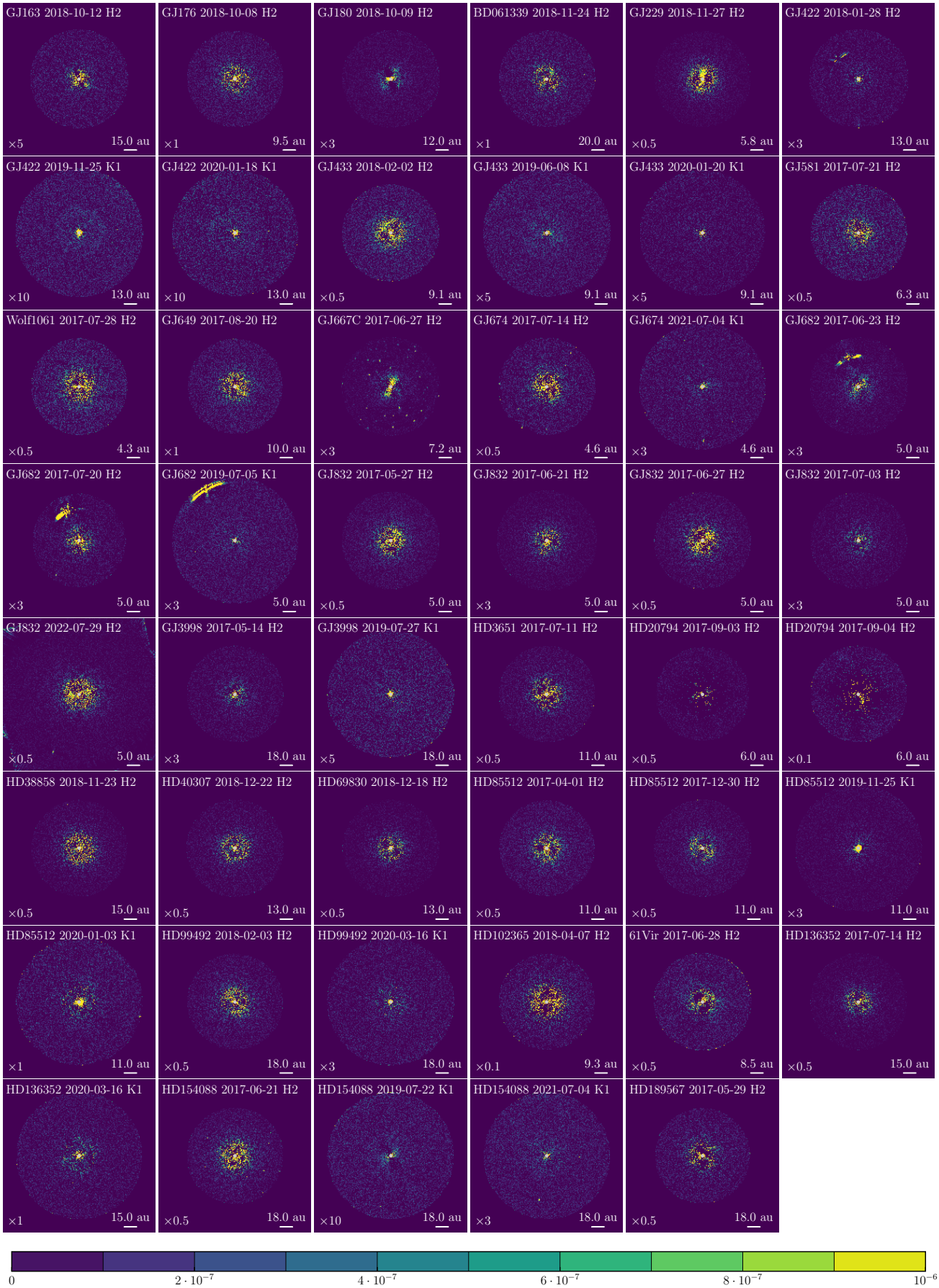

Fig. E.2. Reduced images from SPHERE-IRDIS for the whole survey for SpeCal-TLOCI ADI reductions.

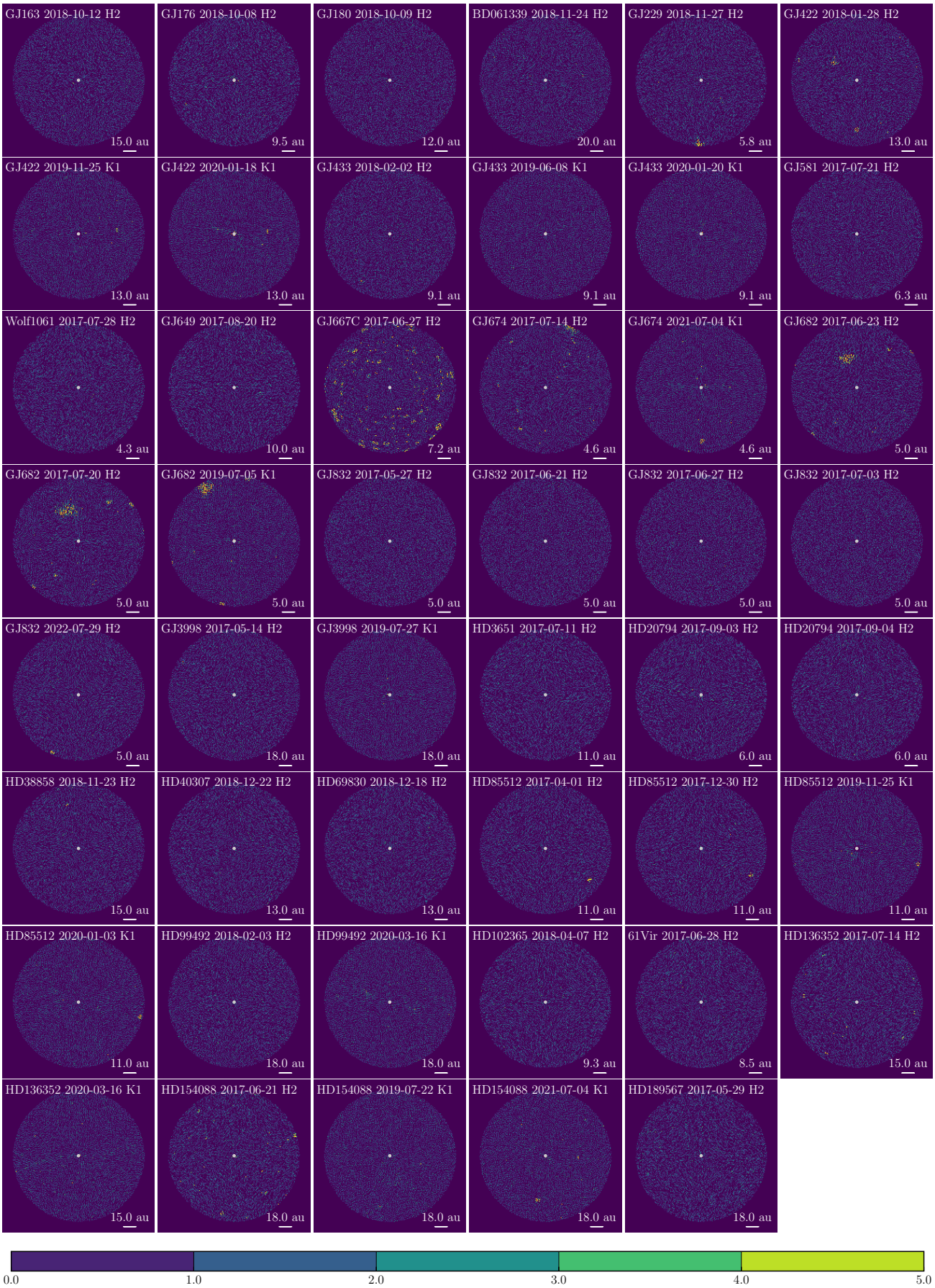

Fig. E.3. Reduced images from SPHERE-IRDIS for the whole survey for ANDROMEDA reductions.

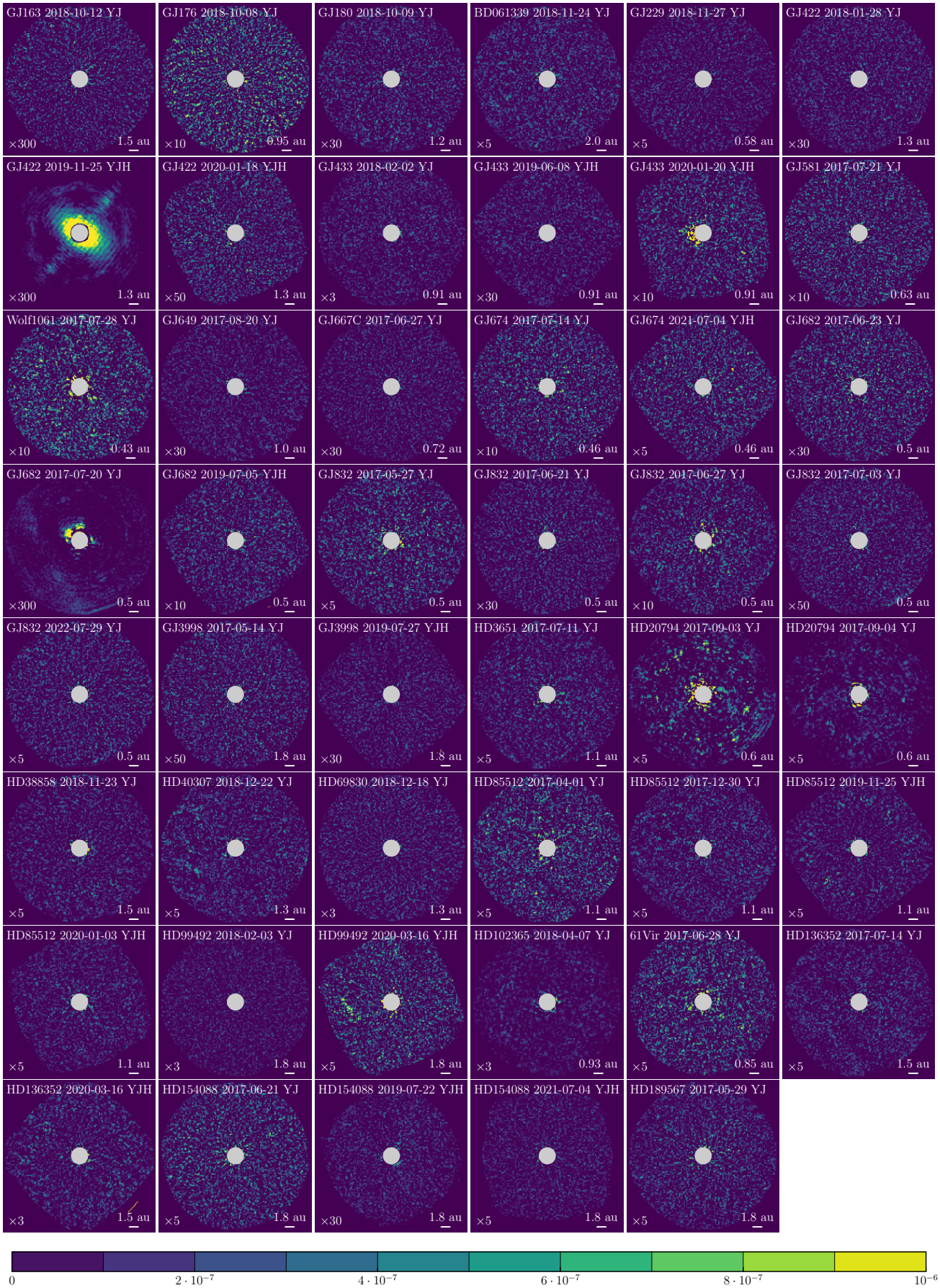

Fig. E.4. Reduced images from SPHERE-IFS for the whole survey for SpeCal-PCA-ADSI reductions.

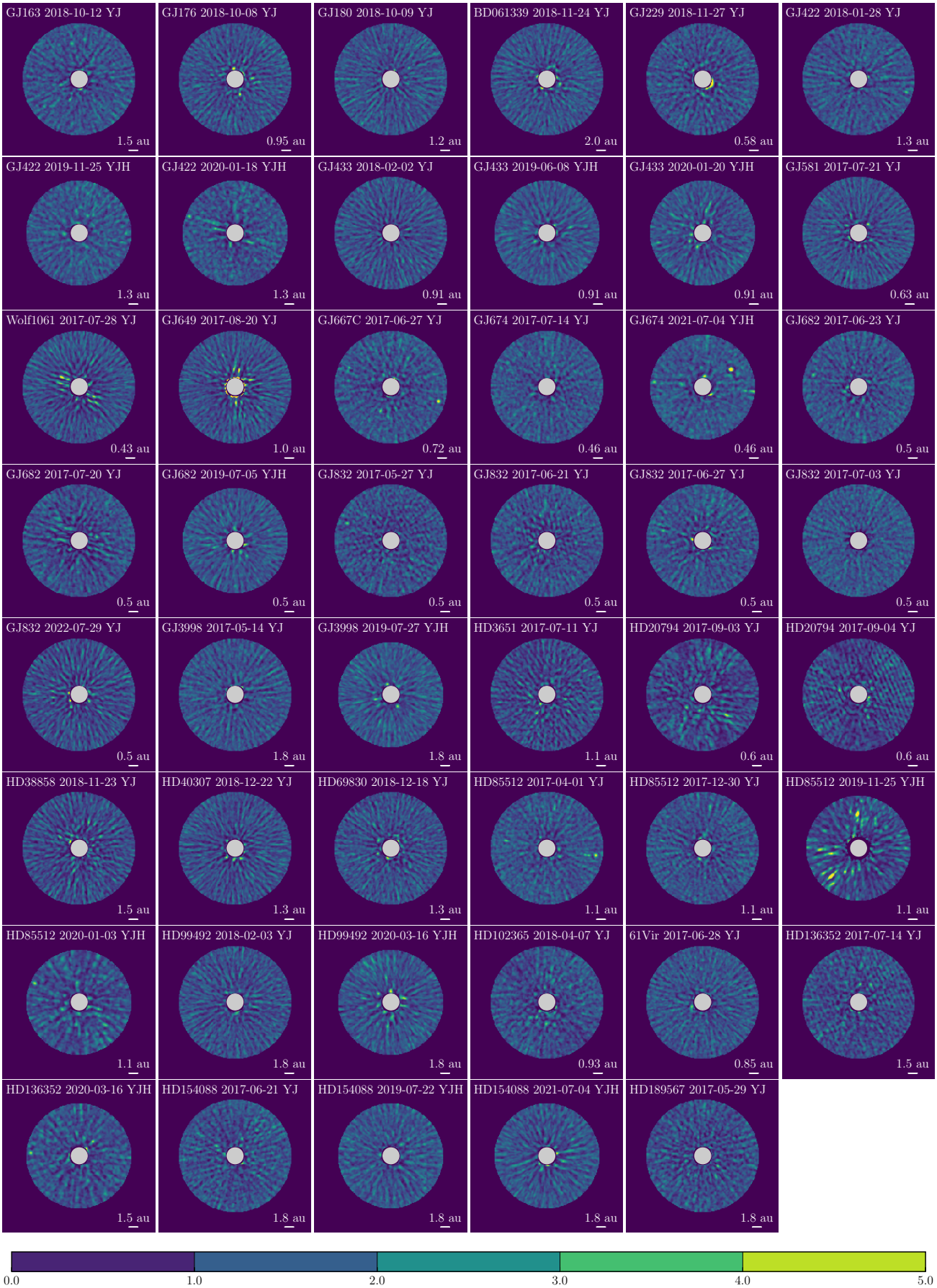

Fig. E.5. Reduced images from SPHERE-IFS for the whole survey for ANDROMEDA-ASDI reductions.

Appendix F: Companion candidates from ANDROMEDA and SpeCal processing

Figure F.1 reports the distribution of the detections for SPHERE-IRDIS observations with the ANDROMEDA-ADI or SpeCal-cADI processing, as well as the separations and contrasts of the detections. We can see that below 2", ANDROMEDA processing results in additional detections compared to SpeCal-cADI, which is expected (e.g., Cantalloube et al. 2015).

In addition, we note that concerning bright ($> 10^{-4}$ or 10^{-5}) candidates, there is a bias between ANDROMEDA and SpeCal photometry: the same candidate can have a difference up to 0.3 mag depending on which processing is used to retrieve the photometry. This photometric bias correlates with the apparent magnitude of the candidate. The brighter is the detection, the larger is the bias. There is no visible correlation with the separation. In our observations, this effect is only visible in the H2 band, corresponding to observations with bright candidates. By investigating this effect on the known brown dwarf GJ 229 B for which the photometry is reported in the literature, we found that SpeCal-cADI (and Specal-non-ADI) was consistent with the values from Nakajima et al. (1995) and Faherty et al. (2012), contrary to ANDROMEDA.

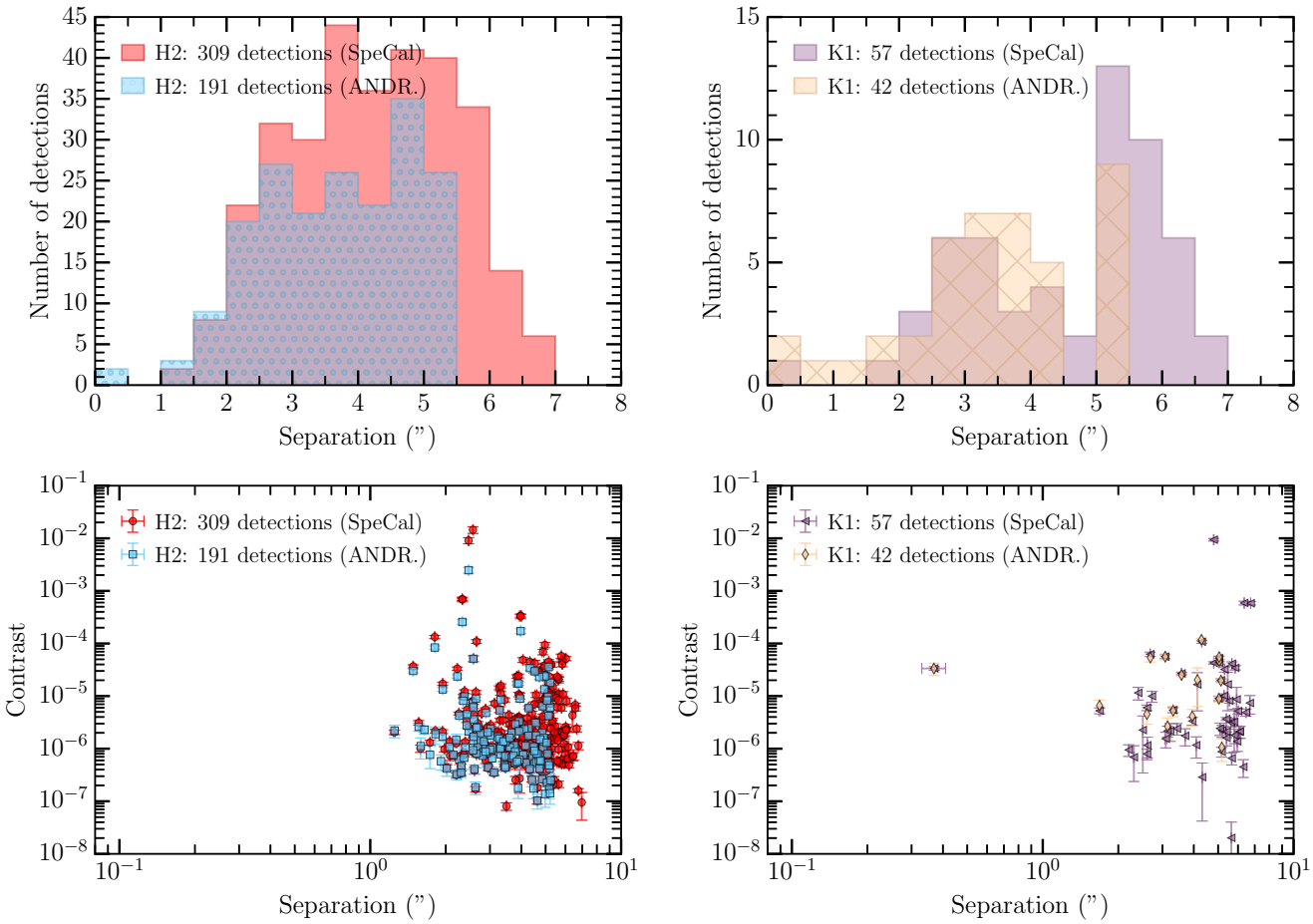

Fig. F.1. At the *top*, distribution of the separations of all the point-source detections from SPHERE-IRDIS in the H2-band (*on the left*) and the K1-band (*on the right*). At the *bottom*, contrasts and separations of all the point-source detections from SPHERE-IRDIS in the H2-band (*on the left*) and the K1-band (*on the right*). The post-processing algorithms used are SpeCal-cADI and ANDROMEDA-ADI.

Appendix G: Input parameters for Gaia and Hipparcos results via the `GaiaPMEX` tool

Table G.1 summarizes the parameters used for running the tool `GaiaPMEX` (Kiefer et al. (in prep.) for the systems GJ 832 and GJ 229, the only two that led to a positive detection from *Gaia* and HIPPARCOS data (see 5.3)

Table G.1. Parameters used with the `GaiaPMEX` tool for the systems GJ 229 and GJ 832.

Parameter	Unit	GJ 229	GJ 832
		Aliases	
HIP		29295	106440
Gaia DR3		2940856402123426176	6562924609150908416
		Main parameters	
$M_\star$	$M_\odot$	0.570	0.480
$\sigma_{M\star}$	$M_\odot$	0.049975713178077	0.0498015394994533
V		8.12	8.67
RA		06:10:34.4589	21:33:33.9004
DEC		-21:52:04.163	-49:00:45.468
		Gaia parameters	
`ra`	deg	92.644	323.391
`ra_error`	deg	0.008	0.018
`dec`	deg	-21.868	-49.013
`dec_error`	deg	0.014	0.014
`pmra`	mas yr^{-1}	-135.692	-45.917
`pmra_error`	mas yr^{-1}	0.011	0.023
`pmdec`	mas yr^{-1}	-719.178	-816.875
`pmdec_error`	mas yr^{-1}	0.017	0.018
`parallax`	mas	173.57	201.33
`parallax_error`	mas	0.02	0.02
`phot_g_mean_mag`		7.31	7.74
`bp_rp`		2.074	2.240
`astrometric_matched_transits`		82	47
`astrometric_n_good_obs_al`		723	414
`astrometric_params_solved`		31	31
`astrometric_excess_noise` or AEN_{obs}	mas	0.123	0.160
`ruwe` or $RUWE_{obs}$		1.013	1.097
		Hipparcos parameters	
e_{RA} cos DEC	mas	0.381	0.420
e_{DEC}	mas	0.670	0.600
σ_{pos}	mas	0.771	0.732
		Kervella et al. (2022) parameters	
pmRAH2EG3b	mas yr^{-1}	-136.406	-46.046
e_pmRAH2EG3b	mas yr^{-1}	0.015	0.018
pmDEH2EG3b	mas yr^{-1}	-714.974	-816.289
e_pmDEH2EG3b	mas yr^{-1}	0.019	0.020
PMaRAH2EG3b	mas yr^{-1}	0.712	0.140
e_PMaRAH2EG3b	mas yr^{-1}	0.018	0.029
PMaDEH2EG3b	mas yr^{-1}	-4.224	-0.547
e_PMaDEH2EG3b	mas yr^{-1}	0.025	0.027
‖PMa‖ (or PMa_{obs})	mas yr^{-1}	4.284	0.565
$\sigma_{PMa,obs}$	mas yr^{-1}	0.025	0.027
		Noise parameters and simulations of single systems	
σ_{AL}	mas	0.083	0.086
$\sigma_{attitude}$	mas	0.064	0.082
σ_{jitter}	mas	0.129	0.135
AEN_{simu} as single	mas	0.123	0.124
$\sigma_{AEN,simu,single}$	mas	0.015	0.021
PMa_{simu} as single	mas yr^{-1}	0.060	0.059
$\sigma_{PMa,simu,single}$	mas yr^{-1}	0.034	0.033
AEN_{obs} significance		0.007	1.696
PMa_{obs} significance		>3.82	>3.82

Appendix H: Comparison of detection method sensitivity on our survey

Detection methods of exoplanet suffer from observational biases. Combining different detection techniques enable to have a more global view on planetary systems (see Fig. H.1), even though observers are still blind to low-mass exoplanets at wide orbits (e.g., an exoplanet of 1 $M_\oplus$ planet orbiting at 20 au).

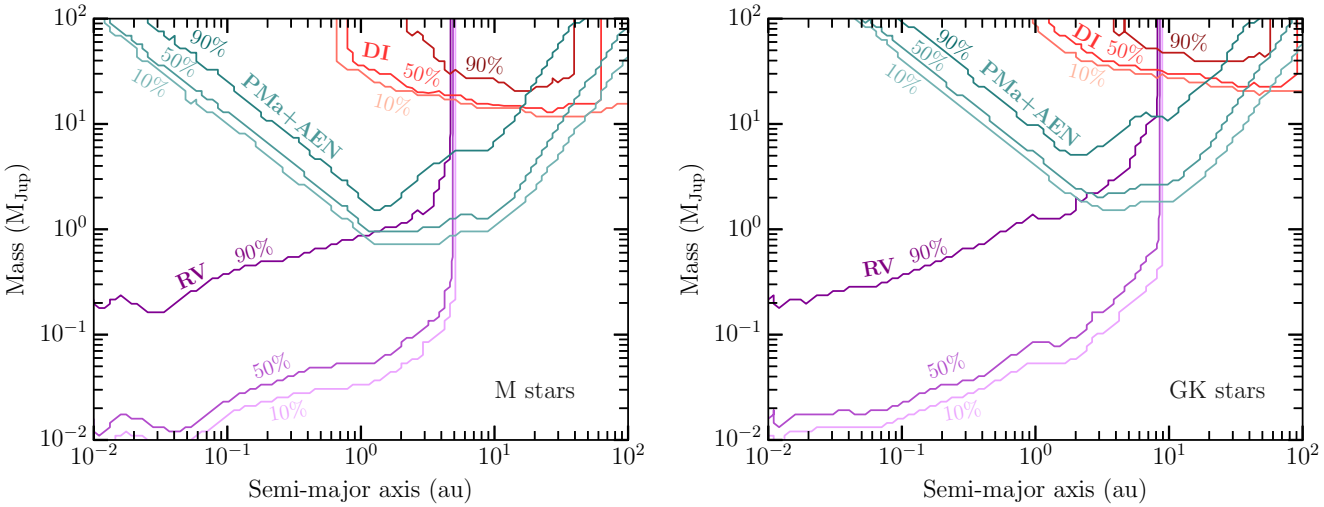

Fig. H.1. Comparison of the sensitivity of the direct imaging (DI, red), proper motion anomaly and *Gaia* astrometric excess noise (PMa+AEN, blue) and radial velocity (RV, purple) detections methods on our survey. We took the median of the detection probabilities at 10%, 50%, and 90% the M-stars (*left*) and the GK-stars (*right*).

Figure H.2 shows sensitivity from high-contrast imaging SPHERE-IRDIS and SPHERE-IFS observations for each system of our sample (see Section 5.4). For a few mature systems, high-contrast imaging observations are sensitive to companions of $\lesssim 10$ M_{Jup} beyond a few astronomical units (e.g., GJ 433) or dozen of astronomical units (e.g., GJ 229, GJ 649, GJ 674, GJ 832).

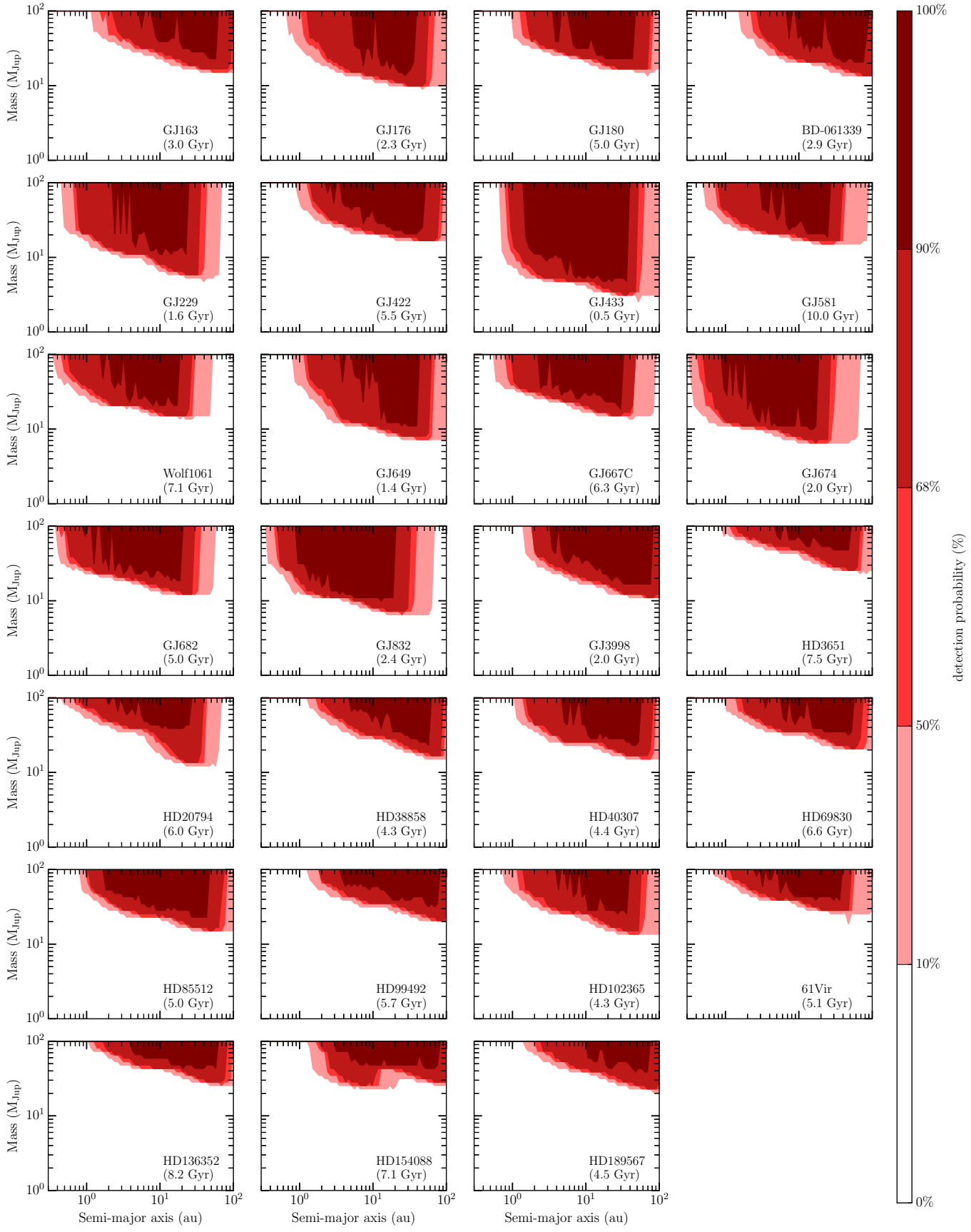

Fig. H.2. Detection limits from direct imaging observations (SPHERE-IRDIS and SPHERE-IFS) for each system of the survey obtained with the `MESS3` tool.

5.2.6 Main results

The main results of this work can be seen with different point of views. On a general point of view, I published, with my collaborators, the very deep high-contrast imaging observations on very nearby (< 20 pc), mature (500 Myr–10 Gyr) planetary systems hosting super-Earth or sub-Saturn-mass planets. This represents a total of 94 SPHERE observations (47 SPHERE/IRDIS and 47 SPHERE/IFS), that is to say, about 70 hours of telescope time, published for the first time.

I led a homogeneous reduction and analysis of these SPHERE observations. I identified 337 companion candidates, distinguishing them between background contaminants ($322/337$), instrumental artifacts ($2/337$), bound companions ($1/337$), and ambiguous detections ($12/337$), see Fig. 6. In particular, I detected again the known brown dwarf GJ 229 B. I also had a promising detection around GJ 832, that might have been compatible with GJ 832 b. However, I finally classified it as an instrumental artifact, because I did not detect it again in the new epoch of observation acquired with better conditions of observations (see Fig. 9, Section 5.2).

In addition, I constrained the architecture of these systems, down to semi-major axis of 0.3 au and masses of 3 M_{Jup} (for one system). For the 15 M stars of the sample, the observations are sensitive down to 3 or 15 M_{Jup} at 30 au , while for the 12 GK stars, the performances degrade, with sensitivity down to 10 or 30 M_{Jup} at 30 au. The performances in terms of mass is strongly impacted by the age of the star, its stellar type, and its distance.

Regarding the age, the sample consisted in old stars, which is usually avoided in direct imaging, because planets emit less thermally when they get older. Thus, the sensitivity in terms of mass decreases as a function of the age of the planet (and so the host star) when the planet is directly imaged in thermal emission. Nonetheless, since all the stars were selected as suspected to have low-mass planets based on the radial velocity method, this implied that the stars were mostly old, to be stable enough for this method to be able to detect them. Despite this drawback inherent to our sample of super-Earths host, we maximized our sensitivity in terms of planet mass by selecting only very nearby system.

With this work, my collaborators and I were not able to answer the initial question which motivated the project: the correlation between the presence of a short-period, low-mass planet and an outer giant planet. The reason is that current ground-based direct imaging techniques are mainly sensitive down to 20 M_{Jup} around mature stars. Nonetheless, this is a still pioneering work regarding the direct imaging of planetary systems around very nearby, mostly old stars. This pilot study will pave the way to future observations, for instance with *JWST*/MIRI, *RST*, and the ELT instruments, on similar scientific cases. Observing in the mid-infrared red (e.g., with the *JWST*/MIRI and ELT/METIS facilities) can to some extent mitigate the age impact of the final sensitivity. On the other hand, observing exoplanets in reflected light (*RST*, ELT/METIS, ELT/PCS) will be a game changer, because the sensitivity is not dependent of the stellar age anymore (but to the amount of irradiation received by the exoplanets, and so their distance to their host star). In any case, the key is to observe very nearby systems, to maximize the sensitivity of the observations, and probe relatively small semi-major axes.

I did not try to derive an upper limit of the correlation between the presence of both types of planets, due to the low sensitivity of the direct imaging observations, the sample size and sample design. Indeed, the stars were selected based on low-mass planets found by the RV method. However, depending on the RV campaigns, different strategies are followed which would impact positively or negatively the simultaneous presence of low-mass and giant planets. These strategies could bias the results, but are challenging to account for, and may be reinforced by our small sample size (see Section 6.1). Other factors can bias the results, as the stellar host metallicity (e.g., the contradictory results from Bonomo et al. (2023)

compared to previous work (Zhu & Wu, 2018; Bryan et al., 2019), but possibly resolved by Zhu, 2023), which influences around metal-rich stars the presence of Jupiter-mass planets (e.g., Fischer et al., 2003; Santos et al., 2004, but not super-Jupiter, see Santos et al. (2017); Narang et al. (2018); Schlaufman (2018); Swastik et al. (2021)). The distribution of the eccentricity of the known low-mass planets orbiting around host stars of the sample could also bias the results, which was also invoked by (Bitsch & Izidoro, 2023) to explain the absence of correlation reported by Bonomo et al. (2023). In our sample, only three stars have a super-solar metallicity, and most of the planets have low to moderate eccentricities ($e < 0.3$), with a few that may be high ($e \geq 0.3$).

On the whole, I think the main limitation of this work to study the correlation between the presence of close-in low-mass planets and outer giant ones, is the sensitivity of the observations in terms of planet mass, and as a result, the age of the stars, which is also poorly constrained, with uncertainties of a few gigayears on the nominal value. Then, there are also the sample size and the sample design.

5.3 Perspectives

In my opinion, it is particularly difficult to investigate the correlation between the presence of short-period, low-mass planets and outer giant ones from an observational perspective. This is complex because it is a multi-dimensional problem: one must be able to gather observations that are sensitive to both types of planets for a same sample of stars. This sample must be large enough, and not biased.

In this sense, the study from Rosenthal et al. (2022) based on the RV California legacy blind survey of 719 stars with a median metallicity [Fe/H] of 0, a median stellar mass of 1.0 $M_\odot$ and conducted over three decades seems very promising. Their Figure 1 shows the completeness of the survey, which is 90% complete within 2 au (or at least 20% complete within 10 au) for minimal mass higher than that of Saturn. Such completeness led them to detect in systems with short-period low-mass planets, 13 outer massive giant planets based on their wide definition (30–6 000 $M_\oplus$, 0.1–10 au) or 3 outer ones based on their narrow definition (0.3–13 M_{Jup}, 3–7 au). These results certainly correspond to low numbers of giant planet detections.

I think that having a sample significantly larger, with a higher completeness, and up to 20 au (in particular for the more massive stars), would definitely help a lot to better explore and constrain the correlation between the presence of both types of planets, and how this depends on other factors such as the stellar metallicity, stellar mass or the eccentricities of the short-period planets. Obviously, such campaign will be very expensive in telescope time.

A solution that may be perhaps less expensive in total telescope time would be to couple RV and direct imaging methods. The sample would be designed based on a large RV blind survey of very nearby stars, and only those hosting low-mass planets would be observed with direct imaging. If possible, high-contrast imaging instruments should search for the outer massive giant planets in reflected light, to by-pass the age limitation when converted the contrast to mass detection via evolutionary models; otherwise, in thermal light, but with very deep contrasts. Such performances would only be possible on future, cutting-edge facilities (e.g., *RST*, ELT, GMT, *HWO*), for which the telescope time would be even more competitive.

On a more single system perspective, I am particularly interested in observing with direct imaging the few young planetary systems already known to harbor some short-period, low-mass planets. I obtained LBT/SHARK-NIR+LMIRCam time to observe two of them during semester, 2024B. Although I am very hopeful to detect giant massive companions in these young (23 Myr and 414 Myr) multi-planetary systems, I believe that even detection limits

will already be helpful to constrain the architectures of these young systems, that could be related to the formation of the low-mass planets and the overall system dynamics.

Chapter 6

Conclusion and perspectives

In the course of my Ph.D., I peered into the architectures of planetary systems via high-contrast imaging. I focused on direct imaging of exoplanets and circumstellar debris disks, which are both products of planet formation processes. In particular, I have been deeply interested in the diversity of planetary system architectures, and what insights they give about the formation and evolution of planetary systems.

Project-wise, I led specific studies on young systems known to host debris disks or at least one exoplanet, to characterize them. I also worked on a survey of planetary systems, to have a larger sample to obtain statistical results. These research projects allowed me to understand the extent to which breakthroughs in astrophysics depend on advances in instrumentation and data post-processing. During the first half of my Ph.D., I contributed to investigate how the SPHERE+ performances to detect and characterize exoplanets could be boosted by using medium-spectral resolution.

In more details, I led an in-depth analysis on one system (HD 95086) with a giant planet directly imaged but a disk yet unseen in scattered light, and one other system (HD 120326) with a disk clearly detected in scattered light and likely sculpted by one or several planets yet to be discovered. Regarding HD 120326, in Desgrange et al. (2025, subm.), I combined panchromatic (*HST*/STIS, VLT/SPHERE and ALMA) data to better constrain the dust populations from 30 to 1 000 au. I derived the scattering phase function of the inner belt, its maximum fraction of polarization and albedo at 1.6 μm, and also its reflectance between 1.0 and 1.8 μm. By re-processing the data, I also better revealed the spiral-like feature seen in the optical data. Although spirals are frequently observed in numerical simulations involving wide-orbit ($\geq$ 10 au) giant planets, there are rarely observed so far in debris disks. In particular, HD 120326 is the only one with a spiral-like feature spanning over hundreds of astronomical units, up to 1 000 au if co-planar with the inner belt.

On the other hand, HD 95086 could be considered as a massive Solar System analog, with a 4–5 M_{Jup} giant planet (Rameau et al., 2013) located in the cavity between the two belts. In Desgrange et al. (2022a), I used ten epochs of observation acquired in the context of the Guaranteed Time Observation from the SPHERE consortium. I extracted the spectrum of the giant exoplanet HD 95086 b for the first time between 1.0 and 1.6 μm, and also its relative astrometry. With my collaborators, I studied the atmosphere of the exoplanet HD 95086 b, determined that dust must be present either in the upper layers of the atmosphere, which results in a temperature of 800–300 K, or around in a circumplanetary disk, which is accompanied by a higher ($\geq$ 1 400 K) effective temperature. New data probing mid-infrared wavelengths with *JWST*/MIRI discriminated between these two options (Mâlin et al., 2024). Moreover, we confirmed that the orbit of the HD 95086 b has a low-eccentricity, and being possibly circular. Based on dynamical arguments, this implies that at least another planet would be required to maintain the width of the cavity.

In addition, I investigated how low-mass planets orbiting close to their host star could form, and in particular whether this is correlated with the presence of outer, massive companions. I worked on a direct imaging survey searching for such outer, massive companion around twenty-seven very nearby ($\leq$ 20 pc) GKM stars known to host close-in low-mass planets. I showed that such study on mature (500 Myr–10 Gyr) stars is challenging, because even when detection limits achieve large contrasts, the sensitivity expressed in planetary mass degrades rapidly as soon the system age exceeds 500 Myr. In this perspective, detecting planets in reflected light (see tentatives with SPHERE/ZIMPOL, e.g., Tschudi et al., 2024) would be a game changer as the stellar age will not be a constraint anymore to image exoplanets. Alternatively, observing in mid-infrared, would still mitigate the impact of the stellar age (e.g., *JWST*/MIRI observations of epsilon Indi from Matthews et al., 2024).

Last, I contributed to the development of the future scientific cases of the SPHERE+ upgrade (first light planned in 2026). I worked on the performances of a new potential medium-resolution intregral-field spectrograph, called MedRes. MedRes has eventually not been approved by ESO. MedRes was supposed to leverage the improved performances of the upgraded AO system, called SAXO+, to detect and characterize Jupiter-mass exoplanets located closer to their host star, and hopefully, new protoplanets analog to the iconic PDS 70 b and c protoplanets. In practice, I studied how the spectral dimension can be used to reveal a planet via cross-correlation between planetary template spectra and the observations, a technique referred to as molecular mapping. I ran molecular mapping simulations, and in particular developed a framework to run them more efficiently to test different astrophysical scenes[1] and various instrumental set-ups[2], that would have helped to design MedRes. Molecular mapping is a promising technique to detect and characterize exoplanets, with many expectations for both space- (*JWST*/MIRI, Patapis et al., 2022; Mâlin et al., 2023) and forthcoming ground-based facilities (e.g., ELT/HARMONI, Houllé et al., 2021; Bidot et al., 2024, but also with ELT/METIS and ELT/PCS).

There is a strong connection between the SPHERE+ upgrade and the ELT instruments, both instrumental- and astrophysical-wise. First, the SAXO+ upgrade is a technology demonstration for the second-generation, high-contrast spectro-imager PCS (2035+) on the ELT. PCS aims to image in reflected light rocky planets that might be habitable around very nearby low-mass stars. Second, SPHERE can be used as a survey machine, to select the most promising stars that will be imaged with the ELT instruments, which will have huge time pressure factors. In this perspective, constraining the architectures of planetary systems located in the neighborhood of Solar System, as done in Desgrange et al. (2023), is a preliminary step. Furthermore, the SPHERE+ upgrade will allow SPHERE to observe fainter and redder stars and so to access to the bulk of stars in star-forming regions, such as Taurus, Chamaleon, Lupus and Upper Sco (Section 2.3.2). Planet formation could therefore be investigated more extensively with less observational biases and in different stellar associations. On top of that, the SPHERE+ instrument would work with an optimal AO correction even in the median observational condition, which is currently not the case (Fig. 2.3).

Thanks to these research projects, I have developed my skills as an observer, capable of processing data from spectro-imager instruments, and analyzing them in the context of the planet formation and evolution. I used archival data, but also new observations. This logically led me to submit proposals to ask telescope time using various observational facilities to test theories of planet formation and evolution, but also to explore intriguing planetary systems.

[1] For instance, a L-type or T-type exoplanet, with different values of contrast and location in the field of view.
[2] For example, various spectral coverage, with different possible spectral resolutions

At MPIA, I had the opportunity to be involved in the SHARK-NIR consortium, composed mainly of three institutes: INAF Padova (PI institute, Italy), MPIA (Heidelberg, Germany) and the Steward Observatory (Arizona, USA). The SHARK-NIR instrument is a new near-infrared high-contrast imager at LBT, in Arizona, and is a PI instrument. It finished its commissioning phase in Spring 2023, its science verification phase at the beginning of 2024, and is currently in its early science phase. At MPIA, I was responsible of defining the target list for the science verification phase, which corresponds to two runs in October 2023 and December 2023/January 2024. I was then in charge of writing and submitting the SHARK-NIR proposals to the intra-MPIA call to obtain time to exploit the instrument, while people at the INAF Padova and Steward Observatory were doing the same for their specific LBT calls. For information, the MPIA is entitled to about ten nights at LBT during each semester. These nights are spread between the three departments of the institute (Planet and Star Formation, Atmospheres of Exoplanets, and Galaxy and Cosmology).

In this context, I obtained as PI SHARK-NIR and LMIRCam data on systems known to host protoplanetary or debris disks, and I am waiting for five other stars to be observed between October 2024 and January 2025. That being said, unfortunately, weather conditions at LBT are not as good as at the Paranal Observatory where is the VLT, resulting in significant time losses due to bad weather, and sometimes also to technical problems. Only a fraction of about 30 % of my observations in 2024B could be carried out.

I also submitted proposals for other facilities, such as with VLT/SPHERE, *HST*/STIS, *JWST*/MIRI (coronagraphic mode), *JWST*/NIRCam (coronagraphic mode), and *JWST*/NIRISS (aperture masking interferometry). My granted proposals are listed in Appendix B. In these proposals, I mainly asked time to focus on young ($\leq$ 100 Myr) stars, to study planet formation and evolution in the early stages, but not only.

Tracing back the history of an old planetary system by constraining its architecture amazes me. As a consequence, I am very happy that my SPHERE proposal[3] on a mature, very nearby and benchmark planetary system was accepted. This system hosts a Neptune-mass planet on an eccentric, misaligned orbit within a period of three days. The planet undergoes strong evaporation observed in Lyα due to its proximity to its host star. These characteristics are surprising, because the system is 6 ± 2 Gyr old, and so the atmosphere of the planet should have escaped by now, and its orbit being circularized. The paradox can be solved if the planet migrated inwards recently due to a Kozai-Lidov resonance with an outer companion, that could be either a massive exoplanet or a brown dwarf. Such high eccentricity migration scenario can naturally explain the population of eccentric, misaligned, strongly irradiated, and non-evaporated mini-Neptunes (Nagasawa & Ida, 2011). Due to its proximity to the Sun, the M-type of the host star and predictions regarding the outer companion, this system is the most ideal to obtain observational evidence of this high-eccentricity migration mechanism, which could be applied to other eccentric, misaligned, strongly irradiated, but non-evaporated Neptune-mass planets.

The ground-based observations that I obtained as PI and with my collaborators would have the sensitivity to image the companion in the case it is a brown dwarf. If it is a giant planet, *JWST*/MIRI space-based observations would be required to detect it. I previously submitted *JWST*/MIRI proposals in *JWST* Cycle 2 and 3 on this system, and in spite of high-ranking (second and first quintile, respectively), there were not granted time, due to high pressure factors.

Furthermore, I am also excited by the *JWST*/MIRI observations that Elisabeth Matthews (PI), myself (co-PI) and other collaborators at MPIA will obtain in the beginning of 2025 on the predicted massive (2–20 M_{Jup}) companion GJ 179 c based on the radial velocity trend

[3] I worked on this proposal mainly with people at (or at some point at) the Geneva observatory, including Elisabeth Matthews, a close collaborator at MPIA.

and *Gaia* and *Hipparcos* data. This detection will pave the way for a detailed atmospheric characterization of a cold (<450 K) atmosphere, bridging the gap between exoplanets known so far and giant planets in our Solar System.

All in all, I think astronomers in the field of exoplanets and disks are living a particular exciting time, with great facilities on the ground and in space. Moreover, the future is even brighter, with instrumental upgrades and new facilities to come (VLT/SPHERE+, VLTI/GRAVITY+, *RST*, ELT, *HWO*, ...). The synergy of different observational facilities, and exoplanet detection methods keeps increasing, to constrain not only one given planetary system, but also a given exoplanet. The next two (and final) data releases from the *Gaia* mission will contribute to that, with the expected discovery of numerous giant exoplanets within a few astronomical units of their star.

The use of panchromatic data gives precious information on the atmospheric properties of the exoplanets, but also on protoplanetary and debris disks, by probing different types of grains at different locations in the disk. This refines our theories on planet formation and evolution, and gives clues on how it might look like out there on other worlds.

Starting November 15, 2024, I will continue my research as a Fellow at ESO for four years. The first three years will be based in Chile and associated to observational duties, while the last one will be fully dedicated to my research, in an institute of my choice. As part of my observational duties, I will observe 80 nights per year for three years for the astronomical community using the VLT/UT3 telescope at the Paranal observatory located in the Atacama desert. On the UT3 (Unit Telescope 3) are operated the cutting-edge instruments SPHERE, which I know well, CRIRES, and X-SHOOTER.

I will be at an ideal place to use also ESO instruments that I have not much used for now, but that I would be keen to, such as VLT/ERIS, VLTI/GRAVITY and VLTI/MATISSE. This very exciting experience will happen during the golden era where VLTI/GRAVITY+ and VLT/SPHERE+ upgrades will occur, and also when the construction of the biggest eye on the sky, the ELT, will be completed.

Bibliography

Absil, O., Defrère, D., Foresto, V. C. d., et al. (2013), *A near-infrared interferometric survey of debris disc stars: III. First statistics based on 42 stars observed with CHARA/FLUOR*, Astronomy & Astrophysics, 555.

Absil, O., Marion, L., Ertel, S., et al. (2021), *A near-infrared interferometric survey of debris-disk stars: VII. The hot-to-warm dust connection*, Astronomy & Astrophysics, 651.

Abt, H. A. & Levy, S. G. (1976), *Multiplicity among solar-type stars*, Astrophysical Journal, Suppl. Series, 30.

Adam, C., Olofsson, J., Van Holstein, R. G., et al. (2021), *Characterizing the morphology of the debris disk around the low-mass star GSC 07396-00759*, Astronomy & Astrophysics, 653.

Adams, J. D., Herter, T. L., Lau, R. M., Trinh, C., & Hankins, M. (2018), *Dust production rates in the Fomalhaut debris disk from SOFIA/FORCAST mid-infrared imaging*, The Astrophysical Journal, 862, 2.

Aime, C., Soummer, R., & Ferrari, A. (2002), *Total coronagraphic extinction of rectangular apertures using linear prolate apodizations*, Astronomy & Astrophysics, 389, 1.

Alibert, Y., Mordasini, C., Benz, W., & Winisdoerffer, C. (2005), *Models of giant planet formation with migration and disc evolution*, Astronomy & Astrophysics, 434, 1.

Amara, A. & Quanz, S. P. (2012), *pynpoint: an image processing package for finding exoplanets*, Monthly Notices of the Royal Astronomical Society, 427, 2.

Anche, R. M., Douglas, E., Milani, K., et al. (2023), *Simulation of high-contrast polarimetric observations of debris disks with the Roman Coronagraph Instrument*, Publications of the Astronomical Society of the Pacific, 135, 1054.

Antichi, J., Dohlen, K., Gratton, R. G., et al. (2009), *BIGRE: A low cross-talk integral field unit tailored for extrasolar planets imaging spectroscopy*, The Astrophysical Journal, 695, 2.

Apai, D., Schneider, G., Grady, C. A., et al. (2015), *The inner disk structure, disk-planet interactions, and temporal evolution in the Beta Pictoris system: A two-epoch HST/STIS coronagraphic study*, The Astrophysical Journal, 800, 2.

Armitage, P. J. (2017), *Lecture notes on the formation and early evolution of planetary systems*, arXiv:astro-ph/0701485.

Asensio-Torres, R., Henning, T., Cantalloube, F., et al. (2021), *Perturbers: SPHERE detection limits to planetary-mass companions in protoplanetary disks*, Astronomy & Astrophysics, 652.

Asensio-Torres, R., Janson, M., Hashimoto, J., et al. (2016), *Polarimetry and flux distribution in the debris disk around HD 32297*, Astronomy & Astrophysics, 593.

Aumann, H. H., Beichman, C. A., Gillett, F. C., et al. (1984), *Discovery of a shell around Alpha Lyrae*, The Astrophysical Journal, 278.

Avenhaus, H., Quanz, S. P., Garufi, A., et al. (2018), *Disks around T Tauri Stars with SPHERE (DARTTS-S): I. SPHERE/IRDIS polarimetric imaging of eight prominent T Tauri disks*, The Astrophysical Journal, 863, 1.

Backman, D. E., Dasgupta, A., & Stencel, R. E. (1995), *Model of a Kuiper Belt small grain population and resulting far-infrared emission*, Astrophysical Journal Letters, 450.

Backman, D. E. & Paresce, F. (1993), *Main-sequence stars with circumstellar solid material - the VEGA phenomenon*, Protostars and Planets III.

Bai, X.-N. & Stone, J. M. (2010), *Dynamics of solids in the midplane of protoplanetary disks: Implications for planetesimal formation*, The Astrophysical Journal, 722, 2.

Bailer-Jones, C. A. L., Rybizki, J., Fouesneau, M., Mantelet, G., & Andrae, R. (2018), *Estimating distance from parallaxes: IV. Distances to 1.33 billion stars in Gaia Data Release 2*, The Astronomical Journal, 156, 2.

Baraffe, I., Chabrier, G., Barman, T. S., Allard, F., & Hauschildt, P. H. (2003), *Evolutionary models for cool brown dwarfs and extrasolar giant planets. The case of HD 209458*, Astronomy & Astrophysics, 402, 2.

Barbato, D., Pinamonti, M., Sozzetti, A., et al. (2020), *The GAPS programme at TNG: XXIV. An eccentric Neptune-mass planet near the inner edge of the BD-11 4672 habitable zone*, Astronomy & Astrophysics, 641.

Barbato, D., Sozzetti, A., Desidera, S., et al. (2018), *Exploring the realm of scaled Solar System analogues with HARPS*, Astronomy & Astrophysics, 615.

Barge, P. & Sommeria, J. (1995), *Did planet formation begin inside persistent gaseous vortices?*, Astronomy & Astrophysics, 295.

Barman, T. S., Konopacky, Q. M., Macintosh, B., & Marois, C. (2015), *Simultaneous detection of water, methane, and carbon monoxide in the atmosphere of exoplanet HR 8799 b*, The Astrophysical Journal, 804, 1.

Bate, M. R. (2022), *Dust coagulation during the early stages of star formation: Molecular cloud collapse and first hydrostatic core evolution*, Monthly Notices of the Royal Astronomical Society, 514, 2.

Baudoz, P., Desgrange, C., Galicher, R., & Laginja, I. (2024), *Polarization effects on high contrast imaging: measurements on THD2 Bench*, Proceedings of the SPIE.

Baudoz, P., Dorn, R. J., Lizon, J.-L., et al. (2010), *The differential tip-tilt sensor of SPHERE*, Ground-based and Airborne Instrumentation for Astronomy III, 7735.

Baudoz, P., Mazoyer, J., Mas, M., Galicher, R., & Rousset, G. (2012), *Dark hole and planet detection: laboratory results using the self-coherent camera*, Proceedings of the SPIE.

Benisty, M., Bae, J., Facchini, S., et al. (2021), *A circumplanetary disk around PDS 70 c*, The Astrophysical Journal Letters, 916, 1.

Benisty, M., Dominik, C., Follette, K. B., et al. (2023), *Optical and near-infrared view of planet-forming disks and protoplanets*, Protostars and Planets VII, 534.

Benisty, M., Juhász, A., Facchini, S., et al. (2018), *Shadows and asymmetries in the T Tauri disk HD 143006: evidence for a misaligned inner disk*, Astronomy & Astrophysics, 619.

Benisty, M., Stolker, T., Pohl, A., et al. (2017), *Shadows and spirals in the protoplanetary disk HD 100453*, Astronomy & Astrophysics, 597.

Bertini, L., Roccatagliata, V., & Kim, M. (2023), *Flybys in debris disk systems with Gaia eDR3*, Astronomy & Astrophysics, 671.

Best, M., Sefilian, A. A., & Petrovich, C. (2024), *The influence of cold Jupiters in the formation of close-in planets: I. planetesimal transport*, The Astrophysical Journal, 960, 1.

Beust, H., Bonfils, X., Montagnier, G., Delfosse, X., & Forveille, T. (2012), *Dynamical evolution of the Gliese 436 planetary system: Kozai migration as a potential source for Gliese 436b's eccentricity*, Astronomy & Astrophysics, 545.

Beust, H., Milli, J., Morbidelli, A., et al. (2024), *Dynamics of the Beta Pictoris planetary system and its falling evaporating bodies*, Astronomy & Astrophysics, 683.

Beuzit, J.-L., Vigan, A., Mouillet, D., et al. (2019), *SPHERE: The exoplanet imager for the Very Large Telescope*, Astronomy & Astrophysics, 631.

Bhowmik, T., Boccaletti, A., Thébault, P., et al. (2019), *Spatially resolved spectroscopy of the debris disk HD 32297: Further evidence of small dust grains*, Astronomy & Astrophysics, 630.

Bidot, A., Mouillet, D., & Carlotti, A. (2024), *Exoplanet detection limits using spectral cross-correlation with spectro-imaging: Analytical model applied to the case of ELT/HARMONI*, Astronomy & Astrophysics, 682.

Birnstiel, T. (2023), *Dust growth and evolution in protoplanetary disks*, arXiv:2312.13287 [astro-ph].

Birnstiel, T., Dullemond, C. P., & Brauer, F. (2010), *Gas- and dust evolution in protoplanetary disks*, Astronomy and Astrophysics, 513.

Bitsch, B. & Izidoro, A. (2023), *Giants are bullies: How their growth influences systems of inner sub-Neptunes and super-Earths*, Astronomy & Astrophysics, 674.

Bitsch, B., Trifonov, T., & Izidoro, A. (2020), *The eccentricity distribution of giant planets and their relation to super-Earths in the pebble accretion scenario*, Astronomy & Astrophysics, 643.

Blum, J., Bischoff, D., & Gundlach, B. (2022), *Formation of comets*, Universe, 8, 7.

Boccaletti, A., Chauvin, G., Mouillet, D., et al. (2020), *SPHERE+: Imaging young Jupiters down to the snowline*, arXiv:2003.05714 [astro-ph].

Boccaletti, A., Chauvin, G., Wildi, F., et al. (2022), *Upgrading the high contrast imaging facility SPHERE: Science drivers and instrument choices*, Proceedings of the SPIE.

Boccaletti, A., Mâlin, M., Baudoz, P., et al. (2024), *Imaging detection of the inner dust belt and the four exoplanets in the HR 8799 system with JWST's MIRI coronagraph*, Astronomy & Astrophysics, 686.

Boehnke, P. & Harrison, T. M. (2016), *Illusory late heavy bombardments*, Proceedings of the National Academy of Sciences, 113, 39.

Boekel, R. V., Henning, T., Menu, J., et al. (2017), *Three radial gaps in the disk of TW Hydrae imaged with SPHERE*, The Astrophysical Journal, 837, 2.

Bohn, A. J., Kenworthy, M. A., Ginski, C., et al. (2019), *Discovery of a directly imaged disk in scattered light around the Sco-Cen member Wray 15-788*, Astronomy & Astrophysics, 624.

Bonavita, M. & Desidera, S. (2007), *The frequency of planets in multiple systems*, Astronomy & Astrophysics, 468, 2.

Bonavita, M. & Desidera, S. (2020), *Frequency of planets in binaries*, Galaxies, 8, 1.

Bonavita, M., Gratton, R., Desidera, S., et al. (2022), *New binaries from the SHINE survey*, Astronomy & Astrophysics, 663.

Bonfils, X., Delfosse, X., Udry, S., et al. (2013), *The HARPS search for southern extra-solar planets: XXXI. The M-dwarf sample*, Astronomy & Astrophysics, 549.

Bonnefoy, M., Milli, J., Ménard, F., et al. (2017), *Belt(s) of debris resolved around the Sco-Cen star HIP 67497*, Astronomy & Astrophysics, 597.

Bonomo, A. S., Dumusque, X., Massa, A., et al. (2023), *Cold Jupiters and improved masses in 38 Kepler and K2 small planet systems from 3661 HARPS-N radial velocities: No excess of cold Jupiters in small planet systems*, Astronomy & Astrophysics, 677.

Bonse, M. J., Gebhard, T. D., Dannert, F. A., et al. (2024), *Use the 4S (Signal-Safe Speckle Subtraction): Explainable machine learning reveals the giant exoplanet AF Lep b in high-contrast imaging data from 2011*, arXiv:2406.01809 [astro-ph].

Booth, M., del Burgo, C., & Hambaryan, V. V. (2021), *The age of the Carina young association and potential membership of HD 95086*, Monthly Notices of the Royal Astronomical Society, 500, 4.

Booth, M., Matrà, L., Su, K. Y. L., et al. (2019), *Deep ALMA search for CO gas in the HD 95086 debris disc*, Monthly Notices of the Royal Astronomical Society, 482, 3.

Booth, R. A., Meru, F., Lee, M. H., & Clarke, C. J. (2018), *Breakthrough revisited: Investigating the requirements for growth of dust beyond the bouncing barrier*, Monthly Notices of the Royal Astronomical Society, 475, 1.

Boss, A. (1997), *Giant planet formation by gravitational instability*, Science, 276.

Bottke, W. F., Nesvorný, D., Vokrouhlický, D., & Morbidelli, A. (2010), *The irregular satellites: The most collisionally evolved populations in the Solar System*, The Astronomical Journal, 139, 3.

Bourrier, V., Lovis, C., Beust, H., et al. (2018), *Orbital misalignment of the Neptune-mass exoplanet GJ 436b with the spin of its cool star*, Nature, 553, 7689.

Bouvier, A. & Wadhwa, M. (2010), *The age of the Solar System redefined by the oldest Pb–Pb age of a meteoritic inclusion*, Nature Geoscience, 3, 9.

Brandt, T. D. (2018), *The Hipparcos–Gaia catalog of accelerations*, The Astrophysical Journal Supplement Series, 239, 2.

Brauer, F., Dullemond, C. P., & Henning, T. (2008), *Coagulation, fragmentation and radial motion of solid particles in protoplanetary disks*, Astronomy & Astrophysics, 480, 3.

Bryan, M. L., Knutson, H. A., Lee, E. J., et al. (2019), *An excess of Jupiter analogs in super-Earth systems*, The Astronomical Journal, 157, 2.

Burn, R., Schlecker, M., Mordasini, C., et al. (2021), *The New Generation Planetary Population Synthesis (NGPPS): IV. Planetary systems around low-mass stars*, Astronomy & Astrophysics, 656.

Burns, J. A., Lamy, P. L., & Soter, S. (2014), *Radiation forces on small particles in the Solar System: A re-consideration*, Icarus, 232.

Cantalloube, F., Dohlen, K., Milli, J., Brandner, W., & Vigan, A. (2019), *Peering through SPHERE Images: A Glance at Contrast Limitations*, Published in The Messenger vol. 176, pp. 25-31.

Cantalloube, F., Gomez-Gonzalez, C., Absil, O., et al. (2020), *Exoplanet imaging data challenge: Benchmarking the various image processing methods for exoplanet detection*, Proceedings of the SPIE.

Cantalloube, F., Mouillet, D., Mugnier, L. M., et al. (2015), *Direct exoplanet detection and characterization using the ANDROMEDA method: Performance on VLT/NaCo data*, Astronomy & Astrophysics, 582.

Carrera, D., Gorti, U., Johansen, A., & Davies, M. B. (2017), *Planetesimal formation by the streaming instability in a photoevaporating disk*, The Astrophysical Journal, 839, 1.

Chapman, C. R., Cohen, B. A., & Grinspoon, D. H. (2007), *What are the real constraints on the existence and magnitude of the late heavy bombardment?*, Icarus, 189, 1.

Chatterjee, S., Ford, E. B., Matsumura, S., & Rasio, F. A. (2008), *Dynamical outcomes of planet-planet scattering*, The Astrophysical Journal, 686, 1.

Chauvin, G. (2018), *Two decades of exoplanetary science with adaptive optics*, arXiv:1808.02454 [astro-ph].

Chauvin, G., Gratton, R., Bonnefoy, M., et al. (2018), *Investigating the young Solar System analog HD 95086: A combined HARPS and SPHERE exploration*, Astronomy & Astrophysics, 617.

Chauvin, G., Lagrange, A.-M., Dumas, C., et al. (2004), *A giant planet candidate near a young brown dwarf: Direct VLT/NACO observations using IR wavefront sensing*, Astronomy & Astrophysics, 425, 2.

Chen, C., Mazoyer, J., Poteet, C. A., et al. (2020), *Multiband GPI imaging of the HR 4796A debris disk*, The Astrophysical Journal, 898, 1.

Chen, C. H., Mittal, T., Kuchner, M., et al. (2014), *The Spitzer infrared spectrograph debris disk catalog: I. Continuum analysis of unresolved targets*, The Astrophysical Journal Supplement Series, 211, 2.

Chen, C. H., Pecaut, M., Mamajek, E. E., Su, K. Y. L., & Bitner, M. (2012), *A Spitzer MIPS study of 2.5-2.0 Msun stars in Scorpius-Centaurus*, The Astrophysical Journal, 756, 2.

Chiang, E. & Laughlin, G. (2013), *The minimum-mass extrasolar nebula: In situ formation of close-in super-Earths*, Monthly Notices of the Royal Astronomical Society, 431, 4.

Choquet, E., Pueyo, L., Hagan, J. B., et al. (2014), *Archival legacy investigations of circumstellar environments: Overview and first results*, Proceedings of the SPIE.

Christiaens, V., Gonzalez, C. A. G., Farkas, R., et al. (2023), *VIP: A Python package for high-contrast imaging*, Journal of Open Source Software, 8, 81.

Christou, J. C., Neichel, B., Rigaut, F., et al. (2010), *ALTAIR performance and updates at Gemini North*, Proceedings of the SPIE.

Ciarniello, M., Moroz, L. V., Poch, O., et al. (2021), *VIS-IR spectroscopy of mixtures of water ice, organic matter, and opaque mineral in support of small body remote sensing observations*, Minerals, 11, 11.

Claudi, R. U., Turatto, M., Gratton, R. G., et al. (2008), *SPHERE IFS: The spectro differential imager of the VLT for exoplanets search*, Proceedings of the SPIE, 7014, 70143E.

Clement, M. S., Kaib, N. A., Raymond, S. N., & Chambers, J. E. (2021), *The early instability scenario: Mars' mass explained by Jupiter's orbit*, Icarus, 367.

Clement, M. S., Kaib, N. A., Raymond, S. N., & Walsh, K. J. (2018), *Mars' growth stunted by an early giant planet instability*, Icarus, 311.

Cosentino, R., Lovis, C., Pepe, F., et al. (2012), *Harps-N: the new planet hunter at TNG*, Proceedings of the SPIE, 8446.

Crossfield, I. J. M., Biller, B., Schlieder, J. E., et al. (2014), *A global cloud map of the nearest known brown dwarf*, Nature, 505, 7485.

Crutcher, R. M. (2012), *Magnetic fields in molecular clouds*, Annual Review of Astronomy and Astrophysics, 50, 1.

Cumming, A., Butler, R. P., Marcy, G. W., et al. (2008), *The Keck planet search: detectability and the minimum mass and orbital period distribution of extrasolar planets*, Publications of the Astronomical Society of the Pacific, 120, 867.

Cuzzi, J. N. & Zahnle, K. J. (2004), *Material enhancement in protoplanetary nebulae by particle drift through evaporation fronts*, The Astrophysical Journal, 614, 1.

Dai, Y.-Z., Liu, H.-G., An, D.-S., & Zhou, J.-L. (2021), *Planet occurrence rate correlated to stellar dynamical history: Evidence from Kepler and Gaia*, The Astronomical Journal, 162, 2.

Dauphas, N. & Pourmand, A. (2011), *Hf–W–Th evidence for rapid growth of Mars and its status as a planetary embryo*, Nature, 473, 7348.

Davies, R., Absil, O., Agapito, G., et al. (2023), *The Enhanced Resolution Imager and Spectrograph for the VLT*, Astronomy & Astrophysics, 674.

De Boer, J., Ginski, C., Chauvin, G., et al. (2021), *Possible single-armed spiral in the protoplanetary disk around HD 34282*, Astronomy & Astrophysics, 649.

De Boer, J., Langlois, M., Van Holstein, R. G., et al. (2020), *Polarimetric imaging mode of VLT/SPHERE/IRDIS: I. Description, data reduction, and observing strategy*, Astronomy & Astrophysics, 633.

De Rosa, R. J., Dawson, R., & Nielsen, E. L. (2020a), *A significant mutual inclination between the planets within the π Mensae system*, Astronomy & Astrophysics, 640.

De Rosa, R. J., Nielsen, E. L., Wahhaj, Z., et al. (2023), *Direct imaging discovery of a super-Jovian around the young Sun-like star AF Leporis*, Astronomy & Astrophysics, 672.

De Rosa, R. J., Rameau, J., Patience, J., et al. (2016), *Spectroscopic characterization of HD 95086 b with the Gemini Planer Imager*, The Astrophysical Journal, 824, 2.

De Rosa, R. J. D., Nielsen, E. L., Wang, J. J., et al. (2020b), *An updated visual orbit of the directly imaged exoplanet 51 Eridani b and prospects for a dynamical mass measurement with Gaia*, The Astronomical Journal, 159, 1.

de Sousa, R. R., Morbidelli, A., Raymond, S. N., et al. (2020), *Dynamical evidence for an early giant planet instability*, Icarus, 339.

de Zeeuw, P. T., Hoogerwerf, R., de Bruijne, J. H. J., Brown, A. G. A., & Blaauw, A. (1999), *A HIPPARCOS Census of the Nearby OB Associations*, \aj, 117, 1.

Dekker, H., D'Odorico, S., Kaufer, A., Delabre, B., & Kotzlowski, H. (2000), *Design, construction, and performance of UVES, the echelle spectrograph for the UT2 Kueyen Telescope at the ESO Paranal Observatory*, Proceedings of the SPIE, 4008.

Delgrande, J. J. & Soanes, S. V. (1943), *Kirkwood's gap in the asteroid orbits*, Journal of the Royal Astronomical Society of Canada, 37.

Deming, D., Louie, D., & Sheets, H. (2019), *How to characterize the atmosphere of a transiting exoplanet*, Publications of the Astronomical Society of the Pacific, 131, 995.

Dent, W. R. F., Wyatt, M. C., Roberge, A., et al. (2014), *Molecular gas clumps from the destruction of icy bodies in the Beta Pictoris debris disk*, Science, 343, 6178.

Desgrange, C., Chauvin, G., Christiaens, V., et al. (2022a), *In-depth direct imaging and spectroscopic characterization of the young Solar System analog HD 95086*, Astronomy & Astrophysics, 664.

Desgrange, C., Chauvin, G., Malin, M., et al. (2022b), *Spectral characterization and simulated observations with the James Webb Space Telescope of the young exoplanet HD 95086 b*, Proceedings of the Annual meeting of the French Society of Astronomy and Astrophysics.

Desgrange, C., Milli, J., Chauvin, G., et al. (2025 subm.), *Dust populations from 30 to 1000 au in the debris disk HD 120326*, Astronomy & Astrophysics.

Desgrange, C., Milli, J., Chauvin, G., et al. (2023), *Planetary system architectures with low-mass inner planets: Direct imaging exploration of mature systems beyond 1 au*, Astronomy & Astrophysics, 680.

Diego, F., Charalambous, A., Fish, A. C., & Walker, D. D. (1990), *Final tests and commissioning of the UCL echelle spectrograph*, Proceedings of the SPIE, 1235.

Dohlen, K., Langlois, M., Saisse, M., et al. (2008), *The infra-red dual imaging and spectrograph for SPHERE: Design and performance*, Proceedings of the SPIE, 7014, 70143L.

Dohnanyi, J. S. (1969), *Collisional model of asteroids and their debris*, Journal of Geophysical Research, 74.

Donati, J. F., Kouach, D., Moutou, C., et al. (2020), *SPIRou: NIR velocimetry and spectropolarimetry at the CFHT*, Monthly Notices of the Royal Astronomical Society, 498, 4.

Dones, L. & Tremaine, S. (1993), *Why does the Earth spin forward?*, Science, 259, 5093.

Dong, S., Katz, B., & Socrates, A. (2013), *Warm Jupiters need close "friends" for high-eccentricity migration: A stringent upper limit on the perturber's separation*, The Astrophysical Journal, 781, 1.

Doyle, L. R., Carter, J. A., Fabrycky, D. C., et al. (2011), *Kepler-16: A transiting circumbinary planet*, Science, 333, 6049.

Dressing, C. D. & Charbonneau, D. (2015), *The occurrence of potentially habitable planets orbiting M dwarfs estimated from the full Kepler dataset and an empirical measurement of the detection sensitivity*, The Astrophysical Journal, 807, 1.

Drążkowska, J., Alibert, Y., & Moore, B. (2016), *Close-in planetesimal formation by pile-up of drifting pebbles*, Astronomy & Astrophysics, 594.

Drążkowska, J., Bitsch, B., Lambrechts, M., et al. (2023), *Planet formation theory in the era of ALMA and Kepler: From pebbles to exoplanets*, Protostars and Planets VII, 534.

Duquennoy, A. & Mayor, M. (1991), *Multiplicity among solar type stars in the solar neighbourhood: II. Distribution of the orbital elements in an unbiased sample*, Astronomy & Astrophysics, 248.

Eistrup, C., Walsh, C., & Van Dishoeck, E. F. (2016), *Setting the volatile composition of (exo)planet-building material: Does chemical evolution in disk midplanes matter?*, Astronomy & Astrophysics, 595.

Emsenhuber, A., Mordasini, C., Burn, R., et al. (2021), *The New Generation Planetary Population Synthesis (NGPPS): I. Bern global model of planet formation and evolution, model tests, and emerging planetary systems*, Astronomy & Astrophysics, 656.

Engler, N., Milli, J., Gratton, R., et al. (2023), *The high-albedo, low polarization disk around HD 114082 harbouring a Jupiter-sized transiting planet*, Astronomy & Astrophysics, 672.

Engler, N., Schmid, H. M., Quanz, S. P., Avenhaus, H., & Bazzon, A. (2018), *Detection of scattered light from the hot dust in HD 172555*, Astronomy & Astrophysics, 618.

Ertel, S., Absil, O., Defrère, D., et al. (2014), *A near-infrared interferometric survey of debris-disk stars: IV. An unbiased sample of 92 southern stars observed in H band with VLTI/PIONIER*, Astronomy & Astrophysics, 570.

Ertel, S., Defrère, D., Absil, O., et al. (2016), *A near-infrared interferometric survey of debris-disc stars: V. PIONIER search for variability*, Astronomy & Astrophysics, 595.

Esposito, S., Riccardi, A., Pinna, E., et al. (2012), *Natural guide star adaptive optics systems at LBT: FLAO commissioning and science operations status*, Proceedings of the SPIE, 8447.

Estrada, P. R. & Cuzzi, J. N. (2022), *Global modeling of nebulae with particle growth, drift, and evaporation fronts: III. Redistribution of refractories and volatiles*, The Astrophysical Journal, 936, 1.

Estrada, P. R., Cuzzi, J. N., & Morgan, D. A. (2016), *Global modeling of nebulae with particle growth, drift, and evaporation fronts: I. Methodology and typical results*, The Astrophysical Journal, 818, 2.

Fabrycky, D. & Tremaine, S. (2007), *Shrinking binary and planetary orbits by Kozai cycles with tidal friction*, The Astrophysical Journal, 669, 2.

Fabrycky, D. C., Lissauer, J. J., Ragozzine, D., et al. (2014), *Architecture of Kepler's multi-transiting systems: II. New investigations with twice as many candidates*, The Astrophysical Journal, 790, 2.

Farinato, J., Baffa, C., Baruffolo, A., et al. (2015), *The NIR arm of SHARK: System for coronagraphy with High-order Adaptive optics from R to K bands*, International Journal of Astrobiology, 14, 3.

Feng, F., Butler, R. P., Shectman, S. A., et al. (2020), *Search for nearby earth analogs: II. Detection of five new planets, eight planet candidates, and confirmation of three planets around nine nearby M dwarfs*, The Astrophysical Journal Supplement Series, 246, 1.

Fischer, D. A., Butler, R. P., Marcy, G. W., Vogt, S. S., & Henry, G. W. (2003), *A sub-Saturn mass planet orbiting HD 3651*, The Astrophysical Journal, 590, 2.

Flasseur, O., Denis, L., Thiébaut, E., & Langlois, M. (2018), *Exoplanet detection in angular differential imaging by statistical learning of the nonstationary patch covariances: The PACO algorithm*, Astronomy & Astrophysics, 618.

Flasseur, O., Denis, L., Thiébaut, E., & Langlois, M. (2020), *Robustness to bad frames in angular differential imaging: a local weighting approach*, Astronomy & Astrophysics, 634.

Flasseur, O., Thé, S., Denis, L., Thiébaut, E., & Langlois, M. (2021), *REXPACO: An algorithm for high contrast reconstruction of the circumstellar environment by angular differential imaging*, Astronomy & Astrophysics, 651.

Follette, K. B., Grady, C. A., Swearingen, J. R., et al. (2015), *SEEDS adaptive optics imaging of the asymmetric transition disk Oph IRS 48 in scattered light*, The Astrophysical Journal, 798, 2.

Fontanive, C. & Bardalez Gagliuffi, D. (2021), *The census of exoplanets in visual binaries: Population trends from a volume-limited Gaia DR2 and literature dearch*, Frontiers in Astronomy and Space Sciences, 8.

Foreman-Mackey, D., Hogg, D. W., Lang, D., & Goodman, J. (2013), *emcee: The MCMC hammer*, Publications of the Astronomical Society of the Pacific, 125, 925.

Franson, K., Balmer, W. O., Bowler, B. P., et al. (2024), *JWST/NIRCam 4-5 µm imaging of the giant planet AF Lep b*, arXiv:2406.09528 [astro-ph].

Franson, K., Bowler, B. P., Bonavita, M., et al. (2023), *Astrometric accelerations as dynamical beacons: Discovery and characterization of HIP 21152 B, the first T-dwarf companion in the Hyades*, The Astronomical Journal, 165, 2.

Fulton, B. J., Petigura, E. A., Howard, A. W., et al. (2017), *The California-Kepler Survey: III. A gap in the radius distribution of small planets*, The Astronomical Journal, 154, 3.

Fulton, B. J., Rosenthal, L. J., Hirsch, L. A., et al. (2021), *California Legacy Survey: II. Occurrence of giant planets beyond the ice line*, The Astrophysical Journal Supplement Series, 255, 1.

Gaia , Brown, A. G. A., Vallenari, A., et al. (2018), *Gaia Data Release 2: Summary of the contents and survey properties*, Astronomy & Astrophysics, 616.

Gaia , Brown, A. G. A., Vallenari, A., et al. (2021), *Gaia Early Data Release 3: Summary of the contents and survey properties*, Astronomy & Astrophysics, 649.

Galicher, R., Boccaletti, A., Mesa, D., et al. (2018), *Astrometric and photometric accuracies in high contrast imaging: The SPHERE speckle calibration tool (SpeCal)*, Astronomy & Astrophysics, 615.

Galicher, R. & Mazoyer, J. (2023), *Imaging exoplanets with coronagraphic instruments*, Comptes Rendus. Physique, 24, S2.

Galicher, R., Rameau, J., Bonnefoy, M., et al. (2014), *Near-infrared detection and characterization of the exoplanet HD 95086 b with the Gemini Planet Imager*, Astronomy & Astrophysics, 565.

Gallenne, A., Desgrange, C., Milli, J., et al. (2022), *Probing the innermost region of the AU Microscopii debris disc*, Astronomy & Astrophysics, 665.

Gammie, C. F. (2001), *Nonlinear outcome of gravitational instability in cooling, gaseous disks*, The Astrophysical Journal, 553, 1.

Garaud, P., Meru, F., Galvagni, M., & Olczak, C. (2013), *From dust to planetesimals: An improved model for collisional growth in protoplanetary disks*, The Astrophysical Journal, 764, 2.

Gardner, J. P., Mather, J. C., Clampin, M., et al. (2006), *The James Webb Space Telescope*, Space Science Reviews, 123, 4.

Garufi, A., Avenhaus, H., Pérez, S., et al. (2020), *Disks Around T Tauri Stars with SPHERE (DARTTS-S): II. Twenty-one new polarimetric images of young stellar disks*, Astronomy & Astrophysics, 633.

Garufi, A., Benisty, M., Stolker, T., et al. (2017), *Three Years of SPHERE: The latest view of the morphology and evolution of protoplanetary discs*, Published in The Messenger vol. 169, pp. 32-37.

Garufi, A., Ginski, C., Van Holstein, R. G., et al. (2024), *The SPHERE view of the Taurus star-forming region: The full census of planet-forming disks with GTO and DESTINYS programs*, Astronomy & Astrophysics, 685.

Gaspar, A., Wolff, S. G., Rieke, G. H., et al. (2023), *Spatially resolved imaging of the inner Fomalhaut disk using JWST/MIRI*, Nature Astronomy.

Gauchet, L., Lacour, S., Lagrange, A.-M., et al. (2016), *Sparse aperture masking at the VLT: II. Detection limits for the eight debris disks stars Beta Pic, AU Mic, 49 Cet, eta Tel, Fomalhaut, g Lup, HD 181327 and HR 8799*, Astronomy & Astrophysics, 595.

Gaudi, B. S. (2012), *Microlensing surveys for exoplanets*, Annual Review of Astronomy and Astrophysics, 50, 1.

Gaudi, B. S., Bennett, D. P., Udalski, A., et al. (2008), *Discovery of a Jupiter/Saturn analog with gravitational microlensing*, Science, 319, 5865.

Gautier, D. & Owen, T. (1983), *Cosmogonical implications of elemental and isotopic abundances in atmospheres of the giant planets*, Nature, 304, 5928.

Ghezzi, L., Montet, B. T., & Johnson, J. A. (2018), *Retired a stars revisited: An updated giant planet occurrence rate as a function of stellar metallicity and mass*, The Astrophysical Journal, 860, 2.

Gillett, F. C. (1986), in *Light on Dark Matter*, ed., F. P. Israel, Vol. 124, Springer Netherlands, 61–69, series Title: Astrophysics and Space Science Library.

Gillon, M., Jehin, E., Lederer, S. M., et al. (2016), *Temperate Earth-sized planets transiting a nearby ultracool dwarf star*, \nat, 533, 7602.

Gillon, M., Triaud, A. H. M. J., Demory, B.-O., et al. (2017), *Seven temperate terrestrial planets around the nearby ultracool dwarf star TRAPPIST-1*, Nature, 542, 7642.

Goldreich, P. & Tremaine, S. (1980), *Disk-satellite interactions*, The Astrophysical Journal, 241.

Gomes, R., Levison, H. F., Tsiganis, K., & Morbidelli, A. (2005), *Origin of the cataclysmic late heavy nombardment period of the terrestrial planets*, Nature, 435, 7041.

Gomez Gonzalez, C. A., Wertz, O., Absil, O., et al. (2017), *VIP: Vortex Image Processing package for high-contrast direct Imaging*, The Astronomical Journal, 154, 1.

Gorrini, P., Astudillo-Defru, N., Dreizler, S., et al. (2022), *Detailed stellar activity analysis and modelling of GJ 832: Reassessment of the putative habitable zone planet GJ 832c*, Astronomy & Astrophysics, 664.

Gould, A., Dorsher, S., Gaudi, B. S., & Udalski, A. (2006), *Frequency of hot Jupiters and very hot Jupiters from the OGLE: III. Transit surveys toward the galactic bulge and Carina*, arXiv:astro-ph/0601001.

Gould, A. & Loeb, A. (1992), *Discovering planetary systems through gravitational microlenses*, Astrophysical Journal, 396.

Gratton, R., D'Orazi, V., Pacheco, T. A., et al. (2021), *Investigating three Sirius-like systems with SPHERE*, Astronomy & Astrophysics, 646.

Gratton, R., Keller, C., Diolaiti, E., et al. (2022), *MedRes: a new MEDium RESolution integral field spectrograph for SPHERE*, Proceedings of the SPIE.

Greco, J. P. & Brandt, T. D. (2016), *The measurement, treatment, and impact of spectral covariance and bayesian priors in integral-field spectroscopy of exoplanets*, The Astrophysical Journal, 833, 2.

Groff, T. D., Chilcote, J., Kasdin, N. J., et al. (2016), *Laboratory testing and performance verification of the CHARIS integral field spectrograph*, Proceedings of the SPIE, 9908.

Güttler, C., Blum, J., Zsom, A., Ormel, C. W., & Dullemond, C. P. (2010), *The outcome of protoplanetary dust growth: pebbles, boulders, or planetesimals?: I. Mapping the zoo of laboratory collision experiments*, Astronomy and Astrophysics, 513.

Haffert, S. Y., Bohn, A. J., De Boer, J., et al. (2019), *Two accreting protoplanets around the young star PDS 70*, Nature Astronomy, 3, 8.

Haghighipour, N. (2013), *The formation and dynamics of super-Earth planets*, Annual Review of Earth and Planetary Sciences, 41, 1.

Haisch Jr., Karl E., Lada, Elizabeth A. & Lada, Charles J. (2001), *Disk frequencies and lifetimes in young clusters*, The Astrophysical Journal, 533, 2.

Hansen, B. M. S. (2009), *Formation on the terrestrial planets from a narrow annulus*, The Astrophysical Journal, 703, 1.

Hansen, B. M. S. & Murray, N. (2013), *Testing in situ assembly with the Kepler planet candidate sample*, The Astrophysical Journal, 775, 1.

Harris, A. W. & Ward, W. R. (1982), *Dynamical constraints on the formation and evolution of planetary bodies*, Annual Review of Earth and Planetary Sciences, 10, 1.

Hartmann, W., Ryder, G., Dones, L., & Grinspoon, D. (2000), , 493–512.

Heintz, W. D. (1969), *A statistical study of binary stars*, Journal of the Royal Astronomical Society of Canada, 63.

Helled, R., Stevenson, D. J., Lunine, J. I., et al. (2022), *Revelations on Jupiter's formation, evolution and interior: Challenges from Juno results*, Icarus, 378.

Henyey, L. G. & Greenstein, J. L. (1941), *Diffuse radiation in the galaxy*, Astrophysical Journal, 93.

Heppenheimer, T. A. (1980), *Secular resonances and the origin of eccentricities of Mars and the asteroids*, ICarus, 41, 1.

Hinkley, S., Lacour, S., Marleau, G.-D., et al. (2023), *Direct discovery of the inner exoplanet in the HD 206893 system: Evidence for deuterium burning in a planetary-mass companion*, Astronomy & Astrophysics, 671.

Hodapp, K., Jensen, J., Irwin, E., et al. (2003), *The Gemini Near-Infrared Imager (NIRI)*, Publications of the Astronomical Society of the Pacific, 115, 814.

Hodapp, K. W., Suzuki, R., Tamura, M., et al. (2008), *HiCIAO: the Subaru telescope's new high-contrast coronographic imager for adaptive optics*, Proceedings of the SPIE, 7014.

Hoeijmakers, H. J., Schwarz, H., Snellen, I. A. G., et al. (2018), *Medium-resolution integral-field spectroscopy for high-contrast exoplanet imaging: Molecule maps of the Beta Pictoris system with SINFONI*, Astronomy & Astrophysics, 617.

Homma, K. A., Okuzumi, S., Nakamoto, T., & Ueda, Y. (2019), *Rocky planetesimal formation aided by organics*, The Astrophysical Journal, 877, 2.

Houllé, M., Vigan, A., Carlotti, A., et al. (2021), *Direct imaging and spectroscopy of exoplanets with the ELT/HARMONI high-contrast module*, Astronomy & Astrophysics, 652.

Hsu, D. C., Ford, E. B., Ragozzine, D., & Ashby, K. (2019), *Occurrence rates of planets orbiting FGK stars: Combining Kepler DR25, Gaia DR2, and Bayesian inference*, The Astronomical Journal, 158, 3.

Hsu, D. C., Ford, E. B., & Terrien, R. (2020), *Occurrence rates of planets orbiting M Stars: Applying ABC to Kepler DR25, Gaia DR2, and 2MASS data*, Monthly Notices of the Royal Astronomical Society, 498, 2.

Hu, R., Ehlmann, B. L., & Seager, S. (2012), *Theoretical spectra of terrestrial exoplanet surfaces*, The Astrophysical Journal, 752, 1.

Huang, X., Ji, J., Liu, S., Dong, R., & Wang, S. (2023), *Evolution of planetary obliquity: The eccentric Kozai–Lidov mechanism coupled with tide*, The Astrophysical Journal, 956, 1.

Hubin, N., Beuzit, J. L., Gendron, E., & Demailly, L. (1994), *ADONIS: A user friendly adaptive optics system for the ESO 3.6m telescope*, European Southern Observatory Conference and Workshop Proceedings, 48.

Hughes, A. M., Duchene, G., & Matthews, B. (2018), *Debris Disks: Structure, composition, and variability*, Annual Review of Astronomy and Astrophysics, 56, 1.

Hull, C. L. H. & Zhang, Q. (2019), *Interferometric observations of magnetic fields in forming stars*, Frontiers in Astronomy and Space Sciences, 6.

Hunziker, S., Schmid, H. M., Ma, J., et al. (2021), *HD 142527: Quantitative disk polarimetry with SPHERE*, Astronomy & Astrophysics, 648.

Hurley, J. R. & Shara, M. M. (2002), *The promiscuous nature of stars in clusters*, The Astrophysical Journal, 570, 1.

Ida, S. & Lin, D. N. C. (2004), *Toward a deterministic model of planetary formation: II. The formation and retention of gas giant planets around stars with a range of metallicities*, The Astrophysical Journal, 616, 1.

Izidoro, A., Bitsch, B., & Dasgupta, R. (2021), *The effect of a strong pressure bump in the Sun's natal disk: Terrestrial planet formation via planetesimal accretion rather than pebble accretion*, The Astrophysical Journal, 915, 1.

Izidoro, A., Morbidelli, A., Raymond, S. N., Hersant, F., & Pierens, A. (2015), *Accretion of Uranus and Neptune from inward-migrating planetary embryos blocked by Jupiter and Saturn*, Astronomy & Astrophysics, 582.

Izidoro, A., Ogihara, M., Raymond, S. N., et al. (2017), *Breaking the chains: Hot super-Earth systems from migration and disruption of compact resonant chains*, Monthly Notices of the Royal Astronomical Society, 470, 2.

Jang-Condell, H., Chen, C. H., Mittal, T., et al. (2015), *Spitzer IRS spectra of debris disks in the Scorpius-Centaurus OB association*, The Astrophysical Journal, 808, 2.

Janson, M., Gratton, R., Rodet, L., et al. (2021), *A wide-orbit giant planet in the high-mass b Centauri binary system*, Nature, 600, 7888.

Johansen, A. & Lacerda, P. (2010), *Prograde rotation of protoplanets by accretion of pebbles in a gaseous environment*, Monthly Notices of the Royal Astronomical Society.

Johansen, A., Youdin, A. N., & Lithwick, Y. (2012), *Adding particle collisions to the formation of asteroids and Kuiper belt objects via streaming instabilities*, Astronomy & Astrophysics, 537.

Johnson, J. A., Howard, A. W., Marcy, G. W., et al. (2010), *The California planet survey: II. A Saturn-mass planet orbiting the M dwarf Gl 6491*, Publications of the Astronomical Society of the Pacific.

Jones, J. W., Chiang, E., Duchêne, G., Kalas, P., & Esposito, T. M. (2023), *Giant impacts and debris disk morphology*, The Astrophysical Journal, 948, 2.

Jovanovic, N., Martinache, F., Guyon, O., et al. (2015), *The Subaru Coronagraphic Extreme Adaptive Optics System: Enabling high-contrast imaging on solar-system scales*, Publications of the Astronomical Society of the Pacific, 127, 955.

Juillard, S., Christiaens, V., & Absil, O. (2023), *Inverse-problem versus principal component analysis methods for angular differential imaging of circumstellar disks: The mustard algorithm*, Astronomy & Astrophysics, 679.

Juillard, S., Stasevic, S., Christiaens, V., Absil, O., & Milli, J. (2024), *Combining reference-star and angular differential imaging for high-contrast imaging of extended sources*, arXiv:2406.14444 [astro-ph].

Jurić, M. & Tremaine, S. (2008), *Dynamical origin of extrasolar planet eccentricity distribution*, The Astrophysical Journal, 686, 1.

Kalas, P. G., Rajan, A., Wang, J. J., et al. (2015), *Direct imaging of an asymmetric debris disk in the HD 106906 planetary system*, The Astrophysical Journal, 814, 1.

Kammerer, J., Lawson, K., Perrin, M. D., et al. (2024), *JWST-TST high contrast: JWST/NIRCam observations of the young giant planet Beta Pic b*, arXiv:2405.18422 [astro-ph].

Kasper, M., Cerpa Urra, N., Pathak, P., et al. (2021), *PCS: A roadmap for Exo-Earth imaging with the ELT*, Published in The Messenger vol. 182, pp. 38-43.

Kasting, J. F., Whitmire, D. P., & Reynolds, R. T. (1993), *Habitable zones around main sequence stars*, Icarus, 101, 1.

Kataoka, A., Tanaka, H., Okuzumi, S., & Wada, K. (2013), *Fluffy dust forms icy planetesimals by static compression*, Astronomy & Astrophysics, 557.

Kennedy, G. M. & Kenyon, S. J. (2008), *Planet formation around stars of various masses: The snow line and the frequency of giant planets*, The Astrophysical Journal, 673, 1.

Kennedy, G. M., Matrà, L., Marmier, M., et al. (2015), *Kuiper belt structure around nearby super-Earth host stars*, Monthly Notices of the Royal Astronomical Society, 449, 3.

Kennicutt, R. C. & Evans, N. J. (2012), *Star formation in the Milky Way and nearby galaxies*, Annual Review of Astronomy and Astrophysics, 50, 1.

Keppler, M., Benisty, M., Müller, A., et al. (2018), *Discovery of a planetary-mass companion within the gap of the transition disk around PDS 70*, Astronomy & Astrophysics, 617.

Keppler, M., Penzlin, A., Benisty, M., et al. (2020), *Gap, shadows, spirals, and streamers: SPHERE observations of binary-disk interactions in GG Tauri A*, Astronomy & Astrophysics, 639.

Kervella, P., Arenou, F., Mignard, F., & Thévenin, F. (2019), *Stellar and substellar companions of nearby stars from Gaia DR2: Binarity from proper motion anomaly*, Astronomy & Astrophysics, 623.

Kim, S.-L., Lee, C.-U., Park, B.-G., et al. (2016), *KMTNET: A network of 1.6 M wide-field optical telescopes installed at three southern observatories*, Journal of The Korean Astronomical Society, 49, 1.

Klačka, J., Petržala, J., Pástor, P., & Kómar, L. (2014), *The Poynting–Robertson effect: A critical perspective*, Icarus, 232.

Kleine, T., Touboul, M., Bourdon, B., et al. (2009), *Hf–W chronology of the accretion and early evolution of asteroids and terrestrial planets*, Geochimica et Cosmochimica Acta, 73, 17.

Kley, W. & Nelson, R. P. (2012), *Planet-disk interaction and orbital evolution*, Annual Review of Astronomy and Astrophysics, 50, 1.

Konishi, M., Grady, C. A., Schneider, G., et al. (2016), *Discovery of an inner disk component around HD 141569 A*, The Astrophysical Journal, 818, 2.

Konopacky, Q. M., Barman, T. S., Macintosh, B. A., & Marois, C. (2013), *Detection of carbon monoxide and water absorption lines in an exoplanet atmosphere*, Science, 339, 6126.

Kozai, Y. (1962), *Secular perturbations of asteroids with high inclination and eccentricity*, Astronomical Journal, 67.

Kral, Q., Davoult, J., & Charnay, B. (2020), *Formation of secondary atmospheres on terrestrial planets by late disk accretion*, Nature Astronomy, 4, 8.

Kraus, A. L., Ireland, M. J., Hillenbrand, L. A., & Martinache, F. (2012), *The role of multiplicity in disk evolution and planet formation*, The Astrophysical Journal, 745, 1.

Kraus, A. L., Ireland, M. J., Huber, D., Mann, A. W., & Dupuy, T. J. (2016), *The impact of stellar multiplicity on planetary systems: I. The ruinous influence of close binary companions*, The Astronomical Journal, 152, 1.

Kraus, S., Kreplin, A., Young, A. K., et al. (2020), *A triple-star system with a misaligned and warped circumstellar disk shaped by disk tearing*, Science, 369, 6508.

Kretke, K. A. & Lin, D. N. C. (2007), *Grain retention and formation of planetesimals near the snow line in MRI-driven turbulent protoplanetary disks*, The Astrophysical Journal, 664, 1.

Krijt, S., Kama, M., McClure, M., et al. (2023), *Chemical habitability: supply and retention of life's essential elements during planet formation*, Protostars and Planets VII, 534.

Krijt, S., Ormel, C. W., Dominik, C., & Tielens, A. G. G. M. (2015), *Erosion and the limits to planetesimal growth*, Astronomy & Astrophysics, 574.

Lacour, S., Tuthill, P., Ireland, M., Amico, P., & Girard, J. (2011), *Sparse Aperture Masking on Paranal*, Messenger, 146.

Lacour, S., Wang, J. J., Nowak, M., et al. (2020), *The ExoGRAVITY project: Using single mode interferometry to characterize exoplanets*, Proceedings of the SPIE.

Lafreniere, D., Marois, C., Doyon, R., Nadeau, D., & Artigau, E. (2007), *A new algorithm for point-spread function subtraction in high-contrast imaging: A demonstration with angular differential imaging*, The Astrophysical Journal, 660, 1.

Lagrange, A.-M., Philipot, F., Rubini, P., et al. (2023), *Radial distribution of giant exoplanets at Solar System scales*, Astronomy & Astrophysics, 677.

Lambrechts, M. & Johansen, A. (2012), *Rapid growth of gas-giant cores by pebble accretion*, Astronomy & Astrophysics, 544.

Landman, R., Snellen, I. A. G., Keller, C. U., et al. (2023), *Trade-offs in high-contrast integral field spectroscopy for exoplanet detection and characterisation: Young gas giants in emission*, Astronomy & Astrophysics, 675.

Lane, M. D., Cloutis, E. A., R. N., C., et al. (2024), *Reflectance spectroscopy of 27 fine-particulate mineral samples from far-ultraviolet through mid-infrared (0.12-20 μm)*, Planetary Science Journal, accepted.

Larkin, J., Barczys, M., Krabbe, A., et al. (2006), *OSIRIS: A diffraction limited integral field spectrograph for Keck*, New Astronomy Reviews, 50, 4-5.

Laskar, J., Joutel, F., & Robutel, P. (1993), *Stabilization of the Earth's obliquity by the Moon*, Nature, 361, 6413.

Laskar, J. & Robutel, P. (1993), *The chaotic obliquity of the planets*, Nature, 361, 6413.

Laughlin, G. & Adams, F. C. (1998), *The modification of planetary orbits in dense open clusters*, The Astrophysical Journal, 508, 2.

Laws, A. S. E., Harries, T. J., Setterholm, B. R., et al. (2020), *Irregular dust features around intermediate-mass young stars with GPI: signs of youth or misaligned disks?*, The Astrophysical Journal, 888, 1.

Le Coroller, H., Nowak, M., Delorme, P., et al. (2020), *K-Stacker: an algorithm to hack the orbital parameters of planets hidden in high-contrast imaging: First applications to VLT/SPHERE multi-epoch observations*, Astronomy & Astrophysics, 639.

Le Coroller, H., Nowak, M., Wagner, K., et al. (2022), *Efficiently combining Alpha Cen A multi-epoch high-contrast imaging data: Application of K-Stacker to the 80 hours NEAR campaign*, Astronomy & Astrophysics, 667.

Le Gouellec, V. J. M. (2021), *Constraining the dust grain alignment mechanisms responsible for the (sub-) millimeter dust polarization observed in Class 0 protostellar cores*, Thesis Université de Paris.

Lecavelier des Etangs, A. & Lissauer, J. J. (2022), *The IAU working definition of an exoplanet*, New Astronomy Reviews, 94.

Lee, E. J. & Chiang, E. (2016), *A primer on unifying debris disk morphologies*, The Astrophysical Journal, 827, 2.

Lee, E. J., Chiang, E., & Ormel, C. W. (2014), *Make super-Earths, not Jupiters: Accreting nebular gas onto solid cores at 0.1 au and beyond*, The Astrophysical Journal, 797, 2.

Lenzen, R., Hartung, M., Brandner, W., et al. (2003), *NAOS-CONICA first on sky results in a variety of observing modes*, Proceedings of the SPIE, 4841.

Lestrade, J.-F., Matthews, B. C., Sibthorpe, B., et al. (2012), *A debris disk around the planet hosting M-star GJ 581 spatially resolved with Herschel*, Astronomy & Astrophysics, 548.

Lin, D. N. C. & Papaloizou, J. (1986), *On the tidal interaction between protoplanets and the primordial solar nebula: III. Orbital migration of protoplanets*, The Astrophysical Journal, 309.

Linder, E. F., Mordasini, C., Mollière, P., et al. (2019), *Evolutionary models of cold and low-mass planets: Cooling curves, magnitudes, and detectability*, Astronomy & Astrophysics, 623.

Lissauer, J. J., Ragozzine, D., Fabrycky, D. C., et al. (2011), *Architecture and dynamics of Kepler's candidate multiple transiting planet systems*, The Astrophysical Journal Supplement Series, 197, 1.

Liu, B., Ormel, C. W., & Johansen, A. (2019), *Growth after the streaming instability: From planetesimal accretion to pebble accretion*, Astronomy & Astrophysics, 624.

Liu, B., Raymond, S. N., & Jacobson, S. A. (2022), *Early Solar System instability triggered by dispersal of the gaseous disk*, Nature, 604, 7907.

Long, F., Herczeg □ , G. J. □ ., Harsono, D., et al. (2019), *Compact disks in a high-resolution ALMA survey of dust structures in the Taurus molecular cloud*, The Astrophysical Journal, 882, 1.

Lopez-Santiago, J., Martino, L., Miguez, J., & Vazquez, M. A. (2020), *A likely magnetic activity cycle for the exoplanet host M dwarf GJ 3512*, The Astronomical Journal, 160, 6.

Luger, R., Sestovic, M., Kruse, E., et al. (2017), *A seven-planet resonant chain in TRAPPIST-1*, Nature Astronomy, 1, 6.

Lyra, W. & Lin, M.-K. (2013), *Steady state dust distributions in disk vortices: Observational predictions and applications to transitional disks*, The Astrophysical Journal, 775, 1.

Macintosh, B., Graham, J. R., Barman, T., et al. (2015), *Discovery and spectroscopy of the young jovian planet 51 Eri b with the Gemini Planet Imager*, Science, 350, 6256.

Madhusudhan, N. (2019), *Exoplanetary atmospheres: Key insights, challenges, and prospects*, Annual Review of Astronomy and Astrophysics, 57, 1.

Madhusudhan, N., Burrows, A., & Currie, T. (2011), *Model atmosphere for massive gas giants with thick clouds: Application to the HR 8799 planets and predictions for future detections*, The Astrophysical Journal, 737, 1.

Madsen, S., Dravins, D., & Lindegren, L. (2002), *Astrometric radial velocities. III. Hipparcos measurements of nearby star clusters and associations*, Astronomy & Astrophysics, 381.

Madurowicz, A., Macintosh, B. A., Ruffio, J.-B., et al. (2018), *Characterization of lemniscate atmospheric aberrations in Gemini Planet Imager data*, 10703.

Malik, M., Grosheintz, L., Mendonça, J. M., et al. (2017), *HELIOS: An open-source, GPU-accelerated radiative transfer code for self-consistent exoplanetary atmospheres*, The Astronomical Journal, 153, 2.

Maness, H. L., Kalas, P., Peek, K. M. G., et al. (2009), *Hubble Space Telescope optical imaging of the eroding debris disk HD 61005*, The Astrophysical Journal, 707, 2.

Mao, S. & Paczynski, B. (1991), *Gravitational microlensing by double stars and planetary systems*, The Astrophysical Journal, 374.

Marcy, G., Butler, R. P., Fischer, D. A., et al. (2005a), *Observed properties of exoplanets: masses, orbits, and metallicities*, Progress of Theoretical Physics Supplement, 158.

Marcy, G. W., Butler, R. P., Vogt, S. S., et al. (2005b), *Five new extrasolar planets*, The Astrophysical Journal, 619, 1.

Marino, S. (2021), *Constraining planetesimal stirring: How sharp are debris disc edges?*, Monthly Notices of the Royal Astronomical Society, 503, 4.

Marino, S., Carpenter, J., Wyatt, M. C., et al. (2018), *A gap in the planetesimal disc around HD 107146 and asymmetric warm dust emission revealed by ALMA*, Monthly Notices of the Royal Astronomical Society, 479, 4.

Marino, S., Yelverton, B., Booth, M., et al. (2019), *A gap in HD 92945's broad planetesimal disc revealed by ALMA*, Monthly Notices of the Royal Astronomical Society, 484, 1.

Marino, S., Zurlo, A., Faramaz, V., et al. (2020), *Insights into the planetary dynamics of HD 206893 with ALMA*, Monthly Notices of the Royal Astronomical Society, 498, 1.

Marleau, G.-D., Coleman, G. A. L., Leleu, A., & Mordasini, C. (2019), *Exploring the formation by core accretion and the luminosity evolution of directly imaged planets: The case of HIP 65426 b*, Astronomy & Astrophysics, 624.

Marois, C., Correia, C., Véran, J.-P., & Currie, T. (2013), *TLOCI: A fully loaded speckle killing machine*, Proceedings of the International Astronomical Union, 8, S299.

Marois, C., Lafreniere, D., Doyon, R., Macintosh, B., & Nadeau, D. (2006), *Angular Differential Imaging: A powerful high-contrast imaging technique*, The Astrophysical Journal, 641, 1.

Marois, C., Macintosh, B., Barman, T., et al. (2008), *Direct imaging of multiple planets orbiting the star HR 8799*, Science, 322, 5906.

Marois, C., Zuckerman, B., Konopacky, Q. M., Macintosh, B., & Barman, T. (2010), *Images of a fourth planet orbiting HR 8799*, Nature, 468, 7327.

Matrà, L., MacGregor, M. A., Kalas, P., et al. (2017), *Detection of exocometary CO within the 440 Myr old Fomalhaut belt: A similar CO+CO2 ice abundance in exocomets and Solar System comets*, The Astrophysical Journal, 842, 1.

Matrà, L., Öberg, K. I., Wilner, D. J., Olofsson, J., & Bayo, A. (2019), *On the ubiquity and stellar luminosity dependence of exocometary CO gas: Detection around M dwarf TWA 7*, The Astronomical Journal, 157, 3.

Matthews, E. C., Bonnefoy, M., Xie, C., et al. (2023), *The first scattered light images of HD 112810, a faint debris disk in the Sco-Cen association*, Astronomy & Astrophysics, 679.

Matthews, E. C., Carter, A. L., Pathak, P., et al. (2024), *A temperate super-Jupiter imaged with JWST in the mid-infrared*, Nature, 8031.

Mawet, D., Pueyo, L., Lawson, P., et al. (2012), *Review of small-angle coronagraphic techniques in the wake of ground-based second-generation adaptive optics systems*, Proceedings of the SPIE.

Mayor, M., Marmier, M., Lovis, C., et al. (2011), *The HARPS search for southern extra-solar planets: XXXIV. Occurrence, mass distribution and orbital properties of super-Earths and Neptune-mass planets*, arXiv:1109.2497 [astro-ph].

Mayor, M. & Queloz, D. (1995), *A Jupiter-mass companion to a solar-type star*, Nature, 378, 6555.

McLean, I. S., Becklin, E. E., Bendiksen, O., et al. (1998), *Design and development of NIRSPEC: A near-infrared echelle spectrograph for the Keck II telescope*, Proceedings of the SPIE, 3354.

Meheut, H., Meliani, Z., Varniere, P., & Benz, W. (2012), *Dust-trapping Rossby vortices in protoplanetary disks*, Astronomy & Astrophysics, 545.

Mesa, D., Gratton, R., Kervella, P., et al. (2023), *AF Lep b: The lowest-mass planet detected by coupling astrometric and direct imaging data*, Astronomy & Astrophysics, 672.

Miki, S. (1982), *The gaseous flow around a protoplanet in the primordial solar nebula*, Progress of Theoretical Physics, 67, 4.

Miley, J. M., Panić, O., Booth, R. A., et al. (2020), *The impact of pre-main sequence stellar evolution on mid-plane snowline locations and C/O in planet forming discs*, Monthly Notices of the Royal Astronomical Society, 500, 4.

Milli, J., Choquet, E., Tazaki, R., et al. (2024), *The polarisation properties of the HD 181327 debris ring: Evidence for sub-micron particles from scattered light observations*, Astronomy & Astrophysics, 683.

Milli, J., Engler, N., Schmid, H. M., et al. (2019), *Optical polarised phase function of the HR 4796 A dust ring*, Astronomy & Astrophysics, 626.

Milli, J., Hibon, P., Christiaens, V., et al. (2017a), *Discovery of a low-mass companion inside the debris ring surrounding the F5V star HD 206893*, Astronomy & Astrophysics, 597.

Milli, J., Mawet, D., Pinte, C., et al. (2015), *New constraints on the dust surrounding HR 4796 A*, Astronomy & Astrophysics, 577.

Milli, J., Mouillet, D., Lagrange, A.-M., et al. (2012), *Impact of angular differential imaging on circumstellar disk images*, Astronomy & Astrophysics, 545.

Milli, J., Vigan, A., Mouillet, D., et al. (2017b), *Near-infrared scattered light properties of the HR 4796 A dust ring: A measured scattering phase function from 13.6° to 166.6°*, Astronomy & Astrophysics, 599.

Miotello, A., Kamp, I., Birnstiel, T., Cleeves, L. I., & Kataoka, A. (2023), *Setting the stage for planet formation: Measurements and implications of the fundamental disk properties*, Protostars and Planets VII, 534.

Miret-Roig, N. (2023), *The origin of free-floating planets*, Astrophysics and Space Science,, 368, 3.

Miret-Roig, N., Bouy, H., Raymond, S. N., et al. (2022), *A rich population of free-floating planets in the Upper Scorpius young stellar association*, Nature Astronomy, 6, 1.

Miyazaki, S. & Masuda, K. (2023), *Evidence that the occurrence rate of hot Jupiters around Sun-like stars decreases with stellar age*, The Astronomical Journal, 166, 5.

Mollière, P., Boekel, R. V., Dullemond, C., Henning, T., & Mordasini, C. (2015), *Model atmospheres of irradiated exoplanets: The influence of stellar parameters, metallicity, and the C/O ratio*, The Astrophysical Journal, 813, 1.

Mollière, P., Molyarova, T., Bitsch, B., et al. (2022), *Interpreting the atmospheric composition of exoplanets: sensitivity to planet formation assumptions*, The Astrophysical Journal, 934, 1.

Mollière, P., Van Boekel, R., Bouwman, J., et al. (2017), *Observing transiting planets with JWST: Prime targets and their synthetic spectral observations*, Astronomy & Astrophysics, 600.

Momose, M., Morita, A., Fukagawa, M., et al. (2015), *Detailed structure of the outer disk around HD 169142 with polarized light in H-band*, Publications of the Astronomical Society of Japan, 67, 5.

Monnier, J. D., Harries, T. J., Aarnio, A., et al. (2017), *Polarized disk emission from Herbig Ae/Be stars observed using Gemini Planet Imager: HD 144432, HD 150193, HD 163296, and HD 169142*, The Astrophysical Journal, 838, 1.

Morales, J. C., Mustill, A. J., Ribas, I., et al. (2019), *A giant exoplanet orbiting a very-low-mass star challenges planet*, Science, 365.

Morbidelli, A., Baillié, K., Batygin, K., et al. (2021), *Contemporary formation of early Solar System planetesimals at two distinct radial locations*, Nature Astronomy, 6, 1.

Morbidelli, A., Bitsch, B., Crida, A., et al. (2016), *Fossilized condensation lines in the Solar System protoplanetary disk*, Icarus, 267.

Morbidelli, A., Levison, H. F., Tsiganis, K., & Gomes, R. (2005), *Chaotic capture of Jupiter's Trojan asteroids in the early Solar System*, Nature, 435, 7041.

Mouillet, D., Milli, J., Sauvage, J.-F., et al. (2018), *Statistical analysis and lessons learned of SPHERE adaptive optics performance*, Proceedings of the SPIE, 10703.

Mroz, P. & Poleski, R. (2023), *Exoplanet occurrence rates from microlensing surveys*, arXiv:2310.07502 [astro-ph].

Mróz, P., Udalski, A., Bennett, D. P., et al. (2019), *Two new free-floating or wide-orbit planets from microlensing*, Astronomy & Astrophysics, 622.

Mróz, P., Udalski, A., Skowron, J., et al. (2017), *No large population of unbound or wide-orbit Jupiter-mass planets*, Nature, 548, 7666.

Mulders, G. D., Pascucci, I., & Apai, D. (2015), *A stellar-mass-dependent drop in planet occurence rates*, The Astrophysical Journal, 798, 2.

Murchikova, L. & Tremaine, S. (2020), *Peas in a pod? Radius correlations in Kepler multiplanet systems*, The Astronomical Journal, 160, 4.

Muro-Arena, G. A., Benisty, M., Ginski, C., et al. (2020), *Shadowing and multiple rings in the protoplanetary disk of HD 139614*, Astronomy & Astrophysics, 635.

Mustill, A. J. & Wyatt, M. C. (2009), *Debris disc stirring by secular perturbations from giant planets*, Monthly Notices of the Royal Astronomical Society, 399, 3.

Mâlin, M., Boccaletti, A., Charnay, B., Kiefer, F., & Bézard, B. (2023), *Simulated performance of the molecular mapping for young giant exoplanets with the Medium-Resolution Spectrometer of JWST/MIRI*, Astronomy & Astrophysics, 671.

Mâlin, M., Boccaletti, A., Perrot, C., Baudoz, P., Rouan, D. et al. (2024), *Unveiling the HD 95086 system at mid-infrared wavelengths with JWST/MIRI*, Astronomy & Astrophysics, 690.

Müller, A., Keppler, M., Henning, T., et al. (2018), *Orbital and atmospheric characterization of the planet within the gap of the PDS 70 transition disk*, Astronomy & Astrophysics, 617.

Nagasawa, M. & Ida, S. (2011), *Orbital distributions of close-in planets and distant planets formed by scattering and dynamical tides*, The Astrophysical Journal, 742, 2.

Nagasawa, M., Lin, D. N. C., & Thommes, E. (2005), *Dynamical shake-up of planetary systems: I. Embryo trapping and induced collisions by the sweeping secular resonance and embryo-disk tidal interaction*, The Astrophysical Journal, 635, 1.

Najita, J. R., Kenyon, S. J., & Bromley, B. C. (2022), *From pebbles and planetesimals to planets and dust: The protoplanetary disk–debris disk connection*, The Astrophysical Journal, 925, 1.

Nakagawa, Y., Sekiya, M., & Hayashi, C. (1986), *Settling and growth of dust particles in a laminar phase of a low-mass solar nebula*, Icarus, 67, 3.

Naoz, S., Farr, W. M., & Rasio, F. A. (2012), *On the formation of hot Jupiters in stellar binaries*, The Astrophysical Journal, 754, 2.

Narang, M., Manoj, P., Furlan, E., et al. (2018), *Properties and Occurrence Rates for Kepler Exoplanet Candidates as a Function of Host Star Metallicity from the DR25 Catalog*, The Astronomical Journal, 156, 5.

Nasedkin, E., Mollière, P., Lacour, S., et al. (2024), *Four-of-a-kind? Comprehensive atmospheric characterisation of the HR 8799 planets with VLTI/GRAVITY*, arXiv:2404.03776 [astro-ph].

N'Diaye, M., Pueyo, L., & Soummer, R. (2015), *Apodized pupil Lyot coronagraphs for arbitrary apertures: IV. Reduced inner working angles and increased robustness to low-order aberrations*, The Astrophysical Journal, 799, 2.

Nelder, J. A. & Mead, R. (1965), *A simplex method for function minimization*, Computer Journal, 7, 4.

Nesvorný, D., Vokrouhlický, D., & Morbidelli, A. (2007), *Capture of irregular satellites during planetary encounters*, The Astronomical Journal, 133, 5.

Neugebauer, G., Habing, H. J., van Duinen, R., et al. (1984), *The infrared astronomical satellite IRAS mission*, Astrophysical Journal, 278.

Ngo, H., Knutson, H. A., Hinkley, S., et al. (2016), *Friends of hot Jupiters: IV. Stellar companions beyond 50 au might facilitate giant planet formation, but most are unlikely to cause Kozai-Lidov migration*, The Astrophysical Journal, 827, 1.

Nielsen, E. L., De Rosa, R. J., Macintosh, B., et al. (2019), *The Gemini Planet Imager exoplanet survey: Giant planet and brown dwarf demographics from 10 to 100 au*, The Astronomical Journal, 158, 1.

Nowak, M., Lacour, S., Lagrange, A.-M., et al. (2020), *Direct confirmation of the radial-velocity planet Beta Pictoris c*, Astronomy & Astrophysics, 642.

N'Diaye, M., Dohlen, K., Fusco, T., & Paul, B. (2013), *Calibration of quasi-static aberrations in exoplanet direct-imaging instruments with a Zernike phase-mask sensor*, Astronomy & Astrophysics, 555.

N'Diaye, M., Soummer, R., Pueyo, L., et al. (2016a), *Apodized pupil Lyot coronagraphs for arbitrary apertures: V. Hybrid shaped pupil designs for imaging Earth-like planets with future space observatories*, The Astrophysical Journal, 818, 2.

N'Diaye, M., Vigan, A., Dohlen, K., et al. (2016b), *Calibration of quasi-static aberrations in exoplanet direct-imaging instruments with a Zernike phase-mask sensor: II. Concept validation with ZELDA on VLT/SPHERE*, Astronomy & Astrophysics, 592.

Ohno, K. & Ueda, T. (2021), *Jupiter's "cold" formation in the protosolar disk shadow: An explanation for the planet's uniformly enriched atmosphere*, Astronomy & Astrophysics, 651.

Okuzumi, S., Tanaka, H., Kobayashi, H., & Wada, K. (2012), *Rapid coagulation of porous dust aggregates outside the snow line: A pathway to successful icy planetesimal formation*, The Astrophysical Journal, 752, 2.

Olofsson, J., Thébault, P., Bayo, A., et al. (2023), *Apocenter pile-up and arcs: A narrow dust ring around HD 129590*, Astronomy & Astrophysics, 674.

Olofsson, J., Thébault, P., Kennedy, G. M., & Bayo, A. (2022a), *The halo around HD 32297: µm-sized cometary dust*, Astronomy & Astrophysics, 664.

Olofsson, J., Thébault, P., Kral, Q., et al. (2022b), *The vertical structure of debris disks and the impact of gas*, Monthly Notices of the Royal Astronomical Society, 513, 1.

Ormel, C. W. & Klahr, H. H. (2010), *The effect of gas drag on the growth of protoplanets: Analytical expressions for the accretion of small bodies in laminar disks*, Astronomy and Astrophysics, 520.

Ormel, C. W., Paszun, D., Dominik, C., & Tielens, A. G. G. M. (2009), *Dust coagulation and fragmentation in molecular clouds: I. How collisions between dust aggregates alter the dust size distribution*, Astronomy & Astrophysics, 502, 3.

Owen, T. & Encrenaz, T. (2003), *Element abundances and isotope ratios in the giant planets and Titan*, Space Science Reviews,, 106, 1.

Paardekooper, S.-J., Dong, R., Duffell, P. C., et al. (2023), *Planet-disk interactions and orbital evolution*, Protostars and Planets VII, 534.

Paczynski, B. (1986), *Gravitational microlensing by the galactic halo*, The Astrophysical Journal, 304.

Padgett, D. & Stapelfeldt, K. (2016), *Warm debris disks with WISE and HST*, Proceedings of the International Astronomical Union, 10, S314.

Padoan, P. & Nordlund, A. (2004), *The "mysterious" origin of brown dwarfs*, The Astrophysical Journal, 617, 1.

Pairet, B., Cantalloube, F., & Jacques, L. (2021), *MAYONNAISE: a morphological components analysis pipeline for circumstellar discs and exoplanets imaging in the near-infrared*, Monthly Notices of the Royal Astronomical Society, 503, 3.

Palma-Bifani, P., Borja, D., Chauvin, G., et al. (2024), *The atmosphere of AF Lep b through ForMoSA*, Astronomy & Astrophysics, 683, A214.

Palma-Bifani, P., Chauvin, G., Bonnefoy, M., et al. (2023), *Peering into the young planetary system AB Pic: Atmosphere, orbit, obliquity, and second planetary candidate*, Astronomy & Astrophysics, 670.

Patapis, P., Nasedkin, E., Cugno, G., et al. (2022), *Direct emission spectroscopy of exoplanets with the medium resolution imaging spectrometer on board JWST MIRI: I. Molecular mapping and sensitivity to instrumental effects*, Astronomy & Astrophysics, 658.

Patience, J., White, R. J., Ghez, A. M., et al. (2002), *Stellar companions to stars with planets*, The Astrophysical Journal, 581, 1.

Pawellek, N. & Krivov, A. V. (2015), *The dust grain size–stellar luminosity trend in debris discs*, Monthly Notices of the Royal Astronomical Society, 454, 3.

Pawellek, N., Krivov, A. V., Marshall, J. P., & Montesinos, B. (2014), *Disk radii and grain sizes in Herschel-resolved debris disks*, The Astrophysical Journal.

Pawellek, N., Wyatt, M., Matrà, L., Kennedy, G., & Yelverton, B. (2021), *A □ 75 per cent occurrence rate of debris discs around F stars in the Beta Pic moving group*, Monthly Notices of the Royal Astronomical Society, 502, 4.

Pearce, T. D. (2024), in *Encyclopedia of Astrophysics*, arXiv, arXiv:2403.11804 [astro-ph].

Pearce, T. D., Launhardt, R., Ostermann, R., et al. (2022), *Planet populations inferred from debris discs: Insights from 178 debris systems in the ISPY, LEECH and LIStEN planet-hunting surveys*, Astronomy & Astrophysics, 659.

Pecaut, M. J., Mamajek, E. E., & Bubar, E. J. (2012), *A revised age for Upper Scorpius and the star formation history among the F-type members of the Scorpius-Centaurus OB Association*, The Astrophysical Journal, 746, 2.

Pedichini, F., Stangalini, M., Ambrosino, F., et al. (2017), *High contrast imaging in the visible: First experimental results at the Large Binocular Telescope*, The Astronomical Journal, 154, 2.

Penny, M. T., Scott Gaudi, B., Kerins, E., et al. (2019), *Predictions of the WFIRST microlensing survey: I. Bound Planet detection rates*, The Astrophysical Journal Supplement Series, 241, 1.

Pepe, F., Cristiani, S., Rebolo, R., et al. (2021), *ESPRESSO at VLT: On-sky performance and first results*, Astronomy & Astrophysics, 645.

Pepe, F., Mayor, M., Rupprecht, G., et al. (2002), *HARPS: ESO's coming planet searcher. Chasing exoplanets with the La Silla 3.6-m telescope*, The Messenger, 110.

Pepin, R. O. (1991), *On the origin and early evolution of terrestrial planet atmospheres and meteoritic volatiles*, Icarus, 92, 1.

Perrin, M. D., Duchene, G., Millar-Blanchaer, M., et al. (2015), *Polarimetry with the Gemini Planet Imager: Methods, performance at first light, and the circumstellar ring around HR 4796A*, The Astrophysical Journal, 799, 2.

Perryman, M. (2012), *The history of astrometry*, The European Physical Journal H, 37, 5.

Petrus, S., Bonnefoy, M., Chauvin, G., et al. (2021), *Medium-resolution spectrum of the exoplanet HIP 65426 b*, Astronomy & Astrophysics, 648.

Philipot, F., Lagrange, A.-M., Rubini, P., Kiefer, F., & Chomez, A. (2023), *Updated characterization of long-period single companion by combining radial velocity, relative astrometry, and absolute astrometry*, Astronomy & Astrophysics, 670.

Pichierri, G., Batygin, K., & Morbidelli, A. (2019), *The role of dissipative evolution for three-planet, near-resonant extrasolar systems*, Astronomy & Astrophysics, 625.

Pilbratt, G. L., Riedinger, J. R., Passvogel, T., et al. (2010), *Herschel Space Observatory: An ESA facility for far-infrared and submillimetre astronomy*, Astronomy and Astrophysics, 518.

Pinilla, P., Benisty, M., Boer, J. D., et al. (2018), *Variable outer disk shadowing around the dipper star RXJ1604.3–2130*, The Astrophysical Journal, 868, 2.

Pinna, E., Esposito, S., Hinz, P., et al. (2016), *SOUL: the Single conjugated adaptive Optics Upgrade for LBT*, Proceedings of the SPIE.

Pinte, C., Price, D. J., Ménard, F., et al. (2018), *Kinematic evidence for an embedded protoplanet in a circumstellar disk*, The Astrophysical Journal, 860, 1.

Pollack, K. B., Hubickyj, O., Bodenheimer, P., et al. (1996), *Formation of the giant planets by concurrent accretion of solids and gas*, Icarus, 124.

Por, E. H. (2020), *Phase-apodized-pupil Lyot Coronagraphs for Arbitrary Telescope Pupils*, The Astrophysical Journal, 888, 2.

Potier, A., Galicher, R., Baudoz, P., et al. (2020), *Increasing the raw contrast of VLT/SPHERE with the dark hole technique. I. Simulations and validation on the internal source*, Astronomy & Astrophysics, 638.

Potier, A., Mazoyer, J., Wahhaj, Z., et al. (2022), *Increasing the raw contrast of VLT/SPHERE with the dark hole technique: II. On-sky wavefront correction and coherent differential imaging*, Astronomy & Astrophysics, 665.

Pourré, N., Le Bouquin, J.-B., Milli, J., et al. (2022), *Low-wind-effect impact on Shack-Hartmann-based adaptive optics: Partial control solution in the context of SPHERE and GRAVITY+*, Astronomy & Astrophysics, 665.

Pourré, N., Winterhalder, T. O., Bouquin, J.-B. L., et al. (2024), *High contrast at short separation with VLTI/GRAVITY: Bringing Gaia companions to light*, arXiv:2406.04003 [astro-ph].

Quarles, B. & Kaib, N. (2019), *Instabilities in the early Solar System due to a self-gravitating disk*, The Astronomical Journal, 157, 2.

Quirrenbach, A., Passegger, V. M., Trifonov, T., et al. (2022), *The CARMENES search for exoplanets around M dwarfs: Two Saturn-mass planets orbiting active stars*, Astronomy & Astrophysics, 663.

Racine, R., Walker, G., Nadeau, D., Doyon, R., & Marois, C. (1999), *Speckle noise and the detection of faint companions*, Publications of the Astronomical Society of the Pacific, 111, 759.

Raettig, N., Klahr, H., & Lyra, W. (2015), *Particle trapping and streaming instability in vortices in protoplanetary disks*, The Astrophysical Journal, 804, 1.

Raghavan, D., McAlister, H. A., Henry, T. J., et al. (2010), *A survey of stellar families: multiplicity of solar-type stars*, The Astrophysical Journal Supplement Series, 190, 1.

Rameau, J., Chauvin, G., Lagrange, A.-M., et al. (2013), *Discovery of a probable 4-5 Jupiter-mass exoplanet to HD 95086 by direct-imaging*, The Astrophysical Journal, 772, 2.

Rameau, J., Nielsen, E. L., Rosa, R. J. D., et al. (2016), *Constraints on the architecture of the HD 95086 planetary system with the Gemini Planet Imager*, The Astrophysical Journal Letters, 822, 2.

Rasio, F. A. & Ford, E. B. (1996), *Dynamical instabilities and the formation of extrasolar planetary systems*, Science, 274, 5289.

Ray, S., Sallum, S., Hinkley, S., et al. (2023), *The JWST early release science program for direct observations of exoplanetary systems: III. Aperture Masking Interferometric observations of the star HIP 65426 at 3.8 μm*, arXiv:2310.11508 [astro-ph].

Raymond, S. N., Armitage, P. J., & Gorelick, N. (2009), *Planet-planet scattering in planetesimal disks.*, The Astrophysical Journal, 699, 2.

Raymond, S. N., Barnes, R., & Mandell, A. M. (2008), *Observable consequences of planet formation models in systems with close-in terrestrial planets: Observable consequences of planet formation*, Monthly Notices of the Royal Astronomical Society, 384, 2.

Raymond, S. N. & Izidoro, A. (2017), *The empty primordial asteroid belt*, Science Advances, 3, 9.

Rebollido, I., Eiroa, C., Montesinos, B., et al. (2020), *Exocomets: A spectroscopic survey*, Astronomy & Astrophysics, 639.

Rebollido, I., Stark, C. C., Kammerer, J., et al. (2024), *JWST-TST high contrast: Asymmetries, dust populations and hints of a collision in the Beta Pictoris disk with NIRCam and MIRI*, The Astronomical Journal, 167, 2.

Ren, B. B., Rebollido, I., Choquet, □ ., et al. (2023), *Debris disk color with the Hubble Space Telescope*, Astronomy & Astrophysics, 672.

Rice, W. K. M., Armitage, P. J., Wood, K., & Lodato, G. (2006), *Dust filtration at gap edges: implications for the spectral energy distributions of discs with embedded planets*, Monthly Notices of the Royal Astronomical Society, 373, 4.

Rigliaco, E., Gratton, R., Kóspál, A., et al. (2020), *The circumstellar environment of EX Lupi: SPHERE and SINFONI views*, Astronomy & Astrophysics, 641.

Roddier, F. (1981), *The effects of atmospheric turbulence in optical astronomy*, Progess in Optics, 19.

Rodet, L., Beust, H., Bonnefoy, M., et al. (2017), *Origin of the wide-orbit circumbinary giant planet HD 106906: A dynamical scenario and its impact on the disk*, Astronomy & Astrophysics, 602.

Romero, C., Milli, J., Lagrange, A.-M., et al. (2021), *The HD 206893 planetary system seen with VLT/SPHERE: Upper limit on the dust albedo and constraints on additional companions*, Astronomy & Astrophysics, 651.

Rosenthal, L. J., Knutson, H. A., Chachan, Y., et al. (2022), *The California legacy survey: III. On the shoulders of (some) giants: The relationship between inner small planets and outer massive planets*, The Astrophysical Journal Supplement Series, 262, 1.

Rouan, D. & Lagrange, A.-M. (2023), *Detection of exoplanets: exploiting each property of light*, Comptes Rendus. Physique, 24, S2.

Rousset, G., Beuzit, J.-L., Hubin, N., et al. (1994), *Performance and results of the COME-ON+ adaptive optics system at the ESO 3.6-m telescope*, Proceedings of the SPIE, 2201.

Rousset, G., Fontanella, J. C., Kern, P., Gigan, P., & Rigaut, F. (1990), *First diffraction-limited astronomical images with adaptive optics*, Astronomy and Astrophysics, 230, 2.

Rousset, G., Lacombe, F., Puget, P., et al. (2003), *NAOS, the first AO system of the VLT: On-sky performance*, Proceedings of the SPIE, 4839.

Ruane, G., Riggs, A., Mazoyer, J., et al. (2018), *Review of high-contrast imaging systems for current and future ground- and space-based telescopes I. Coronagraph design methods and optical performance metrics*, Space Telescopes and Instrumentation 2018: Optical, Infrared, and Millimeter Wave.

Santos, N. C., Adibekyan, V., Dorn, C., et al. (2017), *Constraining planet structure and composition from stellar chemistry: trends in different stellar populations*, Astronomy & Astrophysics, 608.

Santos, N. C., Israelian, G., & Mayor, M. (2004), *Spectroscopic [Fe/H] for 98 extra-solar planet-host stars: Exploring the probability of planet formation*, Astronomy & Astrophysics, 415, 3.

Sato, B., Omiya, M., Harakawa, H., et al. (2012), *Substellar companions to seven evolved intermediate-mass stars*, Publications of the Astronomical Society of Japan, 64, 6.

Schlaufman, K. C. (2014), *Tests of in situ formation scenarios for compact multiplanet systems*, The Astrophysical Journal, 790, 2.

Schlaufman, K. C. (2018), *Evidence of an upper bound on the masses of planets and its implications for giant planet formation*, The Astrophysical Journal, 853, 1.

Schlecker, M., Burn, R., Sabotta, S., et al. (2022), *RV-detected planets around M dwarfs: Challenges for core accretion models*, Astronomy & Astrophysics, 664.

Schlecker, M., Mordasini, C., Emsenhuber, A., et al. (2021), *The New Generation Planetary Population Synthesis (NGPPS): III. Warm super-Earths and cold Jupiters: a weak occurrence correlation, but with a strong architecture-composition link*, Astronomy & Astrophysics, 656.

Schlichting, H. E. (2014), *Formation of close in super-Earths and mini-Neptunes: Required disk masses and their implications*, The Astrophysical Journal, 795, 1.

Schmid, H. M., Bazzon, A., Roelfsema, R., et al. (2018), *SPHERE/ZIMPOL high resolution polarimetric imager: I. System overview, PSF parameters, coronagraphy, and polarimetry*, Astronomy & Astrophysics, 619.

Schneider, G., Grady, C. A., Hines, D. C., et al. (2014), *Probing for exoplanets hiding in dusty debris disks: Disk imaging, characterization, and exploration with HST/STIS multi-roll coronagraphy*, The Astronomical Journal, 148, 4.

Schneider, G., Grady, C. A., Stark, C. C., et al. (2016), *Deep HST/STIS visible-light imaging of debris systems around solar analog hosts*, The Astronomical Journal, 152, 3.

Schoonenberg, D., Ormel, C. W., & Krijt, S. (2018), *A Lagrangian model for dust evolution in protoplanetary disks: formation of wet and dry planetesimals at different stellar masses*, Astronomy & Astrophysics, 620.

Schräpler, R., Blum, J., Krijt, S., & Raabe, J.-H. (2018), *The physics of protoplanetary dust agglomerates. X. High-velocity collisions between small and large dust agglomerates as a growth barrier*, The Astrophysical Journal, 853, 1.

Schwarz, K. R., Bergin, E. A., Cleeves, L. I., et al. (2019), *Unlocking CO depletion in protoplanetary disks: II. Primordial C/H predictions inside the CO snowline*, The Astrophysical Journal, 877, 2.

Sefilian, A. A. (2022), *Secular dynamics of self-gravitating debris discs*, University of Cambridge, UK.

Simon, J. B., Armitage, P. J., Li, R., & Youdin, A. N. (2016), *The mass and size distribution of planetesimals formed by the streaming instability: I. The role of self-gravity*, The Astrophysical Journal, 822, 1.

Simon, J. B., Blum, J., Birnstiel, T., & Nesvorný, D. (2022), *Comets and planetesimal formation*, arXiv:2212.04509 [astro-ph].

Skrutskie, M. F., Jones, T., Hinz, P., et al. (2010), *The Large Binocular Telescope mid-infrared camera (LMIRcam): final design and status*, Proceedings of the SPIE, 7735.

Smith, B. A. & Terrile, R. J. (1984), *A circumstellar disk around Beta Pictoris*, Science, 226, 4681.

Smith, R., Wyatt, M. C., & Haniff, C. A. (2009), *Resolving the hot dust around HD 69830 and eta Corvi with MIDI and VISIR*, Astronomy & Astrophysics, 503, 1.

Soummer, R., Aime, C., & Falloon, P. E. (2003), *Stellar coronagraphy with prolate apodized circular apertures*, Astronomy & Astrophysics, 397, 3.

Soummer, R., Pueyo, L., & Larkin, J. (2012), *Detection and characterization of exoplanets and disks using projections on Karhunen-Loève eigenimages*, The Astrophysical Journal, 755, 2.

Sparks, W. B. & Ford, H. C. (2002), *Imaging spectroscopy for extrasolar planet detection*, The Astrophysical Journal, 578, 1.

Spergel, D., Gehrels, N., Breckinridge, J., et al. (2013), *WFIRST-2.4: What every astronomer should know*, arXiv e-prints.

Stasevic, S., Milli, J., Mazoyer, J., et al. (2023), *An inner warp discovered in the disk around HD 110058 using VLT/SPHERE and HST/STIS*, Astronomy & Astrophysics, 678.

Steinpilz, T., Teiser, J., & Wurm, G. (2019), *Sticking properties of silicates in planetesimal formation revisited*, The Astrophysical Journal, 874, 1.

Stolker, T., Sitko, M., Lazareff, B., et al. (2017), *Variable dynamics in the inner disk of HD 135344B revealed with multi-epoch scattered light imaging*, The Astrophysical Journal, 849, 2.

Su, K. Y. L., MacGregor, M. A., Booth, M., et al. (2017), *ALMA 1.3 mm map of the HD 95086 system*, The Astronomical Journal, 154, 6.

Su, K. Y. L., Morrison, S., Malhotra, R., et al. (2015), *Debris distribution in HD 95086: A young analog of HR 8799*, The Astrophysical Journal, 799, 2.

Su, K. Y. L., Rieke, G. H., Stapelfeldt, K. R., et al. (2009), *The debris disk around HR 8799*, The Astrophysical Journal, 705, 1.

Swastik, C., Banyal, R. K., Narang, M., et al. (2021), *Host star metallicity of directly imaged wide-orbit planets: Implications for planet formation*, The Astronomical Journal, 161, 3.

Swift, J. J., Johnson, J. A., Morton, T. D., et al. (2013), *Characterizing the cool KOIs: IV. Kepler-32 as a prototype for the formation of compact planetary systems throughout the galaxy*, The Astrophysical Journal, 764, 1.

Tamura, M., Fukagawa, M., Kimura, H., et al. (2006), *First two-micron imaging polarimetry of Beta Pictoris*, Astronomy and Astrophysics, 641, 2.

Tanaka, H., Takeuchi, T., & Ward, W. R. (2002), *Three-dimensional interaction between a planet and an isothermal gaseous disk: I. Corotation and Lindblad torques and planet migration*, The Astrophysical Journal, 565, 2.

Tatsuuma, M. & Kataoka, A. (2021), *Rotational disruption of porous dust aggregates due to gas flow in protoplanetary disks*, The Astrophysical Journal, 913, 2.

Teng, H.-Y., Sato, B., Kuzuhara, M., et al. (2023), *Revisiting planetary systems in Okayama planet search program: A new long-period planet, RV astrometry joint analysis, and multiplicity-metallicity trend around evolved stars*, 75, 6.

Terquem, C. & Papaloizou, J. C. B. (2007), *Migration and the formation of systems of hot super-Earths and Neptunes*, The Astrophysical Journal, 654, 2.

Tobin, T. L., Currie, T., Li, Y., et al. (2024), *Direct imaging discovery of a substellar companion orbiting the accelerating variable star, HIP 39017*, arXiv:2403.04000 [astro-ph].

Tremaine, S. (1991), *On the origin of the obliquities of the outer planets*, Icarus, 89, 1.

Tschudi, C., Schmid, H. M., Nowak, M. et al. (2024), *SPHERE RefPlanets: Search for ε Eridani b and warm dust*, Astronomy & Astrophysics, 667, A74.

Tsiganis, K., Gomes, R., Morbidelli, A., & Levison, H. F. (2005), *Origin of the orbital architecture of the giant planets of the Solar System*, Nature, 435, 7041.

Udalski, A., Szymański, M. K., & Szymański, G. (2015), *OGLE-IV: Fourth Phase of the Optical Gravitational Lensing Experiment*, Acta Astronomica, 65, 1.

Underwood, D., Jones, B., & Sleep, P. (2003), *The evolution of habitable zones during stellar lifetimes and its implications on the search for extraterrestrial life*, International Journal of Astrobiology, 2, 4.

Valenti, J. A. & Fischer, D. A. (2005), *Spectroscopic Properties of Cool Stars (SPOCS): I. 1040 F, G, and K Dwarfs from Keck, Lick, and AAT Planet Search Programs*, The Astrophysical Journal Supplement Series, 159, 1.

van Holstein, R., Stolker, T., Jensen-Clem, R., et al. (2021), *A survey of the linear polarization of directly imaged exoplanets and brown dwarf companions with SPHERE-IRDIS: First polarimetric detections revealing disks around DH Tau B and GSC 6214-210 B*, Astronomy & Astrophysics, 647.

Van Holstein, R. G., Girard, J. H., De Boer, J., et al. (2020), *Polarimetric imaging mode of VLT/SPHERE/IRDIS: II. Characterization and correction of instrumental polarization effects*, Astronomy & Astrophysics, 633.

van Leeuwen, F. (2007), , 10.1007/978-1-4020-6342-8.

Vigan, A., Fontanive, C., Meyer, M., et al. (2021), *The SPHERE infrared survey for exoplanets (SHINE): III. The demographics of young giant exoplanets below 300 au with SPHERE*, Astronomy & Astrophysics, 651.

Vigan, A., N'Diaye, M., Dohlen, K., et al. (2019), *Calibration of quasi-static aberrations in exoplanet direct-imaging instruments with a Zernike phase-mask sensor: III. On-sky validation in VLT/SPHERE*, Astronomy & Astrophysics, 629.

Vogt, S. S., Allen, S. L., Bigelow, B. C., et al. (1994), *HIRES: The high-resolution echelle spectrometer on the Keck 10-m telescope*, Proceedings of the SPIE, 2198.

von Braun, K., Boyajian, T. S., Kane, S. R., et al. (2011), *Astrophysical parameters and habitable zone of the exoplanet hosting star GJ 581*, The Astrophysical Journal, 729, 2.

Wahhaj, Z., Milli, J., Romero, C., et al. (2021), *A search for a fifth planet around HR 8799 using the star-hopping RDI technique at VLT/SPHERE*, Astronomy & Astrophysics, 648.

Walsh, K. J. & Levison, H. F. (2016), *Terrestrial planet formation from an annulus*, The Astronomical Journal, 152, 3.

Walsh, K. J., Morbidelli, A., Raymond, S. N., O'Brien, D. P., & Mandell, A. M. (2011), *A low mass for Mars from Jupiter's early gas-driven migration*, Nature, 475, 7355.

Wang, J., Xie, J.-W., Barclay, T., & Fischer, D. A. (2014), *Influence of stellar multiplicity on planet formation: I. Evidence of suppressed planet formation due to companions within 20 au and validation of four planets from the Kepler multiple planet candidates*, The Astrophysical Journal, 783, 1.

Wang, J. J., Vigan, A., Lacour, S., et al. (2021), *Constraining the nature of the PDS 70 protoplanets with VLTI/GRAVITY*, The Astronomical Journal, 161, 3.

Ward, W. R. (1981), *Solar nebula dispersal and the stability of the planetary system: I. Scanning secular resonance theory*, Icarus, 47, 2.

Ward, W. R., Colombo, G., & Franklin, F. A. (1976), *Secular resonance, solar spin down, and the orbit of Mercury*, Icarus, 28, 4.

Ward, W. R. & Hahn, J. M. (1998), *Dynamics of the trans-Neptune region: Apsidal waves in the Kuiper belt*, The Astronomical Journal, 116, 1.

Weidenschilling, S. J. (1977), *Aerodynamics of solid bodies in the solar nebula*, Monthly Notices of the Royal Astronomical Society, 180, 2.

Weiss, L. M., Marcy, G. W., Petigura, E. A., et al. (2018), *The California-Kepler Survey: V. Peas in a pod: Planets in a Kepler multi-planet system are similar in size and regularly spaced*, The Astronomical Journal, 155, 1.

Weiss, L. M., Millholland, S. C., Petigura, E. A., et al. (2022), *Architectures of compact multiplanet systems: diversity and uniformity*, Protostars and Planets VII, 42.

Weiss, L. M. & Petigura, E. A. (2020), *The Kepler peas in a pod pattern is astrophysical*, The Astrophysical Journal, 893, 1.

Welsh, W. F., Orosz, J. A., Carter, J. A., et al. (2012), *Transiting circumbinary planets Kepler-34 b and Kepler-35 b*, Nature, 481, 7382.

Werner, M. W., Roellig, T. L., Low, F. J., et al. (2004), *The Spitzer space telescope mission*, Astrophysical Journal Supplement Series, 154, 1.

Wildi, F., Blind, N., Reshetov, V., et al. (2017), *NIRPS: an adaptive-optics assisted radial velocity spectrograph to chase exoplanets around M-stars*, Proceedings of the SPIE, 10400.

Windmark, F., Birnstiel, T., Güttler, C., et al. (2012a), *Planetesimal formation by sweep-up: How the bouncing barrier can be beneficial to growth*, Astronomy & Astrophysics, 540.

Windmark, F., Birnstiel, T., Ormel, C. W., & Dullemond, C. P. (2012b), *Breaking through: The effects of a velocity distribution on barriers to dust growth*, Astronomy & Astrophysics, 544.

Winn, J. N., Sanchis-Ojeda, R., & Rappaport, S. (2018), *Kepler-78 and the ultra-short-period planets*, New Astronomy Reviews, 83.

Wittenmyer, R. A., Butler, R. P., Tinney, C. G., et al. (2016), *The Anglo-Australian planet search: XXIV. The frequency of Jupiter analogs*, The Astrophysical Journal, 819, 1.

Wittenmyer, R. A., Wang, S., Horner, J., et al. (2020), *Cool Jupiters greatly outnumber their toasty siblings: occurrence rates from the Anglo-Australian Planet Search*, Monthly Notices of the Royal Astronomical Society, 492, 1.

Wolszczan, A. & Frail, D. A. (1992), *A planetary system around the millisecond pulsar PSR1257+12*, Nature, 355, 6356.

Wright, E. L., Eisenhardt, P. R. M., Mainzer, A. K., et al. (2010), *The Wide-field Infrared Survey Explorer (WISE): Mission description and initial on-orbit performance*, The Astronomical Journal, 140, 6.

Wu, Y., Worthen, K., Brandeker, A., & Chen, C. (2024), *Argon in Beta Pictoris: Entrapment and release of volatile in disks*, arXiv:2407.06035 [astro-ph].

Wyatt, M. C. (2005), *The insignificance of P-R drag in detectable extrasolar planetesimal belts*, Astronomy & Astrophysics, 433, 3.

Wyatt, M. C. (2008), *Evolution of debris disks*, Annual Review of Astronomy and Astrophysics, 46, 1.

Xie, C., Choquet, E., Vigan, A., et al. (2022), *Reference-star differential imaging on SPHERE/IRDIS*, Astronomy & Astrophysics, 666.

Youdin, A. N. & Goodman, J. (2005), *Streaming instabilities in protoplanetary disks*, The Astrophysical Journal, 620, 1.

Youdin, A. N. & Shu, F. H. (2002), *Planetesimal formation by gravitational instability*, The Astrophysical Journal, 580, 1.

Zakamska, N. L. & Tremaine, S. (2004), *Excitation and propagation of eccentricity disturbances in planetary systems*, The Astronomical Journal, 128, 2.

Zapata, L. A., Ho, P. T. P., & Rodríguez, L. F. (2018), *A submillimeter background galaxy projected on the debris disk of HD95086 revealed by ALMA*, Monthly Notices of the Royal Astronomical Society, 476, 4.

Zhu, W. (2020), *On the patterns observed in Kepler multi-planet systems*, The Astronomical Journal, 159, 5.

Zhu, W. (2023), *The metallicity dimension of the super Earth-cold Jupiter correlation*, Research in Astronomy and Astrophysics, Volume 24, Issue 4, id.045013, 6 pp., 24, 4.

Zhu, W., Petrovich, C., Wu, Y., Dong, S., & Xie, J. (2018), *About 30% of Sun-like stars have Kepler-like planetary systems: A study of their intrinsic architecture*, The Astrophysical Journal, 860, 2.

Zhu, W. & Wu, Y. (2018), *The super Earth–cold Jupiter relations*, The Astronomical Journal, 156, 3.

Zsom, A., Ormel, C. W., Dullemond, C. P., & Henning, T. (2011), *The outcome of protoplanetary dust growth: pebbles, boulders, or planetesimals?: III. Sedimentation driven coagulation inside the snowline*, Astronomy & Astrophysics, 534.

Zsom, A., Ormel, C. W., Güttler, C., Blum, J., & Dullemond, C. P. (2010), *The outcome of protoplanetary dust growth: pebbles, boulders, or planetesimals?: II. Introducing the bouncing barrier*, Astronomy & Astrophysics, 513.

Öberg, K. I., Murray-Clay, R., & Bergin, E. A. (2011), *The effects of snowlines on C/O in planetary atmospheres*, The Astrophysical Journal, 743, 1.

Appendix A

Publications

I list below my first and co-author publications, and the proceedings, related to the field of high-contrast imaging of exoplanets and disks. I have two first-author, peer-reviewed publications. I first submitted the paper on the debris disk HD 120326 in October 2024 in Astronomy & Astrophysics. I received the positive report from the referee in December, I will submit the paper again in January, after having implemented the comments.

Publications as first author in peer-reviewed journals:

- Desgrange, C., Milli, J., Chauvin, G., et al. (2025 subm.), *Dust populations from 30 to 1000 au in the debris disk HD 120326*, Astronomy & Astrophysics
- Desgrange, C., Milli, J., Chauvin, G., et al. (2023), *Planetary system architectures with low-mass inner planets: Direct imaging exploration of mature systems beyond 1 au*, Astronomy & Astrophysics, 680
- Desgrange, C., Chauvin, G., Christiaens, V., et al. (2022a), *In-depth direct imaging and spectroscopic characterization of the young Solar System analog HD 95086*, Astronomy & Astrophysics, 664

Publications as co-author in peer-reviewed journals:

- Palma-Bifani, P., Borja, D., Chauvin, G., et al. (2024), *The atmosphere of AF Lep b through ForMoSA*, Astronomy & Astrophysics, 683, A214
- Milli, J., Choquet, E., Tazaki, R., et al. (2024), *The polarisation properties of the HD 181327 debris ring: Evidence for sub-micron particles from scattered light observations*, Astronomy & Astrophysics, 683
- Matthews, E. C., Bonnefoy, M., Xie, C., et al. (2023), *The first scattered light images of HD 112810, a faint debris disk in the Sco-Cen association*, Astronomy & Astrophysics, 679
- Stasevic, S., Milli, J., Mazoyer, J., et al. (2023), *An inner warp discovered in the disk around HD 110058 using VLT/SPHERE and HST/STIS*, Astronomy & Astrophysics, 678
- Landman, R., Snellen, I. A. G., Keller, C. U., et al. (2023), *Trade-offs in high-contrast integral field spectroscopy for exoplanet detection and characterisation: Young gas giants in emission*, Astronomy & Astrophysics, 675
- Palma-Bifani, P., Chauvin, G., Bonnefoy, M., et al. (2023), *Peering into the young planetary system AB Pic: Atmosphere, orbit, obliquity, and second planetary candidate*, Astronomy & Astrophysics, 670

- Le Coroller, H., Nowak, M., Wagner, K., et al. (2022), *Efficiently combining Alpha Cen A multi-epoch high-contrast imaging data: Application of K-Stacker to the 80 hours NEAR campaign*, Astronomy & Astrophysics, 667
- Xie, C., Choquet, E., Vigan, A., et al. (2022), *Reference-star differential imaging on SPHERE/IRDIS*, Astronomy & Astrophysics, 666
- Gallenne, A., Desgrange, C., Milli, J., et al. (2022), *Probing the innermost region of the AU Microscopii debris disc*, Astronomy & Astrophysics, 665
- Bonavita, M., Gratton, R., Desidera, S., et al. (2022), *New binaries from the SHINE survey*, Astronomy & Astrophysics, 663
- Asensio-Torres, R., Henning, T., Cantalloube, F., et al. (2021), *Perturbers: SPHERE detection limits to planetary-mass companions in protoplanetary disks*, Astronomy & Astrophysics, 652
- Gratton, R., D'Orazi, V., Pacheco, T. A., et al. (2021), *Investigating three Sirius-like systems with SPHERE*, Astronomy & Astrophysics, 646
- Le Coroller, H., Nowak, M., Delorme, P., et al. (2020), *K-Stacker: an algorithm to hack the orbital parameters of planets hidden in high-contrast imaging: First applications to VLT/SPHERE multi-epoch observations*, Astronomy & Astrophysics, 639

Proceedings:

- Baudoz, P., Desgrange, C., Galicher, R., & Laginja, I. (2024), *Polarization effects on high contrast imaging: measurements on THD2 Bench*, Proceedings of the SPIE
- Desgrange, C., Chauvin, G., Malin, M., et al. (2022b), *Spectral characterization and simulated observations with the James Webb Space Telescope of the young exoplanet HD 95086 b*, Proceedings of the Annual meeting of the French Society of Astronomy and Astrophysics
- Bonavita, M., Gratton, R., Desidera, S., et al. (2022), *New binaries from the SHINE survey*, Astronomy & Astrophysics, 663
- Gratton, R., Keller, C., Diolaiti, E., et al. (2022), *MedRes: a new MEDium RESolution integral field spectrograph for SPHERE*, Proceedings of the SPIE
- Boccaletti, A., Chauvin, G., Wildi, F., et al. (2022), *Upgrading the high contrast imaging facility SPHERE: Science drivers and instrument choices*, Proceedings of the SPIE
- Cantalloube, F., Gomez-Gonzalez, C., Absil, O., et al. (2020), *Exoplanet imaging data challenge: Benchmarking the various image processing methods for exoplanet detection*, Proceedings of the SPIE

Appendix B

Accepted telescope time proposals

I list below my PI or co-PI proposals that were accepted on ground- or space-based observational facilities.

They aim to search for young or old exoplanets in various systems and image protoplanetary or debris disks, sometimes for the first time.

- PI: ESO Program ID 114.276D, VLT/UT3, SPHERE 2h, *"Direct detection of the hidden companion responsible for the migration of the iconic planet GJ 436 b"*. Grade A. Observation planned between January and March 2025.
- PI: LBT Program ID MPIA-2024B-004, SHARK-NIR and LMIRCam, 12.5h, *"Direct imaging of exoplanets and disks with LBT/SHARK-NIR"*. Observations planned between October 2024 and January 2025.
- co-PI: *JWST* Cycle 3 Program ID 5229, MIRI 12.9h, *"Super-Jupiters in our backyard: MIRI coronagraphic imaging of a massive planet/brown dwarf orbiting an M dwarf at 12pc"*. Observation planned between January and March 2025.
- PI: ESO Program ID 113.26E1, VLT/UT3, SPHERE 16h30, *"Catching Exoplanets born around young Suns"*. Grade B, 29% executed.
- PI: LBT Program ID MPIA-2024A-007, SHARK-NIR and LMIRCam, 16h, *"Search for protoplanets and disk substructures in Taurus-Auriga"*. 25% executed.
- PI: LBT Program ID MPIA-2024A-006, SHARK-NIR and LMIRCam, 12h, *"Searching for young exoplanets and debris disks around A stars"*. 33% executed.
- PI: ESO Program ID 109.23F2, VLT/UT3, SPHERE, 2h00, *"Direct imaging confirmation of an ultracool Jupiter-like planet orbiting a nearby M-dwarf"*. Grade A, 100% executed. Published in Desgrange et al. (2023).

Appendix C

Version courte de la thèse en français

Dans cette annexe, une version courte (40 pages) se trouve rédigée en français de ma thèse de doctorat, dont la version complète est rédigée en anglais dans les Chapitres de 1 à 6. J'ai choisi dans cette version courte de parler de chacun de mes chapitres de ma thèse, mais j'ai omis certaines sections et raccourci significativement d'autres.

Contents

C.1 Introduction

Les êtres humains ont commencé à regarder les étoiles il y a des siècles. Les étoiles et planètes servaient de guide pour s'orienter et trouver son chemin. De nos jours, les astronomes étudient les étoiles et autres objets célestes pour notamment retourner dans le passé et essayer de comprendre l'origine de l'univers. Les astronomes souhaitent comprendre la formation et l'évolution des objets célestes, ce qui inclut notamment les galaxies, les étoiles et les planètes.

Dans ma thèse de doctorat, mon travail porte sur l'architecture des systèmes planétaires. En particulier, je montre comment leur architecture peut aider à contraindre la formation et l'évolution planétaire. Dans le premier chapitre, j'introduis mon champ de recherche, les exoplanètes, c'est-à-dire les planètes extrasolaires, qui se situent à l'extérieur du Système Solaire.

C.1.1 Planètes et exoplanètes

Le Système Solaire

Sans aucun doute, les planètes (ou exoplanètes) les plus célèbres sont les huit planètes orbitant autour de notre Soleil. Quatre d'entre elles sont dites telluriques (ou rocheuses), Mercure, Vénus, la Terre, Mars et les quatre autres sont des planètes géantes, Jupiter, Saturne, Uranus et Neptune. Jupiter et Saturne sont également qualifiées de planètes géantes gaseuses, car elles contiennent principalement du gaz, tandis qu'Uranus et Neptune sont aussi qualifiées de planètes géantes glacées, car elles sont constituées d'une fraction importante de glace.

En plus des planètes, le Système Solaire est constitué de nombreux petits corps : de satellites qui orbitent autour de planètes, tels que la Lune autour de la Terre, des planètes naines telles que Pluton et Éris, des comètes, telles que la fameuse comète Tchourioumov-Guérassimenko étudiée par la sonde européenne Rosetta et visitée par le rover Philae entre 2014 et 2016, des astéroïdes, des "cailloux" plus petits et des (très nombreux) grains de poussières. Les petits corps sont principalement rassemblés dans la ceinture d'astéroïde principale, entre Mars et Jupiter, dans la ceinture de Kuiper située après Neptune et dans le nuage d'Oort, situé encore plus loin (voir Fig. C.1). De nombreux grains de poussières sont situés dans le nuage zodiacal, situé proche du plan de l'écliptique (le plan où orbite les planètes).

Le Soleil s'est formé il y a 4.568 milliards d'années (Ga, Bouvier & Wadhwa, 2010). Les quatre planètes géantes se sont formées rapidement, dans les premiers millions d'années de vie du Soleil. Les planètes telluriques se sont formées plus ou moins rapidement, Mars en 5–10 Ma (Ma, Dauphas & Pourmand, 2011), tandis que la Terre (et la Lune) se sont formées sur une échelle de temps plus incertaine, entre 50–150 Ma (Kleine et al., 2009).

Le modèle le plus accepté expliquant la formation du Système Solaire est le modèle de Nice (Gomes et al., 2005; Tsiganis et al., 2005; Morbidelli et al., 2005) et ses versions ultérieures. Le modèle de Nice explique les orbites actuelles des planètes géantes, ce qui inclus leur rayon orbital, leur excentricité et inclinaison (Tsiganis et al., 2005), les satellites troyens de Jupiter (Morbidelli et al., 2005), les satellites irréguliers des planètes géantes (Nesvorný et al., 2007; Bottke et al., 2010) et la structure orbitale de la ceinture de Kuiper et des objets épars qui en sont issus. Dans le modèle de Nice, les planètes géantes sont supposées s'être formées dans une configuration compacte entre 5 et 18 ua dans le disque de poussières et de gaz (nommé disque protoplanétaire). À cause d'un événement d'instabilité dynamique majeur, les planètes géantes ont migré vers leur position actuelle. En particulier, Uranus et Neptune auraient pu inverser leur ordre, avec désormais Neptune située à 30 ua et Uranus à 19 ua (Tsiganis et al., 2005).

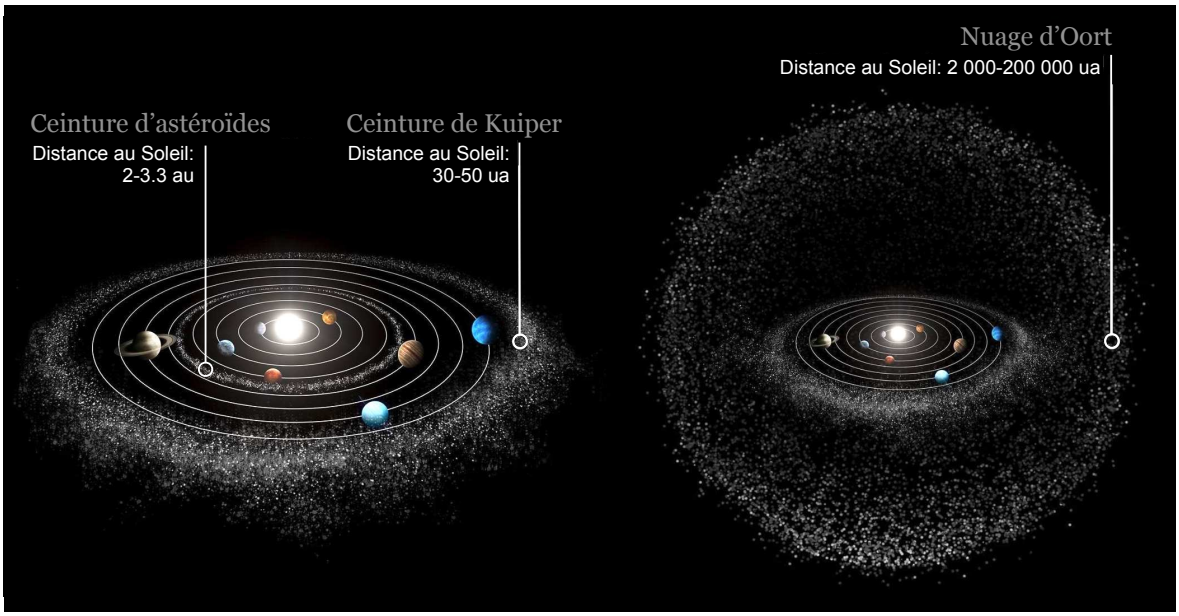

Figure C.1: Schéma du Système Solaire illustrant son architecture. Il y a huit planètes, deux ceintures de débris et un nuage de débris, plus étendu. Figure adaptée de l'Agence Spatiale Européenne (ESA).

L'instabilité dynamique majeure en question a initialement été proposée être le croisement de la résonance de moyen mouvement (MMR) 2:1 de Jupiter et Saturne[1]. Ce croisement de MMR aurait pu avoir lieu quand Jupiter migrait vers le Soleil et Saturne migrait à l'opposé du Soleil, entre 200 et 900 Ma après leur formation (Tsiganis et al., 2005). Cette hypothèse est compatible avec le pic de bombardement d'astéroïdes sur la Lune, vers 700 Ma (Hartmann et al., 2000), aussi connu sous le nom du grand bombardement tardif (LHB, Gomes et al., 2005). Toutefois, des résultats plus récents soulignent la présence de biais d'échantillonnage et d'analyses des roches lunaires, indiquant que finalement ce grand bombardement tardif n'aurait peut-être pas existé, ou alors de ne pas avoir été si conséquent ou si tardif (Chapman et al., 2007; Boehnke & Harrison, 2016).

D'autres événements sont envisagés pour incarner l'instabilité dynamique majeure. Par exemple, cette instabilité dynamique a pu être déclenchée par des interactions planète-disque (Quarles & Kaib, 2019; de Sousa et al., 2020), des interactions entre planètes géantes (de Sousa et al., 2020) ou la photo-évaporation de l'intérieur vers l'extérieur du gaz présent autour du Soleil durant sa jeunesse (Liu et al., 2022).

Bien que les scientifiques connaissent désormais les grandes lignes de la formation et de l'évolution du Système Solaire, des questions demeurent en suspens. Par exemple, concernant la petite taille de Mars, qui pourrait être expliquée par différent scénarios tels que le modèle du Grand Revirement (Walsh et al., 2011), une ceinture d'astéroïdes principale de faible masse (Hansen, 2009; Izidoro et al., 2015; Walsh & Levison, 2016; Drążkowska et al., 2016; Raymond & Izidoro, 2017) ou le modèle d'instabilité précoce (Clement et al., 2018, 2021). Une autre question est l'origine de l'eau sur Terre.

En utilisant des télescopes et instruments toujours plus sensibles, les astronomes ont réussi à observer des systèmes planétaires autour d'autres étoiles. Certains très tôt lors de la phase de formation planétaire ($\sim$1 Ma), d'autres à des phases plus évoluées, à des âges similaires ou plus élevés que celui du Système Solaire ($\sim$4.6 Ga). Observer d'autres systèmes planétaires permet d'estimer leur diversité et de contraindre d'un point de vue global

[1]Cette résonance signifie que Jupiter réalise deux révolutions autour du Soleil lorsque Saturne n'en réalise qu'une seule.

les modèles théoriques de formation et d'évolution planétaire. Cela aide également à déterminer comment le Système Solaire a pu se former et évoluer à son état actuel et de déterminer s'il s'agit d'un système planétaire commun.

Les premières découvertes d'exoplanètes

L'existence de planètes orbitant autour d'autres étoiles que le Soleil a été pensé bien avant que les premières planètes extrasolaires furent découvertes. En particulier, cette question est reliée à la question de la vie qui pourrait avoir émergé et se développé ailleurs que sur la Terre. Cette question philosophique et scientifique est toujours fortement d'actualité. Elle est au coeur des objectifs scientifiques de futures infrastructures astronomiques, telles que l'Extremely Large Telescope (ELT), en cours de construction par l'European Southern Observatory (ESO), et du Habitable Worlds Observatory (HWO), télescope spatial en cours d'études de la National Aeronautics and Space Administration (NASA).

Les deux premières exoplanètes furent découvertes simultanément, en 1992, par Wolszczan & Frail (1992). Ces exoplanètes, de quelques masses terrestres, orbitent un pulsar, nommé PSR1257+12. Toutefois, l'année retenue de la première découverte d'une exoplanète est généralement 1995, correspondant à la découverte de Mayor & Queloz (1995) de la planète géante 51 Pegasi b, orbitant autour de l'étoile 51 Pegasi. C'est cette découverte qui est retenue, car 51 Pegasi est une étoile de la séquence principale, soit pour résumer, une étoile "classique". Ces deux découvertes ont révolutionné la perception des astronomes de ceux à quoi pouvaient ressembler les systèmes exoplanétaires. Premièrement, car un pulsar est une étoile à neutrons, issue de l'explosion en supernova d'une étoile massive en fin de vie qui s'est retrouvée à cours de carburant. Un pulsar orbite très rapidement sur lui-même, de l'ordre de la seconde ou milliseconde dans le cas de PSR1257+12. Deuxièmement, parce que la planète 51 Pegasi b est une planète de la masse de Jupiter (M_{Jup}) orbitant seulement en quatre jours autour de son étoile hôte, qui est une étoile de type solaire. En guise de comparaison, Jupiter orbite en onze années autour du Soleil, donc sur une échelle de temps bien plus longue, et Mercure, la planète la plus proche du Soleil, orbite en 88 jours. Par conséquent, ces premières découvertes d'exoplanètes ont bouleversé les théories de l'époque sur les mécanismes de formation et d'évolution planétaire.

Plusieurs techniques de détection (et caractérisation) d'exoplanètes existent. Je les décris dans la Section C.1.2. Les premières exoplanètes, et à l'heure actuelle la plupart d'entre elles, ont été découvertes indirectement. La première détection d'exoplanète directe a été effectuée il y a vingt ans, en 2004, autour d'une naine brune d'environ 24 M_{Jup} par Chauvin et al. (2004). L'exoplanète découverte a une masse comprise entre 3–15 M_{Jup} et est située à 55 ua, soit environ deux fois la distance entre le Soleil et Neptune, qui est la planète située la plus loin dans notre Système Solaire. Ensuite, le premier système multi-planétaire photographié grâce à l'imagerie directe est HR 8799. Ce système a quatre planètes géantes, de quelques fois la masse de Jupiter et qui orbitent loin de leur étoile (Marois et al., 2008, 2010), voir Fig. C.2 (*à droite*). Ces planètes géantes sont localisées entre deux ceintures de poussières, ressemblant comme deux gouttes d'eau à l'architecture du Système Solaire, mais autour d'une étoile plus massive (1.5 fois la masse solaire, noté 1.5 $M_\odot$).

Jusqu'à 2018, la plupart des exoplanètes découvertes étaient âgées, plusieurs milliards d'années, et quelques unes bien plus jeunes, jusqu'à 15 Ma. Les découvertes des très jeunes proto-planètes géantes PDS 70 b (Keppler et al., 2018; Müller et al., 2018) et PDS 70 c (Haffert et al., 2019) orbitant autour de l'étoile PDS 70 furent des découvertes majeures. Pour la première fois, les astronomes réussirent à observer des planètes encore en cours de formation dans le disque protoplanétaire.

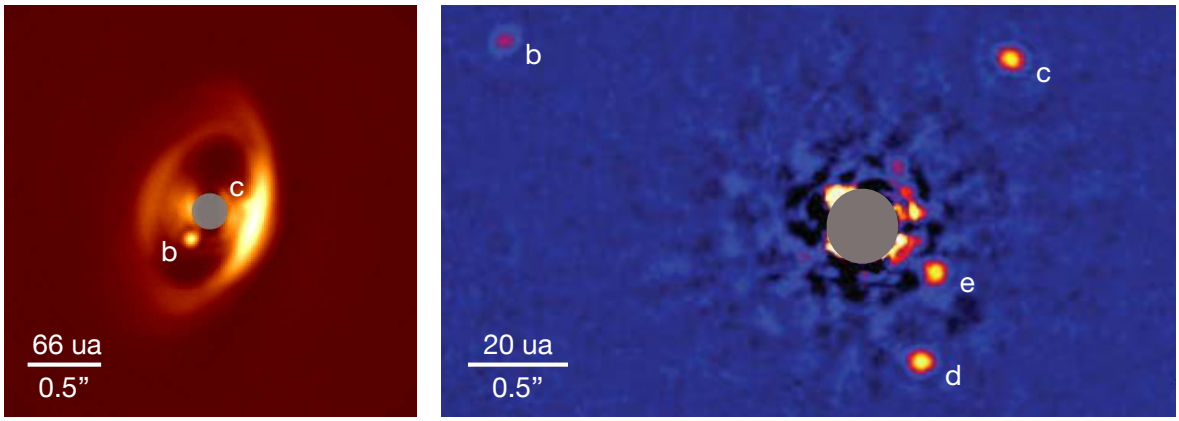

Figure C.2: *À gauche* : Image du disque protoplanétaire PDS 70, ayant deux proto-planètes géantes de détectées (Keppler et al., 2018; Müller et al., 2018; Haffert et al., 2019), PDS 70 b dans la cavité et PDS 70 c située au niveau de la ceinture de poussières. Figure adaptée de Pairet et al. (2021), utilisant des données en infrarouge (bande K, 2.1 μm) du VLT/SPHERE data acquise en Février 2018. *À droite* : Image du système planétaire HR 8799 ayant quatre planètes géantes (b, c, d et e). Figure adaptée de Marois et al. (2010), utilisant des données dans l'infrarouge (bande L', 3.8 μm) Keck II acquises en Novembre 2009. Sur les deux images, le masque gris circulaire correspond à la région cachée par le coronagraphe.

Zoologie des exoplanètes connues actuellement

De nos jours, plus de cinq milles exoplanètes ont été découvertes (voir Fig. C.3). La plupart des exoplanètes connues orbitent proches de leur étoile. C'est dû au fait que les méthodes de détection d'exoplanètes les plus efficaces à l'heure actuelle, soit la méthode des transits et la méthode des vitesses radiales, sont biaisées. Elles sont sensibles principalement à des exoplanètes orbitant à une fraction ou quelques unités astronomiques de leur étoile.

Les exoplanètes connues actuellement ont été classifiées en différentes catégories en fonction de leur masse ou distance de leur étoile hôte. Il y a les super-Terres et mini-Neptunes, pour les planètes de relativement faible masse et les Jupiters très chaudes, Jupiters chaudes, Jupiters froides ou super-Jupiter froides pour les planètes géantes très massives (Fig. C.3).

Concernant les super-Terres et mini-Neptunes, les grands relevés des méthodes des transits et des vitesses radiales rapportent une abondance de ce type de planètes, qui orbitent en moins de cent jours de leur étoile hôte. Un total de 20 à 50% des étoiles de type solaire pourraient avoir des super-Terres ou mini-Neptunes (Mayor et al., 2011), tandis que presque toutes (90-100%) les étoiles de faible masse auraient ce type de planètes (Swift et al., 2013; Dressing & Charbonneau, 2015). La frontière entre une super-Terre et une mini-Neptune est aussi représentée comme étant la vallée de la photo-évaporation, aussi connue sous le nom de fossé de Fulton et situé pour un rayon planétaire d'environ 1.5–1.9 $R_\oplus$. La valeur de la densité est le meilleur estimateur pour déterminer si une planète est pauvre en gaz (telle qu'une planète tellurique) ou riche en gaz (telle qu'une planège géante). Cependant, souvent seulement le rayon ou la masse (minimale) de la planète est connue, empêchant la détermination de sa densité. Approximativement, les super-Terres et les mini-Neptunes ont une masse entre 1 et 20 fois la masse de la Terre ($M_\oplus$) et un rayon entre 1 et 4 fois le rayon de la Terre ($R_\oplus$).

Parmi les exoplanètes orbitant très proches de leur étoile, il y a les planètes à période de révolution ultra courtes. Ces planètes orbitent autour de leur étoile en moins d'un jour. Elles possèdent des niveaux d'irradiation très élevés. Elles se situent typiquement dans une region où la poussière se sublime, générant des questions sur comment elles ont pu se former (Winn et al., 2018). Ces planètes sont dites verrouillées par les effets de marée avec leur étoile

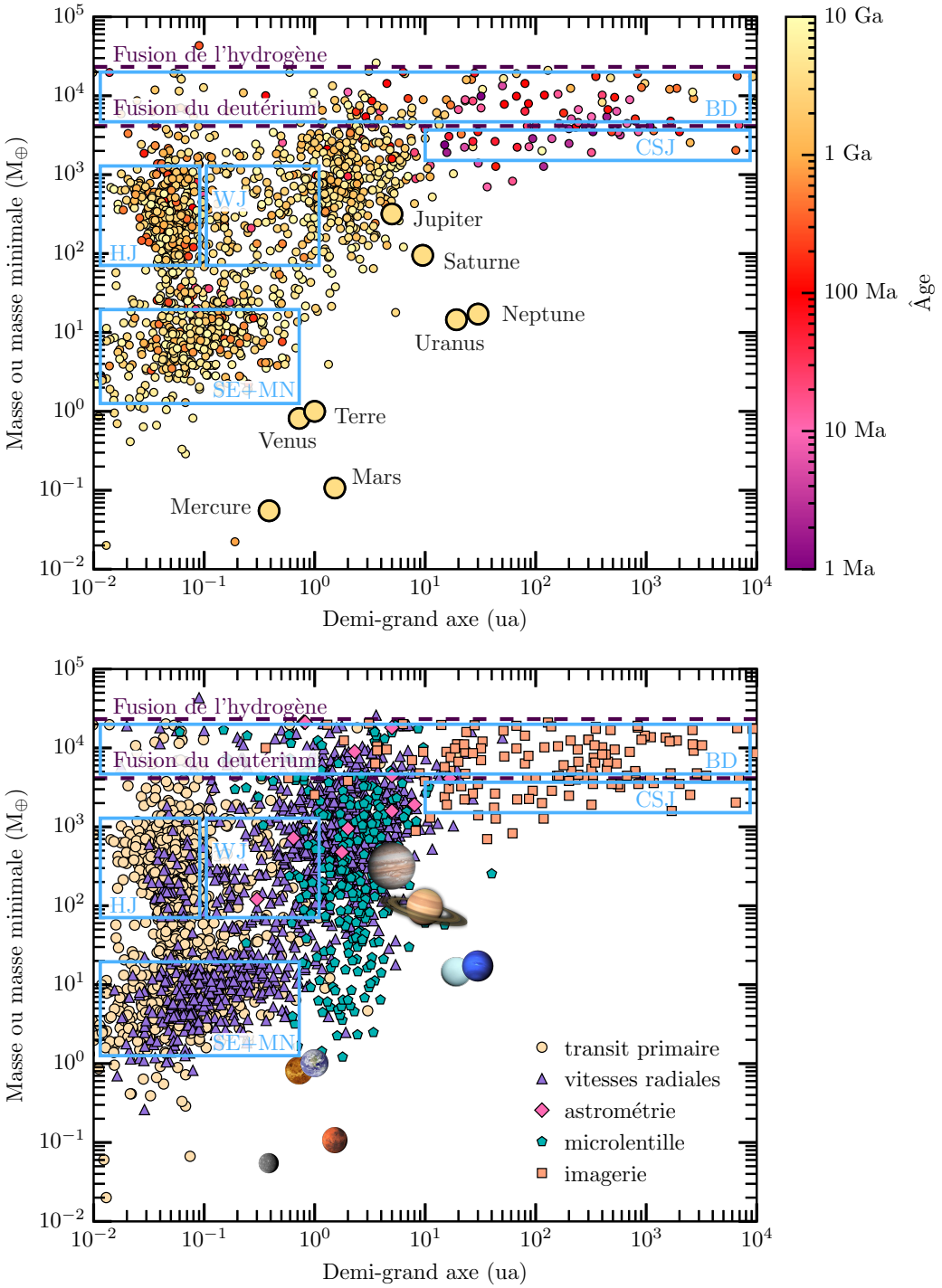

Figure C.3: Demi-grand axe des exoplanètes confirmées en fonction de la masse (minimale) d'après le catalogue européen (https://exoplanet.eu/catalog/ téléchargé le 8 Avril 2024). Les rectangles bleus indiquent des catégories d'exoplanètes données, dont les limites ne sont pas strictes, telles que les super-Terres(SE), mini-Neptunes (MN), Jupiters très chaudes (HJ), Jupiters chaudes (WJ) et les super-Jupiters froides (CSJ). Au-delà de la limite de fusion du deutérium commence le régime des naines brunes (BD) et au-delà de la limite de fusion de l'hydrogène, commence le régime des étoiles. *En haut :* La couleur indique l'âge de l'étoile hôte. La plupart des exoplanètes confirmées font partie de systèmes âgés. Les planètes du Système Solaire ont été rajoutées, pour comparaison. *En bas :* La couleur et le symbole indique la technique utilisée pour détecter une planète. Durant mon doctorat, j' ai principalement étudié les super-Jupiters froides. Dans une de mes études (section C.5), je les recherche dans des systèmes ayant des planètes de faible masse telles que des super-Terres ou des mini-Neptunes.

hôte, ce qui a pour conséquence qu'elle montre toujours la même face à leur étoile, comme la Lune montre toujours la même face à la Terre (aux effets de libration près). Ainsi, elles ont des côtés jour et nuit stables, ce qui induit à la surface de la planète de larges variations en température entre les faces jour et nuit.

Quant aux Jupiters très chaudes et les Jupiters chaudes, elles ont respectivement des périodes orbitales inférieures à 10 et 400 jours. Les planètes géantes massives sont plus rares que les petites planètes, avec moins d'1% (respectivement 10%) d'étoiles FGK hôtes de Jupiters très chaudes (Jupiters chaudes), d'après les travaux de Marcy et al. (2005a); Gould et al. (2006); Mayor et al. (2011); Dai et al. (2021); Miyazaki & Masuda (2023).

D'autre part, seulement quelques planètes ont été découvertes orbitant loin de leur étoile, au-delà de 10 ua, dû aux biais observationnels. Ces exoplanètes actuelles détectées grâce à l'imagerie directe ont jusqu'à présent au moins quelques fois la masse de Jupiter, et sont ainsi surnommées super-Jupiters ou super-Jupiters froides. Ce type de planètes n'est pas très fréquent autour des étoiles solaires (2.9–8.5%, Vigan et al., 2021). Des planètes de masse plus faible, jusqu'à la masse de Saturne, et orbitant à des dizaines d'unités astronomiques, sont enfin détectables autour de certaines étoiles grâce à l'excellente sensibilité du télescope spatial *James Webb* (*JWST*, Gardner et al., 2006), opérationnel depuis 2022. Le *JWST* détectera certainement bientôt de telles exoplanètes.

La plupart des exoplanètes connues à ce jour orbitent autour d'une étoile, et certaines même autour de deux étoiles (Doyle et al., 2011; Welsh et al., 2012; Rodet et al., 2017). Concernant les planètes orbitant autour d'une étoile, cette étoile peut être très massive ($\sim$3 $M_\odot$, Sato et al., 2012) ou de très faible masse et même être une naine brune[2] (Chauvin et al., 2004). D'autres exoplanètes ont aussi été découvertes solitaires, c'est-à-dire sans orbiter autour d'une étoile (voir par exemple la revue de Miret-Roig, 2023). Ces exoplanètes errantes sont communes, mais difficiles à détecter (Mróz et al., 2017, 2019; Miret-Roig et al., 2022).

En Avril 2024, les 5 659 exoplanètes confirmées font partie de 4 166 systèmes extra-solaires, dont 896 systèmes sont connus pour avoir plusieurs planètes[3].

C.1.2 Méthodes de détection d'exoplanètes

Plusieurs techniques existent pour détecter des exoplanètes. Les méthodes directes sont l'imagerie directe et l'interférométrie, tandis que les méthodes indirectes sont à partir des transits, des vitesses radiales, de l'astrométrie ou des microlentilles gravitationnelles. Je décris brièvement chacune de ces méthodes ci-dessous. Elles sont illustrées dans la Fig. C.4.

Imagerie directe

L'imagerie directe est peut-être la méthode la plus intuitive pour détecter des exoplanètes. De façon très simpliste, elle consiste à prendre en photo une étoile et de combiner la séquence d'images pour révéler la présence d'exoplanètes orbitant autour de l'étoile. Comme les planètes sont situées visuellement très proches de leur étoile hôte et sont très peu lumineuses comparées à elle, les détecter est particulièrement difficile. L'imagerie directe doit résoudre

[2]Différentes définitions existent concernant une naine brune. Une définition est basée sur sa capacité à brûler du deutérium, contrairement aux planètes, et à sa non-capacité à brûler de l'hydrogène, contrairement aux étoiles. Cette définition implique des masses limites inférieures et supérieures d'environ 13 M_{Jup} et 75 M_{Jup}. Un objet de masse plus faible serait une planète, un objet de masse plus élevé serait une étoile. Une autre définition considère le mécanisme de formation de l'objet. La définition de l'Union Internationale Astronomique ne prend pas en compte le mécanisme de formation et rajoute comme contrainte que la planète, pour être considérée comme telle, doit orbiter autour d'une étoile, d'une naine brune ou d'un vestige d'étoile d'au moins 25 fois sa masse (Lecavelier des Etangs & Lissauer, 2022).

[3]D'après le catalogue européen `https://exoplanet.eu/catalog/`. Dans ce chapitre, tous les nombres et pourcentages concernant la démographie des exoplanètes datent d'Avril 2024.

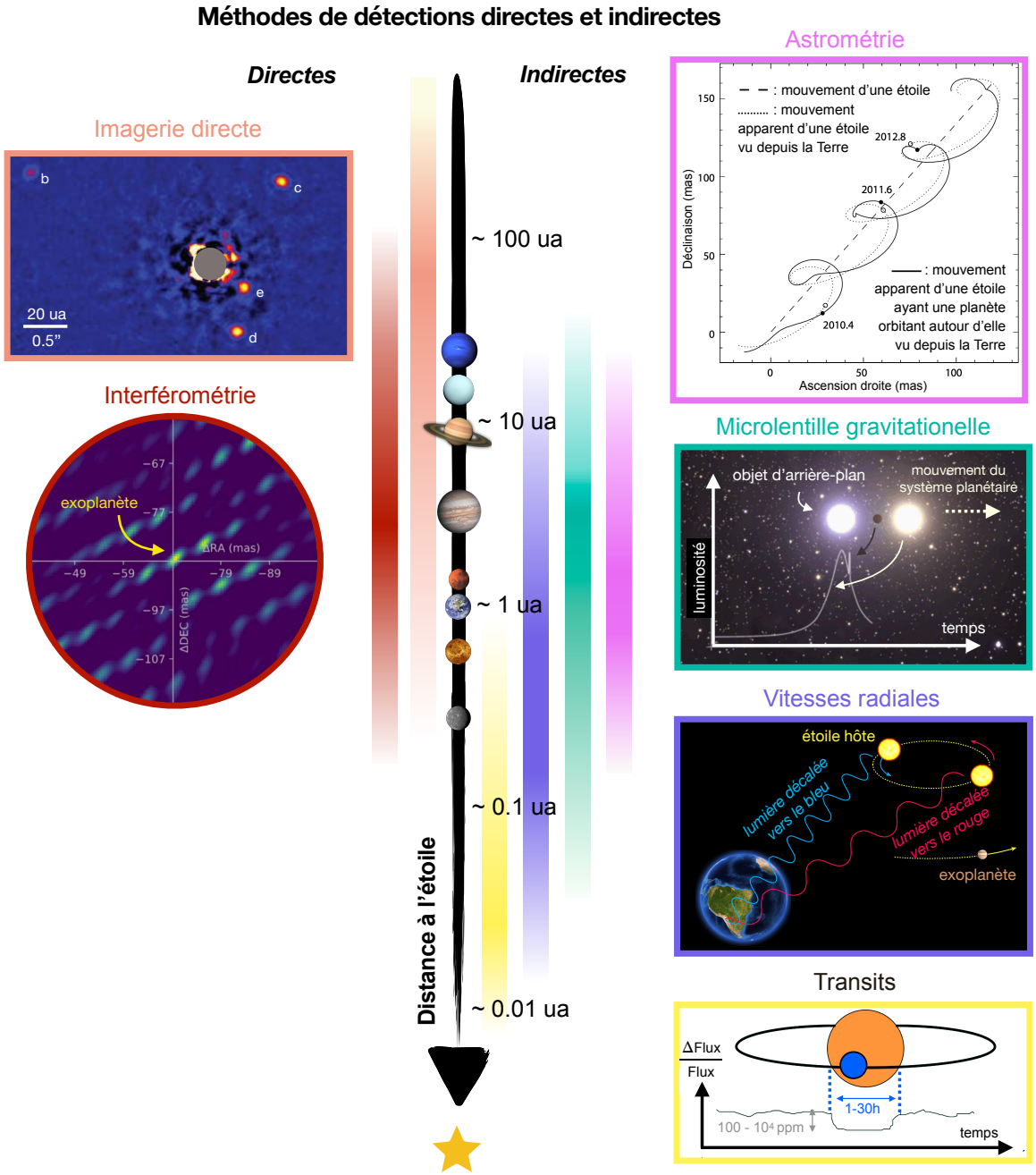

Figure C.4: Vue d’ensemble des méthodes de détection et caractérisation des exoplanètes. Cette Figure est composée de plusieurs figures adaptées : Marois et al. (2010) pour l’imagerie directe du système HR 8799, de Hinkley et al. (2023) pour la détection interférométrique de l’exoplanète HD 206893 c, de Perryman (2012) montrant l’impact d’un compagnon sur l’astrométrie absolue de son étoile hôte, de l’ESO/L. Calçada pour l’illustration d’un événement de microlentille gravitationnelle, de l’ESO expliquant le principe de la méthode des vitesses radiales en utilisant l’effet Doppler et de Rouan & Lagrange (2023) montrant la courbe de lumière au cours du temps d’une étoile se faisant occulter par une exoplanète.

ces deux problèmes majeurs et donc travailler à haut-contraste et à haute résolution angulaire.

Les observations d'imagerie directe actuelles sont sensibles à l'émission thermique des planètes et non la lumière de leur étoile qui se réfléchit sur elles. Par conséquent, il est plus simple de détecter des planètes qui sont jeunes, car elles sont plus chaudes et donc plus brillantes en émission thermique dans l'infrarouge. Par exemple, des modèles évolutifs (Linder et al., 2019) couplés à des modèles d'atmosphère (`petitCODE`, Mollière et al., 2015, 2017) ou (`HELIOS`, Malik et al., 2017) prédisent qu'une planète de 2 M_{Jup} a une température effective entre 1 300–1 700 K[4] (en fonction de la métallicité ou la présence de nuages) à 20 Ma. À 2 Ga, la température effective de la planète décroît à 170–250 K.

L'imagerie directe est donc plus efficace pour détecter des planètes jeunes (typiquement jusqu'à quelques dizaines de millions d'années) qu'âgées, massives (typiquement de quelques masses de Jupiter) que de faible masse, situées loin de leur étoile (typiquement au-delà d'une séparation de 0.1″ correspondant à 10 ua pour une étoile située à 100 pc[5]) que proches. Différents instruments existent pour photographier des exoplanètes, voir la Section C.2.

Interférométrie

L'interférométrie peut détecter des planètes à des séparations plus petites que l'imagerie directe et avec une meilleure résolution angulaire[6].

L'interférométrie classique combine le signal de plusieurs télescopes. Par exemple, le Very Large Telescope Interferometer (VLTI) combiné à l'instrument GRAVITY permet de détecter des planètes à 0.040″ de leur étoile (voir Fig. 12 de Pourré et al., 2024) et avec une précision astrométrique de 50 μas (Lacour et al., 2020; Pourré et al., 2024), ce qui est plus d'un ordre de grandeur meilleur que l'imagerie directe. Cela permet notamment de déterminer des paramètres orbitaux bien plus précis (e.g., Wang et al., 2021). En utilisant GRAVITY, il est aussi possible d'étudier la spectroscopie en émission des jeunes exoplanètes avec l'interférométrie, pour mieux contraindre leur atmosphère ou environnement proche. Alternativement, l'interférométrie peut également utilisé un seul télescope, combiné à un masque comportant plusieurs trous pour créer artificiellement plusieurs télescopes qui peuvent ensuite faire interférer la lumière entre eux, voir notamment les travaux de Lacour et al. (2011); Gauchet et al. (2016); Ray et al. (2023).

Transits

La méthode des transits consiste à détecter une planète quand elle occulte son étoile hôte. Cela requiert un alignement parfait de l'observeur, la planète et l'étoile. Ainsi, les instruments performants pour détecter des transits ont besoin d'observer un grand nombre d'étoiles

[4] T (K) $= T$ (°C) + 273.15 (°), autrement dit il faut soustraire 273.15 à la température en kelvin pour obtenir la température en degré celsius.

[5] Quelques remarques sur les unités : 1″ est la notation pour une arcseconde, qui correspond à un diamètre angulaire. Une arcseconde est 3 600 plus petit qu'un degré. Pour donner un ordre de grandeur, un degré correspond à deux fois le diamètre angulaire de la Lune vue depuis la Terre. En unités en-dessous de l'arcseconde et sont mentionnées dans mon manuscrit de thèse, il y a la milliarcseconde (notée mas) et la microarcseconde (notée μas). Concernant l'unité notée pc, il s'agit du parsec. Un parsec est égal à 3.26 année-lumière, l'année-lumière étant la distance que parcourt la lumière en un an, soit environ 9 500 milliards de kilomètres. La définition du parsec a été choisie pour qu'à cette distance du Système Solaire, une arcseconde représente le diamètre angulaire de la distance Terre-Soleil, qui est définie comme étant égale à une unité astronomique. Ces trois quantités peuvent donc être exprimées les unes en fonction des autres : 1 ua $= 1'' \times 1$ pc.

[6] La résolution angulaire est de λ/D en imagerie directe et de λ/B en interférométrie, où λ est la longueur d'onde, D le diamètre du télescope et B la plus grande ligne de base entre deux téléscopes.

simultanément, pour augmenter le nombre de détections potentielles de transits, puisque la probabilité de l'alignement observateur-planète-étoile est de

$$\text{probabilité} \;=\; \frac{R_\star + R_\mathrm{p}}{a}\,, \tag{C.1}$$

pour une distance planète-étoile (a) donnée, où $R_\star$ et R_p sont respectivement le rayon de l'étoile et la planète. De plus, le rayon de la planète doit être suffisament large comparé au rayon de son étoile hôte, pour que la variation de luminosité soit suffisament significative. Cette variation de luminosité s'exprime suivant

$$\text{variation} \;=\; \frac{R_\mathrm{p}}{R_\star}\,. \tag{C.2}$$

Par exemple, le transit de Jupiter devant le Soleil correspondrait à une variation de luminosité d'environ 1%, puisque Jupiter a un rayon environ dix fois plus petit que celui du Soleil. La probabilité de détecter ce transit, pour un observateur externe, est très faible (0.1%), car Jupiter orbite loin du soleil (à 5 ua ; 11 années). Cependant, si Jupiter se situait bien plus proche du Soleil, par exemple avec une période orbitale de trois jours, la probabilité de détecter son transit serait bien plus élevé (10%).

Pour déterminer la période orbitale d'une planète donnée, il est nécessaire d'observer plusieurs transits ou alors d'utiliser une autre méthode de détection comme celle des vitesses radiales. Utiliser ces méthodes permettent de mesurer la masse de l'objet, pour déterminer notamment si c'est un compagnon planétaire, une naine brune ou une étoile. Observer une orbite complète d'une exoplanète qui transite peut permettre de détecter également l'éclipse secondaire de cette exoplanète, c'est-à-dire quand celle-ci est occultée par son étoile hôte. Cela permet de contraindre sa courbe de phase en photométrie ou en spectrométrie[7], ce qui permet ensuite de contraindre les propriétés de l'atmosphère de l'exoplanète et notamment la formation de nuages (voir par exemple Deming et al., 2019).

Les télescopes spatiaux *Kepler* et *TESS* ont découvert des milliers d'exoplanètes confirmées par la suite, avec un autre millier d'exoplanètes toujours à confirmer ou infirmer. Le télescope au sol TRAPPIST a aussi joué un rôle majeur, en découvrant le célèbre système TRAPPIST-1, qui est un système multi-planétaire iconique (Gillon et al., 2016, 2017; Luger et al., 2017). Ce système a sept planètes telluriques, aux rayons et masses similaires à celui de la Terre. Elles sont situées dans une configuration compacte autour d'une étoile de très faible masse (0.08 $\mathrm{M}_\odot$) située à 12 pc du Système Solaire.

Vitesses radiales

Mesurer la vitesse radiale des étoiles peut permettre de déterminer la présence d'exoplanètes orbitant autour de ces étoiles. En effet, dans un système planétaire avec une étoile simple, l'étoile et la (ou les exoplanètes) vont orbiter autour du barycentre du système, qui est distinct du centre de l'étoile. Lorsque l'étoile se déplace en direction de l'observateur, l'effet Doppler va induire un décalage vers le bleu dans le spectre électomagnétique de l'étoile mesuré par l'observateur. De manière réciproque, quand l'étoile s'éloigne de l'observateur, l'effet Doppler induit un décalage vers le rouge dans le spectromagnétique (voir Fig. C.4, en bas à droite). Ce signal périodique de décalage vers le bleu, puis vers le rouge, puis vers le bleu, et ainsi de suite, est visible pour des systèmes planétaires qui ne sont *pas* vus de face, c'est-à-dire dont le plan orbital n'est *pas* orthogonal à la ligne de visée observateur-étoile. Le décalage vers le bleu et vers le rouge dans le spectre électromagnétique est plus

[7] c'est-à-dire à une (photométrie) ou plusieurs (spectrométrie) longueurs d'ondes

important dans le cas d'une exoplanète massive, vue alignée observateur-exoplanète-étoile (ou observateur-étoile-exoplanète) et qui orbite proche de son étoile hôte.

La technique des vitesses radiales permet de dériver les paramètres orbitaux de l'exoplanète, tels que sa période orbitale (et donc son demi-grand axe) et son excentricité, ainsi que la masse minimale de l'exoplanète, qui dépend de l'inclinaison sous laquelle est vu le système planétaire.

Ci-dessous je liste certains spectromètres haute résolution qui ont permis la détection d'exoplanètes grâce aux mesures des vitesses radiales de leur étoile hôte, dans l'ordre alphabétique : CARMENES, ELODIE (utilisé pour découvrir l'exoplanète 51 Pegasi b), ESPRESSO (Pepe et al., 2021), HARPS (Pepe et al., 2002), HARPS-N (Cosentino et al., 2012), HIRES (Vogt et al., 1994), NIRPS (Wildi et al., 2017), SPIRou (Donati et al., 2020), UCLES (Diego et al., 1990), UVES (Dekker et al., 2000).

Astrométrie

Mesurer l'astrométrie[8] absolue d'une étoile au cours du temps permet de déterminer la présence d'un compagnon massif orbitant autour de l'étoile (plus précisément autour de leur barycentre), tel qu'une exoplanète géante ou une naine brune. Concrètement, dans le cas où l'étoile à un (ou plusieurs compagnons) la direction long-terme du déplacement de l'étoile diffère de sa direction court-terme. Visuellement, cela induit un mouvement plus complexe (voir Fig. C.4, en haut à droite), appelé anomalie de mouvement propre ou accélération astrométrique (Kervella et al., 2019; Brandt, 2018, respectivement).

Pour le moment, l'anomalie de mouvement propre de l'étoile (ou l'accérélation astrométrique) donne seulement des indices sur la présence d'un compagnon autour de l'étoile, mais ne permet pas de le détecter officiellement, dû à la dégénérescence entre la masse du compagnon et sa distance orbitale. D'autres observations avec l'imagerie directe ou les vitesses radiales sont nécessaires pour les détecter (voir les découvertes présentées dans Hinkley et al., 2023; Mesa et al., 2023; De Rosa et al., 2023; Franson et al., 2023; Tobin et al., 2024).

Deux télescopes spatiaux ont permis de mesurer très précisément les positions des étoiles, *Hipparcos* (van Leeuwen, 2007, époque référence 1991) et *Gaia* (Gaia Collaboration et al., 2018, 2021, époque référence actuelle 2015). Le télescope *Gaia* est encore en activité jusqu'à début 2025. Dans les années qui viennent, les prochaines (et dernières) deux grandes diffusions des données de *Gaia* analysées par la collaboration éponyme, seront accompagnées des listes d'exoplanètes et naines brunes que *Gaia* aura découvertes, grâce à ses cinq puis dix années de mission.

Microlentille gravitationnelle

Les exoplanètes peuvent également être détectées en utilisant l'effet de microlentille gravitationnelle (Mao & Paczynski, 1991; Gould & Loeb, 1992), lié à la relativité générale. Une "lentille" consiste par exemple en un système planétaire (une étoile et une planète) passant devant un objet d'arrière-plan très brillant, tel qu'une étoile. Cette "lentille", dû à la gravité, va accroître la luminosité apparente de l'étoile d'arrière-plan. La courbe de luminosité de l'étoile d'arrière-plan va alors varier : au lieu d'être constante, elle va augmenter relativement longuement lorsque que l'étoile s'aligne avec l'étoile d'arrière-plan et l'observateur, diminuer progressivement lorsque l'étoile s'éloigne, puis à nouveau augmenter brièvement

[8] L'astrométrie correspond à la position d'un astre. Typiquement, les astronomes s'intéressent à la position des astres au cours du temps, pour étudier leur direction ou vitesse de déplacement. Les astres se déplacent, typiquement les étoiles se déplacent autour du centre de leur galaxie hôte.

lorsque la planète se retrouve alignée avec l'étoile d'arrière-plan et l'observateur (voir Fig. C.4, à droite).

Environ 280 planètes ont été détectées via l'effet de microlentille gravitationnelle, dont quelques systèmes multiplanétaires (voir par exemple Gaudi et al., 2008). Contrairement aux autres méthodes de détection, cette méthode n'utilise pas la détection de photons de l'étoile hôte et/ou de la planète en question. De plus, cette technique permet de déterminer la masse et le demi-grand axe des exoplanètes détectées. C'est la technique qui a découvert la plupart des planètes de faible masse type super-Terres entre 1 et 5 ua (voir notamment : Gaudi, 2012; Mroz & Poleski, 2023).

Au total, sur les plus de 5 000 exoplanètes découvertes et confirmées (ou naines brunes) reportées dans le catalogue européen des exoplanètes, environ 69% ont été détectées via la méthode des transits, 20% via la méthode des vitesses radiales, 5% via microlentille gravitationnelle et 4% via imagerie directe.

Coupler les méthodes de détection d'exoplanètes

Comme aucune technique de détection n'est capable de détecter tout l'espace des paramètres des exoplanètes, combiner les différentes techniques permet d'avoir une vision plus globale des exoplanètes qui existent : celles situées proches ou loin de leur étoiles, celles jeunes ou âgées, celles orbitant dans des plans orbitaux orthogonaux ou non à la ligne de visée, etc.

Combiner les méthodes de détection permet également d'avoir plus d'informations sur les paramètres physiques, orbitaux ou atmosphériques de la planète, comme écrit plus haut, par exemple dans le cas de la méthode des transits et de la méthode des vitesses radiales. Cette synergie permet de déterminer la masse et la densité de la planète.

Une autre synergie particulièrement intéressante est le couplage de l'imagerie directe avec l'astrométrie et/ou les vitesses radiales, pour déterminer la masse dynamique de la planète. Cette masse dynamique permet ensuite de contraindre la relation masse-luminosité des modèles évolutifs et atmosphériques pour un âge donné de la planète.

De plus, les méthodes des vitesses radiales et d'astrométrie permettent aussi d'indiquer la présence susceptible d'une exoplanète située loin de son étoile par exemple par l'effet de pente dans les vitesses radiales (voir Fig. 3 de Teng et al., 2023) ou l'anomalie de mouvement propre. Ces indices permettent de guider les relevés observationnels en imagerie directe, qui vont cibler en priorité ces systèmes où les astronomes s'attendent à découvrir une exoplanète. Cette stratégie d'observation permet d'économiser du temps de télescope, et a été réalisée avec succès et indépendamment pour l'exoplanète AF Lep b par trois équipes de recherche différentes (Mesa et al., 2023; De Rosa et al., 2023; Franson et al., 2023).

C.1.3 Formation et évolution planétaire

Les principales étapes de la formation d'un système planétaire sont résumées dans le schéma en Fig. C.5.

Du nuage moléculaire à la formation de l'étoile et de son disque

La première étape est la formation d'une étoile via la contraction d'un nuage moléculaire, qui est composé de gaz et de poussières, lire notamment la revue de Kennicutt & Evans (2012) et l'introduction détaillée de la thèse de doctorat de Le Gouellec (2021). La pression, densité et température de coeurs pré-stellaires augmentent, jusqu'à déclencher les réaction de fusion thermo-nucléaire. La proto-étoile s'allume alors. Sa lumière n'est néanmoins pas visible pour un observateur, car les photons sont très rapidement absorbés par le matériel

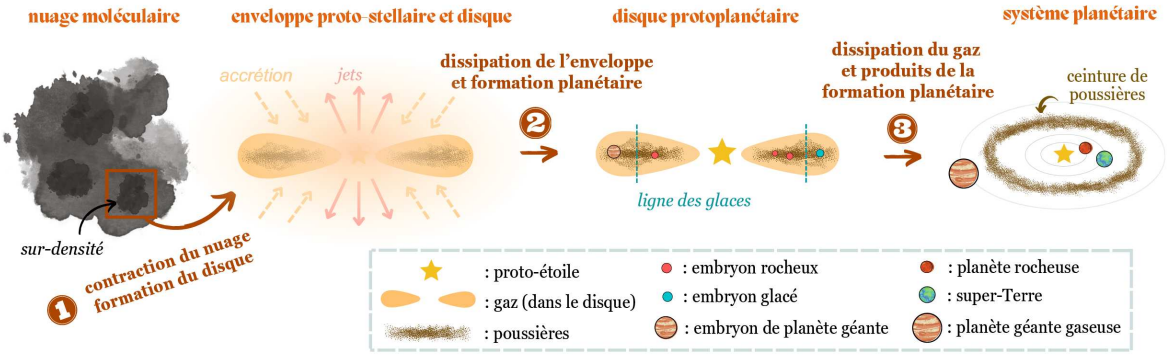

Figure C.5: Schéma montrant les grandes lignes de la formation d'un système planétaire.

opaque qui entoure l'étoile. Une partie du gaz et de la poussière accrète sur la proto-étoile, tandis qu'une autre partie est éjectée par des jets bipolaires, voir Fig. C.5.

La conservation du moment angulaire, et les effets gravitationnels, pression du gaz et force centrifuge, font que l'enveloppe autour de l'étoile s'aplatit dans un disque qualifié de protoplanétaire, car des planètes peuvent s'y former par la suite. De plus, les champs magnétiques jouent un rôle important et complexe dans la régulation de la formation stellaire, à l'échelle du nuage moléculaire et celle du disque protoplanétaire (Crutcher, 2012; Hull & Zhang, 2019).

Des grains de poussières aux planétésimaux

Dans un disque protoplanétaire, le ratio poussières-gaz est supposé être d'environ 1%. Le gaz est sujet aux forces gravitationnelles et centrifuge et à la pression du gaz, dont le gradient diminue au premier ordre avec la distance à l'étoile, car la température et la densité diminue. Ce gradient de pression implique que le gaz se déplace à des vitesses sub-képlériennes. Les particules de poussières suffisamment larges, quant à elles, sont principalement sensibles aux forces gravitationnelles et centrifuge et orbitent donc à des vitesses képlériennes. Par conséquent, les poussières font face à un vent de tête dû au gaz sub-képlérien, qui va alors les freiner et les faire spiraler vers l'étoile. Cet effet est appelé la dérive radiale (Weidenschilling, 1977). De plus, les interactions entre les poussières et le gaz causent la sédimentation verticale : les poussières se retrouvent de manière préférentielle dans le plan médian du disque. Concernant les petites particules de poussières, celles-ci sont suffisamment petites pour être couplées au gaz. Elles orbitent donc à des vitesses sub-képlériennes.

Initialement, dans le disque protoplanétaire, les particules de poussières sont supposées avoir une taille inférieure à 1 μm (Ormel et al., 2009; Bate, 2022). Les grains de poussières deviennent ensuite de plus en plus gros, ils forment des agrégats de poussières grâce à des collisions constructives. Cependant, il y a également des collisions destructives qui causent leur fragmentation ou érosion (Güttler et al., 2010). La croissance des aggrégats de poussières en planétésimaux doit franchir trois barrières : la barrière rebondissante, la barrière de fragmentation et la barrière de dérive. En version courte, la barrière rebondissante empêche les aggrégats de poussières de croître car les collisions maintiennent le statut quo, la barrière de fragmentation leur fait diminuer significativement de taille et la barrière de dérive les fait migrer vers l'étoile. La version plus détaillée est décrite dans la version longue du manuscrit de thèse, en Section 1.3.1.

Des planétésimaux aux planètes

Dans le modèle d'accrétion sur coeur (Pollack et al., 1996), deux modèles rivalisent pour expliquer comment les planètes se forment : l'accrétion de cailloux (Johansen & Lacerda, 2010; Ormel & Klahr, 2010; Lambrechts & Johansen, 2012) ou l'accrétion de planétésimaux (Pollack et al., 1996; Alibert et al., 2005; Emsenhuber et al., 2021) sur un coeur protoplanétaire (voir par exemple la revue de Drążkowska et al., 2023). Les modèles actuels d'accrétion de cailloux ou planétésimaux initialisent souvent leurs simulations avec un coeur planétaire de la masse de 0.01 $M_{\oplus}$, soit environ la masse de la Lune. Un tel coeur planétaire pourrait se former via "l'instabilité de flux", suivi par des collisions positives (Liu et al., 2019).

Lorsque l'embryon planétaire accrète suffisament rapidement de cailloux ou planétésimaux, il peut également accréter le gaz toujours présent dans le disque protoplanétaire, et ainsi devenir une planète géante. Dans l'autre cas, la planète peut devenir une planète tellurique, telle que la Terre par exemple. Lorsque la planète croît, due aux interactions gravitationnelles entre le disque et la planète, la planète se met généralement à migrer vers l'intérieur ou l'extérieur du système (Goldreich & Tremaine, 1980; Lin & Papaloizou, 1986).

Les planètes jusqu'à quelques masses de Jupiter sont principalement formées via le scénario d'accrétion sur coeur, tandis que les planètes plus massives ($\geq$ 4–5 M_{Jup}) et naines brunes pourraient se former via d'autres mécanismes, tels que l'instabilité gravitationnelle de disque (Boss, 1997) ou la fragmentation gravo-turbulente (Padoan & Nordlund, 2004). L'instabilité gravitationnelle du disque consiste en une fragmentation du disque dans les jeunes phases de la formation de l'étoile et du disque. Au-delà d'environ 50 ua de l'étoile hôte, des amas de gaz froids et instables gravitationnellement peuvent s'effondrer en de hautes densités (Boss, 1997; Gammie, 2001; Armitage, 2017) où la formation planétaire peut avoir lieu. Enfin, la fragmentation gravo-turbulente de nuages moléculaires peut résulter en des coeurs gravitationnels instables de la masse d'une naine brune, qui vont s'effondrer ensuite et former des planètes géantes très massives ou des naines brunes (Padoan & Nordlund, 2004).

Produits : planètes et disques de débris

La formation planétaire a lieu pour les planètes géantes durant la phase de disque protoplanétaire qui dure environ 3 à 6 Ma (Haisch et al., 2001), tandis que les planètes plus petites peuvent se former sur des échelles de temps plus longues. La phase de dispersion du disque protoplanétaire a été appelée "disque de transition" ou "disque hybride". Après cette étape, la plus grande partie du gaz a disparu. Il a soit été accrété sur l'étoile ou sur les planètes (géantes) ou diffusé à l'extérieur du système.

Une question importante dans le domaine est comment les disques de débris sont reliés aux disques protoplanétaires. Par exemple, est-ce que les disques protoplanétaires larges et brillants résultent en des disques de débris larges et brillants ? Najita et al. (2022) a étudié cette question. D'après leur étude, comme 25% des jeunes (1 Ma) étoiles de type solaire ont de larges et brillants disques protoplanétaires, et que la même fraction d'étoiles âgées ont de larges et brillants disques de poussières, cela serait une option possible. Toutefois, ils soulignent qu'une combinaison de différents chemins d'évolution serait également possible, avec des disques suivant différents scénarios tels que ceux nommés "éruption précoce", "lueur constante" ou "floraison tardive" (voir leur Fig. 12).

Lorsque le disque de gaz s'est dissipé, autour de l'étoile demeurent les produits de la formation planétaire. Cela inclut la présence de planète(s) et des corps plus petits, tels que des planètes naines, planétésimaux, cailloux et poussières, qui peuvent être considérés comme des "débris". Un disque de débris peut représenter tous les débris dans un système, ou des populations individuelles de débris (voir la revue pédagogique de Pearce, 2024).

Après que les planètes se soient fermées, les systèmes planétaires ne demeurent pas statiques et des événements majeurs peuvent avoir lieu, tels que des collisions planète-planète, événements de dispersion planète-planète (Rasio & Ford, 1996), migration à haute-excentricité via les interactions de Kozai-Lidov (Kozai, 1962; Naoz et al., 2012) par exemple, des tombées tardives de planétésimaux sur les planètes (Gomes et al., 2005) ou des perturbations externes comme un passage rapproché avec une autre étoile (Laughlin & Adams, 1998; Hurley & Shara, 2002; Zakamska & Tremaine, 2004). Ces événements peuvent modifier l'architecture du système planétaire, en éjectant des planètes ou en changeant leurs propriétés orbitales, ou leurs propriétés atmosphériques et leur composition. Par exemple, la température de la planète peut varier significativement, résultant en une échappée tardive de son atmosphère (Bourrier et al., 2018) ou en changeant l'état physique de certains de ses constituants (par exemple en transformant des océans en vapeur). Les tombées tardives de planétésimaux pourraient être une source d'eau, comme cela l'a peut-être été pour la Terre (Pepin, 1991).

Comme pour les planètes, les disques de débris évoluent également. Les collisions entre les planétésimaux génèrent des corps plus petits, qui vont être sujet à des séries de collisions, résultant en des particules de plus en plus petites (Wyatt, 2008). Cette cascade collisionnelle génère de nouvelles populations de poussières. Lorsque les poussières sont suffisament petites, les grains de poussières deviennent sensibles à d'autres forces que la gravité. L'effet de Poynting-Robertson implique que les grains de poussières spiralent vers l'étoile (voir notamment Klačka et al., 2014). D'autre part, les vents stellaires et la pression de radiation stellaire agissent comme une force s'opposant à la gravité de l'étoile, en repoussant les petits grains de poussières, augmentant leur excentricité et éjectant du système les plus petits d'entre eux, ceux en-dessous d'une taille caractéristique (environ 1–10 μm pour des étoiles de type G à A, d'après (Pearce, 2024)).

Remarque : systèmes stellaires binaires ou multiple

Précédemment, j'ai décrit la formation et évolution des planètes autour d'une étoile seule. Cependant, les systèmes composés de plusieurs étoiles sont communs. Par exemple, 50 % des étoiles de type solaire font partie de système binaires ou de plus haut ordre de multiplicité (Heintz, 1969; Abt & Levy, 1976; Duquennoy & Mayor, 1991; Raghavan et al., 2010). Plus de 200 systèmes multiples sont les hôtes d'au moins une planète (Fontanive & Bardalez Gagliuffi, 2021)[9]. Dans les systèmes planétaires avec une étoile binaire, des planètes circumstellaires (orbitant autour d'une des deux étoiles, voir Patience et al., 2002; Marcy et al., 2005b) et circumbinaires (orbitant autour des deux étoiles, voir Doyle et al., 2011; Welsh et al., 2012; Rodet et al., 2017) ont été détectées. Les systèmes multiples à plus haut ordre et stables, sont des systèmes hiérarchiques. Par exemple, les systèmes triples consistent en une étoile orbitant autour d'une étoile binaire. Des planètes peuvent faire également partie de tels systèmes, par exemple, α Cen est un système triple, composé de la binaire α Cen A et α Cen B, autour de laquelle orbite α Cen C aussi connue sour le nom de Proxima du Centaure (l'étoile la plus proche du Soleil) et autour de laquelle orbite Proxima du Centaure b.

Par conséquent, une vision complète de la formation et évolution planétaire ne peut exclure les systèmes multiples. Le facteur clé est la distance entre les étoiles, qui implique si la multiplicité va avoir tendance à empêcher la formation planétaire (distance $\leq$ 50–100 ua, Bonavita & Desidera, 2007, 2020; Kraus et al., 2012, 2016; Wang et al., 2014), influencer l'évolution planétaire (100–1 000 ua, Fabrycky & Tremaine, 2007; Naoz et al., 2012; Dong et al., 2013; Ngo et al., 2016) ou ne va pas avoir d'impact significatif ($\geq$ 1 000 ua, Bonavita & Desidera, 2007, 2020; Fontanive & Bardalez Gagliuffi, 2021).

[9] voir aussi le catalogue suivant : https://exoplanet.eu/planets_binary/

La compréhension actuelle de la formation et évolution planétaire se base notamment sur de nombreuses contraintes observationnelles. Je les décris et illustre dans la version anglaise du manuscrit de thèse (Section 1.3.2, Figs. 1.10-1.15).

C.1.4 Contribution de ma thèse de doctorat

Dans les sections précédentes, j'ai montré à quel point les architectures des systèmes planétaires peuvent être diverses, et dans quelle mesure elles peuvent aider à comprendre comment les planètes se forment et évoluent. Dans ce contexte, ma recherche se concentre sur une étude détaillée de deux systèmes spécifiques, ainsi que sur un relevé sur un échantillon plus large pour avoir une vision statistique des architectures des systèmes planétaires, pour mieux comprendre comment les planètes se forment et évoluent sur des échelles du grain de poussière à une planète.

Dans la Section C.3, je présente les résultats clés sur l'étude multi-longueur d'ondes du complexe jeune disque de débris HD 120326. Ce disque a des structures résolues à la fois à des échelles intermédiaires (30–150 ua) et très grandes ($\leq$ 1 000 ua). Un large éventail de données est disponible sur ce système, incluyant des données dans le spectre visible (*HST* / STIS), proche infrarouge (VLT / SPHERE) en intensité polarisée et totale, et millimétrique (ALMA). J'ai combiné toutes ces données pour obtenir la vision la plus complète sur ce système (Desgrange et al., 2025, subm.). En particuler, avec les données SPHERE j'ai contraint les propriétés des grains de poussières de la ceinture principale, identifiée comme une ceinture de planétésimaux.

Les disques de débris sont un produit de la formation planétaire. Contrairement au système précédent, où pas de planètes n'ont encore été découvertes, mais qui pourraient bien être présentes pour expliquer les structures observées dans le disque de débris, le système présenté en Section C.4, HD 95086, est un système emblématique avec une planète imagée située entre deux ceintures de poussières. J'ai caractérisé les propriétés orbitales et atmosphériques de la planète HD 95086 b dans mon article en première autrice Desgrange et al. (2022a). D'autres planètes, que j'ai recherchées, sont attendues entre les deux ceintures de poussières pour expliquer la largeur de la cavité. Le système HD 95086 est dans une certaine mesure, un jeune, massif analogue au Système Solaire, dû à son architecture de double ceinture de poussières avec une planète géante située entre.

Ensuite, dans la Section C.5, je présente mon travail sur des systèmes planétaires ayant des planètes de faible masse et orbitant proche de leur étoile. De tels types de systèmes sont nombreux d'après la mission spatiale *Kepler* et les données de vitesses radiales. La motivation de ce projet était de déterminer comment ces planètes ont pu se former. Est-ce qu'elles se sont formées proches de leur étoile hôte, malgré un manque potentiel de solides ? Ou se sont-elles formées beaucoup plus loin, et ont migré ensuite vers l'intérieur du système dû à des interactions dynamiques avec des planètes géantes ? Pour étudier ces questions, j'ai dirigé une publication d'une étude pilote en imagerie directe avec l'instrument SPHERE au VLT pour déterminer la présence de planètes géantes situées sur des orbites distantes (au-delà de quelques unités astronomiques) dans des systèmes planétaires où de planètes de faible masse orbitant proches de leur étoiles ($\leq$ 1 ua) ont déjà été découvertes. Mon objectif était de déterminer la corrélation (ou non) entre la présence des ces deux types de planètes. Une corrélation positive, négative ou une absence de corrélation pourrait indiquer comment les planètes de faible masse et à courte période orbitale se sont formées.

En parallèle de ces trois projets de recherche utilisant principalement l'instrument SPHERE au VLT, j'ai contribué à étudier comment les performances de détection et caractérisation de l'instrument SPHERE pourraient être améliorées avec un spectrographe à champ intégral à moyenne résolution. Ce travail a été effectué dans le contexte de l'amélioration de

l'instrument SPHERE, nommé SPHERE+, et le consortium SPHERE+. Il y a de fortes connections entre SPHERE(+) et les instruments de l'ELT, à la fois sur des aspects astrophysiques et instrumentaux. Je les décrirais plus loin dans le manuscrit.

Passons maintenant aux concepts et méthodes de l'imagerie directe d'exoplanètes et de disques circumstellaires, qui est le sujet de la Section C.2.

C.2 Imagerie directe d'exoplanètes et de disques de débris : concepts et méthodes

Je décris dans cette section comment il est possible de photographier des exoplanètes et disques de poussières autour d'étoiles. En Section C.2.1, je compare les observatoires situés au sol et dans l'espace, en nommant leurs avantages et inconvénients. Ensuite, en Section C.2.2, j'explique le principe d'un instrument à haut-contraste et haute résolution angulaire. Enfin, en Section C.2.3, je présente l'instrument SPHERE situé au VLT, qui est l'instrument principal que j'ai utilisé lors de mon doctorat pour caractériser les systèmes planétaires.

C.2.1 Observatoires au sol et dans l'espace

Les instruments à haut-contraste situés dans l'espace ne souffrent pas des effets de l'atmosphère terrestre, qui déforme le front d'onde, dégrade la résolution angulaire et absorbe certaines portions du spectre électromagnétique (rayons γ, rayons X, ultraviolets, infrarouge moyen et lointain). De plus, les signaux spectraux ne peuvent être confondus entre du signal astrophysique réel (soit de l'exoplanète ou de son étoile hôte) et l'absorption par l'atmosphère de la Terre. Enfin, les observations depuis l'espace sont plus stables que leur équivalent depuis la Terre. Par exemple, les incertitudes sur le flux mesuré d'une exoplanète par un observatoire spatial n'ont pas à prendre en compte les variations de l'atmosphère de la Terre qui est constamment en évolution.

Néanmoins, les télescopes spatiaux sont des projets long-termes, particulièrement coûteux. Par exemple, les premiers designs du *JWST* ont commencé en 1996, tandis que le *JWST* a été lancé le 25 décembre 2021, pour un coût total de 10 milliards de dollars américains. Par ailleurs, la plupart du temps il n'est pas possible de réparer un télescope spatial une fois qu'il a été lancé. L'exception est le télescope spatial Hubble (*HST*), qui a été réparé (ou alors ses instruments mis à jour) cinq fois. Ces missions étaient possibles car le *HST* était relativement proche, à une altitude de 590 km, et que des missions de maintenance utilisant des navettes spatiales étaient prévues dès le départ. De telles missions de maintenance ne sont pas réalistes avant longtemps pour des télescopes situés au point Lagrange 2 (L2), soit à 1.5 million de kilomètres de la Terre, comme le *JWST*. Par conséquent, le télescope et les instruments embarqués doivent être absolument fiables. Ainsi, l'instrumentation spatiale peut être sur certains aspects dépassée comparer à ce qui est en parallèle développée, testée, utilisée pour l'instrumentation au sol. Dernier point, il est difficile et particulièrement cher d'envoyer dans l'espace un télescope avec un large mirroir primaire. À ce jour, *JWST* a le plus large (6.2 m) miroir primaire jamais envoyé dans l'espace. Cela a nécessité un design et une stratégie sur-mesure : lorsque le *JWST* a été lancé, son miroir primaire fut plié dans un premier temps et il ne se déplia que lorsque le *JWST* atteignit sa localisation finale, au point L2.

Dans mon champ de recherche, l'imagerie directe d'exoplanètes et de disques circumstellaires, les télescopes spatiaux principaux sont *IRAS* (*InfraRed Astronomical Satellite*, Neugebauer et al., 1984), *Spitzer* (Werner et al., 2004), *Herschel* (Pilbratt et al., 2010), *WISE* (Wright

et al., 2010), *HST*, *JWST*, et *Nancy Grace Roman Space Telescope* (RST Spergel et al., 2013) qui sera lancé en 2027.

Brièvement, *IRAS* a cartographié le ciel et identifié des étoiles avec un excès infrarouge. Cet excès infrarouge fut interprété comme la présence de poussières froides autour de ses étoiles, sous la forme de disques de poussières. Une des célèbres découvertes de *IRAS* fut les "fabuleux quatre disques de débris" Vega (Aumann et al., 1984), Fomalhaut, Beta Pictoris et Epsilon Eridani (Gillett, 1986; Backman & Paresce, 1993). Après avoir vu les résultats d'*IRAS*, (Smith & Terrile, 1984) ont observé et résolu le disque de débris de Beta Pictoris, faisant ce système le premier disque de débris spatiallement résolu. Par la suite, les missions spatiales *Spitzer*, *Herschel* et *WISE* aidèrent à identifier les étoiles ayant des disques de débris, à enlever les cas douteux et à déterminer le taux d'occurence minimal de disques débris.

Concernant les télescopes (toujours) en fonctionnement, il y a *HST*, lancé en 1990 et qui a photographié de nombreux disques de poussières. Il a révélé en particulier les halos de très petites particules de poussière qui sont repoussées au loin de l'étoile par la pression de radiation stellaire et les vents stellaires. En télescope plus récent, il y a donc le *JWST*, dont les résultats scientifiques ont récemment commencé à être publiés. Pour en nommer quelques uns, *JWST* a photographié dans des disques de débris des ceintures ou structures pour la première fois observées ou spatialement résolues dans ces disques-là : une ceinture intermédiaire de poussières dans l'emblématique système Fomalhaut (Gaspar et al., 2023), la ceinture interne du système iconique HR 8799 (Boccaletti et al., 2024), ou encore la surnommée "queue de chat" dans le système célèbre Beta Pictoris (Rebollido et al., 2024).

Dans le futur proche, le *RST* atteindra des limites de détections inédites avec son instrument coronographique (CGI), en étant sensible dans le domaine du visible à des exoplanètes un milliard de fois plus faibles que leur étoile hôte. L'instrument CGI est un démonstrateur pour l'Observatoire des Mondes Habitables (*HWO*), qui devrait être lancé dans les années 2040s+. Les objectifs de *HWO* est de chercher et photographier des planètes similaires à la Terre dans les zones habitables autour d'autres étoiles, et ou en principe de l'eau sous la forme liquide pourrait exister.

Les observatoires au sol sont complémentaires à ceux dans l'espace sur bien des aspects. Comme écrit précédemment, car ils offrent plus de flexibilité pour tester et développer de nouveaux instruments, technologies et stratégies d'observation. Ces dernières peuvent demander des ajustements en temps réel (voir notamment Potier et al., 2020, 2022). Deuxièmement, c'est moins coûteux de construire un télescope au sol que son équivalent spatial. Troisièmement, les télescopes spatiaux ont un temps de vie limité dépendant de leur carburant, souci que n'a pas le télescope au sol. Enfin, même s'il n'y avait pas de contraintes budgétaires, certains télescopes ne seraient tout simplement pas faisables dans l'espace dans l'état actuel des connaissances et du savoir-faire.

Une revue des instruments haut-contraste est réalisée dans Chauvin et al. (2018). Elle relate également les contraintes de ces instruments sur les modèles de formation et évolution planétaire, la démographie des exoplanètes et les architectures planétaires.

Durant mon doctorat, j'ai principalement utilisé l'instrument SPHERE situé au VLT au Chili (voir les Sections C.3, C.4 et C.5). J'ai également été particulièrement intéressée par les instruments au sol SHARK-NIR et LMIRCam au Large Binocular Telescope (LBT) en Arizona aux États-Unis, et les télescopes et instruments spatiaux *HST*/STIS, *JWST*/NIRCam et *JWST*/MIRI. En particulier, j'ai soumis des demandes de temps avec toutes ces infrastructures pour initier de futurs projets de recherche sur lesquels je compte m'investir dans mon futur poste. Dans les demandes de temps acceptées, détaillées un peu plus en Appendix B, j'ai obtenu du temps comme Investigatrice Principale (PI) sur SPHERE (ID: 109.23F2, 113.26E1 et 114.276D) et SHARK-NIR et LMIRCam (ID: MPIA-2024A-006, MPIA-2024A-007 et MPIA-2024B-001) et en co-Investigatrice Principale (co-PI) sur *JWST*/MIRI (PI: Elisabeth Matthews;

ID GO 5229). Je suis aussi impliquée sur d'autres demandes de temps en tant que collaboratrice (co-I).

C.2.2 Atteindre la sensibilité requise

Pour photographier du matériel circumstellaire (planète, disque de poussières), il faut une instrumentation capable de détecter des objets très faibles et situés très proches de l'étoile. Typiquement, les jeunes planètes géantes de quelques masses de Jupiter ont un contraste de 10^{-5}–10^{-6}. Dans le cas du Système Solaire, Jupiter est situé à 5 ua, soit 0.5" pour un observateur situé à 10 pc ou 0.1" pour un observateur à 50 pc.

Cela nécessite deux étapes clés : atteindre une haute résolution angulaire et un haut contraste. En pratique, pour les observations au sol, la haute résolution angulaire peut être obtenue grâce à un télescope avec un large miroir et un instrument équipé d'une optique adaptative pour corriger des effets de la turbulence atmosphérique qui brouille les images. Actuellement, les instruments d'imagerie directe parviennent à détecter des objets situés au mieux à environ 0.1" de leur étoile. Pour obtenir un haut contraste, il faut pouvoir enlever au maximum la lumière stellaire, pour révéler des planètes ou disques de poussières autour de l'étoile. En pratique, un coronographe peut être utilisé pour cacher (en partie) la lumière de l'étoile et ensuite des techniques de traitement de données pour modéliser et enlever le flux stellaire résiduel.

Ces trois étapes sont représentées dans la Fig. C.6 pour l'instrument SPHERE au VLT. Utiliser une optique adaptative permet de détecter du signal relativement proche de l'étoile et environ mille fois plus faible que l'étoile, soit un contraste de 10^{-3}, à 1.6 μm. Ajouter un coronographe permet de gagner un facteur dix, donc observer des objets à un contraste de 10^{-4}. Appliquer des techniques plus ou moins sophistiquées de traitement de données permet de gagner un facteur entre dix et cent, donc observer des objets avec un contraste entre 10^{-5} et 10^{-6}, donc de jeunes, massives exoplanètes.

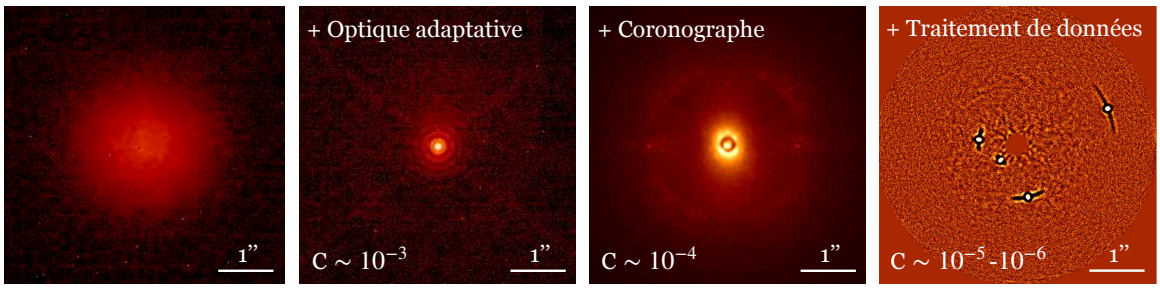

Figure C.6: Principe d'un instrument à haut contraste et à haute résolution angulaire. De *gauche* à *droite* : image typique d'une étoile observée par un télescope et instrument au sol sans système d'optique adaptative ; ajout d'un système d'optique adaptative permettant de restaurer une haute résolution angulaire, qui est limitée par la diffraction et non par la turbulence de l'atmosphère ; ajout d'un coronographe pour enlever la lumière stellaire ; image obtenue après traitement de données du système HR 8799 data. Crédits : l'équipe de mise en service ("commissioning") de SPHERE et Faustine Cantalloube.

Ci-dessous, j'apporte brièvement quelques informations complémentaires sur un système d'optique adaptative, sur un coronagraphe et sur le traitement de données. Plus d'informations sont disponibles dans la version anglaise du manuscrit, dans la Section 2.2.

Optique adaptative

La Figure C.7, montre un schéma d'un instrument muni d'un système d'optique adaptative. Lorsque la lumière d'une étoile parvient sur Terre, son front d'onde précédemment

plat devient déformé dû à la turbulence de l'atmosphère. La lumière va être collectée par le télescope et envoyée dans l'instrument. Le système d'optique adaptative de l'instrument va mesurer les écarts du front d'onde déformé d'un front d'onde plat, grâce au senseur de front d'onde et du système de contrôle. Il va ensuite les corriger, grâce au miroir déformable, qui va prendre la forme du front d'onde.

Pour qu'une optique adaptative soit efficace, elle doit réussir à mesurer et corriger le front d'onde suffisamment rapidement. Plus précisément, sa fréquence de correction doit être plus élevée que l'évolution de la turbulence de l'atmosphère, qui est typiquement de l'ordre de quelques millisecondes à Paranal, où est situé le VLT.

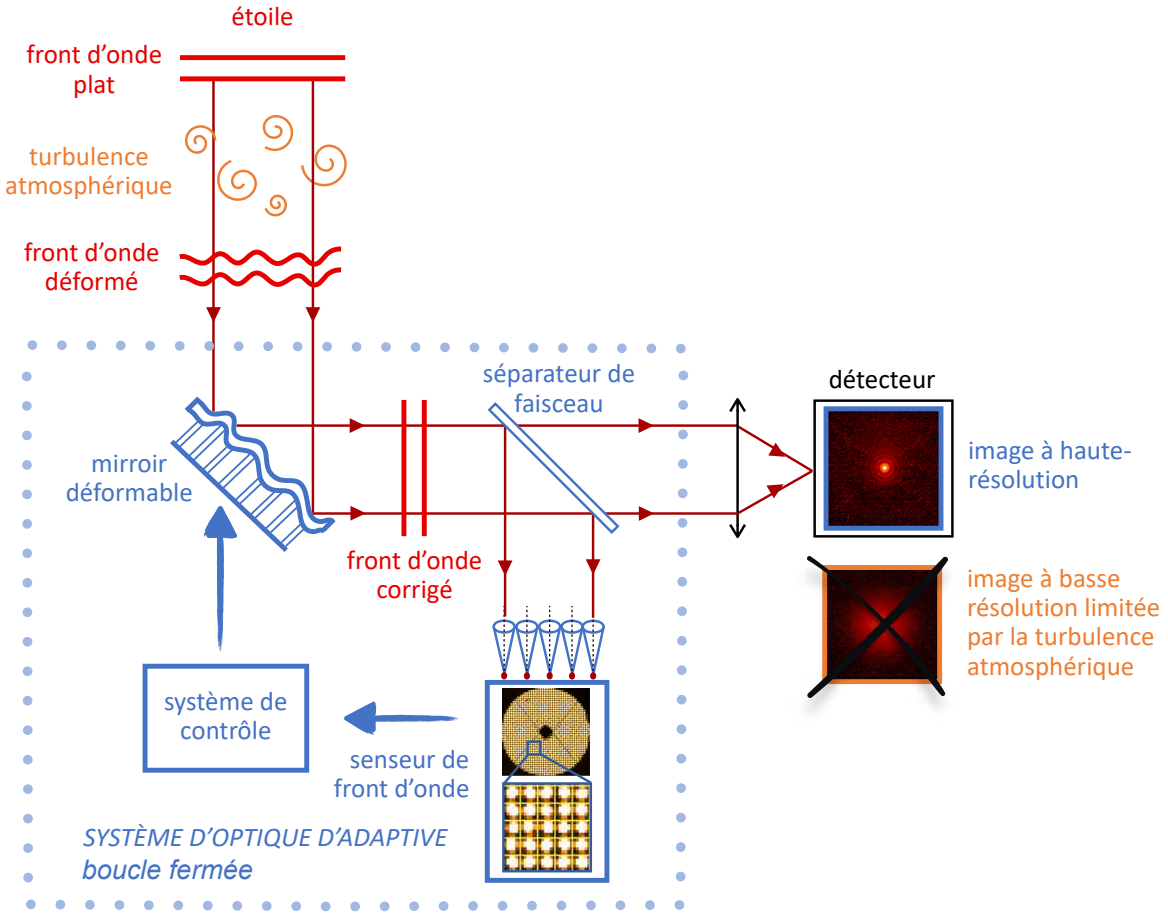

Figure C.7: Schéma illustrant le principe d'un système d'optique adaptative. Pour simplification, dans ce schéma il n'y a pas de coronographe, mais la Figure C.8 en montre un (le coronographe APLC) qui peut être ajouté entre le séparateur de faisceau et la lentille qui focalise la lumière sur le détecteur. Crédits : Les petites images carrées sont de la mise en service ("commissioning") de SPHERE.

Coronagraphe

Concernant le coronographe, celui particulièrement utilisé dans l'instrument SPHERE est le coronographe de Lyot apodisé (APLC). Il est représenté en Fig. C.8. Il est constitué d'un apodiseur, d'un masque en plan focal et d'un stop de Lyot. Après être passé par le système d'optique adaptative, le front d'onde collimaté (et plan) passe à travers l'apodiseur, qui va enlever les anneaux de diffraction et adoucir les bords abrupts de la pupille du télescope. Ensuite, le front d'onde passe à travers une lentille (ou miroir courbe) qui va concentrer le faisceau sur le masque en plan focal. La lumière stellaire sur l'axe optique est bloquée ou

diffractée au-delà de la pupille, qui sera bloquée ensuite par le stop de Lyot. Le stop de Lyot a des obstructions plus larges que la pupille du télescope. Le reste du faisceau continue ensuite jusqu'au détecteur qui enregistre l'image (voir la troisième image de la Fig. C.6).

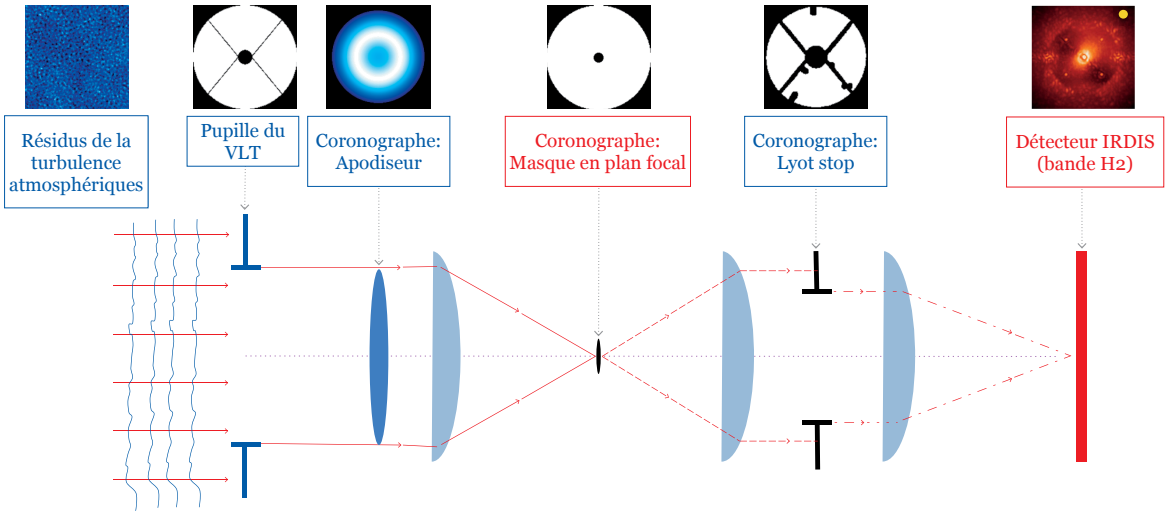

Figure C.8: Schéma montrant le coronographe apodisé de Lyot (APLC) pour l'instrument SPHERE. Dans les plans pupilles (en bleu) sont montrés les résidus (en phase et en amplitude) atmosphériques de la turbulence, la pupille du VLT, l'apodiseur et le stop de Lyot. Dans les plans focaux (en rouge) sont situés le masque en plan focal et le détecteur de SPHERE / IRDIS, sur lequel est montré l'image finale coronographique. Figure de Cantalloube et al. (2019).

Traitement de données

L'étape de traitement de données est essentielle pour détecter et caractériser du signal circumstellaire. De nombreux algorithmes existent. Ils se basent sur les différences entre les propriétés de l'étoile et du signal circumstellaire (planètes, disques), en utilisant l'information polarimétrique, spectrale ou temporelle, ou encore via calibration avec une étoile de référence. Différents acronymes existent pour faire référence à ces techniques : PDI (Polarization Differential Imaging), SDI (Spectral Differential Imaging, Racine et al., 1999; Sparks & Ford, 2002), ADI (Angular Differential Imaging Marois et al., 2006) et RDI (Reference Differential Imaging). Ces techniques ont chacunes leurs avantages et inconvénients. Certaines peuvent être utilisées simultanément.

Durant mon doctorat, j'ai utilisé ces quatre techniques de traitement de données, la technique ADI ayant été la plus incontournable.

C.2.3 L'instrument SPHERE au Very Large Telescope

L'instrument SPHERE peut photographier des exoplanètes et disques de poussières dans l'optique et l'infrarouge, de 0.51 à 2.35 μm avec des filtres larges ou étroits, ou en spectroscopie. SPHERE est composé de plusieurs sous-instruments : le chemin optique et infrastructure communs (CPI), qui inclut le système d'optique adaptative (SAXO) et les trois sous-instruments, un imageur à double bande (IRDIS, Dohlen et al., 2008) dans l'infrarouge, un spectrographe à champ intégral (IFS, Claudi et al., 2008) dans l'infrarouge et un polarimètre dans le visible (ZIMPOL, Schmid et al., 2018), voir Fig. C.9. Durant ma thèse, j'ai traité et analysé des données d'IRDIS et d'IFS, et non de ZIMPOL.

Plus précisément, l'imageur à double bande IRDIS peut observer dans l'infrarouge entre 0.95 à 2.35 μm, c'est-à-dire dans les bandes YJHKs. IRDIS a plusieurs modes, il permet de

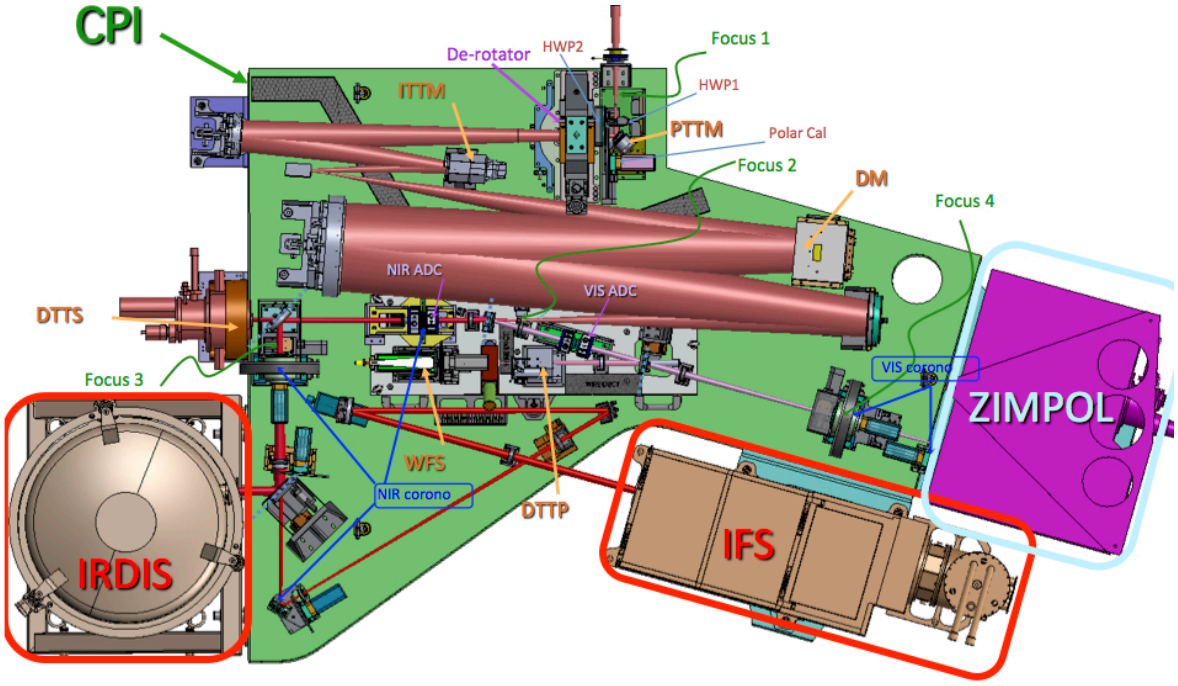

Figure C.9: L'instrument SPHERE et ses sous-instruments : IRDIS, IFS et ZIMPOL. La lumière entre dans l'instrument par le haut. Crédits : Manuel ESO/SPHERE.

faire de l'imagerie classique (CI), de l'imagerie à double bande (DBI), typiquement réalisée pour deux filtres étroits (Y2 et Y3, J2 et J3, H2 et H3, ou K1 et K2), de l'imagerie à double polarisation linéaire (DPI, De Boer et al., 2020) et de la spectroscopie à longue fente (LSS). IRDIS a un champ de vue de $11'' \times 11''$, ce qui est plus large que le champs de vue de l'IFS et de ZIMPOL. Sa taille de pixel est de $0.01225'' \times 0.01225''$, soit 12.25 mas $\times$ 12.25 mas.

Quand à l'IFS, il s'agit d'un spectographe à champ intégral de faible résolution, opérant entre 0.95 et 1.35 μm (soit les bandes YJ, résolution spectrale d'environ 50) ou 0.95 et 1.65 μm (soit les bandes YJH, résolution d'environ 30). C'est un spectrographe utilisant un réseau de lentilles (suivant le concept BIGRE, Antichi et al., 2009) pour diffracter la lumière reçue dans les différentes régions du champ de vue. L'IFS à 39 canaux spectraux en tout. Le champ de vue de l'IFS est $1.7'' \times 1.7''$ et la taille de pixel finale est de 7.46 mas $\times$ 7.46 mas.

Enfin, ZIMPOL est un polariseur à haut contraste observant dans l'optique (510–900 nm). ZIMPOL peut faire de l'imagerie classique et de l'imagerie différentielle polarisée (PDI) en modulation courte ou rapide. Son champ de vue est de $3.5'' \times 3.5''$, avec une taille de pixel de 7 mas $\times$7 mas.

L'instrument SPHERE peut observer avec un champ de vue stabilisé ou avec le plan pupille stabilisé. Dans le champ de vue stabilisé, une portion donnée du détecteur recevra toujours de la lumière de la même localisation du champ de vue durant la séquence d'observation. Quant au champ pupille stabilisé, la configuration pupille du télescope est stabilisée, ce qui implique que les résidus stellaires sont quasi-statiques durant l'observation, tandis que le signal circumstellaire tourne au cours de l'observation, dû à la rotation de la Terre.

Lorsque l'observation est effectuée en champ pupille stabilisé, de la diversité temporelle est introduite dans la séquence d'observation, entre le signal stellaire (quasi-statique) et le signal circumstellaire (qui tourne au cours de l'observation). Cela permet ensuite dans le traitement de données d'utiliser les algorithmes basés sur l'ADI. Pour des données acquises en plusieur longueurs d'ondes, le traitement de données pourra se servir de la SDI, et pour des données acquises en polarimétrie, de la PDI.

Des routines ont été développées pour pré- et post-réduire les données de l'instrument SPHERE, notamment SpeCal (Galicher et al., 2018) et IRDAP (Van Holstein et al., 2020). La routine SpeCal est associée au High Contrast Data Center (HC-DC[10]), qui offre un service de réduction d'observations à imagerie à haut contraste, tel que pour les données de SPHERE. Quant à la routine IRDAP, elle a été développée par Van Holstein et al. (2020) pour réduire les données polarimétriques de SPHERE/IRDIS, en prenant en compte les effets de polarisation induits par le télescope et l'instrument. Elle est actuellement en cours d'implémentation dans le HC-DC.

Pour mes projets de recherche, j'ai systématiquement utilisé le service de HC-DC pour obtenir les données pré-traitées en intensité totale de SPHERE et souvent pour obtenir les données post-traitées via plusieurs algorithmes. J'ai aussi post-traité les données moi-même en utilisant des algorithmes en libre accès ou qui m'ont été partagés (sections C.3, C.4, et C.5). Concernant les données polarimétriques, j'ai pré- et post-traité les données avec la routine IRDAP (section C.3).

Je m'arrête ici concernant la description des concepts et méthodes pour détecter des exoplanètes et disques dans cette version courte en français. Les informations concernant les limitations de SPHERE et comment aller au-delà sont décrites dans la version intégrale de mon manuscrit de thèse, dans la Section 2.3.2, et concernant les synergies avec d'autres instruments, dans la Section 2.3.3.

Passons maintenant à mes travaux sur les architectures des systèmes planétaires, en commençant par une étude multi-longueur d'onde des populations de poussières à des distances intermédiaires et très larges d'un jeune disque de débris, HD 120326.

C.3 Poussières et morphologie du disque de débris HD 120326

C.3.1 Contexte

Plus d'une centaine de disques de débris ont été résolus spatialement, soit dans le domaine visible, l'infrarouge ou le millimétrique. Les disques de débris sont communs et plus fréquemment détectés autour d'étoiles solaires jeunes ($\leq$ 25 Ma) que d'étoiles solaires plus âgées (50 Ma–10 Ga). En effet, Pawellek et al. (2021) détermina un taux de détection de disques de débris de 75% autour des étoiles du groupe mouvant de Beta Pictoris[11], tandis que plusieurs études rapportent des taux de détection de 25% pour des étoiles plus âgées (voir Najita et al., 2022, et les références qui y figurent). Néanmoins, les taux de détection peuvent être significativement différents des taux d'occurence, à cause du biais observationnel. Par exemple, les infrastructures actuelles ne sont pas capables de détecter des ceintures de poussières avec une luminosité fractionnelle similaire à celle ($\sim 10^{-7}$) de la ceinture d'astéroïdes principale et de la ceinture de Kuiper (Backman et al., 1995) autour d'autre étoiles que le Soleil (voir Fig. C.10).

Étudier les disques de poussières permettent de contraindre les architectures des systèmes planétaires, les propriétés des poussières et du gaz et des potentielles interactions disque-planète. Les disques de poussières sont de précieux réservoirs de comètes, qui peuvent fournir des substances volatiles, telles que de l'eau et des matières organiques, lorsqu'elles tombent sur des planètes. La morphologie d'un disque de poussières peut aussi aider à retracer la formation ou l'évolution d'un système grâce en particulier à des traits caractéristiques qui peuvent être reliées à des impacts géants (Jones et al., 2023), ou révéler des interactions avec leur voisinage proche, comme des passages rapprochés avec d'autres

[10] disponible à https://hc-dc.cnrs.fr/. Le HC-DC était précédemment nommé le SPHERE Data Center.
[11] Le groupe mouvant de Beta Pictoris est une association stellaire jeune dont le système Beta Pictoris fait partie.

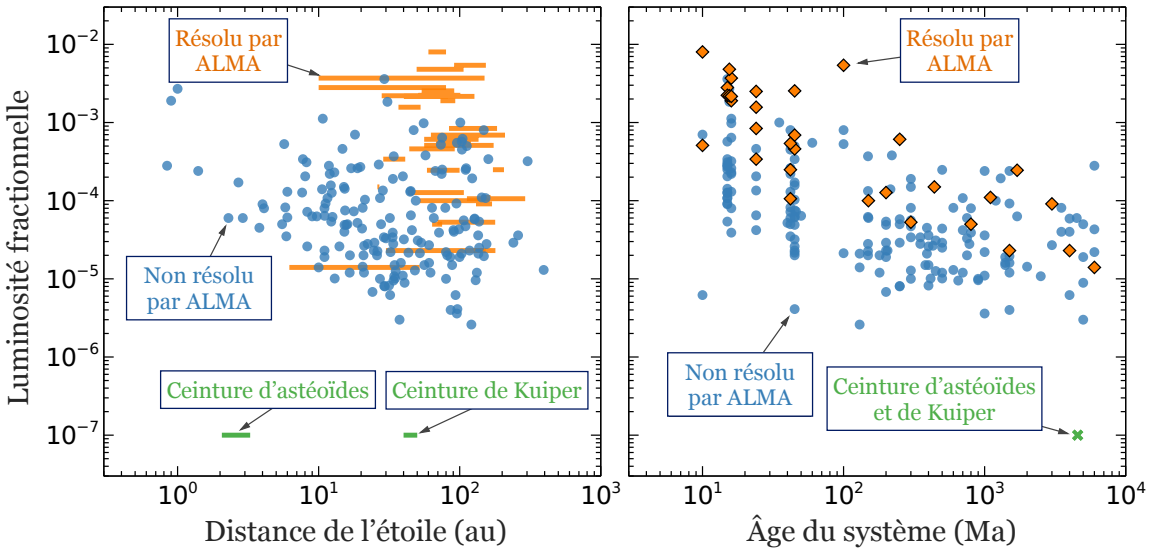

Figure C.10: Disques de débris observés avec ALMA autour d'étoiles jeunes et âgées. Ceux larges et lumineux sont résolus par ALMA. La luminosité des disques de débris semble décroître avec le temps. La luminosité de la poussière chaude (dans la ceinture d'astéroïde principale) et celle froide (dans la ceinture de Kuiper) autour du Soleil est significativement plus faible que celle détectée dans les disques de débris extrasolaires. Figure adaptée de la revue Pearce (2024).

étoiles stellaires (Bertini et al., 2023), ou des interactions avec le milieu interstellaire (Maness et al., 2009).

Parmi les associations proches, jeunes et larges, l'association Sco-Cen (Scorpius-Centaurus) se distingue notamment par son très grand nombre d'étoiles. De nombreux disques spatialement résolus et des exoplanètes y ont été observés en imagerie directe. Étudier une telle association permet ainsi d'étudier la diversité des architectures des systèmes planétaires à un jeune âge, quand les planètes se forment encore ou viennent de se former. En particulier durant mon doctorat, j'ai étudié le disque de débris complexe HD 120326, qui a plusieurs structures de poussières détectées à différentes échelles.

C.3.2 Mes résultats principaux

J'ai étudié la morphologie et les grains de poussières du système HD 120326 en utilisant des données multi-longueur d'onde, du domaine du visible (données *HST* / STIS), de l'infrarouge proche (VLT / SPHERE) et du millimétrique (ALMA), voir Figs. C.11 et C.12. La Figure C.11 représente les deux structures à échelle intermédiaire (30–150 ua) vues avec SPHERE en intensité polarisée, intensité totale et / ou avec ALMA. La Figure C.12 montre la structure étendue ($\leq$ 1 000 ua) et asymétrique vue avec *HST* / STIS, où au centre j'ai mis à l'échelle le signal vu avec SPHERE ou ALMA.

Mes principaux résultats concernent la caractérisation des différentes structures de disque et des propriétés des poussières. J'ai déterminé les paramètres de morphologie de la ceinture de débris interne (située à $\sim$43 ua) en modélisant simultanément les données SPHERE en intensité totale et intensité polarisée. Cette ceinture est identifiée comme une ceinture de planétésimaux en utilisant les données ALMA. J'ai contraint le taux de polarisation des grains de poussières à 1.6 μm, leur spectre de réflectance entre 1.0 et 1.8 μm et la masse que représenterait les poussières de taille millimétrique.

J'ai confirmé l'existence de la seconde structure de poussières vue seulement dans les données SPHERE en intensité totale, en utilisant de nouvelles observations et différents algorithmes de traitement de données. Cette structure de poussières très faible est précédemment

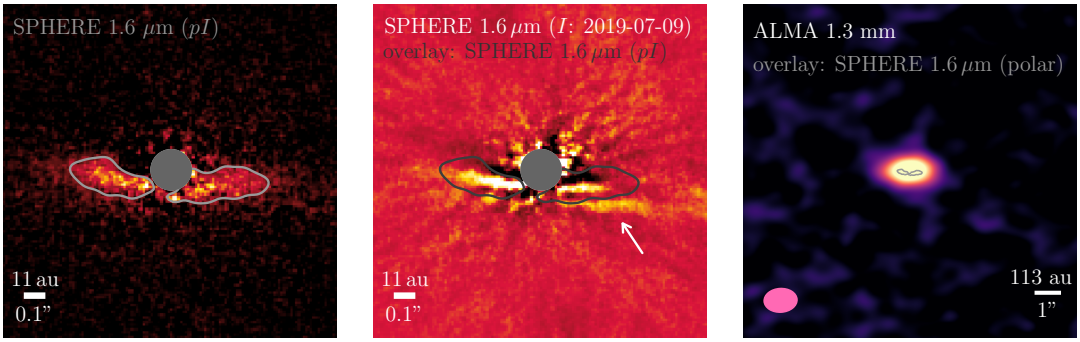

Figure C.11: Comparaison des structures de poussières de HD 120326 détectées en lumière diffusée avec SPHERE (1.6 μm) et en émission thermique avec ALMA (1.3 mm). À *gauche*, l'image en intensité polarisée de SPHERE avec en superposé les contours de la ceinture interne de poussières déterminés à une valeur de flux de 2 mJ/arcsec^2 sur cette image convoluée avec une gaussienne pour avoir des contours lisses. Les contours sont ajoutés sur l'image SPHERE en intensité totale (*au milieu*) et sur l'image ALMA reconstruite (*à droite*). Dans l'image *du milieu*, la flèche blanche indique la partie sud-ouest de la seconde structure vue seulement dans les données SPHERE en intensité totale, et qui ne se superpose pas au signal vu en intensité polarisé.

mentionnée par Bonnefoy et al. (2017), mais son existence réelle n'était pas claire dû au faible signal sur bruit, et par ailleurs elle n'a pas été détectée ultérieurement dans l'observation SPHERE en intensité polarisée obtenue à la même longueur d'onde (Olofsson et al., 2022b). La nature de cette seconde structure n'est toujours pas identifiée : un halo de petits grains de poussières, une seconde ceinture... J'ai montré que sa détection uniquement dans les données en intensité totale et non dans les données en intensité polarisée n'est pas incohérent. Je confirme que la structure est asymétrique : elle réfléchit plus de lumière et est plus étendue côté sud-ouest que sud-est.

J'ai traité à nouveau les données *HST*/STIS pour mieux mettre en lumière la structure étendue et asymétrique précédemment publiée par Padgett & Stapelfeldt (2016) et Bonnefoy et al. (2017). J'ai calibré les données *HST*/STIS en une unité en flux et j'ai dérivé la carte signal-sur-bruit.

Mon travail de recherche a abouti à un article en premier autrice (Desgrange et al., 2025, subm.) en cours de publication dans la revue Astronomie & Astrophysique à comité de lecture. Leur rapport est positif. Je suis en cours d'implémentation des révisions suite aux commentaires du relecteur, et je re-soumettrai prochainement l'article, qui est ajouté dans la Section 3.2.1.

C.3.3 Perspectives

De nouvelles données sont nécessaires pour mieux contraindre la morphologie des structures du disque et les propriétés des grains de poussières. Des nouvelles données *HST*/STIS acquises avec une stratégie d'observation optimisée (avec une étoile de référence et à trois angles de roulis différents) sont nécessaires pour avoir une meilleure couverture spatiale du disque en évitant les zones aveugles dû aux masques coronographiques et aigrettes (correspondant à la zone unie grise en Fig. C.12). Utiliser comme masque coronagraphique la Cbar5 permettrait également de caractériser avec STIS (et donc à une autre longueur d'onde qu'avec SPHERE) de la poussière située plus proche de l'étoile, jusqu'à des séparations de 0.2″, coïncidant avec la seconde structure vue avec SPHERE en intensité totale.

Des nouvelles données ALMA acquises à plus haute résolution permettraient de résoudre l'émission thermique des poussières dans le millimétrique et contraindre plus précisément

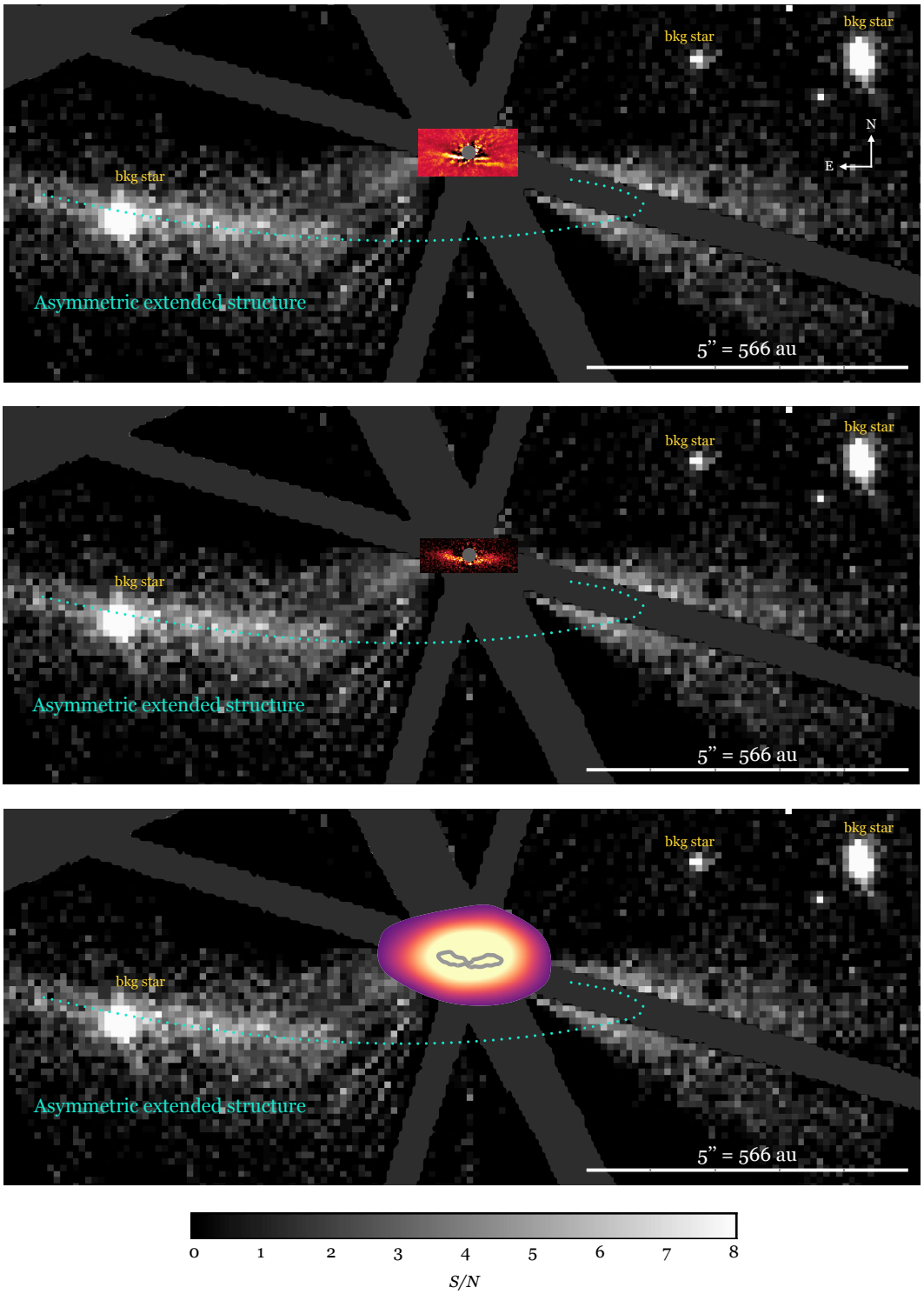

Figure C.12: Vue d'ensemble de l'architecture du système HD 120326. L'image en noir et blanc est la carte signal-sur-bruit (S/N) des données coronographiques *HST*/STIS dans le visible, binnées spatialement 2×2 pixels^2 $\rightarrow$ 1×1 pixel^2. Au centre de chaque image, est ajoutée l'image des structures internes vues avec SPHERE en intensité totale (*en-haut*), avec SPHERE en intensité polarisée (*au milieu*) et avec ALMA (*en-bas*). Les régions cachées par le masque coronographique et les aigrettes de diffractions sont masqués en gris foncé.

sa localisation. Enfin, des données *JWST* permettraient de déterminer la présence de poussières autour de HD 120326 à différentes longueurs d'onde, de l'infrarouge proche au moyen, apportant de fortes contraintes sur les populations de grains de poussières dans ce système, et la morphologie des structures. De plus, dans ce système *JWST* pourrait trouver des exoplanètes géantes de la masse de Saturne (ou supérieures) à quelques dizaines d'unités astronomiques, ce qui permettrait d'étudier les interactions planète-disque et d'expliquer la morphologie de certaines structures observées dans ce système. Évidemment, cela offrirait également une (ou des) nouvelle exoplanète à étudier, et qui commencerait à combler notre vision partielle des exoplanètes connues à ce jour (Fig. C.3).

C'est pourquoi j'ai soumis en Octobre 2023 et Mars 2024 des demandes de temps *JWST* et *HST*, qui malheureusement n'ont pas été acceptées.

Comme déjà écrit, un argument classique pour expliquer les structures dans les disques de débris est la présence d'exoplanètes qui pourraient les sculpter. Dans le système HD 120326, pas d'exoplanète encore n'a été découverte, mais une part significative de l'espace des paramètres reste encore à explorer.

Ainsi, la présence d'exoplanètes dans des systèmes ayant des disques de poussières peut être déduite en supposant des hypothèses sur les interactions planète-disque. Pearce et al. (2022) a effectué ce travail et prédit la présence de nombreuses exoplanètes, qui se situeraient entre 10 et 100 ua, voir Fig. C.13. Pour façonner une ceinture de poussières, la masse et le demi-grand axe nécessaires de l'exoplanète dépend du type des interactions planète-disque, et si plusieurs exoplanètes sont en jeu ou non.

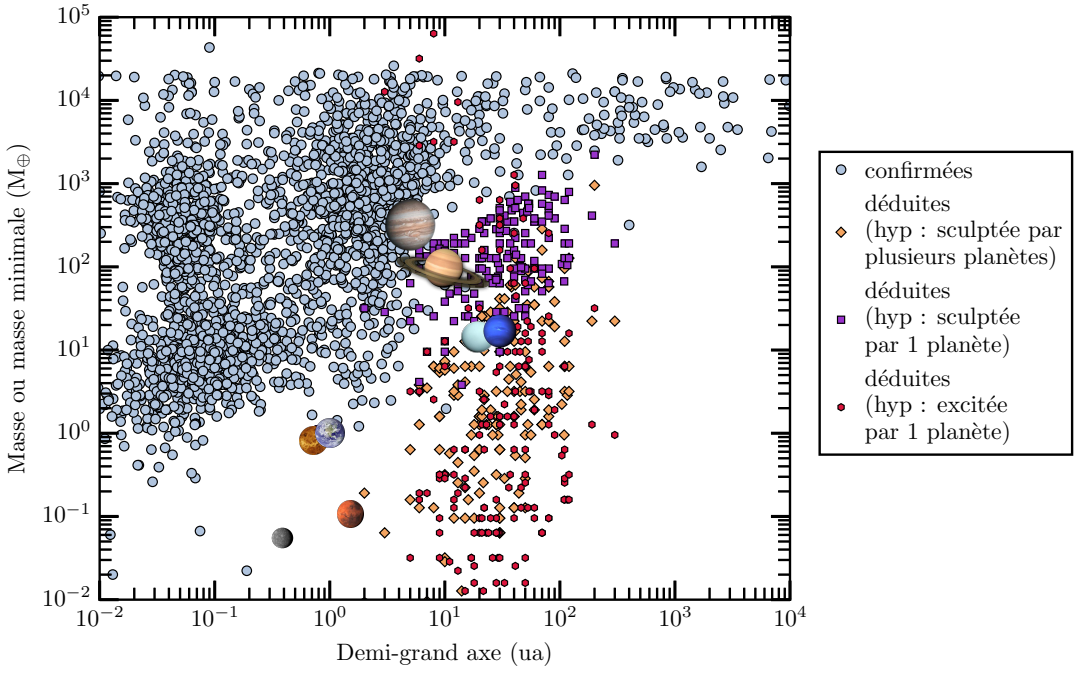

Figure C.13: Exoplanètes déduites à partir d'interactions disque-planète, issues du catalogue de Pearce et al. (2022), superposées aux exoplanètes connues à ce jour (cercles gris, voir Fig. C.3). La couleur indique le mécanisme supposé pour l'interaction planète-disque : soit en étant excité (cercle rouge) par une planète, soit via en étant sculpté par une ou des planètes (respectivement carré violet ou losange orange).

Avant le *JWST*, la plupart de ces candidats exoplanétaires se trouvaient en dessous des limites de détection des infrastructures astronomiques. Depuis le *JWST*, plusieurs larges

programmes observationnels ont été acceptés pour détecter ces exoplanètes prédites. Dans les cas les plus favorables, le *JWST* a la sensibilité pour détecter des exoplanètes de la masse de Neptune (Kammerer et al., 2024). Même des non-détections apporteraient des informations précieuses, car cela exclurait des scénarios concernant les propriétés de l'exoplanète (ou de la chaine d'exoplanètes), qui pourrait sculpter la ceinture de poussières, et donc cela contraindrait les interactions planète-disque.

Dans la prochaine section, je présente mon travail sur une jeune planète géante massive, HD 95086 b, qui sculpterait le bord interne de la ceinture externe de poussières du système HD 95086.

C.4 Le système planétaire HD 95086, jeune, massif analogue du Système Solaire

C.4.1 Contexte

Les systèmes similaires au Système Solaire et jeunes permettent de remonter le temps pour essayer de comprendre comme de tels systèmes se forment et évoluent au cours du temps (1–500 Ma). Cela permet d'étudier la formation de notre Système Solaire et la Terre, ainsi que les origines de la vie, avec une autre perspective.

Jusqu'à présent, concernant les jeunes systèmes ayant des disques circumstellaires et/ou des planètes, les astronomes ont pu contraindre :

1. Les propriétés orbitales des planètes géantes, en particulier si elles sont en résonance de moyen mouvement, ce qui pourrait aboutir à une configuration dynamique stable (Wang et al., 2021; Nowak et al., 2020; Beust et al., 2024), ou leur excentricité (De Rosa et al., 2020b), qui peut être reliée à des interactions dynamiques telles que des événements de dispersion (Raymond et al., 2009) ou des interactions de Kozai-Lidov (Beust et al., 2012; De Rosa et al., 2020a).

2. La présence de disque circumplanétaire, dans lequel des exo-Lunes pourraient se former (Benisty et al., 2021).

3. Les atmosphères de jeunes exoplanètes et la présence de nuages (voir Crossfield et al., 2014; Petrus et al., 2021; Huang et al., 2023; Palma-Bifani et al., 2024; Nasedkin et al., 2024, pour des caractérisations principalement récentes).

4. La poussière très chaude ou chaude localisée à une fraction ou quelques unités astronomiques, respectivement. Cette poussière correspond à une fraction de quelques pourcents de la lumière stellaire dans l'infrarouge (Absil et al., 2013, 2021; Ertel et al., 2014, 2016). Sa détection fréquente soulève des questions, car cette poussière devrait se dissiper rapidement, et donc des mécanismes de réapprovisionnement sont requis (voir par exemple Pearce, 2024).

5. Les réservoirs froids d'astéroïdes, en étudiant la poussière générée par les collisions (Chen et al., 2020; Milli et al., 2015, 2017a, 2019, 2024; Engler et al., 2023; Wu et al., 2024). Étudier les propriétés des poussières permet de contraindre leur porosité, ce qui aide à mieux comprendre la croissance des grains de poussières dans le cas où leur structure est suffisament préservée par rapport à la phase du disque protoplanétaire. De plus, contraindre les propriétés des poussières permettent également de déterminer si elles contiennent des minéraux hydratés, ce qui pourrait représenter une source d'eau pour les planètes rocheuses, quand les astéroides tombent sur les planètes (par exemple, durant un événement tel que le grand bombardement tardif).

6. Les réservoirs de comètes [12] en étudiant le gaz libéré lors des collisions ou lorsqu'elles se rapprochent de leur étoile hôte (Matrà et al., 2017, 2019; Rebollido et al., 2020; Beust et al., 2024). Le gaz de seconde génération peut aussi contribuer à modifier la composition atmosphérique des planètes rocheuses qui peuvent accréter partiellement ce gaz (Kral et al., 2020). Les comètes sont notamment intéressantes car elles pourraient être une source d'eau pour des planètes lorsqu'elles s'écrasent dessus, en particulier pour des planètes rocheuses situées à une distance propice de l'étoile pour que de l'eau à sa surface soit sous la forme liquide.

De telles études sur des systèmes analogues au Système Solaire sont d'intérêt majeur. Malheureusement, seulement quelques uns des systèmes planétaires découverts ont des propriétés similaires à celles du Système Solaire. Le système le plus iconique est HR 8799 (Fig. C.2, Marois et al., 2008, 2010), avec quatre planètes géantes massives situées entre deux ceintures de poussières. Un autre système planétaire à double ceinture de poussières est HD 95086, connu pour avoir au moins une exoplanète géante (Rameau et al., 2013) située dans la cavité entre les deux ceintures de poussières (voir Fig. C.14). À la fois HR 8799 et HD 95086 orbitent autour d'étoile de type A, donc des étoiles plus massives que le Soleil.

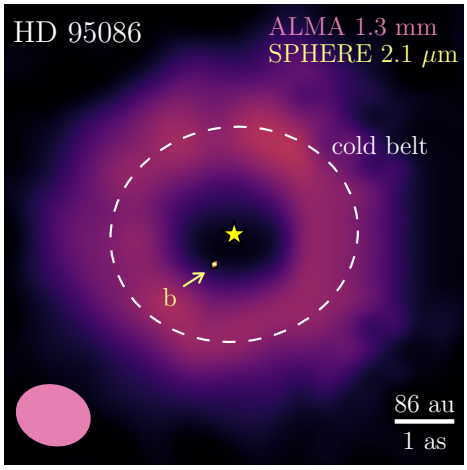

Figure C.14: Image composite du système planétaire HD 95086, utilisant les données SPHERE pour la détection de l'exoplanète géante HD 95086 b (Chauvin et al., 2018) et des données ALMA pour la détection de la ceinture de poussière externe (Su et al., 2017). La ceinture interne (entre 7 et 10 ua) n'est pas résolue avec ALMA. Image issue de Desgrange et al. (2022a).

C.4.2 Mes résultats principaux

J'ai caractérisé les propriétés spectroscopiques et orbitales de l'exoplanète géante HD 95086 b, qui a une masse de 4–5 M_{Jup} et a un demi-grand axe entre 50 et 70 ua. J'ai utilisé dix époques d'observation de l'instrument SPHERE, acquises entre 2015 et 2019 dans le contexte du temps garanti du consortium SPHERE. Ces observations, ont été acquises simultanément avec SPHERE/IRDIS et SPHERE/IFS, entre 1.0 et 2.3 μm, et je les ai couplées avec des données d'archive de Gemini Sud/GPI (1.9–2.3 μm) et VLT/NaCo (3.8 μm).

Dans mon article en première autrice publié dans Astronomie & Astrophysique (Desgrange et al., 2022a), ajouté en Section 4.2.1, mes collaborateurs et moi avons montré que la sous-luminosité de l'exoplanète géante HD 95086 b et son spectre rouge peut-être expliqué

[12] Je fais ici la distinction entre une comète et un astéroïde, bien que la différence n'est pas si claire à l'heure actuelle. Par comètes, j'entends des corps riches en volatiles, contrairement aux astéroïdes.

par deux scénarios, reliés à la présence de poussières autour de l'exoplanète. Dans le premier scénario, la poussière serait située dans un disque circumplanétaire et l'exoplanète aurait une température effective de $\geq$1400 K. Dans le second scénario, la poussière serait située sous la forme de nuages dans les hautes couches de son atmosphère, correspondant à une atmosphère avec une métallicité super-solaire, ce qui serait en faveur d'un mécanisme de formation d'accrétion sur coeur et non d'instabilité gravitationnelle. La température effective de l'exoplanète serait moins élevée (800–1300 K). Ces deux solutions sont tout aussi vraisemblables l'une que l'autre d'après notre modélisation. Elles se basent sur les mesures spectroscopiques et photométriques de SPHERE/IFS, GPI, SPHERE/IRDIS et NaCo de HD 95086 b, donc entre 1.2 et 4.0 μm. Concernant ces mesures, j'ai en particulier extrait le spectre de HD 95086 b entre 1.2 et 1.6 μm (donnée SPHERE/IFS) pour la première fois, ce qui était particulièrement difficile car l'exoplanète HD 95086 b est particulièrement faible à ces longueurs d'onde. J'ai dû combiner les meilleures époques de SPHERE, après avoir corrigé du mouvement orbital, pour augmenter le ratio signal-sur-bruit.

Concernant les propriétés orbitales de l'exoplanète HD 95086 b, mes collaborateur et moi avons déterminé que son excentricité est faible, inférieure à 0.18 à 1σ, alors que précédemment elle était moins bien contrainte ($\leq$ 0.5, Chauvin et al., 2018). De ce fait, l'exoplanète HD 95086 b, sculpte certainement le bord interne de sa ceinture externe, mais ne peut expliquer la largeur de la cavité par elle-même. Ainsi, au moins une autre exoplanète est attendue pour expliquer la largeur de la cavité d'après des arguments dynamiques (Su et al., 2015).

Enfin, j'ai recherché la présence d'autres compagnons planétaires, et amélioré les contraintes précédentes. En utilisant les modèles d'évolution (`COND`, Baraffe et al., 2003) pour convertir la limite de détection donnée de luminosité en masse planétaire, j'exclus à un niveau de confiance de 90% la présence d'exoplanètes ayant une masse supérieure à 9 M_{Jup} à un demi-grand axe entre 13 et 20 ua, et au-dessus de 5 M_{Jup} au-delà de 20 ua.

C.4.3 Perspective

Le système HD 95086 est un système emblématique, ciblé par de nombreux télescopes et instruments. J'ai pu collaborer avec Gilles Otten qui travaille sur les données VLTI/GRAVITY. L'astrométrie très précise de HD 95086 b mesurée à partir des données GRAVITY pour des époques entre 2019 et 2022 est cohérente avec l'astrométrie issue de SPHERE, et est compatible avec les ajustements orbitaux réalisés à partir des données SPHERE et NaCo (époques d'observation entre 2012 et 2019). Cette comparaison est montrée sur le poster réalisé en collaboration avec Gilles Otten et que j'ai présenté lors de la conférence In Spirit of Lyot en 2022 à Leyde aux Pays-Bas (Fig. 4.2).

Très récemment, à partir des données *JWST*/MIRI dans l'infrarouge moyen, Mâlin et al. (2024) a publié la première image de la ceinture de débris interne, dont l'existence était précédemment déduite seulement grâce à l'étude de la densité spectrale d'énergie du système. Un autre résultat très enthousiasmant de leur travail est leur caractérisation de l'atmosphère de HD 95086 b en incluant deux nouveaux points photométriques entre 10 et 12 μm, qui confirmerait que l'exoplanète b a une température effective entre 850 et 1 020 K et que son atmosphère aurait une métallicité super-solaire.

Pour les télescopes et instruments à venir, par exemple ceux sur l'ELT, le système HD 95086 est un système de haute priorité à observer, car il est jeune, situé relativement proche du Soleil, dans lequel l'existence d'au moins une autre exoplanète géante est attendue et parce que son architecture rappelle celle de notre Système Solaire.

C.5 Architecture des systèmes ayant des planètes de faible masse à courte période orbitale

C.5.1 Contexte

Un résultat frappant de la mission *Kepler* a été la découverte de nombreuses exoplanètes de faible masse et orbitant autour de leur étoile hôte en moins de 100 jours. Ces exoplanètes de faible masse, souvent appelées super-Terres et mini-Neptunes dû à leur masse et/ou leur rayon, pourraient orbiter autour d'environ 50% des étoiles solaires[13] d'après la méthode de détection des vitesses radiales (Mayor et al., 2011). Cela pourrait également être vrai pour les étoiles de type M, bien que cela soit basé sur des statistiques sur de petits échantillons (Bonfils et al., 2013). Au contraire, la méthode de détection des transits indique une fréquence plus élevée de super-Terres et de mini-Neptunes à courte période orbitale pour les étoiles M que pour les étoiles de type solaire, lorsqu'elles sont comparées à des périodes orbitales similaires (Mulders et al., 2015). Cependant, pour des valeurs d'insolation similaires, l'occurrence des super-Terres et des mini-Neptunes en orbite autour d'étoiles M ou d'étoiles de type solaire est presque égale, dans les limites des incertitudes (Hsu et al., 2019, 2020).

La courte période orbitale de nombreuses super-Terres et mini-Neptunes dans les systèmes extrasolaires est une surprise lorsqu'elle est comparée à la position de la Terre et de Neptune dans notre Système Solaire. La formation de ces super-Terres et mini-Neptunes proches de leur étoile hôté reste une question ouverte et donc un sujet de recherche très actif (Haghighipour, 2013; Zhu & Wu, 2018; Bryan et al., 2019; Schlecker et al., 2021; Rosenthal et al., 2022; Bonomo et al., 2023; Zhu, 2023).

D'une part, des planètes de faible masse (super-Terres, mini-Neptunes) avec des courtes périodes orbitales ($\leq$ 100 jours), pourraient se former à peu près à l'emplacement radial où elles ont été détectées. D'autre part, elles pourraient s'être formées plus loin, dans la partie externe du système, puis avoir migré vers l'intérieur. Cette migration pourrait être facilitée ou empêchée par la présence d'une planète géante lointaine.

Ces différents scénarios peuvent être étudiés en étudiant la corrélation (ou non) entre la présence de exoplanètes de faible masse situées à courte période orbitale et celle de exoplanètes géantes situées plus loin dans le système planétaire. Je donne quelques exemples ci-dessous, que j'illustre en Fig. C.15.

Corrélation positive

Une corrélation positive impliquerait que les conditions qui rendent possible la croissance d'une planète géante sont également favorables à la croissance de planètes de faible masse à courte période orbitale (Chiang & Laughlin, 2013; Schlecker et al., 2021), ou alors qu'une planète géante extérieure pourrait favoriser la présence d'une planète intérieure de faible masse.

Par exemple, lors de sa formation, la planète de faible masse pourrait être située dans la partie externe du système, mais plus proche de son étoile hôte que la planète géante. Sa formation serait favorisée par le mécanisme dit de "balayage des résonances séculaires" (voir Nagasawa et al., 2005; Best et al., 2024).

Le balayage des résonances séculaires est lié aux taux de précession apsidal relatif entre la planète géante externe, les embryons et les planétésimaux (Ward et al., 1976; Ward, 1981; Heppenheimer, 1980). Lorsque ces taux coïncident, l'excentricité des embryons et des planétésimaux est fortement excitée, ce qui augmente leur fréquence de rencontre. Le gaz présent dans le disque protoplanétaire diminue les excentricités des embryons et des planétésimaux, provoquant leur rapprochement vers l'étoile hôte. Au fur et à mesure que

[13] Sont ici considérés des systèmes avec une seule étoile, donc sont exclus les systèmes binaires ou multiples.

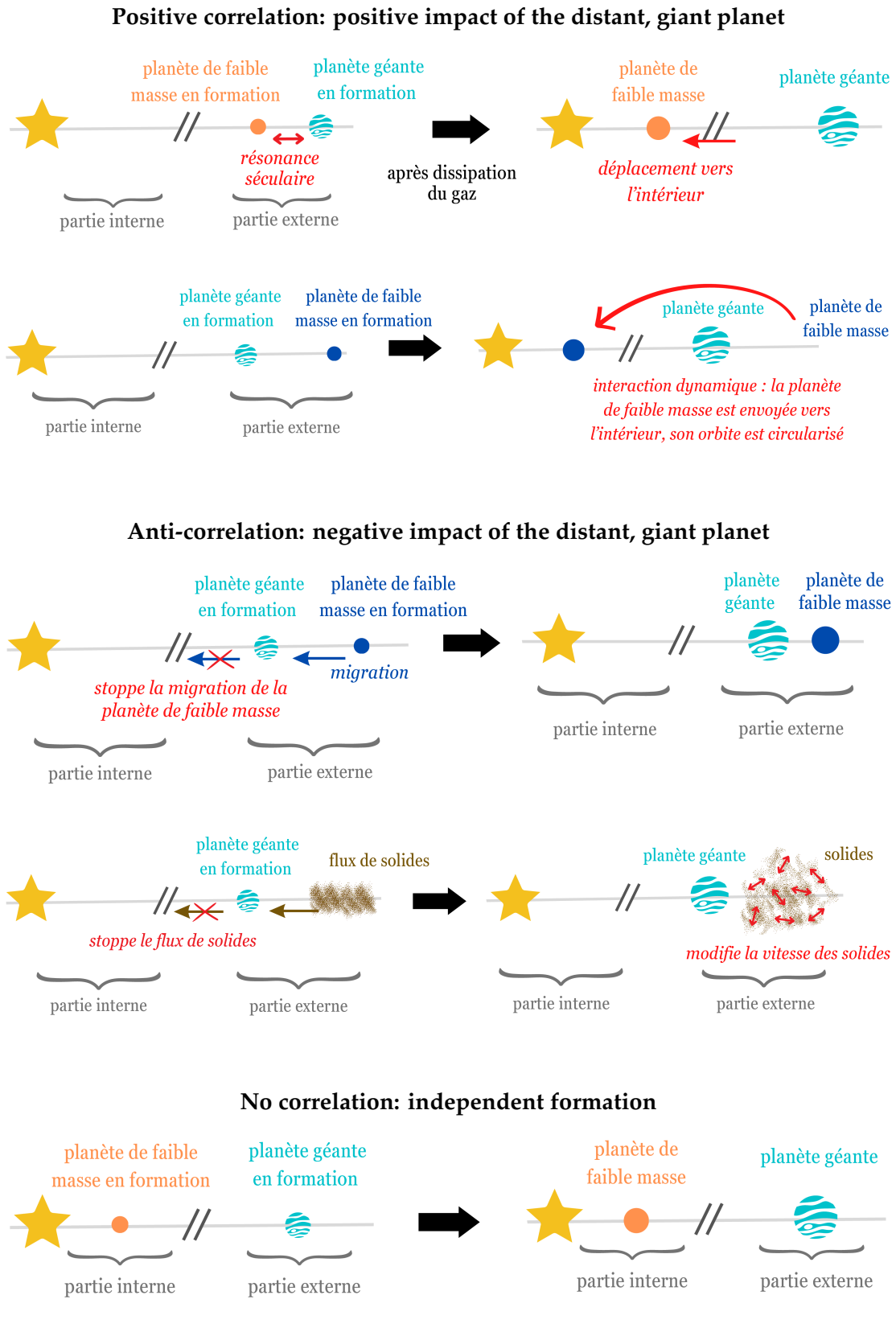

Figure C.15: Exemples de mécanismes de formation et d'évolution de planètes de faible masse situées proches de leur étoile qui pourraient indiquer une corrélation positive (*en haut*), négative (*au milieu*) ou absence de corrélation (*en bas*) entre la présence d'une planète à courte période orbitale et de faible masse (< 95 $M_\oplus$) et une planète géante massive extérieure.

le gaz s'épuise, l'emplacement des résonances séculaires se décale vers l'étoile. In fine, ce processus peut aboutir à la présence de planètes de faible masse orbitant proches de leur étoile hôte (voir Fig. C.15, première ligne).

Dans un autre scénario, la planète de faible masse pourrait se former plus loin que la planète géante, avant d'être envoyée via des interactions dynamiques dans la partie interne du système. Là, son orbite pourrait se circulariser suite aux effets de marée causés par sa proximité avec son étoile hôte (Terquem & Papaloizou, 2007; Kennedy & Kenyon, 2008) ou à cause du gaz dans le disque qui la freinerait (Izidoro et al., 2015), voir la Fig. 5.1 (deuxième ligne).

Corrélation négative

Si les deux planètes se forment dans la partie externe du système, la planète de faible masse étant plus éloignée, sa migration potentielle vers l'étoile hôte pourrait être stoppée par la présence d'une planète géante. Cette planète géante agirait alors comme une barrière (Izidoro et al., 2015), voir Fig. 5.1 (troisième ligne).

Une autre possibilité serait que la planète de faible masse ne se forme jamais, car une planète géante se formant à l'extérieur empêcherait le flux de solides d'aller vers l'intérieur du système, agissant à nouveau comme une barrière (Morbidelli et al., 2016; Izidoro et al., 2021). La planète géante pourrait également impacter la distribution en vitesse des solides, les faisant s'éparpiller (Mustill & Wyatt, 2009), voir la Fig. 5.1 (quatrième ligne).

Absence de corrélation

La présence d'une planète de faible masse à courte période orbitale et d'une planète géante lointaine pourrait être indépendante si les conditions initiales de formation des deux types de planètes ne sont pas corrélées (Schlaufman, 2014). La planète de faible masse pourrait se former dans la partie interne du système, tandis que la planète géante se formerait dans la partie externe (Raymond et al., 2008; Lee et al., 2014), voir Fig. 5.1 (dernière ligne). Cela nécessiterait que le disque protoplanétaire soit initialement très massif, ou bien une augmentation de la densité des solides dans ses régions internes. Ce dernier cas est soutenu par la dérive des objets vers l'intérieur du système lorsqu'il y a encore suffisamment de gaz (Chiang & Laughlin, 2013; Lee et al., 2014; Schlichting, 2014; Hansen & Murray, 2013).

Alternativement, un mixte des mécanismes précédents de formation de planètes (avec un impact positif ou négatif d'une planète géante) pourrait résulter statistiquement en une absence de corrélation entre la présence des deux types de planètes.

Par conséquent, étudier si la présence d'une planète de faible masse à courte période est corrélée à la présence d'une planète géante extérieure pourrait aider à comprendre comment les premières se forment. Comme écrit plus tôt, ceci est particulièrement intéressant, car les planètes de faible masse situées proches de leur étoile sont très nombreuses d'après les études observationnelles se basant sur les méthodes des transits et des vitesses radiales.

C.5.2 Mes résultats principaux

Durant mon doctorat, j'ai étudié la corrélation entre la présence de planètes de faible masse situées proches de leur étoile et de planètes géantes situées plus loin. J'ai étudié cette question avec un nouveau angle, comparé à ce qu'il y avait déjà été effectué d'un point de vue observationnel dans la littérature (Zhu et al., 2018; Bryan et al., 2019; Rosenthal et al., 2022), en sondant les parties externes d'un ensemble de systèmes planétaires avec l'imagerie directe, pour déterminer la présence de planètes géantes ou naines brunes.

Dans l'échantillon que j'ai étudié, les planètes de faible masse et à courte période ont été découvertes grâce à la méthode des vitesses radiales. L'échantillon est composé de 27 systèmes, avec des étoiles hôtes de type spectral G, K ou M et situés dans le voisinage très proche du Système Solaire, à moins de 20 pc, voir Fig. C.16.

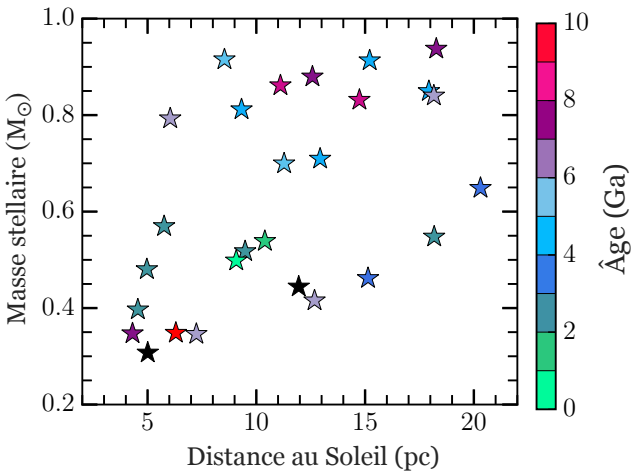

Figure C.16: Masse, distance et âge (en milliard d'années) des 27 étoiles du relevé sur lequel j'ai travaillé.

D'un point de vue méthodologique, j'ai utilisé 94 observations de SPHERE (47 SPHERE/IRDIS et 47 SPHERE/IFS), soit environ 70 heures de temps de télescope. J'ai réalisé un travail conséquent de traitement et analyse de données, en automatisant au maximum et en réalisant une étude la plus homogène possible, et avec l'aide de mes collaborateurs. Ce travail a fait l'objet d'une publication où je suis première autrice dans la revue Astronomie & Astrophysique (Desgrange et al., 2023), ajouté en Section 5.2.5.

J'ai identifié 337 candidats de compagnons liés au système. J'ai déterminé leur statut : objet d'arrière-plan (322/337), artefacts instrumentaux (2/337), compagnons liés (1/337), et quelques détections au statut ambigu (12/337).

En particulier, j'ai détecté la naine brune connue GJ 229 B. J'ai également obtenu une détection prometteuse autour de GJ 832, qui aurait pu être compatible avec l'exoplanète connue GJ 832 b. Cependant, je l'ai finalement classé comme un artefact instrumental, car je ne l'ai pas redétecté dans la nouvelle époque d'observation acquise dans de meilleures conditions d'observation et ayant des meilleures limites de détection.

De plus, j'ai contraint l'architecture de ces systèmes planétaires. Pour les 15 étoiles M de l'échantillon, les observations sont sensibles jusqu'à 3 ou 15 M_{Jup} à 30 ua. Pour les 12 étoiles GK, les performances se dégradent, avec une sensibilité jusqu'à 10 ou 30 M_{Jup} à 30 ua. Nos meilleures limites de détection, valident pour un seul système (GJ 433), permettent d'être sensible jusqu'à un demi-grand axe de 0.3 ua et jusqu'à des masses de 3 M_{Jup}. Les performances en termes de masse sont fortement influencées par l'âge de l'étoile, son type stellaire et sa distance.

En ce qui concerne l'âge, l'échantillon était composé d'étoiles a priori âgées mais néanmoins avec une grosse incertitude sur leur âge (de l'ordre de plusieurs milliards d'années). Un de mes collaborateur a re-déterminé les âges de manière homogène pour notre échantillon d'étoiles, et abouti à des âges stellaires entre 500 Ma et 10 Ga. En imagerie directe, observer des étoiles âgées est généralement à éviter, car les planètes émettent moins thermiquement lorsqu'elles vieillissent. Ainsi, la sensibilité en terme de masse diminue en fonction de l'âge de la planète (et donc de l'étoile hôte) lorsque la planète est observée en émission thermique. Néanmoins, comme un des critères de sélection des étoiles étaient qu'elles aient

au moins une planète de faible masse orbitant proche de leur étoile, cela impliquait que les étoiles soient suffisament stables (peu d'activité stellaire) pour pouvoir détecter ces planètes, et donc, que les étoiles soit âgées. Malgré cet inconvénient inhérent à notre échantillon de systèmes planétaires, les collaborateurs qui ont défini l'échantillon en 2016 lorsque la première demande de temps pour ce projet a été soumise, avaient sélectionné les systèmes les plus proches ($\leq$ 20 pc) du Système Solaire pour essayer de contre-balancer partiellement l'âge élevé.

Avec ce travail, mes collaborateurs et moi-même n'avons pas pu répondre à la question initiale qui a motivé le projet : la présence d'une planète de courte période et de faible masse est-elle corrélée à celle d'une planète géante extérieure ? La raison est que les techniques actuelles d'imagerie directe au sol sont principalement sensibles jusqu'à des compagnons substellaires d'environ 20 M_{Jup} (soit des naines brunes) autour d'étoiles âgées, ce que nous avons pu vérifier. Néanmoins, il s'agit d'un travail de pionnier concernant l'imagerie directe de systèmes planétaires autour d'étoiles très proches ($\leq$ 20 pc), pour la plupart vieilles.

C.5.3 Perspectives

Cette étude pilote ouvrira la voie à de futures observations, par exemple avec *JWST*/MIRI, *RST* et les instruments ELT, sur des cas scientifiques similaires. L'observation dans le rouge infrarouge moyen (par exemple avec les instruments *JWST*/MIRI et ELT/METIS) peut, dans une certaine mesure, atténuer l'impact de l'âge de l'étoile sur les limites de détection en terme de masse planétaire (Matthews et al., 2024). D'autre part, l'observation des exoplanètes en lumière réfléchie (*RST*, ELT/METIS, ELT/PCS) sera une révolution dans le domaine de l'imagerie directe. En effet, la sensibilité ne dépendra plus de l'âge stellaire, mais de la quantité d'irradiation reçue par les exoplanètes et donc de leur distance par rapport à leur étoile hôte. Dans les deux cas, émission thermique ou lumière réfléchie, la clé est d'observer des systèmes très proches du Système Solaire, pour maximiser la sensibilité des observations et pour sonder des demi-grand axes relativement petits.

C.6 Conclusion et perspectives

Au cours de mon doctorat, j'ai étudié les architectures des systèmes planétaires grâce à l'imagerie à haut contraste. En particulier, j'ai utilisé l'imagerie directe pour étudier la présence d'exoplanètes et de disques de débris circumstellaires et les caractériser. Ce sont tous les deux des produits de la formation planétaire. Les disques de débris circumstellaires sont des disques de seconde génération, générés par la cascade collisionnelle entre les planétésimaux. Je me suis particulièrement intéressée à la diversité des architectures des systèmes planétaires et à ce qu'elle peut nous apprendre sur la formation et l'évolution des systèmes planétaires.

En pratique, j'ai mené des études spécifiques sur de jeunes systèmes connus pour abriter des disques de débris ou au moins une exoplanète, afin de les caractériser. J'ai également travaillé sur un relevé de systèmes planétaires, afin de disposer d'un échantillon plus large pour obtenir des résultats statistiques. Ces projets de recherche m'ont permis de comprendre à quel point les percées en astrophysique dépendent des progrès en matière d'instrumentation et du traitement de données. Pendant la première moitié de mon doctorat, j'ai également contribué à étudier comment les performances de SPHERE pouvaient être améliorées pour accroître sa sensibilité et ses capacités de caractérisation, en ajoutant un spectrographe à champ intégral de moyenne résolution.

En plus de détails, j'ai mené une analyse approfondie sur un jeune système (HD 95086) avec une planète géante découverte en imagerie directe, mais dont son disque de débris est actuellement indétectable en lumière diffusée. J'ai aussi caractérisé un autre système (HD 120326), qui a un disque de débris clairement détecté en lumière diffuse et potentiellement sculpté par une ou plusieurs planètes qui restent à découvrir. En ce qui concerne HD 120326, dans Desgrange et al. (2025, subm.), j'ai combiné des données panchromatiques (*HST*/STIS, VLT/SPHERE et ALMA soit du visible au millimétrique) pour contraindre les populations de poussières de 30 à 1 000 ua. En modélisant de manière cohérente les données SPHERE en intensité totale et polarisée, j'ai déterminé la fonction de phase de diffusion de la ceinture interne (identifiée comme une ceinture de planétésimaux grâce aux données ALMA) et sa fraction maximale de polarisation à 1.6 μm, ainsi que sa réflectance entre 1.0 et 1.8 μm. En traitant à nouveau les données STIS (0.2–1.0 μm), j'ai également mieux mis en évidence la morphologie asymétrique et très étendue de la structure de poussières, qui ressemble à une spirale. Bien que les spirales soient fréquemment observées dans les simulations numériques impliquant des planètes géantes situées à large distance de leur étoile (≥ 10 ua), elles sont jusqu'à présent rarement observées dans les disques de débris. En particulier, HD 120326 est le seul système à présenter cette structure de poussières en forme de spirale s'étendant sur une aussi grande distance, des centaines d'unités astronomiques et jusqu'à 1 000 ua si elle est coplanaire avec la ceinture interne.

D'autre part, le système HD 95086 peut être considéré comme un système analogue au Système Solaire, en version jeune et plus massif. HD 95086 a une planète géante de 4–5 M_{Jup} (Rameau et al., 2013) située dans la cavité entre les deux ceintures de débris. Dans Desgrange et al. (2022a), j'ai analysé dix époques d'observation acquises dans le cadre du temps garanti du consortium SPHERE. J'ai extrait le spectre de l'exoplanète géante HD 95086 b pour la première fois entre 1.0 et 1.6 μm, ainsi que son astrométrie relative à de nouvelles époques. Avec mes collaborateurs, j'ai étudié l'atmosphère de l'exoplanète HD 95086 b, déterminé que la poussière doit être présente soit dans les couches supérieures de l'atmosphère, ce qui donnerait une température effective de l'exoplanète HD 95086 b de 800–1300 K, soit autour dans un disque circumplanétaire, ce qui s'accompagnerait d'une température effective plus élevée ($\geq 1\,400$ K). De nouvelles données sondant les longueurs d'onde de l'infrarouge moyen avec *JWST*/MIRI ont permis de discriminer ces deux options (Mâlin et al., 2024). De plus, mes collaborateurs et moi avons confirmé que l'orbite de HD 95086 b a une faible excentricité (< 0.18 à 1σ), et même qu'elle est probablement circulaire. Sur la base d'arguments dynamiques, cela impliquerait qu'au moins une autre exoplanète serait nécessaire pour maintenir la largeur de la cavité.

En outre, j'ai étudié comment les planètes de faible masse orbitant à proximité de leur étoile hôte pouvaient se former et en particulier si cela était corrélé à la présence de compagnons extérieurs massifs. Pour chercher de tels compagnons massifs externes, j'ai travaillé sur un relevé en imagerie directe avec SPHERE constitué de vingt-sept étoiles GKM très proches du Soleil(≤ 20 pc) connues pour abriter des planètes de faible masse (≤ 95 $M_\oplus$) à courte distance de leur étoile (≤ 1 ua). J'ai montré qu'une telle étude sur des étoiles matures (500 Ma–10 Ga) est un défi, car même si la sensibilité en contraste est très bonne (10^{-5}–10^{-6}), la conversion en masse planétaire se dégrade rapidement dès que l'âge du système dépasse 500 Ma.

Sur ce point-là, l'imagerie directe d'exoplanètes en lumière réfléchie (voir les essais avec SPHERE/ZIMPOL par Tschudi et al., 2024) changerait la donne comparée à leur imagerie en émission thermique, car l'âge stellaire ne serait plus une contrainte. Alternativement, les observations dans l'infrarouge moyen atténuent l'impact de l'âge stellaire (voir la découverte récente en imagerie directe d'une super-Jupiter âgée grâce à des données *JWST*/MIRI de Matthews et al., 2024).

Enfin, j'ai contribué au développement des futurs cas scientifiques de l'amélioration de l'instrument SPHERE en SPHERE+, dont la première lumière est prévue en 2026. J'ai travaillé sur les performances d'un nouveau potentiel spectrographe à champ intrégral de moyenne résolution, appelé MedRes. MedRes n'a finalement pas été approuvé par l'ESO. MedRes était censé exploiter les meilleures performances du système d'optique adaptative SAXO bientôt mis à jour en SAXO+, pour détecter et caractériser des exoplanètes de la masse de Jupiter situées plus proches de leur étoile hôte, et avec un peu de chance, de nouvelles protoplanètes analogues aux protoplanètes emblématiques PDS 70 b et c.

Concrètement, j'ai participé au projet SPHERE+ en étudiant comment dans le dimensionnement de MedRes, la résolution spectrale et bande spectrale utilisées pouvaient être optimisées pour détecter et caractériser des exoplanètes. La technique de traitement de données en jeu est la cartographie moléculaire, en utilisant la corrélation croisée entre des spectres de modèles d'atmosphères planétaires et les spectres observés. J'ai effectué des simulations de cartographie moléculaire et j'ai mis au point un cadre permettant de les exécuter plus efficacement afin de tester différentes scènes astrophysiques (par exemple, une exoplanète de type L ou de type T, avec différentes valeurs de contraste et différents emplacements possibles dans le champ de vision) et différentes configurations instrumentales (par exemple, différentes couvertures spectrales, avec différentes résolutions spectrales possibles), qui auraient contribué à la conception de l'instrument MedRes. La cartographie moléculaire est une technique prometteuse pour détecter et caractériser les exoplanètes, et il y a de hautes attentes concernant ses résultats pour des observations avec l'instrument spatial *JWST*/MIRI (Patapis et al., 2022; Mâlin et al., 2023) et les instruments terrestres à venir (ELT/HARMONI, Houllé et al., 2021; Bidot et al., 2024, mais aussi avec ELT/METIS et ELT/PCS).

Il existe un lien étroit entre l'amélioration de SPHERE en SPHERE+ et les instruments de l'ELT, tant sur le plan instrumental qu'astrophysique. Tout d'abord, l'amélioration de SAXO en SAXO+ (qui consiste à ajouter un second étage d'optique adaptative) est une démonstration technologique pour le spectro-imageur à haut contraste de deuxième génération PCS (2035+) sur l'ELT. PCS a pour but de photographier en lumière réfléchie des planètes rocheuses qui pourraient être habitables autour d'étoiles de faible masse très proches du Soleil. Deuxièmement, SPHERE pourrait être utilisé comme une machine de relevé, pour sélectionner les étoiles les plus prometteuses qui seront ensuite observées avec les instruments de l'ELT, qui seront extrêmement compétitifs.

Dans cette perspective, les études sur l'architecture des systèmes planétaires situés dans le voisinage très proche du Système Solaire, comme mon étude pilote Desgrange et al. (2023), sont une étape préliminaire essentielle. Troisièmement, SPHERE+ permettra d'observer des étoiles moins lumineuses et plus rouges, et donc d'accéder ainsi à l'essentiel des étoiles dans les régions de formation stellaire, telles que le Taureau, le Camaléon, le Loup et le Haut-Scorpion. La formation des planètes pourrait donc être étudiée de manière plus approfondie avec moins de biais d'observation et dans différentes associations stellaires. Quatrièmement, dans les conditions d'observation médianes au VLT, SPHERE+ fonctionnerait avec une correction optimale de son système d'optique adaptative, ce qui n'est pas le cas actuellement où les conditions doivent être meilleures que médianes pour que SPHERE fonctionne optimalement.

Grâce à ces projets de recherche, j'ai développé mes compétences d'observatrice, dans le traitement de données de spectro-imageurs et de leur analyse dans le contexte de la formation et de l'évolution planétaire. J'ai utilisé des données d'archives, mais aussi de nouvelles observations. Cela m'a logiquement conduit à soumettre des propositions pour demander du temps d'observation en utilisant diverses infrastructures astronomiques pour tester les modèles théoriques sur la formation et l'évolution planétaire, mais aussi pour explorer des systèmes planétaires intrigants.

Au MPIA, je suis également devenue membre du consortium SHARK-NIR, composé principalement de trois instituts : INAF Padova (l'institut PI, Italie), MPIA (Heidelberg, Allemagne) et l'Observatoire Steward (Arizona, États-Unis). L'instrument SHARK-NIR est un nouvel imageur à haut contraste dans le proche infrarouge situé au LBT, en Arizona. Il a terminé sa phase de mise en service au printemps 2023, sa phase de vérification scientifique au début de 2024 et se trouve actuellement dans sa phase scientifique initiale. Au MPIA, j'ai été chargé de définir la liste des étoiles à observer pour la phase de vérification scientifique, qui correspond à deux périodes d'observation en octobre 2023 et décembre 2023/janvier 2024. J'ai ensuite été chargée de rédiger et de soumettre les demandes de temps SHARK-NIR intra-MPIA afin d'obtenir du temps pour exploiter l'instrument, tandis que les collègues à l'INAF Padova et à l'Observatoire Steward faisaient de même pour leurs appels LBT spécifiques. Pour information complémentaire, le MPIA a droit à une dizaine de nuits au LBT durant chaque semestre. Ces nuits sont réparties entre les trois départements de l'institut.

Dans ce contexte, j'ai obtenu en tant que PI des données SHARK-NIR et LMIRCam sur des systèmes connus pour héberger des disques protoplanétaires ou de débris. J'attends les observations de cinq autres étoiles entre octobre 2024 et janvier 2025. Néanmoins, les conditions météorologiques au LBT ne sont malheureusement pas aussi bonnes que celles à l'Observatoire de Paranal où se trouve le VLT, ce qui entraîne des pertes de temps importantes dues au mauvais temps et parfois aussi à cause de problèmes techniques. Seule une fraction d'environ $30\,\%$ de mes observations en 2024B a pu être réalisée.

J'ai également soumis des demandes de temps pour d'autres infrastructures, telles que le VLT/SPHERE, *HST*/STIS, *JWST*/MIRI, *JWST*/NIRCam, et *JWST*/NIRISS. Celles qui ont été acceptées sont listées dans l'annexe B. Ces demandes de temps concernent principalement des systèmes jeunes (≤ 100 Ma), mais pas seulement, avec pour but d'étudier leur architecture et comment leur architecture aide à contraindre la formation et l'évolution des systèmes planétaires.

D'autre part, retracer l'histoire d'un système planétaire âgé en contraignant son architecture m'enthousiasme particulièrement. Par conséquent, je suis très heureuse que ma demande de temps SPHERE sur un système planétaire emblématique et âgé, situé très proche du Soleil, ait été acceptée. Ce système héberge une exoplanète de la masse de Neptune sur une orbite excentrique et désalignée de période de trois jours. L'exoplanète subit une forte évaporation Lyα en raison de sa proximité avec son étoile hôte. Ceci est surprenant, car le système est âgé de 6 ± 2 Ga, donc l'atmosphère de l'exoplanète aurait déjà dû s'échapper et son orbite être circularisée. Le paradoxe peut être résolu si l'exoplanète a migré récemment vers son étoile en raison d'une résonance de Kozai-Lidov avec un compagnon extérieur, qui pourrait être soit une exoplanète massive, soit une naine brune. Un tel scénario de migration à haute excentricité peut naturellement expliquer la population de mini-Neptunes excentriques, désalignées, fortement irradiées et dont l'atmosphère ne s'est pas encore évaporée (Nagasawa & Ida, 2011).

Le système pour lequel j'ai obtenu du temps d'observation avec SPHERE est le plus idéal pour obtenir des preuves observationnelles de ce mécanisme de migration à haute excentricité, parce que le système est très proche de notre Système Solaire, que l'étoile hôte est de faible masse (type spectal M) et que les prédictions théoriques concernant les propriétés du compagnon extérieur indiqueraient un compagnon que l'on pourrait détecter avec SPHERE. Confirmer observationnellement le mécanisme de migration à haute excentricité dans ce système idéal motiverait une étude sur un relevé de systèmes planétaires plus large, ayant également des exoplanètes de la masse de Neptune étant excentriques, désalignées, fortement irradiées, avec une atmosphère non évaporée.

Les observations au sol que j'ai obtenues en tant que PI et avec mes collaborateurs auront la sensibilité nécessaire pour obtenir une image du compagnon s'il s'agit d'une naine

brune. S'il s'agit d'une exoplanète géante, des observations spatiales *JWST*/MIRI seraient nécessaires pour la détecter. J'ai déjà soumis deux demandes de temps *JWST*/MIRI pour observer ce système, et malgré un classement élevé (second puis premier quintile au *JWST* Cycle 2 et 3), elles n'ont pas été acceptées en raison d'un facteur de pression élevé, mais je vais continuer à perséverer.

Concernant un autre système âgé, ayant également une étoile de type M, j'ai hâte d'obtenir les observations *JWST*/MIRI qu'Elisabeth Matthews (PI), moi-même (co-PI) et d'autres collaborateurs (coI) reliés au MPIA obtiendront début 2025. Ces observations ont pour but de détecter le compagnon massif (2–20 M_{Jup}) GJ 179 c, qui est prédit d'après un signal long-terme dans les vitesses radiales et une anomalie de mouvement propre d'après les données *Gaia* et *Hipparcos*. Cette détection ouvrira la voie à une caractérisation détaillée d'une atmosphère froide (≤ 450 K), comblant ainsi le fossé entre les exoplanètes géantes connues à ce jour et les planètes géantes de notre Système Solaire.

Dans l'ensemble, je pense que les astronomes travaillant dans le domaine des exoplanètes et des disques vivent une période particulièrement passionnante, avec d'excellents télescopes et instruments au sol et dans l'espace. L'avenir est même encore plus radieux, avec les améliorations instrumentales (VLT/SPHERE+, VLTI/GRAVITY+) et futurs télescopes à venir (*RST*, ELT, *HWO*, ...), toujours plus performants. La synergie entre les différentes infrastructures observationelles et les méthodes de détection et caractérisation des exoplanètes ne cesse de croître, pour caractériser un système planétaire donné, mais aussi une exoplanète donnée. Les deux prochaines (et dernières) diffusions massives des données analysées de la mission *Gaia* iront dans ce sens, avec la découverte attendue de nombreuses exoplanètes géantes situées à quelques unités astronomiques de leur étoile.

De plus, l'utilisation de données panchromatiques fournit des informations précieuses sur les propriétés atmosphériques des exoplanètes, mais aussi sur les disques protoplanétaires et de débris, en sondant différents tailles de grains situés dans différentes régions du disque. Cela permet d'affiner nos théories sur la formation et l'évolution planétaire, et nous donne des indices sur l'aspect que pourraient avoir d'autres mondes.

À partir du 15 novembre 2024, je poursuivrai ma recherche en post-doctorat en tant que Fellow à l'Observatoire Austral Européen (European Southern Observatory ; ESO) pendant quatre ans. Les trois premières années seront basées au Chili et la moitié de mon temps sera consacrée à des tâches d'observation, l'autre moitié à ma recherche. La dernière année sera entièrement dédiée à ma recherche, dans un institut de mon choix.

Dans le cadre de mes tâches d'observation, j'observerai 80 nuits par an pendant trois ans pour la communauté astronomique en utilisant le télescope UT3 (Unit Telescope 3) du VLT à l'observatoire Paranal situé dans le désert d'Atacama. Le télescope UT3 est équipé des instruments de pointe SPHERE, que je connais bien, CRIRES et X-SHOOTER.

Je serai dans une position idéale pour m'investir également dans les instruments de l'ESO que je n'ai pas encore exploités, mais que j'aimerais utiliser, comme ERIS sur le VLT, GRAVITY et MATISSE sur le VLTI. Cette expérience passionnante se déroulera pendant les améliorations de GRAVITY+ au VLTI et de SPHERE+ au VLT, ainsi que lorsque la construction de l'Extremely Large Telescope, le plus grand oeil sur le ciel, sera achevée.